2
MIT

NASA CR-66852

ATTITUDE-REFERENCED RADIOMETER STUDY
Volume I
ATTITUDE DETERMINATION SYSTEM DESIGN

August 1969

Prepared under Contract No. NAS 1-8801 by

HONEYWELL INC.
Aerospace Division
Minneapolis, Minnesota

for

NATIONAL AERONAUTICS AND SPACE ADMINISTRATION

NASA CR-66852

ATTITUDE-REFERENCED RADIOMETER STUDY

VOLUME I

ATTITUDE DETERMINATION SYSTEM DESIGN

by

N.W. Tidwell
G.D. Nelson
W.J. Lewis

VOL. 2 - NAS 1-8801
CR-66855 — N70-17760

Distribution of this report is provided in the interest of information exchange. Responsibility for the contents resides in the author or organization that prepared it.

August 1969

Prepared under Contract No. NAS 1-8801 by

Honeywell Inc.
Aerospace Division
Minneapolis, Minnesota

for

National Aeronautics and Space Administration

NASA CR-66852

ATTITUDE-REFERENCED RADIOMETER STUDY

VOLUME I

ATTITUDE DETERMINATION SYSTEM DESIGN

by

N.W. Tidwell
G.D. Nelson
W.J. Lewis

August 1969

Prepared under Contract No. NAS 1-8801 by

Honeywell Inc.
Aerospace Division
Minneapolis, Minnesota

for

National Aeronautics and Space Administration

FOREWORD

This report documents Part I of a two-part Attitude-Referenced Radiometer Study (ARRS) performed under National Aeronautics and Space Administration contract No. NAS 1-8801 for Langley Research Center.

A previous analytical and design study under contract No. NAS 1-6010 indicated the feasibility of the measurement package and identified critical design and development problems. Having previously established the feasibility of the radiometric measurement package, this study provided advancement of techniques for the design and fabrication of precision radiometric and attitude determination systems for use in an earth-orbiting spacecraft. The effort was devoted to solving the critical design and development problems in Part I. Design requirements and conceptual design of the systems, based on analytical analyses, are established and reported within this study effort.

The contractual effort was divided into three major tasks:

1. Radiometric system design
2. Attitude-referenced radiometer system integration
3. Attitude determination system design

Honeywell Inc., Aerospace Division, performed this study program under the technical direction of Mr. J. C. Bates. The Part I effort was conducted from 1 January 1969 to 10 October 1969.

Gratitude is extended to NASA Langley Research Center for their technical guidance, under the program technical direction of Messrs. A. Jalink and J.A. Dodgen, with direct assistance from Messrs. D. Hesketh, D. Hinton, W.C. Hodge, and H. J. Curfman Jr., as well as the many people within their organization.

PRECEDING PAGE BLANK NOT FILMED.

CONTENTS

LIST OF ILLUSTRATIONS

Figure

Figure		Page

Figure		Page
57	Nominal Case - Attitude Errors after Convergence	126
58	Nominal Case - Attitude Errors after Convergence over Five Spin Periods	126
59	Nominal Case - Rate and Attitude Errors after Convergence over One Spin Period	127
60	Nominal Case - Behavior of the Diagonal Elements of the Covariance Matrix with Reduced Number of Sightings	129
61	Nominal Case - Convergence over One Spin Period with Reduced Number of Sightings	130
62	Nominal Case - Convergence over 10 Spin Periods with Reduced Number of Sightings	131
63	Nominal Case - Attitude Errors as a Function of Instrument Noise	133
64	Attitude Errors as a Function of Instrument Noise Uncertainty	135
65	Rate Errors as a Function of Instrument Noise Uncertainty	135
66	Inertia Ratio and Pitch Error with Inertia Ratio Estimation Initiated at $t = 0$	136
67	Rate and Attitude Errors with Inertia Ratio Estimation Initiated at $t = 550$ sec ($Q_{77} - Q_{88} = 10^{-7}$ $\Delta A = 0.01$)	137
68	Inertia Ratio Error and Covariance Behavior and Inertia Ratio Estimation initiated at $t = 550$ sec ($Q_{77} = Q_{88} = 10^{-7}$, $\Delta A = 0.01$)	138
69	Rate and Attitude Errors with Inertia Ratio Estimation Initiated at $t = 550$ sec ($Q_{77} = Q_{88} = 10^{-9}$, ΔA=0.01)	139
70	Inertia Ratio Error and Covariance Behavior with Inertia Ratio Estimation Initiated at $t = 550$ sec ($Q_{77} = Q_{88} = 10^{-9}$, $\Delta A = 0.01$)	140
71	Rate and Attitude Error with Inertia Ratio Estimation Initiated at $t = 550$ sec ($Q_{77} = Q_{88} = 10^{-9}$, ($\Delta A = 0.025$)	142

Figure		Page
72	Inertia Ratio Error and Covariance Behavior with Inertia Ratio Estimation Initiated at t = 550 sec ($Q_{77} = Q_{88} = 10^{-9}$, $\Delta A = 0.025$)	143
73	Attitude Errors as a Function of Eddy Current Coefficient	144
74	Vehicle Rate and Attitude Errors - 12 Variable Estimation State	146
75	Inertia Ratio, Eddy Current Coefficient - 12 Variable Estimation State	147
76	Magentic Moment Estimation - 12 Variable Estimation State	148
77	Yaw Error as a Function of Integration Time Step for Second, Third, and Fourth Order Runge-Kutta	149
78	Pitch Error as a Function of Integration Time Step for Second, Third, and Fourth Order Runge-Kutta	149
79	Comparison of Yaw Errors for Different Torque Models and Number of Sightings as a Function of Instrument Noise	151
80	Comparison of Roll Errors for Different Torque Models and Number of Sightings as a Function of Instrument Noise	152
81	Comparison of Pitch Errors for Different Torque Models and Number of Sightings as a Function of Instrument Noise	153
82	Sensitivity of Yaw Errors to Additive Noise	154
83	Sensitivity of Roll Errors to Additive Noise	155
84	Sensitivity of Pitch Errors to Additive Noise	155
85	Comparison of Yaw Errors for Different Values of Additive Noise	157
86	Comparison of Roll Errors for Different Values of Additive Noise	158
87	Comparison of Pitch Errors for Different Values of Additive Noise	158

Figure		Page

LIST OF TABLES

ATTITUDE-REFERENCED RADIOMETER STUDY
VOLUME I: ATTITUDE DETERMINATION SYSTEM DESIGN

by: N. W. Tidwell, G. D. Nelson, and W. J. Lewis, Honeywell Inc.

SUMMARY

This volume presents the attitude determination system design consisting of the conceptual design of the celestial sensor system and the development of an operational data-reduction program to provide for continuous spacecraft attitude knowledge to 30 arc sec in pitch and 150 arc sec in roll and yaw. The conceptual design of the sensing system used tradeoffs and computer analysis to define sensor parameters, to determine performance, and to define mechanization that could lead to a complete set of attitude determination hardware purchase specifications for the ARRS experiment. Development of an operational data-reduction program was concerned with constructing a computer program that operates on the celestial sensor output and a complete simulation of the attitude determination system to determine the data requirements and the performance of attitude estimation for several system parameter variations. Analysis and interpretations of the study results are presented.

The requirement for continuous attitude knowledge is defined to be the attitude of the spacecraft experiment axes at any time in orbit. With the greater part of the orbit being spent in the daylight, baffling of the star sensor becomes important to permit detection of a sufficient number of targets. In general, the better that the baffle reduces stray light, the greater the probability of detection of dim stars. However, practical limitations in baffle design to reduce stray light led to the combined ARRS attitude determination approach of (1) designing a baffle within practical volume size and stray light rejection ability, (2) using the sun as a target for updating the spacecraft attitude, and (3) providing an accurate model of the spacecraft dynamics to permit greater time spans of attitude extrapolation to maintain attitude knowledge for sparse celestial observations. The ARRS attitude determination system concept consists of a starmapper, sun sensor, and on-board digital electronics which transform sensor output into target transit times. An operational constraint of 60,000 bits per orbit of on-board storage for target transit times required digital processing to discriminate transit time from noise.

The discriminated celestial data are transmitted to ground for editing, celestial target identification, and subsequent attitude estimation data processing. Based on a continuous one-year mission, ground data processing required that data be processed sufficiently rapid to prevent backlogging of raw data. In pursuing the ARRS attitude determination concept, Part I concentrated on (1) the accurate modeling of the spacecraft dynamics which involves modeling of environmental torques and involves modeling such that efficient numerical propogation of spacecraft state is realized, (2) the development of an operational quasi-real-time attitude determination program and the simulation of the attitude determination system to establish design parameters and celestial data requirements, (3) the design of the celestial sensor to determine the optical transfer function, minimum baffle volume for daylight operation in

relation to the sensor aperture size, field of view, and star magnitude, and the method of onboard data processing to minimize noise data stored.

TORQUE MODELING

Five torques were modeled and investigated for effect on spacecraft attitude propogation with time. The torques modeled are due to the spacecraft residual magnetic moments, induced eddy currents, aerodynamic pressure, solar pressure, and gravity gradient. Using the five torques as a basis for the total torque environment, results showed that solar pressure, eddy current, and residual magnetic moment torques were required in the extrapolation model for long-term prediction of 45 minutes. Gravity gradient can be significant, depending on the spacecraft inertia distribution relative to local vertical. Accurate attitude extrapolation for 3 minutes may be obtained by including just the torques due to the eddy currents and residual magnetic moment.

Simplification of the models was desired to reduce running time on the computer. Results of torque plots showed that cyclic torques were present that appeared to have zero mean value. A time average of the torque models over the spacecraft spin period is suggested. Because the torque models are functions of parameters, the parameters must be estimated by the attitude determination programs. To reduce the number of parameters estimated is to reduce the running time of the estimation program. It is advantageous, then, to use only those torques and parameters within the torque models that have a significant effect on the attitude propagation. The state propagation accuracy required during the daylight portion is predicated on the availability of celestial observations. The torque models used must be selected on this basis.

SPACECRAFT MODELING

The modeling of the propogation equation for the spacecraft state incorporating the residual magnetic moment, eddy current, and gravity gradient torques was accomplished to improve the numerical evaluation speed. The equations were written in an angular momentum frame with the knowledge that the angular momentum frame is slowly moving due to small torques. Time averaging of the torques by means of perturbation techniques yielded a set of "simplified equations of motion" that are accurate to 1 arc sec in 800 sec of time. This set of equations is shown to be simple functions of time (constants ramps). The solutions accuracy becomes relatively independent of step size and suggests improvement in numerical propogation of state to desired time points.

ATTITUDE DETERMINATION ALGORITHM

An attitude determination data-reduction program was developed and exercised. The data-reduction program executed 10 to 20 times faster than real time on the CDC 6600 computer using the nonsimplified equations with a 0.5 sec time stop in the integration. This is an acceptable execution time; however, further improvement is obtained using the developed "simplified equation of motion"

The performance analysis demonstrated that three celestial targets per revolution of the spacecraft are sufficient to obtain a 10-arc-sec attitude estimate, and two observations per revolution are sufficient to maintain the estimate. These results were obtained with only the use of the residual magnetic moment and eddy current torque being used in the algorithm.

The inertia ratio and eddy current torque parameters were estimated correctly, but the residual magnetic moment's parameter appeared to be unobservable. The lack of observatility is due to the minor effect of the torque over one revolution of the vehicle. For operation in the daylight portion of the orbit, two observations per revolution are obtainable from the sun and one star. The baffle must be capable of detecting one star per revolution of the spacecraft or, depending on the vehicle dynamic model exactness, must occasionally detect one star. Additional investigation of the occasional star detection on attitude estimation is warranted.

STARMAPPER PARAMETERS

An analysis was conducted to determine the starmapper parameters required to detect one star and two stars per revolution on the daylight portion of the orbit. The second brightest star per spacecraft scan during the sunlit orbit over the entire celestial sphere (to account for full seasonal usage of the starmapper) has a magnitude of 3.4 (visual). This is fainter than the limiting magnitude star required to detect six stars per scan over the nighttime portion of the orbit. This is principally accounted for by the reduction in the scanned area of sky, related in turn to the closest permissible angular approach of the optical axis to either the sun or the sunlit earth.

A second major consideration which relates to the magnitudes of daylight detected stars is the physical dimensioning of the light baffle. Parameter studies were predicated on a minimum baffle volume criterion. A computer-automated program was subsequently designed to select an optimum set of starmapper parameters. These are

- Baffle diameter 10 in.
- Baffle height 14 in.
- FOV 15°

- Cant angle 100° (from positive--spin axis)
- Closest approach to bright object 46°
- Limiting nighttime magnitude 3.2 (visual)
- Limiting daytime magnitude 3.4 (visual)
- Clear aperture 2.2 in.

Use of the starmapper over less than 100% of the daytime orbit permits detection of brighter stars. The clear aperture indicated can be realized with the baseline aperture diameter of 3.18 in. and a central obscuration of 2.3 in. The 15° fov is reduced over the 20° field considered as baseline. This will permit a physically smaller sensor package.

OPTICAL TRANSFER FUNCTION

The concentric catadioptric optical system was selected for the ARRS application over a candidate refractive system principally because of the optical system providing superior image quality (blur spot symmetry) for all filled angles. The availability of the EMR 531N miniature photomultiplier tube made packaging of the detector on the optical axis a practical matter. The concentric system is less complex, has fewer elements, has no cemented interfaces, is physically smaller, and in every other aspect is superior to the refractive optical system.

Light-gathering properties of the concentric system are superior to those of the refractive system. This is evident from the fact that an AO star of magnitude 0.0, detected by the concentric system, is an equivalent magnitude of 1.6 for the refractive system, on axis. In addition, loss of sensitivity equivalent to 0.7 magnitude results for 10° off-axis conditions.

The ARRS optical system produces star images for all field angles having blur spot diameters of 12 arc sec at the design wavelength of 0.405 μ, 100% of the star energy is contained within a 60-arc-sec spot diameter. In addition, the spot configuration is extremely symmetrical and, therefore, contributes negligibly to the overall star transit time error.

The optical system was evaluated for performance at low operating temperature (-75° C) and in vacuum. The change in blur spot diameter due to both effects is less than 5 arc sec, and is, therefore, considered as no cause for concern.

The concentric optical system is ideally suited for the sun-sensor application. Two requirements - the wide for (40°) and accuracy (10 arc sec) - are difficult requirements for conventional sun sensors to meet. The ARRS sun sensor optical system requirements are met using a two-element optical system, having a 1.37-in. aperture size using two V-shaped deposited silicon "slit" detectors, each 60 arc sec projected width. Use of narrow-band filters and antireflection coatings deposited on the optical elements is utilized to attenuate the incoming solar energy to the level required by the detector.

CATHODE PROTECTION

Inadvertent scanning of the sun by the optical system will result in a temperature rise of the cathode. However, the rise will not reach a level sufficient to induce degrading or damaging effects to the cathode material. A wide factor of safety exists, due a large degree to the improved semitransparent bi-alkali (N) cathode used, which permits a maximum ambient cathode temperature of 150°C.

Operation of the photomultiplier during an inadvertent scan of the sun or a scanning of the illuminated earth will cause excessive current flow from the detector beyond the maximum operational limits. To avoid this condition, the voltage between the cathode and second dynode will be switched in polarity (grounding the dynode), which reverses the normal acceleration of electrons from the cathode. This method has the advantage that relatively low voltage is switched.

Switching of the photomultiplier voltage does not protect the cathode from bright source exposure. However, the resultant agitation within the cathode material for the ARRS application will not increase the dark current to a level which might cause detection difficulties. The rise in dark current resulting from an inoperative starmapper scan of the illuminated earth will permit detection of fourth magnitude stars immediately following the bright source portion of the scan. This condition precludes the necessity of a shutter mechanism which would have to be actuated on each scan.

The recommended cathode protection method will use a fail-open (fail-safe) mechanical shutter (to be actuated only in the event of prolonged focused solar radiation). In addition, the photomultiplier will be switched off whenever the radiation level exceeds a pre-set level such as that occurring when the bright earth or moon is scanned by the starmapper fov.

ERROR ANALYSIS

The ability to interpolate the threshold crossing of a pulse can be accomplished to within 1 part in 13 for pulse rise and 1 part in 18 for pulse fall. The resultent 1 sigma error in determining pulse center (transit time) is, therefore, 3.2 arc sec. The encoding error is assumed to be 1 arc sec. No blur spot asymmetry is contributed. The total rms error expected is about 3.5 arc sec.

CELESTIAL SENSOR LOGIC

The triplet selection criterion in conjunction with a CPU (small onboard computer) appears to represent not only the optimum approach to on-board data processing but perhaps the only practical method. It is apparent that the triplet selection criterion, due to its smaller window, will transmit fewer noise pulses to storage by a factor of 10. Use of a CPU on-board makes possible the processing of at least six sequential transits before deciding on the legitimacy of a pulse. This would be prohibitively complex in practice if hardwired logic were used.

INTRODUCTION

With the advent of earth orbiting spacecraft, earth resources' detection, military surveillance, and meteorology research have brought into sharp focus the need for infrared measurement research and detection techniques. An essential part of infrared measurement experimentation and detection techniques is the determination of the experiment axes attitude and in turn the experiment's line of sight at the time of the experiment measurement. In the evolution of infrared research and implementation, the growing complexity of the missions has demanded greater precision attitude determination. Many missions are presently demanding a continuous time history of the experiment's pointing direction to 1 to 30 arc seconds for periods of one year or more. To meet these requirements, long life attitude measurement instrumentation and sophisticated and efficient data reduction techniques are being developed.

A number of significant programs were conducted that required and led to greater precision attitude determination systems. These programs include the NASA D-61 program and the Air Force Infrared Atmospheric Transmission Evaluation Program (IRATE). NASA also conducted experiments on the X-15 vehicle, and most recently the suborbital Scanner probe was successfully flown. All of the above experiments required attitude determination for experiment line-of-sight referencing. In particular, the Scanner probe used a passive star mapper that emitted a pulse(s) at time of star crossing and with least squares data reduction resulted in approximately 30 arc seconds attitude accuracy. This concept provided minimum moving parts and high reliability. Another program that advanced the state of the art of attitude determination using star mappers to sense celestial targets was the NASA Applications Technology Satellite (ATS-III) experimental spacecraft which carried an attitude determination system experiment that demonstrated approximately 20 arc seconds accuracy.

Programs such as the Space Precision Attitude Reference Systems (SPARS) and the Horizon Definition Study that demand greater precision attitude determination are in analytical and development stages. Of particular interest is the Horizon Definition Study, contract NAS 1-6010, which showed that a passive attitude determination system to give 10 arc seconds attitude history for at least one year was required. Phase A, Part II of Contract NAS 1-6010 demonstrated analytical and conceptual design feasibility of a 10 arc second attitude determination system using a single star mapper and a sun mapper for daylight operation on a spin-stabilized spacecraft and a least squares reduction of star mapper transit time data for attitude. In addition to the feasibility proof, several critical design and development areas were identified in the sensing system and the software for attitude estimation that must be solved to completely specify an operational 10 arc seconds attitude determination system.

The purpose of the study described herein is to advance the technique for the design and fabrication of a precision attitude determination system which includes a celestial sensing system and an algorithm for the estimation of spacecraft attitude for an attitude-referenced radiometer. An analytical process was used to establish the conceptual design of the attitude determination system. This process consists of determining the types of celestial sightings required to meet the specified accuracy, the onboard detection and data processing logic to minimize the data storage requirement, the sensors' optical transfer function and light shielding and developing a quasi-real-time data reduction to prevent significant backlogging of collected data.

An attitude determination algorithm was developed and exercised to establish design parameters and celestial data requirements. A transit time generator simulated the sensor's output by using a real-world model of the spacecraft environment and the geometric constraint to derive the transit of the celestial target. In reality, the transit output must be processed to identify the celestial body that created the transit. The simulation included a star identification update that used the estimated attitude to identify the next transit. The identified transits are then processed by the Algorithm to update the spacecraft state based on each new transit. A parameter variation study was performed to establish the sensitivities to sensor pointing direction, spacecraft dynamics parameters, initial condition errors, and daylight attitude estimation using sun transit only.

The celestial sensor design was conducted which was concerned with the analytical process of determining the sensor optics transfer function, light baffling parameters for daylight star mapping, and determining the method of onboard data processing for minimizing noise data storage.

A sensor conceptual design parameter analysis was conducted to determine the best pointing direction of the sensor to minimize the baffle volume and to detect stars in each revolution of the vehicle. In addition, other sensor parameters were determined such as field of view, aperture size, required magnitude to be detected for 1 and 2 stars detection per revolution of the spacecraft, cant angle, and baffle dimensions. Another analytical process determined the parameters and behavior of the sensor optics for various celestial body characteristics and environmental conditions on the sensor, including the detector response. An error analysis followed using the transfer function of the sensor to establish analytically the transit time error and signal-to-noise ratio.

Several methods of onboard digital selection of data for storage were identified and tradeoffs made to determine the best method. The significant factor in the selection of the best method was noise rejection ability. Another factor was the cost of implementing the various methods. The method selected was based significantly on these factors. Initial star identification is based on the selected method of onboard digital filtering. The method of initial star identification was derived from the selected concept. A simulation was conducted to determine the performance of the initial star identification with a controlled true transit-to-noise transit time ratio. An update star identification program which is presently incorporated in the attitude determination program was developed to continue the star identification once the estimate of the spacecraft state is converged.

In conclusion, the results of the celestial sensor parameter design analysis and the attitude determination parameter sensitivity analysis are merged to establish the over-all conclusion and recommendation for the attitude determination system.

STUDY REQUIREMENTS AND OBJECTIVES

The attitude determination system study was guided by requirements imposed on the Attitude-Referenced Radiometer Study original statement of work and NASA instructions. The basic requirements are

- A goal of 30 arc seconds attitude determination accuracy as related to an earth-based reference frame for referencing radiometric observations made to 0.03 W/m^2-sr accuracy in the 14- to 16-μ electromagnetic spectrum.
- The spacecraft orbital parameters, spacecraft configuration, and operational characteristics are imposed as a design guideline where variations of these parameters are permissible in the analysis. These design guidelines are detailed as follows:

  1. Orbital parameters:
     - a. Altitude - 500 Km
     - b. Eccentricity - zero (circular orbit)
     - c. Inclination - 97.38° (near-polar sun synchronous)
     - d. Phasing - 3:00 a.m. or 3:00 p.m.
  2. Spacecraft configuration:
     - a. Shape - see Figure 1
     - b. Inertia characteristics: I_y = 65 slug-ft^2

       $I_x = I_z$ (± 2%)

       $1.1 \leq \frac{I_y}{I_x} \leq 1.4$

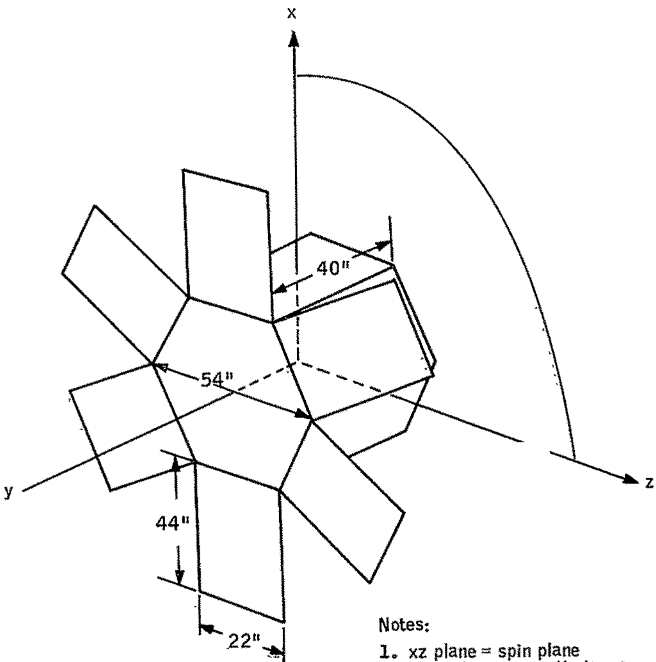

Notes:

1. xz plane = spin plane
2. Spin plane nominally lies in orbit plane ± 5°
3. Radiometer optical axis lies in xz plane

Figure 1. Spacecraft Configuration

c. Magnetic characteristics: (Based on assumed spherical model)

Moment coefficients: $M_x = M_y = M_z$

$M_x = 0\ (\pm 5 \times 10^{-6})$ ft-lb/G due to

preflight compensation uncertainties

ΔM_x due to difference in sunlight and

dark conditions $\approx 5\%$ of M_x

Eddy current coefficients: 1.4×10^{-5} ft/lb/sec/G^2

d. Radiometer optical axis: Lies in spin plane

3. Operational characteristics

a. Spin rate: 1 to 5 revolutions per minute

b. Attitude: Spin axis nomially perpendicular to orbit plane within ± 5°. No control applied during instrument measurement period.

The goal of 30 arc sec attitude determination accuracy in an earth coordinate includes the inaccuracies attributed to spacecraft position determination. However, the Part I goal of the attitude determination study was to estimate attitude relative to an inertial frame with an accuracy of ± 15 arc sec in the spin plane and ± 100 arc sec in the two planes orthogonal to the spin plane.

Spacecraft parameters previously described above, are provided as a representative set used for earth-resource missions as indicated in Contract NAS 1-6010 studies. The following documents of NAS 1-6010 were supplied as background and reference material:

- CR-66376 - Orbital Operations and Analysis for a 15-Micron Horizon Radiance Measurement Program
- CR-66429 - Feasibility Design of an Instrument System for Measurement of Horizon Radiance in the CO_2 Absorption Band
- CR66382 - Conceptual Mechanization Studies for a Horizon Definition Spacecraft Attitude Control System
- CR66432 - Horizon Definition Study Summary

The attitude determination system design study was required to establish a conceptual design comprised of a celestial body sensing element on the spacecraft and ground data reduction to obtain a spacecraft axis time history of attitude in inertial coordinates. To accomplish the study of the attitude determination system, the following detailed tasks were required:

- Using the output of the celestial sensor, development of a ground quasi real-time data reduction program to estimate the celestial sensor point direction to the specified accuracy.
- Establishment of the data requirements (i. e., the number and type of celestial sensors) to meet the stated accuracy.
- Establishment of the celestial sensor parameters such as field of view, detectivity, resolution, aperture, and baffle geometry.
- Development of the celestial sensor(s) optical transfer function and onboard data processing to meet the overall attitude accuracy. A requirement of 60,000 bits of attitude data per orbit in the development of the onboard logic was imposed.
- Development of a ground data processing program to identify the celestial body sighted and to provide the output format suitable for the attitude determination data reduction program.

ATTITUDE DETERMINATION ALGORITHM

INTRODUCTION AND OBJECTIVES

The attitude determination algorithm study was concerned with the development of an operational, quasi-real-time data reduction program for ground reduction of attitude celestial sensor(s) output to give spacecraft axes time history of attitude. The attitude determination algorithm study plan is shown in Figure 2. This plan is composed of three tasks:

1. Torque Modeling. Models of five torques were derived, programmed, and analyzed to determine the effect on the spacecraft motion. These models were applied to the real-world model and the data-reduction model. Permissible simplications of the models were discussed for the data-reduction model. Analyses were performed to determine which torques were most significant in terms of attitude deviation and to establish methods of simplifications of the models for the data-reduction algorithm.

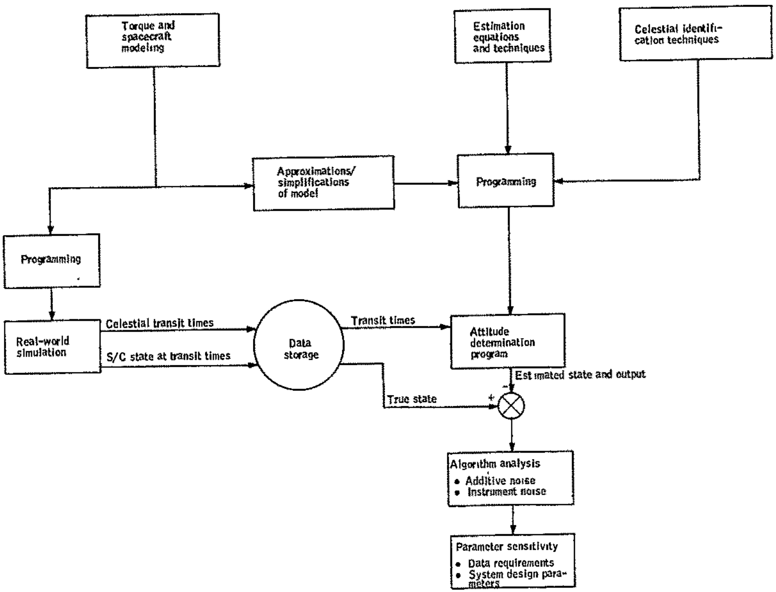

Figure 2. Schematic of Attitude Determination Algorithm Development and Analysis Report

2. Spacecraft Modeling. Spacecraft modeling was to develop an accurate and computationally efficient computer program to give continuous time history of spacecraft state given a state at time, $t = t_k$, where the state at time, t_k, is a best estimate.

   This model includes the effect due to significant environmental torques. This model was programmed and an analysis performed to establish the accuracy and efficienty of generating the spacecraft state.

3. Data-Reduction System Simulation. The data-reduction system simulation was to examine the performance of quasi-real-time estimation of spacecraft state from celestial sensor transit data. Performance requirements of the attitude estimation are specified in the previous section and are the goals of this study. Mission requirements dictate that at least real-time data processing be used to prevent significant backlogging of data over a one-year period. Results of Contract NAS 1-6010 Phase A, Part II showed that data-reduction time could be significant. The proposed solution is a sequential data-reduction algorithm which was programmed using efficient programming and computational techniques, and simulated to verify its performance in terms of the specified requirements. The simulation consists of a real-world program that generates the celestial sensor(s) output for a spacecraft that experiences five environmental torques, a star identification program to identify the celestial target, and a data-reduction program consisting of the spacecraft state time history. The real-world programs produce the output of the sensor(s) as defined by a five environmental torque rotational dynamics and sensor constraints. This provides an appropriate representation of the actual flight data. In the case of the data reduction program, simplification of the rotational dynamics are attempted to reduce running time of the data reduction program without loss of state propagation accuracy. The effort centered on developing the simulation to an operational status, to evaluate the performance in terms of running time and accuracy, and to establish design parameter and system performance under a wide range of parameter.

In addition to the three tasks, celestial identification techniques were investigated to identify the star that was observed at time, t_k. To evaluate the performance of the attitude estimation technique, a simulation of the sensor(s) was required and was developed with a real-world spacecraft model and a transit time generator. The additional tasks reported in the ensuing paragraphs of the attitude determination algorithm section are the real-world simulation and star identification simulation.

Torque Modeling

With the specified spacecraft configuration and orbit parameter as a guide, five environmental torques were derived and analyzed. The effect of the torques due to residual magnetic moments, eddy current loss, solar pressure, aerodynamic pressure, and gravity gradient on spacecraft attitude was determined and compared for relative significance. The combined effect of the five torques was evaluated to ascertain the additive property of torque effect on attitude.

Modeling.

Residual magnetic moment: The equation for residual magnet mome torque is well known and is represented vectorially by

$$\vec{T} = \vec{M} \times \vec{B}$$

where

$\vec{M}$ is the spacecraft magnetic moment vector

$\vec{B}$ is the earth's magnetic field intensity vector

Eddy current loss: Eddy current losses in the spacecraft are very c dent on spacecraft geometry, material conductivity, spacecraft state, ar earth's magnetic field intensity. The equation of the torque must reflect dependencies such that an accurate knowledge of spacecraft torque as a f tion of time be applied to the dynamics. The torque due to the eddy curr loss for a general configuration is given in gaussian units by

$$\vec{T} = \frac{1}{c} \iiint_{\text{volume}} \vec{r} \times (\vec{J} \times \vec{H})\, dV$$

where

$\vec{H} = \frac{\vec{B}}{\mu}$ magnetic field intensity vector

$\vec{J}$ is the volume eddy current density (ref. 1)

C is velocity of light in vacuum

$\vec{r}$ is from the spacecraft center of mass to the element of volume

$\mu \equiv 1$ for aluminum

The current density for eddy currents is represented vectorially by

$$\vec{J} = \frac{1}{2} \sigma c^{-1} (\vec{\omega} \times \vec{H}) \times \vec{r} + \nabla\phi$$

where

σ is the static electrical conductivity

$\vec{\omega}$ is the spacecraft spin vector

ϕ is a potential which must satisfy Laplace's equation $\nabla^2 \phi = 0$

The most studied spacecraft configuration is the sphere because ϕ is a constant which simplifies the derivation of the model. Applying the above equations, Vinti (ref. 2) developed the equation for the sphere:

$$\vec{T} = K\,(\vec{\omega} \times \vec{H}) \times \vec{H} \tag{4}$$

where

K is the constant based on spacecraft dimensions and material conductivity

For the ARRS spacecraft configuration, the geometry requires a solution for the gradient of ϕ; therefore, a closed-formed solution for torque becomes more difficult. The detailed derivation of the torque is given in Appendix A, and the equation for the torque is

$$\begin{aligned}
T_x &= -P_1\,(\omega_x H_y^2 - \omega_y H_x H_y) - P_2\,(\omega_x H_z^2 - \omega_z H_x H_z) \\
T_y &= P_3\,[\omega_y\,(H_x^2 + H_z^2) - \omega_x H_x H_y - \omega_z H_y H_z\,] \\
T_z &= -P_1\,[(\omega_z H_y^2 - \omega_y H_y H_z)] - P_2\,(\omega_z H_x^2 - \omega_x H_x H_z)
\end{aligned} \tag{5}$$

where the P's are constants based on the spacecraft dimensions and material static conductivity. The equations for the P's are

$$\begin{aligned}
P_1 = \Bigg\{ & \frac{1}{2}\sigma c^{-2}\,\tau WL^3 + \frac{1}{8}\sigma c^{-2}\,\tau LW^3 - \frac{3}{4}\sigma c^{-2}\,\tau L_1 L^2 W + \frac{3}{2}\sigma c^{-2}\,\tau LW\left(L_1 L - \frac{L^2}{2}\right) \\
& - 12\,\sigma c^{-2}\,\tau W^2\left(L_1 L - \frac{L^2}{2}\right) \sum_{n=1}^{\infty} \left(\frac{1}{m\pi}\right)^3 \left[\tanh\frac{m\pi L}{2W} + \left(\frac{L}{W}\right)^2 \tanh\frac{m\pi W}{2L}\right] \\
& - 24\,\sigma c^{-2}\,\tau W^4 \sum_{m=1,3,5,\ldots,2n-1}^{\infty} \left(\frac{1}{m\pi}\right)^5 \left[\tanh\frac{m\pi L}{2W} + \left(\frac{L}{W}\right)^4 \tanh\frac{m\pi W}{2L}\right] \Bigg\}
\end{aligned}$$

$$\begin{aligned}
P_2 = \Bigg\{ & -3\sigma c^{-2}\,\epsilon adh^2 - \frac{9}{8}\sigma c^{-2}\,\epsilon dh^3 - \frac{1}{8}\sigma c^{-2}\,\epsilon d^3 h \\
& + 24\,\sigma c^{-2}\,\epsilon d^2\left(ah + \frac{h^2}{2}\right) \sum_{n=1}^{\infty} \left(\frac{1}{m\pi}\right)^3 \left[\tanh\frac{m\pi h}{2d} + \left(\frac{h}{d}\right)^2 \tanh\frac{m\pi d}{2h}\right]
\end{aligned}$$

$$- 48\, \sigma c^{-2}\, \epsilon d^4 \sum_{n=1}^{\infty} \left(\frac{1}{m\pi}\right)^5 \left[\tanh\frac{m\pi h}{2d} + \left(\frac{h}{d}\right)^4 \tanh\frac{m\pi d}{2h}\right]\Bigg\}$$

$$P_3 = \Bigg\{-\frac{3}{8}\sigma c^{-2}\, \tau W^3 L - \frac{3}{8}\sigma c^{-2}\, \tau W L^3 - \frac{9}{4}\sigma c^{-2}\, \tau W L \left(L_1 L - \frac{L^2}{2}\right)$$

$$+ 36\, \sigma c^{-2}\, \tau W^2 \left(L_1 L - \frac{L^2}{2}\right) \sum \left(\frac{1}{m\pi}\right)^3 \left[\tanh\frac{m\pi L}{2W} + \left(\frac{L}{W}\right)^2 \tanh\frac{m\pi W}{2L}\right]$$

$$+ 72\, \sigma c^{-2}\, \tau W^4 \sum_{n=1}^{\infty} \left(\frac{1}{m\pi}\right)^5 \left[\tanh\frac{m\pi L}{2\,W} + \left(\frac{L}{W}\right)^4 \tanh\frac{m\pi W}{2L}\right]\Bigg\}$$

where

σ = Static electrical conductivity

τ = Thickness of cylinder panels

ϵ = Thickness of solar panels

W = Width of cylinder panels

L = Length of cylinder panels

h = Length of solar panels

d = Width of solar panels

m = $2n-1$, where $n=1, 2, 3, \ldots$

a = $\frac{\sqrt{3}}{2} W$

L_1 = $L - L_2$ = Distance from center of mass to end of cylinder in negative body y-direction

The eddy current model developed for the ARRS configuration considered only the losses in the skin and solar panels. Losses due to internal devices of various geometry and composition do affect the amount of the loss and the form of the model. Two problems prohibit modeling internal devices. These problems are (1) the geometry of the devices are not known and (2) that the composition of the devices cannot be defined precisely. The objective was to determine the form of the model required to represent the loss due to the skin and compare this model to the spherical model. Coefficients derived provide a tool and a guide to the design of the spacecraft geometry and composition to minimize the eddy current losses.

Aerodynamic torque: The torque produced consists of aerodynamic pressure torque due to the spacecraft's center of mass velocity and a dissipative torque due to the spacecraft's angular rate (see Appendix B). The torque equation including these two effects is taken from Beletskii's work (ref. 3). The torque equation developed is valid when the spacecraft's angular velocity is large compared with the rotation of the atmosphere (earth's rate approximately); the linear surface velocities due to the spin of the satellite are small compared with the spacecraft's center of mass velocity; and the angle of attack of each surface encountered is less than $\frac{\pi}{2}$. The torque equation is then given by

$$\vec{T} = \frac{1}{2} c\rho_a V_o^2 \int_{S(\vec{n}\cdot\vec{e}_v > o)} (\vec{n}\cdot\vec{e}_v)(\vec{e}_v \times \vec{r}_s)\, dS$$

$$+ \frac{1}{2} c\rho_a V_o \int_{S(\vec{n}\cdot\vec{e}_v > o)} \left[\left(\vec{n}\cdot\left[\vec{\omega}\times\vec{r}_s\right]\right)\left(\vec{e}_v \times \vec{r}_s\right) + (\vec{n}\cdot\vec{e})\left[\vec{\omega}\times\vec{r}_s\right]\times\vec{r}_s \right] dS \qquad (6)$$

where

$\vec{n}$ = Unit vector in direction of normal to surface, dS

$\vec{e}_v = \frac{\vec{V}_o}{|\vec{V}_o|}$ = Unit vector in direction of translational velocity of center of mass relative to incident stream

$\vec{r}_s$ = Radius vector joining surface element center and spacecraft center of mass

The first term of Equation (6) represents torque due to misalignment of spacecraft center of mass and center of pressures. The second term represents dissipative torque due to spacecraft spin. On examining the coefficient of each term, the torque due to center of pressure misalignment is approximately a factor of V_o larger than the dissipative torque coefficient when

$\omega r \ll V_o$. For ARRS spacecraft in a 270-nautical-mile orbit, V_o is 2.624 x 10^4 ft/sec.

Previous investigations estimated that $\frac{1}{2} c \rho_a V_o^2$ is 2 x 10^{-7} lb/ft^2. The coefficient of the second integral of Equation (6) is much less than the coefficient of the first, i.e., $\frac{1}{2} c \rho_a V_o \omega r \ll \frac{1}{2} c \rho_a V_o^2$, where ωr = 0.69 ft/sec compared to V_o = 2.624 x 10^4 ft/sec.

Consequently, dissipative torque is a factor of 2 x 10^{-5} less than pressure torque and is sufficiently small that the second term of Equation (6) will be neglected. Then, the aerodynamic torque equation is given by

$$\vec{T} = \frac{1}{2} c \rho_a V_o^2 \int_{S(\vec{n} \cdot \vec{e}_v > 0)} (\vec{n} \cdot \vec{e}_v)(\vec{e}_v \times \vec{r}_s)\, dS \qquad (7)$$

The domain of integration is indicated by $S(\vec{n} \cdot \vec{e}_v > 0)$. This means that the angle of attack of each surface element is less than $\frac{\pi}{2}$. The ARRS spacecraft surfaces consist of a hexagonal cylinder and rectangular solar panels.

The direction of the stream is in the orbit plane, and for this reason the spacecraft will present a different surface to the stream, depending on the attitude of the vehicle.

Figure 3 illustrates two orientations of the spacecraft that give two different domains for Equation (7).

Aerodynamic torque will be represented by two equations because of the different surfaces presented to the stream as shown in Figure 3. In Figure 3(b) the force along the y-axis due to the stream is positive. Figure 3(a) illustrates that the force along the y-axis is negative.

Two equations are required for the aerodynamic pressure torque because of the different surfaces presented to the stream velocity (see Figure 3). The derived equations are:

$$T_a = \begin{cases} q_2 \vec{e}_v \times \left(\underbrace{\sum_i}_{(\vec{n}_i \cdot \vec{e}_v > 0)} (\vec{n}_i \cdot \vec{e}_v)\vec{v}_i + (\vec{n}' \cdot \vec{e}_v)(\vec{v}' + \vec{v}_E) \right) & \text{for } \vec{e}_v \cdot \hat{j} \leq 0 \text{ or } F_y \geq 0 \\ \\ q_2 \vec{e}_v \times \left(\underbrace{\sum_i}_{(n_i \cdot e_v > 0)} (\vec{n}_i \cdot \vec{e}_v)\vec{v}_i + (\vec{n}'' \cdot \vec{e}_v)\vec{v}'' \right) & \text{for } e_v \cdot \hat{j} > 0 \text{ or } F_y < 0 \end{cases} \qquad (8)$$

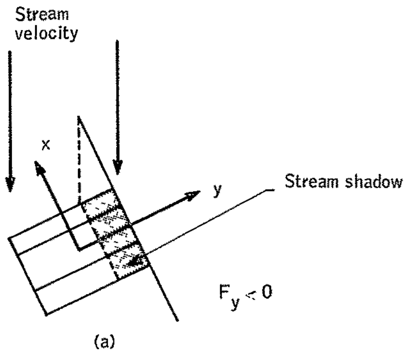

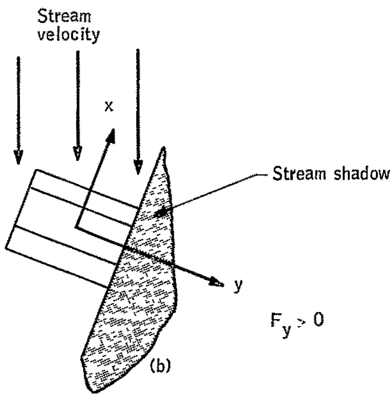

Figure 3. Spacecraft Shadowing

where

$$\vec{v}_i = \frac{\sqrt{3W}^3}{2} L \cos\frac{\pi}{3}(i-1)\,\hat{i} + \frac{W}{2}\left(L_2^2 - L_1^2\right)\hat{j} - \frac{3}{2}W^3 \sin\frac{\pi}{3}(i-1)\,\hat{k}$$

$$\vec{n}_i = \cos\frac{\pi}{3}(i-1)\,\hat{i} - \sin\frac{\pi}{3}(i-1)\,\hat{k} \quad \text{for } i=1, \ldots 6.$$

$$\vec{n} = -\hat{j}$$

$$\vec{n}\,' = \hat{j}$$

$$v_i' = -\frac{3}{2}W^3\left(L_1 + L_2'\right)\cos\frac{\pi}{3}(i-1)\,\hat{i} + \frac{W}{2}\left(L_2'^2 - L_1^2\right)\hat{j} - \frac{3}{2}W^3(L_1+L_2')\sin\frac{\pi}{3}(i-1)\hat{k}$$

$$L_2' = L_2 - \frac{(r_4 - r_3)(e_v \cdot \hat{j})}{\sqrt{1-(\vec{e}_v \cdot \hat{j})^2}}$$

$$\vec{v}\,' = L_2\,\pi\, r_4^2 - r_3^2\,\hat{j}$$

$$V_E = L_1\,\pi\, r_3^2\,\hat{j}$$

$$\vec{v} = \Big[\left(r_3(r_4^2 - r_3^2)\sin\theta\right)\hat{i}$$

$$+\left(L_2\pi r_4^2 - L_2\pi r_3^2 - L_2 r_3(r_4^2 - r_3^2)^{1/2} - L_2 r_4^2\sin^{-1}\left(\frac{r_3}{r_4}\right)\right)\hat{j}$$

$$-\left(r_3(r_4^2 - r_3^2)\cos\theta\right)\hat{k}\Big]$$

where

$$\sin\theta = \frac{v_x}{\sqrt{1 - v_y^2}}$$

$$\cos\theta = \frac{v_z}{\sqrt{1 - v_y^2}}$$

and the symbol

$$\sum_{\substack{i \\ (\vec{n}_i \cdot \vec{e}_v > 0)}}$$

means sum over the surfaces whose angle of attack is positive.

The torque equation derived above is not an exact representation of the vehicle's aerodynamic torque. Frictional or dissipative torques are small compared with pressure torques; therefore, frictional torques were neglected.

In the derivation of pressure torque, the solar panels were assumed to be a solid disk, where is actuality six rectangular panels are the solar panels (see Figure 4).

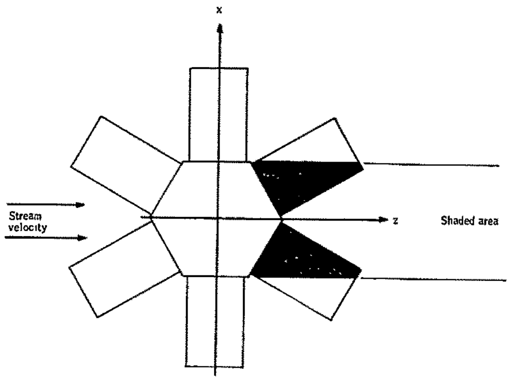

Figure 4. Solar Panel Configuration

Torque due to the solar panels is varying with a frequency six times the spin rates as opposed to the result obtained in this analysis. The result derived in this analysis is varying relative to the body axis only, but not the magnitude of the torque. In Figure 4 the shaded area covers only part of the two solar panels, and as the spacecraft rotates varying amounts of solar panel areas are shaded. It is for this reason that the magnitude of the solar panel torques is varying approximately six times the spin rate. The disk-shaped panels give a larger magnitude of torque but remain constant in absolute value.

Solar pressure torque model: The effect of solar pressure on the ARRS spacecraft is modeled and discussed herein. The torque equations [Equations (9), (10), and (11)] are found in reference 3, pages 24 and 25.

Equations. Torque on a body due to solar pressure is computed from the following three formulas:

$$\vec{m}^{+} = \hat{\tau} \times \int_{S_1} \hat{r}_s \, (\hat{n} \cdot \hat{\tau}) \, ds \qquad (9)$$

$$\vec{m}^{-} = 2 \int_{S_1} \hat{n} \times \vec{r}_s \, (\hat{n} \cdot \hat{\tau})^{2} \, ds \qquad (10)$$

$$\vec{T} = P \left[(1 - \epsilon_o) \, \vec{m}^{+} + \epsilon_o \, \vec{m}^{-} \right] \qquad (11)$$

where

S = Region of body in sunlight; ds is an area differential

$\vec{r}_s$ = Vector from body's C.M. to ds

$\hat{\tau}$ = Unit vector directed from sun

$\hat{n}$ = Unit outward normal to ds

P = Pressure exerted locally by sunlight

s_o = Body's reflection coefficient

The integrations described in Equations (9) and (10) are performed over two distinct surfaces -- the solar panels and end of the spacecraft (Figure 4) and the sides of the spacecraft (Figure 5). To simplify the model, three assumptions are made:

1. That the sun never shines on the end of the spacecraft opposite the solar panels

2. That the shadow of the tips of a solar panel never strikes any part of the spacecraft.

3. That the sides of the spacecraft (i.e., not the solar panels) constitute a circular cylinder rather than a hexagonal one

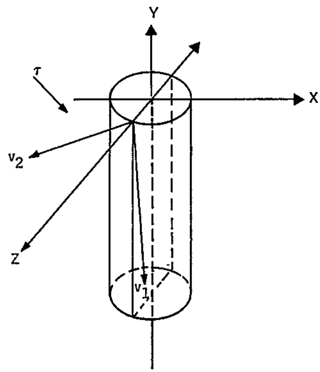

Figure 5. Spacecraft in Unprimed Coordinate System

The integrations of Equations (9) and (10) over the end and solar panels are quite simple. The integrations over the sides are considerably more complicated.

Sunlight passing between two solar panels may strike the spacecraft. If so, the integration of Equations (9) and (10) must be performed over the sunlit region. The limits of integration (i.e., the lines bounding this region) are described by Equations (12), (16), (17), and (18).

Solar Panels and End: Since $\hat{n}$ and $\hat{\tau}$ are constants on the region of Figure 4, one needs to evaluate

$$\int_{S_1} \vec{r}_s \, ds$$

where

$$\vec{r}_s = \begin{bmatrix} x \\ L_2 \\ z \end{bmatrix}$$

and

$$\int_{s_1} r_s \, ds = \int_{s_1} \begin{bmatrix} x \\ L_2 \\ z \end{bmatrix} dxdz$$

Because of the symmetry of s_1 with respect to the x_B and z_B axes, one has

$$\int_{s_1} xd\,x\,dz = \int_{s_1} zd\,x\,dz = 0$$

Also,

$$\int_{s_1} L_2 \, dxdz = L_2 s$$

where s is the area of Figure 5.

Let

$$\hat{\tau} = \hat{\tau}_B = \begin{bmatrix} a_o \\ b_o \\ c_o \end{bmatrix} \text{ and } \hat{n} = \begin{bmatrix} 0 \\ 1 \\ 0 \end{bmatrix}$$

Then

$$\vec{m}^+ = \begin{bmatrix} -c_o b_o L_2 s \\ 0 \\ a_o b_o L_2 s \end{bmatrix} \text{ and } \vec{m}^- = \begin{bmatrix} 0 \\ 0 \\ 0 \end{bmatrix}.$$

The end opposite the solar panels: No calculation was made for this end of the spacecraft, since the sun will never shine here.

The sides of the spacecraft: All computations in this section will be done in the unprimed coordinate system of the cylindrical coordinate system. The body of the spacecraft is approximated by a circular cylinder of length L. Figure 5 shows the configuration in the unprimed coordinate system.

Figure 5 also shows the unit vectors $\hat{v}_1$, $\hat{v}_2$, and $\hat{\tau}$. The unit vector, $\hat{\tau}$, is directed from the sun. This vector has the same components as $\hat{\tau}_B$ in body coordinates:

$$\hat{\tau} = \begin{bmatrix} a_o \\ b_o \\ c_o \end{bmatrix}$$

One defines $\hat{v}_1$ and $\hat{v}_2$ to be unit vectors along two adjacent solar panel edges. The sunlight by these two edges will strike the spacecraft and alter its course if $c_o < 0$.

The problem, then, will be to find the region of integration (i.e., the region on the cylinder where the sunlight falls). This area will be bounded by some combination of the following lines:

- Condition A -- the circles forming the top and bottom of the cylinder
- Condition B -- the shadows formed by the adjacent edges of two solar panels
- Condition C -- the lines which border the sunlit and dark sides of the cylinder

The lines under Condition C are most easily described in the cylindrical coordinate system. (See Appendix B for a description of this system.) They are described by $\hat{r} \cdot \hat{n} = 0$, or

$$\theta = -\tan^{-1} (c_o/a_o) \tag{12}$$

$$\theta = \pi - \tan^{-1} (c_o/a_o)$$

To achieve the description of the lines under Condition B, one must consider the projection of $\hat{v}_1$ and $\hat{v}_2$ onto the cylinder. In the unprimed system,

$$\hat{v}_1 = \hat{i} \sin 30° + \hat{k} \cos 30°$$

The projection of $\hat{v}_1$ onto the cylinder lies in the plane which is common to $\hat{v}_1$ and $\hat{r}$. Call this plane P_1; P_1 has a non-zero normal

$$\vec{N} = \hat{v}_1 \times \hat{r}$$

$$= -\hat{i}\, b_o \cos 30° + \hat{j}\, (a_o \cos 30° - c_o \sin 30°) + \hat{k}\, b_o \sin 30°$$

A point known to be on the plane is $(0, 0, r_3)$, where r_3 is the radius of the cylinder. Knowing the normal to P_1 and a point on P_1 is enough to determine the plane uniquely. The equation for P_1 is found to be

$$-\frac{\sqrt{3}}{2} b_o x + \frac{1}{2} (\sqrt{3}\, a_o - c_o) y + \frac{b_o z}{2} = r_3 \frac{b_o}{2} \tag{13}$$

In a similar manner, P_2, the plane which is the sun's projection of $\hat{v}_2$, has equation

$$-\frac{\sqrt{3}}{2} b_o x + \frac{1}{2} (\sqrt{3} a_o + c_o) y - \frac{b_o}{2} z = -r_3 \frac{b_o}{2} \tag{14}$$

The cylinder has the equation

$$x^2 + z^2 = r_3{}^2 \tag{15}$$

If Equations (12) and (15) are solved simultaneously, the result is a line which describes the projection of $\hat{v}_1$ on the cylinder (at least on the sunny side of the cylinder). A similar explanation holds for the simultaneous solution of Equations (9) and (15). These results are expressed in Equations (16) and (17) in the cylindrical coordinate system.

For $\hat{v}_1$

$$y = r_3 b_o / (\sqrt{3} a_o - c_o) (\sqrt{3} \sin \theta - \cos \theta + 1) \tag{16}$$

For $\hat{v}_2$

$$y = r_3 b_o / (\sqrt{3} a_o + c_o) (\sqrt{3} \sin \theta + \cos \theta - 1) \tag{17}$$

The lines under Condition A are described by

$$\begin{matrix} [y = 0] \\ [y = -L] \end{matrix} \tag{18}$$

Equations (12), (16), (17), and (18) describe the lines on the surface of the cylinder which are candidates for the integration limits in Equations (9) and (10). Depending on the direction from which the sun is shining, different integration limits exist. They fall into six distinct categories which are shown in Figures 6 through 11.

Case I is shown in Figure 8. Both shadows run off the left edge of the sunlit part of the cylinder before they strike the lower end of the cylinder. If $\vec{f}(y, \theta)$ is allowed to represent either integrand in Equation (7) or (8), then

$$\int_{s_1} \vec{f}(y, \theta)\, ds = r_3 \int_{\Phi_o}^{o} \int_{K_1 F(\theta)}^{K_2 G(\theta)} \vec{f}(7, \theta)\, dy d\theta \tag{19}$$

where

$$K_1 = r_3\, b_o / (\sqrt{3}\, a_o - c_o)$$

$$K_2 = r_3\, b_o / (\sqrt{3}\, a_o + c_o)$$

$$F(\theta) = \sqrt{3} \sin\theta - \cos\theta + 1$$

and

$$G(\theta) = \sqrt{3} \sin\theta + \cos\theta - 1$$

The other five cases are shown in Figures 7 through 11. It is assumed that the reader is viewing along the line of $\hat{r}$, so that the $\hat{n} \cdot \hat{r} = 0$ lines are the right and left visible edges of the cylinder.

Equations corresponding to Equation (19) were calculated for each case. In the six cases, the possibility that the shadow due to the end of the solar panel may strike the spacecraft was ignored. This seems a reasonable assumption. If the solar panels are never shorter than the length of the cylinder, the angle between the y-axis and $\hat{r}$ would have to exceed 45 degrees for this to occur. This is not expected.

To find some of the preceding integration limits, it will be necessary to invert Equations (16) and (17). Their inversions are Equations (20) and (21), respectively:

$$\theta = \mathrm{Sin}^{-1} \left[\sqrt{3}\, (y/K_1 - 1)/4 + \sqrt{(3 - y/K_1)\ (1 + y/K_1)/4} \right] \tag{20}$$

$$\theta = \mathrm{Sin}^{-1} \left[\sqrt{3}\, (y/K_2 + 1)/4 - \sqrt{(3 + y/K_2)\ (1 - y/K_2)/4} \right] \tag{21}$$

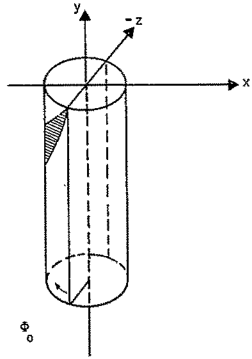

Figure 6. Both Shadows Intersecting Left Edge of Sunlit Area

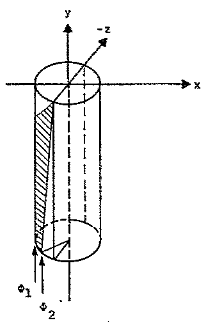

$$\int_{S_1} \vec{f}(y,\theta)\,ds = r_3 \int_{\Phi_2}^{0} \int_{K_1F(\theta)}^{K_2G(\theta)} \vec{f}\,dy\,d\theta + r_3 \int_{\Phi_1}^{\Phi_2} \int_{-L}^{K_2G(\theta)} \vec{f}\,dy\,d\theta$$

Figure 7. Shadows Intersecting Edge of Sunlit Area and End of Spacecraft.

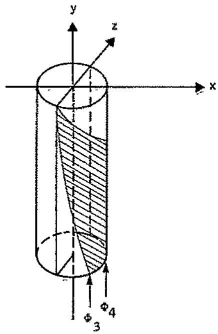

$$\int_{s_1} \vec{f}(y,\theta)\,ds = r_3 \int_0^{\Phi_3} \int_{K_2G(\theta)}^{K_1F(\theta)} \vec{f}\,dy\,d\theta + r_3 \int_{\Phi_3}^{\Phi_4} \int_{-L}^{K_1F(\theta)} \vec{f}\,dy\,d\theta$$

Figure 8. Shadows Intersecting Right Edge of Sunlit Region and End of Spacecraft

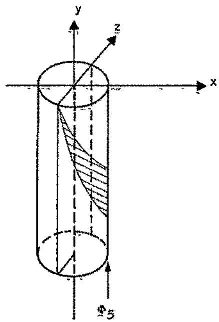

$$\int_{s_1} \vec{f}(y,\theta)\,ds = r_3 \int_0^{\Phi_5} \int_{K_2G(\theta)}^{K_1F(\theta)} \vec{f}\,dy\,d\theta$$

Figure 9. Both Shadows Intersecting Right Edge of Sunlit Region

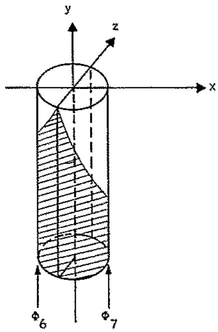

$$\int_{S_1} \vec{f}(y, \theta)\, ds = r_3 \int_{\Phi_6}^{0} \int_{-L}^{K_2 G(\theta)} \vec{f}\, dy d\theta + r_3 \int_{0}^{\Phi_7} \int_{-L}^{K_1 F(\theta)} \vec{f}\, dy d\theta$$

Figure 10. Each Shadow Intersecting Nearest Edge of Sunlit Region

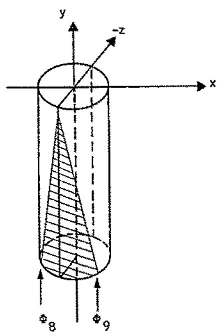

$$\int_{S_1} \vec{f}(y, \theta)\, ds = r_3 \int_{\Phi_8}^{0} \int_{-L}^{K_2 G(\theta)} \vec{f}\, dy d\theta + r_3 \int_{0}^{\Phi_9} \int_{-L}^{K_1 F(\theta)} \vec{f}\, dy d\theta$$

Figure 11. Both Shadows Intersecting End of Spacecraft

One must check carefully to see that θ as yielded by Equations (20) or (21) lies on the sunny half of the spacecraft as defined by the two $n \cdot \tau = 0$ lines. If not, the correct value will be $\theta_i = \pi - \theta$.

Any integral expressed as a solution to one of the six cases can be written as a linear combination of some integrals of the following general form:

$$r_3 \int_{\Phi_1}^{\Phi_2} \int_{-L}^{KH(\theta)} \vec{f}\,(y, \theta)\, dy d\theta = I \tag{22}$$

where

$H(\theta) = d\ \ 3 \sin \theta - \cos \theta + 1$, and d can take on the value of ± 1

and

$$K = \begin{bmatrix} K_1 \text{ if } d = 1 \\ \\ -K_2 \text{ if } d = -1 \end{bmatrix}$$

The general evaluation of I/r_3 [Equation (22)] was performed for both functions which $f(y, \theta)$ represents. The evaluation follows:

$$\boxed{\overline{m}^+ = \int_{-L}^{KH(\theta)} \vec{s}\ (\hat{n} \cdot \hat{\tau})\ dy d\theta}$$

For the $\hat{i}$ - component,

$$K\, r_3 \left\{ \frac{-d\sqrt{3}}{3}\, a_o \cos\theta\, (\sin^2\theta + 2) + (d\, c_o\sqrt{3} - a_o)\, \frac{\sin^3\theta}{3} + \frac{c_o}{3} \cos^3 \theta \right\} +$$

$$+ r_3\, (K+L) \left\{ \frac{a_o}{2}\ (\theta - \sin\theta \cos\theta) + \frac{c_o}{2} \sin^2 \theta \right\} \Big|_{\Phi_1}^{\Phi_2}$$

For the $\hat{j}$ - component,

$$K^2 \left\{ -\frac{a_o}{3} \cos\theta\ (\sin^2\theta + 2) + (c_o - d\sqrt{3}\ a_o) \frac{\sin^3}{3}\theta + \frac{d\sqrt{3}\ c_o}{2} \cos^3\theta \right\} +$$

$$+ K(K+L_2) \left\{ \frac{d\sqrt{3}\,a_o}{2} (\theta - \sin\theta\cos\theta) + (d\sqrt{3}\,c_o - a_o) \frac{\sin^2\theta}{2} - \frac{c_o}{2} (\theta + \sin\theta\cos\theta) + \right.$$

$$\left. - a_o \cos\theta + c_o \sin\theta \right\} - L\left(\frac{L}{2} - L_2\right) (-a_o \cos\theta + c_o \sin\theta) \Big|_{\Phi_1 = \theta}^{\Phi_2 = \theta}$$

For the $\hat{k}$ - component,

$$K\, r_3 \left\{ \frac{da_o\sqrt{3}\ \sin^3}{3} \theta + (a_o - d\sqrt{3}\,c_o) \frac{\cos^3\theta}{3} - \frac{co}{3} \sin\theta\ (\cos^2\theta + 2) \right\} +$$

$$+ r_3\ (K+L) \left\{ \frac{a_o}{2} \sin\theta + \frac{c_o}{2} (\theta + \sin\theta\cos\theta) \right\} \Big|_{\Phi_1}^{\Phi}$$

The equation

$$\boxed{\vec{m}^- = \int_{\Phi_1}^{\Phi_2} \int_{-L}^{KH(\theta)} \hat{n} \times \vec{r}_s\ (\hat{n} \cdot \hat{\tau})^2\ dy d\theta :}$$

is intregrated. Given in component form, this equation is

For the $\hat{i}$ - component,

$$-K^2 \left\{ \frac{a_o}{5} \sin^5\theta + (2a_o c_o - d\sqrt{3} a_o^2) \left[\frac{1}{5}\sin^4\theta\cos\theta - \frac{1}{15}\cos\theta(\sin^2\theta + 2)\right] + \right.$$

$$\left. + (c_o^2 - 2d\sqrt{3}\, a_o c_o)\left(\frac{1}{5}\sin^3\theta\cos^2\theta + \frac{2}{15}\sin^3\theta\right) + \frac{d\sqrt{3}}{5} c_o^2 \cos^5\theta \right\} +$$

$$- K(K+L_2) \left\{ \frac{d\sqrt{3}}{4} a_o^2 \sin^4\theta + \frac{1}{8}(2d\sqrt{3}\, a_o c_o - a_o^2)\left(\theta - \frac{1}{4}\sin_4\theta\right) + \right.$$

$$- \frac{1}{4}(d\sqrt{3} c_o^2 - 2\, a_o c_o)\cos^4\theta - c_o^2 \left[\frac{1}{4}\sin\theta\cos^3\theta + \frac{3}{8}(\theta + \sin\theta\cos\theta)\right] +$$

$$\left. + \frac{a_o^2}{3}\sin^3\theta - \frac{2}{3} a_o c_o \cos^3\theta + \frac{c_o^2}{3}\sin\theta(\cos^2\theta + 2) \right\} + L\left(\frac{L}{2} - L_2\right)\left[\frac{a_o^2}{3}\sin^3\theta + \right.$$

$$\left. - \frac{2}{3} a_o c_o \cos^3\theta + \frac{c_o^2}{3}\sin\theta(\cos^2\theta + 2)\right] \Big|_{\Phi_1}^{\Phi_2}$$

For the $\hat{j}$ - component = 0.

For the $\hat{k}$ - component,

$$K^2 \left\{ a_o^2 \left[-\frac{1}{5}\sin^4\theta\cos\theta - \frac{4}{15}\cos\theta(\sin^2\theta + 2)\right] + \frac{1}{5}(2a_o c_o - d\sqrt{3}\, a_o^2)\sin^5\theta + \right.$$

$$+ (c_o^2 - 2d\sqrt{3}\, a_o c_o)\left[\frac{1}{5}\sin^4\theta\cos\theta - \frac{1}{15}\cos\theta(\sin^2\theta + 2)\right] +$$

$$\left. - d\sqrt{3}\, c_o^2 \left(\frac{1}{5}\sin^3\theta\cos^2\theta + \frac{2}{15}\sin^3\theta\right) \right\} + K(K+L_2)\left\{ d\sqrt{3}\, a_o^2 \left[\frac{1}{4}\sin^3\theta\cos\theta + \right.\right.$$

$$\left. + \frac{3}{8}(\theta - \sin\theta\cos\theta)\right] + \frac{1}{4}(2d\sqrt{3}\, a_o c_o - a_o^2)\sin^4\theta + \frac{1}{8}(d\sqrt{3}\, c_o^2 - 2\, a_o c_o$$

$$\left(\theta - \frac{1}{4}\sin 4\theta\right) + \frac{c_o^2}{4}\cos^4\theta - \frac{1}{3} a_o^2 \cos\theta(\sin^2\theta + 2) + \frac{2}{3} a_o c_o \sin^3\theta +$$

$$- \frac{c_o^2}{3}\cos^3\theta - L\left(\frac{L}{2} - L_2\right)\left[-\frac{a_o^2}{3}\cos\theta(\sin^2\theta + 2) + \frac{2}{3} a_o c_o \sin^3\theta - \frac{c_o^2}{3}\cos^3\theta\right] \Big|_{\Phi_1}^{\Phi_2}$$

This solves the problem in the unprimed system. To solve the problem for the other five V-shaped areas, one must transform $\hat{\tau}$ into the primed coordinate system

$$\begin{bmatrix} a'_o \\ b'_o \\ c'_o \end{bmatrix} = M^T(i) \begin{bmatrix} a_o \\ b_o \\ c_o \end{bmatrix}, \quad i = 2, 3, 4, 5, 6$$

After finding $\vec{T}'$, the torque in the primed system, one transforms it back to body coordinates

$$\vec{T}_B = M(i)\,\vec{T}'$$

The one remaining problem is to devise a means for determining $\hat{\tau}_B$ as a function of time and body orientation. The negative of $\hat{\tau}$, $-\hat{\tau}$, lies in the ecliptic at an angle, S, from the X_e-axis,

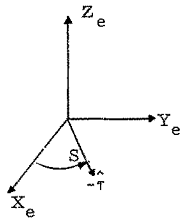

where S is a measure of the time of year. On the first day of spring $S = 0$. In the ecliptic frame,

$$\hat{\tau}_e = \begin{bmatrix} -\cos S \\ -\sin S \\ 0 \end{bmatrix}$$

Hence, in body coordinates,

$$\hat{\tau}_B = \begin{bmatrix} a_o \\ b_o \\ c_o \end{bmatrix} = E(\psi, \phi, \theta)\; G^T(\epsilon)\; \hat{\tau}_e$$

where G(E) and M(I) are defined in Appendix G.

In the computer simulations of flights, real time seldom exceeds two or three hours, and it will be assumed that S is a constant.

A computer subprogram was written to calculate solar pressure torque. The computer program is called at each time step of the numerical integration of the equations of motion of the spacecraft, and the torque at that time and place is computed. It should be emphasized that the integrations of (7) and (8) are not performed numerically but are evaluated analytically at each time step.

Gravity Gradient: The equations for the gravity gradient torque are expressed in a body-fixed axes system (principal body axes).

The torque on a rigid body due to the gravity gradient (reference 3, page 9) is

$$\vec{T}_G = \frac{3\mu}{R^3}\,\hat{r} \times \bar{\bar{I}} \cdot \hat{r} \tag{23}$$

assuming that the earth is spherical.

Further,

μ = Earth's gravitational constant
= 1.4082×10^{16} ft^3/sec^2

$\hat{r}$ = Unit vector in direction of earth's radius vector

R = Distance from earth's center to body's center of mass

$\bar{\bar{I}}$ = Moment of inertia dyadic of the body

To write the body-axis components of this gravity torque, three coordinate frames are required -- an inertial frame, a local vertical frame, and a body-fixed (principal axes) frame.

In body coordinates the equation is

$$\begin{bmatrix} T_{Gx} \\ T_{Gy} \\ T_{Gz} \end{bmatrix} = \frac{3\mu}{R^3} \begin{bmatrix} (I_z - I_y)\, r_{By}\, r_{Bz} \\ (I_x - I_z)\, r_{Bz}\, r_{Bx} \\ (I_y - I_x)\, r_{Bx}\, r_{By} \end{bmatrix} \tag{24}$$

and

$$\hat{r}_B = E\,(\psi, \phi, \theta)\, F\,(\Omega, i, \nu)\, \hat{r}_L$$

$$\hat{r}_L = [+1,\ 0, 0]$$

where r_{Bx}, r_{By}, and r_{Bz} are the direction cosine of the unit vector from the earth's center of mass to the spacecraft's center of mass in body axes.

Analysis and results. -- The analysis of torqued body motion was conducted using a digital computer. Figure 12 is a diagram of the order in which the equations are applied to arrive at the integrated equations of motion.

Computer program: The overall objective of the system of programs is to integrate the equations of motion for different cases of spacecraft configuration and different types of torques applied to the spacecraft and to compare the results of two separate cases. This comparison is accomplished by plotting (CalComp) the differences in Euler angles and torques between two different cases. Figure 13 shows the general flow of logic. Any number of cases may be examined, but all differencing is done between the first case presented in the data deck and subsequent cases.

Often a plot of actual torques rather than torque differences is desired. This is accomplished simply by making the first case in the data deck the untorqued case. The differencing is done in such a way that the actual torques (and not their negatives) will be plotted. Accompanying such a set of torque plots will be Euler angle difference plots where the plots represent differences in attitude between the torqued and untorqued bases. Examples of these plots are shown in Figures 14 and 15. In this particular example, the first case was the untorqued case and some later case in the data deck requested that the magnetic moment torque be considered in the integration.

The system of programs: The task set forth in the previous section can be divided into four subtasks:

1. Integration of the equations of motion
2. Position and attitude determination
3. Computation of torques
4. Input and output

A main program, DRIVER, and several subprograms were written to accomplish these subtasks. Figure 16 shows both the pattern of communication between these programs and input/output.

Listed below is the name of each program and a brief description of the function of each.

• DRIVER	Reads and initializes data and programs. Performs Runge-Kutta integration. Prints results.
• TORQUE	Calculates called-for torques as a function of state.

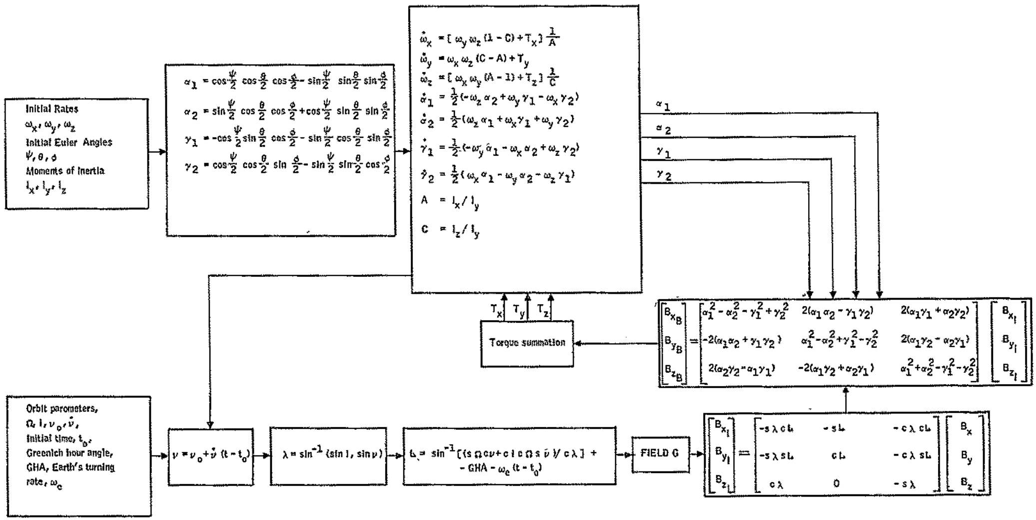

Figure 12. Logical Flow of Integration of Equations of Motion

- UNTNGL — Calculates the three Euler angles from the E-matrix and the previous value of

- DPLOT — Plots the differences between two arrays of numbers.

- MATMUL — Multiplies two matrices.

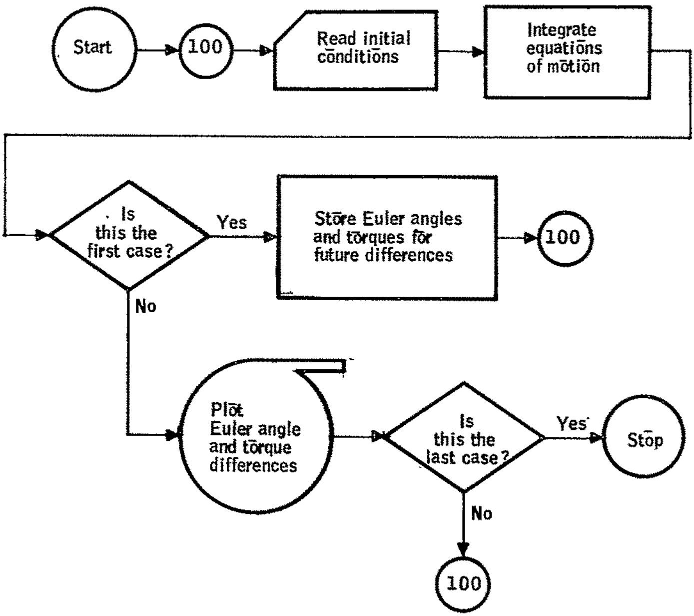

Figure 13. Logical Flow Within the System of Computer Programs

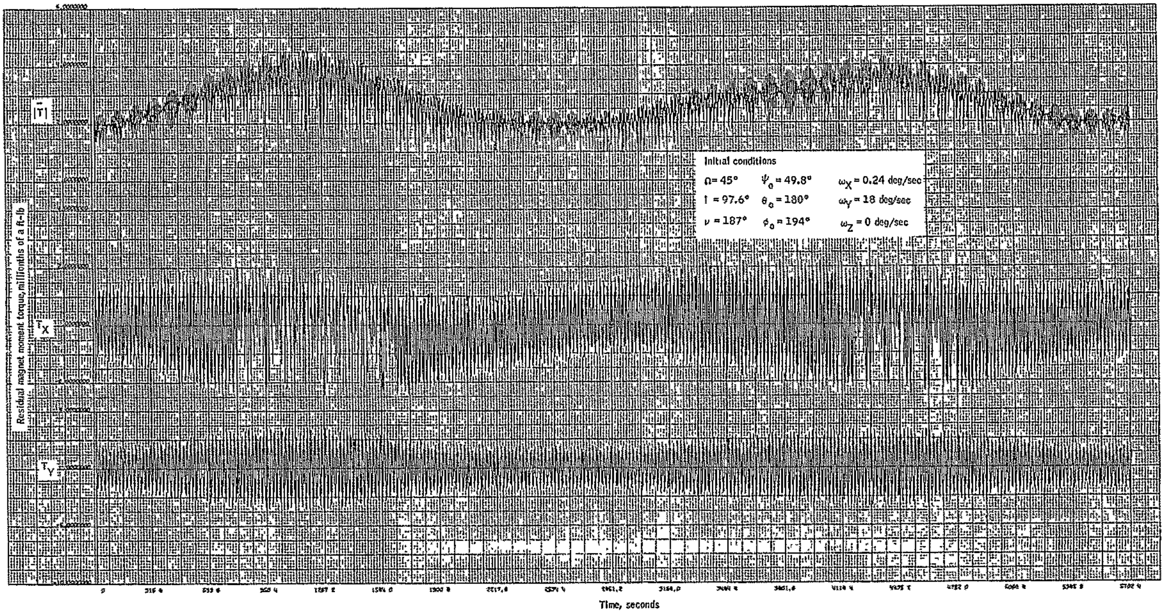

Figure 14. Example of Torque Difference Plots

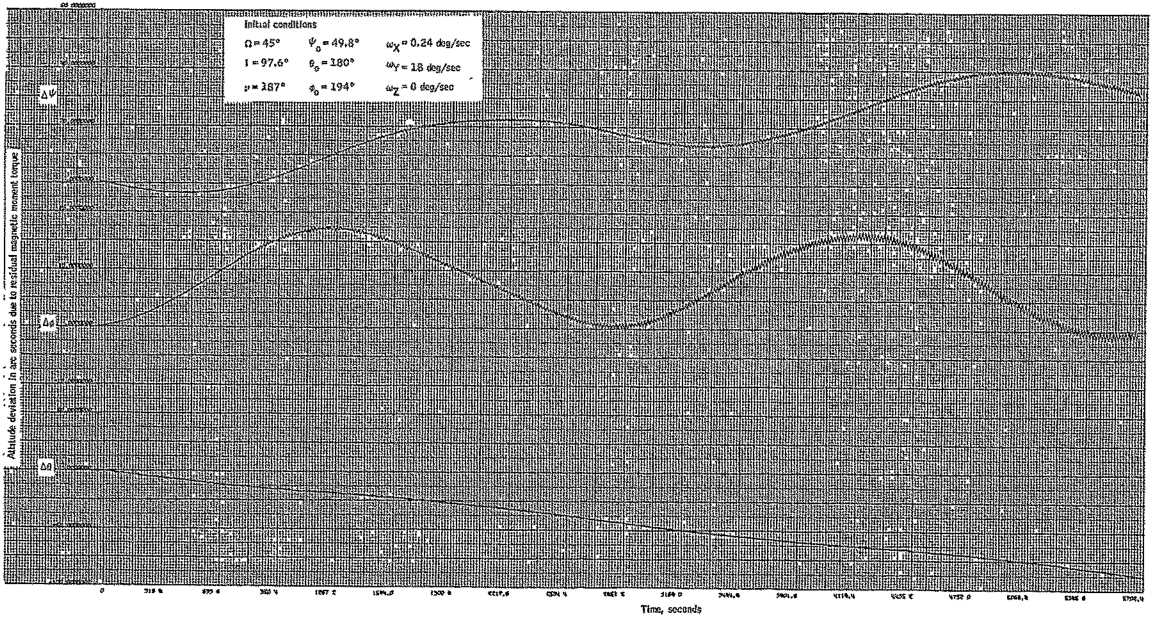

Figure 15. Example of Euler Angle Difference Plots

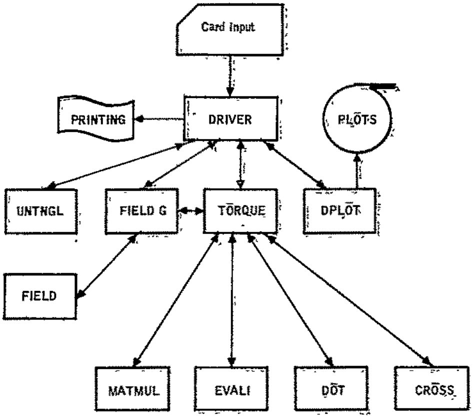

Figure 16 Communication Within the System of Programs and Input/Output

- FIELDG, FIELD — Calculates earth's magnetic field as a function of orbit position and attitude.
- CROSS — Forms the cross product of two vectors.
- DOT — Forms the dot product of two vectors.
- EVALI — Evaluates an integral needed for the solar pressure calculation.

Equations of motion: Differential equations of motion are written in terms of a set of Euler's symmetric parameters (α_1, α_2, γ_1, γ_2).

$$\dot{\omega}_x = [\omega_y\omega_z (1 - C) + T_x]/A$$
$$\dot{\omega}_y = \omega_x\omega_z (C - A) + T_y$$
$$\dot{\omega}_z = [\omega_x\omega_y (A - 1) + T_z]/C$$
$$\dot{\alpha}_1 = \frac{1}{2}(-\omega_z\alpha_2 + \omega_y\gamma_1 - \omega_x\gamma_2)$$
$$\dot{\alpha}_2 = \frac{1}{2}(\omega_z\alpha_1 + \omega_x\gamma_1 + \omega_y\gamma_2)$$

$$\alpha_1 = \cos\frac{\psi}{2}\cos\frac{\theta}{2}\cos\frac{\phi}{2} - \sin\frac{\psi}{2}\sin\frac{\theta}{2}\sin\frac{\phi}{2}$$

$$\alpha_2 = \sin\frac{\psi}{2}\cos\frac{\theta}{2}\cos\frac{\phi}{2} + \cos\frac{\psi}{2}\sin\frac{\theta}{2}\sin\frac{\phi}{2}$$

$$\gamma_1 = \cos\frac{\psi}{2}\sin\frac{\theta}{2}\cos\frac{\phi}{2} - \sin\frac{\psi}{2}\cos\frac{\theta}{2}\sin\frac{\phi}{2}$$

$$\gamma_2 = \cos\frac{\psi}{2}\cos\frac{\theta}{2}\sin\frac{\psi}{2} - \sin\frac{\psi}{2}\sin\frac{\theta}{2}\cos\frac{\phi}{2}$$

$$\dot{\gamma}_1 = \frac{1}{2}(-\omega_y\alpha_1 - \omega_x\alpha_2 + \omega_z\gamma_2)$$

$$\dot{\gamma}_2 = \frac{1}{2}(\omega_x\alpha_1 - \omega_y\alpha_2 - \omega_z\gamma_2)$$

In the previous equations,

$$A = I_x/I_y$$
$$C = I_z/I_y$$

and T_x, T_y, and T_z are the torques divided by I_y.

Integration of the equations of motion: The task of integrating the equations of motion was accomplished through a Runge-Kutta fourth-order algorithm. Briefly, for a differential equation of the form

$$\frac{dy}{dx} = f(x, y)$$

and integration step size Δx, one forms at the n^{th} step

$$k_1 = \Delta x\, f(x_n, y_n)$$
$$k_2 = \Delta x\, f(x_n + \Delta x/2,\ y_n + k_1/2$$
$$k_3 = \Delta x\, f(x_n + \Delta x/2,\ y_n + k_2/2)$$
$$k_4 = \Delta x\, f(x_n + \Delta x,\ y_n + k_3)$$

then set

$$y_{n+1} = y_n + \frac{1}{6}[k_1 + 2(k_3 + k_3) + k_4]$$

Solving a system of differential equations, as this problem presents, is simply a matter of keeping a system of these calculations going simultaneously. The step size used is 0.4 second for best accuracy results. See NAS-1-6010 Report No. CR-66376, for confirmation on integration accuracy.

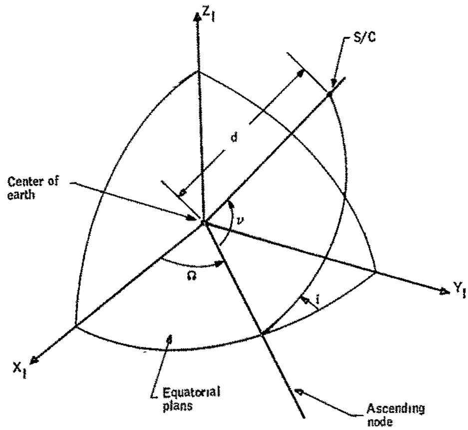

Figure 17. Configuration of Spacecraft Orbit, Earth, and Inertial Reference Frame

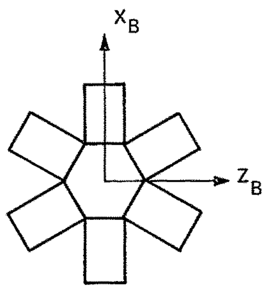

Figure 18. X_B and Z_B Axes

Coordinate systems: There are two major coordinate systems used in this system of computer programs -- the inertial coordinate system and the body fixed coordinate system. The inertial coordinate system has its origin at the center of the earth, the X_I axis directed toward the Vernal Equinox, the Z_I axis directed toward the north pole, and the Y_I axis forming a right-handed coordinate system (Figure 17). The body-fixed coordinate system has its origin at the center of mass of the spacecraft. Its axes coincide with the axes of the principal moments of inertia of the spacecraft. The Y_B axis is directed along the spin axis toward the solar-panel end of the spacecraft. Figure 18 shows the orientation of the X_B and Z_B axes with respect to the solar panels.

A vector $\vec{V}_I$ in inertial coordinates is given in body-fixed coordinates by a transformation $E(\psi, \phi, \theta)$, where $E(\psi, \phi, \theta)$ is defined in Appendix G.

Orbit parameters: The orbit plane of the spacecraft can be described by two parameters, Ω and i. The exact position of the spacecraft in the orbit plane requires two additional parameters, ν and r. The relationship of these parameters to the inertial reference frame is pictured in Appendix G.

Given information about the initial orbit parameters, the time of day of launch, the earth's turning rate, and the spacecraft's orbit rate, latitude and longitude can be calculated as a function of time. These calculations are shown in Figure 12.

Euler's symmetric parameters (See Reference 5): Differential equation of motion are written in terms of α_1, α_2, γ_1, and γ_2 instead of Ψ, ϕ, and θ. The inverse of this operation is done by equating $E(\Psi, \phi, \theta)$ to $E(\alpha_1, \alpha_2, \gamma_1, \gamma_2)$. This yields nine relations in the three unknowns Ψ, ϕ, and θ. The resultant system of equations fails to have a unique solution. However, in integrating the equations of motion, the solution at the previous time step is known. Given this information, the correct solution among the family of possible solutions may be uniquely chosen.

Results and discussion of results: The sequence of presentation of the torque model analysis results and discussion is residual magnetic moment, eddy current loss, solar pressure, aerodynamic pressure, and gravity gradient. The previous paragraphs detailed the computer program and the manner in which it was used for the analysis. In all cases of the analysis, the integration step size used was 0.4 second. The program output was limited to approximately 1000 data points per simulation run. Consequently, the output sampling period depended on the length of the run. For this reason, torque plots occasionally possess gaps because peak points were missed.

However, the magnitude of the torque is plotted which does not contain this effect.

A simulation of each torque is presented and discussed. In conclusion, several simulations were made to demonstrate the additive property of adding torque individually to the equation of motion.

Residual magnetic moment: The residual magnet moment torque model was programmed, and a short-term simulation of one spin period and a long-term simulation of one orbit was generated for the following values of the moments:

$$M_x = M_y = M_z = 5.170856 \times 10^{-6} \text{ ft-lb/G}$$

This value of the moment is representative of moment values experienced on the Tiros spacecrafts. Figure 19 demonstrates the value of the T_x, T_y, and $|\vec{T}|$ as a function of time sampled once per 4.8 seconds. The peaks of the envelope in all three of the torque plots represent the South and North Pole of the earth,respectively. At these points the magnetic field vector is greatest in the orbit plane. The y-component of torque is cyclic with a period of 20 seconds and mean value of zero. The y-component of torque is a function of B_x, M_z, M_x, and B_z, where M_x and M_z are constants and B_x and B_z are cyclic with a 20-second period due to the spacecraft spin. The x-component is also cyclic, with a period of 20 seconds and with the mean varying somewhat with position in orbit. The mean of the T_x torque is nonzero because of the ($M_z B_y$) term. The cyclic portion is due to the $M_y B_z$ term. The peak of the total torque is 4.5×10^{-6} ft-lb. Initial conditions were chosen such that a cone angle of 0.61° was obtained and the principal y-axis of the body was misaligned to the orbit normal by approximately 7.5°. The orbit parameters were chosen with the true anomaly at the equator and a south heading. The right ascension represents a 3 a.m. or 3 p.m. launch condition, and the inclination gives the sun synchronous retrograde orbit. A correlation of the attitude deviation with the torque can be made by observing both Figure 19 and 20. Notice that the cyclic nature of the torque does not create a cyclic variation in $\Delta\theta$. Although $\Delta\phi$ and $\Delta\Psi$ have cyclic variation, the extent of the variation is insignificant over the full orbit -- approximately 1 arc sec variation of $\Delta\phi$ at 5702.4 seconds. This suggests that short-term variation with a period of 20 seconds and mean of zero can be deleted from the torque model. Thus, the y-component is a candidate for deletion in the algorithm equations of motion.

Noting the general effect of the residual magnetic moment torque on the spacecraft attitude, the pitch, $\Delta\theta$, has deviated 87.5 arc sec at 5702.4 seconds in time and $\Delta\Psi$ is completely oscillatory about a mean of 8.5 arc sec. Also, $\Delta\Psi$ is oscillatory but on a ramp with average drift of 35 arc sec at 5702.4 seconds in time.

Figures 21 and 22 demonstrate the residual magnetic moment torque and attitude effect over the first spin cycle. The initial conditions are the same as the long simulation run.

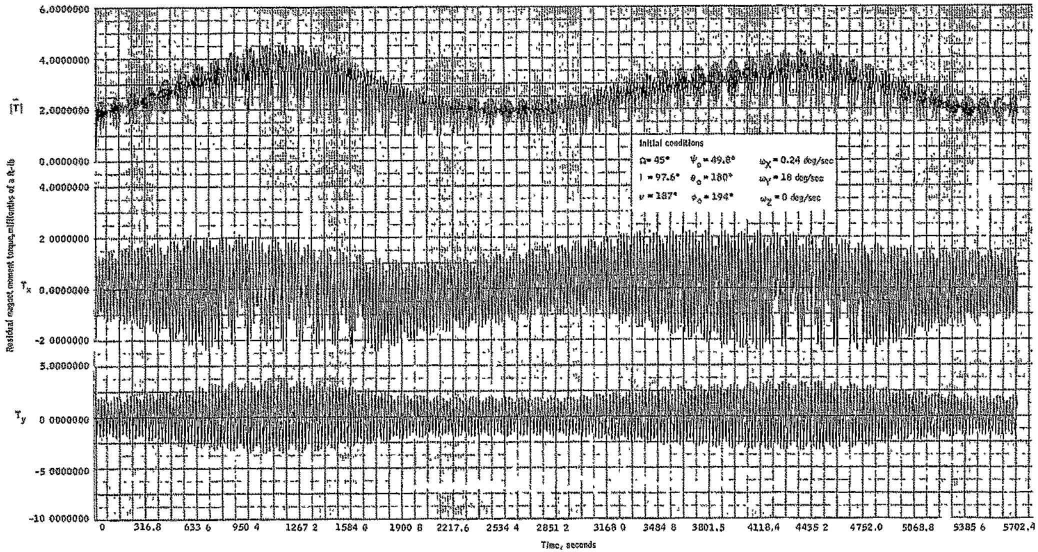

Figure 19. Torque on Spacecraft Due to Residual Magnetic Moments

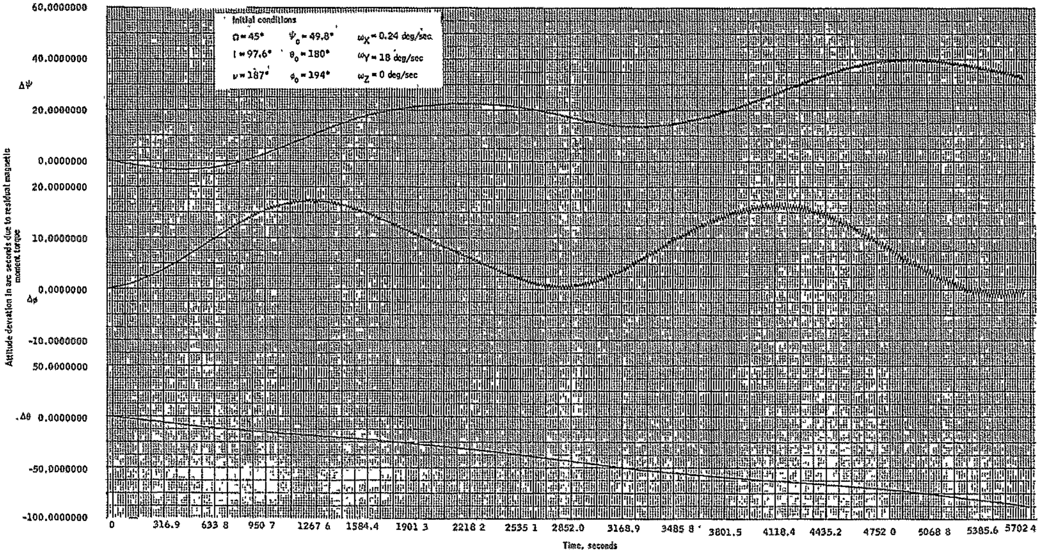

Figure 20. Attitude Deviation of Spacecraft due to Residual Magnetic Moment Torque Relative to an Untorqued Spacecraft

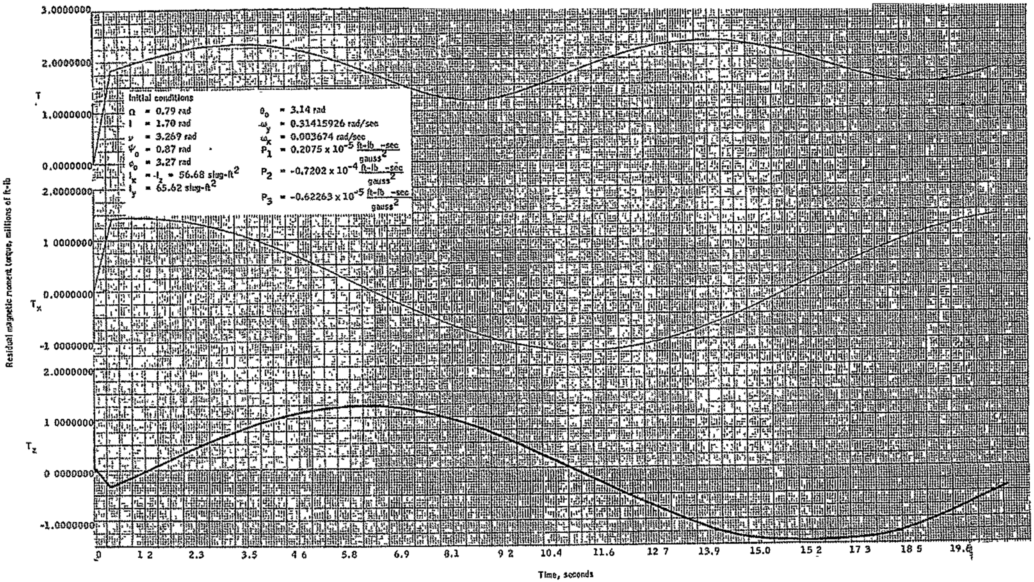

Figure 21. Torque on Spacecraft Due to Residual Magnetic Moments

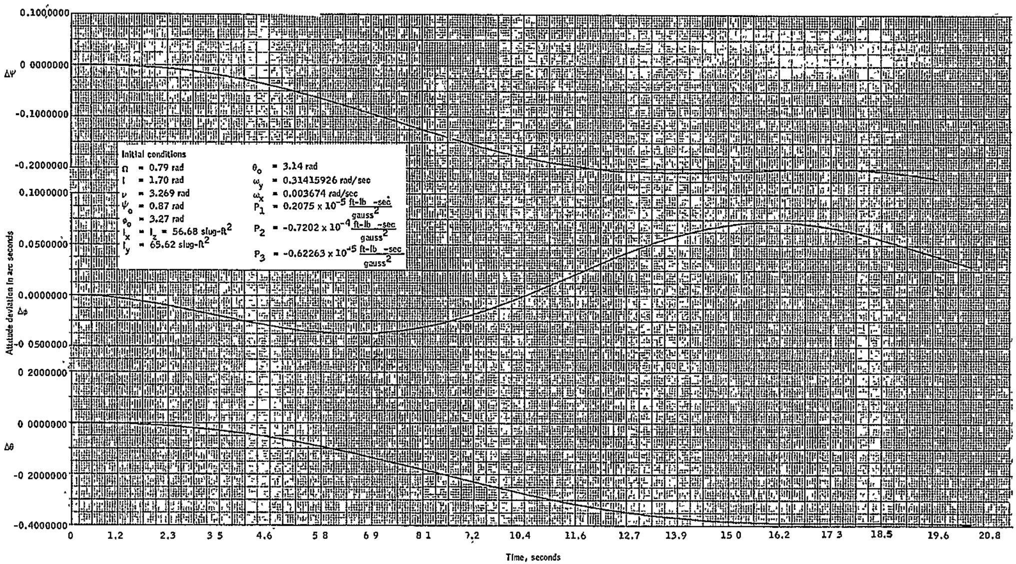

Figure 22. Attitude Deviation of Spacecraft Due to Residual Magnetic Moment Torque Relative to an Untorqued Spacecraft

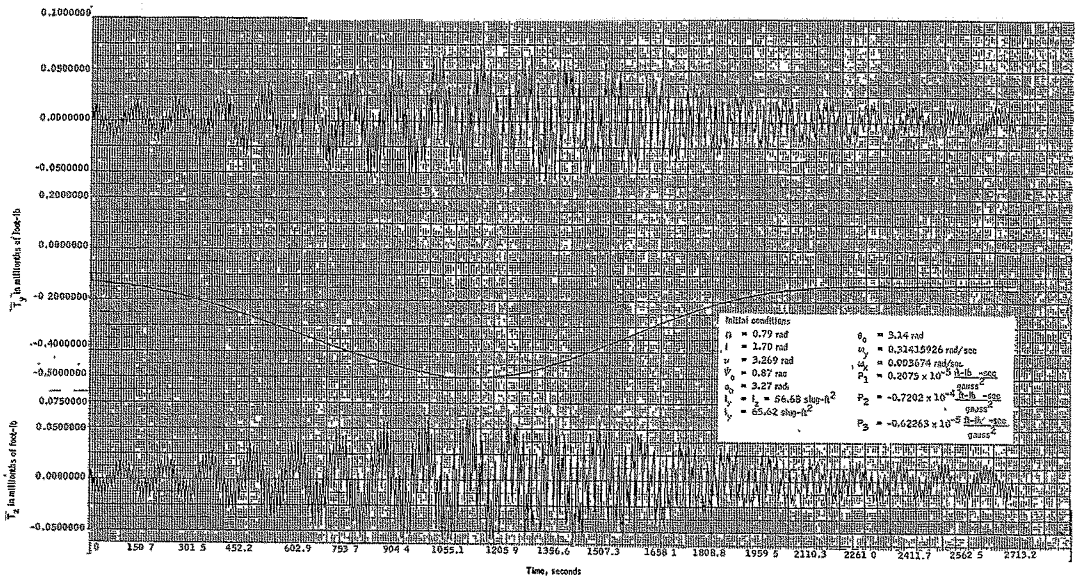

Figure 23. ARRS Eddy Current Torque on Half Orbit

Eddy current loss torque: The analysis of the eddy current loss effect consisted of comparison of the spherical model effect with the ARRS configuration model and effect of torque over one orbit period. Initially, the three coefficients for the ARRS model were evaluated using the baseline dimensions of the vehicle and static conductivity of aluminum at 20°C. The quantities used are

$\tau = 0.0254$ cm	$h = 111.8$ cm
$\varepsilon = 0.0254$ cm	$d = 55.9$ cm
$W = 55.9$ cm	$L_2 = 43.1$ cm
$L = 101.1$ cm	$\sigma C^{-2} = 2.83 \times 10^{-11} \dfrac{\sec^2}{\text{ohm - cm}^3}$

The results of the evaluation are

$$\left.\begin{aligned} P_1 &= 2.075 \times 10^{-6} \ \frac{\text{ft-lb-sec}}{G^2} \\ P_2 &= -7.20 \times 10^{-5} \ \frac{\text{ft-lb-sec}}{G^2} \\ P_3 &= -6.226 \times 10^{-6} \ \frac{\text{ft-lb-sec}}{G^2} \end{aligned}\right\} \text{ARRS model coefficients}$$

Figure 23 is a plot of the ARRS configuration eddy current torque using the evaluated coefficients for a one-half orbit simulation. The y-component of the torque does not possess cyclic variation at the spin rate. However, the z-component does exhibit variation of torque at the spin frequency and the precession frequency. The spin vector precession frequency is present because the equation contains two coefficients that are different, mainly because P_2 is greater than P_1. From Equation (5), the term $[-P_2(\omega_z H_x^2 - \omega_x H_x H_z)]$ modulates at the precession frequency and dominates the term $[-P_1(\omega_z H_z^2 - \omega_y H_y H_z)]$, and H_x and H_z modulate at the spin frequency. Correlation of the effect of the torques on the attitude can be made by comparing Figures 24 and 25. The attitude deviation, $\Delta\theta$, does not possess a cyclic variation, but $\Delta\Psi$ and $\Delta\phi$ possess a cyclic variation at the spin frequency. Only at 2700 seconds does the precession frequency variation become perceptible. The deviation in θ at 2700 seconds is 3500 arc sec and $\Delta\Psi$ and $\Delta\phi$ have a peak-to-peak of 37.5 arc sec.

Comparison of the two eddy current models was made using the following coefficients:

$$K = 0.25 \times 10^{-5} \ \frac{\text{ft-lb-sec}}{G^2}$$

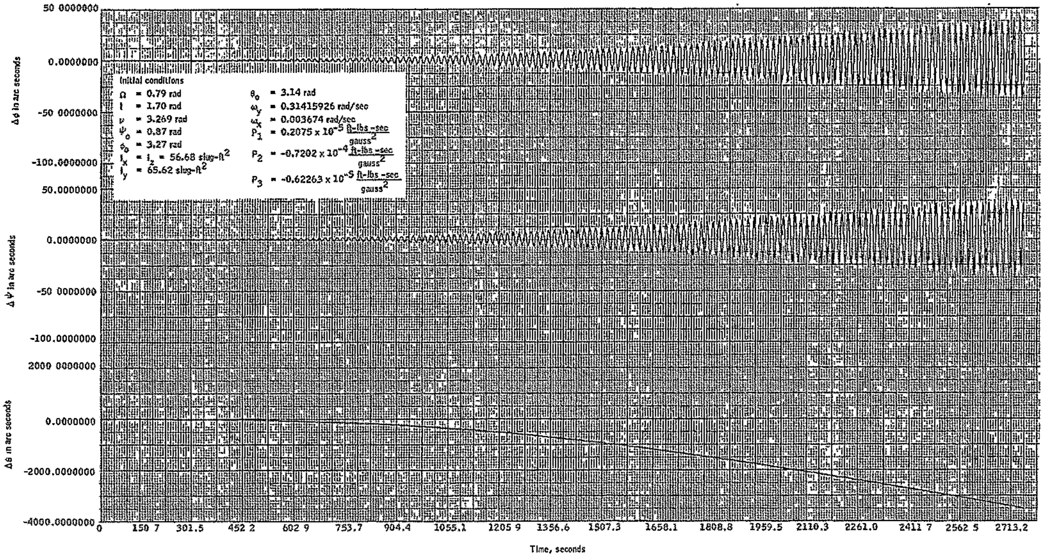

Figure 24. Attitude Deviation Due to ARRS Eddy Current Torque Relative to an Untorqued Spacecraft

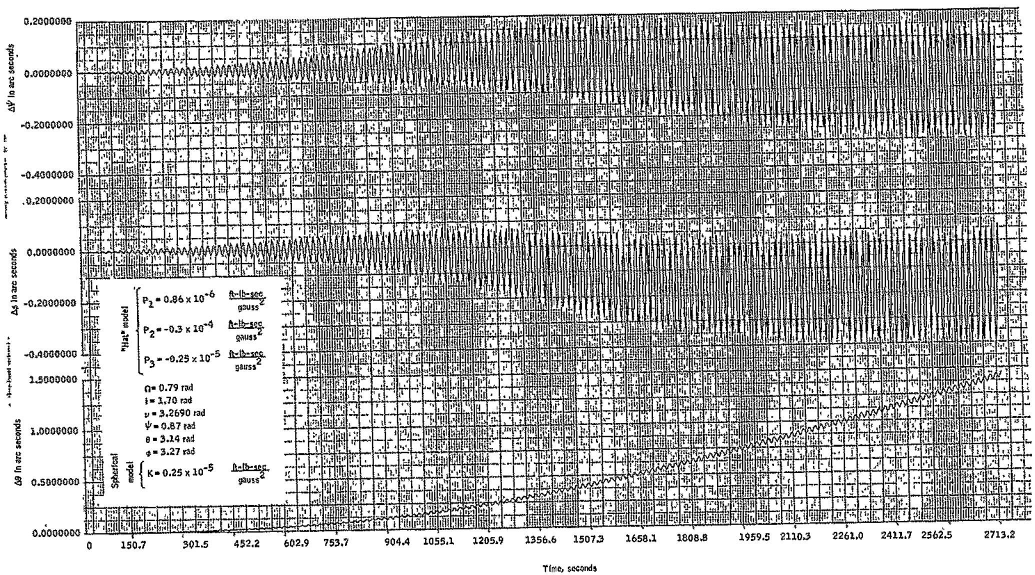

Figure 25. Comparison of "Hat" Configuration -- Eddy Current Model to Spherical Eddy Current Model

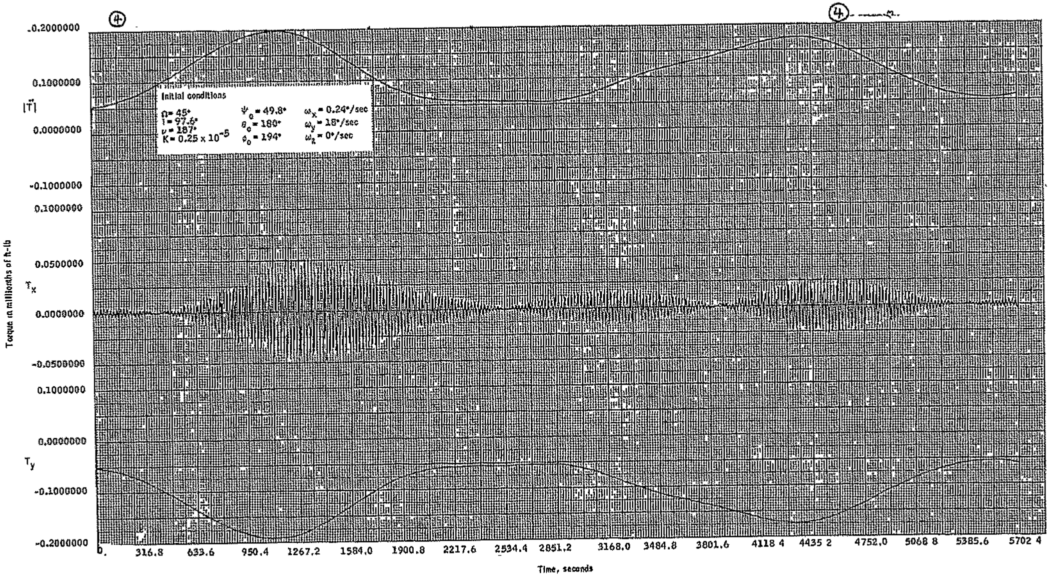

Figure 26. Torque on a Spherical Spacecraft Due to Eddy Current Losses

$$P_1 = 0.86 \times 10^{-6} \frac{\text{ft-lb-sec}}{G^2}$$

$$P_2 \doteq -0.3 \times 10^{-4} \frac{\text{ft-lb-sec}}{G^2}$$

$$P_3 = -0.25 \times 10^{-5} \frac{\text{ft-lb-sec}}{G^2}$$

The coefficient for the y-component torque is made equal where P_1 and P_2 are scaled according to the ratios of the evaluated coefficients. Figure 25 is a plot of the Δ (Δ attitude) due to the different effect of the two models. The result for Δ $(\Delta\theta)$ at 2700 seconds is 1.4 seconds, and $\Delta(\Delta\phi)$ and $\Delta(\Delta\Psi)$ are about 0.4 second peak-to-peak at 2700 seconds. For the given values of the coefficients, the differences suggest that the spherical model is adequate for the data-reduction algorithm.

The simulation results for the spherical model over 4752 seconds are illustrated in Figures 26 and 27. The loss constant used in these results is

$$0.25 \times 10^{-5} \frac{\text{ft-lb-sec}}{G^2}$$

In conclusion, the ARRS model representation must be retained in the real-world simulation. The spherical model proves adequate for use in the data-reduction algorithm.

Solar pressure torque: The analysis of the solar pressure torque consisted of a half-orbit simulation and a short-term simulation. As a result of these simulations, it was necessary to modify the solar pressure torque computer program to improve the running time. The results of the long-term and short-term simulation are presented in Figures 28, 29, 30, and 31. The torque plot in Figure 28 shows that T_x and T_y are cyclic and remain periodic throughout the 2700-second simulation. The constant total torque is expected because the sun direction relative to the spacecraft is approximately constant in direction over the one-half orbit simulation. Correlation of the effect on attitude with the torque is made by observing Figures 28 and 29. The difference in $\Delta\theta$ relative to an untorqued vehicle at 2700 seconds is +100 arc sec. The torque and $\Delta\phi$ difference does not possess the cyclic nature of the torques but $\Delta\Psi$ exhibits a peak-to-peak of 1.25 arc sec at the spin frequency at 2700 seconds of time. The results show that the cyclic torque can essentially be replaced by the mean of the torque over the spin period.

Displaying the solar pressure torque and difference in attitude for 300 seconds reveals the details of the torque and attitude differences. The cyclic effect is seen now in all three of the attitude differences, but most promounced in $\Delta\Psi$. Time average of the torque over the spin period on further observation is possible. The magnitude of the solar pressure torque is essentially constant over the simulation time of both cases.

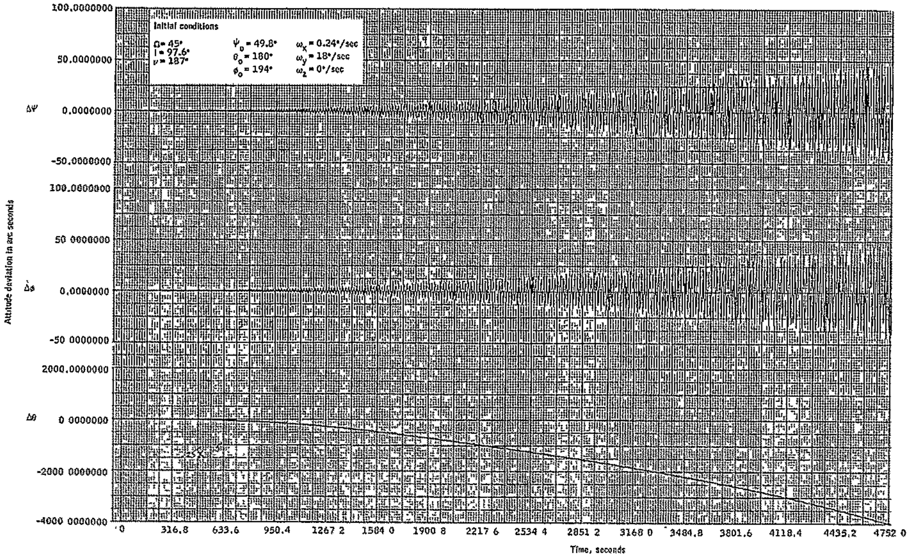

Figure 27. Attitude Deviation in the Spherical Spacecraft Due to Eddy Current Losses Relative to an Untorqued Spacecraft

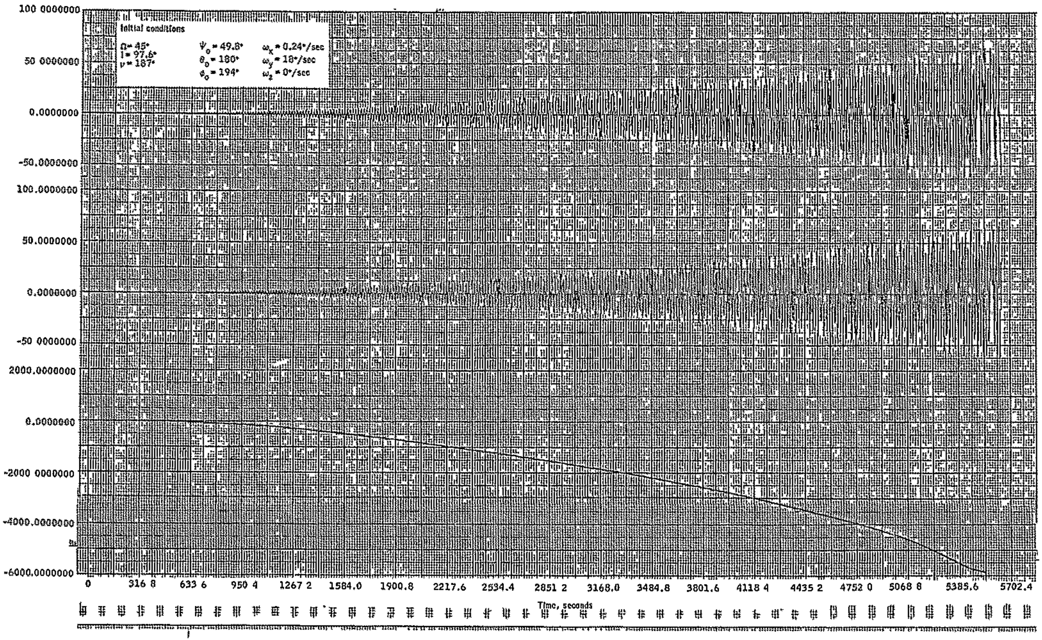

Figure 28. Torque on Spacecraft Due to Solar Pressure

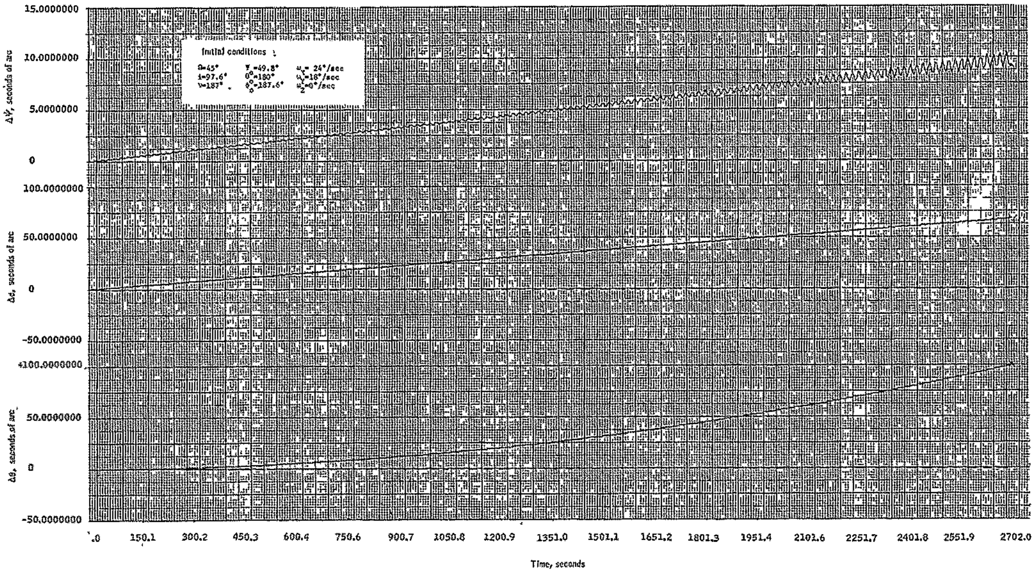

Figure 29. Attitude Deviation Due to Solar Pressure

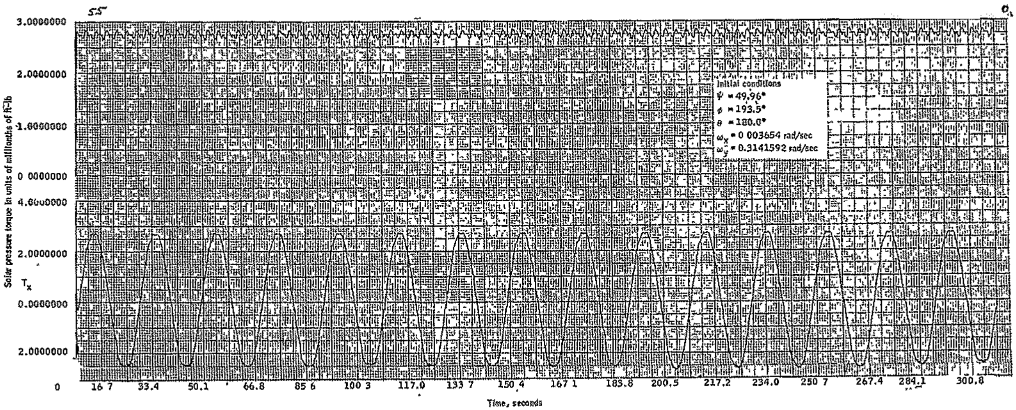

Figure 30. Torque Resulting From Solar Pressure
Effect on Spacecraft

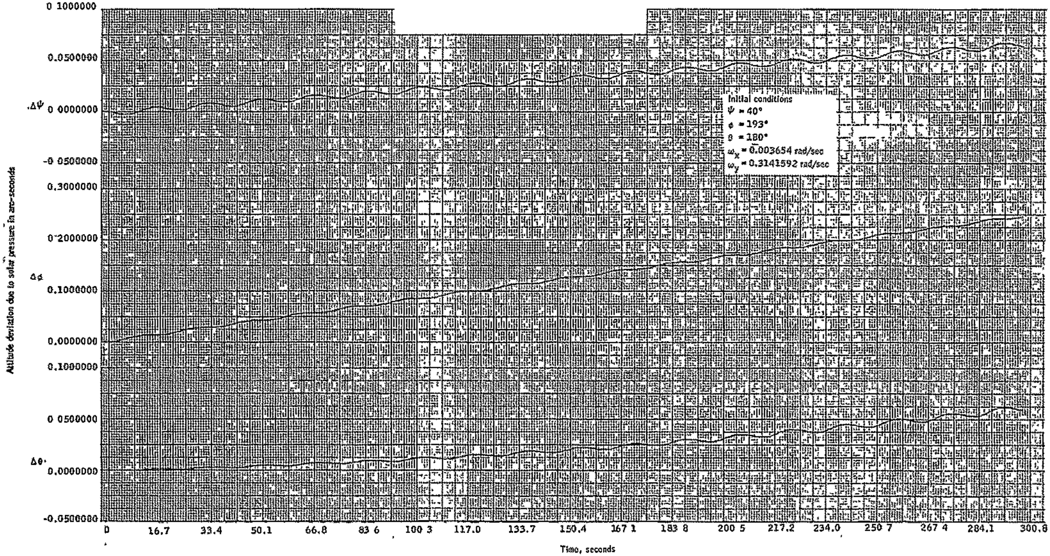

Figure 31. Attitude Deviation of the Spacecraft Due to Solar Pressure Effect Relative to an Untorqued Spacecraft

The computer program of the solar pressure torque was found to be very slow. This slowness of execution is due to integration over the spacecraft cylinder, to account for the shadowing, and is required for each integration step. Three approaches to remedy the execution time were considered: (1) remove the effect of cylinder torque and consider only torque due to solar panels; (2) compute and store torque due to the spacecraft cylinder for one or two spin periods; and (3) compute torque due to solar panels normally and add cylinder torque based on the store of torque data for all subsequent spin periods.

Approach 1 was tried unsuccessfully; approach 2 was successful, as shown in Figure 32.

Comparing the results in Figures 29 and 32, the attitude difference for the modified solar pressure torque at 2700 seconds is

$\Delta\theta$ = +97.2 arc sec

$\Delta\phi$ = +74.0 arc sec

$\Delta\Psi$ = +10.0 arc sec with a 1.25 arc sec variation

and the correct model gives

$\Delta\theta$ = +100 arc sec

$\Delta\phi$ = +67.5 arc sec

$\Delta\Psi$ = +9.0 arc sec with a 1.25 arc sec variation at the spin frequency

Based on these results, the modified solar pressure will be used in the real-world simulation.

Aerodynamic pressure torque: The analysis of the aerodynamic solar pressure consisted of a one-orbit and 20-second simulation to determine the effect on the attitude relative to an untorqued vehicle. Figures 34 and 35 are the plots of the results. In Figure 33, the y-component of torque is zero; the x-component is cyclic at spin frequency and possesses two nulls in one orbit. The y-component torque is zero because the vehicle is symmetric about the spin axis, causing the center of pressure moment about y to be zero. Two nulls occur because the vehicle is inertially fixed and angle of attack of the body y axis passes through zero twice due to the orbit motion. Figure 34 substantiates that the angle of attack changes direction relative to the aerodynamic stream velocity, because the $\Delta\theta$ difference is initially retarded and then is aided. This demonstrates that the attitude deviation due to aerodynamic pressure will remain bounded for a greater elapsed time than the deviation due to the other torques.

Figures 35 and 36 illustrate the results of the 20-second simulation. Based on these results, it is recommended that this torque be used in the real-world simulation, but not the data-reduction algorithm.

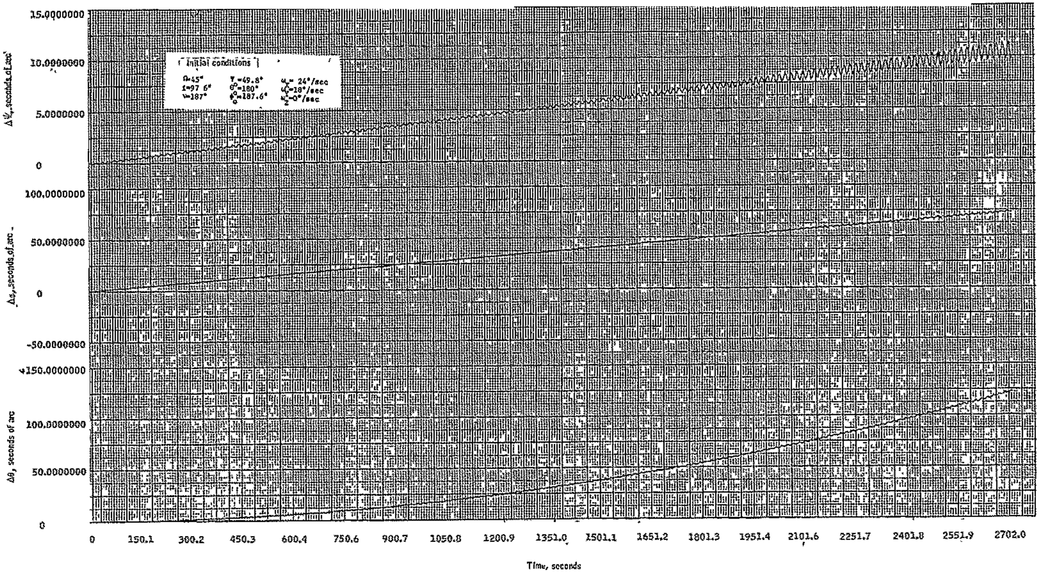

Figure 32. Attitude Deviation Resulting From Modified Solar Pressure

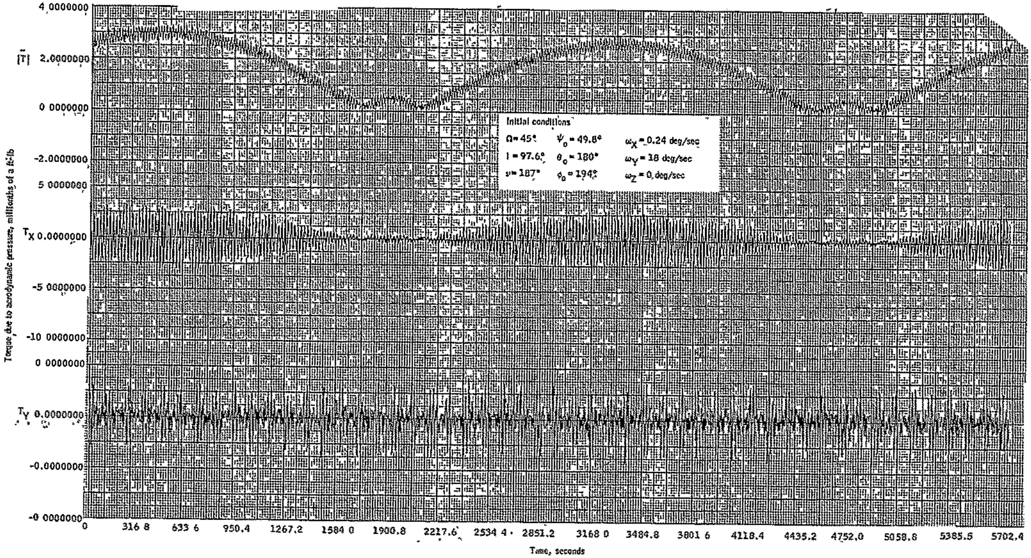

Figure 33. Torque on a Spacecraft Due to Aerodynamic Pressure Relative to an Untorqued Spacecraft, One-orbit Simulation

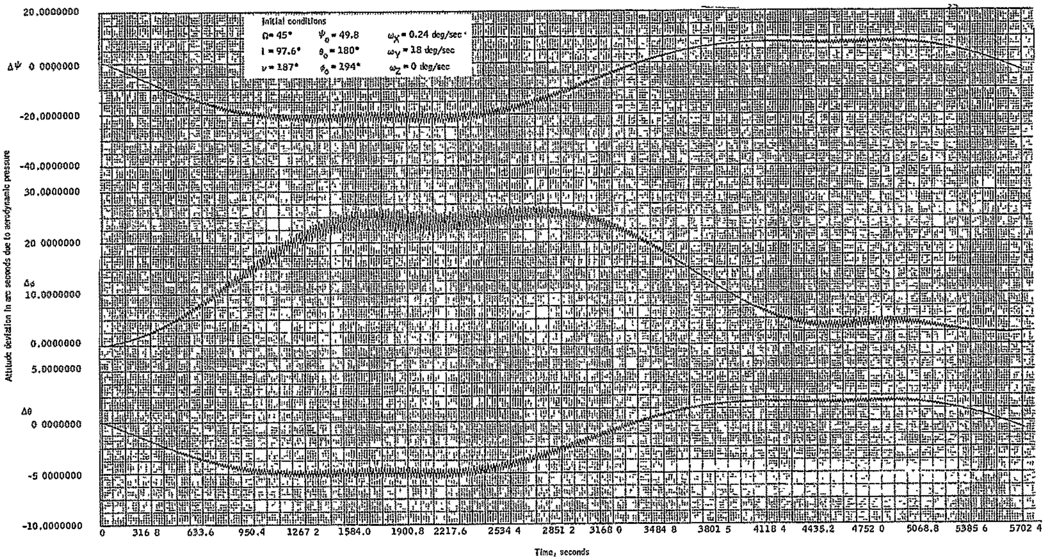

Figure 34. Attitude Deviation of Spacecraft Due to Aerodynamic Pressure Relative to an Untorqued Spacecraft, One-orbit Simulation

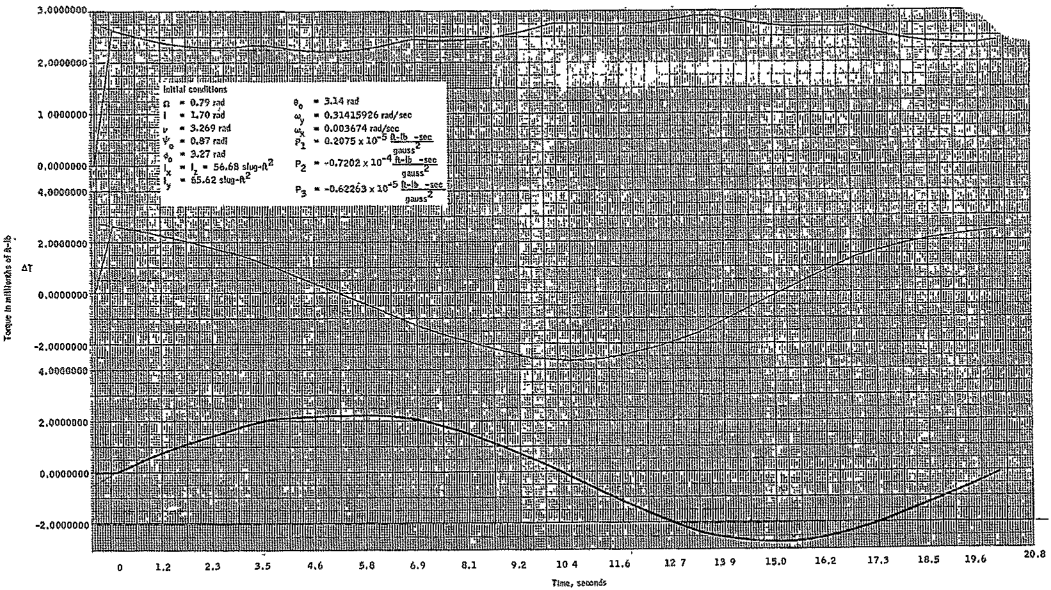

Figure 35. Torque on Spacecraft due to Aerodynamic Pressure, 20-Second Simulation

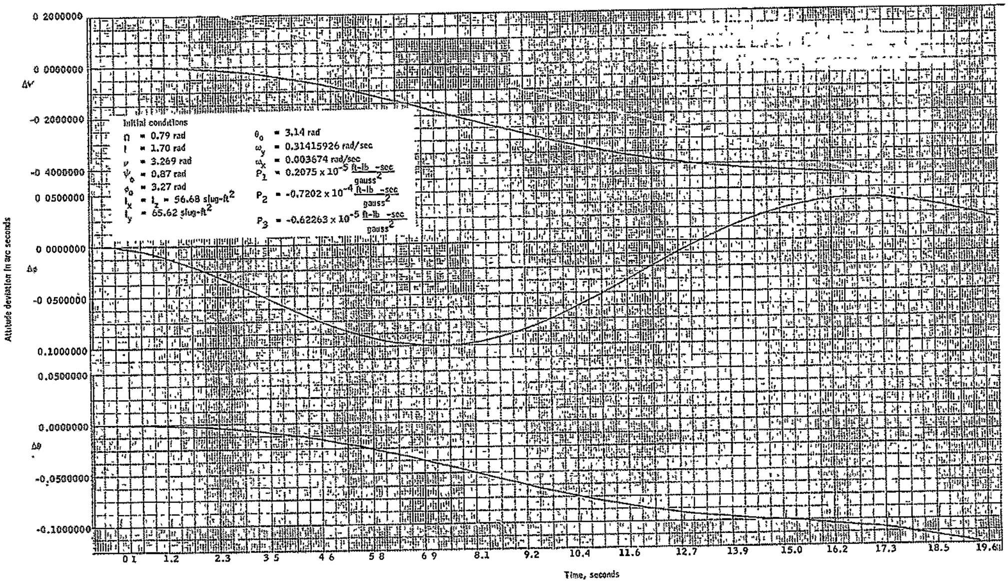

Figure 36. Attitude Deviation of Spacecraft Due to Aerodynamic Pressure Relative to an Untorqued Spacecraft, 20-Second Simulation

Gravity gradient torque: Two computer runs were made over an interval of about one third of an orbit (30 minutes). Of the two runs, two different sets of initial conditions were used. Since the torque is very dependent on spacecraft attitude, a worst-case attitude orientation of the spin vector (5°) relative to the orbit normal was used as initial conditions.

Figures 37 and 38 present the results of a run where spacecraft spin attitude is about 0.5° from the orbit normal. The long-term effect of the torque despins the vehicle, causing three arc sec deviation in the angle, θ, at 1800 seconds time lapse. Theta is the angle generated by the spin of the spacecraft and is the major attitude error contributor to the tangent height error.

Figures 39 and 40 present the results of another third of an orbit time run where the initial conditions place the spin axes of the spacecraft about 5° from the orbit normal. At 1800 seconds time lapse, the θ deviation is 12.5 arc sec. The $\Delta\theta$ variation over a spin period is about 1.5 arc sec at 1900 seconds. Figure 40 also plots the torque for T_x and T_z (y-axis is the spin axis) and $|\vec{T}|$. The torque is zero twice per orbit because the vehicle is inertially stabilized. This causes the angle between spacecraft local vertical and the principal y-axis to pass through 90° twice due to motion in the orbit. Comparing the results, Figures 37 and 39 show that the gravity gradient torque is very sensitive to the initial conditions. The maximum value of the torque in Figure 40 is about twice that in Figure 37 with the initial condition difference of about 5°.

For the given initial conditions, the results of the gravity gradient simulation indicate that for long-term attitude prediction of half orbit the gravity gradient must be included. However, for shorter periods (20 to 50 seconds of prediction) the torque can be deleted from the data reduction algorithm. For the first set of initial conditions, attitude prediction can be accurate to 3 arc sec over 1800 seconds of time when the gravity gradient torque is deleted.

Correlation of Figures 37 and 40 show that the cyclic torque at the spin frequency is attenuated significantly. At 3400 seconds the peak-to-peak variation is 2.5 arc sec in $\Delta\theta$, and 10 arc sec in $\Delta\phi$ and $\Delta\Psi$. A time average of the torque over one spin period can be made to simplify the torque equation.

Torque model linearity analysis: An analysis was conducted to show that each of the five torques affects the spacecraft attitude linearly. The analysis consisted of computing the attitude deviation due to the individual torques relative to an untorqued spacecraft, computing the attitude deviation due to the combined torques relative to an untorqued spacecraft, and summing the individual attitude deviations to compare with the combined attitude deviation. The results of the analysis are presented in Tables 1, 2, and 3. The initial conditions used for the analysis are

$\Omega = 0.79$ rad	$I_x = I_z = 56.68$ slug-ft^2
$i = 1.70$ rad	$I_y = 65.62$ slug-ft^2
$\nu = 3.2690$ rad	$\omega_x = 0.003674$ rad/sec
$\Psi = 0.87$ rad	$\omega_y = 0.314159$ rad/sec
$\theta = 3.14$ rad	
$\phi = 3.27$ rad	

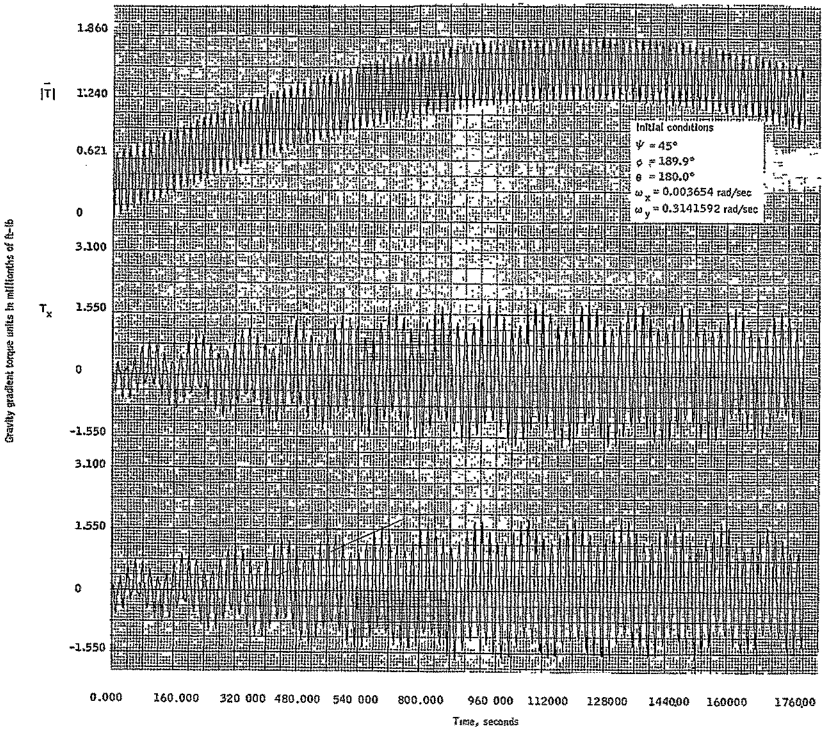

Figure 37. Torque due to Gravity Gradient Effect on Spacecraft

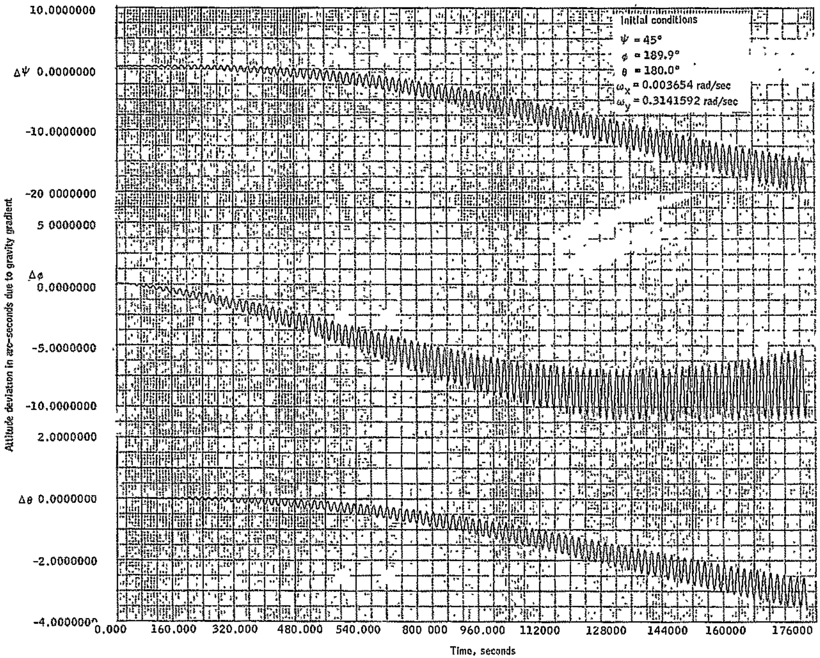

Figure 38. Attitude Deviation of Spacecraft Due to Gravity Gradient Relative to an Untorqued Spacecraft

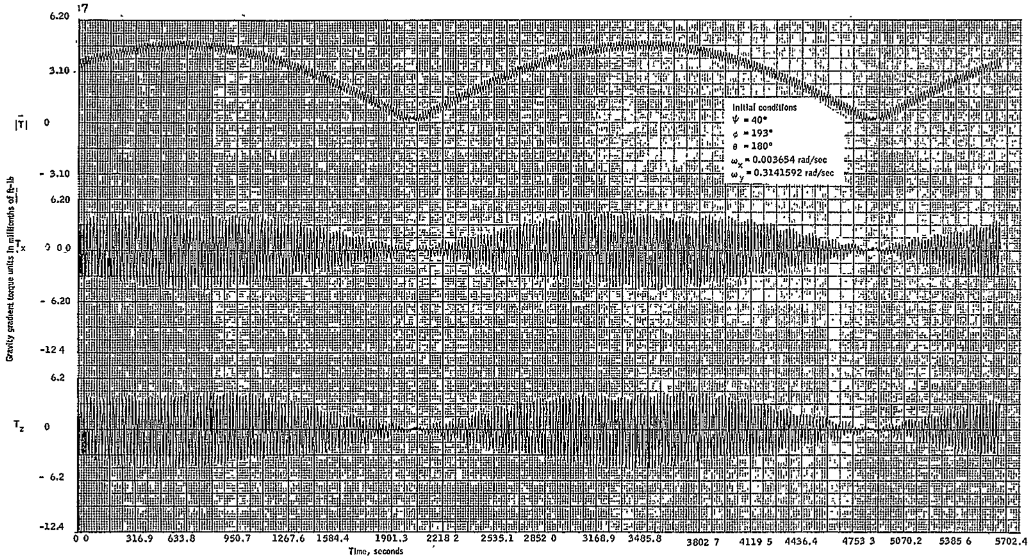

Figure 39. Torque on Spacecraft Due to Gravity Gradient

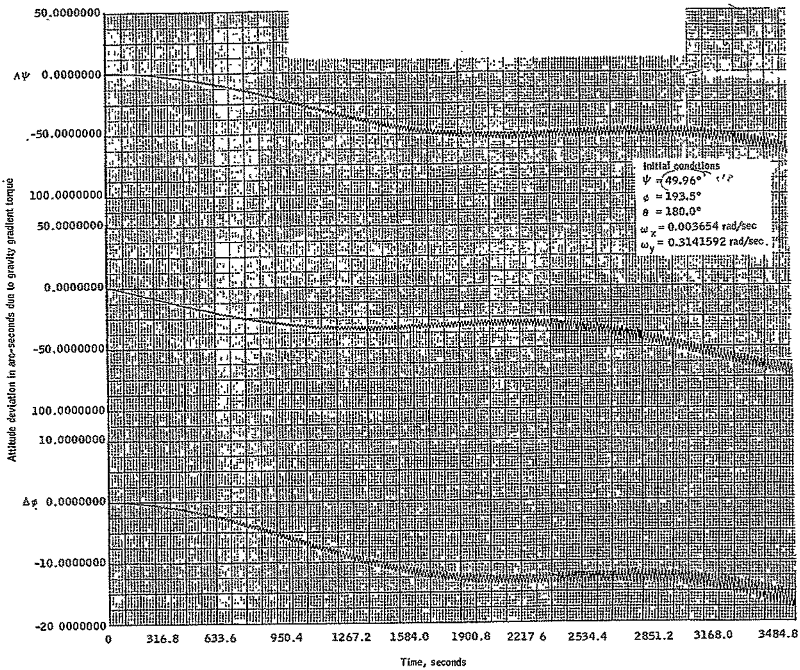

Figure 40. Attitude Deviation of Spacecraft Due to Gravity Gradient Relative to an Untorqued Spacecraft

FOLDOUT FRAME

TABLE 2. - LINEARITY ANALYSIS RESULTS FOR DELTA THETA - $\Delta\theta$

Time (minutes)	Magnetic Moment (sec of arc)	Aerodynamic Pressure (sec of arc)	Solar Pressure (sec of arc)	Gravity Gradient (sec of arc)	Eddy Current (Flat Config) (sec of arc)	Sum of $\Delta\theta$ (sec of arc)	$\Delta\theta$ Combined (sec of arc)	Difference (sec of arc)
.0	.0000000E-80	.0000000E-80	.0000000E-80	.0000000E-80	.0000000E-80	.000000E-80	.000000E-80	.000000E-80
.5	-.6110532E 00	.1957821E-01	.2651172E-01	.1994989E-01	-.1868848E 00	-.731898E 00	-.732005E 00	.107288E-03
1.0	-.1116870E 01	.2274322E-01	.6843273E-01	.1559705E-01	-.7515320E 00	-.176163E 01	-.176201E 01	.377425E-03
1.5	-.1688269E 01	.1590167E-01	.1963090E 00	.5569990E-01	-.1700689E 01	-.312105E 01	-.312199E 01	.944521E-03
2.0	-.2216227E 01	.4033851E-01	.3515246E 00	.1300342E 00	-.3056184E 01	-.474146E 01	-.474310E 01	.163615E-02
2.5	-.2787239E 01	.6129614E-01	.4490516E 00	.1427203E 00	-.4832513E 01	-.696668E 01	-.696932E 01	.263240E-02
3.0	-.3327271E 01	.2521468E-01	.6076238E 00	.1092234E 00	-.7025866E 01	-.961108E 01	-.961486E 01	.378191E-02
3.5	-.3828438E 01	.4747510E-02	.9085849E 00	.2013608E 00	-.9671617E 01	-.123854E 01	-.123906E 02	.527054E-02
4.0	-.4395880E 01	.5349091E-01	.1166899E 01	.3229686E 00	-.1282648E 02	-.156700E 02	-.156857E 02	.665188E-02
4.5	-.4926436E 01	.5646433E-01	.1335096E 01	.2852951E 00	-.1647171E 02	-.197213E 02	-.197296E 02	.824588E-02
5.0	-.5490988E 01	-.2007825E-01	.1638814E 01	.2440044E 01	-.2059679E 02	-.242250E 02	-.242358E 02	.107901E-01
5.5	-.5911527E 01	-.2886132E-01	.2105917E 01	.4031515E 00	-.2531009E 02	-.287392E 02	-.287523E 02	.130685E-01
6.0	-.6524696E 01	.4049369E-01	.2441730E 01	.5352157E 00	-.3067650E 02	-.341838E 02	-.341989E 02	.151430E-01
6.5	-.7011110E 01	.5456383E-02	.2690823E 01	.4412617E 00	-.3660185E 02	-.404754E 02	-.404937E 02	.182390E-01
7.0	-.7563141E 01	-.1032114E 00	.3167582E 01	.4182100E 00	-.4310589E 02	-.472064E 02	-.472273E 02	.208139E-01
7.5	-.7923276E 01	-.7641997E-01	.3782497E 01	.6510871E 00	-.5041002E 02	-.539761E 02	-.540006E 02	.244311E-01
8.0	-.8590702E 01	.2207072E-02	.4173333E 01	.7578543E 00	-.5852344E 02	-.621807E 02	-.622081E 02	.273126E-01
8.5	-.9024484E 01	-.8763926E-01	.4523185E 01	.8040641E 00	-.6724249E 02	-.712274E 02	-.712589E 02	.315428E-01
9.0	-.9576222E 01	-.1991579E 00	.5201861E 01	.8434236E 00	-.7670416E 02	-.806343E 02	-.806691E 02	.348534E-01
9.5	-.9857808E 01	-.1286847E 00	.5930104E 01	.9205954E 00	-.8722813E 02	-.903639E 02	-.904029E 02	.389917E-01
10.0	-.1058531E 02	-.6078652E-01	.6301495E 01	.9737492E 00	-.9869557E 02	-.102006E 03	-.102049E 03	.427314E-01
10.5	-.1095285E 02	-.2147913E 00	.6840491E 01	.7673264E 00	-.1107810E 03	-.114341E 03	-.114388E 03	.472069E-01
11.0	-.1146643E 02	-.2977712E 00	.7731536E 01	.8927617E 00	-.1238633E 03	-.127003E 03	-.127055E 03	.513758E-01
11.5	-.1171767E 02	-.1778841E 00	.8540675E 01	.1194181E 01	-.1382904E 03	-.140460E 03	-.140516E 03	.561271E-01
12.0	-.1250262E 02	-.1475675E 00	.9008636E 01	.1187481E 01	-.1537333E 03	-.156207E 03	-.156269E 03	.617981E-01
12.5	-.1278384E 02	-.3522124E 00	.9677800E 01	.9529352E 00	-.1697856E 03	-.172291E 03	-.172358E 03	.668253E-01
13.0	-.1328630E 02	-.3831114E 00	.1075121E 02	.1151327E 01	-.1871761E 03	-.188913E 03	-.188984E 03	.710862E-01
13.5	-.1351098E 02	-.2184085E 00	.1160808E 02	.1452746E 01	- 2062073E 03	-.206876E 03	-.206953E 03	773702E-01
14.0	-.1434059E 02	-.2557754E 00	.1211843E 02	.1324797E 01	-.2261527E 03	-.227306E 03	-.227388E 03	.817537E-01
14.5	-.1451992E 02	-.4842997E 00	.1301855E 02	.1134344E 01	-.2467456E 03	-.247597E 03	-.247687E 03	.896011E-01
15.0	-.1485919E 02	-.4413230E 00	.1425369E 02	.1403577E 01	-.2691022E 03	-.268845E 03	-.268940E 03	.945670E-01
15.5	-.1525119E 02	-.2502676E 00	.1512557E 02	.1678726E 01	-.2933196E 03	-.292017E 03	-.292118E 03	.100820E-00
16.0	-.1608757E 02	-.3880773E 00	.1573074E 02	.1438645E 01	-.3181444E 03	-.317431E 03	-.317530E 03	.107288E-00
16.5	-.1617556E 02	-.5950826E 00	.1686303E 02	.1301316E 01	-.3438144E 03	-.342421E 03	-.342533E 02	.112408E-00
17.0	-.1659947E 02	-.4632712E 00	.1822973E 02	.1635013E 01	-.3716945E 03	-.368892E 03	-.369012E 08	.119519E-00
17.5	-.1695628E 02	-.2742291E 00	.1909153E 02	.1855016E 01	-.4015016E 03	-.397786E 03	-.397911E 03	.125313E-00
18.0	-.1771680E 02	-.5171605E 00	.1983590E 00	.1510743E 01	-.4314099E 03	-.428297E 03	-.478433E 03	.135796E-00
18.5	-.1777275E 02	-.6874256E 00	.2121134E 02	.1446646E 01	-.4625294E 03	-.458312E 03	-.458451E 03	.139536E-00
19.0	-.1820506E 02	-.4432236E 00	.2267003E 02	.1834294E 01	-.4963121E 03	-.490458E 03	-.490602E 03	.146403E 00
19.5	-.1864607E 02	-.3262792E 00	.2350409E 02	.1930332E 01	-.5317113E 03	-.525249E 03	-.525404E 03	.154465E 00
20.0	-.1930875E 02	-.6303660E 00	.2444204E 02	.1538331E 01	-.5668034E 03	-.560762E 03	-.560924E 03	.161730E 00
20.5	-.1934634E 02	-.6910903E 00	.2605933E 02	.1562732E 01	-.6035512E 03	-.595966E 02	-.596133E 03	.166910E 00
21.0	-.1980929E 02	-.3825904E 00	.2756560E 02	.1992559E 01	-.6433620E 03	-.633996E 03	-.634170E 03	.174022E 00
21.5	-.2032409E 02	-.3803831E 00	.2838456E 02	.1934103E 01	-.6840526E 03	-.674438E 03	-.674625E 03	.186437E 00
22.0	-.2067059E 02	-.7124866E 00	.2955672E 02	.1522636E 01	-.7241467E 03	-.714650E 03	- 714841E 03	.190881E 00
22.5	-.2093220E 02	-.6580456E 00	.3140064E 02	.1648562E 01	- 7664782E 03	-.755019E 03	-.755215E 03	.195970E 00
23.0	-.2145430E 02	-.8144469E 00	.3286212E 02	.2066742E 01	-.8120656E 03	-.798905E 03	-.799108E 03	.203020E 00
23.5	-.2200856E 02	-.4353147E 00	.3374090E 02	.1863783E 01	-.8574606E 03	-.844300E 03	-.844516E 03	.215834E 00
24.0	-.2243915E 02	-.7539612E 00	.3518411E 02	.1467245E 01	-.9021775E 03	-.888719E 03	-.888939E 03	.219941E 00
24.5	-.2266703E 02	-.5686284E 00	.3722584E 02	.1705027E 01	- 9498322E 03	-.934037E 03	-.934260E 03	.222946E 00
25.0	-.2314566E 02	-.2383028E 00	.3860235E 02	.2072597E 01	-.1000592E 04	-.983301E 03	-.983535E 03	.234256E 00
25.5	-.2371557E 02	-.4861387E 00	.3958349E 02	.1724584E 01	-.1049864E 04	-.103278E 04	-.103300E 04	.245395E 00
26.0	-.2404869E 02	-.7487501E 00	.4132688E 02	.1379882E 01	-.1098707E 04	-.108080E 04	-.108104E 04	.244158E 00
26.5	-.2429732E 02	-.4242183E 00	.4347110E 02	.1740524E 01	-.1151385E 04	-.113089E 04	-.113115E 04	.251780E 00
27.0	-.2489528E 02	-.1666341E 00	.4478934E 02	.2007380E 01	-.1206289E 04	-.118455E 04	-.118482E 04	.266933E 00
27.5	-.2545980E 02	-.5281344E 00	.4592429E 02	.1524690E 01	-.1258521E 04	-.123706E 04	-.123734E 04	.275731E 00
28.0	-.2572367E 02	-.6924391E 00	.4798408E 02	.1272440E 01	-.1310979E 04	-.128814E 04	-.128841E 04	.272512E 00
28.5	-.2610406E 02	-.2528163E 00	.5016395E 02	.1744631E 01	-.1368154E 04	-.134260E 04	-.134288E 04	.281402E 00
29.0	-.2670554E 02	-.1104456E 00	.5142720E 02	.1868862E 01	-.1426140E 04	-.139966E 04	-.139996E 04	.297804E 00
29.5	-.2724741E 02	-.5570410E 00	.5277297E 02	.1280042E 01	-.1480485E 04	-.145425E 04	-.145455E 04	.305894E 00
30.0	-.2748578E 02	-.8561217E 00	.5514517E 02	.1203622E 01	-.1536433E 04	-.150813E 04	-.150843E 04	.299896E 00
30.5	-.2798123E 02	-.7096373E-01	.5729284E 02	.1718821E 01	-.1597258E 04	-.156630E 04	-.156661E 04	.310462E 00
31.0	-.2856703E 02	-.7905604E-01	.5852464E 02	.1663215E 01	-.1657253E 04	-.162571E 04	-.162604E 04	.329559E 00
31.5	-.2907922E 02	-.5709885E 00	.6013856E 02	.1008940E 01	-.1713123E 04	-.168163E 04	-.168196E 04	.332594E 00
32.0	-.2932927E 02	-.3862383E 00	.6278383E 02	.1141517E 01	-.1772370E 04	-.173816E 04	-.173840E 04	.326800E 00
32.5	-.2991448E 02	.1026506E 00	.6485608E 02	.1064870E 01	-.1836205E 04	-.179950E 04	-.179984E 04	.345101E 00
33.0	-.3046569E 02	-.7878010E-01	.6600199E 02	.1297201E 01	-.1897261E 04	-.186032E 04	-.186068E 04	.366547E 00
33.5	-.3094255E 02	-.5182948E 00	.6808927E 02	.7958957E 00	-.1954622E 04	-.191720E 04	-.191756E 04	.361684E 00
34.0	-.3123909E 02	-.1973495E 00	.7088876E 02	.1101024E 01	-.2016903E 04	-.197635E 04	-.197671E 04	.358282E 00
34.5	-.3188910E 02	.2491235E 00	.7285217E 02	.1580112E 01	-.2083137E 04	-.204034E 04	-.204073E 04	.382437E 00
35.0	-.3239186E 02	-.1145837E 00	.7414012E 02	.1084900E 01	-.2144513E 04	-.210179E 04	-.210218E 04	.399113E 00
35.5	-.3285473E 02	-.4445031E 00	.7655592E 02	.6190537E 00	-.2203532E 04	-.215966E 04	-.216005E 04	.390407E 00
36.0	-.3320418E 02	-.5150126E-02	.7944731E 02	.1091368E 01	-.2268835E 04	-.222151E 04	-.222190E 04	.390928E 00
36.5	-.3389705E 02	.3500665E 00	.8127632E 02	.1463137E 01	-.2338885E 04	-.228767E 04	-.228809E 04	.421551E 00
37.0	-.3433433E 02	-.1699752E 00	.8276635E 02	.7693604E 00	-.2398013E 04	-.234896E 04	-.234942E 04	.433353E 00
37.5	-.3481771E 02	-.3595081E 00	.8553273E 02	.4987374E 00	-.2459189E 04	-.240834E 04	-.240876E 04	.421551E 00
38.0	-.3521835E 02	.1757380E 00	.8844745E 02	.1117791E 01	-.2527553E 04	-.247303E 04	-.247346E 04	.429889E 00
38.5	-.3593624E 02	.3920317E 00	.9014154E 02	.1313210E 01	-.2596758E 04	-.254085E 04	-.254132E 04	.467563E 00
39.0	-.3631107E 02	-.2394061E 00	.9191061E 02	.4880090E 00	-.2657670E 04	-.260181E 04	-.260228E 04	.470781E 00
39.5	-.3684028E 02	-.2724820E 00	.9500924E 02	.4533697E 00	-.2721396E 04	-.266305E 04	-.266350E 04	.453057E 00
40.0	-.3728571E 02	.3282714E 00	.9787677E 02	.1178915E 01	-.2792824E 04	-.273072E 04	-.273120E 04	.471180E 00
40.5	-.3799587E 02	.3077341E 00	.9946814E 02	.1068868E 01	-.2861034E 04	-.279909E 04	-.279960E 04	.511582E 00
41.0	-.3834088E 02	-.3236735E 00	.1016044E 03	.2667437E 00	-.2923487E 04	-.286028E 04	-.286078E 04	.503090E 00
41.5	-.3892851E 02	-.1906977E 00	.1049734E 03	.4955799E 00	-.2990182E 04	-.292303E 04	-.292432E 04	.491779E 00
42.0	-.3940873E 02	.4388091E 00	.1077330E 03	.1267075E 01	-.3064544E 04	-.299451E 04	-.299503E 04	.520134E 00
42.5	-.4009593E 02	.1606877E 00	.1096859E 03	.6217987E 00	-.3132885E 04	-.306271E 04	-.306327E 04	.557869E 00
43.0	-.4043527E 02	-.4194667E 00	.1118236E 03	.1331160E 00	-.3195551E 04	-.312445E 04	-.312499E 04	.541285E 00
43.5	-.4108163E 02	-.1197035E 00	.1154111E 03	.6297515E 00	-.3265592E 04	-.319075E 04	-.319129E 04	.534970E 00
44.0	-.4159989E 02	.4271917E 00	.1179316E 03	.1279920E 01	-.3341987E 04	-.326394E 04	-.326451E 04	.574851E 00
44.5	-.4223753E 02	-.442943[illegible]-01	.1190064E 03	.5942555E 00	-.3409581E 04	-.333166E 04	-.333227E 04	.604064E 00
45.0	-.4259890E 02	-.516332 E 00	.1225758E 03	.1008817E 00	-.3473912E 04	-.339435E 04	-.339493E 04	.579112E 00

FOLDOUT FRAME 2

PRECEDING PAGE BLANK NOT FILMED.

FOLDOUT FRAME

TABLE 3. - LINEARITY ANALYSIS RESULTS FOR DELTA PSI - $\Delta\psi$

Time (minutes)	Magnetic Moment (sec of arc)	Aerodynamic Pressure (sec of arc)	Solar Pressure (sec of arc)	Gravity Gradient (sec of arc)	Eddy Current (sec of arc)	Sum of $\Delta\psi$ (sec of arc)	$\Delta\psi$ Combined (sec of arc)	Difference (sec of arc)
.0	.0000000E-80	.0000000E-80	.0000000E-80	.0000000E-80	.0000000E-80	.000000E-80	.000000E-80	.000000E-80
.5	-.4397795E 00	.1571730E 00	.4302730E-01	.9580432E-01	-.2089010E-02	-.145864E 00	-.145900E 00	.365211E-04
1.0	-.7648220E 00	.1878250E 00	.8968672E-01	.1104070E 00	-.4592325E-02	-.381495E 00	-.381635E 00	.139619E-03
1.5	-.1092383E 01	.1351465E 00	.3059074E 00	.2229209E 00	.1960644E-01	-.408602E 00	-.408901E 00	.299234E-03
2.0	-.1497920E 01	.3415309E 00	.4634184E 00	.6563951E 00	.6391801E-03	-.359363E-01	-.364650E-01	.529611E-03
2.5	-.1876209E 01	.4961463E 00	.4720116E 00	.9188722E 00	-.5172437E-01	-.409631E-01	-.417448E-01	.781672E-03
3.0	-.2098236E 01	.2222541E 00	.5752846E 00	.7732072E 00	.2010902E-01	-.507381E 00	-.508526E 00	.114509E-02
3.5	-.2348150E 01	.6622458E-01	.8202103E 00	.9572770E 00	.1067150E 00	-.397732E 00	-.399238E 00.	.150539E-02
4.0	-.2714850E 01	.4595166E 00	.9103870E 00	.1751041E 01	-.6262790E-01	-.343468E 00	.341412E 00	.205560E-02
4.5	-.2975121E 01	.4790367E 00	.9128904E 00	.2003741E 01	-.1429457E 00	.277601E 00	.274975E 00	.262581E-02
5.0	-.3049509E 01	-.1155171E 00	.1075512E 01	.1657590E 01	.1473809E 00	-.284632E 00	-.287844E 00	.321123E-02
5.5	-.3223718E 01	-.1761912E 00	.1311925E 01	.2100652E 01	.2017649E 00	.223433E 00	.219075E 00	.375857E-02
6.0	-.3496130E 01	.3624137E 00	.1348631E 01	.3183762E 01	-.2436844E 00	.115499E 01	.115029E 01	.470189E-02
6.5	-.3586321E 01	.1170681E 00	.1368283E 01	.3244446E 01	-.2156961E 00	.927780E 00	.922136E 00	.564354E-02
7.0	-.3482746E 01	-.7531609E 00	.1583434E 01	.2718157E 01	.4425762E 00	.508259E 00	.501939E 00	.632079E-02
7.5	-.3580793E 01	-.5415927E 00	.1787529E 01	.3601505E 01	.2245593E 00	.149121E 01	.148413E 01	.708103E-02
8.0	-.3711054E 01	.6750352E-01	.1785095E 01	.4825229E 01	-.5747355E 00	.239204E 01	.238350E 01	.853743E-02
8.5	-.3591712E 01	-.5519424E 00	.1837677E 01	.4528612E 01	-.1693723E 01	.205326E 01	.204337E 01	.989184E-02
9.0	-.3315834E 01	-.1494367E 01	.2088257E 01	.4026499E 01	.8336009E 00	.213816E 01	.212770E 01	.104528E-01
9.5	-.3322441E 01	-.9623151E 00	.2250625E 01	.5338854E 01	.6306592E-01	.336779E 01	.335637E 01	.114158E-01
10.0	-.3268244E 01	-.3990800E 00	.2225132E 01	.6526961E 01	-.1046673E 01	.403720E 01	.402352E 01	.136728E-01
10.5	-.2919751E 01	-.1465750E 01	.2317990E 01	.5746471E 01	.1372124E 00	.381616E 01	.380073E 01	.154311E-01
11.0	-.2484973E 01	-.2272483E 01	.2584691E 01	.5463982E 01	.1280730E 01	.457p95E 01	.455643E 01	.155185E-01
11.5	-.2399565E 01	-.1375734E 01	.2706125E 01	.7202866E 01	-.4111266E 00	.572257E 01	.570570E 01	.168664E-01
12.0	-.2127398E 01	-.1008095E 01	.2671767E 01	.8132858E 01	-.1584833E 01	.608430E 01	.606397E 01	.203283E-01
12.5	-.1558865E 01	-.2489541E 01	.2814473E 01	.6874060E 01	.7855963E 00	.642573E 01	.640368E 01	.220505E-01
13.0	-.9906921E 00	-.2975446E 01	.3072468E 01	.6964861E 01	.1048359E 01	.771955E 01	.769825E 01	.212965E-01
13.5	-.8181090E 00	-.1729719E 01	.3159173E 01	.9057629E 01	-.1316124E 01	.835286E 01	.832939E 01	.234651E-01
14.0	-.3055556E 00	-.1719903E 01	.3125337E 01	.9491391E 01	-.2027398E 01	.856387E 01	.853516E 01	.287063E-01
14.5	.4432975E 00	-.3507100E 01	.3309556E 01	.7842398E 01	.1812041E 01	.990019E 01	.987065E 01	.295421E-01
15.0	.1110292E 01	-.3502129E 01	.3553909E 01	.8456638E 01	.1726316E 01	.113450E 02	.113175E 02	.275431E-01
15.5	.1358936E 01	-.1987069E 01	.3614054E 01	.1075945E 02	-.2719185E 01	.110262E 02	.109948E 02	.314132E-01
16.0	.2134285E 01	-.2596407E 01	.3598306E 01	.1035390E 02	-.1810246E 01	.116790E 02	.116414E 02	.384810E-01
16.5	.2983450E 01	-.4401695E 01	.3800158E 01	.8611901E 01	.3173170E 01	.141670E 02	.141296E 02	.373741E-01
17.0	.3706237E 01	-.3771235E 01	.4033234E 01	.9863665E 01	.1245014E 01	.150769E 02	.150428E 02	.340807E-01
17.5	.4012643E 01	-.2128648E 01	.4073240E 01	.1216689E 02	-.4588276E 01	.135350E 02	.134947E 02	.411828E-01
18.0	.5031423E 01	-.3453664E 01	.4071963E 01	.1077969E 02	-.9079437E 00	.155215E 02	.154719E 02	.496115E-01
18.5	.5904074E 01	-.5065765E 01	.4285886E 01	.9162257E 01	.4703840E 01	.189903E 02	.189453E 02	.449571E-01
19.0	.6634361E 01	-.3728738E 01	.4515570E 01	.1111004E 02	-.8556915E-01	.184466E 02	.184057E 02	.408981E-01
19.5	.7015206E 01	-.2374132E 01	.4533934E 01	.1288348E 02	-.5897527E 01	.161610E 02	.161077E 02	.532119E-01
20.0	.8192719E 01	-.4219894E 01	.4541426E 01	.1073657E 02	.8690081E 00	.201199E 02	.200582E 02	616740E-01
20.5	.9002500E 01	-.5409883E 01	.4769196E 01	.9492750E 01	.6098738E 01	.239533E 02	.239018E 02	.514832E-01
21.0	.9691478E 01	-.3353306E 01	.5055830E 01	.1212785E 02	-.2514160E 01	.209577E 02	.209094E 02	.482890E-01
21.5	.1012825E 02	-.2526589E 01	.4994841E 01	.1382782E 02	-.6677714E 01	.189106E 02	.188429E 02	.677109E-01
22.0	.1139044E 02	-.4828930E 01	.5003147E 01	.1023320E 02	.3595569E 01	.253934E 02	.253197E 02	.737773E-01
22.5	.1205123E 02	-.5370259E 01	.5255184E 01	.9621096E 01	.6922490E 01	.284797E 02	.284235E 02	.562481E-01
23.0	.1265963E 02	-.2798375E 01	.5487552E 01	.1267377E 02	-.5511607E 01	.225110E 02	.224521E 02	588582E-01
23.5	.1312897E 02	-.2701560E 01	.5450150E 01	.1256034E 02	-.6479526E 01	.219584E 02	.218736E 02	-.847428E-01
24.0	.1439308E 02	-.5224791E 01	.5455967E 01	.9318054E 01	.7108654E 01	.311112E 02	.310271E 02	.847202E-01
24.5	.1483219E 02	-.4914591E 01	.5750927E 01	.9580608E 01	.6655686E 01	.319048E 02	.318460E 02	588653E-01
25.0	.1534130E 02	-.2083812E 01	.5974236E 01	.1274575E 02	-.8872914E 01	.231046E 02	.230319E 02	.726760E-01
25.5	.1581954E 02	-.2805193E 01	.5893387E 01	.1148775E 02	-.4876438E 01	.255191E 02	.254151E 02	.103962E-00
26.0	.1700713E 02	-.5365524E 01	.5901800E 01	.8080518E 01	.1126087E 02	.368938E 02	.368008E 02	.929923E-01
26.5	.1717230E 02	-.3925464E 01	.6257412E 01	.9553640E 01	.3985151E 01	.330431E 02	.329800E 02	.631459E-01
27.0	.1759317E 02	-.1290778E 01	.6460684E 01	.1230938E 02	-.1209158E 02	.229809E 02	.228901E 02	.907473E-01
27.5	.1806710E 02	-.2892125E 01	.6318550E 01	.9864098E 01	-.1557274E 01	.298004E 02	.296760E 02	.125338E 00
28.0	.1011519E 02	-.5225972E 01	.6340060E 01	.6635703E 01	.1536754E 02	.422385E 02	.421416E 02	.969627E-01
28.5	.1900658E 02	-.2658294E 01	.6782144E 01	.9335013E 01	-.2445801E 00	.322218E 02	.321529E 02	.688445E-01
29.0	.1935798E 02	-.515μ030E 00	.6939006E 01	.1136141E 02	-.1452790E 02	.226152E 02	.225012E 02	.113996E 00
29.5	.1982688E 02	-.2982691E 01	.6721333E 01	.7788471E 01	.3591847E 01	.349458E 02	.348016E 02	.144221E 00
30.0	.2063560E 02	-.4468712E 01	.6827384E 01	.5524204E 01	.1634682E 02	.448653E 02	.447686E 02	.967010E-01
30.5	.2034178E 02	-.1219986E 01	.7324794E 01	.8940643E 01	-.5841316E 01	.295459E 02	.294681E 02	.778803E-01
31.0	.2066379E 02	.1402204E 00	.7399300E 01	.9931218E 01	-.1549273E 02	.226418E 02	.224890E 02	.142779E 00
31.5	.2113329E 02	-.3095880E 01	.7100346E 01	.5368362E 01	.1043543E 02	.409725E 02	.408112E 02	.161387E 00
32.0	.2167405E 02	-.3427407E 01	.7334026E 01	.4505212E 01	.1535231E 02	.454404E 02	.453472E 02	.931663E-01
32.5	.2125025E 02	.2591636E 00	.7881088E 01	.8385272E 01	-.1235954E 02	.254162E 02	.253236E 02	.925998E-01
33.0	.2159046E 02	.5749693E 00	.7830641E 01	.8080295E 01	-.1434179E 02	.237346E 02	.235580E 02	.176587E 00
33.5	.2204107E 02	-.2987744E 01	.7503594E 01	.3185975E 01	.1646028E 02	.462122E 02	.460447E 02	.167501E 00
34.0	.2231706E 02	-.2177331E 01	.7874740E 01	.3676816E 01	.1200409E 02	.436943E 02	.436076E 02	.877886E-01
34.5	.2182001E 02	.1634581E 01	.8442496E 01	.7689027E 01	-.1913202E 02	.204550E 02	.203397E 02	.115266E 00
35.0	.2221675E 02	.6997037E 00	.8222396E 01	.5899653E 01	-.1056529E 02	.264733E 02	.262594E 02	.213907E 00
35.5	.2261136E 02	-.2795534E 01	.7915425E 01	.1170572E 01	.2172287E 02	.506247E 02	.504587E 02	.165959E 00
36.0	.2262684E 02	-.8160299E 00	.8455730E 01	.3120034E 01	.8135889E 01	.395345E 02	.394405E 02	.829365E-01
36.5	.2210436E 02	.2758335E 01	.8996343E 01	.6875980E 01	-.2532813E 02	.154069E 02	.152592E 02	.147733E 00
37.0	.2257835E 02	.3532747E 00	.8571809E 01	.3404149E 01	-.2980272E 01	.319473E 02	.317068E 02	.240521E 00
37.5	.2285234E 02	-.2537567E 01	.8350563E 01	-.4749055E 00	.2535938E 02	.536497E 02	.533037E 02.	.156052E 00
38.0	.2260813E 02	.5476463E 00	.9079078E 01	.2891533E 01	-.2147602E 01	.329788E 02	.328970E 02	.817808E-01
38.5	.2209670E 02	.3490447E 01	.9526460E 01	.5964938E 01	-.3002613E 02	.110524E 02	.108611E 02	.191267E 00
39.0	.2262000E 02	-.2611012E 00	.8892224E 01	.1016844E 01	.6216298E 01	.384843E 02	.282238E 02	.260427E 00
39.5	.2271612E 02	-.2235687E 01	.8825291E 01	-.1600280E 01	.2658474E 02	.542902E 02	.541521E 02	.138113E 00
40.0	.2221326E 02	.1790528E 01	.9741561E 01	.3017989E 01	-.1246863E 02	.242947E 02	.242067E 02	.880283E-01
40.5	.2180346E 02	.3283133E 01	.9943286E 01	.4468464E 01	-.2790308E 02	.115024E 02	.112629E 02	.239471E 00
41.0	.2226686E 02	-.1127051E 01	.9193613E 01	-.1086248E 01	.1623392E 02	.454811E 02	.452108E 02	.270319E 00
41.5	.2313272E 02	-.1914176E 01	.9355807E 01	-.2088744E 01	.2472322E 02	.522088E 02	.520951E 02	.113735E 00
42.0	.2138462E 02	.2792867E 01	.1043385E 02	.3492601E 01	-.2417872E 02	.139252E 02	.138194E 02	.105803E 00
42.5	.2110924E 02	.2509952E 01	.1030030E 02	.2962285E 01	-.2266708E 02	.142147E 02	.139248E 02	.289927E 00
43.0	.2140094E 02	-.2205557E 01	.9491473E 01	-.2741536E 01	.2617245E 02	.521778E 02	.519105E 02	.257283E 00
43.5	.2106745E 02	-.1598923E 01	.9956204E 01	-.1866489E 01	.1928617E 02	.468444E 02	.407591E 02	.852862E-01
44.0	.2016256E 02	.3042667E 01	.1102997E 02	.3784110E 01	-.3208825E 02	.594106E 01	.579160E 01	.149459E 00
44.5	.2001631E 02	.1183280E 01	.1059241E 02	.1539370E 01	-.1402582E 02	.193056E 02	.189698E 02	.335717E-00
45.0	.2021892E 02	-.3361850E 01	.9806263E 01	-.3808740E 01	.3407915E 02	.578337E 02	.575971E 02	.236678E 00

PRECEDING PAGE BLANK NOT FILMED.

FOLDOUT FRAME 2

FOLDOUT FRAME 1

FOLDOUT FRAME 2

TABLE 1. - LINEARITY ANALYSIS RESULTS FOR DELTA PHI - $\Delta\phi$

Time (minutes)	Magnetic Moment (sec of arc)	Aerodynamic (sec of arc)	Solar Pressure (sec of arc)	Gravity Gradient (sec of arc)	Eddy Current (sec of arc)	Sum of $\Delta\phi$ (sec of arc)	$\Delta\phi$ Total (sec of arc)	Difference (sec of arc)
.0	.0000000E-80	.0000000E-80	.0000000E-80	.0000000E-80	.0000000E-80	.000000E-80	.000000E-80	.000000E-80
.5	.9402975E-01	-.1042553E-01	.8939385E 00	.8006104E 00	.2425723E-02	.178058E 01	.178057E 01	.108965E 04
1.0	.2313532E 00	.5183824E-01	.1628265E 01	.1548594E 01	-.8704966E-02	.345135E 01	.345131E 01	.320907E-04
1.5	.4802944E 00	-.6786504E-01	.2387129E 01	.2081792E 01	-.4081747E-02	.487727E 01	.487723E 01	.414305E-04
2.0	.7792118E 00	-.2057030E 00	.3304293E 01	.2712989E 01	.3471533E-01	.662551E 01	.662542E 01	.859743E-04
2.5	.9901223E 00	.5638027E-02	.4139415E 01	.3709093E 01	-.7236097E-02	.883703E 01	.883694E 01	.888282E-04
3.0	.1272573E 01	.1297000E 00	.4849258E 01	.4454766E 01	-.7305391E-01	.106332E 02	.106331E 02	.145127E-03
3.5	.1712284E 01	-.2178138E 00	.5665545E 01	.4655845E 01	.4206374E-01	.118579E 02	.118578E 02	.103936E-03
4.0	.2128537E 01	-.2898208E 00	.6593307E 01	.5294222E 01	.1203863E 00	.138466E 02	.138465E 02	.117107E-03
4.5	.2434524E 01	.1849630E 00	.7371127E 01	.6488193E 01	-.9592801E-01	.163829E 02	.193827E 02	.175900E-03
5.0	.2870759E 01	.2515463E 00	.8083325E 01	.7047082E 01	-.1742164E 00	.180785E 02	.180782E 02	.287978E-03
5.5	.3464198E 01	-.2933357E 00	.8959611E 01	.6922990E 01	.1929507E 00	.192464E 02	.192463E 02	.159496E-03
6.0	.3956021E 01	-.1515645E 00	.9865632E 01	.7694973E 01	.2020975E 00	.215672E 02	.215671E 02	.732818E-04
6.5	.4333549E 01	.5701691E 00	.1059695E 02	.9027143E 01	-.3212955E 00	.242065E 02	.242063E 02	.226311E-03
7.0	.4921236E 01	.4504754E 00	.1133224E 02	.9213312E 00	-.2465621E 00	.256707E 02	.256703E 02	.381377E-03
7.5	.5612272E 01	-.2013676E 00	.1225244E 02	.8843665E 01	.4780840E 00	.269851E 02	.269851E 02	-.119745E-05
8.0	.6130247E 01	.2855599E 00	.1312298E 02	.9873314E 01	.1901917E 00	.296023E 02	.296025E 02	-.251338E-03
8.5	.6553291E 01	.1179708E 01	.1382402E 02	.1122528E 02	-.7199255E 00	.320624E 02	.320622E 02	.144887E-03
9.0	.7280699E 01	.7318930E 00	.1460560E 02	.1085871E 02	-.1435280E 00	.333334E 02	.333331E 02	.320428E-03
9.5	.7992238E 01	.1448170E 00	.1553848E 02	.1042286E 02	.8883316E 00	.349867E 02	.349872E 02	-.506747E-03
10.0	.8487658E 01	.1067654E 01	.1636959E 02	.1179613E 02	-.3844608E-01	.376826E 02	.376835E 02	-.940210E-03
10.5	.8928213E 01	.2007195E 01	.1705768E 02	.1299996E 02	-.1284881E 01	.397082E 02	.397081E 02	.469387E-04
11.0	.9759541E 01	.1170552E 01	.1788582E 02	.1200528E 02	.2285493E 00	.410497E 02	.410497E 02	.221522E-04
11.5	.1041444E 02	.8116966E 00	.1881500E 02	.1169126E 01	.1355391E 01	.430878E 02	.430894E 02	-.163268E-02
12.0	.1084551E 02	.2206468E 01	.1961119E 02	.1344054E 02	-.6277545E 00	.454760E 02	.454781E 02	-.213104E-02
12.5	.1130015E 02	.2894481E 01	.2031034E 02	.1413075E 02	-.1683504E 01	.469612E 02	.469614E 02	-.200568E-03
13.0	.1216028E 02	.1801968E 01	.2116642E 02	.1268820E 02	.9726853E 00	.487896E 02	.487904E 02	-.790054E-03
13.5	.1268078E 02	.1839958E 01	.2208231E 02	.1270171E 02	.1733759E 01	.510385E 02	.510422E 02	-.369774E-02
14.0	.1301723E 02	.3678172E 01	.2285387E 02	.1479484E 02	-.1714327E 01	.526298E 02	.526336E 02	-.379365E-02
14.5	.1346047E 02	.3905677E 01	.2357167E 02	.1475746E 02	-.1828212E 01	.538671E 02	.538675E 02	-.438134E-03
15.0	.1428780E 02	.2650679E 01	.2444221E 02	.1298280E 02	.2143340E 01	.565063E 02	.565087E 02	-.242405E-02
15.5	.1460190E 02	.3240715E 01	.2534352E 02	.1352392E 02	.1794269E 01	.585043E 02	.585114E 02	-.704978E-02
16.0	.1484553E 02	.5279258E 01	.2600970E 02	.1567470E 02	-.2982259E 01	.589169E 02	.589224E 02	-.550404E-02
16.5	.1523214E 02	.5002959E 01	.3683633E 01	.1489234E 02	-.1473581E 01	.604902E 02	.604909E 02	-.713660E-03
17.0	.1596334E 02	.3728703E 01	.2771015E 02	.1299882E 02	.3702797E 01	.641038E 02	.641092E 02	-.540645E-02
17.5	.1601431E 02	.4993867E 01	.2860394E 02	.1423801E 02	.1237819E 01	.650880E 02	.650999E 02	-.119124E-01
18.0	.1617182E 02	.6993672E 01	.2935415E 02	.1618924E 02	-.4391696E 01	.643172E 02	.643247E 02	-.697387E-02
18.5	.1646768E 02	.6144414E 01	.3000803E 02	.1462375E 02	-.3610886E 00	.669728E 02	.669739E 02	-.113874E-02
19.0	.1704742E 02	.5034912E 01	.3097013E 02	.1287206E 02	.5481161E 01	.714057E 02	.714161E 02	-.104682E-01
19.5	.1680553E 02	.7053656E 01	.3186002E 02	.1492270E 02	-.3114453E 00	.703305E 02	.703476E 02	-.170975E-01
20.0	.1689111E 02	.8719628E 01	.3261458E 02	.1637250E 02	-.5650937E 01	.689469E 02	.689546E 02	-.767819E-02
20.5	.1706049E 02	.7288575E 01	.3335069E 02	.1406653E 02	.1721431E 01	.734967E 02	.734989E 02	-.313559E-02
21.0	.1745534E 02	.6555218E 01	.3422520E 02	.1275392E 02	.7153516E 01	.781432E 02	.781616E 02	-.183916E-01
21.5	.1692814E 02	.9247234E 01	.3512671E 02	.1555293E 02	-.2710256E 01	.741448E 02	.741672E 02	-.224564E-01
22.0	.1696270E 02	.1035176E 02	.3587549E 02	.1628083E 02	-.6354425E 01	.731164E 02	.731234E 02	-.704948E-02
22.5	.1701032E 02	.8399080E 01	.3658976E 02	.1336381E 02	.4868591E 01	.802316E 02	.802360E 02	-.444923E-02
23.0	.1713706E 02	.8480199E 01	.3748487E 02	.1305780E 02	.7143099E 01	.833030E 02	.833314E 02	-.283387E-01
23.5	.1640754E 02	.1145231E 02	.3840550E 02	.1617282E 02	-.5846291E 01	.765919E 02	.766188E 02	-.269190E-01
24.0	.1642220E 02	.1179057E 02	.3912927E 02	.1599031E 02	-.6030859E 01	.773015E 02	.773063E 02	-.485181E-02
24.5	.1634320E 02	.9448873E 01	.3981331E 02	.1267758E 02	.8991084E 01	.872740E 02	.872833E 02	-.927792E-02
25.0	.1621217E 02	.1053043E 02	.4075695E 02	.1363673E 02	.5828878E 01	.869652E 02	.870056E 02	-.404221E-01
25.5	.1534855E 02	.1353955E 02	.4169447E 02	.1682014E 02	-.9405963E 01	.779967E 02	.780259E 02	-.291402E-01
26.0	.1538256E 02	.1295183E 02	.4236724E 02	.1559203E 02	-.4320477E 01	.820741E 02	.820753E 02	-.118377E-02
26.5	.1517104E 02	.1069243E 02	.4304578E 02	.1250832E 02	.1212972E 02	.935473E 02	.935667E 02	-.194005E-01
27.0	.1483-12E 02	.1262107E 02	.4404827E 02	.1457035E 02	.2930935E 01	.890007E 02	.890543E 02	-.535928E-01
27.5	.1391680E 02	.1538289E 02	.4498814E 02	.1752415E 02	-.1287938E 02	.789326E 02	.789603E 02	-.276578E-01
28.0	.1400791E 02	.1377473E 02	.4558096E 02	.1519172E 02	-.5664736E 02	.879888E 02	.879857E 02	.319769E-02
28.5	.1367348E 02	.1194146E 02	.4628265E 02	.1278413E 02	.1448581E 02	.991675E 02	.992018E 02	-.342608E-01
29.0	.1317078E 02	.1466031E 02	.4736349E 02	.1590703E 02	-.1632626E 01	.894690E 01	.895353E 02	-.663150E-01
29.5	.1229363E 02	.1686984E 02	.4827747E 02	.1830416E 02	-.1560773E 02	.801374E 02	.801587E 02	-.213559E-01
30.0	.1245026E 02	.1428303E 02	.4877802E 02	.1497093E 02	.4738391E 01	.952206E 02	.952194E 02	.114319E-02
30.5	.1301196E 02	.1318462E 02	.4953475E 02	.1362256E 02	.1540894E 02	.103763E 03	.103817E 03	-.541179E-01
31.0	.1139498E 02	.1655578E 02	.5070406E 02	.1765946E 02	-.7695169E 01	.886191E 02	.886956E 02	-.763407E-01
31.5	.1062660E 02	.1791111 02	.5155054E 02	.1916917E 02	-.7683610E 02	.823943E 02	.824038E 02	-.943051E-02
32.0	.1083994E 02	.1456383E 02	.5195709E 02	.1512717E 02	.1082833E 02	.103316E 03	.103322E 03	-.590790E-02
32.5	.1029729E 02	.1441417E 02	.5281378E 02	.1510239E 02	.1431160E 02	.106939E 03	.107018E 03	-.783536E-01
33.0	.9605473E 01	.1822081E 02	.5406715E 02	.1980285E 03	-.1483170E 02	.868646E 02	.869457E 02	-.811359E-01
33.5	.9038335E 01	.1817593E 02	.5476592E 02	.1979610E 02	-.1366427E 02	.881120E 02	.881104E 02	-.161590E-02
34.0	.9231472E 01	.1466810E 02	.5512656E 02	.1577316E 02	.1703818E 02	.111837E 03	.111857E 03	-.200031E-01
34.5	.8572046E 01	.1562562E 02	.5613089E 02	.1725645E 02	.1075534E 02	.106340E 03	.108446E 03	-.105492E 00
35.0	.7837867E 01	.1958056E 02	.5744505E 02	.2227597E 02	-.2238540E 02	.847540E 02	.848321E 02	-.780506E-01
35.5	.7486378E 01	.1799540E 02	.5794126E 02	.2059622E 02	-.8105704E 01	.959136E 02	.959015E 02	.120839E-01
36.0	.7619887E 01	.1466881E 02	.5828913E 02	.1699423E 02	.2256362E 02	.120146E 03	.120188E 03	-.427140E-01
36.5	.6830768E 01	.1681687E 02	.5949499E 02	.2006780E 02	.4516261E 01	.107727E 03	.107860E 03	-.133081E 00
37.0	.6132448E 01	.2017571E 02	.6076089E 02	.2449878E 02	-.2583496E 02	.857329E 02	.857956E 02	-.627299E-01
37.5	.5951910E 01	.1743466E 02	.6107391E 02	.2160733E 02	-.3565580E 00	.105711E 03	.105692E 03	.190643E-01
38.0	.5984177E 01	.1465559E 02	.6149114E 02	.1884207E 02	.2653682E 02	.127510E 03	.127585E 03	-.749438E-01
38.5	.5068400E 01	.1798705 02	.6291117E 02	.2346898E 02	-.4372105E 01	.105063E 03	.105221E 03	-.157257E 00
[illegible]	.4465197E 01	.2030656 02	.6404067E 02	.2676232E 02	-.2688109E 02	.886937E 03	.887336E 02	-.398682E-01
39.5	.4440650E 01	.1659539E 02	.6416655E 02	.2285878E 02	.9148236E 01	.117210E 03	.117190E 03	.192370E-01
40.0	.4341965E 01	.1472772E 02	.6472121E 02	.2133054E 02	.2810458E 02	.133226E 03	.133343E 03	-.116622E 00
40.5	.3354253E 01	.1897899E 02	.6634089E 02	.2714785E 02	-.1404950E 02	.101772E 03	.101934E 03	-.161360E 00
41.0	.2897492E 01	.2000756E 02	.6726843E 02	.2898312E 02	-.2493304E 02	.942236E 02	.942345E 02	-.109725E-01
41.5	.3025767E 01	.1560960E 02	.6722804R 02	.2437066E 02	.1972493E 02	.129959E 03	.129950E 03	.900078E-02
42.0	.2786583E 01	.1498622E 02	.6800669E 02	.2443365E 02	.2650530E 02	.136720E 03	.136887E 03	-.166329E 00
42.5	.1813250E 01	.1976992E 02	.6977694E 02	.3093323E 02	-.2345989E 02	.988334E 02	.989858E 02	-.152313E 00
43.0	.1568521E 01	.1934779E 02	.7043046E 02	.3108001E 02	-.1960696E 02	.102820E 03	.102799E 03	.211836E-01
43.5	.1856163E 01	.1463111E 02	.7027367E 02	.2615374E 02	.3047332E 02	.143388E 03	.143403E 03	-.152856E-01
44.0	.1449247E 01	.1581837E 02	.7142599E 02	.2842850E 02	.1800776E 02	.135130E 03	.135335E 03	-.205518E 00
44.5	.6407724E 00	.2035176E 00	.2035176E 02	.3464280E 02	-.3157138E 02	.972627E 02	.973890E 02	-.126315E 00
45.0	.6717942E 00	.1842033E 02	.7351728E 02	.3298155E 02	-.1077990E 02	.114811E 03	.114758E 03	.529430E-01

$$P_1 = 0.20754 \times 10^{-5} \frac{\text{ft-lb-sec}}{G^2}$$

$$P_2 = -0.72022 \times 10^{-4} \frac{\text{ft-lb-sec}}{G^2}$$

$$P_3 = -0.62263 \times 10^{-5} \frac{\text{ft-lb-sec}}{G^2}$$

$$M_x = M_y = M_z = 5.17095 \times 10^{-6} \frac{\text{ft-lb}}{G}$$

$$\text{Solar pressure constant} = 1 \times 10^{-7} \frac{\text{lb}}{\text{ft}^2}$$

$$\text{Aerodynamic pressure constant} = 2 \times 10^{-7} \frac{\text{lb}}{\text{ft}^2}$$

In Tables 1, 2, and 3 the last column is the difference between the sum of the attitude deviations for each torque and the attitude deviation for the combined torques. The difference, $\Delta(\Delta\theta)$, is approximately 0.5 arc sec after 45 minutes in orbit. This number could very well be attributed to roundoff (10th and 11th decimal place). The results demonstrate the linear additivity of the torques on the spacecraft attitude.

Conclusions and recommendations: The results of the torque model analysis are summarized in Table 4. Table 4 condenses the result of Table 1, 2, and 3 for $\Delta\theta$ deviation due to each of the torques relative to an untorqued vehicle. Comparing these results for long-term prediction over 45 minutes shows that the residual magnetic moment, solar pressure, and eddy current torques must be included in the prediction model. On the other hand, short-term prediction over 5 minutes can be accomplished with only the eddy current and residual magnetic moment torque. Figure 40 indicates a significant effect due to the gravity gradient. However, the alignment of the body y-axis to the orbit normal is greater than the prescribed control limits of the vehicle, whereas, the results presented in Table 2 for the gravity gradient represent an alignment of the body axis within the control limits, which is the more realistic case. Attitude prediction using only the residual magnetic moment eddy and current torque is shown in Table 5. It is of interest to simplify the torque models where possible to improve the speed of the attitude prediction and model integration. The results of the torque analysis demonstrate that the torque can be time averaged over the spin period of 20 seconds without detriment to the attitude prediction and can enhance the use of large step sizes in the numerical integration of the prediction model. The following paragraphs examine the time-average torque approach.

TABLE 4. - SUMMARY OF $\Delta\theta$ ATTITUDE DEVIATION DUE TO EACH TORQUE AND THE TOTAL TORQUE

	(1)	(2)	(3)	(4)	(5)	
Time, min	Residual magnetic moment, $\Delta\theta$ arc sec	Eddy current, $\Delta\theta$-arc sec	Gravity gradient, $\Delta\theta$ arc sec	Aerodynamic pressure, $\Delta\theta$ arc sec	Solar pressure, $\Delta\theta$ arc sec	Total, $\Delta\theta$ arc sec
5	- 5.9	- 20.6	+2.40	-0.02	+ 1.6	- 24.2
10	-10.6	- 98.7	+0.97	-0.06	+ 6.4	- 102.0
15	-15.0	- 269.1	+1.40	-0.44	+ 14.2	- 268.8
20	-19.3	- 566.8	+1.50	-0.69	+ 24.4	- 560.8
25	-23.1	-1000.6	+2.00	-0.24	+ 38.6	- 983.3
30	-27.5	-1536.4	°1.20	-0.56	+ 55.1	-1508.1
35	-32.4	-2144.5	+1.08	-0.44	+ 74.1	-2101.8
40	-37.3	-2792.8	+1.17	+0.31	+ 97.9	-2730.7
45	-42.6	-3473.9	+0.10	+0.52	+122.6	-3394.4

TABLE 5. - COMPARISON OF THE EFFECT OF DIFFERENT COMBINATIONS OF TORQUE WITH THE TOTAL TORQUE EFFECT

Time, Min	Sum, (1)+(2), $\Delta\theta$ arc sec	Sum, (1)+(2)+(5)	Sum, (1)+(2)+(3)+(4)+(5)
5	- 26.5	- 24.9	- 24.2
10	- 109.3	- 102.9	- 102.0
15	- 284.1	- 269.9	- 268.8
20	- 586.1	- 561.7	- 560.8
25	-1023.7	- 985.1	- 983.3
30	-1563.9	-1508.8	-1508.1
35	-2176.9	-2102.8	-2101.8
40	-2830.1	-2732.2	-2730.7
45	-3516.5	-3393.9	-3394.4

(1)+(2) ≡ Attitude deviation due to residual magnetic moment and eddy current torques

(1)+(2)+(5) ≡ Attitude deviation due to residual magnetic moment, eddy current, and solar pressure torques

(1)+(2)+(3)+(4)+(5) ≡ Attitude deviation due to the five torques

Spacecraft Modeling

In the preceding section, extensive modeling of five environmental torques, was accomplished and their effect on spacecraft attitude evaluated. Two results are important in the modeling of the spacecraft rotational dynamics. First, the gravity gradient and magnetic torques were shown to have significant effect on spacecraft attitude. Secondly, two components of several torques were cyclic with mean near zero and a period of 20 seconds. Observations were made that the effect of the cyclic torque upon attitude have minor effect on spacecraft attitude. These results lead to the development of a set of simplified equations of motion which included the gravity and magnetic torques, to improve computational efficiency in the attitude determination data reduction program. Since the net effect of the cyclic term over a period is zero, time averaging successfully eliminates the cyclic terms, substantially reducing the equation complexity. This procedure was used by Beletskii (Reference 3) to analyze the resultant long-term motion of spin-stabilized earth-orbital spacecraft. The analysis presented develops the equations of motion in differential form (suitable for computation) and demonstrates the equation accuracy for the attitude determination problem in the 1 to 10 arc sec accuracy. Two methods of mechanizing the spacecraft equation of motion was attempted. First, a method developed a set called the simplified equations of motions. The second was called an approximate closed-form solution for torqued asymmetric spacecraft.

Simplified equations of motion. --

Axis frame and equations of motion: Axis frames selected for describing the equations of motion are shown in Figures 41 and 42. The angular momentum frame describes the direction of the angular momentum relative to inertial space and results in the set of differential equations presented in Equation (26).

$$\dot{\tau} = \frac{T_{\bar{x}}}{p}$$

$$\dot{\xi} = \frac{T_{\bar{y}}}{p \sin \tau} \qquad (25)$$

$$\dot{p} = T_{\bar{z}}$$

where $T_{\bar{x}}$, $T_{\bar{y}}$, $T_{\bar{z}}$ are the torques applied about the angular momentum axes $\bar{x}$, $\bar{y}$, and $\bar{z}$, respectively.

The body axis frame defines the motion of body-fixed principal axes with respect to the angular momentum axes. The Euler angles are consistent with the spinning-top system used in classical physics (reference 4) and result in a system of differential equations which are

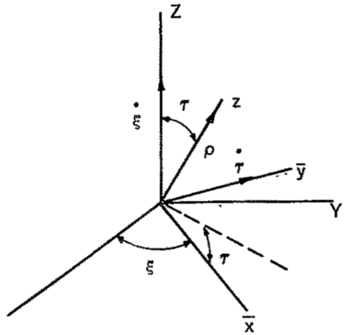

Figure 41. Angular Momentum Axes System

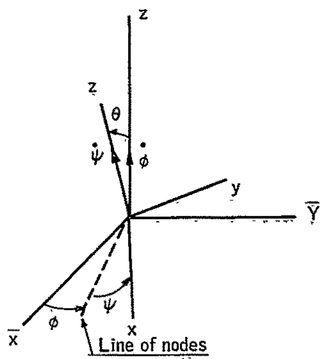

Figure 42. Euler Angle Axes System

$$\dot{\theta} = p \cos \Psi \sin \Psi \left(\frac{1}{I_x} - \frac{1}{I_y}\right) + \frac{T_{\bar{x}} \sin \phi - T_{\bar{y}} \cos \phi}{p}$$

$$\dot{\phi} = p \left(\frac{\sin^2 \Psi}{I_x} + \frac{\cos^2 \Psi}{I_y}\right) + \frac{(T_{\bar{y}} \sin \phi + T_{\bar{x}} \cos \phi) \cot \theta}{p} + \frac{T_{\bar{y}} \cot \tau}{p} \tag{26}$$

$$\dot{\Psi} = p \cos \theta \left(\frac{1}{I_z} - \frac{\sin^2 \Psi}{I_x} - \frac{\cos^2 \Psi}{I_y}\right) - \frac{(T_{\bar{y}} \sin \phi + T_{\bar{x}} \cos \phi) \cos \theta}{p} \qquad \text{(26) (cont)}$$

Equations (25) and (26 form a complete description of the spin motion of the vehicle in a torqued environment. A singularity exists at the point $\theta = 0$ in that Ψ and ϕ are not defined uniquely and the torques become infinite.

Spacecraft torques: To develop the equations of motion explicitly, [(25) and (26)], it is necessary to derive the torques in terms of the spacecraft state variables and rates. The three torques for the ARRS, (magnetic moment, eddy current, and gravity gradient) will be considered. However, the analytical procedure used is to develop the simplified equation that is not limited to these specific torques but is equally applicable to solar, aerodynamic, or other torques resulting from spacecraft motion.

Using the torque equations of the previous section, the three torques considered above can be written as

$$\bar{T}_M = \begin{bmatrix} (\bar{E}_2 \cdot \bar{M})B_z - (\bar{E}_3 \cdot \bar{M})B_y \\ (\bar{E}_3 \cdot \bar{M})B_x - (\bar{E}_1 \cdot \bar{M})B_z \\ (\bar{E}_1 \cdot \bar{M})B_y - (\bar{E}_2 \cdot \bar{M})B_x \end{bmatrix} \tag{27}$$

$$T_E = K\left\{\bar{B}_A (E^{-1}Q\bar{q} \cdot \bar{B}_A) - E^{-1}Q\bar{q}(\bar{B}_A \cdot \bar{B}_A)\right\}$$

$$\bar{T}_G = \frac{3\mu \hat{r} \times (E^{-1}\bar{\bar{I}}E)\hat{r}}{R^3}$$

where

E = Euler angle transform (ϕ, θ, Ψ)

E_i = i^{th} column of E

$$\bar{\bar{I}} = \begin{bmatrix} I_x & 0 & 0 \\ 0 & I_y & 0 \\ 0 & 0 & I_2 \end{bmatrix}$$

$$\bar{B}_A = \begin{pmatrix} B_x \\ B_y \\ B_z \end{pmatrix} \equiv \text{Angular momentum components of the earth's magnetic field}$$

$$Q = \begin{pmatrix} \cos\Psi & \sin\theta\sin\Psi & 0 \\ -\sin\Psi & \sin\theta\cos\Psi & 0 \\ 0 & \cos\theta & 1 \end{pmatrix}$$

$$\bar{q} = \begin{pmatrix} \dot{\theta} \\ \dot{\phi} \\ \dot{\psi} \end{pmatrix}$$

μ = Gravitational constant

R = Radius from spacecraft to earth's center

$$\bar{\bar{I}} = \text{Inertia matrix} = \begin{pmatrix} I_x & 0 & 0 \\ 0 & I_y & 0 \\ 0 & 0 & I_z \end{pmatrix}$$

The vector $\hat{r}$ is the local vertical unit vector in angular momentum coordinate and is obtained by

$$\hat{r} = DF^{-1}(\bar{e}) = \begin{pmatrix} r_1 \\ r_2 \\ r_3 \end{pmatrix} \tag{28}$$

where F and D are the transforms from vertical to inertial to angular momentum, respectively (ref. Figure 41).

Simplified Equations for Symmetric Body: Using Equation 27, the exact motion of the torqued spinning body can be obtained. An approximation to this solution can be obtained by perturbation theory, assuming that the torque terms are small and hence can be neglected in the first approximation. If this assumption is made along with the assumption that $I_x = I_y = I$, then the first-order approximation to the motion becomes

$$\dot{\zeta} = \dot{\tau} = \dot{\theta} = \dot{p} = o$$

$$\dot{\theta} = \frac{p}{I} \qquad (29)$$

$$\dot{\psi} = \frac{k\,p}{I}$$

Note that four of the six state variables are constants and the other two have constant rates. Substituting the results of Equation (29) into Equation (27), it is possible to obtain the first-order estimate of the torques, which can then be sutstituted into the differential equations. These results are shown for T_M, T_E and T_G in Equations (1), (2), and (4) of Appendix C for the special case $I_x = I_y$. Note that the magnetic and gravity torques are functions of all state variables, the explicit relationships for the Euler angles ζ, ψ, and θ are indicated in Equation (1), (2), and (4) and implicitly for τ and ζ in that $\hat{r}$ and $\bar{B}_A$ are functions of these angles.

For the symmetric case, θ, ζ, and τ are constant and $\cos\psi$, $\cos\theta$, etc., are periodic with period $\frac{2\pi}{k\,p/I}$ and $\frac{2\pi}{p/I}$, respectively. Assuming that the other states are constant over a period and since the periods are of a non-integer relationship, it is possible by time-averaging to eliminate all cyclic torque terms. For example

$$T_{\bar{x}\,au} = \lim_{T\to\infty} \frac{1}{T} \int_o^T T\,(\tau,\ \zeta,\ p,\ \theta,\ \psi,\ \phi) \qquad (30)$$

Time averaging the torque terms of Equations (25) and (26) results in the following differential equations to describe the torqued symmetric spacecraft motion:

$$\dot{\tau} = \frac{K\,B_x\,B_y\,(1 + k\cos\theta)}{I} - \frac{B_y\,M_z\cos\theta}{p} + \frac{3\mu\,I\,(1-a)\,(2-3\sin^2\theta)\,r_2\,r_3}{2\,R^3 p}$$

$$\dot{\zeta} = \frac{K\, B_y\, B_z\, (1 + k \cos\theta)}{I \sin\tau} + \frac{B_x\, M_z \cos\theta}{p \sin\tau}$$

$$+ \frac{3\mu\, I\, (1-a)\, (2 - 3 \sin^2\theta)\, r_1\, r_3}{2\, R^3\, p \sin\tau}$$

$$\dot{p} = \frac{-p\, K\, (B_x{}^2 + B_y{}^2)\, (1 + k \cos\theta)}{I}$$

$$\dot{\theta} \quad \frac{k\, K \sin\theta\, (B_x{}^2 + B_y{}^2 + 2B_3{}^2)}{2I}$$

$$\dot{\phi} = \frac{p}{I} + \frac{K\, B_y B_z (1 + k \cos\theta) \cot\tau}{I} + \frac{B_x M_z \cos\theta \cot\tau}{p}$$

$$- \frac{B_z M_z \cos\theta}{p} + \frac{3\mu\, I\, (1 - a) \cot\tau\, (2 - 3 \sin^2\theta)\, r_1 r_3}{2R^3 \dot{p}}$$

$$+ \frac{3\mu\, I (1-a) \cos^2\theta \left[(r_1{}^2 + r_2{}^2) - 2r_3{}^2\right]}{2\, R^3 p} \qquad (31)\ (\text{cont})$$

$$\dot{\Psi} = \frac{kp}{I} - \frac{p \sin\theta\, (I - I_z)\, (\theta - \theta_o)}{I\, I_z} + \frac{B_z M_z}{p}$$

$$- \frac{3\mu\, I\, (1-a) \cos\theta \left[(r_1{}^2 + r_2{}^2) - 2r_3{}^2\right]}{2\, R^3 p}$$

Note that Equation (31) is relatively simple and that there are no terms in ϕ and Ψ on the right-hand side. Hence, no rapidly varying terms exist in Equation (31) and it is possible to carry out the numerical solution using relatively large time intervals.

Simplified equations for asymmetric body: In a manner similar to the previous calculations, it is possible to develop the torque terms for the asymmetric body. However, in this case the equations become more complex and, as will be evident, an explicit set of differential equations is not feasible.

The "angular rate" solution for an untorqued asymmetric spinning body (reference 5) is given by

$$\bar{\omega} = \begin{bmatrix} \sqrt{a_1}\ \mathrm{cn}\ (c_1 t) \\ \dfrac{\mathrm{sn}\ (c_1 t)}{b_2} \\ \sqrt{a_3}\ \mathrm{cn}\ (c_1 t) \end{bmatrix} \tag{32}$$

where sn, cn, sn, and dn are Jacobian elliptic functions. Using the relationship between angular moment and Equation (32), the Euler angle functions become

$$\cos\theta = \frac{I_z \sqrt{a_3}\ \mathrm{dn}\ (c_1 t)}{P} \tag{33}$$

$$\sin\theta = \left[1 - \frac{{I_z}^2\ c_3\ \mathrm{dn}^2\ (c_1 t)}{p^2}\right]^{1/2}$$

$$\cos\Psi = \frac{I_y\ \mathrm{sn}\ (c_1 t)}{b_2 p \left[1 - \dfrac{{I_z}^2\ a_3\ \mathrm{dn}^2\ (c_1 t)}{p^2}\right]^{1/2}}$$

$$\sin\Psi = \frac{I_x \sqrt{a_1}\ \mathrm{cn}\ (c_1 t)}{p \left[1 - \dfrac{{I_z}^2\ a_3\ \mathrm{dn}^2\ (c_1 t)}{p^2}\right]^{1/2}}$$

(33)
(cont)

$$\dot{\theta} = \frac{\sqrt{a_1}\ (I_x - I_y)\ \mathrm{cn}\ (c_1 t)\ \mathrm{sn}\ (c_1 t)}{p b_2 \left[1 - \dfrac{{I_z}^2\ a_3\ \mathrm{dn}^2\ (c_1 t)}{p^2}\right]}$$

$$\dot{\phi} = \frac{I_x\ a_2\ \mathrm{cn}^2\ (c_1 t) + I_y\ \mathrm{sn}^2\ (c_1 t)}{p\ {b_2}^2 \left[1 - \dfrac{{I_z}^2\ a_3\ \mathrm{dn}^2\ (c_1 t)}{p^2}\right]}$$

$$\Psi = I_z \sqrt{a_3}\, dn\,(c_1 t)\,(1/I_z - \dot{\phi})$$

where the constants c, a_1, a_2, a_3, b_2, etc., are related to the normalization of the eliptic function solutions.

The functions of Equation (33) can be used to evaluate the torques given in Appendix C. They become for the eddy current damping and magnetic moment terms

$$T_{\bar{x}_a} = -M_z B_y I_z \sqrt{a_3}\, \overline{dn\, c_1 t} + K B_x B_z \left\{ I_z a_3 \overline{dn^2 (c_1 t)} + I_x a_1 \overline{cn^2 (c_1 t)} + \frac{I_y}{b_2^2} \overline{sn^2 (c_1 t)} \right\}$$

$$T_{\bar{y}_a} = M_z B_x I_z \sqrt{a_3}\, \overline{dn\,(c_1 t)} + K B_y B_z \left\{ I_z a_3 \overline{d_n^{\,2} (c_1 t)} + I_x a_1 \overline{cn^2 (c_1 t)} + \frac{I_y}{b_2^2} \overline{sn^2 (c_1 t)} \right\} \tag{34}$$

$$T_{\bar{z}_a} = -K (B_x^2 + B_2^2) \left\{ I_z a_3 \overline{dn^2 (c_1 t)} + I_x a_1 \overline{cn^2 (c_1 t)} + \frac{I_y}{b_2^2} \overline{sn^2 (c_1 t)} \right\}$$

where the subscript "a" and the bar "—" over the term are used to denote the average over a cycle. It is evident in these equations that the effect of M_x and M_y components of the magnetic moment, as in the symmetric body case, are eliminated by the averaging process.

The torque average of the gravity gradient term cannot be found explicitly because Equation (33) has no explicit solution of the Euler function ϕ. Hence, there are indicated in trigonometric form as

$$T_{\bar{x}_{G_a}} = -I \left\{ (1-a) \left(1 - \overline{\sin^2 \theta\, (1 + \cos^2 \phi)}\right) + \epsilon\, \overline{\sin^2 \theta \sin^2 \phi\, (\cos^2 \Psi - \sin^2 \Psi)} \right\} r_2 r_3 \tag{35}$$

$$T_{\bar{y}_{G_a}} = I \left\{ (1-a) \left(1 - \overline{\sin^2 \theta \, (1 + \sin^2 \theta)}\right) + \varepsilon \, \overline{\sin^2 \theta \cos^2 \phi \, (\cos^2 \Psi - \sin^2 \Psi)} \right\} r_1 \, r_3$$

The torque effects on the Euler angles must be calculated by averaging the terms in Equation (36). Using Appendix C, the torque terms become

$$\begin{aligned}
(T_{\bar{x}} \sin \phi - T_{\bar{y}} \cos \phi)_a = {} & B_z \left(M_x \overline{\cos \Psi} - M_y \overline{\sin \Psi}\right) + k \Big[-B^2 \overline{\dot{\Psi} \sin \theta} \\
& + B_x^{\,2} \, \overline{\sin^2 \phi \sin \theta \, \dot{\Psi}} + b_y^{\,2} \, \overline{\cos^2 \phi \sin \theta \, \Psi} \Big] \\
& + I \varepsilon \Big[2 \, \overline{\cos \Psi \sin \Psi \sin \theta} \, r_3^{\,2} \\
& - \overline{\cos \theta \sin \theta \, (\cos^2 \Psi - \sin^2 \Psi)} \, r_1 r_2 \\
& - \overline{2 \cos \Psi \sin \Psi \sin \theta \sin^2 \phi} \, r_2^{\,2} \\
& + \overline{2 \cos \Psi \sin \Psi \sin \theta \cos^2 \phi} \Big] r_1^{\,2}
\end{aligned} \tag{36}$$

$$\begin{aligned}
(T_{\bar{x}} \cos \phi + T_{\bar{y}} \sin \phi)_a = {} & B_z \left(M_x \overline{\cos \theta \sin \Psi} + M_y \overline{\cos \theta \cos \Psi} \right. \\
& \left. - M_z \overline{\sin \theta}\right) \\
& + K \left(B_x^{\,2} \, \overline{\dot{\theta} \cos^2 \phi} + B_y^{\,2} \, \overline{\dot{\theta} \sin^2 \phi} - B^2 \, \overline{\dot{\theta}}\right. \\
& + I (1-a) \Big[-\overline{\cos \theta \sin \theta} \, r_3^{\,2} \\
& + \overline{\cos^2 \phi \cos \theta \sin \theta} \, r_2^{\,2} \\
& + \overline{\sin^2 \phi \cos \theta \sin \theta} \, r_1^{\,2} \Big] \\
& + \varepsilon I \Big[\overline{\cos \theta \sin \theta \, (\cos^2 \Psi - \sin^2 \Psi) \sin^2 \phi} \, r_1^{\,2} \\
& - \overline{\cos \theta \sin \theta \, (\cos^2 \Psi - \sin^2 \Psi) \cos^2 \phi} \, r_2^{\,2} \Big]
\end{aligned}$$

It should be noted that the equations developed for the asymmetric case do not lead to a format as useful as those of the symmetric case. First, the torques are not explicitly functions of the system parameter. In addition, some of the torque terms of Equation (36) probably average to zero over a complete cycle and others for most usable spacecraft configurations might be negligible. Second, the differential equation form for the asymmetric equations would contain terms in cos Ψ, sin Ψ, and cos θ. Hence, this equation does not have the property noted about Equation (31); that long integration interval sizes are readily available. Since only the first term in Equation (26) needs to be evaluated over short intervals, solution on a high-speed machine given the averaged coefficients would not be lengthy, or the closed-form solutions [Equation (33)] might be employed by evaluating the Jacobian elliptic functions.

Further effort is desirable to develop the best solution method of accurate and rapid computation of the differential equations using time-averaged perturbation torques for the asymmetric case.

Accuracy analysis of the time-averaged equations: In the preceding paragraphs a set of time-averaged perturbation equations was developed which describes the motion of a spin-stabilized spacecraft in an earth-orbital environment. This set affords a marked simplification over the exact equations. In addition, since the torques are time-averaged, it should be feasible to employ integration step sizes substantially greater than those for the exact set. Hence, the time-averaged equations should possess distinct advantages when employed in the computer modeling of the motion of a spinning satellite. Therefore, an accuracy comparison between the time-averaged set and the exact equations is important.

For this comparison, both sets were programmed for digital computer solution on an IBM 7040 Computer. This section presents the comparative results. Since the computer used was limited in storage and since computational speed was reduced because the requirements for precision dictated that a large portion of the program be run in double precision, some simplifications were made. It was decided to program the symmetric body and include only the magnetic field effects since they predominate over the gravity effects and are nonconservative. Also, it was possible using data available from another Honeywell company study to compare certain of the gravity effects independently.

The true magnetic field experienced by a satellite is rather complex. However, an approximate field can be generated by assuming that the earth's field results from a dipole aligned with its spin axis. For a satellite in a circular orbit, the magnetic field in inertial coordinates becomes

$$\begin{aligned} B_X &= K_1 \sin(2\alpha) \cos(\gamma) \\ B_Y &= K_1 \sin(2\alpha) \sin(\gamma) \qquad (37) \\ B_Z &= K_1 [K_2 - \cos(2\alpha)] \end{aligned}$$

where

α = angle of elevation from the X-Y plane

γ = angle between X axis and the projection of the orbital position on the X-Y plane

The angles α and γ are given in terms of the orbital elements* as

$$\tan\gamma = \frac{\cos(i)\sin(\nu)}{\cos(\nu)}$$
$$\sin\alpha = \sin(i)\sin(\nu) \tag{38}$$

In a circular orbit, $\nu = \nu_o + \omega t$.

When comparing the computer solutions between the exact and averaged sets, it is necessary to use the correct initial conditions for each set. It is especially true that the initial magnitude of the angular momentum for the averaged set is the average of the instantaneous angular momentum of the exact equations over a cycle. Otherwise, the average spin motion for both sets is not the same and errors will result.

The selection of the proper initial condition was obtained by a solution of the perturbation equations (not averaged) for x (t) and then set t = 0. To illustrate the procedure, the differential equation for p (t) for the magnetic torque terms only is

$$\begin{aligned}\dot{p} = {} & \frac{pK}{I_x}(B_z^{\,2} - B^2)(1 + k\cos\theta) + \frac{pK}{I_x}(B_z \sin\theta\,(B_x\, s\phi - B_y c\phi) \\ & + (M_x\, c\Psi - M_y\, s\Psi)(B_y\, c\phi - B_x s\phi) \\ & + \left[M_z \sin\theta - \cos\theta\,(M_x\, s\Psi + M_y\, c\Psi)\right](B_y\, s\phi + B_x\, c\phi)\end{aligned} \tag{39}$$

Assuming that p in the second term on the right-hand side can be replaced by p_o, Equation (39) can be written as

$$\dot{p} = C_1 p + C_2 s\phi + C_3 c\phi + C_4 c\Psi c\phi + C_5 s\Psi s\phi + C_6 s\Psi c\phi + c_7 s\Psi c\phi \tag{40}$$

where

$$C_2 = \frac{(-_o K B_z B_y + M_z B_x)s\theta}{I_x}$$

$$C_3 = \frac{(-p_o K B_z B_y + M_z B_x)s\theta}{I_x}$$

$$C_4 = M_xB_y - M_yB_xc\theta$$

$$C_5 = M_yB_x - M_xB_yc\theta$$

$$C_6 = -(M_yB_y - M_xB_xc\theta)$$

$$C_7 = -(M_xB_x - M_yB_yc\theta)$$

Equation (40) can be integrated directly. If $C_1 << p/I_x$, then for the initial condition $\Psi = \phi = 0$

$$P_o = p(0) - (-C_1 - \frac{C_6 + C_7}{2(1+k)} + \frac{C_6 - C_7}{2(1-k)} \frac{I_x}{p(0)} \tag{41}$$

where p_o is the average initial condition when p(0) is the initial condition for the exact set.

The spacecraft used in the comparision simulation was the conceptual mechanization of a horizon definition experiment by Honeywell Inc. for the NASA Langley Research Center (ref. 6). The parameters are

$I_x = I_y = 56.68$ slug-ft^2

$I_z = 65.62$ slug-ft^2

$M_x = M_y = M_z = 0.51052 \times 10^{-5}$ ft-lb/G

$K = 0.141739 \times 10^{-4}$ ft-lb/G^2

The magnetic field constants are for a spcaecraft in a 500 km orbit and are

$K_1 = 0.375$ G

$K_2 = 0.333$ G

$\omega = 0.064$ deg/sec

The remaining constants are

$\iota = 97.38$ deg

$\nu = 97.3$ deg

$\Psi = \phi = 0$

$\omega_x = 0$

$\omega_y = 0.00365471$ rad/sec

$\omega_z = 0.31415926$ rad/sec

$\theta = 0.5757$ deg

$p(o) = 20.61617134$

$\tau = 99.9995$ deg

$\zeta = 314.4154$ deg

Using the above conditions, the spacecraft equations [Equations (25) and (26)] and the approximate equations [Equation (31)] were solved using a fourth order Runge-Kutta integration routine with a fixed interval size of 0.1 second. Figure 43 compares the motions for the angles τ and ζ over a 40-second time period. This short time is used to illustrate the effect of averaging (i.e., the exact solution has oscillations not present in the averages solution). The averaged solution, however, duplicates accurately the long-term motions of the exact set. Solutions over periods of 800 seconds indicate that the difference in magnitude is of the order of 0.0001 degree.

Figure 44 compares the cone angle, θ, for the exact and approximate solutions over a 400-second interval. In this case the exact solution has approximately a 20-second period, which makes the exact motion difficult to represent; hence, the envelope has been indicated. Again the angular difference is of the order of 0.0001 degree. Noting in Equation (26) that the condition $\theta = 0$ leads to infinite torque terms, it is apparent that the initial condition selected here represents the worst practical case for comparing the exact and averaged solutions. Hence, the amplitude of oscillations are substantially reduced at larger θ.

Figure 45 compares the angular momentum for the exact and approximate solutions. Two initial conditions are used for the approximate cases, p(0) and p_o as obtained from Equation (41). Again, the two approximate solutions represent the average change but do not have the oscillations. The latter, p_o, more closely approximates the mean of the exact solution.

Figure 46 shows the errors in the body angular positions, $\phi - \phi_a$ and $\Psi - \Psi_a$. Also included is the sum of these errors, $\phi - \phi_a$ and $\Psi - \Psi_a$. The initial conditions for the angular momentum are p(0). The individual errors $\phi - \phi_a$ and $\Psi - \Psi_a$ are quite large, approximately 0.01 degree, and are opposite in phase. The large amplitude error is a result of the infinite torques which result in the exact equations at $\theta = 0$, but are not present in the averages equations of Equation (3). This mathematical problem is a manifestation of the physical fact that at $\theta = 0$ the Euler angles Ψ and ϕ are not distinct. However, the sum and a difference factor, $\Psi + \phi$ and $\Psi - \phi$, have a useful physical interpretation as $\theta \to 0$, the sum $\Psi + \phi$ being the actual displacement of the x-body axis and the x-reference axis. Then for small θ the error sum more nearly represents the angular position error between the exact and the approximate equations. As shown in Figure 46, this error is of the order of 0.0004 degree over the 20-second interval. It is apparent that there is a mean difference between the exact and approximately $\Psi + \phi$ terms. This difference was found to be due to the initial condition selected for Figure 46. When the initial angular momentum was selected using Equation (41), this error was greatly reduced as shown in Figure 47, which plots the error using p_o over an 800-

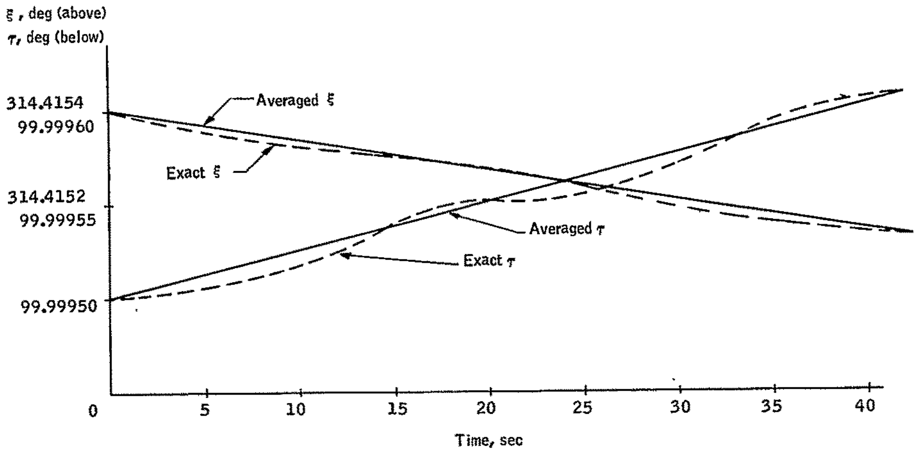

Figure 43. Comparison of Momentum Direction Solutions for Exact and Averaged Equations

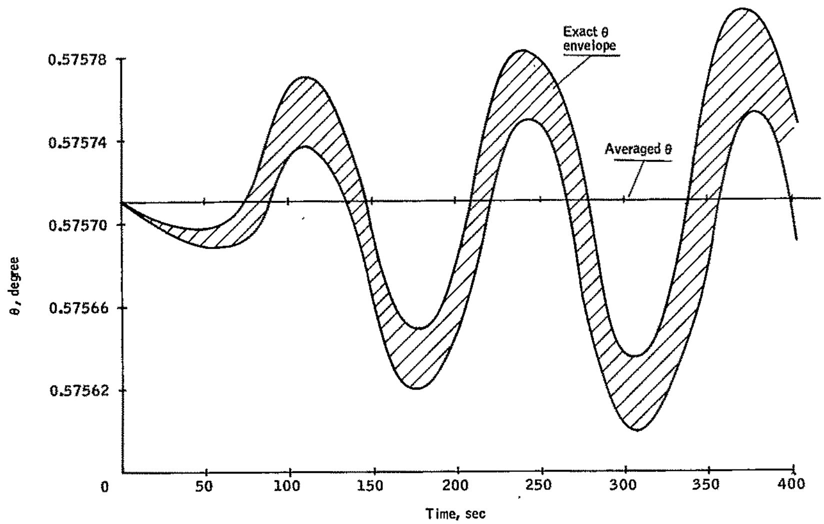

Figure 44. Comparison of Cone Angle, θ, Solutions

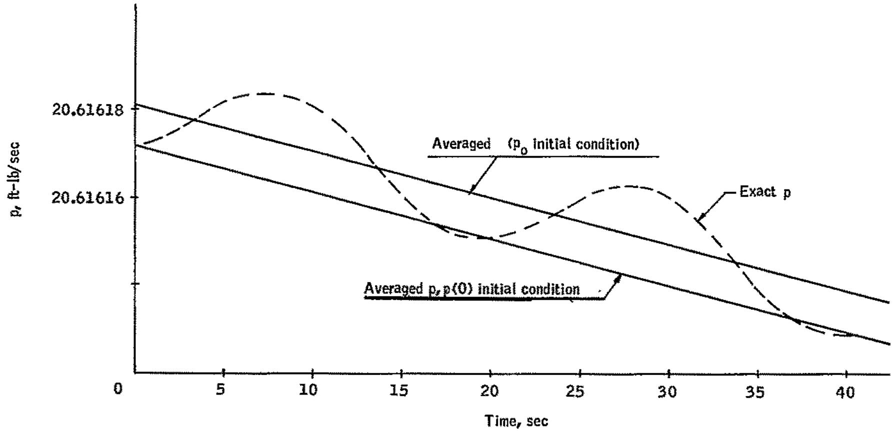

Figure 45. Comparison of Angular Momentum Solutions

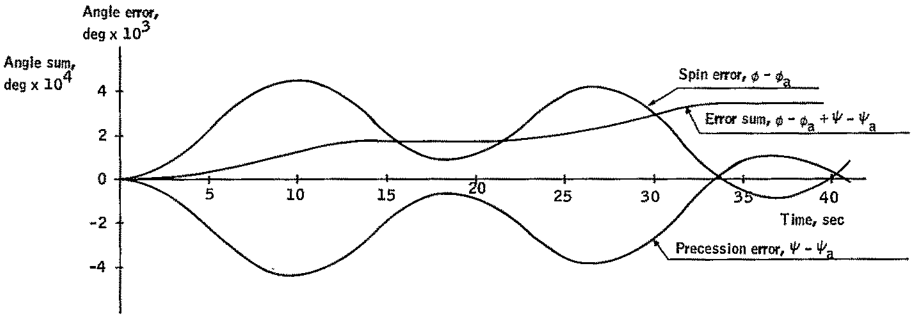

Figure 46. 'Comparison of Spin Error, $\phi - \phi_a$, and Precession Error, $\Psi - \Psi_a$, and Their Sum, $\phi - \phi_a + \Psi - \Psi_a$

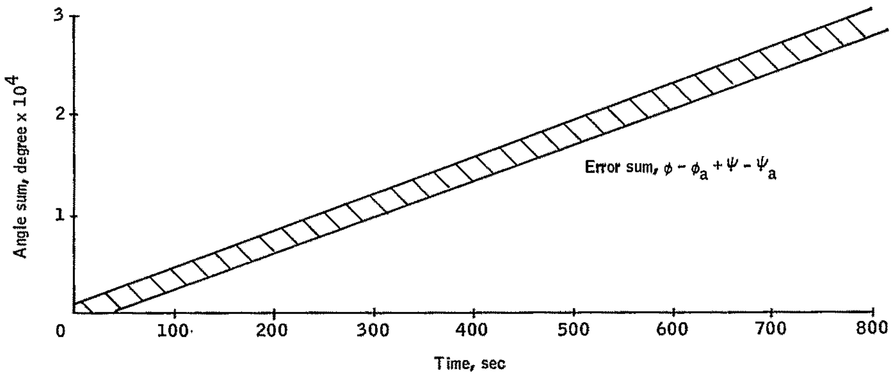

Figure 47. Envelope of Error Sum Using Initial Confition ρ_o = 20.61618074 ft-lb/sec

second interval. In this latter condition the error was less the 0.0002 degree at the end of 800 seconds.

The comparison indicates that for the typical spacecraft parameters selected the approximate equations provide solution accurate to less than 1 arc sec over periods of 500 to 1000 seconds. Since oscillatory motions are not present, the computation interval can be increased substantially.

Comparison of gravity gradient effects: As indicated previously, the effects of gravity terms were not included in the computer study. However, the results of a computer simulation with and without gravity terms were available from another study of spacecraft torques.

The spacecraft parameters are similar to those above with the exception that Ω = 45 degrees. The solutions to the exact equations were obtained by integrating Euler's equations directly and then determining the angular momentum vector. The approximate equations were obtained by a closed-form solution of terms in Equation (31), using graphical plots of the magnetic field and direct integration of the terms in the local vertical vector, r', from Equation (41).

Using the graphical plots of magnetic field and Simpson's Rule for integration, the solution for the terms τ and ζ with and without gravity effects is shown in Figure 48. Since the angular errors are less than 0.002 degree after a time interval of 1000 seconds, it appears that the approximation procedure is adequate to represent the effects of gravity gradient torques on the spacecraft motion.

Conclusions: The procedure based on the nonlinear approximation technique of time averaging the first-order perturbation equations of motion can lead to significant simplification of these equations for a spin-stabilized satellite. In the test case considered, the accuracies when comparing the exact and approximate solutions were within 1 arc sec for an interval of 800 seconds. The terms in the averaged equations are simpler and effects of infinite torques at $\theta = 0°$ are suppressed. In addition, because the cyclic torques are eliminated, the longer time intervals can be used in the numerical integration computer solution, further reducing the required computational problems.

Based on the previous paragraphs, it is concluded that an improvement in numerical integration speed was achieved. At the time of this writing, it was not possible to contrast the work above with the work presented in Appendix D, except to state the same general philosophy was used in both developments but with different starting points. Appendix D gives the development of the approximate closed-form solution technique for use in the data reduction program.

In summary, the computational techniques developed during this study will greatly improve computer efficiency and are recommended for use in the data reduction program. However, the development of the data reduction algorithm, a parallel effort, proceeded by the using of rotational dynamics model that is

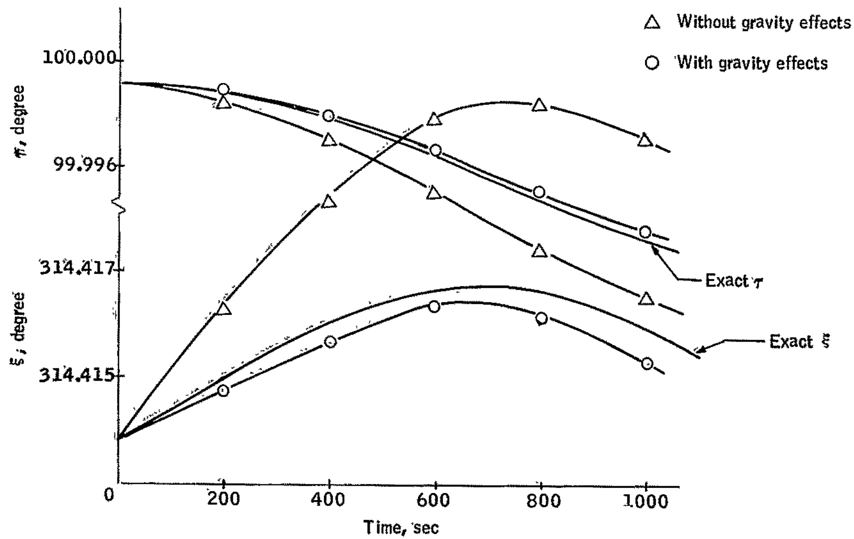

Figure 48. Comparison of Momentum Axes Motion with Gravity Effects

expressed in Reference 19 under the attitude determination section using Runge-Kutta fourth-ordered integration. Software modifications are required to incorporate the improved rotational dynamic model for purposes of improving efficiency. These modifications, if necessary, are planned during Part II of the study.

System Simulation

Objectives. -- This portion of the ARRS attitude determination effort was directed toward the development of a total attitude determination system simulation. This simulation, which exists as a single operational computer program, contains two major capabilities. The first major capability is a simulation of a passive star mapper and sun sensor instrument system fixed in the spacecraft. To represent the actual operational environment of the spacecraft, the external torques from eddy current, residual magnetic moment, gravity gradient, and solar and aerodynamic pressures are included in the spacecraft equations of motion. Simulated star mapper and sun sensor outputs are the main outputs of this portion of the simulation. The second major capability is the data processing of star mapper and sun sensor outputs to yield estimates of spacecraft attitude, rates, and parameters. The system simulation development was undertaken with three primary goals in mind:

- Since missions of one year or longer are contemplated, it was necessary to develop a data-reduction system providing spacecraft attitude estimates in significantly faster than real-time on present-day computers.

- Since the system was to be designed for a class of applications rather than for a specific mission, development of a simulation treating the selection of system parameters as variables for data reduction studies was desirable.

- Sufficient simulation studies must be performed to demonstrate the range of applicability and accuracy possible with the data-reduction algorithm. Specifically, these studies must be performed to establish the data requirements to maintain an inertial attitude accuracy of 5 arc seconds (one sigma) in pitch and 30 arc seconds in the orthogonal axis for a spin-stabilized, 3 rpm spacecraft.

In selection of the data-reduction technique, the first goal was a critical factor. The classical least squares approach was bypassed since during the NAS 1-6010 study it yielded an algorithm possessing sufficient accuracy but requiring real-time on the CDC 6500 computer (Ref. 19). The spacecraft coordinate system used in that study proved to be suitable for the attitude determination problem and consequently was chosen for the system simulation effort. The nonlinear Kalman filter (Ref. 22), mechanized to process transit data sequentially, was selected because of its simple, noniterative structure and because the measurement statistics enter directly into the data reduction equations. Further sequential processing of transit data, as opposed to batch-type processing, provides a distinct advantage which is usually overlooked in the choice of a filter for an operational system. In such a system the identification of stars causing the transit must be solved before the data can be used for attitude estimation. However, after an initial period, the attitude estimates generated by the sequential estimation provide the necessary information to perform the star identification sequentially, rather than prior to the start of the estimation process. This mechanization is applicable to either ground-based data processing or on-board data processing.

Notation. --

t	Time, independent parameter
$\omega_x, \omega_y, \omega_z$	Spacecraft angular rates, principal body axes
ψ, ϕ, θ	Euler angles parameterizing the rotation from inertial to body coordinates, yaw, roll, and pitch, respectively
I_1, I_2, I_3	Spacecraft moments of inertia
A, C	Inertia ratios I_1/I_2 and I_3/I_2, respectively
$\overline{M}'$	Spacecraft residual magnetic moment vector, divided by I_2
K'	Spacecraft eddy current coefficient, divided by I_2
$\overline{X}$	Variable dimension estimation state vector
$\bar{f}(\overline{X})$	Functional representation of $\dot{\overline{X}}$
Ex	Expected value operator
$\hat{\bar{x}}$	Estimate of $\overline{x}$
P	Covariance matrix, $Ex[(\hat{\overline{X}}-\overline{X})(\overline{X}-\hat{\overline{X}})^T]$
$(\;)^T$	Denotes matrix or vector transpose
f_x	Jacobian matrix,
ϵ	Measurement error
H	Measurement model
$\overline{H}_x$	$\left[\frac{\partial H}{\partial X_1}, \ldots, \frac{\partial H}{\partial X_n}\right]$
σ_H^2	Measurement variance, $Ex(H^2)$

$\Phi(k, k-1)$	State n x n transition matrix relating linearized state from time t_{k-1} to time t_k
W	Square root of covariance $P \equiv WW^T$
$(\ )_b$, $(\ )_a$	Denotes quantity before and after application of corrections due to measurement errors
$(\hat{\ })$	Denotes unit vector
$\hat{U}$	Unit normal to slit plane
$\hat{S}$	Star (or sun) vector in inertial space
σ_I^2	Variance of instrument noise
$(\ \ )_B$	Denotes vector in body coordinates
$(\ \ )_I$	Denotes vector in inertial coordinates
$\hat{0}$	Optical axes of starmapper (sun sensor)
fov	Field of view of starmapper (sun sensor)
$\epsilon_1, \epsilon_2, \epsilon_3$	Angles parameterizing the offset of the experimental w.r.t. the spacecraft axes
γ	Cant angle; with zero offset, the angle between the optical axis, and the y body axis
β	Rotation angle of slit plane about the optical axis
α, δ	Right ascension, declination of star (sun)

Coordinate transformations: All coordinate frames are referenced to an inertial coordinate system defined by the x-axis pointing toward the first point of Aries, the z axis along the earth's polar axis. The y-axis is chosen to make a right-handed coordinate frame.

The body axes frame is fixed in the spacecraft and centered at its center of mass. These axes are assumed to coincide with the axes of the principal moments of inertia. The relation between the spacecraft body axes and the inertial frame is given in Appendix G.

Since in practice the experimental frame, defined by the starmapper and sun sensor instruments, may differ from the desired body axes frame, small displacements of this frame from the body frame are treated.

A vector in body coordinates to the experimental frame is given by

$$\overline{X}_E = C(\epsilon_1, \epsilon_2, \epsilon_3)\,\overline{X}_B \tag{42}$$

where

$C(\epsilon_1, \epsilon_2, \epsilon_3)$ is defined in Appendix G.

Orientation of each star mapper or sun sensor slit is specified with respect to the experimental coordinate frame by the cant angle γ and slit plane rotation angle β about the optical axis. Figure 49 illustrates the orientation of a given slit. The geometry shows that in the experimental frame the slit normal $\hat{U}$ and and optical axis $\hat{O}$ are the first and second rows of the matrix, respectively,

$$A = \begin{bmatrix} \cos\beta & \sin\beta \sin\gamma & -\sin\beta\cos\gamma \\ 0 & \cos\gamma & \sin\gamma \\ \sin\beta & -\cos\beta\sin\gamma & \cos\beta\cos\gamma \end{bmatrix} \quad (43)$$

whereas the third row is a unit vector lying in the slit plane and normal to $\hat{O}$.

Zenith vector, $\hat{Z}$, from the center of the earth through the spacecraft, is specified by the usual orbital parameters - longitude of the ascending node Ω, inclination i, and true anomaly ν. For the nominal case defined by the y body axis normal to the orbital plane, the Euler angles ψ and ϕ would equal Ω and i-90°, respectively. The orbital geometry is developed in Appendix G.

Vehicle model: For this study the dynamical model for the spacecraft equations of motion was taken from the formulation used under NAS 1-6010, (ref. 19). In this formulation the vehicle motion and orientation were described by the angular rates about the principal body axes and Euler angles parameterizing the rotation from inertial to body coordinates. These variables satisfy the first-order, nonlinear differential equations.

$$\begin{aligned} \dot{\omega}_x &= [\omega_y\omega_z(1-C) + \tau_x]/A \\ \dot{\omega}_y &= [\omega_x\omega_z(C-A) + \tau_y] \\ \dot{\omega}_z &= [\omega_x\omega_y(A-1) + \tau_z]/C \end{aligned} \quad (44)$$

and

$$\begin{aligned} \dot{\psi} &= [-\omega_x \sin\theta + \omega_z \cos\theta]/\cos\phi \\ \dot{\phi} &= \omega_x \cos\theta + \omega_z \sin\theta \\ \dot{\theta} &= \omega_y - \dot{\psi}\sin\phi \end{aligned}$$

where $I_2 \overline{\tau}$ represents the external torque acting on the spacecraft, in body coordinates.

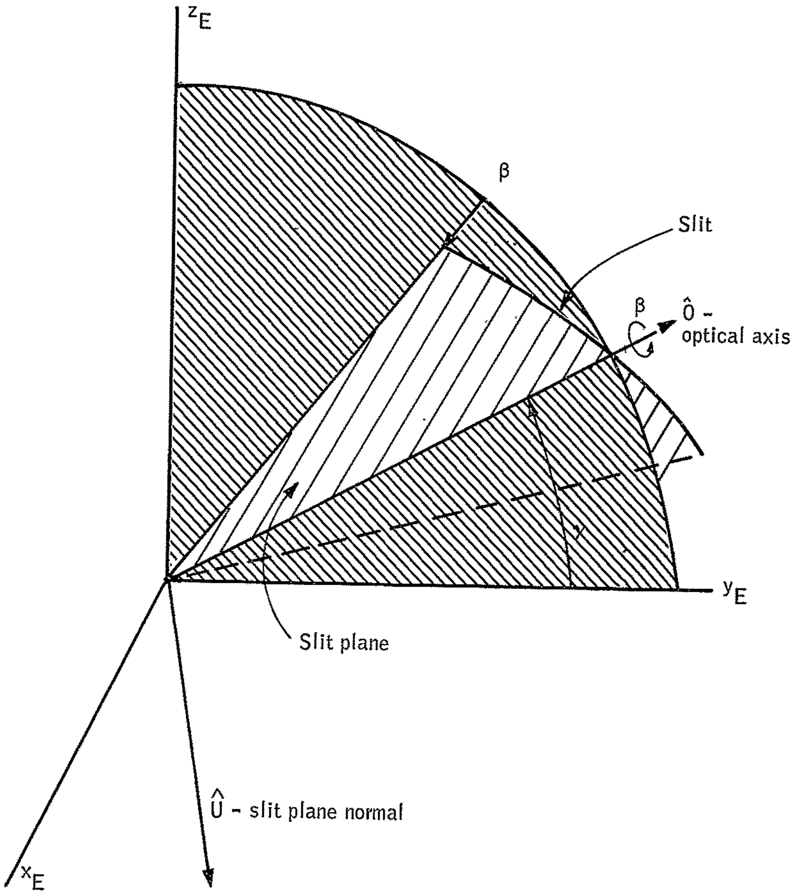

Figure 49. Relationship of Slit Plane to the Experimental Frame

During the course of the study several other parameterizations of the rotation from inertial to body coordinates were considered with the objective of obtaining greater efficiency in the numerical integration of the differential equations of motion. Parameterizations such as the Euler symmetric parameters, used for the torque analysis, and direction cosines were rejected because their use introduces additional dimensionality into the estimation problem. The Gibbs vector representation was initially selected for study since its use requires only algebraic computations. However, it was unsuitable because it possesses a near singularity which occurs twice per spacecraft rotation.

Attitude Estimation Algorithm:

Nonlinear Kalman filter: Two formulations of the nonlinear Kalman filter were mechanized for study in the ARRS Attitude Determination System - a conventional formulation and a square root formulation. Both state estimation techniques were implemented to process transit data sequentially in time and as such can be conveniently stated in two parts. Between transit measurements, the spacecraft rates and Euler angles and the covariance matrix are extrapolated by a numerical solution of the differential equations which describe their motion. At a measurement, both the extrapolated vehicle variables and covariance matrix are updated using one of the two Kalman estimation equations mechanizations. A variable time step, variable order (second, third, or fourth) Runge-Kutta (Ref. 24) is implemented for the numerical solution of the spacecraft differential equations of motion while the covariance matrix extrapolation is accomplished by a variable time step second-order Euler integration.

System variables and parameters which were included in the estimation state $\underline{X}$ are

$$\begin{bmatrix} X_1 \\ X_2 \\ X_3 \end{bmatrix} = \begin{bmatrix} \omega_x \\ \omega_y \\ \omega_z \end{bmatrix}, \quad \begin{bmatrix} X_4 \\ X_5 \\ X_6 \end{bmatrix} = \begin{bmatrix} \psi \\ \phi \\ \theta \end{bmatrix}, \quad \begin{bmatrix} X_7 \\ X_8 \end{bmatrix} = \begin{bmatrix} A \\ C \end{bmatrix}, \quad \begin{bmatrix} X_9 \\ X_{10} \\ X_{11} \end{bmatrix} = \begin{bmatrix} M'_x \\ M'_y \\ M'_z \end{bmatrix}, \quad X_{12} = K'$$

Thus

$$\dot{X}_i = 0, \ i \geq 7$$

is assumed. The estimation algorithms were implemented so that fewer than 12 variable solutions can be obtained.

Algorithm torque model: In general distinct torque models are employed for transit time generation and the attitude determination data reduction. For the latter, the two most prominent torques, magnetic moment and eddy current (single coefficient), were included in the model.

Conventional formulation: In the mechanization of the conventional formulation of the Kalman nonlinear filter, the spacecraft rates and Euler angles and the covariance matrix are propagated from measurement to measurement by a numerical solution of the equations

$$\dot{\bar{X}} = \bar{f}(\bar{X}),\ \bar{X}(t_o) = \bar{X}_o \tag{45}$$

and

$$\dot{P} = Pf_x^T + f_x P + Q,\ P(t_o) = P_o$$

where Q is an nxn diagonal additive "noise" matrix determined empirically to prevent the covariance matrix from becoming negative definite and where the initial conditions, indicated by $(\cdot)_o$, are the values of the quantities at transit measurements after updates due to the measurement errors have been applied. At a transit measurement updating is accomplished with

$$\bar{X}_a = \bar{X}_b + \bar{K}\,\epsilon \tag{46}$$

and

$$P_a = P_b - \bar{K}\,\bar{H}_x\,P_b$$

where the gain vector $\bar{K}$ is

$$\bar{K} = P_b\bar{H}_x^T/(\bar{H}_x P_b \bar{H}_x^T + \sigma_H^2)$$

Square Root Formulation: The state covariance matrix will become negative definite due to computational inaccuracies if some form of additive noise is not used. Consequently, an alternate formulation of the Kalman filter was implemented. This alternate formulation is the "square root" formulation in which all covariance matrix computations are performed with the square root of the covariance matrix rather than with the covariance matrix itself. While the conventional and square root formulations are analytically equivalent if additive noise is not considered, numerical errors do not cause the covariance matrix to become negative definite in the latter, thus circumventing one formidable problem in the practical application of the Kalman filter.

For this formulation of the estimation algorithm, the extrapolation of covariance is accomplished by numerically solving the differential equation satisfied by the state transition matrix,

$$\dot{\Phi}(k, k-1) = f_x(k)\,\Phi(k, k-1)$$

with the initial condition

$$\Phi(0, 0) = I$$

A variable time step, second-order Euler integration is used. The square root of the covariance matrix is propagated from transit to transit by

$$W_b(s) = \Phi(s, s-1)\, W_a(s-1)$$

where $W_a(s-1)$ is the "after" update covariance from the previous transit and $W_b(s)$ is the "before" update for the current transit.

The estimation state vector and the square root of the covariance matrix are updated at a transit time t_s with

$$\bar{X}_a(s) = \bar{X}_b(s) + \bar{K}\varepsilon$$

$$W_a(s) = W_b(s) - c\,\bar{K}\,\bar{g} \tag{47}$$

where

$$\bar{g}^T = W_b^T(s)\,\bar{H}_x^T$$

$$\bar{K} = W_b(s)\,\bar{g}^T/(\overline{gg}^T + \sigma_H^2)$$

$$\varepsilon = -H(\bar{X}_b)$$

$$c = 1 + \sigma_H(\sigma_H^2 + \bar{g}\,\bar{g}^T)^{-1/2}$$

Following the updating, extrapolation is resumed by re-initializing

$$\Phi(s, s) = I$$

$$\dot{\Phi}(s, s) = f_x(\bar{X}_a(s))$$

and at the first time point t_{m+1} after update,

$$\Phi(m+1, s) = I + (t_{m+1} - t_s)\, f_x(\bar{X}_a(s))$$

and

$$\dot{\Phi}(m+1, s) = f_x(\bar{X}(m+1))\, \Phi(m+1, s)$$

Measurement model: Starmapper and sun sensor transit measurements provide the raw data from which spacecraft rates, attitude and parameters are estimated. The estimation, Equations (46) and (47), require that these measurements be modeled analytically to provide a measurement error ε at the time of transit. This error is computed as the difference between the observed measurement value and a predicted value based on the estimated vehicle rates, attitude, and parameters extrapolated from previous transits. Since at the instant of transit the line of sight to the star lies in a plane defined by the slit and optical axis of the instrument, a natural measurement model to use is the equation which states that the projection of the vector along the line of sight to the star on the vector normal to the slit plane vanishes analytically.

$$0 = \hat{U} \cdot \hat{S}_B$$

where $\hat{U}$ is the normal to the slit plane and $\hat{S}_B$ is the star vector, both in body axes. In view of the coordinate transformations described in Equations (41), (42) and (43), it is seen that

$$\hat{U} = A_1 C$$

and

$$\hat{S}_B = E(t)\,\hat{S}$$

Thus, the measurement model which follows is the scalar form

$$H(t) = A_1 C\, E(t)\, \hat{S} \tag{48}$$

This provides a measurement error at a transit time given by

$$\varepsilon(t_s) = 0 - \hat{H}(t_s)$$

where $\hat{H}$ is the predicted, generally nonzero, value of the measurement.

Alternately, the time at which a transit will occur can be predicted and the error term taken to be the difference of the predicted and measured time. The measurement error for this model is

$$\varepsilon(t_s) = t_s - \hat{t}_s \tag{49}$$

where t_s is the predicted time of transit. As no closed, analytic form exists for t_s, Equation (49) must be evaluated from a Taylor's series expansion of Equation (48). To first-order

$$\varepsilon(t_s) = -H(t_s)/\dot{H}(t_s)$$

Both models were implemented since the latter exhibits a nonzero sensitivity

$$\frac{\partial H}{\partial X} \neq 0$$

to the rate variables, whereas the geometric model, Equation (48), does not. Measurement variance values for the two models are

$${\sigma_H}^2 = (\sigma_I / |\bar{\omega}|)^2$$

and

$$= (\sigma_I / |\bar{\omega}|)^2 \cdot (\bar{H}_X \dot{\bar{X}})^2$$

respectively, where σ_I is an assumed instrument noise

Transit time model: The generation of simulated starmapper and sun sensor outputs requires a simulation of considerable complexity. Its outputs are a series of time values representing the times at which the images of various stars or the sun cross slits in the focal planes of the respective instruments as the instruments are scanned across the celestial sphere by the spacecraft's motion. Thus, each transit time is characterized by the following conditions. The line of sight to the celestial body causing the transit lies in a plane defined by the optical axis of the instrument and the slit; the celestial body must lie within the field of view of the instrument; and the celestial body must not be blocked by the earth. Mathematically, these conditions are given by

$$\hat{U}_I \cdot \hat{S} = 0$$

$$- \text{fov} \leq 2 \cos^{-1} (0_I \cdot \hat{S}) \leq \text{fov} \qquad (50)$$

and

$$\hat{S} \cdot \hat{Z} \geq \cos \Gamma$$

respectively. It is apparent that the first condition states that the normal to the sensor plane $\hat{U}_I$ is perpendicular to the star (or sun) vector $\hat{S}$ at the transit, while the second condition states that the angle subtended by the star vector and the optical axis $\hat{0}_I$ is less than half of the field of view (fov) of the instrument. The earth blocking condition is expressed in terms of the zenith vector Z through the spacecraft and the earth block angle Γ, which defines the visible region of the celestial sphere not obscured by the earth. Figure 50 illustrates the geometry at the instant of a transit.

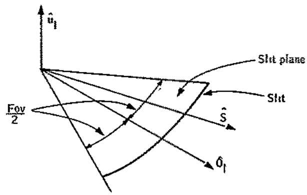

Figure 50. Transit Geometry

Since the simulated sensor outputs produced by the simulation must represent the output of sensors under actual operating conditions, the external torques due to eddy current loss, residual magnetic moment, gravity gradient, and solar and aerodynamic pressure [Equations (2), (1), (23), (11), and (7), respectively], are normally included in the spacecraft model, Equation (44). The resulting complexity precludes a closed-form solution of the first condition (50) and requires an iterative technique to determine the times of transit. Iteration is accomplished as follows: A reference solution of the spacecraft equations of motion is established at evenly spaced time increments by numerical integration. Once per spacecraft rotation crude estimates are made of all transit times which will occur in the next spin period. The crude estimate is determined by solving the equation of motion of the slit normal

$$\dot{\bar{U}}_I = \bar{\omega}_I \times \bar{U}_I \tag{51}$$

assuming a constant rate $\bar{\omega}_I$. This equation is integrated numerically by trapezoidal rule. The integration is terminated when the Newton-Raphson integration step

$$\Delta t = \frac{\hat{S} \cdot \hat{U}_I}{-\hat{S} \cdot (\bar{\omega}_I \times \hat{U}_I)}$$

becomes sufficiently small for a solution $\bar{U}_I$ at a time t_{est}. As the reference solution is generated, the crude time estimates are refined by the same procedure over shortened time spans. Spacecraft attitude is evaluated at each refined estimate and an estimate is accepted as a transit on the condition

$$|\hat{U}_I \cdot \hat{S}| < \epsilon'$$

for an arbitrary tolerance ϵ', provided the second and third conditions (50) are satisfied. The value

$$\epsilon' = 0.5 \times 10^{-6}$$

corresponding to an angular tolerance of approximately 0.1 arcsecond has been used in the simulation program.

Computer program description. -- The approach taken in the design and programming of the attitude determination system simulation was to isolate and program as separate subprograms the various functions associated with the solution of the vehicle [Equations (44)] and the filter [Equations (45) through (47)]. This was done since such a structuring of the system facilitates modeling changes as the analysis effort progresses. Also, to realize maximum compatibility between the SDS Sigma V and CDC 6600, machine dependent features such as disc storage and cathode ray tube display were isolated into separate routines. Thus, the resulting program structure is highly segmented in subroutines defined by function and machine dependency. Some of the features of the system are the

- Option of using either the conventional Kalman filter or the square root Kalman filter for update of state at star transits
- Variable order, variable step Runge-Kutta for integration of vehicle equations of motion between star transits
- Variable step Euler integration of covariance differential equations for conventional Kalman filter or of the state transition matrix for the square root Kalman filter
- Option of using either one of two different scalar measurement models
- Option of changing state dimensions
- Capability of having any combination of five torques by changing the basic input data
- Transit time generation
- Star transit identification
- Dynamic on-line analysis

A block diagram of the system simulation is shown in Figure 51. The dashed lines represent the computational flow for the transit time generation mode of operation, and the solid lines depict the data-reduction mode. Some major outputs are $\overline{X}(t)$ and $E(t)$; the state, covariance, and the matrix relating inertial to body axes at time t; and the right ascension and declination of the star $\hat{S}$ sighted at t_S, α, and δ, respectively.

Several computer program variables are used by the system to represent time. These are defined as follows:

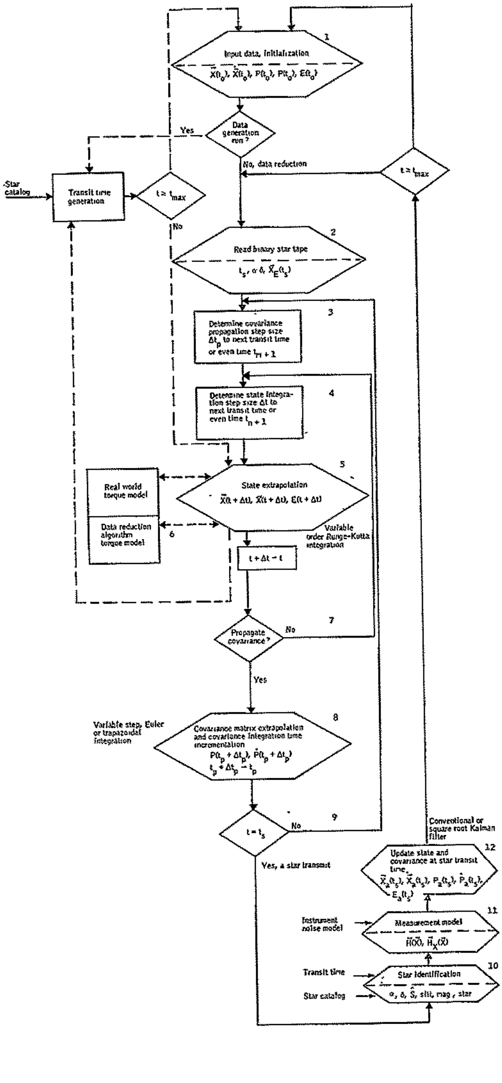

Figure 51. Block Diagram of Attitude Determination System Simulation

t_o - Initial time for data reduction or transit time generation

t_{max} - Maximum time for data reduction or transit time generation; for the purposes of analysis these two variables provide the capability to selectively read portions of the star transit tape for data reduction.

t - Time variable at which spacecraft state (rates, Euler angles, and parameters) is available. This variable assumes values contained within the interval $[t_o, t_{max}]$ at even increments Δt_o and at star or sun transits t_s.

t_p - Time variable at which the covariance matrix is available. This variable assumes values contained within the interval $[t_o, t_{max}]$ at even increments Δt_{po} and at transits t_s.

t_s - Star or sun transit time

t', t'_p - As t and t_p are incremented during the simulation execuyion t' and t'_p are carried along to indicate the previous values of t and t_p respectively, occuring at even time increments Δt_{po} and at transits Δt_{po}.

Δt_o, Δt_{po} - Fixed time steps for the numerical integration of this spacecraft equations of motion and of the matrix Riccati equation

$$(\Delta t_{po} = k\Delta t_o \text{ for some integer } k \geq 1)$$

Δt, Δt_p - Variable time steps for the numerical integrations

The data-reduction mode of operation proceeds as follows, where the numbers correspond to the block numbers of Figure 51.

1) Input data read in and all system variables initialized.

2) The transit time data tape (generated via a previous transit time generation run) is read in to establish the next star (sun) observation time. Data on the tape includes star (sun) data, and "exact" state $\vec{X}_E(t_s)$ at the transit time for error calculation.

3) A determination is made of the value of integration time step Δt_p. The value is computed from

$$\Delta t_p = \text{minimum} [t_s - t_p, \Delta t_{po} - (t_p - t'_p)]$$

which forces $t_p + \Delta t_p$

to the next transit time t_s or to the next time value occuring at an even time increment Δt_{po}.

4) The value of the integration time step Δt is determined from

$$\Delta t = \text{minimum } [t_s - t, \ \Delta t_o - (t - t')] \cdot$$

This guarantees that $t + \Delta t$ will equal either the next transit time or the next time value at the increment Δt_o.

5) A variable order Runge-Kutta numerical integration is used to solve Equation (44) over the interval

$[t, t+\Delta t]$; $\overline{X}(t + \Delta t)$, $\dot{\overline{X}}(t + \Delta t)$, and $E(t + \Delta t)$ are computed.

6) This block computes the external disturbance torques $\vec{\tau}$ for the data-reduction vehicle model.

7) A check is made if time, t, is at a star (sun) transit or the end of a covariance matrix integration interval.

8) The covariance matrix is extrapolated from t_p to $t_p + \Delta t$ by a variable step Euler integration of the matrix Ricatti equation or the linearized state transition matrix, for the conventional Kalman filter, or the square root Kalman filter formulation, respectively. Also computed are

$$P(t + \Delta t) \text{ or } \dot{\Phi}(t + \Delta t) \text{ respectively.}$$

9) If current time is at a star transit, the Kalman filtering of the measurement is initiated.

10) The star and slit causing the transit are identified.

11) The scalar measurement and partial derivatives of the measurement model with respect to state are computed from knowledge of propagated state, orientation of the identified star (sun) in inertial space, and the sensor slit causing the transit.

12) The estimation state and the covariance matrix are updated from the propagated "before" update values

$$\vec{X}_b(t_s) \text{ and } P_b(t_s), \ H[\vec{X}_b(t_s)], \text{ and } \vec{H}_x[\vec{X}_b(t_s)]$$

The "after" update quantities $\vec{X}_a(t_s)$, $\dot{\vec{X}}_a(t_s)$, $E_a(t_s)$, $P_a(t_s)$, and $\dot{P}_a(t_s)$ are the outputs of this block.

On-line analysis: To expedite studies with the simulation, an on-line analysis capability CRT display is used. This feature is mechanized so that all variables of interest are available for display during a simulation. Beside the basic display capability, considerable simulation control is exercised through the CRT by light pen.

Specific on-line control functions provided by the light pen are (1) the initiation of a simulation, (2) the capability to change variables for display by selection from a displayed directory of variable names with the light pen, (3) the capability to interrupt the simulation at any time during the course of a run whereupon all variables may be observed or parameter changes may be input into the simulation, and (4) a case-to-case display capability permitting the superposition of variables from different simulation cases. Figure 52 illustrates the display format, showing the display directory, plotted simulation variable, and light-pen control mechanization. Other features incorporated in the display are automatic scaling and variable display window length for modifying the resolution of displayed variables.

As implemented the display provides an extremely versatile and powerful on-line analysis tool, enabling rapid engineering decisions to be made on-line and allowing complete monitoring of the entire simulation.

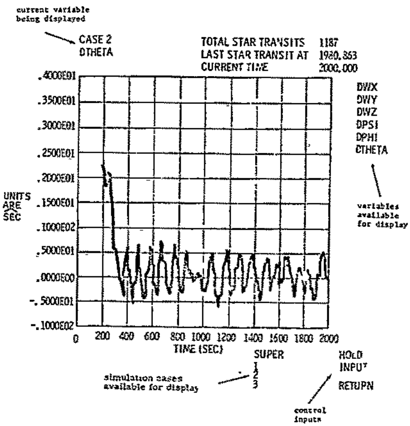

Figure 52. CRT Display Format

Performance analysis: Experiments performed with the simulation were conducted to

- Establish the data requirements to maintain one-sigma attitude accuracies of 5 arc seconds in the pitch angle θ and 30 arc seconds in the yaw and roll angles ψ and ϕ for a spin-stabilized, 3 rpm, low-altitude spacecraft.
- Determine the sensitivity of the estimation accuracy to such parameters as spin rate, cone angle, inertia ratio uncertainty, instrument noise
- Evaluate the operational status of the estimation algorithms

With regard to the latter, it is noted that on the CDC 6600 computer the data reduction portion of the simulation executes from 10 to 20 times faster than real time, depending on the dimension (6 to 12) of the estimation state. Since execution time is directly proportional to the time step used for numerical integration of Equations (44), which in turn is inversely proportional to spin rate, the latter conclusion holds for spin rates up to 30 rpm.

The subsequent discussion describes results obtained with the simulation. These results were taken from simulation experiments conducted on the SDS Sigma V computer using a precision of 15 significant digits. In general, two types of results are presented - time varying and statistical. The former are taken directly from the CRT display, Figure 52 , and are intended primarily to illustrate several characteristics of the estimation process as a function of time. The statistical results are computed from errors in the estimation state at the transit times and represent the steady state or converged behavior of the estimation process as the errors of the first 500 transits processed are not included in the statistical computations. For a given variable y, the statistics which are presented are the mean error

$$\mu(\Delta y) \equiv \frac{1}{N} \sum_{s} \Delta y_s$$

and the standard deviation of the error about the mean

$$\sigma(\Delta y) \equiv \sqrt{\frac{1}{N} \sum_{s} [\Delta y_s - \mu(\Delta y)]^2}$$

where N transits are included in the statistics. Since the precise value of the estimation state is known from the transit time simulation at the true transit time t_s and not at the noise corrupted transit time $t_s + \Delta t_s$ which is processed by the estimation algorithm, the error is computed from

$$\Delta y_s = y_e(t_s) - [\tilde{y}(t_s + \Delta t_s) - \Delta t_s \dot{\tilde{y}}(t_s + \Delta t_s)]$$

where $(\sim)$ denotes the estimated value and $(\ )_e$ denotes the true or exact value available from the transit simulation. Two sets of these statistics, computed before and after the update Equations (46) are applied, are available from the simulation.

Nominal transit data: To initiate the performance analysis effort, a nominal set of simulated transit time data was obtained using the following spacecraft initial conditions and parameter values:

$$\omega = (0.2094°, 18°, 0°)/\text{sec}$$
$$\psi = 45°$$
$$\phi = 190°$$
$$\theta = 82°$$
$$I_1 = 54.68 \text{ slug-ft}^2$$
$$I_2 = 65.62 \text{ slug-ft}^2$$
$$I_3 = 54.38 \text{ slug-ft}^2$$
$$M = (0.516)10^{-5} (\hat{i}, \hat{j}, \hat{k})_B \text{ ft-lb/G}$$
$$K = (0.143)10^{-4} \text{ ft-lb-sec/G}^2$$
$$P_1 = (0.20754)10^{-5} \text{ ft-lb-sec/G}^2$$
$$P_2 = -(0.7202)10^{-4} \text{ ft-lb-sec/G}^2$$

All five torques were included in the model. Orbital parameters used for these simulations are

$$\Omega = 45°$$
$$i = 97.38°$$
$$\nu_o = 86°$$
$$h = 500 \text{ km}$$
$$\alpha_{sun} = 0$$
$$\delta_{sun} = 0$$

with a circular orbit assumed.

The starmapper is characterized by the cant angle

$$\gamma_{star} = 110°$$

and the slit plane rotations

$$\gamma_{sun} = 45°, \ \alpha_3 = -20°, \text{ and } \alpha_5 = 20°$$

A 20° fov is assumed for each instrument.

A star catalog consisting of the first one hundred brightest stars, down to a visual magnitude of 2.74, plus the sun was used. With an earth blocking angle $\Gamma = 90°$ assumed, the transit data depicted in Figure 53 were obtained. Shown in Figure 53 are the catalog number of the star, (Ref. 25), the visual magnitude, right ascension and declination, the approximate time $\tilde{\tau}_s$ at which the star transits (relative to the 20-second spin period), and the approximate separation of the transits from different slits, $\widetilde{\Delta t}_s$. To the right of the vertical time axis, *'s are used to indicate the relative position of the sighting time in the spin period. The particular stars which are sighted at any given time are indicated by the "star sighting windows" on the right-hand side of the axis. Each vertical bar applies for the period of time shown with it. For example, the fourth bar shows that for the time period 850 to 950 seconds, five stars (17518, 18133, 18643, and 18144) are sighted.

Initial data reduction: Initial data reduction experiments were undertaken primarily to obtain a working value of the Q matrix appearing in Equation (45) for the estimation of spacecraft rates and the Euler angles. Initial condition errors for these variables were taken as

$$\begin{aligned} \Delta\omega &= (0.2094°, -0.1°, -0.1°)/\text{sec} \\ \Delta\psi &= 0.5° \\ \Delta\phi &= 1° \\ \Delta\theta &= 1° \end{aligned} \qquad (52)$$

with the other vehicle parameters fixed at

$$M = (0., 0., 0.)$$

$$K = (0.2)\, 10^{-4} \text{ ft-lb-sec}/G^2$$

and

$$\Delta A = \Delta C = 0.01/I_2$$

An instrument noise value of 3 arc seconds (one sigma) was assumed. Trial and error was used to determine values of Q which maintain steady state values of the diagonal elements of the covariance matrix at levels which seem reasonable for the instrument being used. Values of Q were accepted when the covariance behavior exhibited in Figure 54 was achieved. Shown in Figure 54 are the values of the square root of the diagonal elements of the covariance matrix

Star No.	Mag	α Deg	δ Deg	$\tilde{t}_s$ Sec	$\Delta\tilde{t}_s$ Sec
	sun	0.0	0.0	1.0	0.04
5605	1.06	68.497	16.443	1.2	0.10
6427	0.21	78.553	45.967	3.10	0.18
4041	1.90	50.480	49.744	3.16	0.19
17518	1.68	193.139	56.141	7.20	0.11
18133	2.40	200.645	55.100	7.30	0.03
18643	1.91	206.558	49.480	7.70	0.02
19242	0.24	213.536	19.335	9.40	0.13
18144	1.21	200.857	-10.815	11.30	0.05
17262	2.34	189.936	-48.587	13.50	0.12
17052	1.01	187.324	-56.741	13.90	0.12
12938	2.63	140.272	-54.729	15.20	0.10
12831	2.25	139.052	-58.998	15.27	0.03
12764	1.80	138.198	-69.443	15.30	0.11
12069	2.01	130.944	-54.466	15.50	0.07
11463	1.74	125.455	-59.296	15.70	0.01
8302	-0.86	95.805	-52.661	16.75	0.01

Star Sighting windows

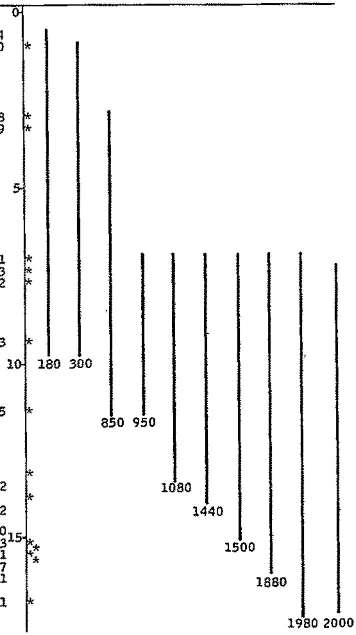

Figure 53. Transit Data for Nominal Case

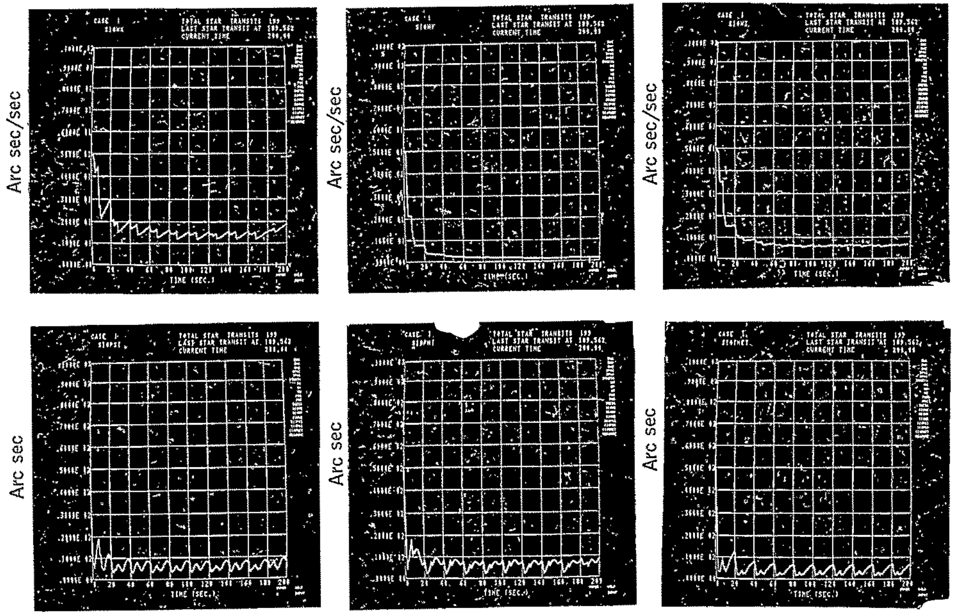

Figure 54. Nominal Case - Behavior of the Diagonal Elements of the Covariance Matrix

$$\sqrt{p_{ii}} = \sqrt{Ex(\Delta X_i^2)} \quad , \; i = 1, 6$$

labeled SIGWX, SIGWY, SIGWZ, SIGPHI, and ISGTHET, respectively. Steadystate values in the element corresponding to pitch, θ, (SIGTHET) are noted to be approximately 3 arc seconds with somewhat higher values in ψ and ϕ. The additive noise values used to attain this performance were

$$q = (0.005,\ 0.02,\ 0.25,\ 5.0,\ 5.0,\ 5.0)\ 10^{-4} \tag{53}$$

where

$$q_{ii} = q_i^2$$

with units of (deg/sec)/$\sqrt{\text{sec}}$ associated with q_1, q_2, and q_3 and units of deg/$\sqrt{\text{sec}}$ associated with q_4, q_5, and q_6. Values of q are quoted since they are the normal input data to the simulation. It is noticed that the value of q_1 is considerably smaller than q_3, although these values correspond to ω_x and ω_z and could be expected to be symmetrical. However, these values were established by selectively increasing the value of q_2 and q_3 until the behavior of P_{22} and P_{23} as exhibited in Figure 54 was achieved. Since P_{11} P_{33}, q_1 was not increased. Figures 55 through 59 illustrate the behavior of the estimation process with these values of additive noise.

The convergence of the estimation process from the initial condition errors, Equation (52), is shown in Figures 55 and 56, where the convergence obtained over the first spin period and the convergence to steady-state errors over 10 spin periods are exhibited. The variables ω_x, ω_y, ω_z, ψ, ϕ, $\Delta\omega_x$, $\Delta\omega_y$, $\Delta\omega_z$, $\Delta\psi$, $\Delta\phi$, and $\Delta\theta$ are shown and labeled WX, WY, WZ, PSI, PHI, DWX, DWY, etc., respectively. Note that the gross rate and attitude errors are eliminated by the processing of the first 20 transits during the first 10 seconds of the data reduction, while complete convergence is obtained by the end of the tenth spin period after processing 200 transits. Examination of the $\Delta\theta$ plot in Figure 55 reveals an error buildup from 0 to 200 arc seconds in the pitch error over the 10 to 20 second time interval. This is extrapolation error due to the error in the estimate of $\bar{\omega}$ over that period of time.

Figure 57 shows the steady-state attitude errors over the entire 2000-second simulation. The first 200 seconds are not plotted to permit a meaningful choice of scale. An increase in the attitude errors is apparent at approximately 900 seconds. Referring to Figure 53, it is seen that this error buildup is due to the loss of transits from stars No. 6427 and No. 4041 as they disappear over the horizon.

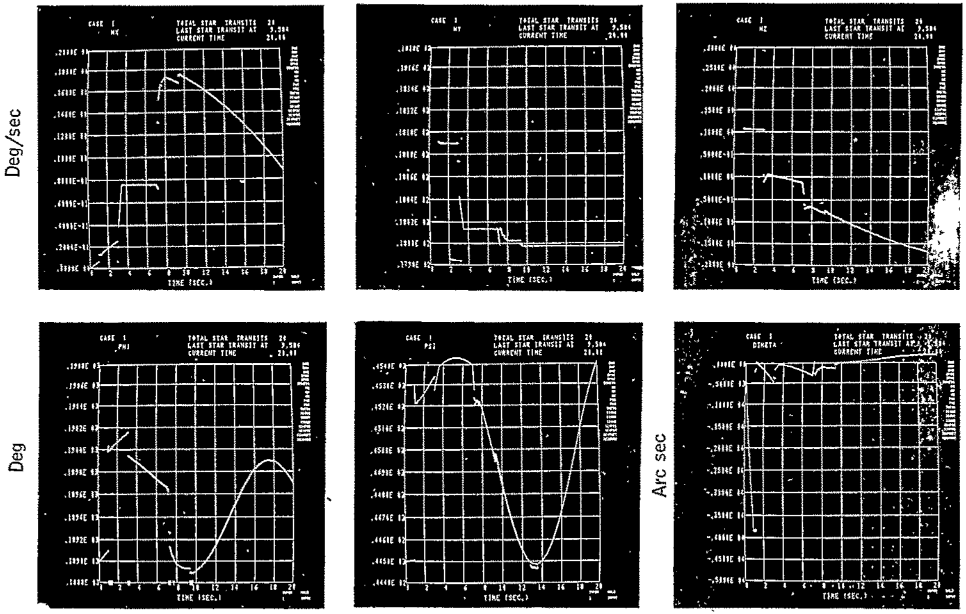

Figure 55. Nominal Case - Convergence Over One Spin Period

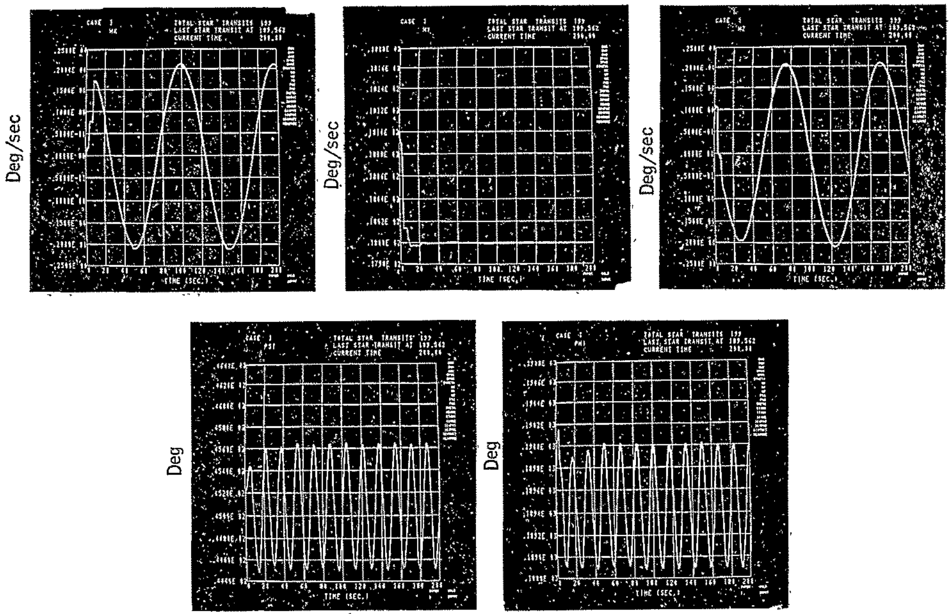

Figure 56. Nominal Case - Convergence over 10 Spin Periods

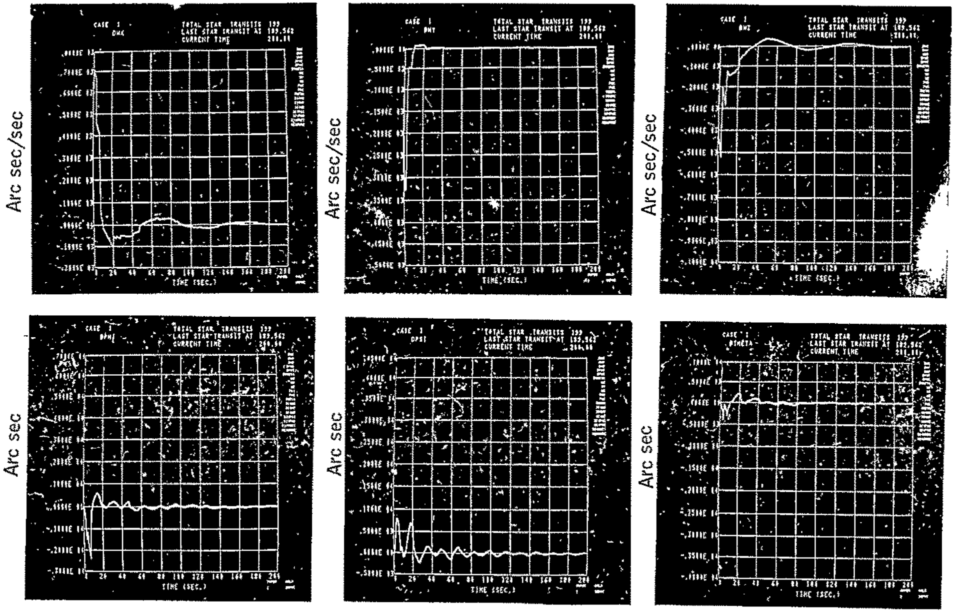

Figure 56. Nominal Case - Convergence over 10 Spin Periods (Concluded)

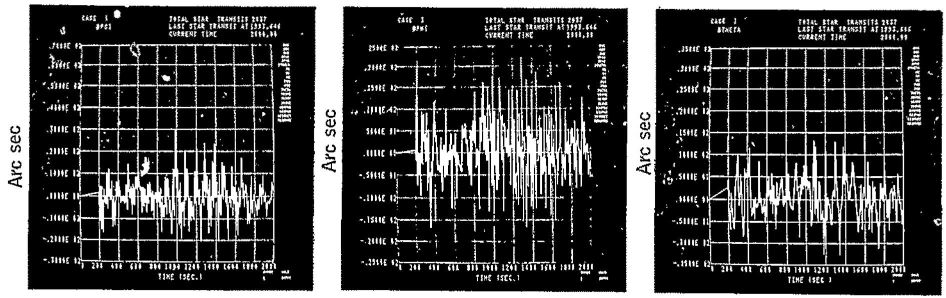

Figure 57. Nominal Case - Attitude Errors After Convergence

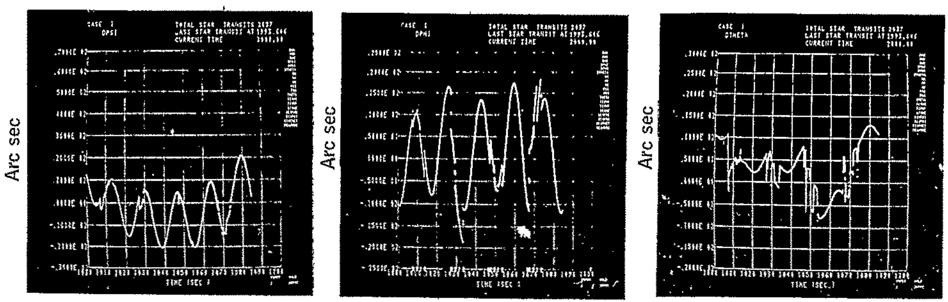

Figure 58. Nominal Case - Attitude Errors After Convergence Over Five Spin Periods

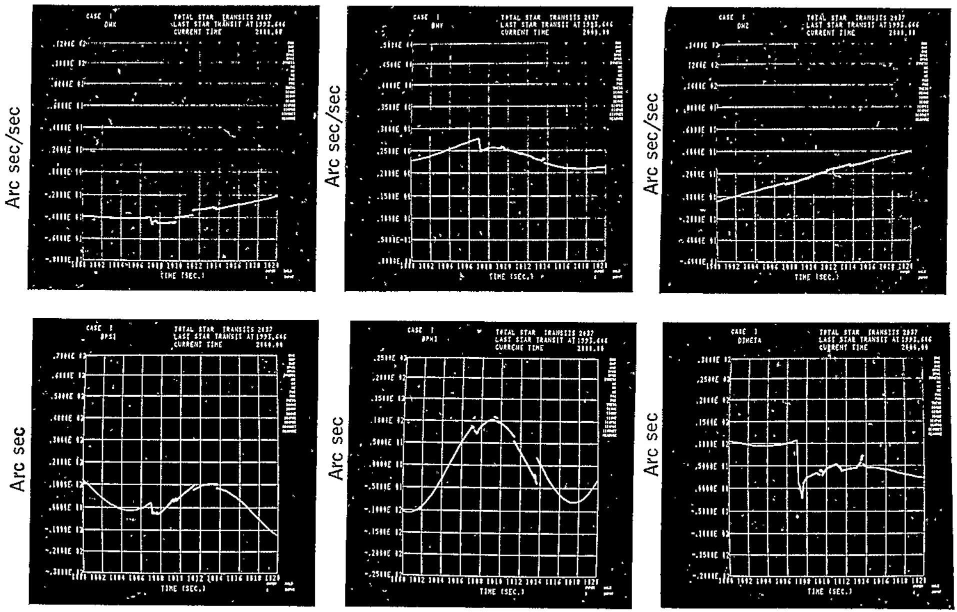

Figure 59. Nominal Case - Rate and Attitude Errors After Convergence Over One Spin Period

Converged attitude errors are shown on expanded time scales in Figure 58 and 59. From these it is seen that the pitch angle θ exhibits a much higher sensitivity to the measurement error than the other attitude angles. Also, it is noted that the period of the yaw and roll errors, $\Delta\psi$ and ϕ respectively have the period associated with ψ and ϕ.

Figures 60 through 62 depict a second data reduction simulation identical to that discussed in the previous paragraphs, except that fewer star sightings are used. For this simulation stars down to a visual magnitude of 1.7 are used, effectively reducing the number of transits processed by approximately one half. No significant difference is noted in the behavior of the covariance matrix diagonal elements, Figures 54 compared with Figure 60.

The short-term convergence over the first spin period, Figure 61, is less smooth with the reduced number of transits (12 as opposed to 20) as shown in Figure 55; however, gross attitude errors are eliminated. The long-term convergence, Figure 62, exhibits larger overshoot in the error estimates than shown in Figure 56, but again convergence to steady-state values is achieved in 10 vehicle rotations.

Steady-state statistics for a series of data-reduction simulations (including the two previously described) based on the nominal transit case are presented in Figure 63. This figure presents the statistics of the attitude errors as a function of instrument noise σ_I and for data reduction simulations using different numbers of star sightings characterized by starts down to a visual magnitude of 2.5 and 1.7. The values of additive noise, Equation (53), are used for all values of instrument noise. Each statistic is presented in the form of an error band which represents the spread between the before and after update values of the attitude errors at the transit times. With the exception of the mean error in pitch, $\mu(\Delta\theta)$, the larger error values represent the performance for the simulations using fewer star sightings characterized by a limiting visual magnitude of 1.7. Approximately 1000 transits are processed for this case, while approximately 2000 are processed for the 2.5 case.

Pitch error is significanntly smaller than the error in the other axes. This is due to higher sensitivity of the measurement to pitch as exhibited in Figure 58. The width of the error bands is relatively small and indicates that the attitude errors over that portion of the vehicle rotation when no measurements are available are not significantly different from those when measurements are available. This is substantiated by the continuous error curves shown in Figures 58 and 59.

Simulation results described in the following paragraphs are based, unless otherwise noted, on the nominal case just discussed.

Instrument noise uncertainty: Besides simplicity of implementation, the explicit appearance of the measurement statistics in the estimation, Equation (46), provides a strong motivation for the selection of the Kalman filter to solve the attitude determination problem. However under operational conditions the measurements statistics of the starmapper may not be known

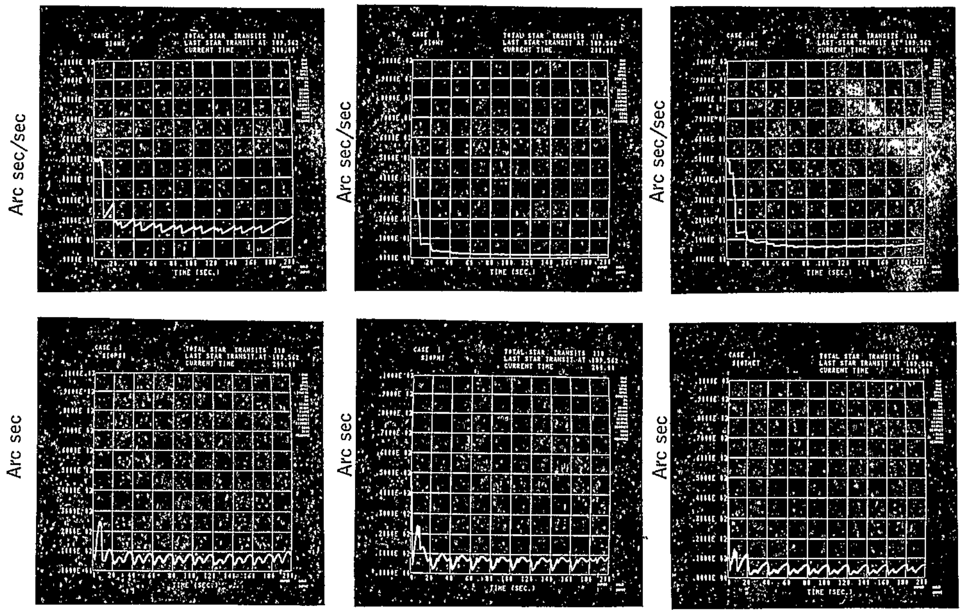

Figure 60. Nominal Case - Behavior of the Diagonal Elements of the Covariance Matrix with Reduced Number of Sightings

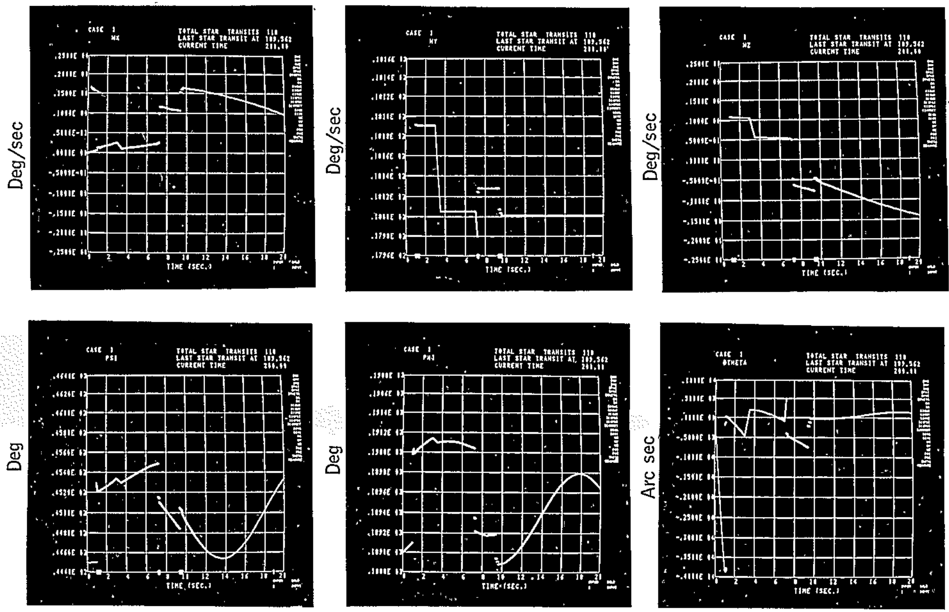

Figure 61. Nominal Case - Convergence Over One Spin Period With Reduced Number of Sightings

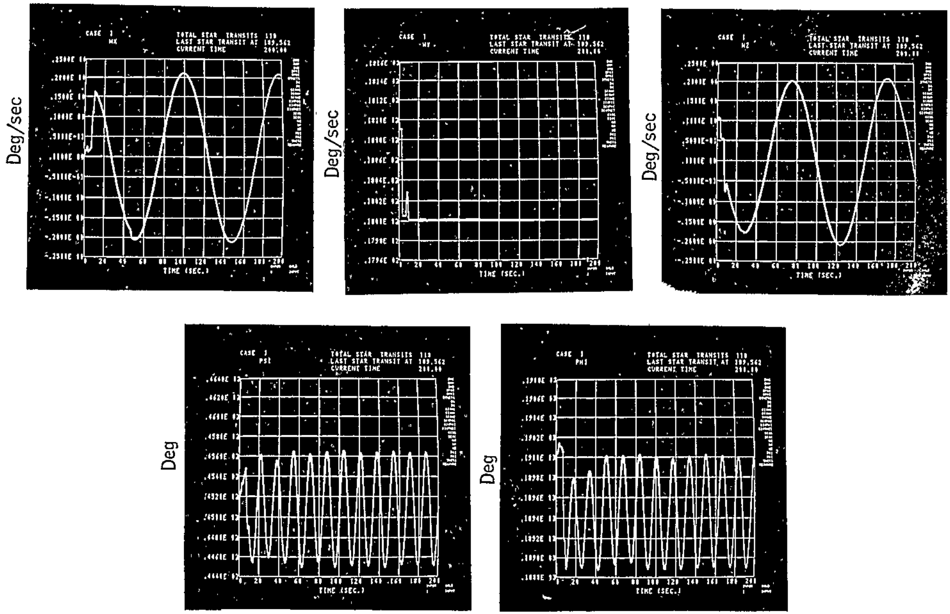

Figure 62. Nominal Case - Convergence Over 10 Spin Periods With Reduced Number of Sightings

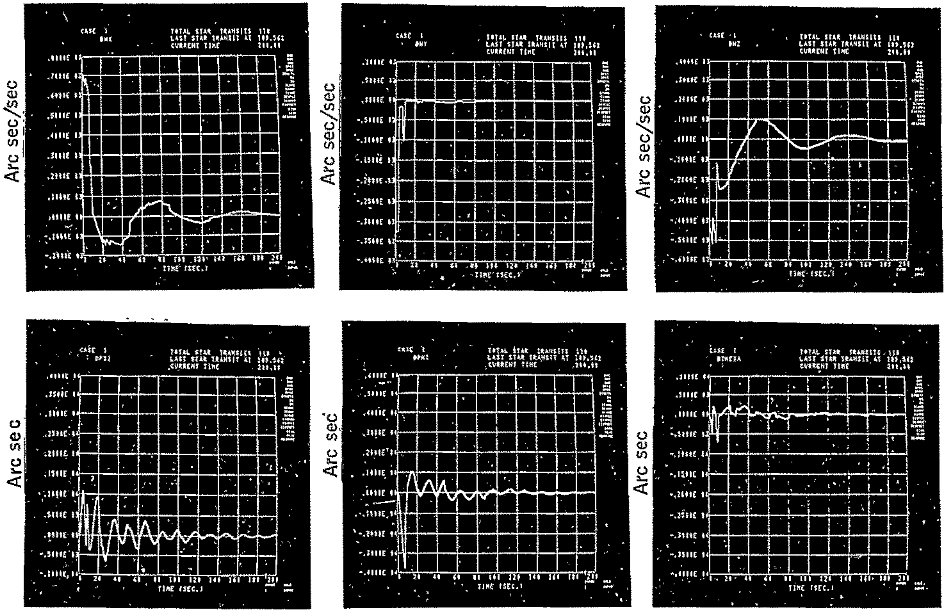

Figure 62. Nominal Case - Convergence Over 10 Spin Periods With Reduced Number of Sightings (Concluded)

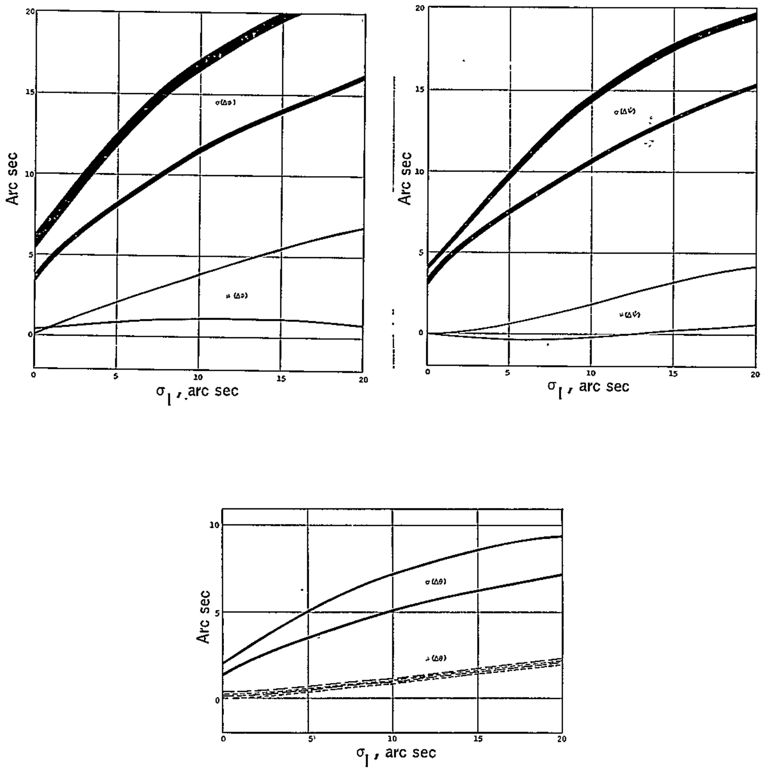

Figure 63. Nominal Case - Attitude Errors as a Function of Instrument Noise

precisely. Thus, the accuracy to which attitude can be estimated will be impaired by the use of an assumed value of instrument variance which does not represent the true variance.

Simulation results are presented in Figures 64 and 65, which demonstrate the effect of instrument noise uncertainties. Attitude and rate errors are plotted as a function of the ratio σ_I'/σ_I where σ_I' represents the assumed value of instrument variance. Errors are plotted for two values of true instrument variance σ_I. For these simulations the exact transit times are corrupted by Gaussian noise of variance $\sigma_I/|\bar{\omega}|$, while σ_I' is used in the computation of measurement variance σ_H appearing in Equation (46). Generally, the errors at the point where $\sigma_I = \sigma_I'$ are the minimum errors or very close to the minimum. Secondly, these results indicate that in an operational data-reduction system it is safer to underestimate rather than overestimate the quality of the starmapper.

Inertia ratio determination: In an operational environment, initially at least, the spacecraft principal moments of inertia will not be known with sufficient precision to permit accurate extrapolation of the spacecraft equations of motion. Thus, estimation of the inertia ratios will have to be performed using the algorithms discussed. The following paragraphs describe simulation experiments undertaken specifically to obtain estimates of these parameters.

Results of a first cut at the estimation of the inertia ratios are shown in Figure 66 where the errors in A and θ for a data reduction simulation in which estimation of the inertia ratios, along with vehicle rates and attitude, was initiated at time $t = 0$. Although the errors are converging at the termination of the simulation, these results are not satisfactory for the mission being simulated. For this mission the spacecraft is in the earth's shadow approximately 2000 seconds; consequently, it is desirable to obtain good convergence in this period of time. The poor performance exhibited by the filter in this simulation is due primarily to the relatively large updates experienced by the inertia ratios A and C at the first few transit measurements. As seen from Figure 66, the update is not only large but incorrect in sign. This is not surprising since the initial measurement error primarily reflects the large initial uncertainties in attitude and not the uncertainty in inertias. Since the initial corrections are proportional to the initial assumed variance values, this problem can be controlled by suitably modifying the variances on A and C. However, such an approach is undesirable since it is initial condition dependent, and by reducing the initial variances on A and C the sensitivity of the filter to uncertainties in the inertias may be lost.

Alternately, estimation of these parameters can be initiated at some time later than the time at which estimation of the vehicle rates and attitude is initiated. With this approach, the objective is to obtain convergence to a measurement error which is primarily due to the uncertainty in the inertia values. Results of implementing this approach are shown in Figures 67 and 68.

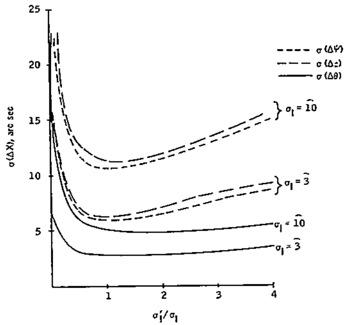

Figure 64. Attitude Errors as A Function of Instrument Noise Uncertainty

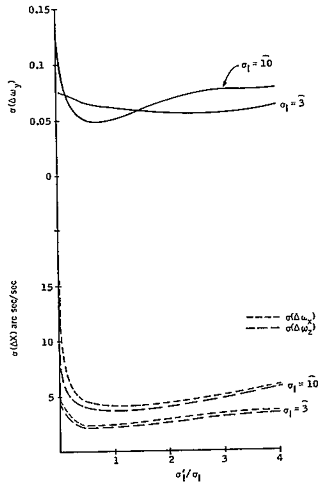

Figure 65. Rate Errors as a Function of Instrument Noise Uncertainty

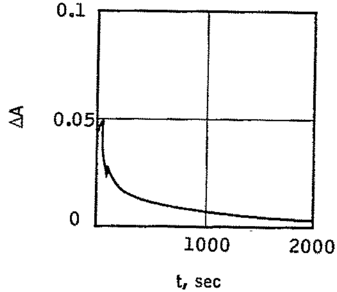

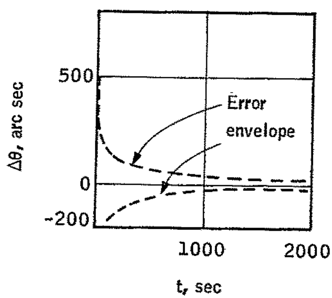

Figure 66. Inertia Ratio and Pitch Error with Inertia Ratio Estimation Initiated at t = 0

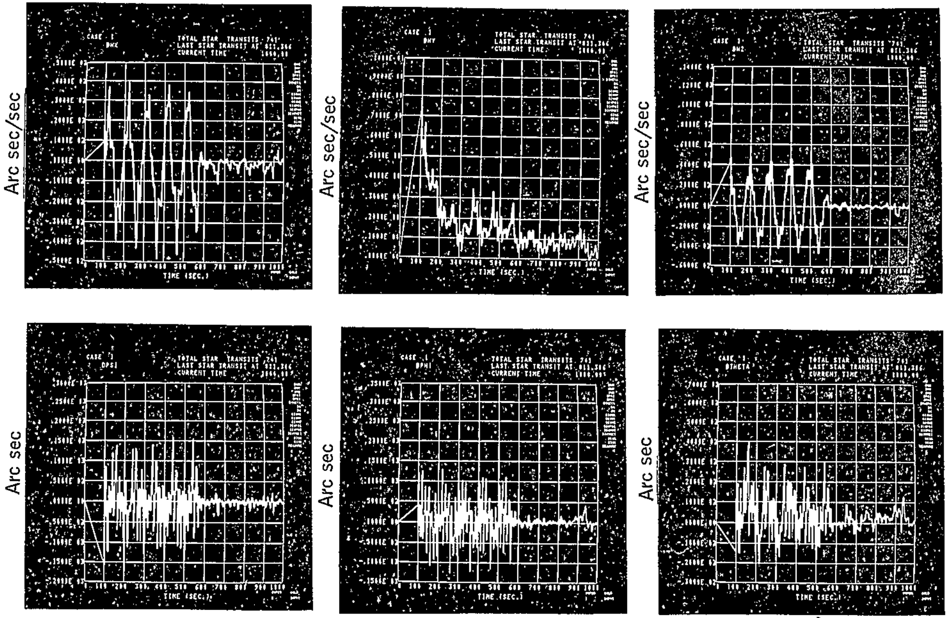

Figure 67. Rate and Attitude Errors with Inertia Ratio Estimation Initiated at t = 550 sec ($Q_{77} = Q_{88} = 10^{-7}$, $\Delta A = 0.01$)

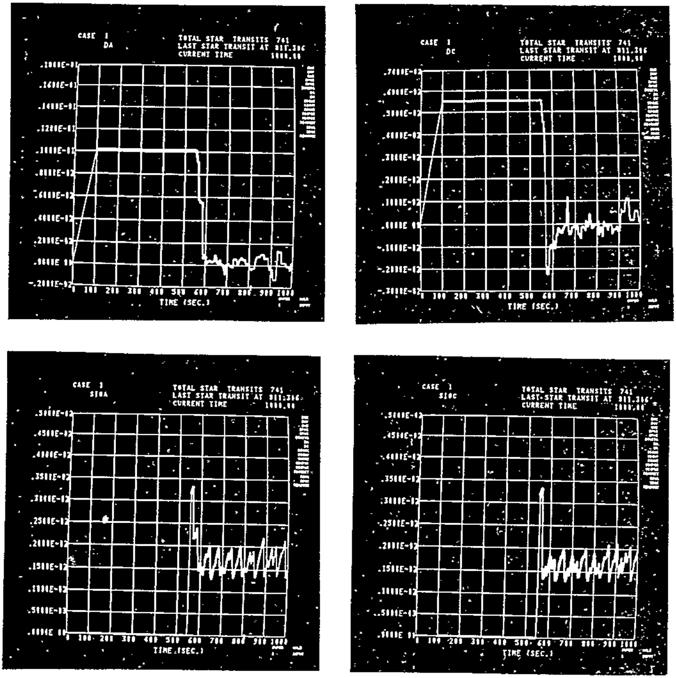

Figure 68. Inertia Ratio Error and Covariance Behavior and Inertia Ratio Estimation Initiated at t = 550 sec ($Q_{77} = Q_{88} = 10^{-7}$, $\Delta A = 0.01$)

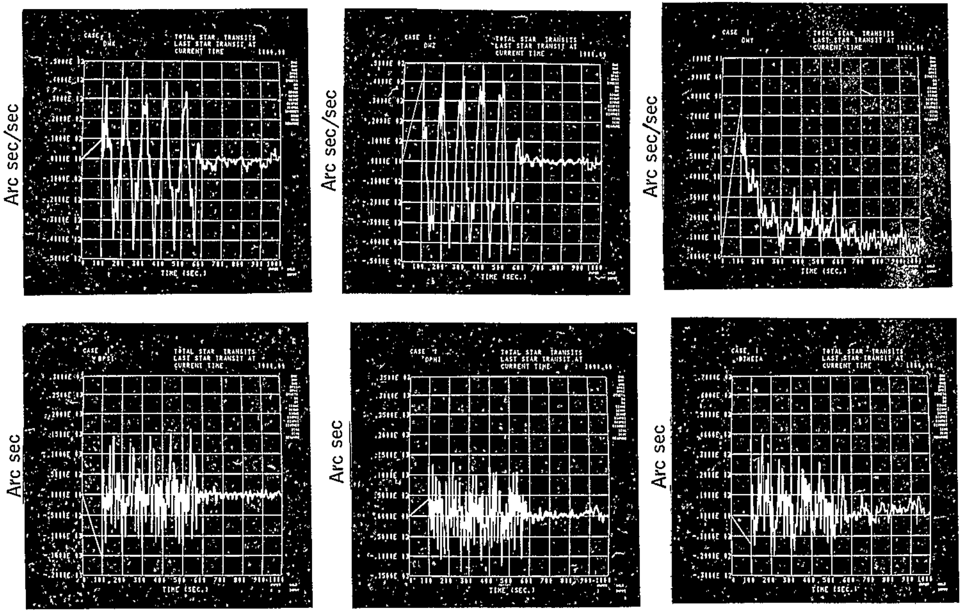

Figure 69. Rate and Attitude Errors with Inertia Ratio Estimation Initiated at t = 550 sec ($Q_{77} = Q_{88} = 10^{-9}$, $\Delta A = 0.01$)

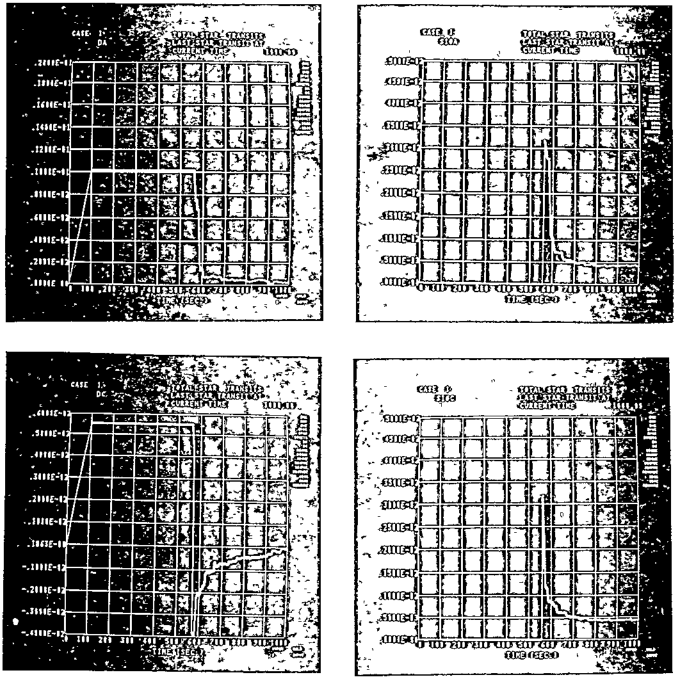

Figure 70. Inertia Ratio Error and Covariance Behavior with Inertia Ratio Estimation Initiated at $t = 550$ sec ($Q_{77} = Q_{88} = 10^{-9}$, $\Delta A = 0.01$)

These results are from a simulation identical to that described in the "Initial Data Reduction" discussion except that inertia ratio values of

$$I_1 = I_3 = 54.5 \text{ slug-ft}^2$$

were assumed and estimation of A and C initiated at 550 seconds. Examination of attitude errors in Figure 67 shows peak-to-peak, steady-state excursions of approximately ±100 arc seconds in $\Delta\psi$ and $\Delta\phi$ and ±20 arc seconds in θ in the time span up to 550 seconds. A very rapid convergence is obtained in all variables once the estimation of A and C is initiated. The errors in A and C, labeled DA and DC, along with the square root of the P_{77} and P_{88} elements, labeled SIGA and SIGC, are shown in Figure 68. The steady-state values of these covariance elements are maintained by additive noise values $Q_{77} = Q_{88} = Q10^{-7}$. Since these steady-state values are high and are observed to create rather large excursions in the estimates of A and C, an identical simulation was performed with $Q_{77} = Q_{88} = 10^{-9}$. The results, presented in Figures 69 and 70, show improved estimation accuracy in all variables and particularly in A and C where improved accuracy by approximately an order of magnitude is evident.

Results of a third such simulation are shown in Figures 71 and 72. For this case fixed inertia values of

$$I_1 = I_3 = 53 \text{ slug-ft}^2,$$

were used over the first 550 seconds of the simulation steady-state, peak-to-peak attitude errors with these values are seen to be ±400 arc seconds in ψ and ϕ ±60 arc seconds in θ. Again, rapid convergence to acceptable values is noted in all variables once the estimation of A and C is initiated.

These results demonstrate that the estimation of the spacecraft inertia ratios can be accurately estimated with the Kalman filter and that the most suitable approach is to initiate the estimation of these parameters at a point in time after convergence from initial attitude and rate errors has been achieved.

Parameter Estimation: Previously, the estimation of inertia ratios was discussed and results presented which indicate that these parameters are readily estimated (observable) with the estimation algorithm. Also, it was noted that the algorithms were programmed so that the spacecraft magnetic moment and eddy current coefficients, divided by I_2, could optionally be included in the estimation state. Generally, these parameters were not included for two reasons. First, initial data-reduction simulations indicated that acceptable results could be obtained by assuming an external torque model with no magnetic moment and an eddy current coefficient in error by 50%. Secondly, data-reduction simulations in which the eddy current coefficient was treated as a variable indicated that errors in the value of the eddy current coefficient of this magnitude did not significantly degrade attitude estimation. This is shown in Figure 73 where the variance of the errors and

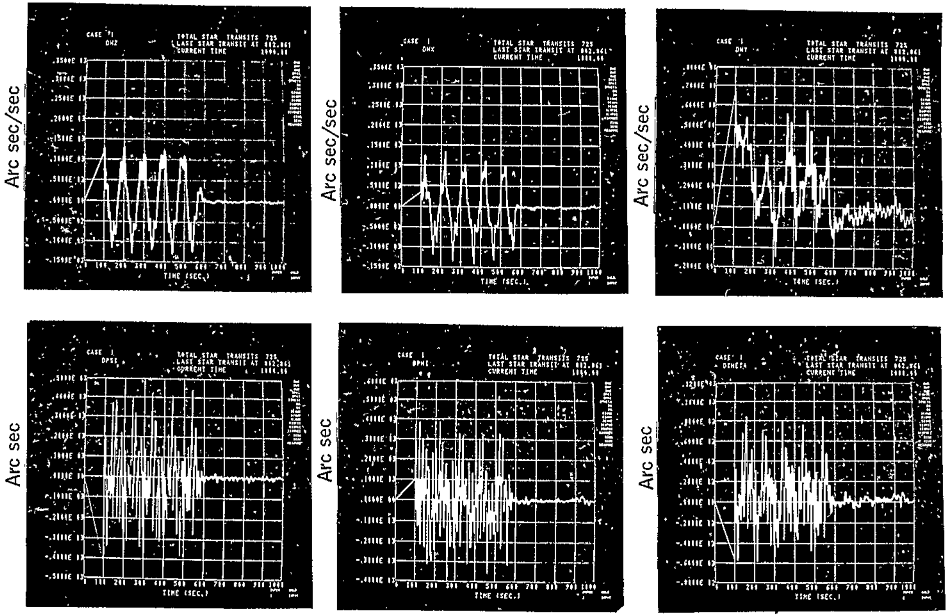

Figure 71. Rate and Attitude Errs with Inertia Ratio Estimation Initiated at t = 550 sec ($Q_{77} = Q_{88} = 10^{-9}$, ($\Delta A = 0.025$)

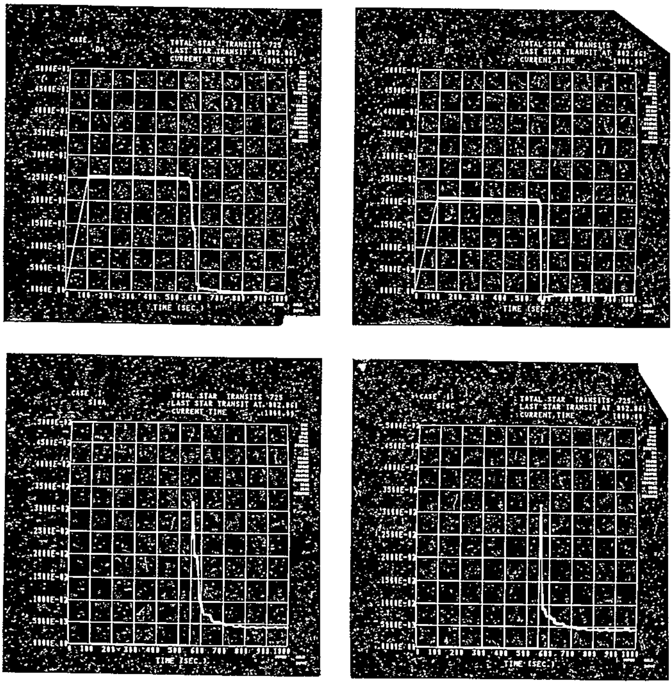

Figure 72. Inertia Ratio Error and Covariance Behavior with Inertia Ratio Estimation Initiated at $t = 550$ sec ($Q_{77} = Q_{88} = 10^{-9}$, $\Delta A = 0.025$)

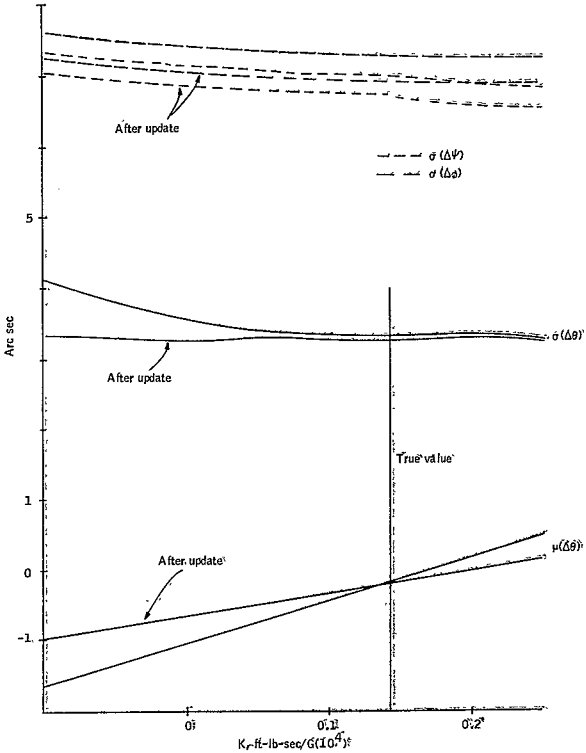

Figure 73. Attitude Errors as a Function of Eddy Current Coefficient

the mean pitch error are plotted as a function of the assumed eddy current coefficient value. Note that the mean value of the pitch errors, $\mu(\Delta\theta)$, before and after update have a crossover point at approximately the true value of K. Specifically, for values of K larger than the true value, larger mean errors are experienced before the update and conversely for values of K less than the true value.

Results of a simulation in which 12 variables (ω, ψ, ϕ, θ, A, C, $\overline{M}'$, K') were estimated are presented in Figures 74 through 76. For this simulation vehicle rates and Euler angles were the only variables estimated until approximately 570 seconds, at which time 12 variable estimation was initiated. Figure 74 shows that no significant improvement in the estimation of the rate and attitude variables, except ω_y, takes place over the last 400 seconds of the simulation. The improvement in the estimate of ω_y is caused by the convergence of K' to the correct value. This is evidenced in Figure 75, where $\Delta K'$, labeled DK, is shown. Improved estimates of K' can be expected to improve the estimate of ω_y since for the symmetric vehicle $\dot{\omega}_y \sim K'$. Also shown in Figure 75 are the inertia ratio errors for initial fixed errors of -0.001. Convergence to errors of 0.001 in the ratios is the limit of the estimation process. The behavior of the square root of covariance diagonal element corresponding to K', $\sqrt{P_{12,12}}$, labeled SIGK, is controlled by an additive noise value $Q_{12,12} = 10^{-15}$. Apparently a smaller value would be more suitable. Results of estimating $\overline{M}'$ are shown in Figure 76. The errors, labeled DMX, etc., exhibit little or no tendency to converge. These results are inconclusive insofar as the estimation of M' is concerned, but it is quite clear from Figure 75 that K' can be estimated accurately.

Numerical Integration: Two major factors in determining the computing time required for data reduction are the integration time step, Δt, and the order of the Runge-Kutta integration method used to extrapolate the vehicle equations of motion (44) from transit to transit. Time step is the most important parameter as the number of evaluations of the right-hand side of both the Riccati equation and vehicle equations of motion (45) depend linearily on it, whereas the integration order determines only the number of evaluations of the spacecraft equations of motion. Attitude accuracy as a function of integration step for second, third, and fourth order Runge-Kutta are presented in Figures 77 and 78. These results are based on the nominal 3-rpm, 2000-second transit data. The most important point to note is that the fourth-order results are relatively insensitive to step size over the interval considered. Since the execution time quoted earlier is based on $\Delta t = 0.5$ second, fourth-order Runge-Kutta simulations, it can be concluded that execution times considerably better than 10 to 20 times faster than real time can be realized on the CDC 6600 computer. Second-order results are slightly worse than the fourth order. The most startling result is the almost divergent behavior of the third-order method which one would intuitively expect to lie between the second and fourth order. This is due to the particular choice of third-order implementation that is used in the simulation where a form due to Huen (Ref. 26) rather than the more symmetrical form due to Kutta is used. Huen's equations

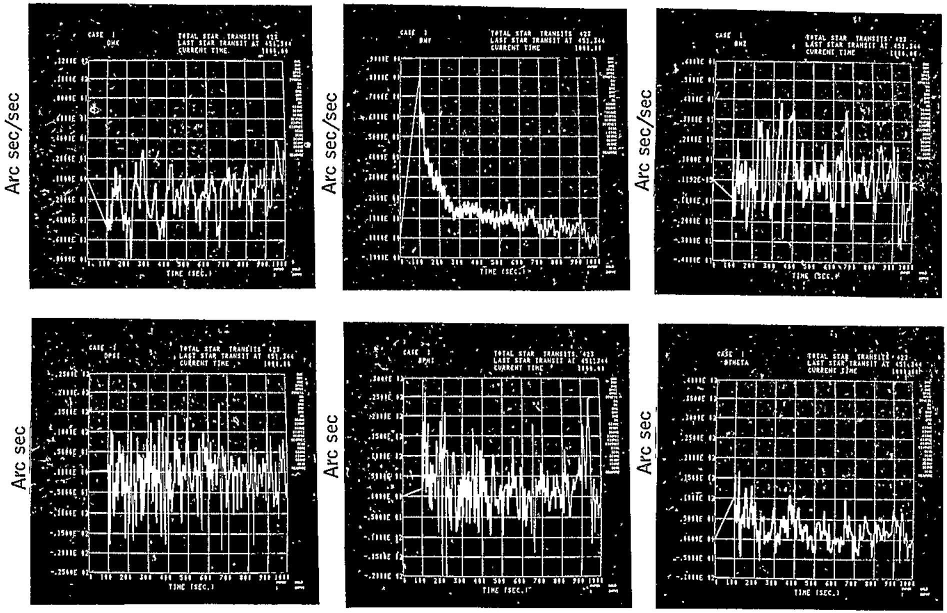

Figure 74. Vehicle Rate and Attitude Errors - 12 Variable Estimation State

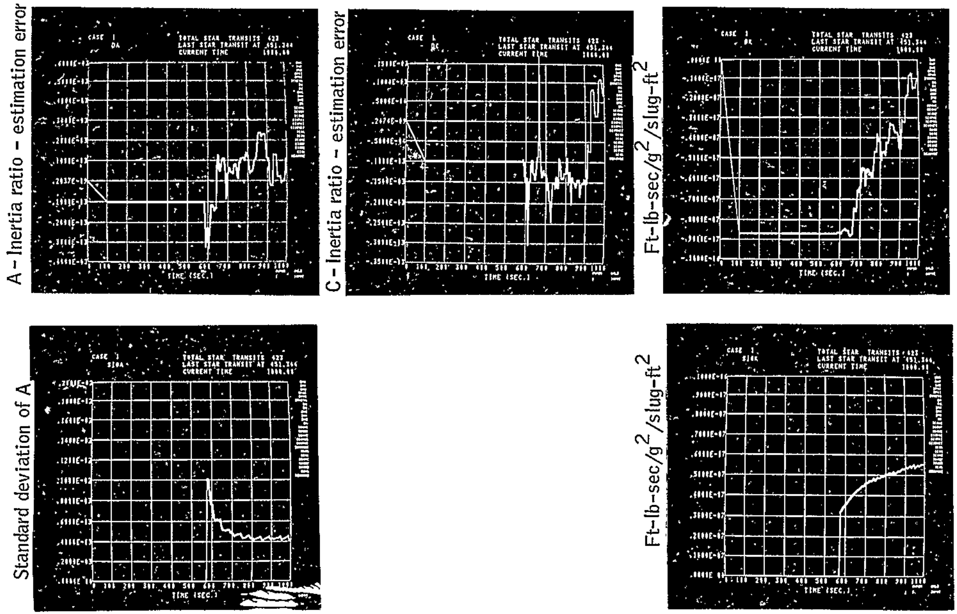

Figure 75. Inertia Ratio, Eddy Current Coefficient - 12 Variable Estimation State

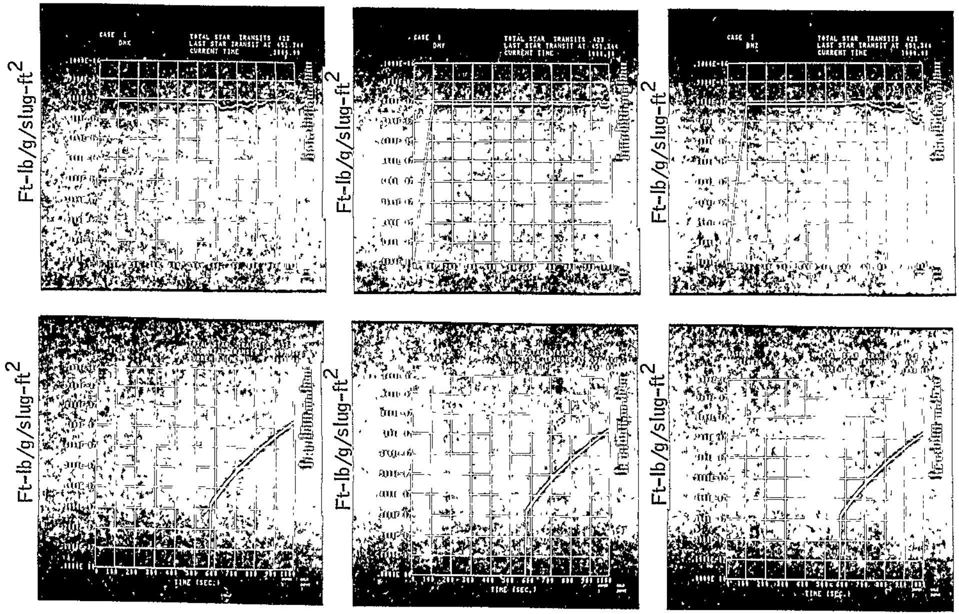

Figure 76. Magnetic Moment Estimation - 12 Variable Estimation State

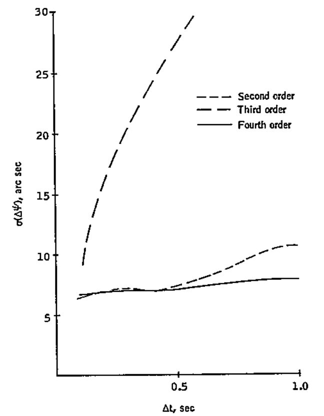

Figure 77. Yaw Error as a Function of Integration Time Step for Second, Third, and Fourth Order Runge-Kutta

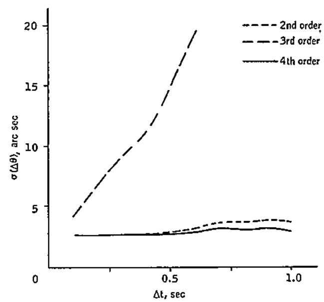

Figure 78. Pitch Error as a Function of Integration Time Step for Second, Third, and Fourth Order Runge-Kutta

$$X_{n+1} = X_n + 1/4\ (K_o + 3K_2)$$

where

$$K_o = \Delta t\ f(t_n,\ X_n)$$

$$K_1 = \Delta t\ f(t_n + \Delta t/3,\ X_n + K_o/3)$$

$$K_2 = \Delta t\ f(t_n \ X\ 2\Delta +/3,\ X_n + 2K_1/3)$$

were chosen since they are simpler than Kutta's. However, as the results indicate, the unsymmetric sampling used to integrate $f(t, x)$ over the interval $[t_n\ t_n + \Delta t]$ is inappropriate for the integration of Equation (44).

Effect of unmodeled torques: In Figure 63 the errors in the attitude estimates do not go to zero with the instrument noise. That this is due primarily to the differences which exist between the external torque models used for the transit generation and the data reduction is shown in Figures 79 through 81. In these figures, comparable attitude errors are shown for identical data-reduction simulations based on the nominal transit case where a complete torque model is used and on transit data derived for a torque model identical to that used in the estimation algorithms. As would be expected, the errors for the transit data derived from the simplified torque model are consistently smaller. Further, it is noted that both the mean and variances go to zero with the instrument variance for the former.

Additive Noise Considerations::One of the most critical problems which must be faced in the application of the filter equations (45) is the determination of the additive noise matrix Q. Trial and error was used to determine the values, Equation (53), used in the data reduction simulations discussed thus far. Apparently, Ref. 27 is the only method available for its determination. During the performance analysis effort these values were applied to several data reduction simulations characterized by variations in a number of different parameters such as spin rate, number of celestial sightings per spacecraft rotation, starmapper cant angle, and instrument noise. Generally, these parameters yielded satisfactory results. Thus, for a real mission where these parameters are well known, Q values established by simulation for a given configuration will be applicable to the actual data reduction. Also, beside a working set of values, simulation can be used to establish the sensitivity of the estimation process to variations in Q and to determine the best direction in optimizing the values used.

Figures 82 through 84 show the sensitivity of attitude errors to variations in the additive noise values q_4, q_5, and q_6. Each of these values was individually varied about the nominal values given in Equation (53). Recalling that $Q_{ii} = q_i^2$, $i = 1, 6$, variations in Q of from three to four orders of magnitude can be tolerated and still produce acceptable results. The q_6 curve shows quite clearly that considerable optimization can be performed with a given set

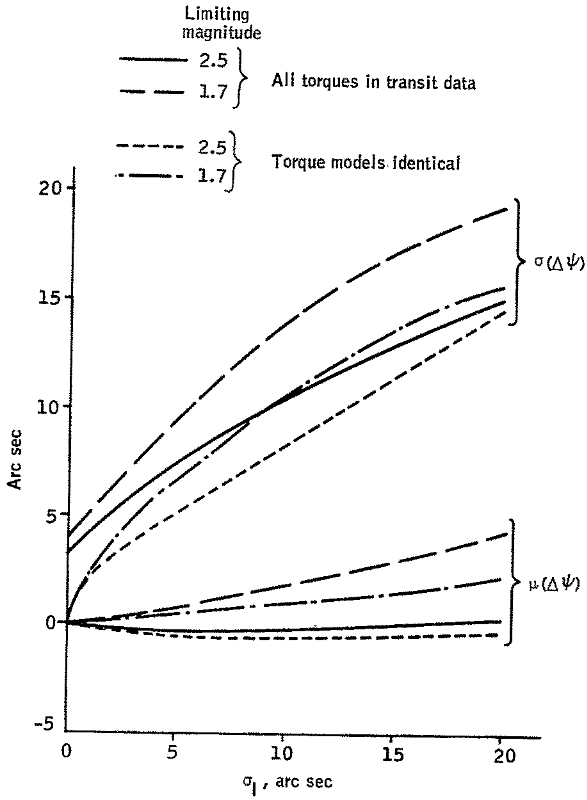

Figure 79. Comparison of Yaw Errors for Different Torque Models and and Number of Sightings as a Function of Instrument Noise

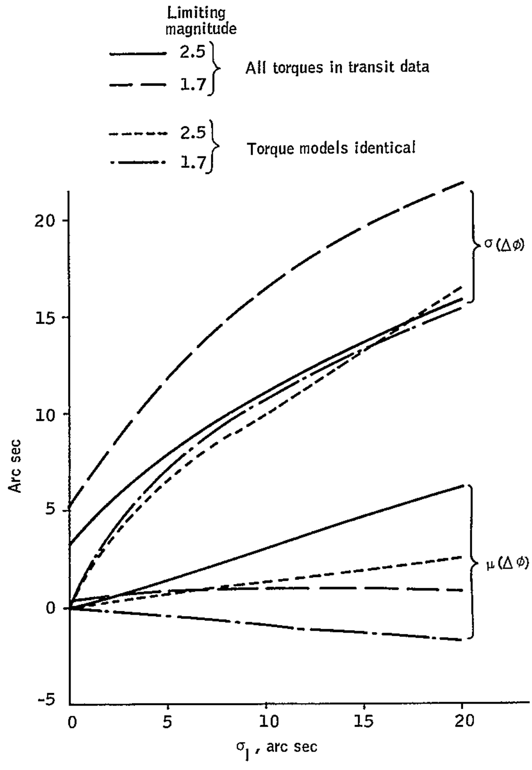

Figure 80. Comparison of Roll Errors for Different Torque Models and Number of Sightings as a Function of Instrument Noise

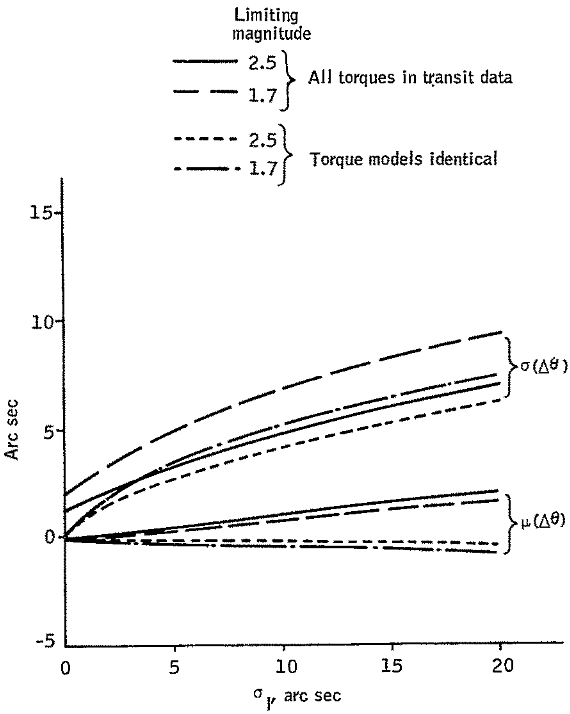

Figure 81. Comparison of Pitch Errors for Different Torque Models and Number of Sightings as a Function of Instrument Noise

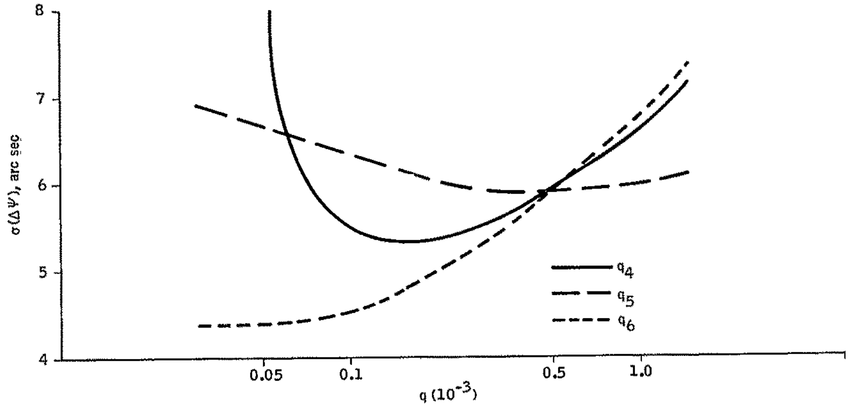

Figure 82. Sensitivity of Yaw Errors to Additive Noise

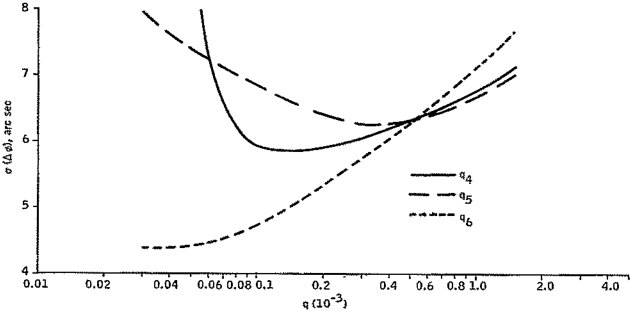

Figure 83. Sensitivity of Roll Errors to Additive Noise

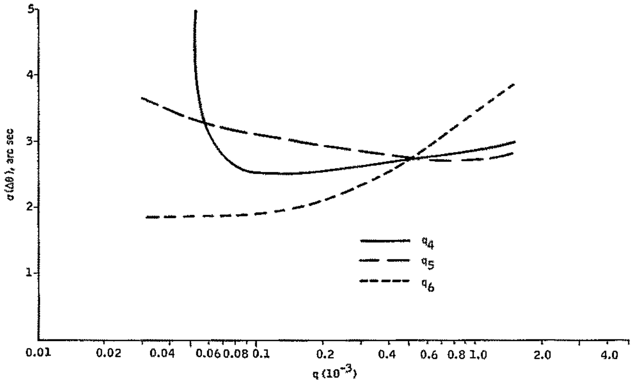

Figure 84. Sensitivity of Pitch Errors to Additive Noise

of additive noise values. In Figures 85 through 87 attitude errors as a function of instrument noise are compared for different values of additive noise. Errors are shown for the nominal additive noise, Equation (53),

$$q(\text{nominal}) = (0.005,\ 0.02,\ 0.25,\ 5.,\ 5.,\ 5.)10^{-4}$$

and for two modifications about the nominal characterized by

$$q_1 = (0.025)10^{-4},\ q_6 = (1.)10^{-4} \tag{54}$$

and

$$q_1 = q_3 = (0.25)10^{-3},\ q_6 = (1.)\,10^{-4} \tag{55}$$

The first modification is based on the results presented in Figures 83 through 85 and similar studies conducted by varying q_1. The second modified set was tested to determine the effect of high Q values in the rate variables. Considerable improvement is noted from the nominal to the first modified set and for all values of instrument noise, although slightly higher mean errors are observed. Note that increased q values in the second set considerably degrade the attitude accuracy and in particular increase the mean attitude errors.

Real versus idealized star fields: It was noted earlier that the loss of transits from stars as they dissapear over the horizon can cause considerable variations in the steady-state estimation error. To better quantify this effect, several data-reduction simulations were conducted using transit data derived from an idealized star catalog consisting of four real stars (5605, 4041, 17518, and 17262 from Figure 53) and by suppressing the earth blocking feature of the transit generating simulation. Figures 88 through 90 show the steady-state attitude errors achieved with the idealized star field as compared with a real star field. Considerably better attitude accuracy is achieved in all axes with the idealized star field, particularly in pitch where an improvement of approximately 50% is noted, although fewer transits were processed for the idealized star field. The additive noise values, Equation (55), were used to reduce both sets of data.

Starmapper cant angle: With the exception of the attitude errors presented in Figures 91 through 96, all simulation results were obtained for a starmapper cant angle $\gamma = 110°$. This value was used extensively since, as shall be shown in subsequent sections, it provides the most favorable conditions for daylight viewing. However, simulations based on cant angle values of $\gamma = 130°$ and $\gamma = 90°$ were conducted to determine the affect of cant angle variations on attitude estimation errors. Attitude errors for $\gamma = 130°$ are shown in Figure 91 and for $\gamma = 90°$ in Figures 93 through 95. For the latter, results are presented for two different values at limiting star magnitude. The transit data for these conditions are depicted in Figures 92 and 96. Note that the $\gamma = 130°$ star field is much less favorable than the $\gamma = 90°$ data; therefore, comparisons on the basis of attitude accuracies achieved are not meaningful.

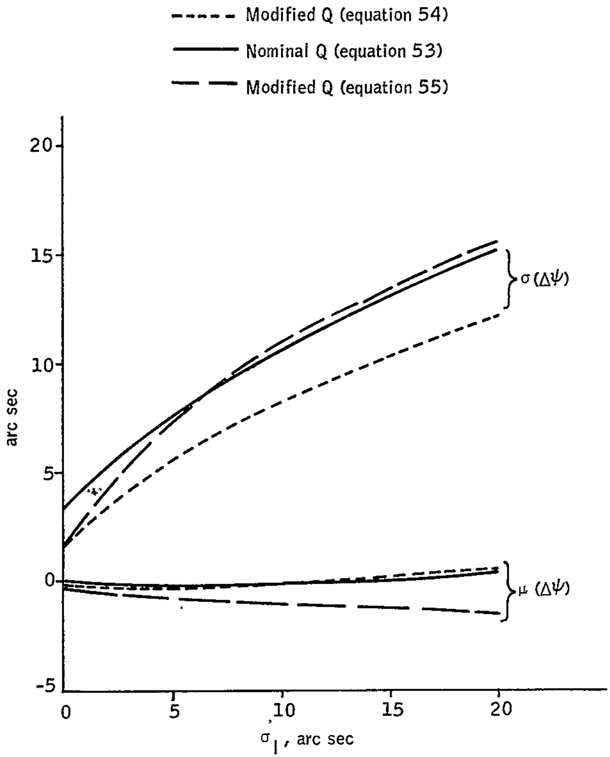

Figure 85. Comparison of Yaw Errors for Different Values of Additive Noise

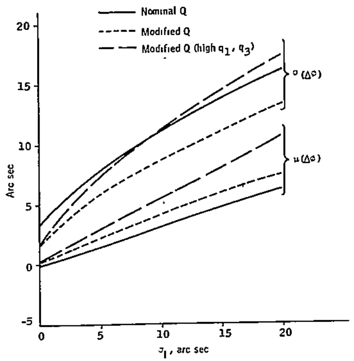

Figure 86. Comparison of Roll Errors for Different Values of Additive Noise

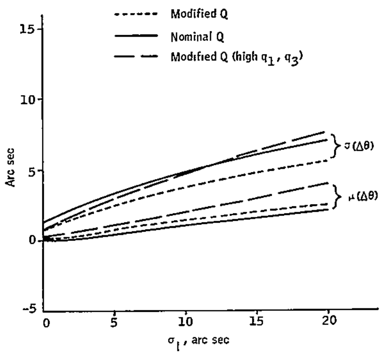

Figure 87. Comparison of Pitch Errors for Different Values of Additive Noise

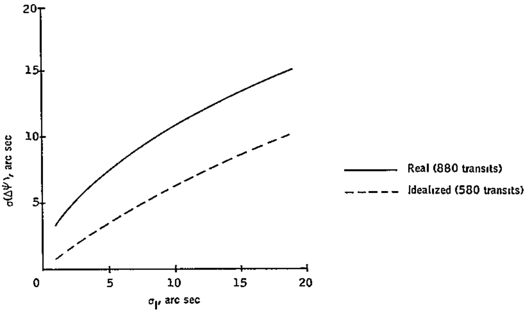

Figure 88. Comparison of Yaw Errors for Real and Idealized Star Fields

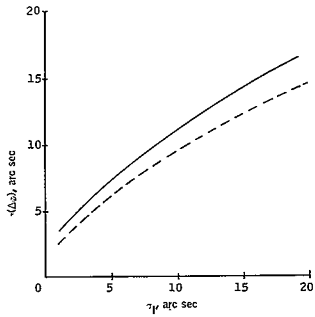

Figure 89. Comparison of Roll Errors for Real and Idealized Star Fields

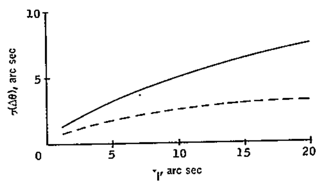

Figure 90. Comparison of Pitch Errors for Real and Idealized Star Fields

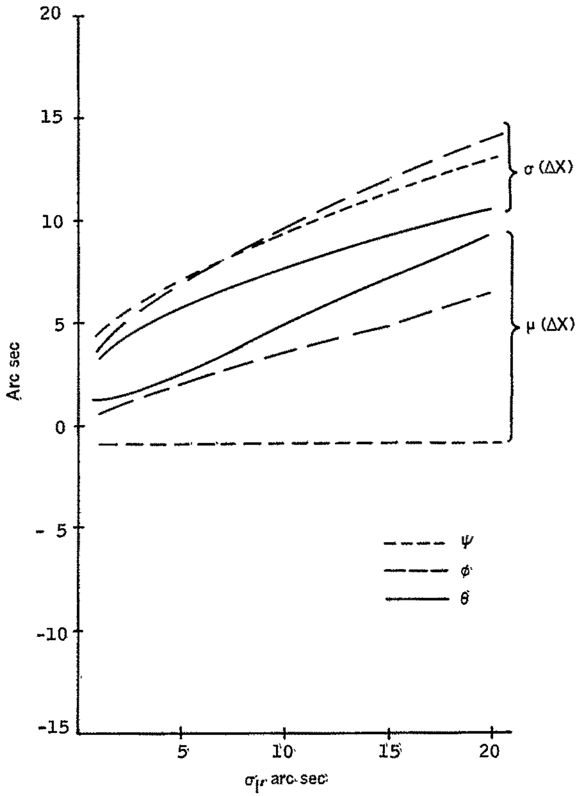

Figure 91. Attitude Errors as a Function of Instrument Noise for $\gamma = 130°$

Star No.	Mag	α Deg	δ Deg	$\tilde{t}_s$ Sec	$\Delta\tilde{t}_s$ Sec	
6668	1.70	80.833	63.212	0.47	0.1	
7451	0.40	88.339	74.026	0.48	0.1	**
	sun	0.0	0.0	1.0	0.04	*
6681	1.78	81.043	28.580	2.0	0.1	*
7557	2.71	89.359	37.212	2.73	0.01	*
7543	1.89	89.268	44.947	3.23	0.07	*
15185	1.95	165.419	61.932	6.34	0.12	*
15145	2.44	164.958	56.562	6.54	0.07	*
16268		178.019	53.881	7.03	0.15	*
16189	2.23	176.838	43.164	9.77	0.27	*
12623	2.22	136.691	43.164	15.30	0.08	*
11105	2.22	122.125	47.140	15.96	0.19	*
10947	2.27	120.602	39.815	16.21	0.02	*
9706	2.74	108.990	36.977	16.85	0.07	*

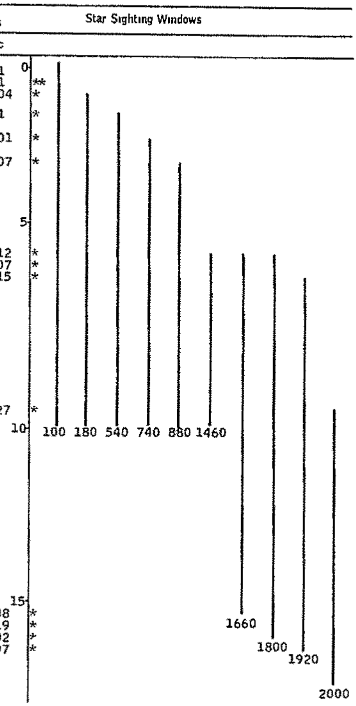

Figure 92. Transit Data for γ = 130°

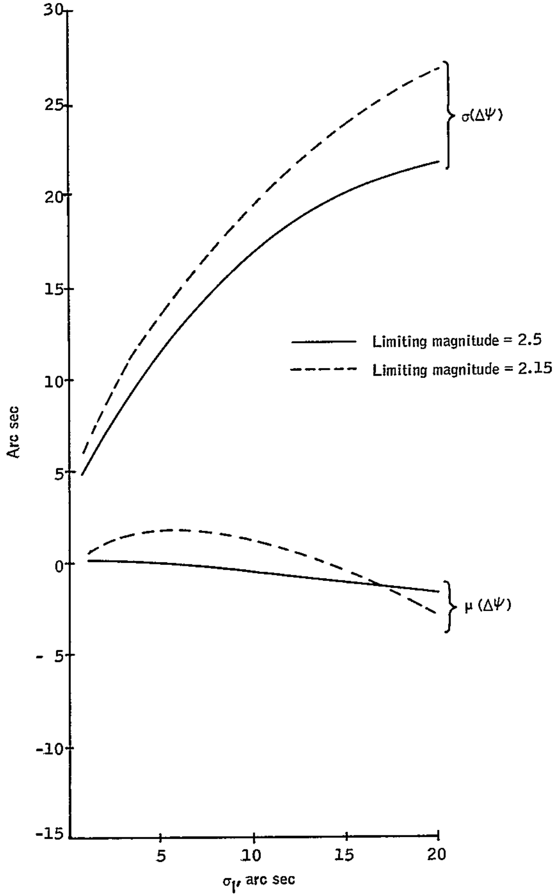

Figure 93. Yaw Error as a Function of Instrument Noise for $\gamma = 90°$

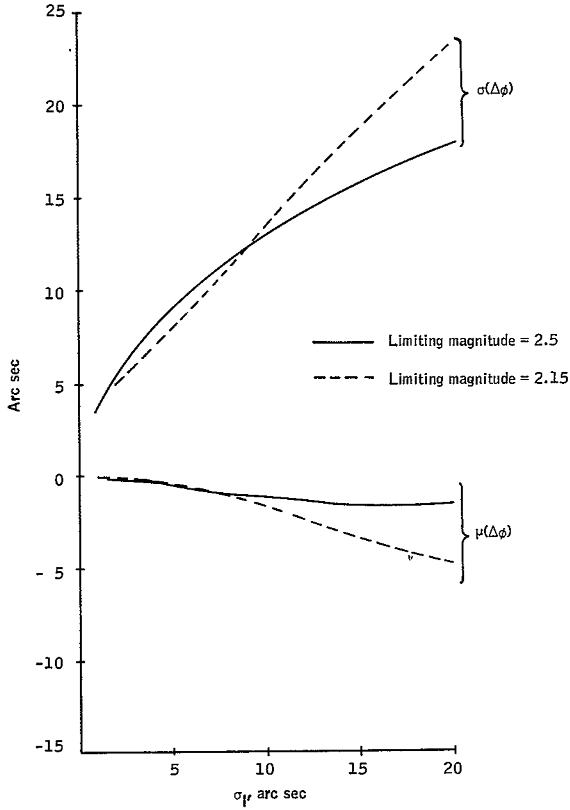

Figure 94. Roll Error as a Function of Instrument Noise for γ = 90°

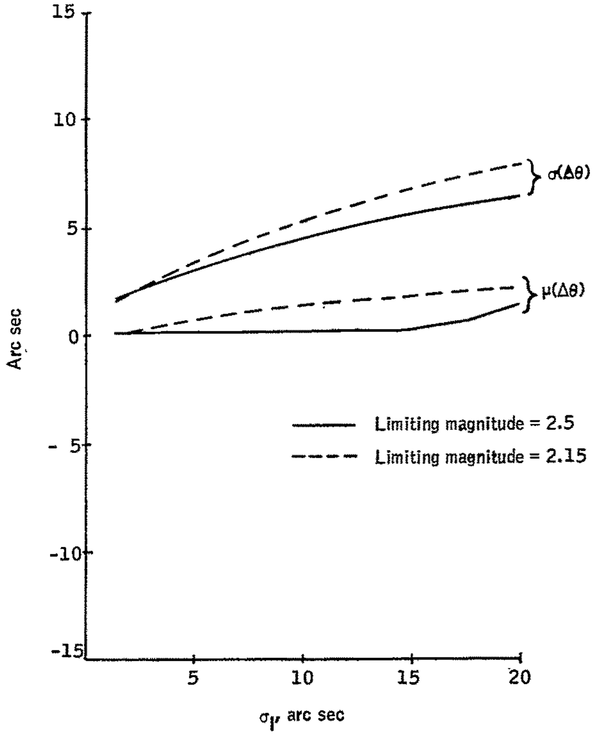

Figure 95. Pitch Error as a Function of Instrument Noise for γ = 90°

Star No.	Mag	α Deg	δ Deg	$\tilde{t}_s$ Sec	$\Delta\tilde{t}_s$ Sec
	Sun	0.0	0.0	1.0	0.04
2538	2.23	31.319	23.305	1.86	0.18
3733	2.10	46.495	40.828	2.68	0.14
2477	2.28	30.458	42.170	2.89	0.12
1117	2.15	13.667	60.536	4.06	0.13
2243	2.12	29.903	89.110	5.39	0.19
20029	2.24	222.695	74.292	6.33	0.18
20947	2.31	233.317	26.826	8.89	0.06
19856	2.70	220.881	27.214	8.97	0.15
19033	2.26	211.176	36.043	12.64	0.12
19656	2.65	218.342	41.867	12.76	0.03
18458	2.56	204.437	53.129	13.50	0.10
18971	0.86	210.360	60.053	13.70	0.11
19728	0.06	219.326	60.562	13.80	0.03
17374	1.50	191.438	59.326	13.98	0.15
16952	1.58	186.180	62.730	14.20	0.50

Star Sighting Windows

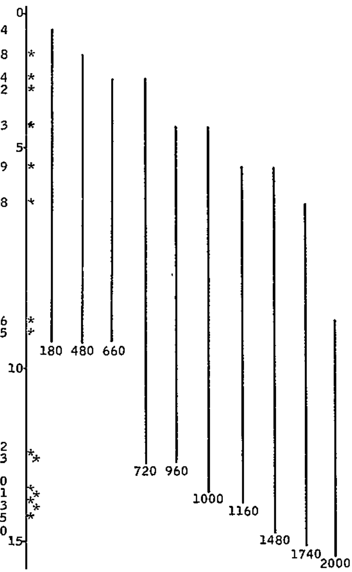

Figure 96. Transmit Data for γ = 90°

However, two points are shown quite clearly when the errors for the two cant angles are compared. First, it is noted that pitch angle θ is determined with less accuracy relative to yaw and roll for the $\gamma = 130°$ case. At σ_I = 3 seconds, for example.

$$\frac{\sigma(\Delta\theta)}{\sigma(\Delta\psi)} = 0.75$$

for $\gamma = 130°$, while for $\gamma = 90°$

$$\frac{\sigma(\Delta\theta)}{\sigma(\Delta\psi)} = 0.25$$

Also, mean errors in pitch are seen to exceed the mean errors in yaw and roll. Secondly, in spite of the larger pitch errors at $\gamma = 90°$. This is to be expected since at $\gamma = 90°$ the measurements are made in the pitch plane and yield more information about pitch, whereas at $\gamma = 130°$ sensitivity to roll and yaw is increased.

Reduced number of stars: Simulation results presented thus far have used sightings from three to seven celestial bodies per spacecraft rotation. Statistical results are presented in Figures 97 through 99 for one and two sightings per spacecraft rotation. These results were obtained from data-reduction simulations identical to the nominal except that after 1000 seconds only one or two stars were used for the data reduction. The modified additive noise values, Equations (54), were used. Time-varying results from a similar single-star simulation are shown in Figure 100. As can be seen from the behavior of the variable $\sqrt{P_{66}}$ (labeled SIGTHET), data reduction with a single star was initiated at 600 seconds. Star No. 17518 is used in the interval 600 to 2000 seconds. The results presented in Figure 100 are for an instrument variance, $\sigma_I = 3$ arc seconds.

Steady-state results obtained with two stars are generally satisfactory, but when compared with the nominal, these results are seen to degrade in pitch accuracy by approximately 1.5 arc seconds for all values of instrument noise. However, the single-star sighting results are not satisfactory and at best appear to be rather anomalous in that attitude errors do not increase monotonically with instrument noise. In particular, the results for large instrument noise are generally better than for smaller instrument noise. This suggests that for the single-star data reduction smaller values of additive noise would be more appropriate. An examination of the $\Delta\theta$, Figure 100, over the interval from 1200 to 1220 seconds bears this out. Negligible corrections are seen to take place at the transit measurements at approximately 1207 seconds. Further, the steady-state values at $\sqrt{P_{66}}$ are considerably higher than the actual value of $\sigma(\Delta\theta)$.

The results presented in Figures 97 through 100 indicate that the use of sightings from two celestial bodies can maintain satisfactory filter

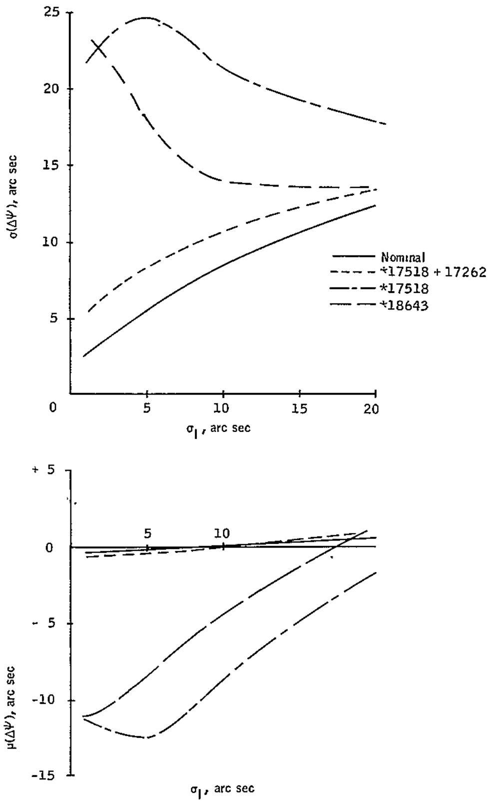

Figure 97. Comparison of Yaw Errors using One and Two Star Sightings/Vehicle Rotation

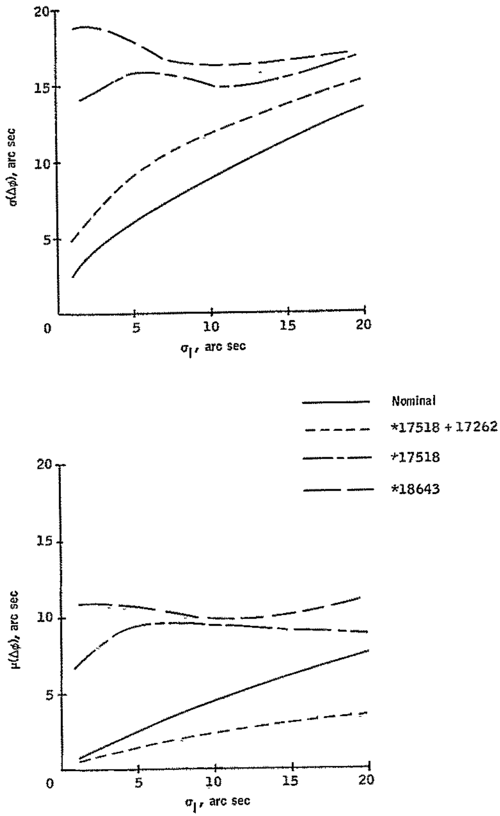

Figure 98. Comparison of Roll Errors using One and Two Star Sightings/Vehicle Rotation

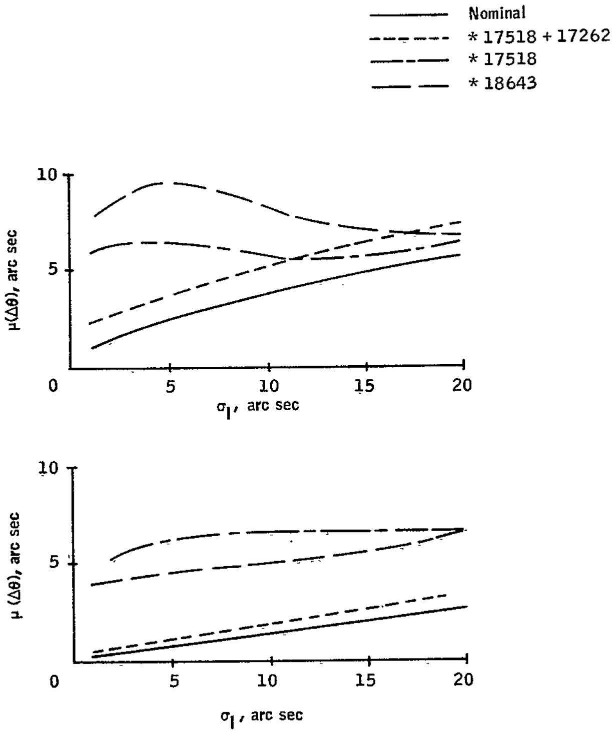

Figure 99. Comparison of Pitch Errors using One and Two Star Sightings/Vehicle Rotation

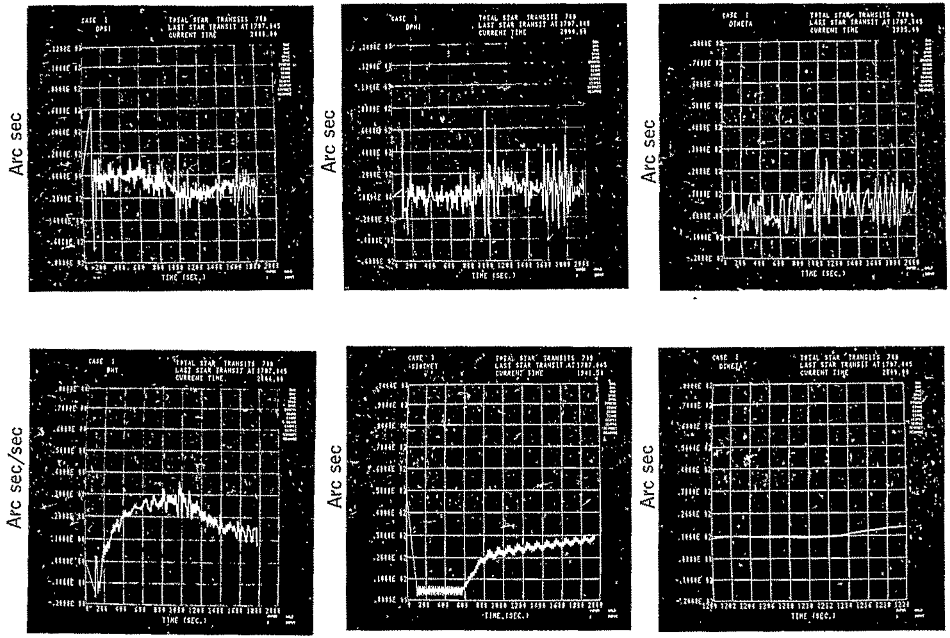

Figure 100. Estimation Results using One Star after 600 sec

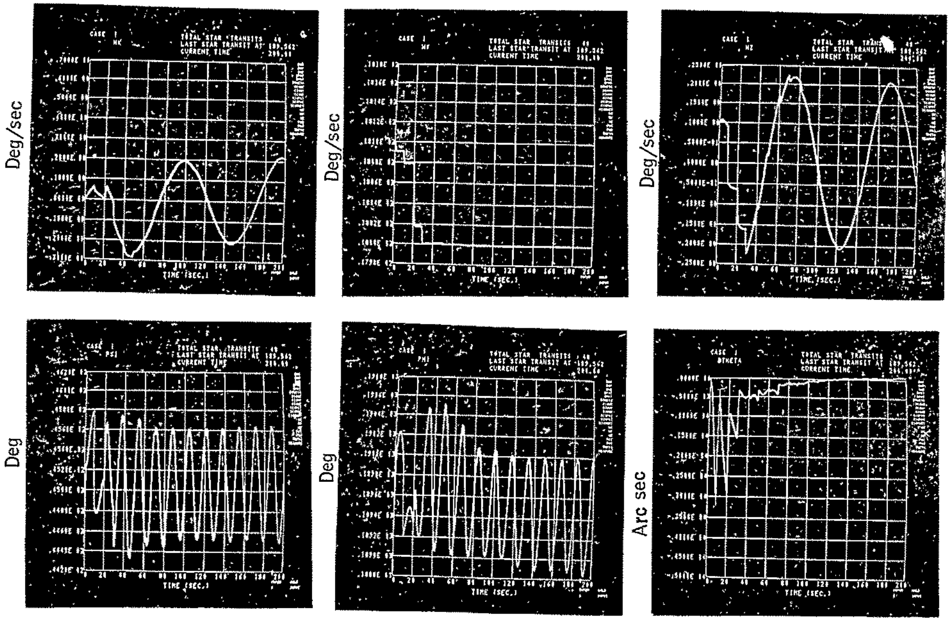

Figure 101. Convergence using Two Celestial Bodies

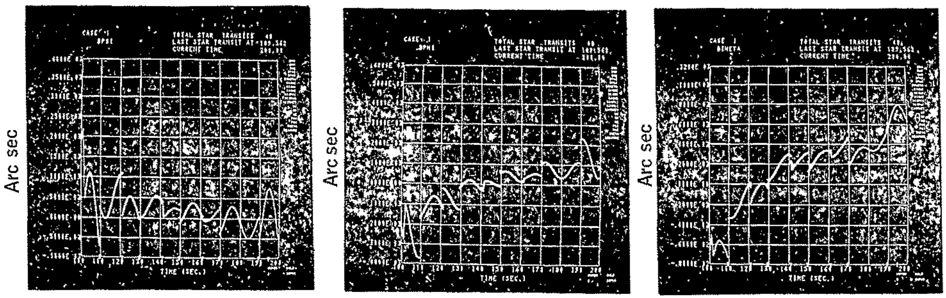

Figure 101. Convergence using Two Celestial Bodies (concluded)

performance if convergence is obtained with sightings from more than two bodies. Further work is required to establish whether adequate convergence can be obtained with two bodies, although the results are from a data-reduction simulation using sightings from the sun and star No. 19242 (See Figure 53). It is seen that after processing of 48 transits convergence to pitch errors of approximately 50 arc seconds was obtained. Referring to Figure 56 where the convergence is shown for approximately 20 transits per vehicle rotation, it is seen that comparable errors in pitch exist after the processing of from 40 to 80 transits.

Spin rate, cone angle results: A nominal spacecraft configuration characterized by a 3-rpm rate and a 0.5° cone angle was used to obtain simulation results presented thus far. Results for other configurations are shown in Figures 102 through 104 for a 1-rpm, 0.5° cone and in Table 6 for 3 to 9 rpm, 0 to 1° cone.

The attitude errors shown in Figures 102 through 104 are for 4500-second, data-reduction simulations based on transit data derived using parameters identical to the nominal except for the 1-rpm rate. Two sets of results using stars down to a limiting magnitude of 2.5 and 1.7 are presented. Approximately 1100 and 620 transits were processed for the two cases. Thus, the two cases represent the processing of sightings from three and five stars per vehicle rotation, respectively. The nominal additive noise values, Equation (53), were used.

Referring to the attitude errors for the 3-4pm nominal (Figure 63), it is seen that the 1-rpm results compare quite favorably and are somewhat better in the yaw and roll axes. Thus, it appears that acceptable attitude estimation can be performed at spin rates down to 1 rpm if sightings from at least three celestial bodies per vehicle rotation are available. The data processing load is also considerably lessened at slower spin rates, and at 1 rpm the estimation algorithms as mechanized execute from 30 to 60 times faster than real time on the CDC 6600.

Table 6 shows attitude errors, for several values of spin rate and cone angle. All results are from 1000-second simulations based on transit data derived from parameters identical to the nominal except for the rate and cone angle. The high additive noise values, Equation (55), were used and are seen to cause mean errors that are relatively large for all rates and cone angles. This effect was noted earlier from these noise values which were used on the nominal 3 rpm transit data, Figures 85 through 87.

While it is difficult to deduce parametric information from Table 6, the results indicate that the estimation of the pitch angle , θ, degrades by approximately 1 arc second as the cone angle increases from 0 to 1°. Also, since the high mean errors can be attributed to the choice of additive noise values, no significant relationship is apparent between spin rate and estimation accuracy.

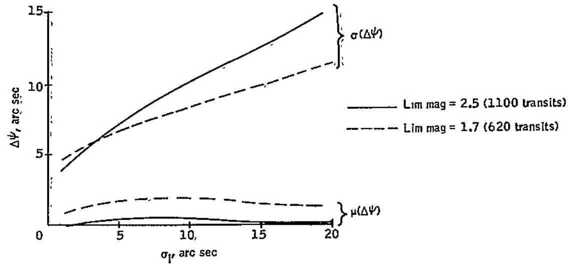

Figure 102. Yaw Errors as a Function of Instrument Noise for $|\bar{\omega}| = 1$ rpm

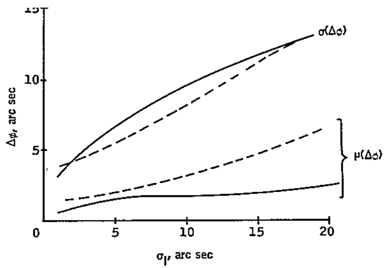

Figure 103. Roll Errors as a Function of Instrument Noise for $|\bar{\omega}| = 1$ rpm

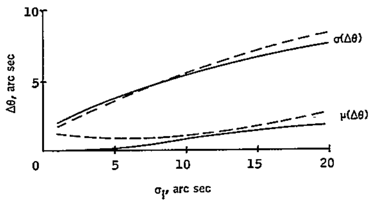

Figure 104. Pitch Errors as a Function of Instrument Noise for $|\bar{\omega}| = 1$ rpm

TABLE 6. - SPIN RATE, CONE ANGLE RESULTS

σ_I	Cone Angle	$\lvert\bar{\omega}\rvert$	Transits Processed	$\mu(\Delta\psi)$	$\sigma(\Delta\phi)$	$\mu(\Delta\phi)$	$\sigma(\Delta\phi)$	$\mu(\Delta\theta)$	$\sigma(\Delta\theta)$
arc sec	deg	rpm		arc sec	arc sec	arc sec	arc sec	arc sec	arc sec
3	0	3	840	-3.16	5.02	2.19	4.97	1.14	1.36
		6	1680	-2.84	4.77	2.23	4.27	1.69	1.24
		9	2460	-1.70	3.79	2.82	3.87	1.92	1.24
	1	3	840	-1.23	5.07	2.30	5.82	1.03	1.95
		6	1680	-3.82	4.92	4.14	5.07	2.42	1.69
		9	2460	-2.82	5.27	3.20	5.13	2.71	1.40
10	0	3	840	-6.64	10.10	6.58	8.51	3.74	3.10
		6	1680	-6.55	9.67	7.20	7.36	5.86	2.67
		9	2460	-3.66	8.22	9.23	7.94	6.94	2.89
	1	3	840	-1.83	9.04	7.23	11.33	3.55	4.13
		6	1680	-7.74	9.58	11.09	9.87	6.57	3.30
		9	2460	-4.50	10.58	9.19	11.24	7.76	3.52

System simulation results and conclusions: An attitude determination system simulation has been described and data reduction simulation results presented which demonstrate the performance of the attitude estimation algorithms for a variety of operating conditions. The major results and conclusions of the system simulation effort are summarized in the following paragraphs.

For a nominal spacecraft configuration characterized by a 3-rpm spin rate, the data reduction algorithms execute 10 to 20 times faster than real time on the CDC 6600 computer using a numerical integration step size of 0.5 second. Thus, from the standpoint of computer run time, the algorithms, as implemented, form the basis of an operational data-reduction system. This conclusion is strengthened by simulation results that indicate that satisfactory attitude estimation can be obtained with larger integration time steps and a consequent decrease in computer run time.

Simulation results obtained from the nominal configuration by treating instrument accuracy and number of celestial sightings per vehicle rotation as parameters indicate that convergence to steady state errors in pitch of 5 arc sec can be achieved with sightings from three celestial bodies and maintained with two sightings for starmapper accuracies of 5 to 10 arc sec. Generally, pitch was determined with better accuracy than roll and yaw. However, in all cases for the number of sightings and instrument accuracies quoted, steady state errors well within 30 arc sec were achieved. In all cases, satisfactory results were obtained with an assumed external model grossly different than the torque model used to generate the simulated transit data.

The effect of instrument noise uncertainty was examined by using variance values in the estimation equations (59) which did not represent the variance of the noise used to corrupt the transit data. Results indicated that it is safer to underestimate, rather than overestimate, the accuracy of the starmapper. For the long-term application of the filter equations, it is apparent that if the measurement instrument degrades as a function of time, because of the results obtained with an overestimation of the instrument performance.

Data reduction simulations undertaken to obtain estimates of fixed spacecraft parameters showed that it was possible to obtain satisfactory estimates of fixed spacecraft parameters showed that it was possible to obtain satisfactory estimates of the inertia ratios and eddy current coefficient normalized to I_2), However, estimation of the spacecraft magnetic moment characteristics does not appear possible. The most satisfactory approach to the estimation of the inertia ratios was to initiate the estimation of the inertia ratios at a point in time after the estimation of the spacecraft rates and Euler angles was initiated.

Estimation accuracy can be considerably improved by using sightings from celestial bodies which are regularly spaced.

The majority of simulations conducted assumed a starmapper cant angle of 110°, orienting the optical axis of the starmapper 20° out of the spin plane. This angle was used because it provides the most favorable conditions for daylight operation. This result is established in the celestrial sensing system design section. However, simulation results show that pitch can be most accurately estimated with the starmapper optical axis lying in the spin plane. Also, for the latter situation pitch was determined more accurately (by a factor of approximately two) than either yaw or roll, whereas for a cant angle of 130° yaw and roll were determined as accurately as pitch.

Simulations conducted at spin rates other than 3 rpm demonstrated that acceptable performance could be obtained for spin rates from 1 to 9 rpm. Further, acceptable performance can be performed outside of this range, although the higher spin rates will require proportionally more computer time to reduce the data.

Additive noise values were determined by trial and error for the nominal data-reduction simulation and applied successfully to a variety of others characterized by different system parameters. Results obtained by varying the values indicated that, for a set of values once established, variations as high as three to four orders of magnitude can be used and produce acceptable estimates of spacecraft attitude. Thus, additive noise values established and optimized through simulation for a given system could be used without difficulty for operational data reduction.

In view of the above results, the estimation algorithms, as mechanized, are applicable to the determination of the attitude of a spin-stabilized spacecraft. Further, at the nominal spin rate of 3 rpm, the data reduction is performed in significantly faster than real time.

ATTITUDE-REFERENCED CELESTIAL SENSING SYSTEM

REQUIREMENTS AND OBJECTIVES

The attitude determination system design has been concerned to this point with the ground-based data reduction of celestial transit data to obtain a time history of the ARRS spacecraft attitude. This section is concerned with the conceptual design of the attitude determination sensing system which consists of celestial sensors and the onboard electronics.

It was required to define a celestial sensing system capable of detecting a given number of stellar targets (presumed to be six for initial attitude determination and two for update purposes) per revolution of the spacecraft, for nearly* all pointing directions on the celestial sphere. In addition, the sensing system must be operative over the entire orbit which implies a capability to detect stars in daylight. Further, the on-board storage of stellar data cannot exceed 60 000 bits per orbit requiring the use of suitable digital filtering techniques to minimize the number of noise pulses stored.

To operate the system over daylight portions of the orbit, it was required to define a light baffle configuration to permit stellar detection as close as possible to bright sources with a reasonable sized baffle. Consequently, an objective was assumed to define a baffle predicted on a minimum-volume criterion.

The objective for the optical system design was to provide the most simple and most efficient concept capable of producing a one arc minute blur spot diameter over the full color spectrum of the system response. It was also required to provide solar detection with similar accuracy to that of stellar targets. Consequently, the sun sensor optical system was, in concept at least, comparable to that of the starmapper.

The major objective for the on-board data processing system was to conceptually implement certain techniques and methods used for ground-based data processing of star signals. Investigations were carried out to determine the optimum of several known criteria for digital filtering of legitimate star pulses from spatial and electronic noise.

Starmapper Sunshield, Aperture, and Limiting Star Magnitude

The major concern of this subsection will be to define a math model of the sun shield and to determine a reasonable criterion to evaluate this model. The parameters characterizing the shield are the output from this effort and are summarized near the end of this subsection.

---

*Portions of the sky around the North and South Celestial Poles are excluded.

An operating environment, as related to the sun, the illuminated earth, and the stellar background were defined and used to compute the sun shield parameters.

An investigation was made into the case in which the system was to be operational less than 100 percent of the time. The results of this study are presented as statistical nomographs.

Statement of problem. -- Capability of the starmapper to detect stars on the daylight side of the orbit is almost singly dependent on the light baffle. This baffle must be capable of attenuating the sun's radiation to at least a level equivalent to the faintest star which must be detected during sunlit operation. The light baffle must also be capable of shielding the starmapper from both the sun and the illuminated earth. Also, the physical dimensions of the baffle must be kept within bounds; this requirement serves as a constraint on the closest permissible approach of the optical axis to either the sun or the sunlit earth. Figures 105 and 106 are included as an aid in defining pertinent geometric relationships.

The immediate discussion relates to the problem of shielding the starmapper from the sun and the illuminated earth. It is assumed that the outer surfaces are specular reflectors, implying that the incident and reflected rays have identical angles with the surface normal. It is also assumed that the shield possesses the general form depicted in Figure 107 in which the upper surface is a perfect conical mirror having a cone angle, α, and having all incident rays, with angles greater than some nominal angle, β, reflect out of the shield. Details of the baffle interior are not shown.

Since the dimensions of the shield must be kept within bounds, a natural criterion is that the total volume be minimized. The total volume cannot be directly minimized unless the aperture size is specified; but the aperture size is a function of the limiting magnitude star required to provide a predetermined number of stellar targets. A further complication is due to the fact that the limiting magnitude depends on the amount of sky viewable by the starmapper.

An indirect approach to the solution of this problem is possible if one minimizes a normalized volume (which will be defined later) and determines limiting magnitude in a region of the sky in which the stars are sparse. The worst case appears to be near the South Galactic Pole on the celestial sphere. (RA ≈ 12°: DEC. ≈ -27°)

A computer program was written to find the minimum volume over a space, determined by the following four variables which are defined explicitly in Figures 60, 61, and 62.

α = cone angle of reflector

β = shield angle -- the closest permissible approach to the sun or sunlit earth

γ = cant angle

S = the area of sky swept out

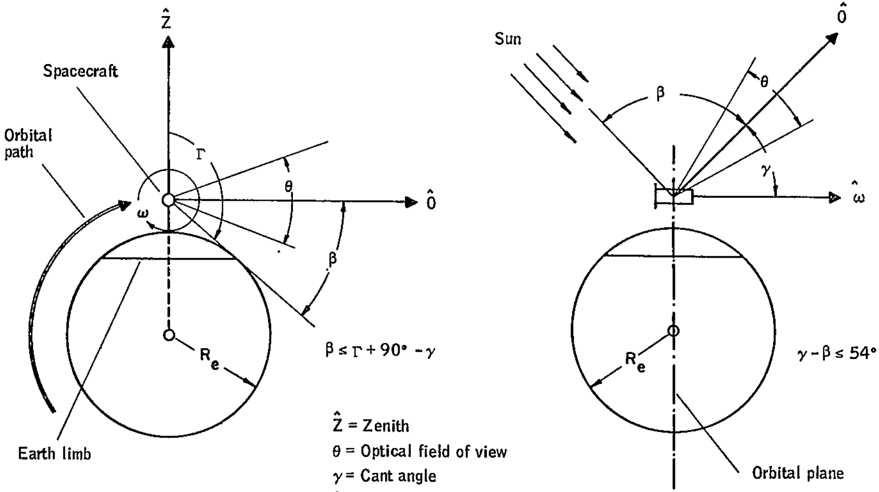

$\hat{Z}$ = Zenith

θ = Optical field of view

γ = Cant angle

β = Closest permissible approach to sun or sunlit earth

$\hat{O}$ = Optical axis

R_e = Earth radius (including atmosphere)

Γ = Earth blocking angle

Figure 105. Scanning Geometry of Starmapper

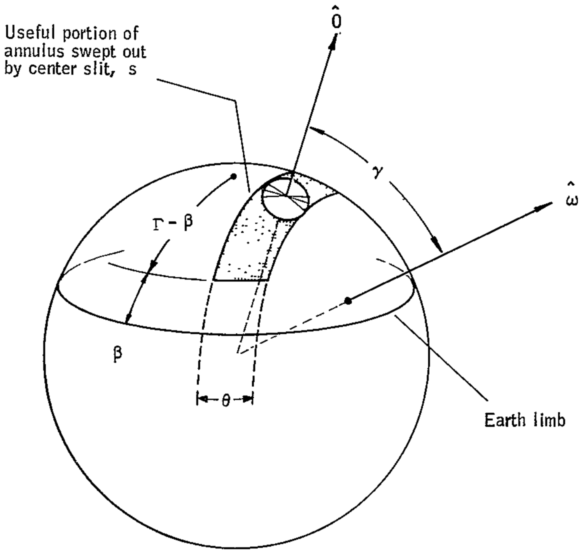

γ - Cant angle
$\hat{O}$ - Optical axis
β - Closest approach to sunlit earth
$\hat{\omega}$ - Scan axis
Γ - Earth blocking angle
θ - Angular field of view

Figure 106.. Scanned Annulus Projected Onto Celestial Sphere

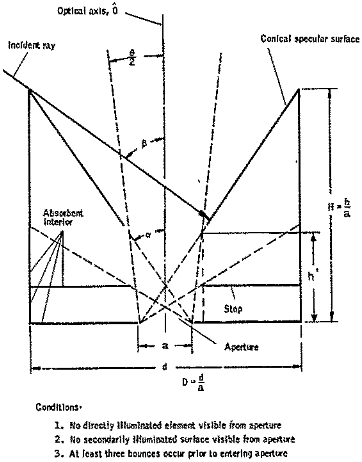

Figure 107. Baffle Description

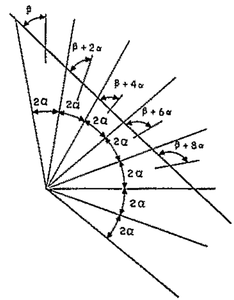

Figure 108. Geometric Construction of Baffle Cone to Show Depth of Penetration and Number of Bounces

Volume formula. -- The depth to which an incident ray penetrates a conical-shaped reflective surface can be determined geometrically, as shown in Figure 108. When the angle between the conical bisection and extended incident ray becomes greater than 90°, the reflected ray exits from the shield.

That is,

$$\beta + 2(N-1)\alpha \geq 90°$$

where

$$N = \text{number of penetrating bounces}$$

and

$$0 < \alpha < \beta < 90°$$

Solving for N gives

$$N = \left[\frac{90° - \beta}{2\alpha}\right] + 1$$

but since N must be an integer, only the integral part of the bracketed quantity is retained. When N = 1, the formula for the value is quite simple and is the case depicted in Figure 107. From Figure 107,

$$h' = \frac{a \cos\alpha \cos\frac{\theta}{2}}{\sin\left(\alpha - \frac{\theta}{2}\right)}$$

and

$$h - h' = \frac{a \cos\alpha \cos\beta \sin\left(\alpha + \frac{\theta}{2}\right)}{\sin\left(\alpha - \frac{\theta}{2}\right) \sin(\beta - \alpha)}$$

so that

$$h = \frac{a \cos\alpha}{\sin\left(\alpha - \frac{\theta}{2}\right)} \left[\frac{\cos\beta \sin\left(\alpha + \frac{\theta}{2}\right)}{\sin(\beta - \alpha)} + \cos\frac{\theta}{2}\right]$$

or finally

$$h = \frac{a \cos^2\alpha \sin\left(\beta + \frac{\theta}{2}\right)}{\sin\left(\alpha - \frac{\theta}{2}\right) \sin(\beta - \alpha)} \tag{56}$$

Also from Figure 107

$$d = 2h \tan\alpha - a \tag{57}$$

The volume for the single bounce case is

$$v = \frac{\pi h d^2}{4} = \frac{\pi}{4} a^3 \frac{\sin\left(\beta + \frac{\theta}{2}\right) \left[\cos\alpha \, \sin(\beta+\alpha) \, \sin\left(\alpha + \frac{\theta}{2}\right)\right]^2}{\left[\sin\left(\alpha - \frac{\theta}{2}\right) \sin(\beta-\alpha)\right]^3} \tag{58}$$

The denominator of Equation (58) implies that α is bounded by the following inequality:

$$\frac{\theta}{2} < \alpha < \beta$$

If the function

$$f(\alpha, \beta, \theta) = \frac{V}{\alpha^3} = \frac{\pi}{4} \frac{\sin\left(\beta + \frac{\theta}{2}\right) \left[\cos\alpha \, \sin(\beta+\alpha) \, \sin\left(\alpha + \frac{\theta}{2}\right)\right]^2}{\left[\sin\left(\alpha - \frac{\theta}{2}\right) \sin(\beta-\alpha)\right]^3}$$

is plotted over the range given above for fixed θ and β, the characteristic curve given in Figure 109 is obtained.

The case for multiple penetrating bounces is slightly more complicated. Let

$$N \geq 3$$

and define

$$\beta_j = \beta + 2(N-j)\alpha, \quad j \geq 3$$

with

$$L_j = L_{j-1} \frac{\sin(\beta_{j-2}+\alpha)}{\sin(\beta_{j-1}-\alpha)}, \quad j \geq 3$$

with

$$L_2 = \frac{\cos\alpha \, \sin\left(\alpha + \frac{\theta}{2}\right)}{\sin\left(\alpha - \frac{\theta}{2}\right) \sin(\beta_1-\alpha)}$$

so that

$$h_j = aL_j \cos\beta_{j-1}, \quad j \geq 2$$

The equation corresponding to Equation (56) is

$$h = \frac{a \cos\alpha \cos\frac{\theta}{2}}{\sin\left(\alpha - \frac{\theta}{2}\right)} + L_2 \frac{2 \sin\left(\alpha + \frac{\theta}{2}\right)}{\sin(\beta_1 - \alpha)} + \sum_{j=3}^{N} aL_j \cos\beta_{j-1} \tag{59}$$

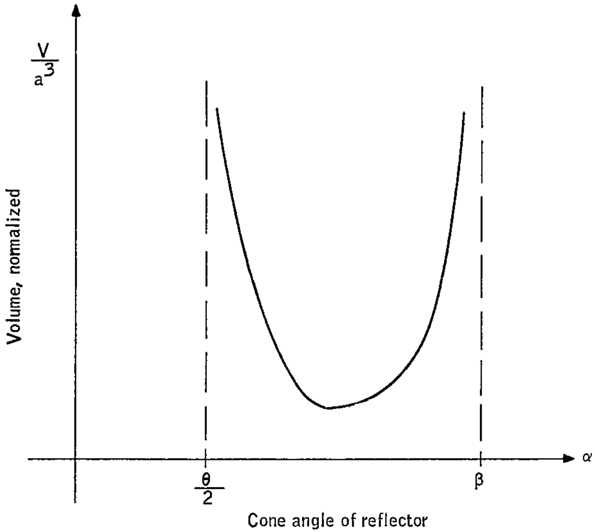

$$\frac{V}{a^3} = \frac{\pi \sin\left(\beta + \frac{\theta}{2}\right)\left[\cos\alpha \sin(\beta + \alpha) \sin\left(\alpha + \frac{\theta}{2}\right)\right]^2}{4\left[\sin\left(\alpha - \frac{\theta}{2}\right) \sin(\beta - \alpha)\right]^3}$$

Figure 109. Normalized Light Baffle Volume versus Shield Angle

The characteristic curve for the multiple bounce case maintains the same form as that given in Figure 109 except that the minimum values are much larger.

Aperture and limiting magnitude star. -- A relationship exists between the aperture and the limiting magnitude of the form

$$a = A\ 10^{Bm_\ell} \tag{60}$$

where

m_ℓ = limiting magnitude

a = aperture

and

A and B = constants that depend on the physical dimensions of the optics and the background noise.

The limiting magnitude calculation satisfies no formula of the above type, but is of the following form:

$$m_\ell = m_\ell(\theta, \beta, \gamma, n) \tag{61}$$

where the term limiting magnitude used here refers to the magnitude of the faintest star required to be detected.

θ = fov

β = shield angle

γ = cant angle

n = number of stellar targets required

For a given fov, θ, and a given cant angle, γ, at a certain orientation in orbit, it is desired to determine the nth brightest star detectable in one revolution. The magnitude of this star is the faintest that must be observed to obtain n stars per revolution.

Constraint equations. -- Let

γ = cant angle

$\hat{z}$ = unit vector in direction of zenith from earth's center

Γ = earth blocking angle

$\hat{n}$ = unit vector along orbital normal

$\hat{s}_i$ = unit vector from earth's center toward ith star

Figure 110 shows that the starmapper sweeps out an annulus on the celestial sphere and, except for earth blocking and illuminance from the sun and earth, the stars within this annulus would transit the slits of the starmapper at some point throughout one revolution of the system. From Figure 110 it can be implied that those stars satisfying the following inequality would be candidates:

$$\cos\left(\gamma + \frac{\theta}{2}\right) \le \hat{s}_i \cdot \hat{n} \le \cos\left(\gamma - \frac{\theta}{2}\right) \tag{62}$$

Those transits that are blocked by the earth must be eliminated as candidates. They satisfy the inequality

$$\cos(\Gamma) \le \hat{z} \cdot \hat{s}_i \tag{63}$$

Of the candidates that are left, some may be eliminated on the basis that at the time of transit the angle between the optical axis and the sun or the optical axis and the sunlit earth does not satisfy the constraints imposed by the shield. Let

$$t_i = \text{time of transit of ith star}$$

then

$$\hat{0}(t_i) \cdot \hat{s}_{sun} > \cos\beta \tag{64}$$

where

$\hat{s}_{sun}$ = unit vector directed from earth's center toward sun

β = shield angle (Figure 107)

From Figures 105, 106, and 110 the constrained relationship between the shield angle, β, and the cant angle, γ, is as follows:

$$\frac{\theta}{2} < \alpha < \beta \begin{cases} \le \alpha - \pi/5 \\ < \pi/2 + \Gamma - \gamma \end{cases}$$

The inequality ($\theta/2 < \alpha < \beta$) merely keeps the shield volume finite by constraining the cone angle, α, to be bounded away from the half field of view, $\theta/2$, and the shield angle, β. The inequality

$$\beta \le \alpha - \pi/5$$

ensures that the system is operative for the worst-case conditions of the sun, optical axis, and orbital position by not permitting the sun's ray to penetrate the shield. The inequality

$$\beta < \pi/2 + \Gamma - \gamma$$

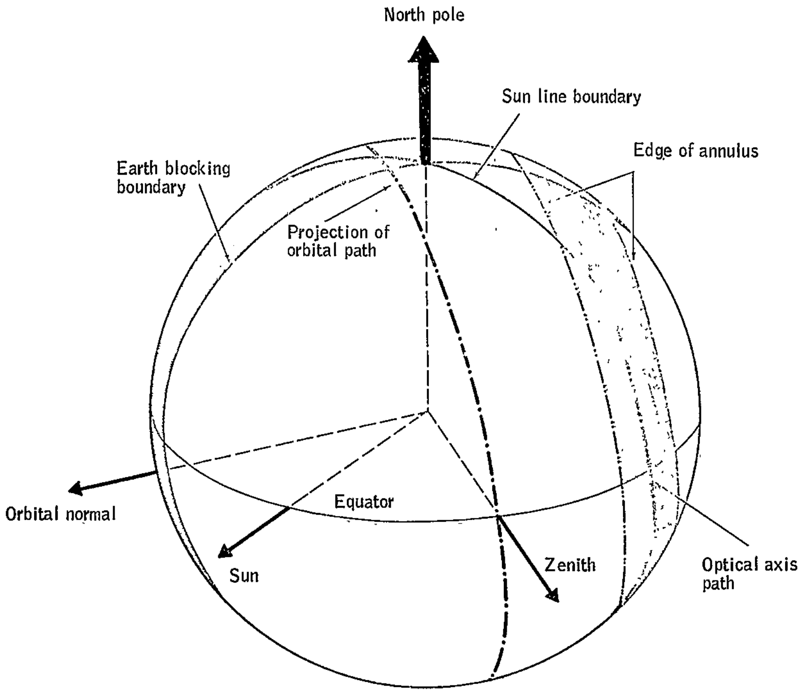

Figure 110. Exact Geometric Relationship Between Optical Axis, Sun Line, and Earth Blocking Boundary on Celestial Sphere

ensures that there is some viewable portion of the celestial sphere free from the sunlit earth. Figure 111 graphically shows the constraint relationship between the cant angle and shield angle. The shaded portion of Figure 111 contained within the constraint boundaries, contains all combinations of γ, β which must be examined for a minimum volume combination. However, it can be shown that the shield minimum volume results when γ, β lie along the line $\gamma = 54° + \beta$. For the orbital conditions chosen for launch, the minimum approval of sun to the orbit plane is 36° (Ref. 19). For closest approach angles, β greater than 36° (optical axis in orbit which is equivalent to $\gamma = 90°$ for a spin axis normal to the orbit plane), the cant angle permissible is greater than 90°, giving $\gamma = 90° - 36° + \beta$ for $\beta \geq 36°$, which gives $\gamma \geq 54° + \beta$. With these constraints on the system an explicit formula for the viewable area on the celestial sphere can be given. Figure 112 gives the relationship of the daytime and nighttime viewable areas. From Figure 112 the daylight viewable area S_D is

$$S_D = 4 \sin\gamma \sin\frac{\theta}{2} \cos^{-1}\left(\frac{\cos(\Gamma-\beta)}{\sin\gamma}\right), \text{ and} \tag{65}$$

the nightime viewable area S_N is

$$S_N = 2 \int_{\gamma-\theta/2}^{\gamma+\theta/2} \sin\phi \cos^{-1}\left(\frac{\cos\Gamma}{\sin\varphi}\right) d\phi \tag{66}$$

Daylight and nighttime viewable (swept out) areas are shown in Figure 112. The baffle minimization program assumed a swept out area, performed the minimization for the set $\{\alpha, \beta. \theta, \gamma\}$, and then conducted a star search from which the limiting daylight and nighttime limiting magnitudes are established. This was done for six stars per scan over the nighttime side of the orbit and both two and one star per scan over the daylight portion. The aperture was then computed, based on the fainter of the two conditions, and the baffle dimensions (h, d) determined from the normalized parameters

$$\left(H = \frac{h}{a} \text{ and } D = \frac{d}{a}\right)$$

In essence the nighttime limiting magnitude m_N depends on the nighttime viewable area, S_N, and the daylight magnitude m_D on the daylight viewable area, S_D. The program steps are summarized in Figure 113. The daytime area is represented in the form $2\pi(1 - \cos\delta)$ where $\delta = f(\theta, \gamma)$.

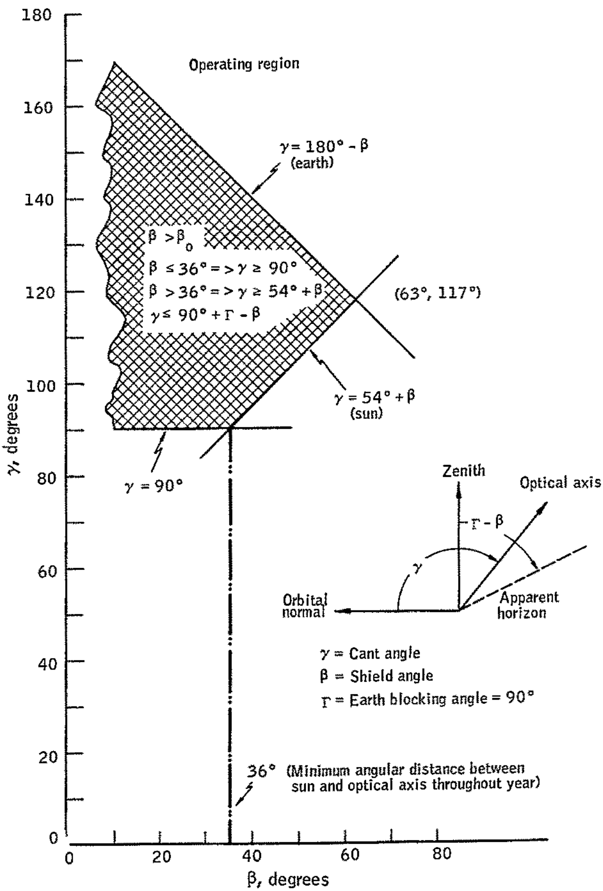

Figure 111. Bounds on the Parameter Set $\{\gamma\ \beta\}$

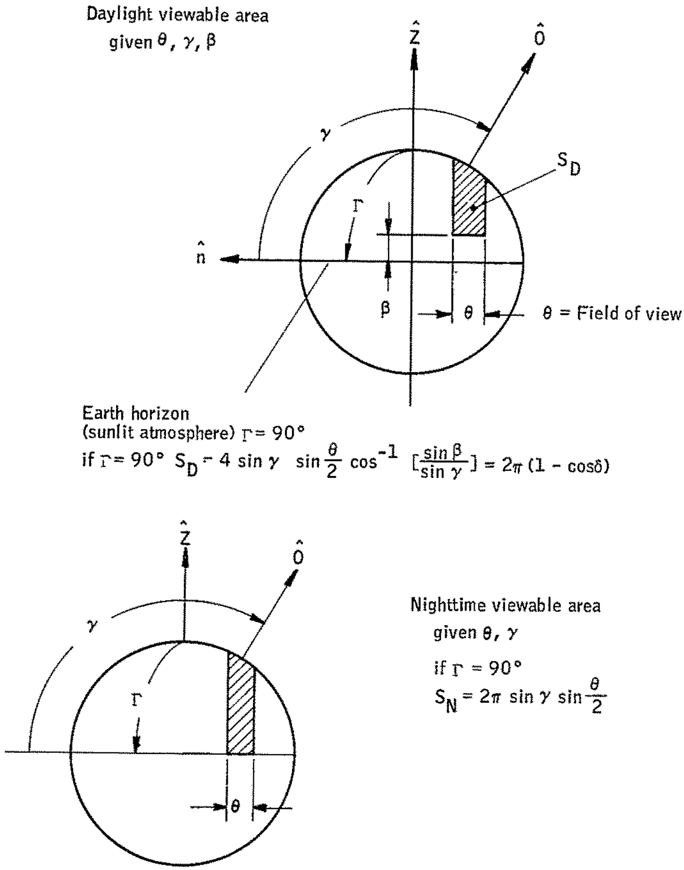

Figure 112. Daylight and Nighttime Viewable Areas

Program

1. Loop on area S_D (equivalent to area on spherical cap of half cone angle δ.) so $7.5° \le \delta \le 30°$ ($S_D = 2\pi(1-\cos\delta)$
2. Loop on γ over $90° \le \gamma \le 115°$
3. Determine β corresponding to min V/a^3 ($\beta = \gamma - 54°$)
4. Compute θ from
   $\theta = 2\sin^{-1}\{S_D/4 \sin\gamma \cos^{-1}[\frac{\sin\beta}{\sin\gamma}]\}$
5. Minimize $f(\alpha, \theta, \beta) = \min f(\alpha_0 \theta, \beta)$ within
   $\frac{\theta}{2} < \alpha < \beta$
6. Compute V/a^3, d/a, h/a
7. Conduct star search for m_D over S_D for $\{\Omega, \nu\}$ for n^{th} brightest star and (γ, β)
8. Conduct search for m_N over S_n for $\{\Omega, \nu_N\}$ for n^{th} brightest star and (γ)
9. Select max m_N or m_D (faintest m_ℓ) - compute aperture
10. Compute V, d, h
11. Plot min V vs. m_D

Figure 113. Computer Program

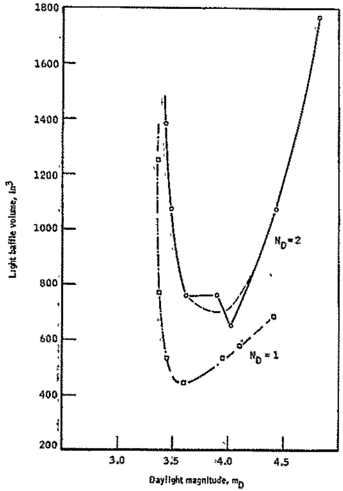

Figure 114. Minimum Volume versus Daylight Limiting Magnitude

For the ranges of θ and γ, delta can range from $7.50 \geq \delta \geq 30°$. The formula for area is now in terms of a single variable for used in the volume minimization program. The delta angle is the half cone angle that intersect the celestial sphere to give an area equivalent to the area swept in an annulus for a given θ and γ.

The results of the program are plotted in Figure 114. Each data point represents the minimum baffle volume for a preselected swept out daylight area which is equivalent to fixing the daylight limiting magnitude. Curves are plotted for one and two stars per scan. The curves illustrate the possible advantage in backing off from a minimum volume criterion to permit detection of a somewhat brighter star.

To show the variation in parameters within a given swept-out area, Figures 115, 116, and 117 are included. The parameters are plotted against the cant angle which is allowed to vary between 90 and 115°. A value of $\gamma = 110°$ represents the cant angle which corresponds to the minimum volume baffle for that particular swept-out area. A table of tentatively selected parameters is included as Table 7, based on obtaining at least two stars per scan over 100 percent of daylight orbita conditions. The results are based on a constant swept out area, S_D, to give at least two stars per scan. For the equivalent representation of area, δ is 17.5 (Figure 115) to give appropriate area for two stars per scan.

TABLE 7. - TABULATION OF PARAMETERS -- WORST CASE (100% OF ORBITAL) CONDITION -- FOR MINIMUM VOLUME BAFFLE CRITERION

Parameter		Value
Cant angle	γ	110°
Field of view	θ	18°
Shield angle	β	56°
Limiting daytime magnitude	m_D	3.65
Limiting nighttime magnitude	m_N	3.08
Aperture (effective aperture)	a	2.39 in.
Light baffle volume	V	753 $in.^3$
Baffle height	h	11.0 in.
Baffle diameter	d	9.6 in.

Figure 116 indicates that the nightime limiting magnitude m_N increases with increasing cant angle, whereas the daytime limiting magnitude curve is more or less constant throughout the operating range. The small oscillations of the daytime and nighttime limiting magnitudes, m_D and m_N, are due primarily to the nonuniform distribution of the stars on the celestial sphere. The shield parameters - i.e., shield angle, fov, and aperture - were determined from the condition that the viewable area in the daytime be constant for all cant angles; however, the area swept out on the celestial sphere during nighttime observation is determined by the daytime parameters and would be larger than necessary. The tendency for m_N to grow with increasing cant angle, except for small oscillations, is due to the fact that the relationship between the cant angle and shield angle, i. e.,

$$\beta = \gamma - 54° \quad \text{(Figure 111)}$$

tends to increase the nighttime viewable area for increasing cant angle.

The set of parameters listed in Table 7 is based on a worst-case star search. A region near the South Galactic Pole which has a relatively sparse star population was selected. This worst-case analysis for 100 % of operational

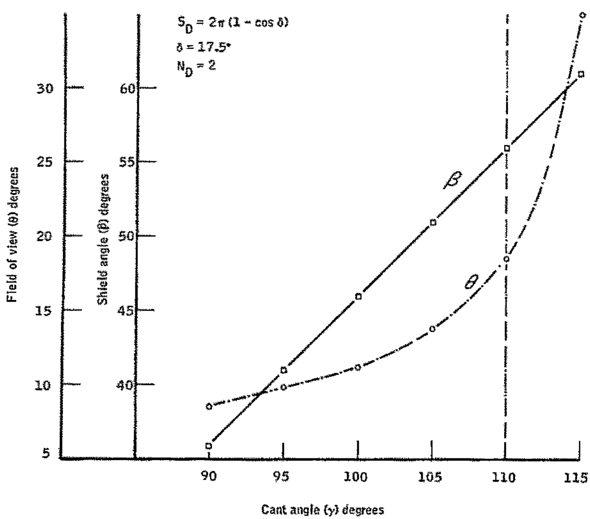

Figure 115. θ, β versus γ

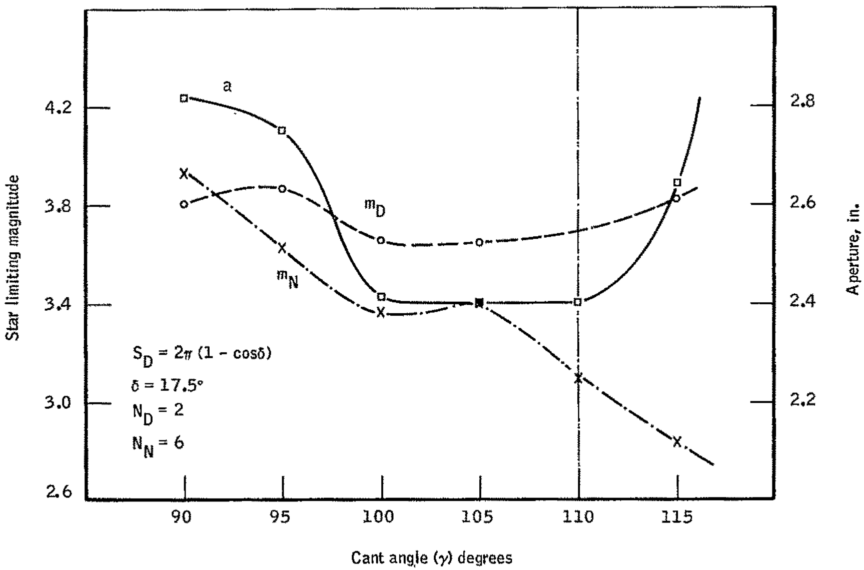

Figure 116. m_D, m_N, a versus γ

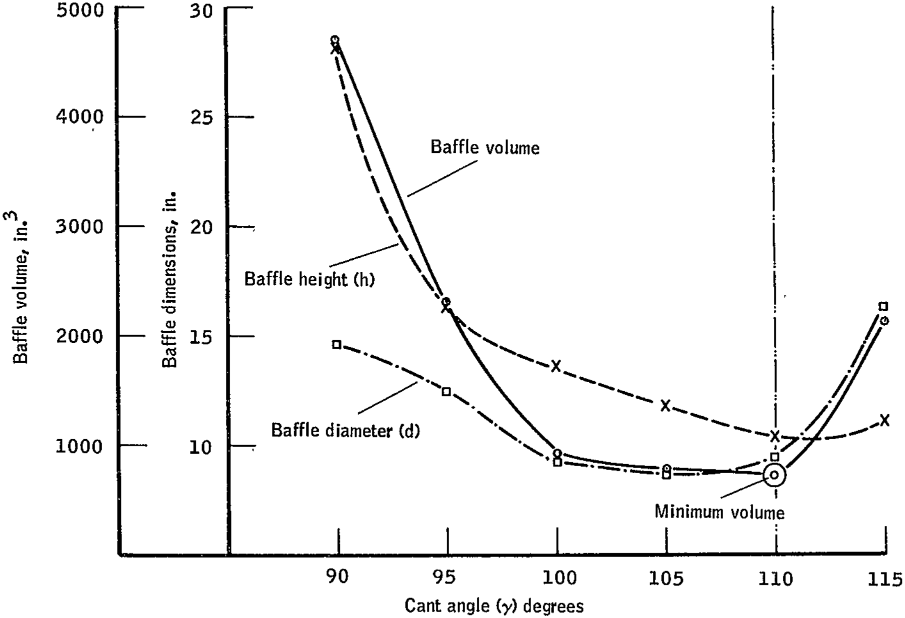

Figure 117. Baffle Dimension versus Cant Angle

capability resulted from the nonuniform distribution of stars on the celestial sphere. Table 7. also points out the condition that the daytime limiting magnitude star is fainter than the nighttime, and it, therefore, serves as the basis for computation of the aperture. Generally, of course, the fainter of the two conditions will govern the aperture size.

If the baffle parameters are fixed and a star search is made of the entire celestial sphere, it is possible to compute a number of statistics. Define the frequency function as

$$f\,(m_\ell) = \frac{\text{frequency per unit interval}}{\text{total number of observations}}$$

where

$$m_\ell = m_\ell\,(k) = \text{magnitude of } k^{th} \text{ brightest viewable star}$$

The distribution function is defined as

$$F(m_\ell) = 100 \sum_{x \le m_\ell} f\,(x)$$

Figure 118 graphically represents, for the baffle parameters listed, the results of a complete search for both one and two stars per scan. As an example in interpreting these graphs, consider the following. If it is required that there be at least two stars in the fov 80% of the daylight observation time, the star sensor would be required to detect stars as dim as 3.2 magnitude. If only one star is required, 80% of the time the limiting magnitude star becomes 2.5 magnitude. This represents the optimal case for a minimum baffle volume criterion. However, if the baffle volume is permitted to increase, detection of brighter stars will be possible.

In Figure 119, graphs are shown which result from an increase in baffle volume to 2385 cubic inches. Again, for 80% of the cases and two stars per scan, the limiting magnitude becomes 2.2 magnitude. The tradeoffs for this increased capability do not only involve increased volume, but also result in increased fov and decreased shield angle (closest approach to bright object), as shown in the parameter set listing in Figure 119.

Both Figures 118 and 119 represent extreme conditions. Additional sets of parameters were also established which are contained within these extremes. Figures 120 and 121 represent additional plots for two selected volumed contained within the extreme conditions of Figures 118 and 119. It is apparent that any set of parameters can be selected subsequent to a determination of that fractional part of the daylight orbit considered essential to meet system accuracy.

Table 8 contains a summary of the four conditions illustrated in Figures 118, 119, 120, and 121 for 100%, 80%, and 50% of usable daylight orbit.

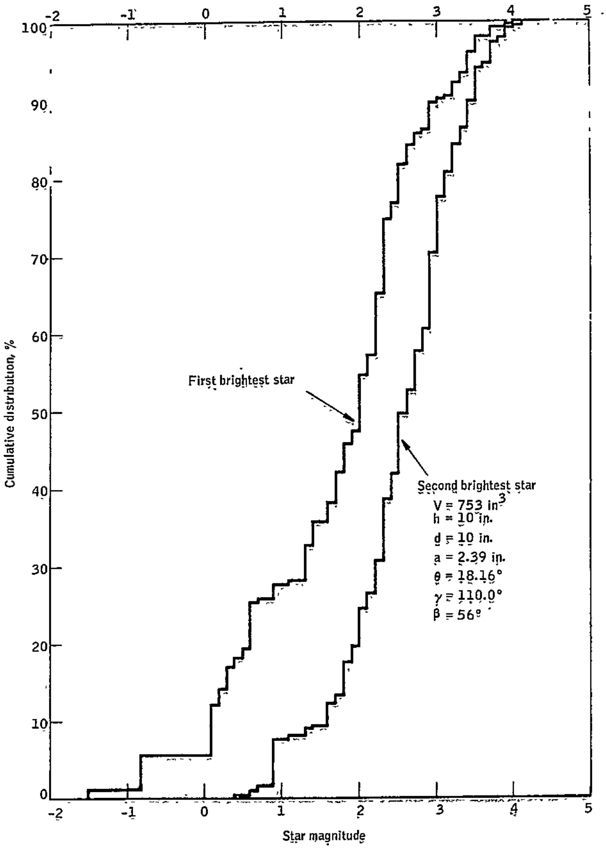

Figure 118. Cumulative Distribution versus Star Magnitude Minimum Baffle Volume Criterion - Case I Parameter Set

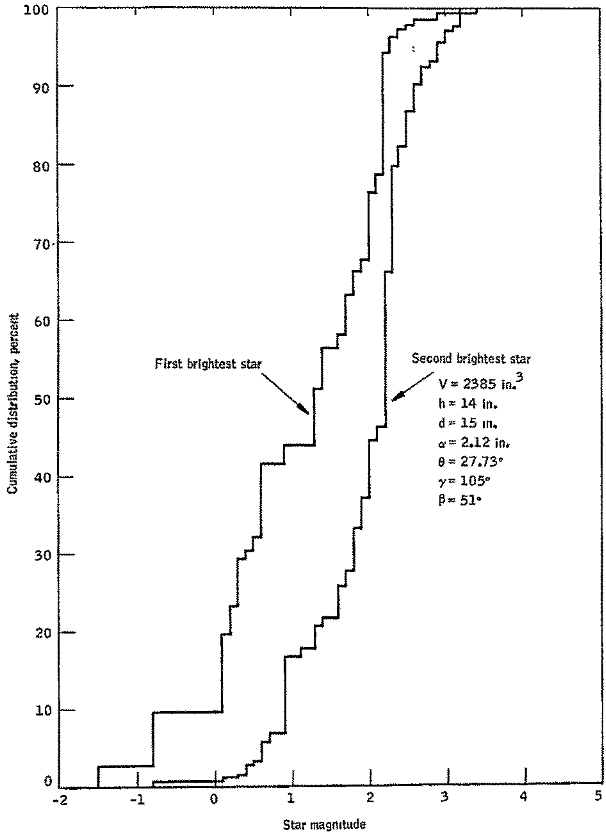

Figure 119. Cumulative Distribution versus Star Magnitude for Case IV Parameter Set

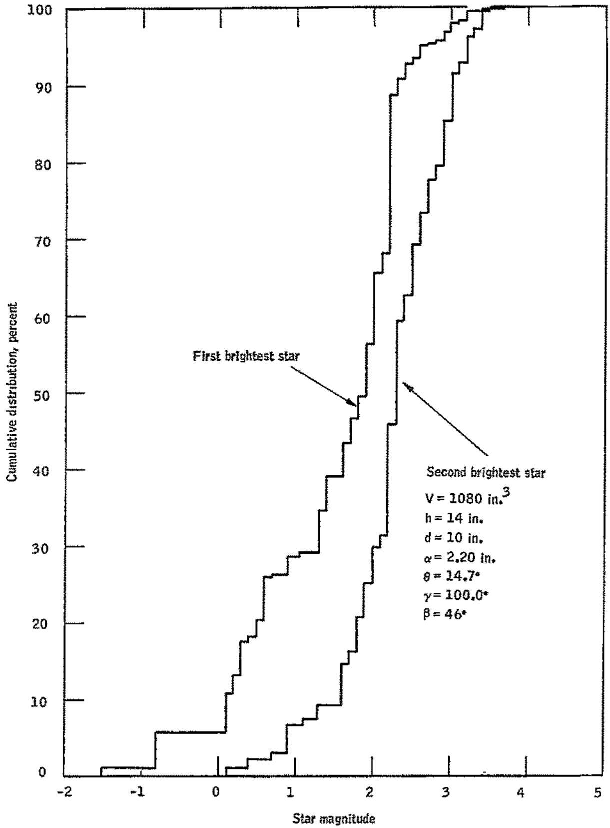

Figure 120. Cumulative Distribution versus Star Magnitude for Case II Parameter Set

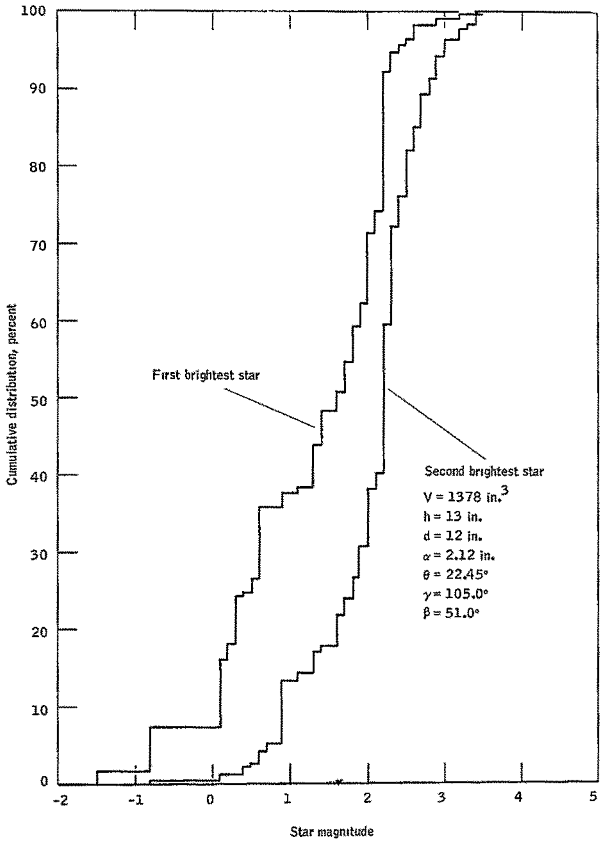

Figure 121.. Cumulative Distribution versus Star Magnitude for Case III Parameter Set

TABLE 8. - SUMMARY TABULATION OF STARMAPPER PARAMETERS

Parameter			Case I	Case II	Case III	Case IV
Volume	V	$in.^3$	753	1080	1378	2385
Baffle height	h	in.	10	14	13	14
Baffle diameter	d	in.	10	10	12	15
Clear aperture	a	in.	2.39	2.20	2.12	2.12
Field of view	θ	deg	18.2	14.7	22.5	27.7
Cant angle	γ	deg	110	100	105	105
Shield angle	β	deg	56	46	51	51
Limiting nighttime magnitude	m_N		3.1	3.2	2.9	2.8
Limiting daytime magnitude*	m_D					
100% of orbit			3.6	3.4	3.4	3.2
80% of orbit			3.1	2.9	2.5	2.4
50% of orbit			2.5	2.2	2.1	2.3

*For 2 stars per scan (exclusive of sun) in all cases $n_D = 2$, $n_N = 6$

Summary and conclusions. -- A minimum volume sun shield having the desired properties can be constructed. Considerable latitude in the choice of the parameters of the system is available if the volume restrictions are relaxes or if the requirement that the system be operational 100% of the time be relaxes. Using both these ideas permits considerable latitude for the design of the sensing system. The limitations in both these areas are spelled out clearly by recognizing how rapidly the volume increases as one moves away from the minimum point (Figure 109), and how the star magnitude increases as the system becomes operational 100% of the time. Figures 118, 119, 120, and 121 span the region containing the minimum volume of Figure 109.

Optical Transfer Function - Starmapper

This subsection presents the performance evaluation of two optical designs for the starmapper celestial sensor. The purpose of the evaluation is to implement a decision as to the better design of the two systems based on a realistic appraisal of sensor performance. Evidence is presented that the catadioptric concentric system will detect all spectral classes of stars better than the refractive system.

In addition, an analysis of the optical performance of the concentric system in two types of environmental perturbations is presented - at very low temperatures and in a high vacuum. The results of these analyses show that the system will indeed perform adequately under these conditions which more nearly approach contemplated operating conditions.

Evaluation of a refractive optical system. -- A stellar sensor using refractive elements is shown in Figure 122. This was the refractive system recommended for previous Horizon Definition Measurement program. It is a balanced type of design having the power of the elements approximately balanced around the aperture. The first and the last two elements are of the same type of glass. The final design shown here is the result of dimensional modifications on the lens elements to minimize the image spot dimensions along the path of the scan of a radial slit. In contrast, the image spot size along the slit was not restricted. The dimensional modifications were performed in a computer-operated automatic lens design program whose image figure of merit was computed according to the instructions entered into the program by the designer. These computations were based on the tracing of certain rays chosen by the designer. The modification process was carried out in two steps. In the first step, the figure of merit was based on the minimization of all of the fifth-order aberrations which could contribute to the widening of the blur spot along the direction of the scan. This type of modification produced relatively large changes in the physical dimensions of the lens train. When an optimum figure of merit was obtained for this method, the lens dimensions were placed in the second step of the modification, which used the minimization of the third-order aberrations as the criterion by which the effect of the modifications was judged. The physical dimensions of the lens train were only slightly altered by this step.

The basic evaluation of the modified optical system was accomplished by means of a computer-operated ray trace and its associated program options.

Blurr spot diagrams in standard computer printout are shown in Figures 123, 124, and 125 for field half angles of 0°, 5°, and 10°. For each diagram 396 rays were traced. The dimensions shown on the right side of the plot are the spot dimensions in arc sec. These spot diagrams are computed for a design wavelength of 0.5876 micron.

The functional performance of the optical system in this sensor depends on the amount of light passing through the slit as the star image passes across it. Graphs of the percentage of the total available rays that are within the area of the slit at a given slit position are shown in Figures 126, 127, and 128 for each of the three half-field angles for which the above blur spots were calculated. These plots were also made at 0.5875 micron wavelength.

The variation of the maximum value of the slit scan for each of 30 wavelengths is plotted in Figures 129, 130, and 131 for each of the three field half angles.

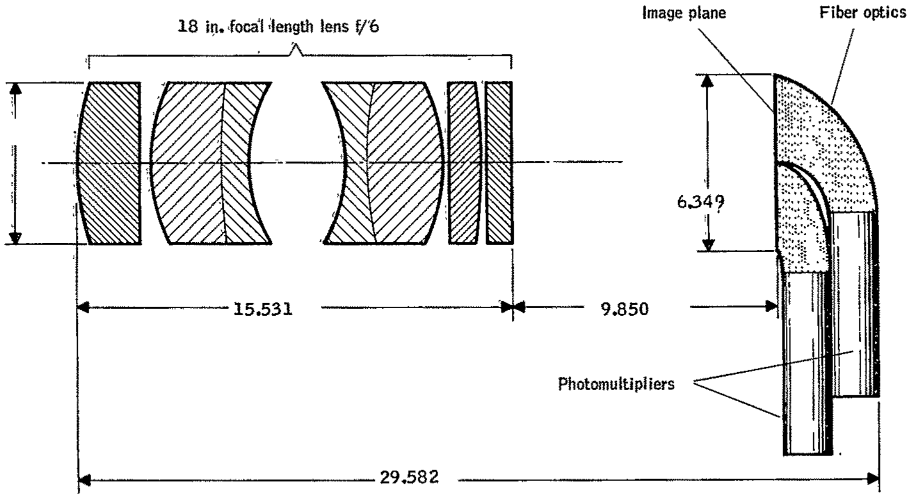

Figure 122. Starmapper Optical Design Using Refractive System

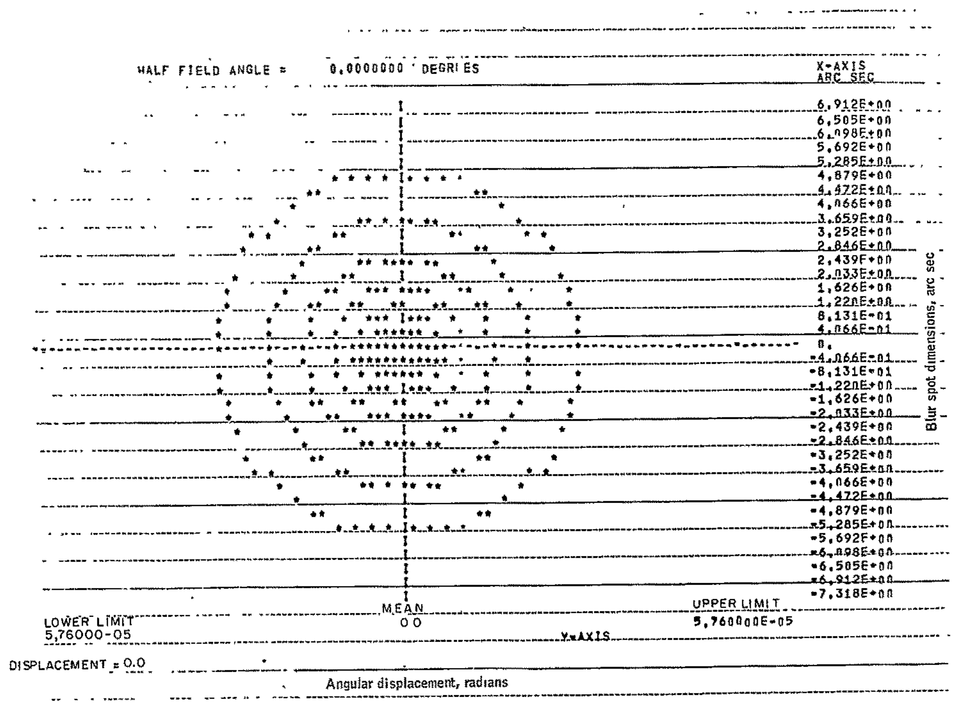

Figure 123. On-Axis Blur Spot Diagram - Refractive Optical System

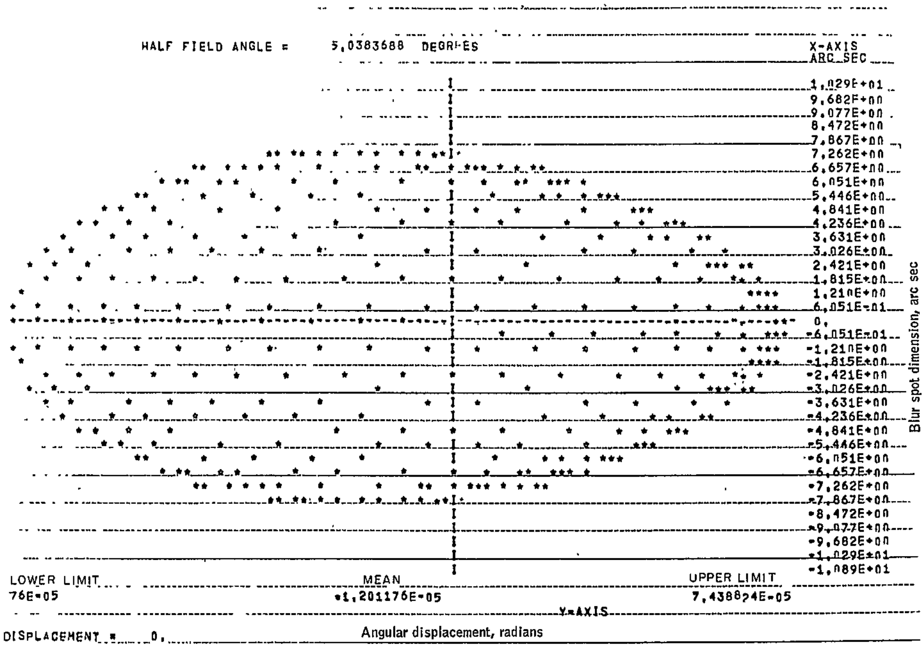

Figure 124. Five-Degree Off-Axis Blur Spot Diagram Refractive Optical System

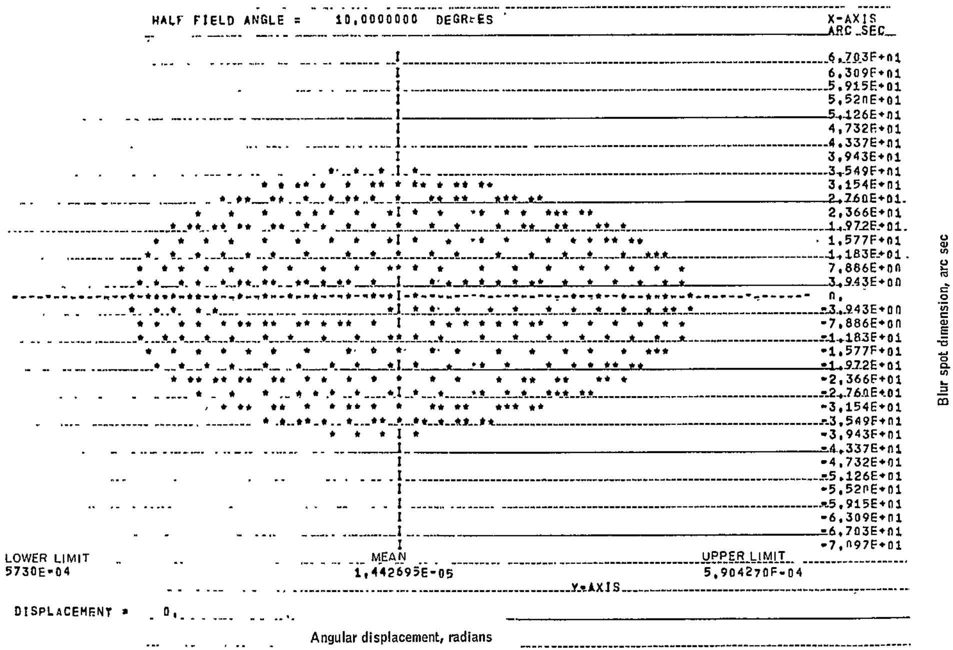

Figure 125. Ten-Degree Off-Axis Blur Spot Diagram - Refractive Optical System

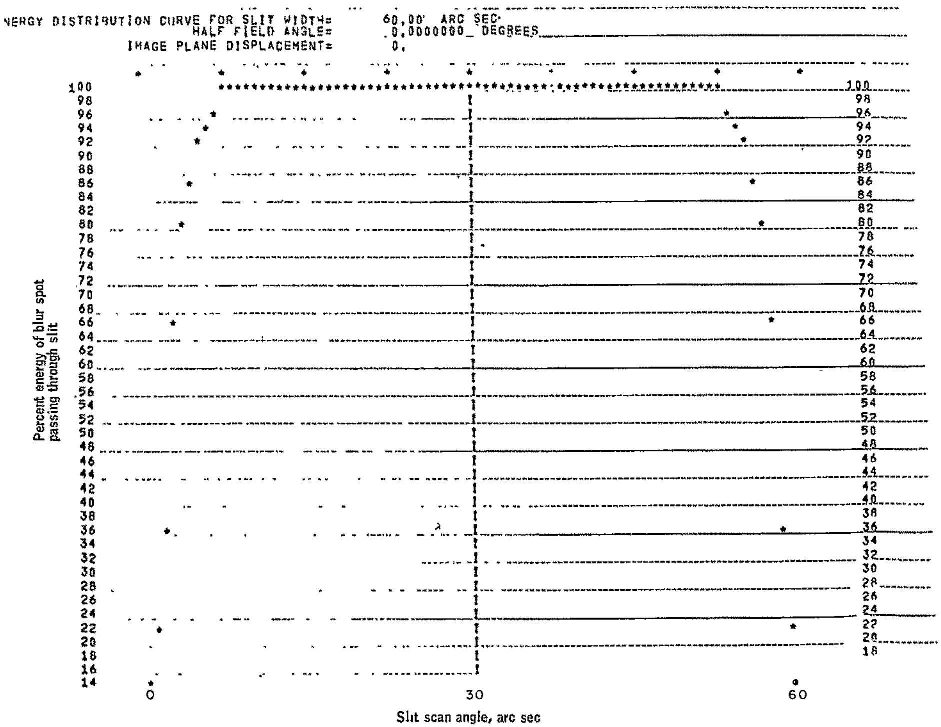

Figure 126. On-Axis Slit Scan - Refractive Optical System

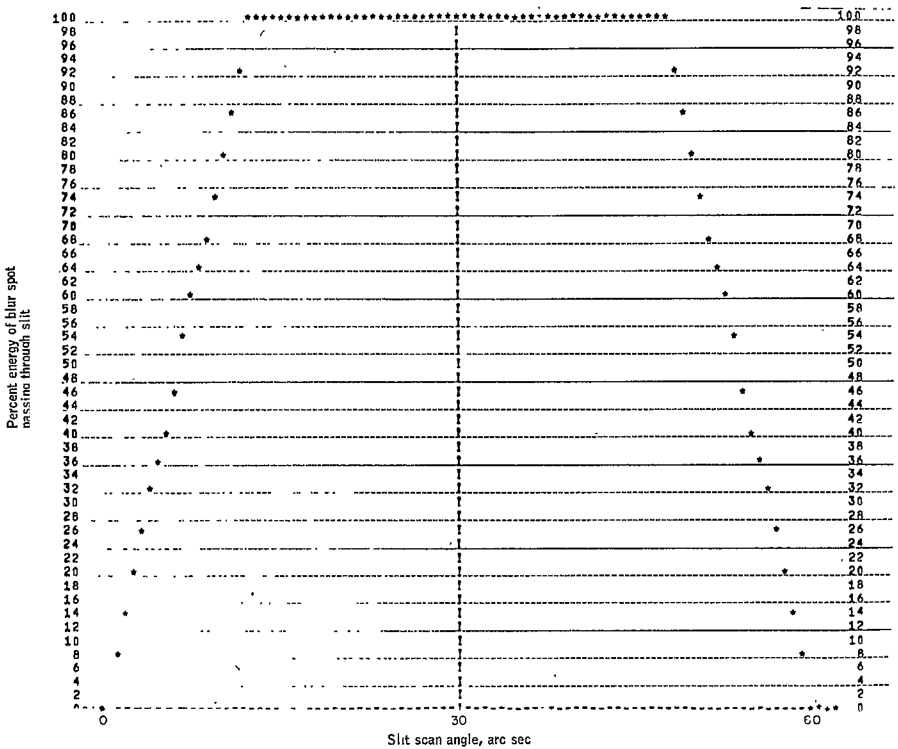

Figure 127. Five-Degree Off-Axis Slit Scan - Refractive Optical System

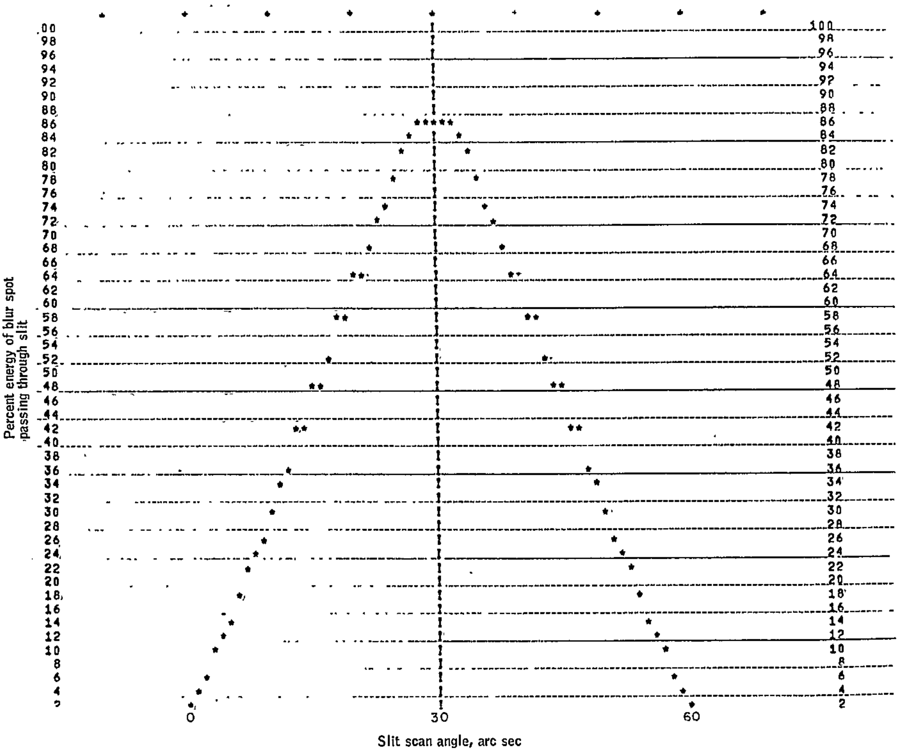

Figure 128. Ten-Degree Off-Axis Slit Scan - Refractive Optical System

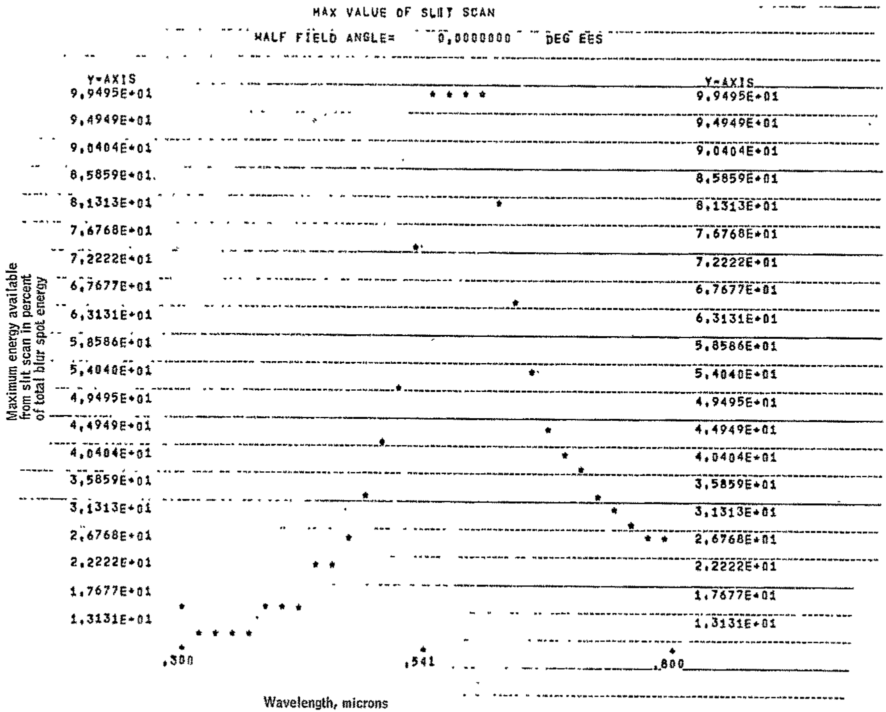

Figure 129. Maximum Slit Scan Value - On-Axis Refractive System

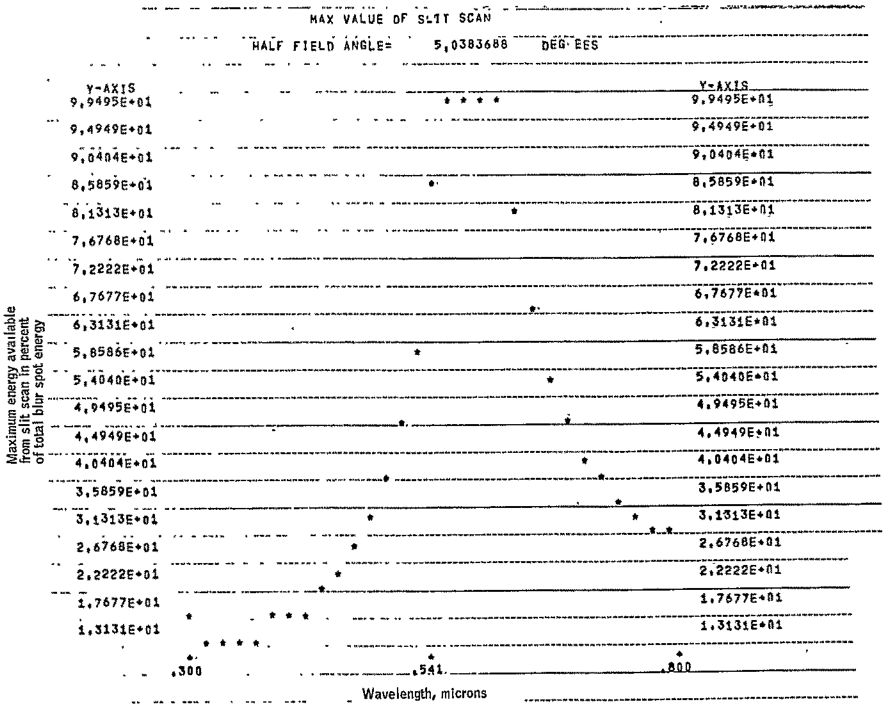

Figure 130. Maximum Slit Scan Value - Five Degree Off-Axis Refractive System

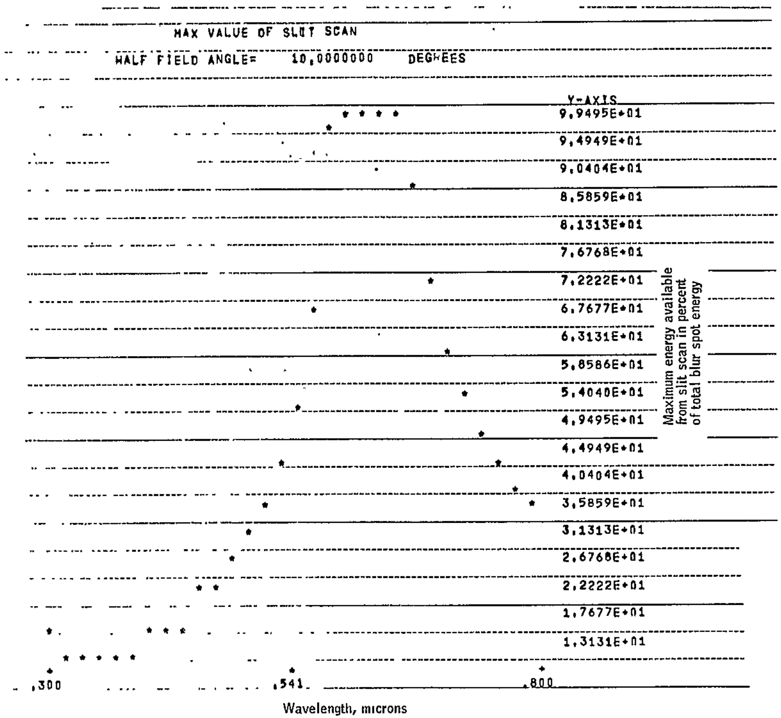

Figure 131. Maximum Slit Scan Value - Ten-Degree Off-Axis Refractive System

The physical diameters of the lens train shown in Figure 122 are just sufficient to pass all of light for a 3.00-inch diameter effective aperture for light parallel to the axis. For any other half-field angle, the diameters of the lenses are inadequate to pass all of the light. The magnitude of the vignetting effect as a function of field angle is shown in Figure 132. The diameter of the entrance and exit lenses necessary to eliminate the vignetting is 6.520 inches.

Evaluation of a concentric optical system. -- Another basic sensor design concept is that of a concentric catadioptric optical system shown in Figure 133. The basic optical elements are an aperture, a primary mirror, and a corrector lens. All of the lens and mirror surfaces are spherical, as is the focal surface, or slit reticle located at the end of the PMT-fiber optics assembly.

The concentric system is made up of a spherical mirror whose axial aberration is spherical and a fused silica negative meniscus corrector whose spherical aberration is equal in magnitude and opposite in sign to the spherical aberration of the mirror. The other axial aberration, chromatic aberration, is zero for the mirror and kept to a minimum in the corrector by two design choices.

1) Choice of optical material. The material chosen -- fused silica -- has the lowest dispersion (change of index of refraction with wavelength of light) of any common optical material.

2) Choice of thickness of corrector. The technique for optimizing the design requires that the closer the corrector is to the mirror the thicker it will be at optimum image size. The corrective spherical aberration occurs at the air-glass interfaces of the corrector; the glass between the interfaces contributes only chromatic aberration to the system. Hence, within certain limits, the thinner the corrector the smaller the chromatic aberration. In this design the corrector was intentionally placed between the image surface and the aperture to optimize the surfaces with a relatively thin corrector.

The most significant property of the concentric system is that any light ray entering the system from a distant source is parallel to a radius drawn to any of the spherical surfaces; hence, any ray entering the system is axial as long as the aperture is at the common center of the spherical surfaces of the system. This means that if the two axial aberrations, spherical and chromatic, are corrected, no other corrections will be needed for any field angle. The remaining aberrations - coma, astigmatism, and distortion - do not exist in this system because no off-axis rays enter.

The blur spot diagram, slit scan, and color analysis plots for the concentric system are shown in Figure 134, 135, and 136, respectively. Only one plot of each kind is needed, since the blur spot and the other associated parameters are unchanged as the field angle changes. The blur spot and slit scan were computed at the design wavelength of 0.4047 micron.

Optical transfer functions. -- A comparison of the performance of the two detector-optical systems in responding to stellar light sources was performed.

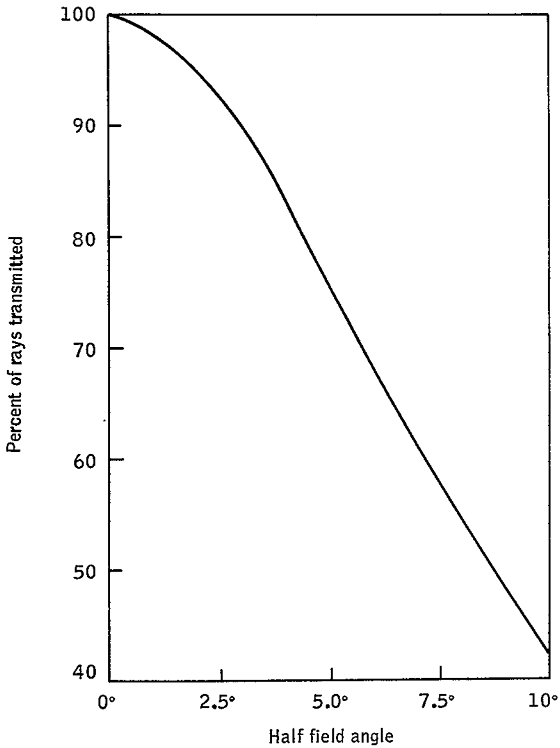

Figure 132. Variation of Transmission of 18-inch Focal Length F/6 Lens Due to Vignetting by Front Lens Element

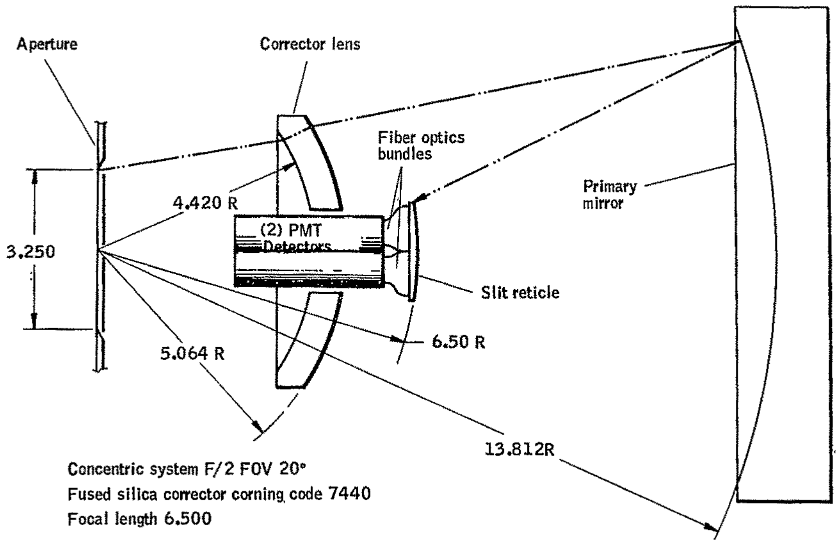

Figure 133. Schematic Starmapper Baseline Optical System

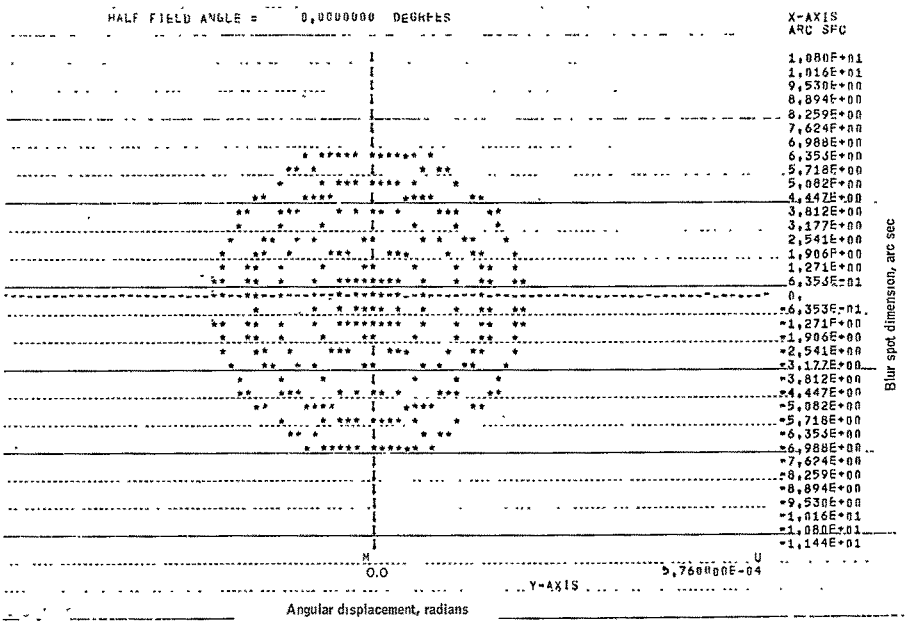

Figure 134. Blur Spot Diagram - Concentric Optical System

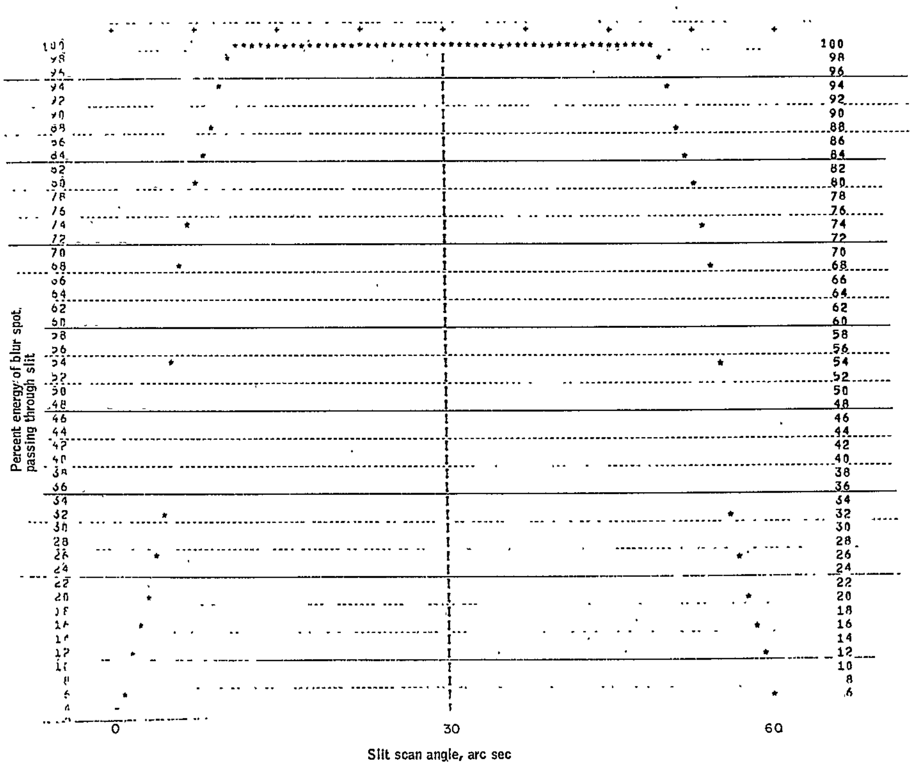

Figure 135. Slit Scan Concentric Optical System

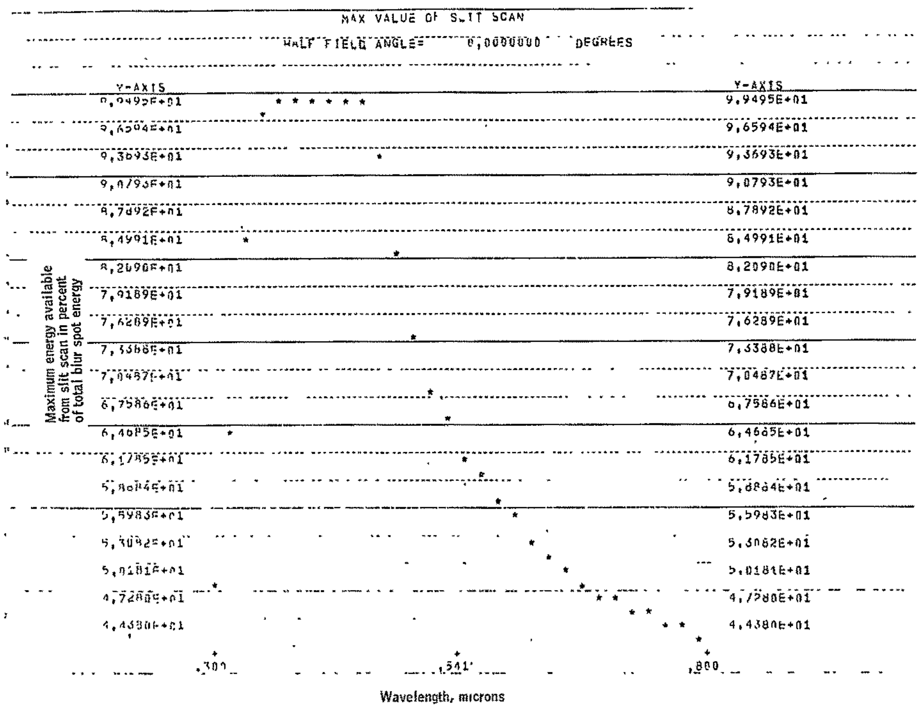

Figure 136. Maximum Slit Scan Value - Concentric System

The basis of the evaluation was the properties of source and sensor for each wavelength of light in the operational wavelength range of the system. The three factors used in the computation of the instrument response were

1) Star color or spectral class. The spectral energy distribution of an ideal black body at a temperature of T°K. Also called

$$\int \left[\Sigma_\lambda \right]_T d\lambda$$

2) Photomultiplier photocathode color response for the Electro Mechanical Research Corporation, EMR type N photocathode

$$\int P(\lambda) d\lambda$$

3) Color response of the optical system. This is the maximum value of the slit scan for the wavelength range used.

$$\int O(\lambda) d\lambda$$

The instrument response for a given color temperature source is given by the expression

$$\int \left[\Sigma_\lambda \right]_T P(\lambda)\, O(\lambda)\, d\lambda$$

To provide a basis of comparison to the visual magnitude classification, the response of the standard photopic eye is used as a multiplier, giving

$$\int \left[\Sigma_\lambda \right]_T \cdot S(\lambda)\, d\lambda$$

The ratio of these two quantities is the ratio of the instrument response to the visual response for a given color temperature or stellar spectral class. Since both integral quantities are proportional to intensities,

$$\frac{\text{Instrument Response}}{\text{Visual Response}} = 2.5 \log_{10} \frac{\int \left[\Sigma_\lambda \right]_T P(\lambda) O(\lambda) d\lambda}{\int \left[\Sigma_\lambda \right]_T S(\lambda) d\lambda}$$

compares these intensity ratios in terms of stellar magnitudes. The ratio was computed for all color temperatures from 2000°K to 25 000°K. To obtain a convenient reference from which to establish a comparison, the ratio at the color temperature of 11 000°K - the nominal color temperature of the AO spectral class star - was used as a standard. A graph of the normalized function is shown in Figure 137 for the concentric optical system at f/2 and the refractive system at f/6 for three half-field angles shown. The intercepts for the AO star for the two optical systems can be interpreted as follows.

If a fourth magnitude AO star can be reliably detected by the f/2 concentric system, in order to be detected by the refractive system with the same reliability an AO star must have a visual magnitude of +2.49 if viewed on axis, +2.45 if viewed 5° off axis, and +2.31 if viewed 10° off axis.

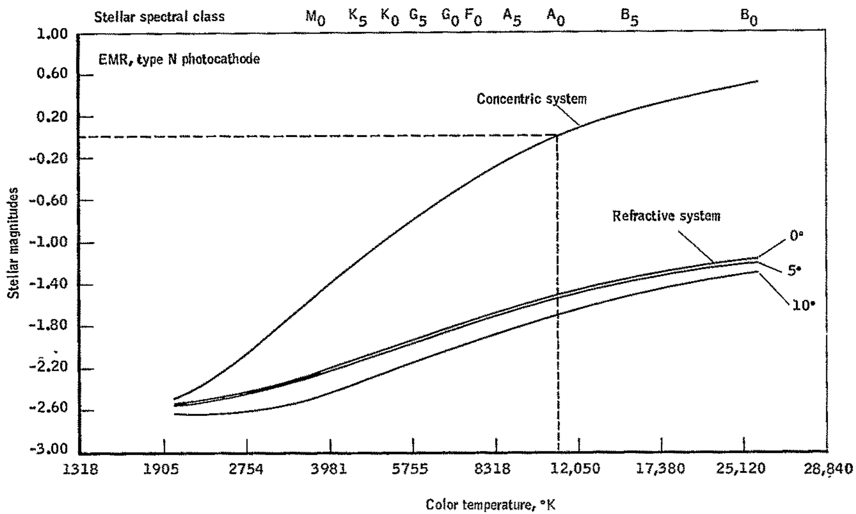

Figure 137. Starmapper Performance

Figure 138 illustrates the derivation of the instrument response parameters; Figure 139 illustrates the visual response parameters. Derivation of the change in stellar magnitude for varying star color temperature (or class) is also shown in Figure 139. This serves as the basis for the optical transfer function plotted in Figure 137.

Sensor performance evaluation at low operating temperatures. -- Performance of the optical system at temperatures of the order of -75°C is dependent on both the physical dimension change calculated from the thermal coefficient of linear expansion and on the change in the index of refraction of the corrector lens as a function of temperature. The thermal coefficient of linear expansion is well documented both for the mirror material and the corrector lens material. A graphical presentation of the linear coefficient of thermal expansion for the two fused silica materials used in the sensor is shown in Figure 140 (refs. 7 and 8).

The index of refraction of the corrector lens, Corning Code 7940, was documented in the 20°C range (ref. 9) but little information is available at lower ranges. Given W. Cleek of the National Bureau of Standards has provided data on the index of refraction of Corning Code 7940 in the temperature range from -192°C to +651°C for the wavelength of 0.5896 micron only.* A table of indices of refraction of vitreous silica in the temperature range of -160°C to +1000° at wavelengths of 0.4713, 0.5016, 0.5876, and 0.6678 micron is published in Sosman's comprehensive book on silica (ref. 10) from work of Martens and Rinne. A plot of the results is shown in Figure 141. Using these data, computer ray traces based both on change in physical dimensions due to thermal expansion and changes in index of refraction with temperature show that with a 0.007 inch movement of the focal surface the image size is still less than the width of the scanning slit at the wavelengths measured. Further, examination of Figure 141 shows that the refractive index curves for the four colors follow regular, approximately parallel paths. This tends to indicate that no serious anomalies exist in the indices whose wavelengths lie between those measured, and hence no large changes in blur spot size and shape which would adversely alter the performance of the sensor from the room temperature predicted performance. The National Bureau of Standards was requested to perform the low temperature index of refraction measurement during the course of the study. The results are presented in Table A. However, the use of these results were not possible for this study.

Table 9 shows the results of refractive index measurements on fused silica, Corning Code 7940. As shown, data were obtained at 10 different wavelengths over a temperature range of +20 to -200°C. The data are reported at temperature intervals of 10°C with additional values at -75°C.

The National Bureau of Standards was unable to make measurements at a wavelength of 365.0 nonometers as originally requested. Furthermore, measurements were made at 404.7 and 471.3 nanometers, instead of 407.7 and 492.2 as was planned originally. These substitutions were made because of the greater intensity and resulting ease of measurement at 404.7 and 471.3 nonometers.

*Cleek, Given W.: Inorganic Glass. NBS, private communications.

TABLE 9.– REFRACTIVE INDEX OF FUSED SILICA CORNING CODE 7940 AS A FUNCTION OF TEMPERATURE AND WAVELENGTH

Temp. °C	λ, nm 667.8 He	643.8 Cd	587.6 He	508.6 Cd	501.6 He	480.0 Cd	471.3 He	467.8 Cd	435.8 Hg	404.7 Hg
+20	1.45607	1.45670	1.45846	1.46186	1 46224	1 46350	1.46406	1.46429	1 46669	1.46962
+10	1.45599	1.45663	1.45838	1.46177	1.46215	1.46341	1.46398	1.46420	1.46661	1.46953
0	1.45590	1.45655	1.45829	1.46169	1.46206	1.46332	1 46389	1.46412	1.46653	1.46944
-10	1.45582	1.45647	1.45821	1.46161	1.46198	1.46323	1.46381	1.46403	1 46645	1.46935
-20	1.45573	1.45639	1.45813	1.46152	1.46189	1.46315	1.46372	1.46395	1.46637	1.46926
-30	1.45565	1.45631	1.45805	1.46144	1 46181	1.46306	1.46364	1.46386	1.46629	1.46918
-40	1.45557	1.45623	1.45797	1.46136	1.46173	1.46298	1.46356	1 46378	1.46620	1.46909
-50	1.45550	1.45615	1.45789	1.46128	1.46165	1.46290	1.46347	1.46370	1.46612	1.46901
-60	1.45542	1.45607	1.45781	1.46120	1.46157	1.46282	1.46340	1.46362	1.46604	1.46892
-70	1.45535	1.45600	1.45774	1.46112	1.46150	1 46275	1.46332	1.46354	1.46597	1.46884
-80	1.45528	1.45592	1.45767	1.46105	1.46143	1.46267	1.46324	1.46347	1.46589	1.46876
-90	1.45521	1.45585	1.45760	1.46098	1.46136	1.46260	1.46317	1.46340	1.46581	1.46869
-100	1.45514	1.45578	1.45753	1.46091	1.46129	1.46254	1.46310	1.46333	1.46574	1 46862
-110	1.45508	1.45571	1.45747	1.46085	1.46123	1.46247	1.46304	1.46326	1.46567	1.46855
-120	1.45503	1.45565	1.45741	1.46079	1.46116	1.46241	1.46297	1.46320	1.46561	1.46848
-130	1.45497	1.45560	1.45736	1.46073	1.46111	1.46236	1.46291	1.46314	1.46555	1 46842
-140	1.45492	1.45554	1.45731	1.46068	1.46105	1.46231	1.46286	1.46309	1.46549	1.46837
-150	1.45488	1.45550	1.45726	1.46063	1.46100	1.46226	1.46281	1.46304	1.46544	1.46832
-160	1.45484	1.45546	1.45722	1.46059	1.46095	1.46222	1.46276	1.46300	1.46539	1.46828
-170	1.45480	1.45543	1.45719	1.46055	1.46091	1.46218	1.46272	1 46297	1.46535	1.46824
-180	1.45477	1.45541	1 45716	1.46052	1.46087	1.46215	1.46269	1.46294	1.46531	1.46821
-190	1.45475	1.45540	1.45713	1.46049	1.46084	1.46212	1.46266	1.46291	1 46528	1.46818
-200	1.45473	1.45539	1.45711	1.46047	1.46081	1.46210	1.46264	1.46289	1.46525	1.46816
-75	1.45531	1.45596	1.45770	1.46109	1.46146	1.46271	1.46328	1.46350	1.46593	1.46880

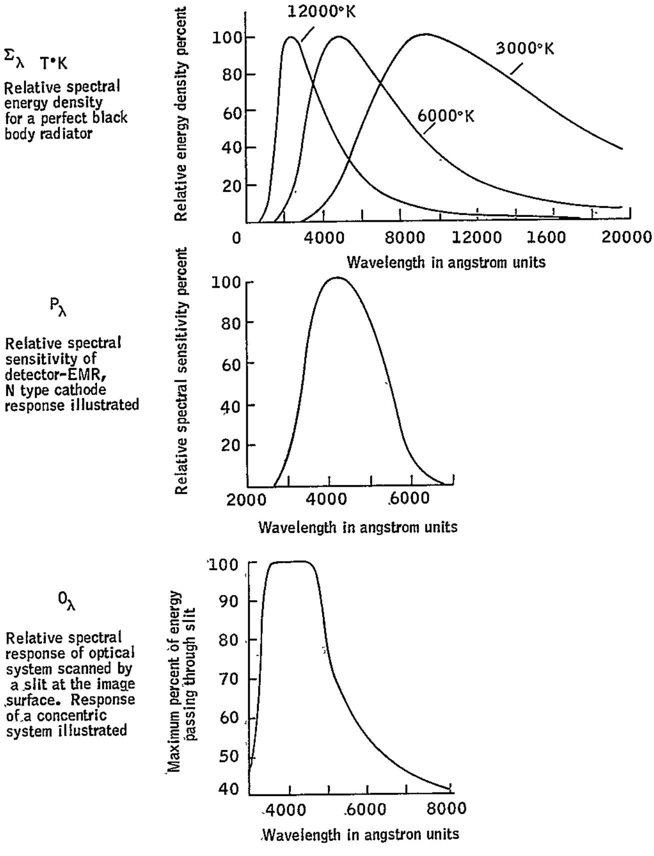

Figure 138. Instrument Response Parameters

$[\Sigma_\lambda]$ T°K

Relative spectral energy density for a perfect black body radiator

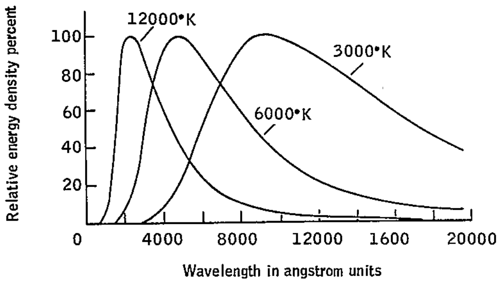

S_λ

Relative spectral response of the human eye (photopic)

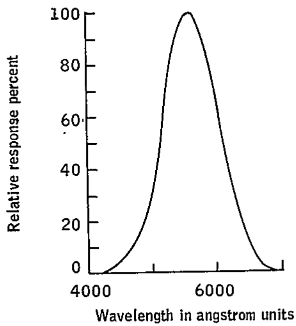

Change in stellar magnitude

$$\Delta m = 2.5 \log_{10} \left[\frac{\text{instrument response}}{\text{visual response}}\right]_{T^\circ} - 2.5 \log_{10} \left[\frac{\text{instrument response}}{\text{visual response}}\right]_{A_0\text{star}}$$

$$\Delta m = 2.5 \log_{10} \left[\frac{\int \Sigma_\lambda P_\lambda O_\lambda \, d\lambda}{\int \Sigma_\lambda S_\lambda \, d_\lambda}\right]_{T^\circ K} - 2.5 \log_{10} \left[\frac{\int \Sigma_\lambda P_\lambda O_\lambda \, d\lambda}{\int \Sigma_\lambda S_\lambda \, d\lambda}\right]_{11,000^\circ K}$$

Figure 139. Visual Response Parameters

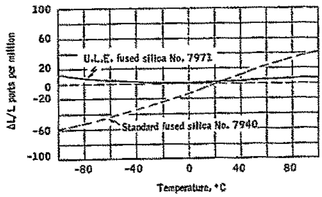

Figure 140. Linear Coefficient of Thermal Expansion for Corrector (No. 7940) and Mirror (7971)

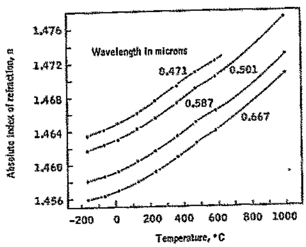

Figure 141. Experimental Data on the Change of Index of Refraction of Vitreous Silica with Temperature and Wavelength

All the reported values are referred to air at 20°C. The standard deviation of each refractive index determination is within 2×10^{-5}.

Evaluation of optical system performance in vacuum. -- The indices of refraction used in the design of the corrector for the ARRS star sensor were based on measurements made in 76 cm barometric pressure dry air. Thus, using the velocity definition of index of refraction, the catalog values of the index of refraction can be expressed as

$$N\ \text{glass/air} = \frac{\text{velocity of light in air}}{\text{velocity of light in glass}} \tag{67}$$

Similarly, the index of refraction of air itself can be expressed as

$$N\ \text{air/vacuum} = \frac{\text{velocity of light in a vacuum}}{\text{velocity of light in air}} \tag{68}$$

Thus, the index of refraction of the glass used with respect to vacuum is

$$N \text{ glass/vacuum} = N \text{ glass/air} \times N \text{ air/vacuum} \tag{69}$$

The values of the index of refraction of air were obtained from Table 413 of the Smithsonian Physical Tables, first reprint of the eighth revised edition, Washington, D. C., 1934.

The values of the index of refraction used in ray trace calculations are in the form of a dispersion equation

$$N^2 = A_o + A_1 \lambda^2 + A_2 \lambda^{-2} + A_3 \lambda^{-4} + A_4 \lambda^{-6} + A_5 \lambda^{-8} \tag{70}$$

where N is the index of refraction, λ is the wavelength of light, and the A's are constants for each glass. The values of the indices of refraction for air were used to evaluate the constant terms in the above equation. The indices for glass-vacuum interface were obtained from the product shown in Equation (69) for each wavelength used in the ray trace. A new dispersion equation of the form of Equation (70) was developed for the Corning Code 7940 fused silica used for the corrector. This dispersion equation was used to compute the required refractive indices for a ray trace and color analysis.

A comparison of the ray trace and color analysis results using the above values with the original design results shows that the changes in performance produced by operating the sensor in a vacuum, rather than in air, are imperceptible and will not require any changes in focal surface position.

Optical Transfer Function - Sun Sensor

This subsection presents the design considerations and performance data to show that a modified catadioptric concentric optical system can detect the position of the sun's limb with sufficient accuracy to enable the position of the sun sensor in relation to the sun to be computed to an accuracy of 10 arc sec.

Optical system design considerations. -- Analyses indicate that the detection of the sun's position could be successfully accomplished using detection of the sun's limb at 0.5400 micron at a bandwidth of 0.0200 micron or less. The pointing requirements of the spacecraft orbit require a 40° fov for the sensor to keep the sun in the fov continuously throughout the year. The wide fov dictates the use of the symmetrical properties of a concentric optical system. In addition, the catadioptric system offers unique opportunities for reducing the light intensity reaching the focal surface.

The baseline optical system for the sun sensor is shown in Figure 142. The optical system design is quite similar to that of the star sensor, except for the special optical coatings used. The first coating that the sun's rays would strike would be the reflective interference-type filter coating on the entrance

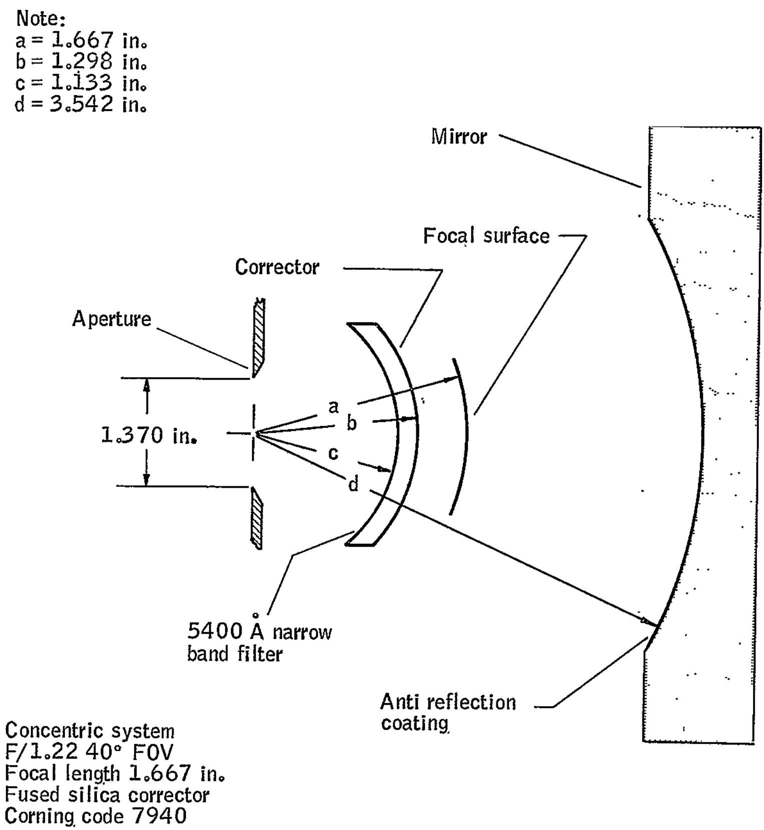

Figure 142. Schematic Sun Sensor Baseline Optical System

face of the corrector. This coating would reflect 99% of the light back out through the aperture and pass 25% of the light in the pass band of the interference filter.

The detection accuracy requires that the detection threshold be set to trigger when the limb of the sun is one-sixth of the way across the slit opening. The slit then receives energy from only 2.144×10^{-4} of the total area of image. The threshold is set at 10^{-4} µ4 signal level, using $0.25 \frac{\mu A}{\lambda W}$ as the sensitivity of the silicon yields 4×10^{-4} µW needed in the slit to trigger the threshold. The total power in the image is the power in the slit divided by the fraction of the total image area in the slit,. or

$$\frac{4 \times 10^{-4} \ \mu W}{2.144 \times 10^{-4}} = 1.866 \ \mu W$$

The input to the sensor is the product of the power density and the area of clear aperture available. The power emerging from the corrector-filter combination is reduced from the input power by the effect of reduced pass band of the filter. For a filter centered on 0.5400 Å wavelength, Jensen (ref. 11) gives the solar spectral irradiance as

$$1.9 \times 10^{-5} \quad \frac{W}{cm^2 - \text{Å}}$$

For a pass band 1% of the center wavelength and a maximum transmission of 25%, the power available from the corrector is

$$0.25 \times 10^{-2} \times 5.4 \times 10^3 \ \text{Å} \times 1.9 \times 10^{-5} \ \frac{W}{cm^2 - \text{Å}} = 0.2565 \times 10^{-3} \ \frac{W}{cm^2}$$

The reflector surface, when coated with an antireflecting coating*, will yield a reflection efficiency of 2.5×10^{-3}. Thus, the power density at the image surface is 0.2565×10^{-3} W $\times 2.5 \times 10^{-3} = 0.641 \times 10^{-6} \ \frac{W}{cm^2}$ or $0.641 \ \frac{\mu W}{cm^2}$

The collection area of the clear aperture is then

$$\frac{1.866 \ \mu W}{\frac{0.641 \ \mu W}{cm^2}} = 2.909 \ cm^2$$

or $0.45096 \ in^2$ clear aperture area

*Applied by the Optical Coating Laboratories, Inc., Santa Rosa, Calif.

The effect of central obscuration of the focal surface on the maximum relative aperture ($f/\#_{max}$) is given by

$$f/\#_{max} = \frac{1}{2 \sin \frac{\theta}{2}}$$

where θ is the optical system fov. For a 40° fov,

$$f/_{max.} = \frac{1}{2 \sin 20°} = \frac{1}{2 \times 0.34202} = 1.462$$

Therefore, for a reflective system having a 40° fov, unless the f/# was less than f/1.462, no light would reach the image surface. For a concentric system having a focal length of 1.667 in., the radius of the central obscuration of the image surface is given by

$$h_o = \frac{1.667}{2 \times 1.462} = 0.570 \text{ in.}$$

If the radius of the actual aperture is β_o, the clear aperture area is given by

$$A = \pi \left(\beta_o^2 - h_o^2\right)$$

from this relationship

$$\beta_o^2 = \frac{A}{\pi} + h_o^2$$

or

$$\beta_o = \sqrt{\frac{A}{\pi} + h_o^2}$$

$$\beta_o = \sqrt{\frac{0.451}{\pi} + (0.570)^2}$$

$$\beta_o = 0.6845 \text{ in.}$$

or an aperture diameter of 1.369 in.

Thus, the actual relative aperture is

$$\frac{1.667 \text{ in.}}{1.369 \text{ in.}} = 1.22$$

The diffraction limit for 0.54 micron and a 60-arc sec diffraction spot size is given by

$$\theta \text{ arc sec} = \frac{2 \times 1.22 \lambda \times 2 \times 10^5}{D} \text{ arc sec/rad} = \frac{4.88 \times 10^5 \lambda}{D}$$

where λ is the wavelength and D is the diameter of the aperture.

For $\lambda = 0.5400\ \mu$, $D = 0.1729$ in.

Since the above calculations show that to obtain an airy disc diameter equal to the width of the slit, the aperture diameter should be at least 0.1729 in.; the fact that the actual diameter is greater shows that the diffraction image will be smaller than the slit. In the Phase A, Part II report for "An Analytical and Conceptual Design Study for an Earth Coverage Infrared Horizon Definition Study" under NASA contract NAS1-6010, pages 418-437, it is shown that the regularity of the curvatures of the limb of the sun allows the prediction of the location of the center from the limb to be located at a far greater accuracy than necessary for this application. This places the burden of accuracy on the sun sensor; the sensor must be capable of detecting the limb in the slit to an accuracy of 10 arc sec in order that the position of the center of the sun can be located to the same accuracy. In this application the blur spot diameter criterion for optical system performance evaluation is now used only to indicate the "sharpness" of the image of the sun's limb. Using this criterion, the effect of a 60-arc sec blur spot diameter will allow the location of the sun's limb to an accuracy of 10 arc sec using the same interpolation factor of 6 that was used in locating star images.

Cathode Protection

Objectives and introduction. -- The objectives of the cathode protection study were to first determine the affects on the multiplier phototube if bright sources (sun, moon, or sunlit earth) were to enter the field of view of the starmapper and then to devise electronic and mechanical design features which will provide suitable protection for the multiplier phototube. To achieve this objective it was necessary to obtain pertinent information for the multiplier phototube being proposed. Radiation levels which the optical system sould cause to fall on the photocathode could be calculated and compared with performance characteristics of the multiplier phototube to determine the needs for protection. Then, knowing the requirements, suitable protection features could be devised.

As an introduction to the subject of cathode protection, it is desirable to look at the pertinent portions of the starmapper design. The starmapper reticle baseline configuration is illustrated in Figure 143. It also illustrates schematically the baseline optical system and is included as an aid in understanding the slit reticle configuration of the figure. From Figure 143, the value of slit width shown was obtained from the equation

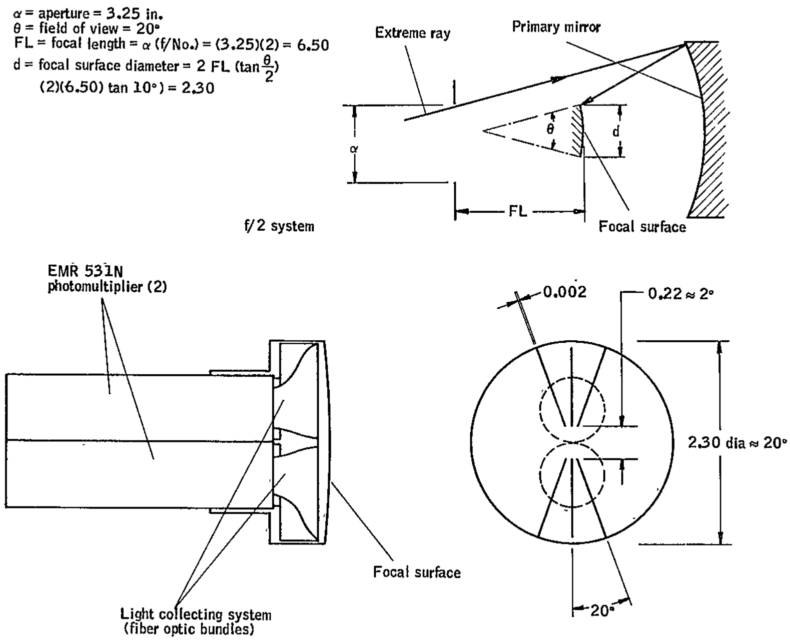

Figure 143. Detector - Reticle Baseline Configuration

$$SW = (FL)\ \phi$$

where

SW = slit width

FL = focal length

ϕ = angular image diameter in radians

Since 10-arc sec accuracy is required and a 6 to 1 signal-to-noise ratio can be assumed*, an angular image (spot) diameter of 60 arc sec results. Then,

$$SW = (6.50)\ (3 \times 10^{-4}) \approx 0.002 \text{ in.}$$

The base line configuration shows two multiplier phototubes arranged so that each accepts stellar radiation from one-half the scanned field. The use of fiber optics makes it possible to use small phototubes and minimizes the dead zone at the center of the slit pattern. Detector redundancy exists in the sense that failure of one of the detectors would not cause total loss of detection capability. The second multiplier phototube would be usable and, therefore, reduced attitude and accuracy would result.

The baseline starmapper configuration uses a type 531N-01-14 multiplier phototube. Selection of this detector was based on its small size and its similarity to the 541N tube. Similarity between the two models exists such that published results from work performed by Brown, et al., (ref. 12) under contract No. NAS 1-7648 is applicable to this study. The work performed by Brown, et al. evaluates the behavior of the EMR 541N-01-14 multiplier phototube in response to laboratory simulation of an orbital scanner mission.

The following three causes for degradation in multiplier phototube performance and the associated need for cathode protection were investigated:

1) Excessive dark current resulting from cathode exposure to high radiant energy levels with the high voltage switched off to prevent permanent damage

2) Excessive anode current resulting from exposure to high radiant energy levels which cause irreversible changes to the phototube

3) Cathode temperature rising above the allowable limit of 150°C as a result of exposure to direct solar radiation

*Signal-to-noise ratio was shown to be equivalent to slit center interpolation.

The first two situations are related and require a determination of the expected radiation levels resulting from exposure to moon and earth illuminance and a calculation of the associated anode currents. An analysis of multiplier phototube sensitivity and dark current requirements is presented in Appendix E along with a scheme for limiting the anode current by appropriate switching of the cathode voltage. An analysis is presented below which shows that the anode current will exceed the one microampere maximum recommended for the EMR 531N-01-14 unless protective measures are used.

Theoretical anode currents were calculated for the baseline optical geometry, using the Brown, et al. equations and irradiation levels used in reference 12. The equation for anode current is

$$I_a = p \times G \times \sigma_k \times A \tag{71}$$

where

I_a = anode current, amp

p = energy density incident on PMT cathode $\frac{W}{cm^2}$

G = gain

σ_k = cathode radiant sensitivity, $\frac{amp}{W}$ = 0.054 $\frac{amp}{W}$ for 531N tube

A = cathode area exposed to radiation, cm^2

To obtain the energy density, p, from the incident radiation, it is necessary to apply factors which account for the concentration of the energy by the optics (optical area ratio) and for losses in the optics (optical efficiency).

The optical area ratio is defined as

$$R_{OA} = \left(\frac{a}{d}\right)^2 \tag{72}$$

where

a = aperture diameter = 3.25 in.

d = image diameter (equals focal surface diameter of 2.23 in. when light source completely fills the fov and an optical efficiency, η, of 0.8 is assumed*

The irradiance of earth reflected sunlight (H) according to Brown, et al., is 0.0078 W/cm^2 using an earth albedo of 0.25. The energy density, p, is then

$$p = H\, R_{OA}\, \eta \tag{73}$$

$$= (0.0078) \left(\frac{3.25}{2.3}\right)^2 (0.8)$$

$$= 0.0125\ W/cm^2$$

The cathode is exposed to this radiation only over an area defined by the outlines of the three slits. The slits are 0.0167° (1 minute) wide and approximately 10° long. The equivalent linear dimensions for the f/2.0, 6.5-inch focal length optics are 0.0048 cm and 2.91 cm for a total slit area of 0.0419 cm^2.

Anode current for a PMT gain of 10^4 which results when the fov scans the sunlit earth then becomes, from Equation (71):

$$I_a = (0.0125)(10^4)(0.054)(0.0419) = 0.282 \text{ amp}$$

A justification for the use of a 10^4 dynode gain is presented in Appendix E.

Similar calculations can be performed for the condition occurring when the fov scans the moon. For a near polar orbit at an angle of 45° to the sun line (syn synchronous orbit), the moon is at the -34° phase position when it is just entering the fov.

Brown, et al. give a value of 2.45×10^{-8} W/cm^2 for the lunar irradiance at 35° phase position. The moon subtends an angle of 33 arc min so the energy entering the aperture is concentrated in a spot whose diameter is 33 arc min (0.55°) as compared to a 20° diameter for the total focal surface (2.3-inch diameter). The linear diameter of the moon's image is 0.063 inch (or 0.16 cm). The energy density of the moon's image is calculated using Equation (73):

$$p = (2.45 \times 10^{-8})(26.6 \times 10^2)(0.8) = 5.21 \times 10^{-5}\ \frac{W}{cm^2}$$

---

*The value used here was obtained from calculations performed on a similar concentric optical system and is considered typical.

where

$$R_{OA} = \left[\frac{3.25}{0.063}\right]^2 = 26.6 \times 10^2$$

If all three slits were irradiated, the cathode area exposed to the lunar radiation can be approximated by assuming that the irradiated length of each slit is equal to the diameter of the moon's image, or 0.16 cm. Since the slit width is 0.0048 cm, the exposed area for three slits becomes 0.0023 cm^2.

The anode current from lunar illumination for a gain of 10^4 can now be determined from Equation (57)

$$I_a = (5.21 \times 10^{-5})(10^4)(0.054)(0.0023) = 6.48 \times 10^{-5} \text{ amp}$$

It has been shown in the above discussion that the anode current will exceed the safe level of one microampere under conditions of irradiance which will be encountered in orbit. Specifically, these conditions occur when the starmapper fov scans the sunlit earth or the full moon when the photomultiplier is operative. The starmapper design must, therefore, include provisions for protection against the occurrence of excessive anode current. This can best be accomplished by appropriate switching of the cathode voltage (see Appendix E).

Preventing the cathode temperature from exceeding the allowable 150°C maximum will be considered next. Even though a sun synchronous orbit does not place the sun within the fov of the starmapper, it is conceivable that this could occur during the initial orientation of the spacecraft in its orbit or during the mission because of unexpected vehicle motions. A thermal analysis study, which is included in Appendix F, led to the conclusion that inadvertent scanning of the sun could be tolerated for scan rates as low as 1 rpm. However, to avoid the possibility of having the sun in the fov during a nonspinning condition (during the launch phase) the use of the shutter mechanism described below was considered.

Shutter mechanism. -- A suitable shutter must be a quick-acting, reliable device which requires a minimum of power and is light in weight. By placing the shutter in close proximity to the focal surface, the size of the shutter device can be minimized. A design concept for such a shutter device was studied and is described below.

Since radiation can reach the PMT only through the reticle slits, it is sufficient to shield only the slits when the tube is being protected by the shutter. This permits a design in which shutter motion is minimal. Under such conditions a small solenoid, or electromagnet, can be used to move the shutter.

Spring loading will ensure that the shutter returns to the openen position, which exposes the slits whenthe electromagnet is not energized.

A design concept for a shutter located at the focal surface is shown in Figure 144. The shutter contains a thin metal plate with a slit pattern which matches the slits in the reticle plate as shown in Figure 144. The slits in the shutter must be wider than the reticle slits to ensure that the latter are fully exposed over the entire fov.

The shutter is supported on two cantilever springs which are mounted at the sides of two PMT's, as shown in Figure 144. The solenoid is mounted at one side with the plunger attached to one cantilever to move the shield to the left when the solenoid is energized. The "slits open" position is controlled by the screw head in the end of the plunger contacting the bracket.

Power to operate the shutter device will be switched on by means of a small sun detector with a silicon solar cell as the active element. This cell is mounted in a housing which exposes the cell to direct solar radiation over a fov of approximately 30° (to provide a margin of safety of 5° over the star-mapper half-field of view)*. Two design concepts for the sun detector are shown in Figure 145. In Figure 145(a) the direct solar radiation enters through a small aperture. For sun angles greater than 15° the rays strike the wall of the housing where a large percentage of the energy is absorbed. When the sun is within the 30° fov, the rays strike the silicon cell and a step-increase in the cell voltage occurs. The voltage remains at this level until the sun passes out of the detector fov.

Illumination of the cell can be increased by means of simple optics, as shown in Figure 145(b).

In other respects the second concept is the same as the first.

The cell output is not sufficient to operate the electromagnet of the shutter device directly, but will be used in a simple transistor photorelay circuit, such as shown in Figure 146.

Transit Time Error Analysis

Signal due to star and background. -- To estimate the time error in determination of a star crossing time, it is first necessary to find the strength of the signal due to the star and that due to other sources of stray light:

*The 5° margin is equivalent to 0.28 second for a vehicle spin rate of 3 rpm. The response time for silicon cells is of the order of 10 microseconds, and the response time for the solenoid-shutter device is less than 100 milliseconds. Thus, the 5° will provide adequate safety margin.

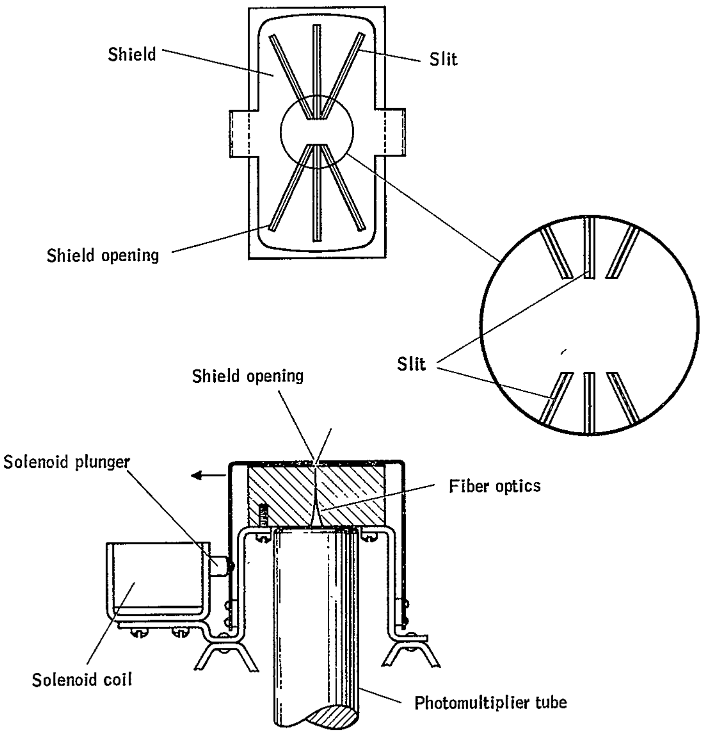

Figure 144. Focal Plane Shutter Mechanism

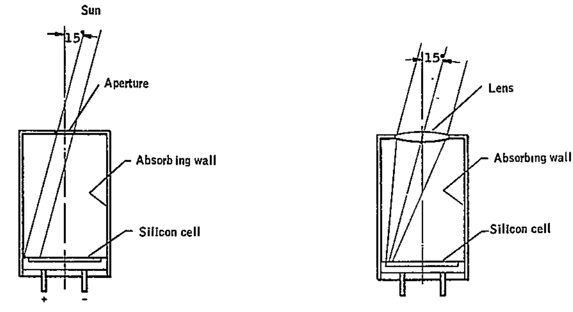

(a) Simple solar detector

(b) Solar detector with optics

Figure 145. Solar Detector for Shutter Device

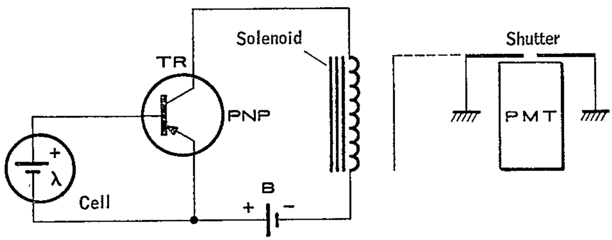

Figure 146. Photorelay Circuit for Shutter Device

$B(\lambda T)$ = Planck emissivity

$\Sigma_{\lambda\ max.}$ = maximum value of emissivity function

$\epsilon_q(\lambda)$ = photocathode quantum efficiency

ϵ_{qm} = maximum value of quantum efficiency

$O(\lambda)$ = maximum value of slit scan from ray trace program

O_m = maximum value of trace program

λ = wavelength (optical)

$S_e(\lambda)$ = spectral response of standard eye

M_B = limiting magnitude (blue)

ϵ_o = optical efficiency

h = Planck's constant

c = light velocity

σ = Stefan-Boltzmann constant

T = temperature °K

ρ = 1.2864×10^{-4} $\frac{\text{ergs}}{\text{cm}^3\ {}^\circ\text{K}^5}$

$F_o = F_o(\lambda, T)$ = energy flux from $0^m.0$ star of color temperature T at wavelength λ, per unit wavelength, per unit area above earth's atmosphere

N_s = signal photoelectrons per star transit

N_B = photoelectrons per star transit due to faint star background

N_o = faint star background in $10^m.0$ stars per square degree

A_s = slit area on celestial sphere in square degrees

A_{opt} = clear area of objective in cm^2

M_s = number of slits in focal plane over photomultiplier

α = slit width in degrees

ω = vehicle spin rate in degrees per second

θ_1, θ_2 = angles denoting slit extent

$$\alpha(T) = \int \frac{B(\lambda T)}{B_{\lambda_{max}}} \frac{\epsilon_q(\lambda)}{\epsilon_{qm}} \; 0(\lambda)\,\lambda\, d\lambda \tag{74}$$

$$\beta(T) = \frac{\int B(\lambda T)\, S_e(\lambda)\, d\lambda}{\int B(\lambda)\, d\lambda} \tag{75}$$

Thus, $\alpha(T)$ gives the dependence of the number of cathode photoelectrons on the color temperature. $\beta(T)$ is the fraction of the total energy accepted by the standard observer.

Figure 147 shows a plot of the function

$$M(T) = \frac{\int B(\lambda)\, \epsilon_q(\lambda)\, 0(\lambda)\lambda\, d\lambda}{\int B(\lambda T)\, S_e(\lambda)\, d\lambda} \tag{76}$$

In Figure 147 the ordinate is expressed in magnitudes with the zero at 11 000°K (Type A0). The abscissa is the common logarithm of color temperature (λ is in microns). 11 000°K corresponds to magnitude 0.1966. From Equations (74) to (76),

$$\alpha(T) = M(T)\beta(T) \frac{\int B(\lambda T)\, d\lambda}{B_{\lambda\, mas}} \tag{77a}$$

If two stars with different temperatures T_1, T_2 are each of zero magnitude, then

$$F_o(T_1)\,\beta(T_1) = F_o(T_2)\,\beta(T_2) = C = \text{Constant} \tag{77b}$$

In addition,

$$\int B(\lambda T)\, d\lambda = \sigma T^4 \text{ (the Stefan-Boltzmann law)} \tag{77c}$$

and

$$B_{\lambda\, max} = \rho\, T^5 \tag{77d}$$

Equations (72a) to '72d) lead to

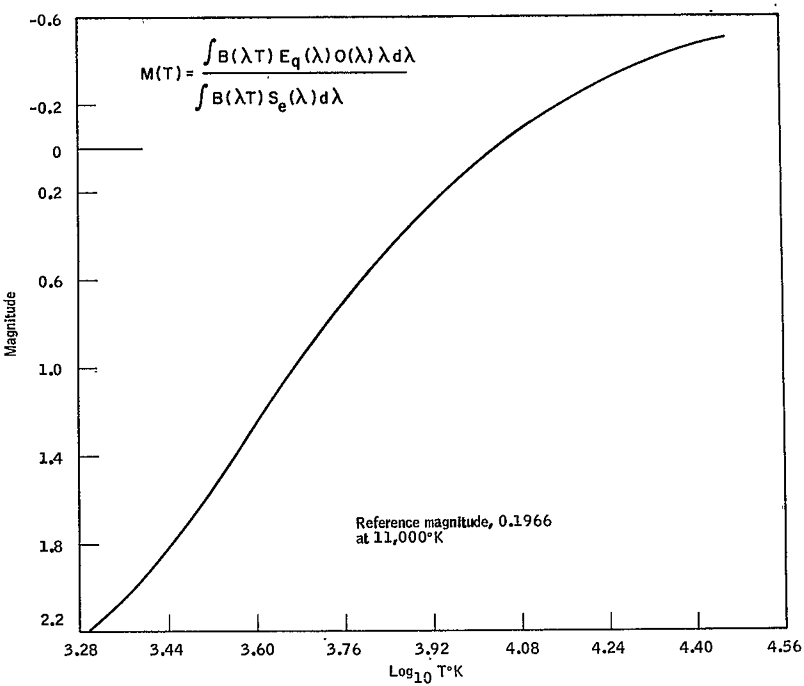

Figure 147. System Response in Visual Magnitudes as a Function of Color Temperature

$$\frac{F_o\,\alpha(T)}{hc} = \frac{C\,M\,(T)\,\sigma}{\rho\,h\,c\,T} = \gamma(T) \qquad (78)$$

Code (ref. 13) gives for the monochromatic flux from a star of visual magnitude zero and color ondex B-V = 0 a value

$$F_o = 3.8 \times 10^{-9}\ \mathrm{erg/cm^2/sec/Å} \qquad (79)$$

at 5560 Å. This value was adopted.

The usual spectral responses of photomultipliers (S-4, S-11, S-9, etc.) correspond roughly in bandpass and bandpass location to the Johnson "B" filter widely used to determine blue magnitudes. This induces the use of blue magnitudes in the calculations of star signals.

If blue magnitudes are used, the flux calibration needed is at 4300 Å (center of Johnson B filter). Code (ref. 13) gives a magnitude difference for Bega (Type A_o visual magnitude 0.00 and color index 0.00) between 5560 and 4300 Å of

$$\Delta M\left(\frac{1}{\lambda}\right) = -0.20 \qquad (80)$$

It is preferred to work in terms of $M(\lambda)$ the magnitude as a function of wavelength rather than reciprocal wavelength. The two are related by

$$M(\lambda) = M(1/\lambda) + 5 \log (\lambda/\lambda_o) \qquad (81)$$

From the definition of magnitude in terms of intensity,

$$\frac{F_o\,(0.4300;\ 11\,000)}{F_o\,(0.5560;\ 11\,000)} = \left(\frac{\lambda_o}{\lambda}\right)^2\ 10^{-0.4\,\Delta M(1/\lambda)} \qquad (82)$$

Using Equations (82) and (79), the monochromatic flux from a star of visual magnitude zero and color index zero at 4300 Å is

$$f_{4300\,Å} = 7.64 \times 10^{-12}\ \frac{W}{cm^2\,\mu}$$

$$= 0.764\ \frac{ergs}{sec\ cm^3} \qquad (83)$$

A numerical integration of Equation (75) for T = 11 000°K gives

$$\beta\ (11\,000°K) = 9.523 \times 10^{-2} \qquad (84)$$

fixing the value of C.

In Figure 147, the reference magnitude is 0.1970. Thus,

$$M(11\ 000°K) = 1.2\mu = 1.20 \times 10^{-4} \text{ cm} \tag{85}$$

The quantity $\gamma(T)$ can now be found as

$$\gamma(11\ 000°K) = \frac{0.764 \times 9.523 \times 10^{-2} \times 1.20 \times 10^{-4} \times 5.67 \times 10^{-5}}{1.286 \times 10^{-4} \times 6.63 \times 10^{-27} \times 3 \times 10^{10} \times 1.1 \times 10^{4}} \frac{1}{\text{sec-cm}^2}$$

$$= 1.760 \times 10^{6}/\text{sec cm}^2 \tag{86}$$

The physical significance of γ (11 000 Å0) is that it is the number of photoelectrons per second produced by a Type A0, $0^m.0$ star in a sensor having ARRS design with a 1-cm^2 aperture of perfect transmission and using an EMR Type N photocathode with a peak quantum effieicncy of unity.

The number of photoelectrons per transit at magnitude M_B, aperture A_{opt}, and optical efficiency ϵ_o can now be calculated

$$n_s = \lambda(T)\, A_{opt}\, \epsilon_o\, \epsilon_{qm} \frac{\alpha}{\omega}\, 10^{0.4 M_B} \tag{87}$$

(α/ω = a star transit time).

The baseline starmapper utilizes a 3.25-inch aperture with a central obscuration of 2.30 inches. There are two fused silica-vacuum interfaces and a single mirror surface. Therefore,

$$A_{opt} = \frac{\pi}{4} 2.54^2 \,(3.25^2 - 2.30^2) = 26.72 \text{ cm}^2 \tag{88}$$

The refractive index, n, for fused silica at 4350 Å is 1.467. The reflection loss at each fused silica surface is approximately

$$R = \left(\frac{n-1}{n+1}\right)^2 = 0.036 \tag{89}$$

Reflectivity of aluminum (on the mirror) is about 0.96 in the visible. If 5% absorption occurs within the lenses, the optical efficiency will be

$$\epsilon_o = 0.964^2 \times 0.96 \times 0.96 = 0.85 \tag{90}$$

If, further, the slit width, α, is one minute of arc and the spacecraft spin velocity is 3 rpm (18°/sec) and the limiting magnitude is assumed as $3^{m}.50$*, n_s can be estimated as

$$n_s = \frac{1.76 \times 10^6 \times 26.72 \times 0.85 \times 0.215^{**} \times 10^{-0.4 \times 3.5}}{60 \times 18}$$

$$= 316 \text{ per star transit} \tag{91}$$

The number of photoelectrons due to the faint star background per star transit will be

$$n_B = \gamma(T)\, A_{opt}\, \epsilon_o\, \epsilon_{qm}\, \frac{\alpha}{\omega} N_o\, 10^{-4}\, A_s \tag{92}$$

$$(\gamma A_{opt}\, \epsilon_o\, \epsilon_{qm}\, \frac{\alpha}{\omega} = 1.351 \times 10^4/\text{sec}$$

If the slit extends from θ_1 to θ_2 as measured from spin axis,

$$A_s = n_s\, \frac{180\,\alpha}{\pi}\, (\cos\theta_1 - \cos\theta_2) \tag{93}$$

The baseline fov is 20°, and the slit array possesses a 2° central blocking angle. One set of slits extends from 70° of spin axis to 79°. Another extends from 81° to 90° of axis. Thus, one set of slits has an area 0.433 square degree, the the other 0.448 square degree; the average is 0.440 square degree.

Principal sources of stray light will be scattered light from bright objects, zodiacal light, and faint stars of the Milky Way. It is not possible to estimate the scattered light from bright objects without knowledge of the configuration. Thus, ideal conditions will be assumed. Allen (ref. 14) gives the zodiacal light at elongation 120° as 170 tenth magnitude stars per square degree. Roach and Negill (ref. 15) give the integrated background of faint stars as a function of galactic coordinates. They find backgrounds as large as 320 tenth magnitude stars per square degree. The zodiac and the Milky Way are not scanned simultaneously. Thus, put $N_o = 320$.

Then,

$$n_B = 1.351 \times 10^4 \times 320 \times 10^{-4} \times 0.440 \tag{94}$$

$$= 101 \text{ per star transit}$$

*A value of 3.65 (visual) was reported earlier as the faintest star required to be detected in a worst-case condition.

**Quantum efficiency of 21.5% corresponding to Type N photocathode.

If the star population is arranged according to spectral class and the number per spectral class is plotted as a function of spectral class, Figure 148 is obtained (ref. 16).

Peaks in population-density occur at Type A and Type M, explaining the use of A0 stars in the calculation and suggesting a similar one for Type M.

The temperature dependence of n_s can be deduced from Equation (78) as

$$n_{s2} = n_{s1} \frac{T_1 M (T_2)}{T_2 M (T_1)} \tag{95}$$

Type M corresponds to about 3800°K, according to Allen (ref. 14). From Figure 102 at T = 3800°K, M (3800°K) = 0.288; thus, for 3800°K,

$$n_s = 316 \times \frac{11}{3.8} \times 0.288 = 263 \tag{96}$$

This result is unexpected; intuitively, one expects many fewer.

Further examination of this result appears in order. In Figure 149, $\alpha(T)$, the system response at constant peak value of the incident radiation, is displayed as a function of temperature. This varies over orders of magnitude and is as expected. However, to obtain the system response at constant magnitude (blue or visual), $\alpha(T)$ must be divided by the response of the standard observer (Figure 150) as well as the effective black body temperature. The result of these operations is the curve of Figure 151. The variation of system response changes surprisingly little over 2500°K $\leq$ T $\leq$ 30 000°K, comprising spectral classes M_5 to B_5.

Signal-to-noise ratio; variance of crossing time estimate. -- Having found the signal from star and background, the signal-to-noise ratio and the factor, K, by which the blur circle of the star or slit width may be interpolated can be estimated. The peak signal to rms noise is

$$S/N = \frac{M_s}{\sqrt{2 (n_s + n_B + n_P}} \tag{97}$$

where

$$n_P = \gamma \frac{\alpha}{\omega} \tag{98}$$

and is the total number of noise pulses per star transit due to the photomultiplier tube and γ is the number per second. EMR 541N specifications indicate γ = 1200. This value is also assumed for the EMR 531N photomultiplier.

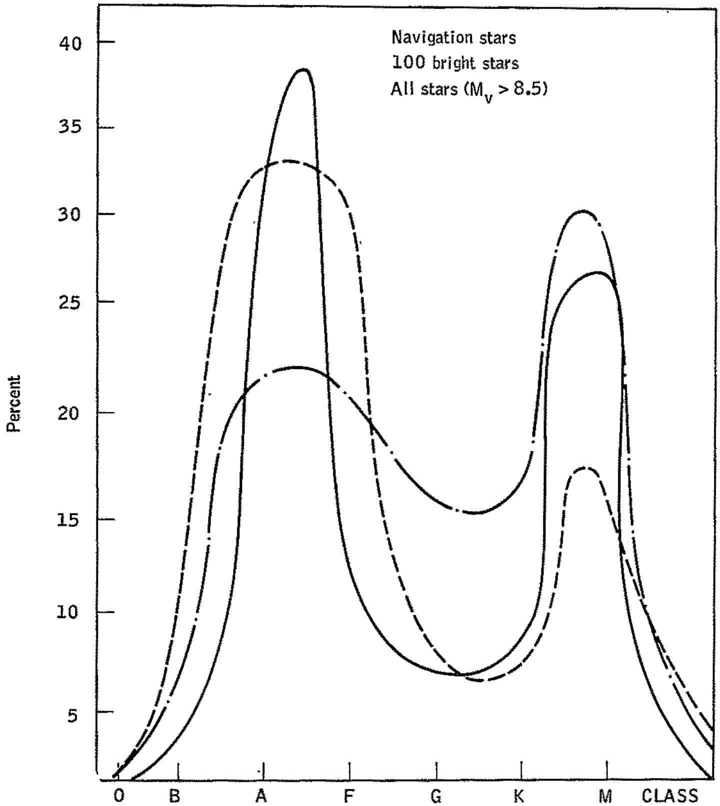

Figure 148. Number Distribution of Stars According to Spectral Class

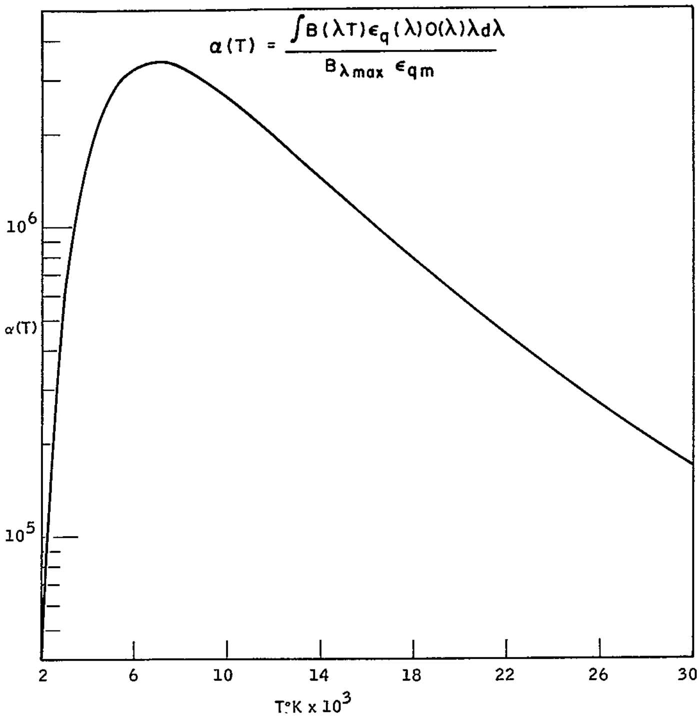

Figure 149. Number of Cathode Photoelectrons as a Function of Color Temperature

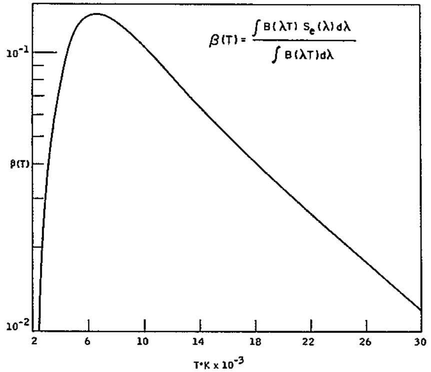

Figure 150. Response of Standard Observer as a Function of Color Temperature

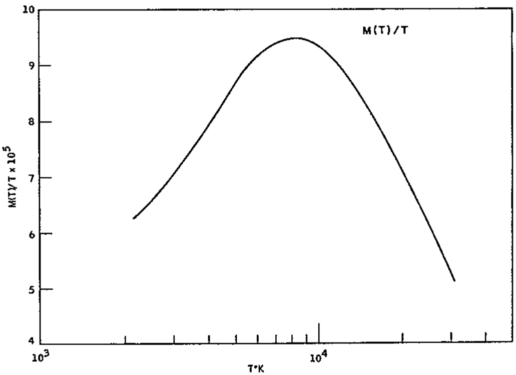

Figure 151. Relative System Response as a Function of Color Temperature

$$n_P = \frac{1200}{18 \times 60} = 1.11$$

which is negligible. Then,

$$(S/N)\ 3^{m}.5\ A0 = 9.91$$

$$(S/N)\ 3^{m}.5\ M0 = 7.14$$

A rule of thumb for estimating the interpolation factor is

$$K \approx \sqrt{2\ (S/N)} \tag{99}$$

Thus,

$$K(3^{m}.5,\ A0) = 14.0$$

$$K\ (3^{m}.5,\ M0) = 10.1$$

The expression (99) is derived as follows.

Let t_s be the measured time of transit, e_o be the output signal, and T_s be the star transit time across the slit. Then,

$$\overline{t_s^{\,2}} = \frac{\overline{e_o^{\,2}}}{2\left(\frac{de_o}{dt}\right)^2}, \quad (S/N)^2 = e_o^{\,2}/\overline{e_o^{\,2}}$$

$$\frac{de_o}{dt} \approx \frac{e_o}{T_s}, \quad \overline{N_s^{\,2}} \approx \frac{T_s^{\,2}}{K^2}$$

whence $K \approx \sqrt{2\ (S/N)}$.

These numbers are based on 1-sigma errors, leading edge detections, and stationary statistics. Since threshold detection at both leading and trailing edge will be used and the statistics are in fact nonstationary, a more rigorous treatment of crossing time error follows.

The following theorem may be derived from Parzen (ref. 16) [see also E. J. Farrel (ref. 17)].

Let x(t) be a poisson process with rate $\nu(t)$, of form

$$x(t) = \sum_{k=-\infty}^{\infty} a_k \int_0^{\infty} p(t - t_k - x)\, h(x)\, dx \tag{100}$$

where $h(t) = 0,\ t \leq 0$, and a_k and t_k are random variables. Then the expectation value, variance, and covariance of $x(t)$ are given by

$$E[x(t)] = \bar{a} \int_{-\infty}^{\infty} \nu(\tau) \int_{-\infty}^{\infty} p(t - \tau - x)\, h(x)\, dx\, d\tau \tag{100}$$

$$\mathrm{var}\ x(t) = \overline{a^2} \int_{-\infty}^{\infty} \nu(\tau) \left\{ \int_{-\infty}^{\infty} p(t - \tau - x)\, h(x)\, dx \right\} d\tau \tag{102}$$

$$\mathrm{coc}\ [x(t),\ x(t + t_o)] = \overline{a^2} \int_{-\infty}^{\infty} \nu(\tau) \int_{-\infty}^{\infty} p(t - \tau - x)\, h(x)\, dx$$

$$\int_{-\infty}^{\infty} p(t + t_o - \tau y)\, h(y)\, dz\, d\tau \tag{103}$$

Considering threshold detection at leading and trailing edges of the star pulse, and assuming a constant slope in a neighbordhood of the threshold, Farrell (ref. 17) derives

$$\mathrm{var}\ (t_s) = \frac{\mathrm{var}\ x\ (t_1) - \mathrm{cov}\ [x(t_1)\ x\ (t_2)]}{2 \left\{ E[x'(t_1)] \right\}^2} \tag{104}$$

where t_1 and t_2 are times of threshold crossings.

E. J. Farrell (ref. 18) has shown that if the star "blur circle" is assumed to have the Gaussian form

$$I(x, y) = e^{-x^2 + y^2 / 2\sigma^2} \tag{105}$$

then the detector output may be well approximated, except for a constant factor

$$g(t) = e^{-t^2 / 2\sigma_1{}^2} \tag{106}$$

where

$$\sigma_1{}^2 = \sigma^2 \left[1 + \frac{1}{3}\left(\frac{T_s}{2\sigma}\right)^2\right], \quad T_s = \frac{\alpha}{\omega} \tag{107}$$

and, where T_s is the time for a star to cross the slit.

The foundations for the application of Equations (100), (101), and (102) has now been laid. One takes t to be time, p(t) to be the detector output due to a single photo event, h(t) to be the impulse response of the filter following the detector, x(t) to be the filter output, a_k to be the size of signal at detector anode due to a single photo event, and $\nu(t)$ as g(t). Since p(t) occurs in a time much smaller than the filter delay, one puts $p(t) = \delta(t)$, where $\delta(t)$ is the Dirac delta function.

Then,

$$E[x(t)] = \bar{a} \int_{-\infty}^{\infty} g(x)\, h(t-x)\, dx \tag{108}$$

$$\operatorname{var} x(t) = \overline{a^2} \int_{-\infty}^{\infty} g(x)\, h^2(t-x)\, dx \tag{109}$$

$$\operatorname{cov}[x(t), x(t+\tau)] = a^2 \int_{-\infty}^{\infty} g(x)\, h(t-x)\, h(t+\tau-x)\, dx \tag{110}$$

where $\bar{a}$ and $\overline{a^2}$ are the first and second moments of a_k.

To account for star plus background and dark current, one takes g(x) as

$$g(x) = I_o\, e^{-x^2/2\sigma_1{}^2} + I_1 \tag{111}$$

where I_o and I_1 are photon rates ($I_o = n_s/T_s$, $I_1 = n_B/T_s$).

A lowpass filter is used. Thus, the impulse response will be of the form

$$h(x) = 2\omega_c \sum_{i=1}^{N} e^{-\alpha_i \omega_c x} \left(a_i \cos \beta_i \omega_c x + b_i \sin \beta_i \omega_c x\right) \tag{112}$$

where α_i, β_i, a_i, b_i, ω_c characterize the filter.

The evaluation of Equation (110) is effected by use of Gauss-Hermite quadrature. One obtains, for example,

$$\begin{aligned} \text{cov}\,[*(t),\ x(t+\tau)] = \overline{a^2}\, I_o \sqrt{2}\ \sigma_1 \sum_{i=1} & W_j\, h(t - \sqrt{2}\,\sigma_1\, x_j) \\ & h(t+\tau - \sqrt{2}\,\sigma_1\, x_j) \\ + \overline{a^2}\, I_1 \sqrt{2}\,\sigma_1 \sum_{i=1} & W_j\, h(t - \sqrt{2}\,\sigma_p\, x_j) \\ & \text{a}\,(t+\tau - \sqrt{2}\,\sigma_1\, x_j) \end{aligned} \tag{113}$$

where W_j and x_j are the weights and roots for Gauss-Hermite quadrature and

$$w_j = e^{x_j^2}\ W_j$$

A threshold I_t is set; a filter delay t_o is calculated from the equation

$$0 = x'(t_o) = \frac{d}{dt}\ E[x(t_o)] \tag{114}$$

in the form

$$\sum_{i=1}^{N} w_i\, x_i h(t_o - \sqrt{2}\,\sigma_1\, s_i) = 0 \tag{115}$$

The threshold crossing times are then taken as

$$t_{1,\,2} = t_o \pm \sqrt{2\,\sigma_1^{\,2}\, \ell n\,(i_o/I_t)} \tag{116}$$

In the present program, the delay for an equi-ripple approximation to linear phase filter, a Paynter filter is used to provide a first appproximation to the solution of (102), $t_o = \pi/\omega_c$.

The quantity $\overline{a^2}/\bar{a}^2$ which will appear in Equation (104) is taken as the degradation factor due to secondary emission multiplication noise in the photomultiplier.

A threshold n_T is found from the equation

$$p(n \geq n_T \mid N) = \frac{1}{2} \operatorname{erfc} \frac{n_T - N}{\sqrt{2N}} \tag{117}$$

i.e., if the mean number of the photoelectrons in a star transit time is $N = n_s + n_B + n_p$, what is the probability that n_T is exceeded. Putting p = 0.95 for a Type A0, $3^m.5$ star producing an average of 538 photons for star transit, n_T = 589, (488 + 101). Calculation of the transit time error can now be performed.

A linear phase shift, sixth-order Paynter filter is assumed. This has the transfer function

$$T(s) = \frac{1}{\prod_{i=1}^{3} \left[a_i \left(\frac{s}{\omega_c}\right)^2 + b_i \frac{s}{\omega_c} + 1\right]} \tag{118}$$

with

$$a_1 = 1.866, \qquad b_1 = 2.3860$$
$$a_2 = 0.6579, \qquad b_2 = 0.6204$$
$$a_3 = 0.2310, \qquad b_3 = 0.1224$$

Thus, the impulse response is

$$h(t) = \left\{2a_i \omega_c e^{-\alpha_i \omega_c t} \cos(\beta_i \omega_c t) + 2b_i \omega_c e^{-\alpha_i \omega_c t} \sin(\beta_i \omega_c t)\right\} \tag{119}$$

with

$$a_1 = 0.6393, \quad \beta_1 = 0.3566, \quad a_1 = 0.0441, \quad b_1 = 0.2691$$
$$a_2 = 0.4715, \quad \beta_2 = 1.1391, \quad a_2 = -0.555, \quad b_2 = 0.1067$$
$$\alpha_3 = 0.2641, \quad \beta_3 = 2.0604, \quad a_3 = 0.0114, \quad b_3 = 0.0143$$

A choice of $\omega_c = 0.7/\sigma$, $\overline{a^2}/\bar{a}^2 = 1.5$, and $n_s = 316$, $n_B = 192$ and $n_T = 471$ leads to a standard deviation for the leading edge of 1.210×10^{-4} second for the trailing edge of 1.215×10^{-4} second. The standard deviation of the pulse center σ_s, is 4.97×10^{-5}. Thus,

$$K = \frac{T_s}{\sigma_s} = 18.6$$

The 1-sigma error for 1-arc-minute slits is 3.2 arc sec. A 3-sigma error is 9.6 arc sec.

For a color temperature of 2400°K (Type M9), the numbers are, $n_s = 200$, $n_B = 192$, $n_T = 392$, and $\sigma_s = 7.19 \times 10^{-5}$, (S/N) = 7.14 and K = 12.9.

Effect of vehicle spin rate on signal to noise. -- From Equations (87) and (92), it may be seen that the number of signal and background photoelectrons varies inversely with ω, the spin rate. Thus, Equation (97) implies that the signal-to-noise will vary inversely as the square root of the spin rate or

$$(S/N)_1/\sqrt{\omega_1} = (S/N)_2/\sqrt{\omega_2}$$

Thus, a signal-to-noise of 15:1 at $3^m.50$ Type A0 becomes

$$(S/N)_{5\ \mathrm{rpm}} = 9.91\sqrt{\frac{3}{5}} = 7.68$$

and

$$(S/N)_{1\ \mathrm{rpm}} = 9.91\sqrt{3} = 17.17$$

GROUND BASED DATA PROCESSING

To determine the attitude of the spacecraft, the attitude determination algorithm uses the transit times of identified stars. The initial star identification subroutine was developed to identify transits from an initial data set of perhaps 10 to 20 scan periods with only a rough estimate of the direction of the spin axis given. As many transits as possible are matched with the star and slit which produced this transit.

As estimation proceeds, each transit which is encountered must be identified as having been produced by a given star and a given slit. The update star identification subroutine was developed to accomplish this.

Initial Star Identification

Initial star identification is accomplished through the following broad substeps. It is assumed that the transits are tagged, indicating from which of the two photomultipliers the pulse originated. It is further assumed that the on-board logic has transmitted transits only if they have been determined to be acceptable triplet members. Data from 10 to 20 scan periods will be used.

1) Measured transits will be grouped into triplets; this will remove the effects of interleaving of triplets and will tenatively identify each transit as being produced by a specified slit.

2) The scan period will be determined by forming a histogram of all the differences of the center slit transit times which lie within specified limits.

3) All of the triplets are then reduced modulo this period. Only the center slits need be considered -- along with the separation of the triplet members. These data are then histogrammed over a time span of one scan period. Triplets with different separations are handled separately. This procedure performs a multiscan correlation of the triplets.

4) The separation angles between the triplets as these angles are projected onto the celestial sphere are calculated. These separations are calculated from a knowledge of the elevations and relative azimuths of the triplets.

   If ω is the spin rate, define the azimuth to be $s = \omega t_3$, where t_3 is the transit time of the third slit. Also let $x = \omega(t_3 - t_1)$. Define σ to be the cant angle (i.e., the angle from the intersection of the slits to the spin axis).

   Finally, let ρ_i be the angle between the i^{th} slit and the great circle connecting the spin axis and the intersection of the slits. In the coordinate system in which the z-axis is identical to the spin axis and the x-axis lies in the plane defined by the spin axis and the position of the intersection of the slits at time $t = 0$, it can be shown that the direction cosines of the star producing the transits are given by

$$\begin{pmatrix} S_1 \\ S_2 \\ S_3 \end{pmatrix} = \frac{1}{\sqrt{a^2 + b^2}} R^T(s) \begin{pmatrix} a \sin\sigma - b \cos\rho_3 \cos\sigma \\ -b \sin\rho_3 \\ a \cos\sigma + b \cos\rho_3 \sin\sigma \end{pmatrix}$$

where

$$a = (\cos\rho_1 \sin\rho_3 - \sin\rho_1 \cos\rho_3 \cos^2\sigma) \cos x$$

$$- \cos(\rho_1 - \rho_3) \cos\gamma \sin x - \sin\rho_1 \cos\rho_3 \sin^2\sigma$$

$$R^T(s) = \begin{bmatrix} \cos s & -\sin s & 0 \\ \sin s & \cos s & 0 \\ 0 & 0 & 0 \end{bmatrix}$$

and

$$b = -\sin\sigma\sin\rho_1\cos\sigma\cos x - \sin\sigma\cos\rho_1\sin x$$
$$+ \sin\sigma\sin\rho_1\cos\sigma$$

Then the separation angle θ_{ij} between the projections of the i^{th} and j^{th} triplet on the celestial sphere can be calculated from the dot product between the two star vectors

$$\cos\theta_{ij} = \hat{S}_i \cdot \hat{S}_j$$

5) Initial identification is accomplished by examining various combinations of three triplets and then linking the separations of these triplets into a polygon. If this polygon corresponds to a polygon formed of the separations of known stars, the stars and triplets are regarded to be matched. The remaining separations are tested with other known stars to try to pick up additional matches.

6) The original transit data are examined and each transit which has been identified with a star is tagged with the matched star number and slit number.

If the reticle slits are characterized by an angle Γ between the slits and an angle σ between the intersection of the slits and the intersection of the spin axis with the celestial sphere, the motion due to the precession of the spacecraft can be considered to be decomposed into an up-down motion of the intersection of the slits expressed as

$$\sigma = \sigma + \gamma\sin\omega_p t$$

and a rotation of the slits through an angle ϵ about the point of intersection of the slits expressed as

$$\epsilon = \gamma\sin\omega_p t$$

where γ is the precession angle and ω_p is the precession rate. Since the precession angle is small, the rotary motion can be considered (for a given star) as a side-to-side motion of the slits.

The maximum difference in the positions of the observations of a given star by a given slit produced by the side-to-side motion will occur for the side slits. If $\sigma = 90°$, $\Gamma = -20°$, $\gamma = 1°$ and the fov is 15°, this difference will be about ±0.3°. For the center slit, the difference will be about 6% less. For the center slit, there will be no difference in the positions of a given star produced by the up-down motion. For the side slits, the maximum difference also will be about 0.3°.

Since the time spent along the up-down and side-to-side axis can be described by a sine curve with the maximum and minimum corresponding to the extreme points of the motion, a histogram of a sample of measurements of a given star (moduled to one spin period) will be double peaked. Since both the side-to-side and up-down motions contribute to the variation in the side slits, while only the up-down motion contributes to the center slit, the width of the peaks from the side slits will be about 1.5 times that of the peak from the center slit. For the above parameters this will imply a total variation from a nominal position of observation (i.e., assuming no precession) for the side slits of $\pm 0.45°$. This complicates the initial star identification procedure since, without an accurate knowledge of the attitude of the spacecraft including the precession effects, only the average position of a star transit can be deduced from the multiscan correlation technique.

The entire program was tested using a tape of simulated ARRS transits. These transits were displaced in time according to a Gaussian distribution of half width equal to 10 arc sec. In addition, triplets were randomly eliminated in inverse proportion to the brightness of the stars. Finally, triplets of noise were randomly introduced into the data. Of the 435 transits on the tape, 171 are noise transits. This simulation actually represents a condition of greater noise content than that expected for the real application.

Figure 152 shows the simulated transit times where each solid data point represents a star triplet and each open data point represents a noise triplet.

Using a value of 0.012 second for the tolerance for comparing the predicted with the measured transit times, 107 star transits were correctly identified and no star transit was incorrectly identified. Fifteen noise transits were incorrectly identified as being star transits. Since the maximum error in time for these incorrectly-identified transits is less than 0.012 second, the effect on the attitude determination should not be severe. It is obvious that the number of noise transits incorrectly identified as star transits will be reduced if the amount of noise in the raw data is less than the approximately 40% of the total used in this simulation.

The required input for the initial star identification program is a star catalog, a list of stars in the fov, a list of transit times, the number of transit times in this list, and a corresponding list of tags indicating whether the transit originated from the upper or lower photomultiplier tube. The output will be a list of identified transits and corresponding lists containing the matched star number, slit number, and tag.

Update Star Identification

Star identification during the update portion of the operation will be accomplished by the subroutine UPSID. The routine will interact with the attitude determination routine in a closed-loop manner. The attitude determination routine will calculate state vector, $\bar{x}(t)$, and the rotation matrix, E(t), which transforms vectors from inertial space to the body reference frame. It will continue this calculation until the time, t_s, of the next observed transit.

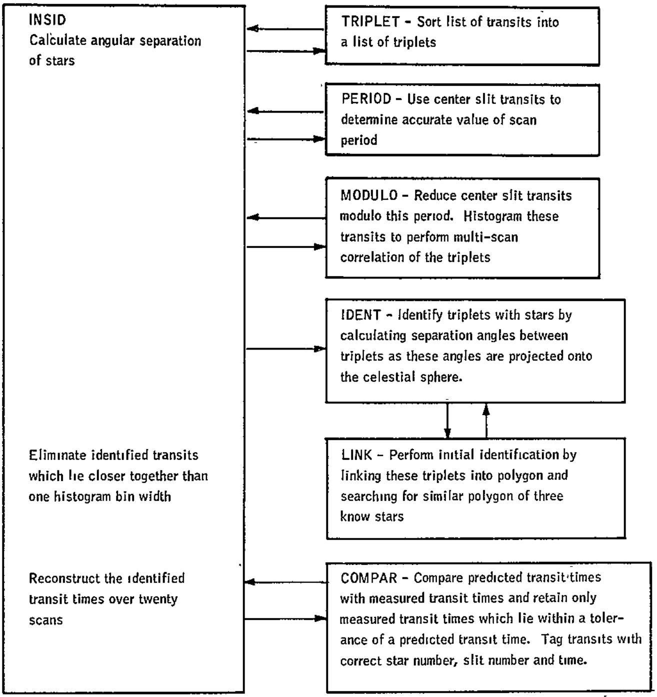

Figure 152. Flow Chart of Initial Star Identification Program

Then the routine UPSID will be called to identify the star and slit which produced this transit. This information will then be used by the attitude determination routine as it updates the attitude parameters until the next transit time.

The normal, $\hat{n}_1$, to the plane of slit i at the time t_s in the inertial reference system is given by

$$\hat{n}_i = E(t_s)\,\hat{N}_i$$

where $\hat{N}_i$ is the previously-calculated normal to the plane of slit i in the body reference frame.

Similarly, the optical axis at the time t_s in the inertial reference system is given by

$$\hat{a} = E(t_s)\,\hat{A}$$

where $\hat{A}$ is the optical axis in the body reference system.

The stars are then cycled through and the angle θ_j between the normal to each slit plane, i, and the previously-calculated star vector, $\hat{S}_j$, is given by

$$\cos\,\theta_j = \hat{n}_i \cdot \hat{S}_j$$

If this cosine is greater in absolute value than that of the best previous star-slit combination, this star-slit combination is eliminated from further consideration.

A check must now be made to see that the star lies in the fov. To do this, the angle $\eta = \hat{a} \cdot \hat{S}_j$. If η is less than the specified fov, the star j and slit i are identified with the transit t_s.

INPUT

$E(t_s)$	rotation matrix from inertial space to body reference frame at time t_s
$\hat{N}_i$	the normal to each slit, i, in the body reference frame
$\hat{A}$	the optical axis in the body reference frame
$\hat{S}_j$	the unit vector in inertial space to each star, j, in the fov
CFOV	the fov
CT	sine of angular tolerance between slit plane and acceptable star vector

OUTPUT

$\left.\begin{matrix}\alpha\\ \delta\end{matrix}\right\}$	right ascension and declination of star identified with t_s
S	direction cosines of star identified with t_s
MSL	slit number identified with t_s
MST	star number identified with t_s
SMAG	magnitude of identified star
SDOTU	cosine of angle between normal to slit plane and identified star vector

Stars in fov. -- A list of stars in the fov of the star sensor is required by both the initial and update star identification programs. The subroutine STARLST writes such a list without taking earth blocking into consideration.

INPUT

Star Catalog

$\left.\begin{matrix}\text{RA}\\ \text{DE}\end{matrix}\right\}$	direction of spin axis
SIGMA	cant angle
FOVD	field of view (deg)
THETA	precession (cone) angle (deg)

OUTPUT

LIST	list of indices of stars in fov

CELESTIAL SENSOR LOGIC

Memory banks on the spacecraft can store a maximum of 60 000 bits of information from the star sensor per orbit. The celestial sensor logic system gathers the data from the photomultiplier tube (PMT), processes it, and places selected items into storage. The signal from the PMT is amplified and filtered to remove as much noise as possible. A threshold detection system and associated logic then determines in real time the position of the transit. Finally, the data-reduction system will separate noise pulses and star information by digital filtering techniques. Since as many as possible of the 60 000 bits must contain good star transit information to solve the attitude determination problem, the aim of this system is to eliminate all noise pulses.

Data Compression

Limited storage of 60 000 bits per orbit is one of the major design constraints in the design of the on-board logic. It is assumed that the position of a star pulse must be resolved to 1 arc sec. The range of time measurement required is calculated as 46.4 microseconds for 1 rpm and 9.25 microseconds for 5 rpm. A 100-KHz clock would give 10 microseconds of resolution with a real-time count of 600×10^6 within 30 bits. A 25-KHz clock would give 40 microseconds of resolution with a real-time count of 150×10^6 within 28 bits.

If t bits are required for a real-time measurement of a star within the orbital period of 100 minutes and if the measurement period were cut in half, to 50 minutes, and the real-time register just recycled, there would be a reduction of 1 bit per data word per orbit. A simple recycling of real-time every 12.5 minutes allows the removal of three bits from each data word. Therefore, t - 3 is the resultant number of bits needed to express real-time. This technique effectively maps temporal star data into octants. Further data compression is realized by reformatting and marking the resultant 27 bits (or 25 bits for 5 rpm). Consider the 1-rpm spin rate, 25-KHz clock, then there are 1.5×10^6 counts within 21 bits for one spin period. Considering the 5-rpm spin rate, 100-KHz clock, then there are 1.2×10^6 counts within 21 bits (a 1-minute marker would require five spins or 6×10^6 counts within 23 bits). The result of this arithmetic implies that if properly organized the star data information could be effectively compressed without encoding loss.

Consider the increase in data handling for a system which utilizes a 1-minute marker. In the 1-rpm range, 21 bits are required for each mapping within the 1-minute interval. Memory would be segmented into data streams at 22 bits where bit 22 is the marker bit as follows:

Bit number	22	21	20	- - - - - - 1
Data word	0	x	x	- - - - - - x
Marker word	1	0	-	- - - - - - 0

For 60 000 bits, this implies that 2720 data words are available for encoding. The method requires 100 words used as marker words. The advantage of using 100 marker words is that the unused 21 bits per marker word could carry status information and additional information on the number of actual transits intercepted. Of course, the marker words could carry star information in the unused 21 bits. Since for 1 rpm 30 bits are normally required but due to formatting only 22 are actually required, there is a realizable data compression ratio of 1.36.

The significance of the 60 000-bit storage capacity as a constraint on the data processing system can be observed from Table 10. The table indicates for the two possible extreme scan rates (1 and 5 rpm) the maximum number of stars per scan that can be accommodated if every scan of data is stored.

TABLE 10.- STORAGE LIMITATION IN TERMS OF STARS/SCAN

Item	5 rpm	1 rpm
Bit storage/orbit	60 000	60 000
Scans/orbit	500	100
Scan period	12 sec	60 sec
Time resolution	10 μsec	46 μsec
Clock frequency	100 KHz	25 KHz
Bits without compression	30	28
Bits with compression	24	22
Words/orbit with compression	2 500	2 620
Words/scan with compression	5	26
Stars/scan with compression	1	8

However, during that portion of the scan when the opaque earth blocks the star field, no star storage is required. Then on the average two stars per scan could be stored (at 5 rpm) rather than just one. Two observations are apparent:

1) Data cannot be stored for every scan. Therefore, some scans must be skipped, presumably in an ordered sequence.

2) Noise pulses should not be accepted since they will occupy valuable storage space.

Table 10 is established on the basis of a data compression scheme which replaces the higher-order bits with the 1-minute marker concept discussed as a part of the section Digital Measurement Subsystem.

Celestial Sensor Logic System

Logic for the ARRS Celestial Sensor Logic (on-board data processing) contains four basic subsystems:

1) The Data Gathering Subsystem (DGS) is, collectively, the PMT, its supply, ground command logic, and the analog processing and smoothing of star signals.

2) The Data Measurement Subsystem (DMS) is the real-time determination of the time position of any transit in orbit. In addition, the spin rate may be determined if required.

3) The Digital Filtering Subsystem (DFS) is the data reduction subsystem which will separate noise and star information by digital filtering through use of scan correlation or triplet selection criterion. This subsystem also accounts for the interface logic with the on-board storage.

   This task may be accomplished by employing either hard-wired special-purpose logic or an on-board central processor unit (CPU).

4) The Timing Subsystem (TSS) accounts for the real-time, 100-minute clock and logic timing for the preceding subsystems of the celestial sensor logic.

Figure 153 shows a simplified diagramatic sketch of a possible celestial sensor logic system.

Data gathering subsystem (DGS). -- The DGS, shown schematically in Figure 154 is a dual-channel concept using two photomultipliers and associated electronics. The use of two photomultipliers is the baseline approach for ARRS. Figure 154 includes, in addition to the photomultiplier and its power supply, a solid-state detector to sense high-intensity radiation (and thereby actuate photomultiplier cutoff) and protection switching logic (control logic). The information path for each channel includes a preamplifier analog filter and an adaptive threshold element. The two channels sum their inputs.

Also shown in the command control word which would receive the ground command instructions and act on therm. The TLU sets the desired threshold level on command. The flag logic will produce a flag bit according to channel.

Digital measurement subsystem (DMS). -- The DMS, shown schematically in Figure 155, measures the center of a star (or noise) pulse in real time. The pulse enters the detection system and with ingress detection initiates a data transfer from a real-time register in the TSS. Once initiated, the logic counts at half clock speed until pulse egress. On egress the data word is transferred from the primary data hold register to the parallel-to-series converter where the data are strobed to the secondary data hold register in the DFS.

In addition, the TSS at each minute forces an interrupt in the DMS so that a minute word is inserted into the data field. The egress detected signal (ED) is transmitted to the DGS logic where the data are filtered to separate digital noise pulses from star data. At a spacecraft scan rate of one revolution per minute, ampulse data word encoded to one arc sec accuracy is 23 bits. At five revolutions per minute the word length is 21 bits.

Timing Subsystem (TSS). -- The TSS, shown schematically in Figure 156, provides timing for the entire on-board processing system. Clock frequency at 1 rpm is 100 KHz and at 5 prm is 25 KHz. The real-time register counts real time in octants and in 1-minute intervals resolved to an accuracy of 11 arc sec.

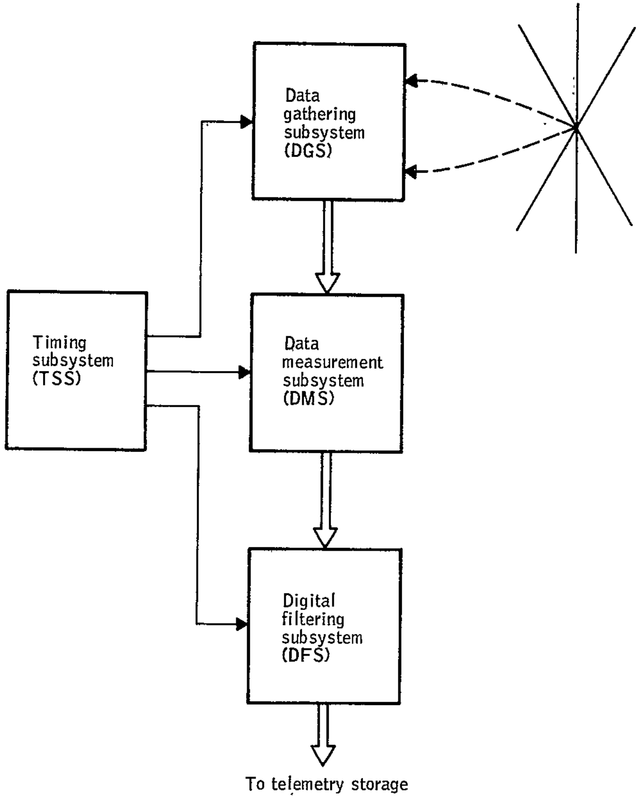

Figure 153. Celestial Sensor Logic System

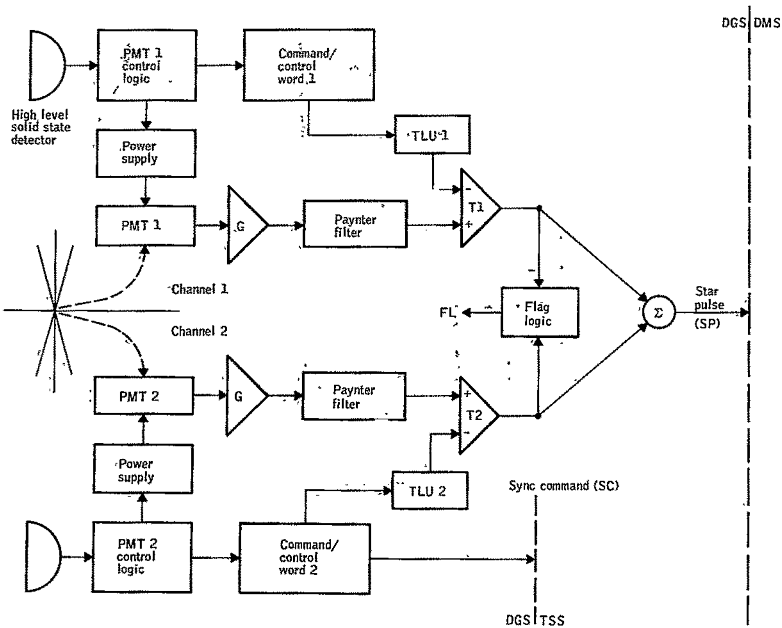

Figure 154. Schematic Diagram of Data-Gathering Subsystem

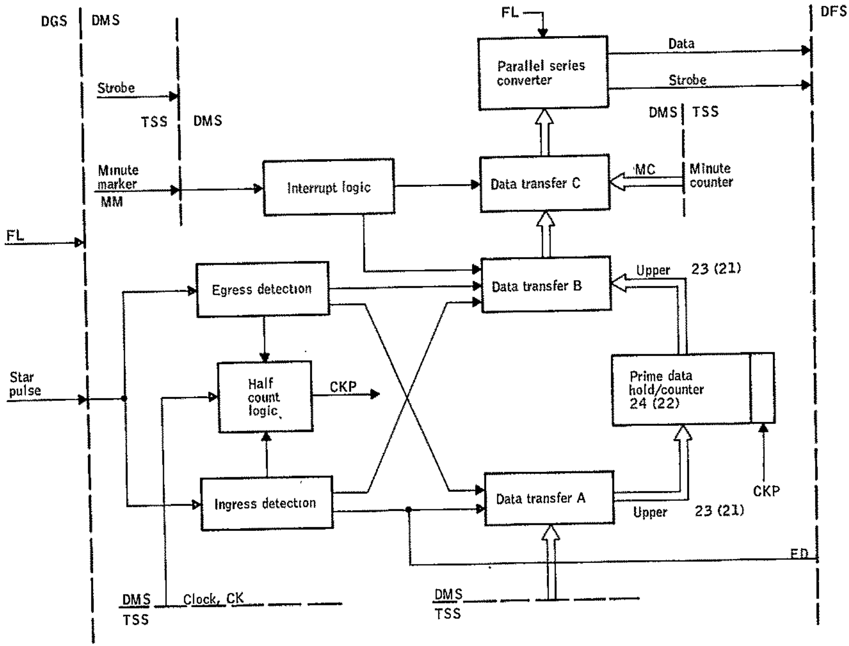

Figure 155. Schematic Diagram of Data-Measuring Subsystem

This system is the tracer for 1-minute interrupts, counts, and strobes pulses for serial data handling in the DMS and DFS. Twenty-seven bits correspond to 1 rpm and 25 to 5 rpm.

Digital filtering subsystem (DFS). -- The purpose of the DFS is to reduce the amount of data resulting from star transits to fit into 60 000 bits per orbit. The object is to retain as many of the star transits as possible while rejecting as many noise transits as possible.

Triplet selection: The matching of data pulses as possible members of a triplet produced by a star transiting the three slits is the basis for this filtering action. Mathematically, one may describe this criterion for any three data pulses, t_n, t_{n+i}, t_{n+i+j} as

$$\frac{\Delta t_L}{2} \le t_{n+i} - t_n = t_{n+i+j} - t_{n+i} \le \frac{\Delta t_U}{2}$$

where

$\Delta t_L \equiv$ minimum time window, or minimum allowable - three slit traversal time

$\Delta t_U \equiv$ maximum time windown, or maximum allowable - three slit traversal time

The information density within the maximum time window, Δt_U, and the maximum nesting of triplets within this window are this criterion's major considerations (see Figure 157).

This technique was studied for possible application to ARRS and is shown schematically in Figure 158. The up/down counters (see Figure 159) are started to count up by signal P_i and back down by signal P_{itj}. If a signal P_{ith} is detected when any of the counters have counted back to zero, the appropriate transit times are sent to the telemetry storage.

Considering the egress detection signals P_1, P_2, P_3, P_4, and P'_1, all possible triplets would be detected by this scheme. If a sixth P'_2 is added, all possible triplets among this group except P_1, P'_1, and P'_2 will be detected. If more than six noise or interleaved triplet pulses are expected within the maximum time window, more ranks of up/down counters must be added and the system very quickly becomes prohibitively complex. Indeed, the number of possible triplets (which corresponds to the complexity of the logic) is $\binom{n}{3}$ where n is the number of transits in the set to be examined.

Scan correlation: Scan correlation filtering assumes that if a data pulse is stable (i. e., a data pulse has a consistent relative temporal placement

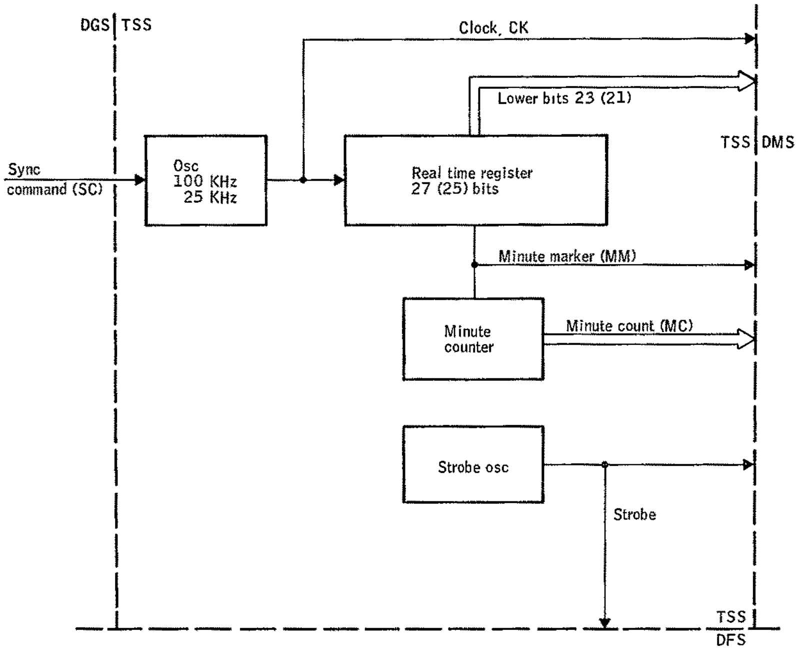

Figure 156. Schematic Diagram of Timing Subsystem

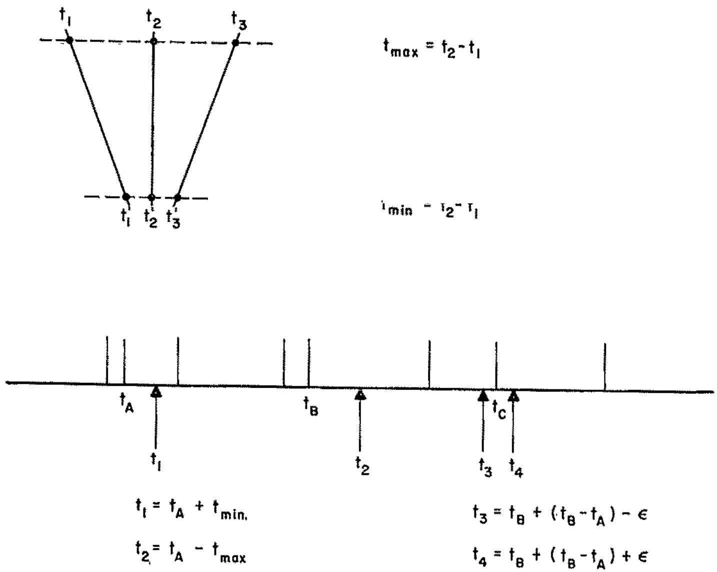

Figure 157. Triplet Selection Criterion

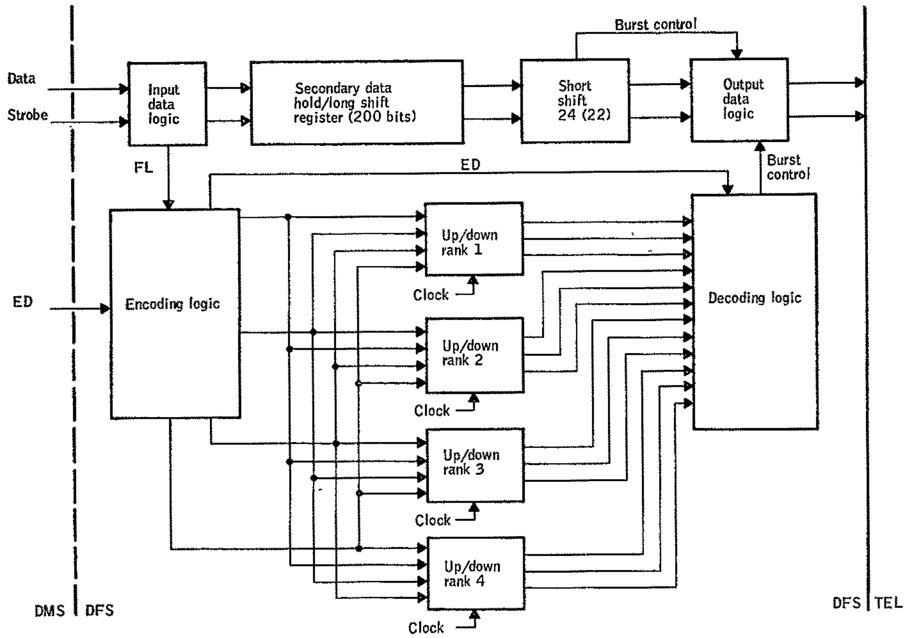

Figure 158. Schematic Diagram of Digital Filtering Subsystem

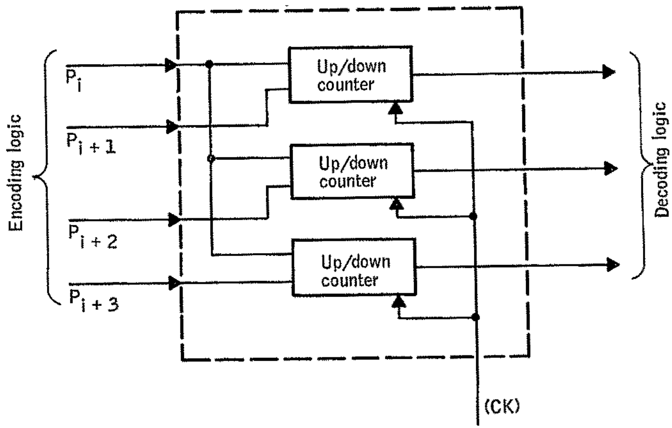

Figure 159. Schematic Diagram of Up/Down Counter Subsystem

for a fixed number of scan periods), the data pulse is assumed to be a star pulse. The scan information density (the number of measurable data pulses in a scan period) and the optimum number of scans for correlation are the major considerations in implementing this criterion. This technique is shown in Figure 160. In the scan correlation criterion shown in Figure 161, n_t transits form from n_s scans must fall within a window ϵ in order for the transits to be accepted.

On egress detection, a pulse is formed and transmitted from the DMS. The ID pulse is "painted" (i.e., strobed into a scan/shift register as a mapping pulse showing the relative occurrence in time to the SR pulse). On scan I (the first of a 3-scan sequence), the data are not strobed into the secondary data hold register. On interval I+1 (the next scan interval), the strobing of new pulse measurement is also blocked from the DMS to the secondary data hold of the DFS. The ID pulses are "painted" in the I+2 scan/shift register to map the data pulses relative to the spin rate marker as in interval I. On the third scan, I+2, the data are not blocked but allowed to pass into the secondary data hold register. At the end of this interval, the data in I, I+1, and I+2 allow a voting to occur (i.e., if the pulse is present in all three registers at the same temporal placement relative to the system marker, SR) and the data are allowed to pass into telemetry storage. If the voting does not hold a majority, the data are not inserted into telemetry storage. The 1-minute interval word is forced into telemetry storage as a function of its occurrence. Behavior of the logic on the next scan rate is optional, either the I+1 and I+2 maps move back via recycle logic and the scan is allowed to run continuously from the star (i.e., no intervals are skipped) or the logic must paint three new intervals and make a new decision at the end of every third scan.

On-board central processor unit (CPU): Use of a CPU greatly enhances the capability of the on-board logic to achieve highly versatile and complex decision and filtering functions. In the consideration of implementing the triplet selection criterion in the DFS of the on-board logic, it was found that complex comparison and inner comparisons were not possible without a significant increase in hardware. It can be shown that four ranks of three up/down counters would saturate without selecting correctly a triplet interleagued within another triplet in a low-noise environment. This, from a system viewpoint, is not ideal. If star data are to be lost, this should be done on a decision basis in the spacecraft logic, not from an inability of the logic to economically handle a higher information density. With this in mind, the CPU was selected as a data handler.

Figure 162 is a schematic diagram for one possible CPU applied as a digital filtering subsystem. This CPU is a candidate for the DFS since it offers low power and lightweight, and will accomplish the task required. The scratch pad would be DRO 256 24-bit words. This allows the tracking of digital pulses to a density of 85 stars per interval. The program for gathering the data, filtering, and transmitting selected star pulses to telemetry storage would reside within 1024 words of NDRO memory. It is recommended that the computer be placed on a 1-minute interrupt and create the time marker word for

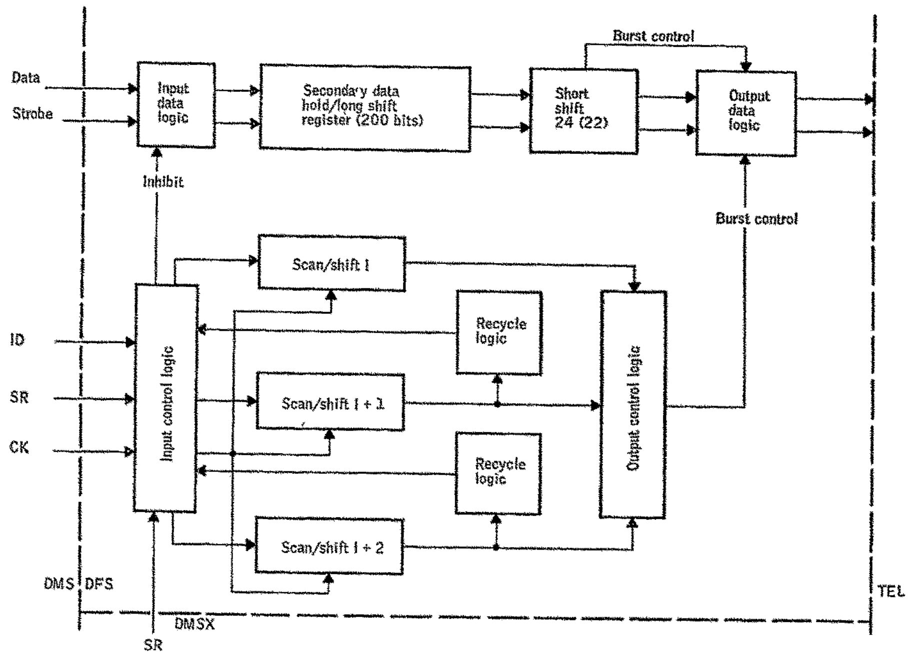

Figure 160. Digital Filtering Subsystem

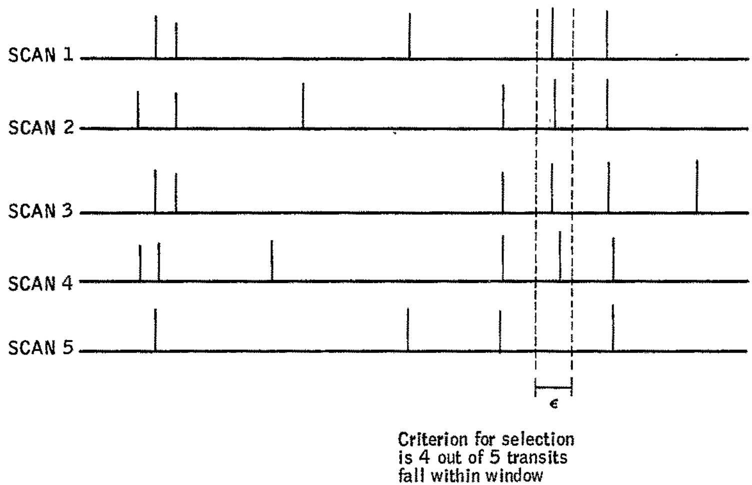

Figure 161. Scan Correlation Criterion

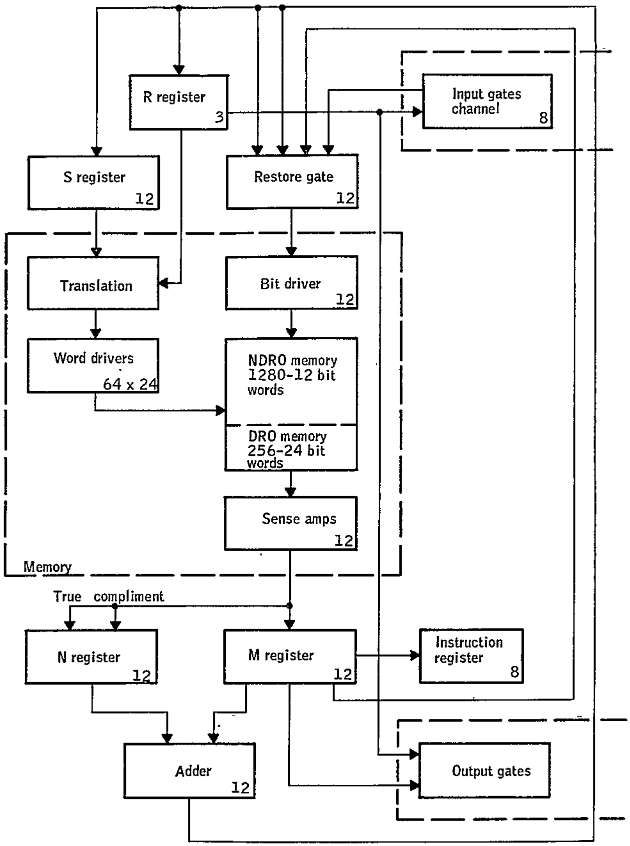

Figure 162. Schematic Diagram of Central Processing Unit Serving as Digital Filtering Subsystem

the compressed data for telemetry. The amplification to the total system subdivision is also rather wide spread. The DGS could be changed in that simple logic would no longer be required to determine the level of the Threshold Logic Unit (TLU), but an adaptive system could easily be created in which the CPU could handle all decision functions required.

The DMS could also be greatly reduced in size, complexity, and function over that required for hard-wired DFS. Its only function would be to measure the temporal placement of data pulses.

In Figure 163 the Celestial Sensor Logic-CPU interface is diagrammed to show the fundamental logic and analog functions required. Figure 164 shows the logical placement of the CPU within the sensor logic. In Figure 165 the memory map for the filtering function is shown to demonstrate the fundamental software packages and estimation of size required for the CPU to accomplish its task.

Table 11 shows the volume, weight, and power requirements for the CDC 449 CPU assuming different sources of primary power.

TABLE 11. - CDC 449 CPU GROSS CHARACTERISTICS

Primary Power	Power (W)	Weight (lbs)	Volume (in^3)
+12 vdc, +6 vdc +4 vdc, -3 vdc	4.5	4.6	125
+28 vdc	9	8.0	216
115 v rms, 400 Hz	25	13	288

Comparison of Filtering Techniques

The conceptual performance of the digital filtering techniques is shown in Table 12. Performance is defined here as being the ratio of the number of transmitted star transits to the number of possible star transits. Since the signal-to-noise ratio is designed to be at least 10 to 1, a probability of 90% for detecting a limiting magnitude star seems entirely reasonable.

The performance ratio for the hard-wired triplet selection technique is less than that for the triplet selection technique using the CPU because the hard-wired scheme cannot handle the interleaving of triplets with each other and with noise as well as can the CPU. These same transits will be lost if the raw data have a large amount of noise.

Table 13 is a comprison matrix of the several criteria for processing star transits and discriminating against noise transists. The large window in the scan correlation techniques is necessary because of the spread in time of the

TABLE 12. PERFORMANCE RATIO FOR VARIOUS ON-BOARD DIGITAL FILTERING TECHNIQUES

Probability of detecting limiting magnitude star	Triplet selection		Scan correlation							
			One transit transmitted				All transits transmitted			
	CPU	On-board logic	3/3	2/3	2/5	4/10	3/3	2/3	2/5	4/10
0.95	0.857	0.686	0.286	0.357	0.270	0.105	0.857	0.993	0.999	0.999
0.90	0.729	0.591	0.243	0.366	0.220	0.111	0.729	0.972	0.989	0.999
0.75	0.422	0.338	0.141	0.376	0.262	0.133	0.422	0.844	0.984	0.998
0.50	0.125	0.100	0.042	0.334	0.393	0.166	0.125	0.500	0.812	0.828

$$\text{Performance} = \frac{\text{number of transmitted star transits}}{\text{number of possible star transits}}$$

TABLE 13. MATRIX OF PERFORMANCE CRITERION ON-BOARD DATA PROCESSING

	Data compression	Window	Noise acceptance	Scan period needed	Triplets detection necessary	Performance[a]	Design effort
Triplet selection (hard-wired)	Yes	2 arc min	1	No	Yes	0.591	moderate
Triplet selection (CPU)	Yes	2 arc min	1	No	Yes	0.729	simple
Scan correlation (hard-wired, one transit transmitted)	Yes	20 arc min	10	Yes	No	0.366	moderate
Scan correlation (hard-wired, all transits transmitted)	No	20 arc min	10	Yes	No	0.972	difficult
Scan correlation (CPU)	Yes	20 arc min	10	Yes	No	0.972	simple

[a] Assuming 90% detection probability

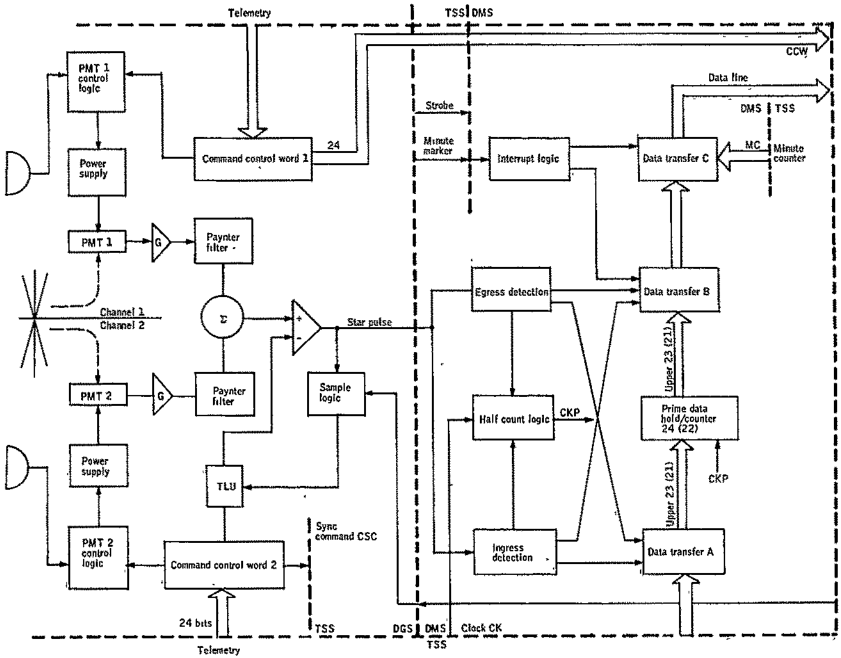

Figure 163. Celestial Sensor Logic - CPU Interface

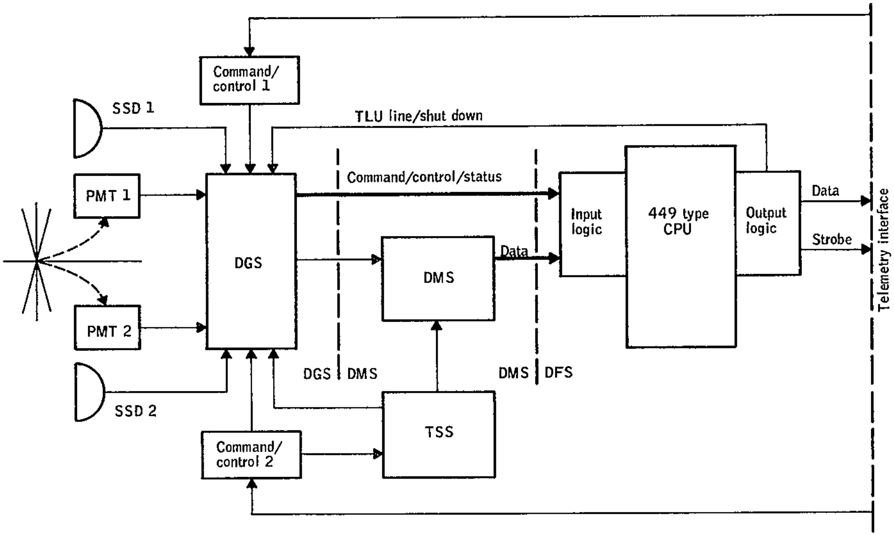

Figure 164. Celestial Sensor Logic System

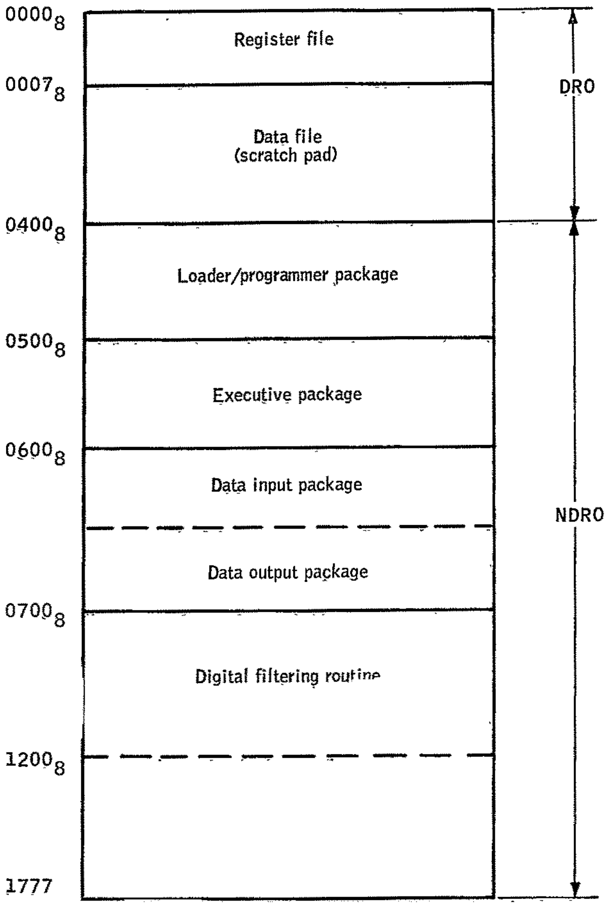

Figure 165. Memory Map Estimate for the Filtering Function

transits due to the coning effect. This large window -- implying the acceptance of more noise -- is a strong argument in favor of the triplet selection criterion.

Tables 12 and 13 refer to the use of a CPU or computer. The advantage of the triplet selection criterion using the CPU is apparent from a study of Figure 49. In particular, it is able to detect all possible triplets from a set of up to 80 transits, whereas the hard-wired scheme would miss at least one possible triplet from all sets containing more than five transits. If the raw data contained more noise transits than that assumed for the calculation of the performance ratios, the performance ratio for the hard-wired triplet selection technique would be considerably lower. The use of a CPU on-board the spacecraft has the further advantage over hard-wired logic in that the data processing algorithm can be written or revised at any point during the build or checkout phases of a programmed mission.

Summary and Conclusions

The window within which transits are accepted is much larger for the scan correlation technique than for the triplet selection technique. The windows for the triplet selection criterion must be only large enough to allow for uncertainty in the measurement of the transit time. This will be between one and two slit widths, which is equivalent to 1 or 2 arc min. However, as discussed earlier, the spread in time of transits due to the coning effect of the spacecraft will be approximately

$$\Delta t = 27/\omega$$

where ω is the spin rate in arc min/sec and a cone angle of 1° is assumed. Since the measurement uncertainty and the uncertainty in the scan period must be added to this, it is apparent that the window for the triplet selection technique can be 10 to 20 times smaller than that for the scan correlation technique. If noise pulses are detected uniformly in time, this implies that the scan correlation method will accept 10 to 20 times as many noise pulses as will the triplet selection criterion. Use of the triplet selection technique is therefore recommended.

Use of a CPU on-board will allow the triplet selection process to be extended to a much greater degree of complexity than if hard-wired logic were used. That is, the nesting of triplets within each other can be examined to a much higher level than would be practical with hard-wired logic. In addition, the use of the CPU would simplify the other on-board logic subsystems since it could handle such tasks as selecting the threshold, providing the 1-minute interrupt for data compression, and assuming some of the DGS control functions.

Thus, the triplet selection criterion in conjunction with an on-board CPU appears to represent the optimum approach to the on-board data processing.

CONCLUSIONS AND RECOMMENDATIONS

This volume documents the design of the ARRS attitude determination system. This portion of the ARRS study included the development of an operational data-reduction program and the conceptual design of the celestial sensors.

The operational data-reduction program development consisted of torque model derivation and analysis, spacecraft modeling, and the data-reduction algorithm development and performance analysis. Spacecraft modeling and torque modeling tasks provided for the development of a model which gives accurate and numerically efficient propogation of the spacecraft's state. The spacecraft and torque modeling tasks were conducted in parallel to the attitude determination data-reduction algorithm task, and results of the spacecraft and torque modeling tasks determined the software modifications desired in the evolving operational algorithm. Data-reduction algorithm tasks provided for the development of an operational attitude determination computer program to estimate spacecraft rotational state from celestial observations. In addition, these tasks included the development of a complete simulation of the attitude determination system for conducting the system performance analysis.

The discrete Kalman filter was used to update the spacecraft state by the celestial observations with propogation of the spacecraft state between observation by the nonlinear rotational dynamics model. Since the nonlinear rotational dynamics model does not represent the true behavior of the spacecraft in the orbital environment, the Kalman filter must be modified to prevent the divergence of the state estimate after initial convergence. The introduction of artificial covariance noise in the state covariance propogation differential equation was made.

The conceptual design of the celestial sensors included analysis to determine the conceptual design parameters, the optical transfer function description for a starmapper and sun sensor, the development of ground-based data processing, and the conceptual design, of the celestial sensor logic.

The conceptual design parameters are the starmapper parameters required for optimum performance in the day portion of the orbit-operation, field of view, mapper baffle dimensions, baffle cone angle, and cant angle of mapper. The optimum set of parameters is based on the minimum baffle volume for viewing one or two stars per scan.

The optical transfer function task consisted of the investigation of the optical performance characteristics for the starmapper and sun sensor. Two basic designs were investigated a concentric catadioptic system and an all-refractive system. An error analysis was performed to demonstrate the celestial sensor's target line-of-sight detection accuracy.

The conceptual design of the celestial sensor logic provided a tradeoff of two methods of selecting sensor output (star and sun transits selection from noise) for on-board storage. The logic was required to select celestial transit for maximum target-to-noise storage with a 60, 000-bit limitations.

The ground based data processing tasks provided a celestial target identification algorithm and program to process the celestial sensor data to obtain the coordinates of the target. The coordinates of the targets must be determined for use in the subsequent Kalman filter attitude estimation process.

Conclusions and recommendations in each of the tasks identified are presented in the following paragraphs.

TORQUE MODEL

The torque modeling development and analysis have shown that long-term prediction without star update requires that

- The residual magnetic moment, eddy current, gravity gradient, and solar pressure torques be included in the prediction model
- Each of the five torques affects the spacecraft attitude in an additive manner for the level of torque experience by the ARRS spacecraft
- For short-term prediction of 100 to 200 sec only the inclusion of eddy current and residual magnetic moment torque effects is needed for the 10 arc-rec attitude accuracy requirement. Inclusion of at least the eddy current and residual magnetic moment torques in the algorithm is recommended, and the celestial sensor data simulation must include the five torques developed in this study.

SPACECRAFT MODELING

The spacecraft modeling developed a set of "simplified equations of motion", and analysis showed that the speed of the data reduction can be improved by using these equations in the algorithm without significant detriment to the accurate propogation of the spacecraft attitude. This increase speed is realized by the increased step size allowable for accurate attitude propogation. The "simplified equations of motion" were developed in terms of state variables that are slowly varying functions of time. Some of the variables are constant, others are ramps. This allows the use of simple integration algorithms to propogate from some time point to the next desired point without intermediate integration step sizes.

In the parallel effort on the attitude determination algorithm development, the execution time, using the dynamics model of Reference 19, was demonstrated to be 10 to 20 times faster than real time on the CDC 6600 computer. This is considered reasonable for processing a full year of data collection. This spacecraft model does not create an execution time handicaps as originally contended. However, speed of execution can be improved by using the

"Simplified Equation's of Motions", because many intermediate integration step can be eliminated, rather than the model used in Reference 19.

OPERATIONAL ALGORITHM

The attitude determination data-reduction program was developed and exercised. The data-reduction program executed 10 to 20 times faster than real time on the CDC 6600 computer using a step size of 0.5 sec, thus establishing the program as acceptable in terms of execution time. Further improvement can be obtained by the use of the "Simplified Equations of Motion".

The performance analysis demonstrated that

- Estimation of spacecraft attitude within 5 to 10 arc-sec is achieved using three celestial targets for initial convergence and two celestial targets to maintain convergence where only the magnetic torques are included in the algorithm model and five torques for the generation of the transit data.
- Performance of the attitude estimation is better when the quality of the sensor is underestimated; i.e., it is safer to assume that the instrument is more noisey than it actually is. In the event of a gradual degradation of sensor quality, the assumed process noise in the filter must be changed to improve attitude estimates.
- Estimation of the inertia ratios and eddy current coefficient is achievable for the levels of torque experienced by the vehicle. However, the residual magnetic moment components were not observable. The estimate of these moments did not agree with the actual values used.
- Estimation of spacecraft attitude is best when the celestial targets are regularly spaced in time.
- Using the optimum 110° cant angle and 20° for determined from the sensor conceptual design analysis, performance analysis of estimation of attitude versus cant angle shows that the accuracy of estimation is traded among the three Euler angle states. At cant angle of 90° the pitch attitude is better estimated than the roll and yaw, and at 130° each is equally estimated.
- Performance of attitude estimation does not change for spacecraft spin rates from 1 to 9 rpm.
- Performance for long-term estimation (at least 2000 sec) requires the use of additive noise to the state covariance propogation matrix. These values must be determined by trial and error for best performance. Once established, variation up to 4 orders of magnitude are permissible.

In conclusion, the mechanized Kalman filter gives attitude estimates within 10 are-sec for the five-torque spacecraft environment using an estimate of only three parameters, two inertia ratios, and the eddy current coefficient for a period of at least 2000 sec. This performance is achieveable by initially using three celestial targets to converge to 10 arc-sec accuracy and continuing with the use of two celestrial targets to maintain the performance.

Additional work is recommended in the following areas:

- Sensor offset angles should be added to the estimation state vector and simulation experiments undertaken to determine the observability of these parameters.
- The presence of the arbitrary noise matrix Q in the estimation equations (59) is the least satisfactory aspect of the system. Consequently, an analytic effort should be undertaken to develop methods of determining Q from previously obtained measurement errors.
- Further simulation effort is required to obtain the estimation accuracies possible using transits from a single celestial body and to evaluate the degradation in the estimation due to relatively long periods of time without data.

STARMAPPER PARAMETERS

A second major consideration which relates to the magnitudes of daylight detected stars is the physical dimensioning of the light baffle. Parameter studies were predicated on a minimum baffle volume criterion. A computer-automated program was subsequently designed to select an optimum set of starmapper parameters. These are listed below:

OPTIMIZED STARMAPPER PARAMETERS

Baffle diameter	10 in.
Baffle height	14 in.
Fov	15°
Cant angle	100° (from positive--spin axis)
Closest approach to bright object	36°
Limiting nighttime magnitude	3.2 (visual)
Limiting daytime magnitude	3.4 (visual)
Clear aperture	2.2 in.

Use of the starmapper over less than 100 percent of the daytime orbit permits detection of brighter stars. For the set of parameters listed in Table 8, the daytime limiting magnitude for two stars per scan becomes 2.9 for usage over 80 percent of the orbit and 2.2 for 50 percent of the orbit. The clear aperture indicated can be realized with the baseline aperture diameter of 3.18 inches and a central obscuration of 2.3 inches. The 15° fov is reduced over the 20° field considered as baseline. This will permit a physically smaller sensor package.

OPTICAL TRANSFER FUNCTION

The concentric catadioptric optical system was selected for the ARRS application over a candidate refractive system principally because the optical system provides superior image quality (blur spot symmetry) for all filled angles. The availability of the EMR 531N miniature photomultiplier tube made packaging of the detector on the optical axis practical. The concentric system is less complex, has fewer elements, has no cemented interfaces, is physically smaller, and in every other aspect is superior to the refractive optical system.

Light-gathering properties of the concentric system are superior to those of the refractive system. This is evident from the fact that an AO star of magnitude 0.0, detected by the concentric system, is an equivalent magnitude of 1.6 for the refractive system, on axis. In addition, loss of sensitivity, equivalent to 0.7 magnitude, results for 10° off-axis conditions.

The ARRS optical system produces star images for all field angles having blur spot diameters of 12 arc sec at the design wavelength of 0.405 micron. Between the wavelengths of 0.32 and 0.45 micron, 100% of the star energy is contained within a 60-arc-sec spot diameter. In addition, the spot configuration is extremely symmetrical and, therefore, contributes negligibly to the overall star transit time error.

The optical system was evaluated for performance at low operating temperature (-75°C) and in vacuum. The change in blur spot diameter due to both effects is less than 5 arc sec and is, therefore, considered no cause for concern.

The concentric optical system is ideally suited for the sun-sensor application. Two requirements - the wide fov (40°) and accuracy (10 arc sec) - are difficult requirements for conventional sun sensors to meet. The ARRS sun sensor optical system requirements are met using a two-element optical system, having a 1.37-inch aperture size using two V-shaped deposited silicon "slit" detectors, each 60 arc sec projected width. Use of narrow-band filters and antireflection coatings deposited on the optical elements is utilized to attenuate the incoming solar energy to the level required by the detector.

CATHODE PROTECTION

Inadvertent scanning of the sun by the optical system will result in a temperature rise of the cathode. However, the rise will not reach a level sufficient to induce degrading or damaging effects to the cathode material. A wide factor of safety exists, due a large degree to the improved semitransparent bi-alkali (N) cathode used, which permits a maximum ambient cathode temperature of 150°C.

Operation of the photomultiplier during an inadvertent scan of the sun or a scanning of the illuminated earth will cause excessive current flow from the detector beyond the maximum operational limits. To avoid this condition, the voltage between the cathode and second dynode will be switched in polarity (grounding the dynode), which reverses the normal acceleration of electrons from the cathode. This method has the advantage that relatively low voltage is switched.

Switching of the photomultiplier voltage does not protect the cathode from bright source exposure. However, the resultant agitation within the cathode material for the ARRS application will not increase the dark current to a level which might cause detection difficulties. The rise in dark current resulting from an inoperative starmapper scan of the illuminated earth will permit detection of fourth magnitude stars immediately following the bright source portion of the scan. This condition precludes the necessity of a shutter mechanism which would have to be actuated on each scan.

The recommended cathode protection method will use a fail-open (fail-safe) mechanical shutter (to be actuated only in the event of prolonged focused solar radiation). In addition, the photomultiplier will be switched off whenever the radiation level exceeds a pre-set level such as that occurring when the bright earth or moon is scanned by the starmapper fov.

ERROR ANALYSIS

The ability to interpolate the threshold crossing of a pulse can be accomplished to within 1 part in 13 for pulse rise and 1 part in 18 for pulse fall. The resultent 1 sigma error in determining pulse center (transit time) is, therefore, 3.2 arc sec. The encoding error is assumed to be 1 arc sec. No blur spot asymmetry is contributed. The total rms error expected is about 3.5 arc sec.

GROUND-BASED DATA PROCESSING

Star identification for the ARRS application will be performed as initial identification and update identification. The initial identification program makes use of triplets of pulses resulting from a star crossing of the three-slit pattern. The entire program was tested using a tape of simulated ARRS transits. The transits were displaced in time according to a Gaussian distribution of half width equal to 10 arc sec. In addition, triplets were randomly eliminated in inverse proportion to the brightness of the stars. Finally, triplets of noises were randomly introduced into the data. The results of the simulation indicated that less than 9% of the total transits read-in were incorrectly identified and 40% of the transits read-in were not identified; no stars were incorrectly identified.

CELESTIAL SENSOR LOGIC

The triplet selection criterion in conjunction with CPU (small, on-board computer) appears to represent not only the potimum approach to on-board data processing but perhaps the only practical method. It is apparent that the triplet selection criterion, due to its smaller window, will transmit fewer noise pulses to storage by a factor of 10. Use of CPU on-board makes possible the processing of at least six sequential transits before deciding on the ligitimacy of a pulse. This would be prohibitively complex in practice if hard-wired logic were used.

RECOMMENDATIONS

Selection of the starmapper parameters was based, to a large extent, on star-availability searches using PM tube response and visual magnitudes. The sensor peak spectral response if 0.405 micron (design wavelength of the optical system). The availability of stellar targets must, therefore, be related to the instrument response characteristics. This can be done by adjusting the visual magnitudes to instrument magnitudes and then conducting further star availability researches. It is recommended that this be done to assure that sufficient bright stars are available in color magnitudes responsive to the instrument characteristics.

It is required, to detect a fourth magnitude star on the daylight side of the orbit, that the sun's radiation be attenuated by a factor 10^{13} to assure a 10:1 signal-to-noise ratio. The ARRS baffle configuration was derived by assuming perfectly specular reflectances of 99.9 percent of the incident rays, and complete absorption by baffle interior surfaces of diffuse radiation. It is recommended that both specular and absorptive surfaces be fabricated and tested to establish the extent of the validity of these assumptions.

APPENDIX A

DEVELOPMENT OF A TORQUE MODEL DUE TO INDUCED EDDY CURRENTS IN A SPINNING HAT CONFIGURATION SPACECRAFT

APPENDIX A

DEVELOPMENT OF A TORQUE MODEL DUE TO INDUCED EDDY CURRENTS IN A SPINNING HAT CONFIGURATION SPACECRAFT

This appendix presents the derivation of a torque due to induced eddy currents in a "spinning hat" configuration spacecraft.

J. P. Vinti (ref. 2) solved the torque for a conducting sphere. In his paper he stated the general problem and continued by making several assumptions such that the electrodynamical and mechanical problem could be solved separately.

In addition to Vinti's paper, G. Louis Smith (ref. 1) conducted a study of torques due to eddy currents on spinning cylinders, thin-wall cones, cone frustums, and general bodies of revolution.

The torque on a sphere is represented quite simply as demonstrated by Vinti; however, for other geometries the solution becomes more complex because boundary conditions are not easily satisfied. Smith's paper demonstrates the complexity in solving for torque in bodies whose geometries are not a sphere.

The derivation of the torque for the spinning hat configuration will exhibit complexity not encountered in the spherical spacecraft. The complexity is not too great that it cannot be overcome. The result of the derivation will be a vector torque equation in body axes as a function of the body rate, earth's magnetic field, and material conductivity.

STATEMENT OF PROBLEM

Eddy currents are generated in a conducting media as it moves through an external magnetic field. The generated current then interacts with the magnetic field to retard the motion of the moving media. For body motion about its center of mass, the retarding effect is called a torque. For a spinning body in an earth orbit, the media motion relative to the spacecraft's center of mass and the media motion of the center of mass in orbit generate currents. Also, due to the nonuniformity of the magnetic field around the earth, currents are generated in the spacecraft. The currents due to the nonuniformity of the field and center of mass motion will be neglected for the present problem.

A rigorous and exact solution for the retarding effect requires the following approach:

1) Set up electrodynamical equations for a moving body and solve them with the proper boundary conditions.

2) Using the distribution of the currents and magnetic field, find the force exerted on each element of volume and the moments of that force relative to the center of mass.

3) Integrate over the volume of the spacecraft for the total torque for a given mechanical configuration. Vinti specified the mechanical configuration by a given velocity and acceleration of the center of mass, the angular velocity vector, the rate of change of the angular velocity vector, and the principal moments of inertia.

4) Solve the electrodynamical and mechanical problem simultaneously.

Deviation to this approach will be used under the assumptions that the effect of the rate of change of the angular velocity and center of mass acceleration is negligible. One is then allowed to separate the electrodynamic and mechanical problems. Vinti discusses the separation of the two problems. The torque is then based on the instantaneous angular velocity of the spacecraft and can be applied to the mechanical dynamics to obtain the following of the spacecraft motion.

ARRS SPACECRAFT DESCRIPTION

The geometry and body coordinate frame for the derivation of the torque is shown in Figure A1.

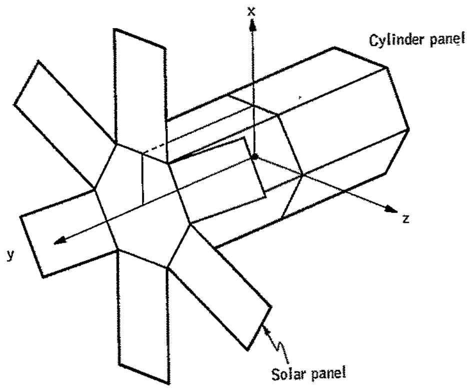

Figure A1. ARRS Spacecraft Geometry and Body Coordinate Frame Definition

ASSUMPTIONS ON SPACECRAFT MEDIA

Each solar panel and cylinder panel is assumed to be electrically isolated with a static electrical conductivity. The panels are assumed to be thin flat plates whose surface normals are aligned to the body coordinate frame. The conductivity external to spacecraft media is zero. The dielectric and permeability of the spacecraft media are 1.

TORQUE ON ELEMENT VOLUME OF MEDIA

The torque is given by (in gaussian units)

$$d\vec{T} = c^{-1} \vec{r} \times (\vec{J} \times \vec{H}) \, dV \tag{A1}$$

where

$\vec{r}$ = Vector from spacecraft center of mass to element of volume

$\vec{J}$ = Current density

$\vec{H}$ = Earth's magnetic field intensity

Current density, $\vec{J}$, must be determined before total torque can be computed.

EDDY CURRENT DENSITY

The eddy current density is solved for an instantaneous mechanical configuration. Then, Maxwell's equation becomes

$$\begin{aligned} \nabla \times \vec{H} &= 4\pi c^{-1} \vec{J} \\ \nabla \times \vec{E} &= 0 \\ \nabla \cdot \vec{B} &= \nabla \cdot \vec{H} = 0 \\ \nabla \cdot \vec{E} &= 0 \end{aligned} \tag{A2}$$

where

$\vec{H}$ = Magnetic field intensity

$\vec{E}$ = Electric field

and the electric field and current density respectively are

$$\vec{E} = \nabla\psi + c^{-1}(\vec{\omega} \times \vec{r}) \times \vec{H} \qquad \text{(A3)}$$

$$\vec{J} = \sigma\vec{E}$$

where

σ = Static conductivity

c = Speed of light in vacuum

ψ = Potential function that satisfies $\nabla^2\psi = 0$ and the boundary conditions.

Then using Equations (A1) and (A3), the eddy current (ref. 18), in general, is

$$\vec{J} = \frac{1}{2}\sigma c^{-1}(\vec{\omega} \times \vec{H}) \times \vec{r} + \nabla\phi \qquad \text{(A4)}$$

The eddy current density is completely specified by Equation (A4) upon solution for ϕ.

METHOD OF SOLUTION FOR ϕ

The potential, ϕ, must satisfy the boundary condition

$$\nabla\phi = -\frac{1}{2}\sigma c^{-1}(\vec{\omega} \times \vec{H}) \times \vec{r} \qquad \text{(A5)}$$

when evaluated on the boundary and LaPlace's question,

$$\nabla^2\phi = 0$$

The problem is a Neumann boundary value problem. In general, Neumann boundary value problems cannot be solved in closed form. However, reduction of Neumann boundary value problems to Dirichlet boundary value problems (ref. 1) can be made for two-dimensional problems by using Cauchy-Riemann conditions and integrating the gradient along the boundary. Also, the integral

$$\oint \nabla \phi \, ds = 0 \tag{A6}$$

at the boundary must be satisfied.

The constraint of Equation (A6) is satisfied for the present problem.

TOTAL TORQUE EQUATION

Substituting Equation (A4) into Equation (A1) and integrating over the volume

$$\vec{T} = c^{-1} \int\int\int \vec{r} \times \{[\nabla \phi + \frac{1}{2} \sigma c^{-1} (\vec{\omega} \times \vec{H}) \times \vec{r}] \times \vec{H} \} \, dV \tag{A7}$$

The torque separates into

$$\vec{T} = T_1 + T_2 = c^{-1} \int\int\int \vec{r} \times (\nabla\phi \times \vec{H}) \, dV$$
$$+ \frac{1}{2} \sigma c^{-2} \int\int \vec{r} \times \{[(\vec{\omega} \times \vec{H}) + r] \times \vec{H} \} \, dV \tag{A8}$$

ORDER OF PRESENTATION OF MODEL DERIVATION

The model derivation is developed by computing the torque on two of the panels of the cylinder (Figure A2(. First, Torque $\vec{T}_1$ is computed by solving for ψ (stream function) in one panel, and for two panels the sum is taken. Torque $\vec{T}_2$ is computed similarly. The total torque is then computed by coordinate rotation for three pairs of panels to a common frame in the body.

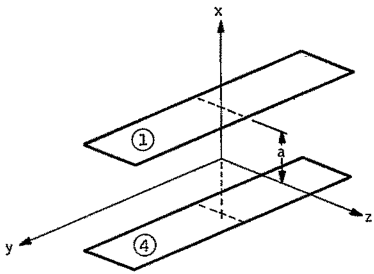

Figure A2. Relationship of the Two Cylinder Panels to the
x, y, z Frame

The total torque is computed by coordinate rotation to a common frame for all six polar panels.

DERIVATION OF TORQUE DUE TO ARRS SPACECRAFT CYLINDER

Torque due to the ARRS spacecraft cylinder is discussed under the following main headings:

- Solution of Neumann Boundary Value Problem for a Thin Rectangular Plate
- Derivation of $\vec{T}_1$ Torque for Two Cylinder Panels
- Derivation of $\vec{T}_2$ Torque for Two Cylinder Panels
- Torque Due to Cylinder

SOLUTION OF NEUMANN BOUNDARY VALUE PROBLEM FOR A THIN RECTANGULAR PLATE

The Neumann Problem

To compute the eddy current torque, current density first must be determined. From Vinti, current density is given by

$$\vec{J} = \frac{1}{2} \sigma c^{-1} (\vec{\omega} \times \vec{H}) \times \vec{r} + \nabla \phi \qquad \text{(A9)}$$

The geometry of the ARRS spacecraft is given in Figure A3.

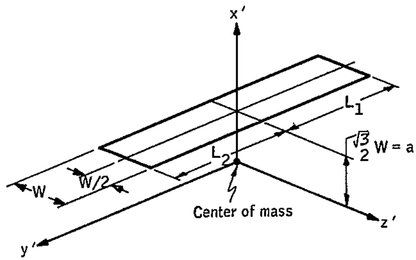

Figure A3. Relationship of ARRS Cylinder Panel to Spacecraft Center of Mass

From Equation (A2),

$\vec{r}$ = Vector to element volume of panel from center of mass

$\vec{\omega}$ = Spin vector

$\vec{H}$ = Earth's magnetic intensity

The general solution for $\vec{J}$ is given by Equation (A9). The solution for the current density in the panel of Figure A3 is completed by knowing the potential, ϕ, that satisfies $\nabla^2\phi = 0$ and the boundary conditions. The boundary conditions are

$$
\begin{aligned}
&J_y\,(y' = L_2,\ x' = a) = 0 \\
&J_y\,(y' = -L_1,\ x' = a) = 0 \\
&J_z\,(x' = a,\ z' = -\tfrac{W}{2}) = 0 \\
&J_z\,(x' = a,\ z' = \tfrac{W}{2}) = 0
\end{aligned}
\qquad \text{(A10)}
$$

The solution for ϕ is aided by translating the panel to a new frame as shown in Figure A4.

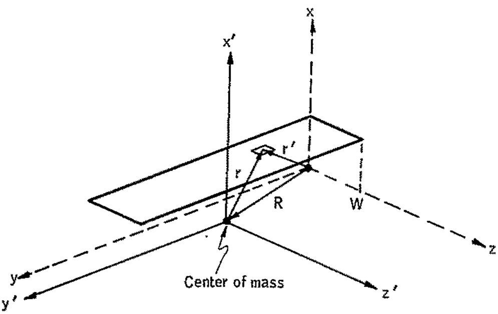

Figure A4. Translation of Plate to a New Coordinate Frame x, y, z

Expanding Equation (A9),we get

$$
\begin{aligned}
J_x &= \frac{1}{2}\sigma c^{-2}\,[(\omega_z H_x - \omega_x H_z)\, z' - (\omega_x H_y - \omega_y H_x)\, y'] + \frac{\partial \phi}{\partial x} \\
J_y &= \frac{1}{2}\sigma c^{-2}\,[(\omega_x H_y - \omega_y H_x)\, x' - (\omega_y H_z - \omega_z H_y)] + \frac{\partial \phi}{\partial y} \qquad \text{(A11)} \\
J_z &= \frac{1}{2}\sigma c^{-2}\,[(\omega_y H_z - \omega_z H_y)\, y' - (\omega_z H_x - \omega_x H_z)\, x'] + \frac{\partial \phi}{\partial z}
\end{aligned}
$$

From Figure A4 we have

$$R + r = r'$$

and

$$R = 0\,\hat{i} + L\,\hat{j} + \frac{W}{2}\hat{R}$$

$$r' = a\,\hat{i} + y\hat{j} + z\hat{R} \tag{A12}$$

and

$$r = a\,\hat{i} + (y - L_1)\,\hat{j} + (z - \frac{W}{2})\,\hat{R}$$

Therefore, substituting Equation(A12)into Equation(A11) (Note: Because the plate is thin, J is automatically satisfied):

$$J_y = \frac{1}{2}\sigma c^{-2}\,[(\omega_x H_y - \omega_y H_x)a - (\omega_y H_z - \omega_z H_y)\,(z - \frac{W}{2})] + \frac{\partial\phi}{\partial y}$$

$$J_z = \frac{1}{2}\sigma c^{-2}\,[(\omega_y H_z - \omega_z H_y)(y - L_1) - (\omega_z H_x - \omega_x H_z)\,a] + \frac{\partial\phi}{\partial z} \tag{A13}$$

Using the boundary condition of Equation (A10) and Equation (A13), the value of the gradient along the boundary of the plate is specified; hence, a Neumann boundary value problem. For two-dimensional Neumann problems, the Cauchy-Riemann conditions may be applied to reduce to a Dirichlet problem (ref. 18). In applying this method, Cauchy-Riemann condition

$$\frac{\partial\phi}{\partial y} = \frac{\partial\psi}{\partial z}$$

and

$$\frac{\partial\phi}{\partial z} = -\frac{\partial\psi}{\partial y} \tag{A14}$$

are used.

Substituting into Equation (A13), and applying the boundary conditions, we get

$$
\begin{aligned}
J_y(y = 0,\ x = a) &= 0 = K_1 + K_2\left(z - \frac{W}{2}\right) + \frac{\partial\psi}{\partial z} \\
J_y(y = L, x = a) &= 0 = K_1 + K_2\left(z - \frac{W}{2}\right) + \frac{\partial\psi}{\partial z} \\
J_z(z = 0,\ x = a) &= 0 = K_3 - K_2(y - L_1) - \frac{\partial\psi}{\partial y} \\
J_z(z = W,\ x = a) &= 0 = K_3 - K_2(y - L_1) - \frac{\partial\psi}{\partial y}
\end{aligned}
\qquad (A15)
$$

Now, the potential on the boundary using Cauchy-Riemann conditions is given by

$$
\psi(y, z) - \psi(0, 0) = \int_{00}^{yz} \frac{\partial\psi}{\partial s}\, ds \qquad (A16)
$$

Figure A5 shows the panel in its new orientation

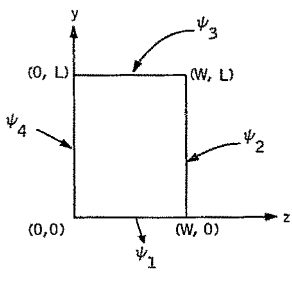

Figure A5. Panel Orientation to y-z Frame

The potential ψ_1 is given by

$$\psi_1 = \int_{00}^{z0} \frac{\partial \psi}{\partial z}(y = 0) \quad dz = -\left[\left(K_1 - \frac{K_2 W}{2}\right) z + \frac{K_2 z^2}{2}\right]$$

The potential ψ_2 is given by

$$\psi_2 = \int_{00}^{W0} \frac{\partial \psi}{\partial z}(y = 0) \quad dz + \int_{W0}^{Wy} \frac{\partial \psi}{\partial y}(z = W) \quad dy$$

$$= -K_1 W + (K_3 + K_2 L_1)\, y - \frac{K_2 y^2}{2}$$

The potential ψ_3 is given by

$$\psi_3 = \int_{00}^{W0} \frac{\partial \psi}{\partial z}(y = 0)\, dz + \int_{W0}^{WL} \frac{\partial \psi}{\partial y}(z = W)\, dy + \int_{WL}^{zL} \frac{\partial \psi}{\partial z}(y = L)\, dz$$

$$= \left(K_3 L + K_2 L_1 L - \frac{K_2 L^2}{2}\right) + \left(\frac{K_2 W}{2} - K_1\right) z - \frac{K_2 z^2}{2}$$

The potential ψ_4 is given by

$$\psi_4 = \psi_3 (z = W) + \int_{0L}^{0y} \frac{\partial \psi}{\partial y}(z = 0)\, dz$$

$$= (K_3 + K_2 L_1) y - \frac{K_2 y^2}{2}$$

where

$$K_1 = \frac{1}{2} \sigma c^{-1} (\omega_x H_y - \omega_y H_x)\, a$$

$$K_2 = -\frac{1}{2} \sigma c^{-1} (\omega_y H_z - \omega_z H_y)$$

$$K_3 = -\frac{1}{2} \sigma c^{-1} (\omega_y H_z - \omega_z H_y)\, a$$

Summarizing the ψ_1, ψ_2, ψ_3, and ψ_4 to give

$$\begin{aligned}
\psi_1 &= f_1 z + f_2 z^2 \\
\psi_2 &= b_1 + f_3 y + f_2 y^2 \\
\psi_3 &= b_2 + f_1 z + f_2 z^2 \\
\psi_4 &= f_3 y + f_2 y^2
\end{aligned} \tag{A17}$$

where

$$f_1 = -\left(K_1 - \frac{K_2 W}{2}\right)$$

$$f_2 = -\frac{K_2}{2}$$

$$f_3 = (K_3 + K_2 L_1)$$

$$b_1 = -K_1 W$$

$$b_2 = \left(K_3 L + K_2 L_1 L - \frac{K_2 L^2}{2}\right)$$

Solution for ψ

We now have a Dirichlet problem and can use the superposition theorem to separate the problem into four boundary value problems as shown in Figure A6.

Solution for ψ_1

For $\nabla^2\psi = 0$, the general solution for ψ_1 is

$$\psi_1 = (A \cos \mu_1 z + B \sin \mu_1 z)(C \sinh \mu_1 y + D \cosh \mu_1 y) \tag{A18}$$

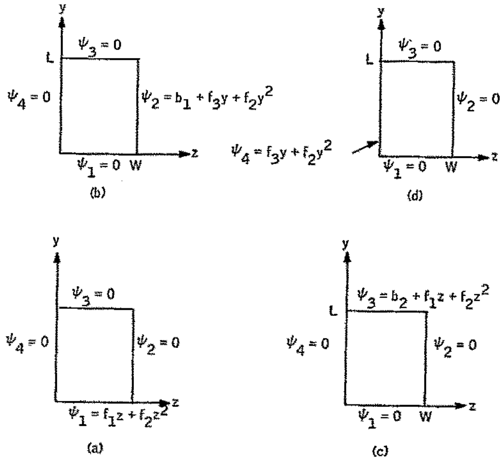

Figure A6. Four Boundary Value Problems

Using boundary conditions of Figure A6(a), the solution for ψ_1 is:

(1) $\psi_1(z=0,\ x=a) = 0 = A \cos \mu_1 z + D \cosh \mu_1 y)$ which implies $A = 0$

(2) $\psi_1(z=W) = 0 = B \sin \mu_1 W\ (C \sinh \mu_1 y + D \cosh \mu_1 y)$ which implies

$$\mu_1 = \frac{n\pi}{W}$$

(3) $\psi_1(y=L) = 0 = B \sin \mu_1 z\ (C \sinh \mu_1 L + D \cosh \mu_1 L)$ which implies

$$D = -C \tanh \mu_1 L$$

These three conditions give

$$\psi_1 = BC \sin \mu_1 z \, (\sinh \mu_1 y - \tanh \mu_1 L \cosh \mu_1 y)$$

$$= BC \sin \mu_1 z \; \frac{\sinh \mu_1 y \cosh \mu_1 L - \sinh \mu_1 L \cosh \mu_1 y}{\cosh \mu_1 L}$$

$$= BC \sin \mu_1 z \frac{\sinh \mu_1 (y-L)}{\cosh \mu_1 L}$$

and

$$(4) \quad \psi_1(y=0) = f_1 z + f_2 z^2 = -BC \tanh \mu_1 L \sin \mu_1 z$$

Now, $f_1 z + f_2 z^2$ is expanded in a $\sin \mu_1 z$ series.

$$f(z) = f_1 z + f_2 z^2 = \sum b_n \sin \mu_1 z$$

where

$$b_n = \frac{2}{W} \int_0^W (f_1 z + f_2 z^2) \sin \mu_1 z \, dz$$

$$= \frac{2f_1}{W} \int_0^W z \sin \mu_1 z \, dz + \frac{2f_2}{W} \int_0^W z^2 \sin \mu_1 z \, dz$$

$$= \frac{2f_1}{W} \left[- \frac{W^2}{n\pi} (-1)^n \right] + \frac{2f_2}{W} \left\{ - \frac{W^3}{n\pi} (-1)^n + \frac{2W^3}{(n\pi)^3} [(-1)^n - 1] \right\}$$

$$= - \frac{2f_1 W}{n\pi} (-1)^n - \frac{2f_2 W^2 (-1)^n}{n\pi} + \frac{4f_2 W^2}{(n\pi)^3} [(-1)^n - 1]$$

Therefore,

$$-BC \tanh \mu_1 L = b_n \qquad \text{(A19)}$$

Then

$$BC = -\frac{b_n}{\tanh \mu_1 L}$$

$$= \frac{-\left\{ \frac{-2f_1 W}{n\pi}(-1)^n - \frac{2f_2 W^2(-1)^n}{n\pi} + \frac{4f_2 W^2}{(n\pi)^3}\left[(-1)^n - 1\right] \right\}}{\tanh \mu_1 L}$$

Then

$$\psi_1 = -\left\{ -\frac{2(-1)^n}{n\pi}(f_1 W + f_2 W^2) + \frac{4f_2 W^2}{(n\pi)^3}\left[(-1)^n - 1\right] \right\} \frac{\sinh \mu_1 (y-L)}{\sinh \mu_1 L} \sin \mu_1 z$$

and

$$\psi_1 = \sum B_n \sin \frac{n\pi}{W} z \sinh \frac{n\pi}{W}(y-L)$$

where

$$B_n = -\left\{ -\frac{2(-1)^n}{n\pi}(f_1 W + f_2 W^2) + \frac{4f_2 W^3}{(n\pi)^3}\left[(-1)^n - 1\right] \right\} \frac{1}{\sinh \mu_1 L}$$

<u>Solution for ψ_2</u>

With boundary conditions given in Figure A6(b), the general solution for ψ_2 is:

$$\psi_2 = (A \sin \mu_2 y + B \cos \mu_2 y)(C \sinh \mu_2 z + D \cosh \mu_2 z) \qquad \text{(A20)}$$

where

(1) $\psi_2(y = 0) = 0 \Rightarrow B = 0$

(2) $\psi_2(y, z = 0) = 0 \Rightarrow D = 0$

(3) $\psi_2(y = L, z) = 0 \Rightarrow \mu_2 = \frac{n\pi}{L}$

Now,

$$\psi_2 = AC \sin \frac{n\pi y}{L} \sinh \frac{n\pi}{L} z \tag{A21}$$

and

(4) $\psi_2(y_1 z = W) = b_1 + f_3 y + f_2 y^2$

$$= AC \sin \frac{n\pi y}{L} \sinh \frac{n\pi W}{L}$$

Now, expanding $b_1 + f_3 y + f_2 y^2$ in a $\sin \frac{n\pi y}{L}$ series

$$b_1 + f_3 y + f_2 y^2 = \Sigma b_n \sin \frac{n\pi y}{L}$$

where

$$b_n = \frac{2}{L} \int_0^L (b_1 + f_3 y + f_2 y^2) \sin \frac{n\pi y}{L} \, dy \tag{A22}$$

$$= \frac{2b_1}{L} \int_0^L \sin \frac{n\pi}{L} y \, dy + \frac{2f_3}{L} \int_0^L y \sin \frac{n\pi y}{L} \, dy + \frac{2f_2}{L} \int_0^L y^2 \sin \frac{n\pi y}{L} \, dy$$

$$= \frac{2b_1}{L} \left\{ \frac{L}{n\pi} \left[1-(-1)^n\right] \right\} + \frac{2f_3}{L} \left[-\frac{L^2}{n\pi}(-1)^n \right] + \frac{2f_2}{L} \left\{ -\frac{L^3}{n\pi}(-1)^n + \frac{2L^3}{(n\pi)^3}\left[(-1)^n - 1\right] \right\}$$

$$= \frac{2b_1}{n\pi} - \frac{2b_1(-1)^n}{n\pi} - \frac{2f_3 L}{n\pi}(-1)^n - \frac{2f_2 L^2}{n\pi}(-1)^n + \frac{4f_2 L^2}{(n\pi)^3}\left[(-1)^n - 1\right]$$

$$= \frac{2b_1}{n\pi} - \frac{2(-1)^n}{n\pi}\left(b_1 + f_3 L + f_3 L^2\right) + \frac{4f_3 L^2}{(n\pi)^3}\left[(-1)^n - 1\right]$$

Therefore,

$$AC \sinh \frac{n\pi W}{L} = b_n \tag{A23}$$

and

$$AC = \left\{- \frac{2(-1)^n}{n\pi} (b_1 + f_3 L + f_2 L^2) + \frac{2b_1}{n\pi} + \frac{4f_2 L^2}{(n\pi)^3} [(-1)^n - 1]\right\} \sinh \frac{1}{\left(\frac{n\pi W}{L}\right)}$$

and

$$\psi_2 = \sum (AC)_n \sin \frac{n\pi y}{L} \sinh \frac{n\pi}{L} z \tag{A24}$$

Solution for ψ_3

Figure A6(c) gives the boundary conditions for ψ_3 solution:

$$\psi_3 = (A \sin \mu z + B \cos \mu z)(C \sinh \mu y + D \cosh \mu y) \tag{A25}$$

where

(1) $\psi_3 (y = 0) = 0 \Rightarrow D = 0$

(2) $\psi_3 (z = 0) = 0 \Rightarrow B = 0$

(3) $\psi_3 (z = \omega) = 0 \Rightarrow \mu_z = \frac{n\pi}{W}$

These conditions reduce Equation (A18) to

$$\psi_3 = AC \sin \frac{n\pi}{W} z \sinh \frac{n\pi}{W} y \tag{A26}$$

and

$$(4)\quad \psi_3\,(y = L) = b_2 + f_1 z + f_2 z^2$$

$$= AC \sin \frac{n\pi}{W} z \sinh \frac{n\pi L}{W}$$

Expanding $b_2 + f_1 z + f_2 z^2$ in $\sin \frac{n\pi}{W} z$ series to give

$$b_2 + f_1 z + f_2 z^2 = \sum b_n \sin \frac{n\pi}{W} z$$

where

$$b_n = \frac{2}{W} \int_0^W (b_2 + f_1 z + f_2 z^2) \sin \frac{n\pi}{W} z \, d_z \tag{A27}$$

then

$$b_n = \frac{2b_2}{W} \int_0^W \sin \frac{n\pi}{W} z \, d_z + \frac{2f_1}{W} \int_0^W z \sin \frac{n\pi}{W} z \, d_z + \frac{2f_2}{W} \int_0^W z^2 \sin \frac{n\pi}{W} z \, dz$$

$$= \frac{2b_2}{W} \left\{ \frac{W}{n\pi} \left[1 - (-1)^n\right] \right\} + \frac{2f_1}{W} \left[- \frac{W^2}{n\pi} (-1)^n \right] + \frac{2f_2}{W} \left\{ - \frac{W^3}{n\pi} (-1)^n + \frac{2W^3}{(n\pi)^3} \left[(-1)^n - 1\right] \right\}$$

$$= \frac{2b_2}{n\pi} - \frac{2b_2(-1)^n}{n\pi} - \frac{2f_1 W(-1)^n}{n\pi} - \frac{2f_2 W^2 (-1)^n}{n\pi} + \frac{4f_2 W^2}{(n\pi)^3} \left[(-1)^n - 1\right]$$

$$= \frac{2b_2}{n\pi} - \frac{2(-1)^n}{n\pi} (b_2 + f_1 W + f_2 W^2) + \frac{4f_2 W^2}{(n\pi)^3} \left[(-1)^n - 1\right]$$

Therefore, by Equation (A26)

$$AC \sinh \frac{n\pi L}{W} = b_n$$

and

$$AC = \left\{ - \frac{2(-1)^n}{n\pi} [\psi_3(L)] + \frac{2b_2}{n\pi} + \frac{4f_2 W^2}{(n\pi)^3} \quad [(-1)^n - 1] \right\} \frac{1}{\sinh \frac{n\pi L}{W}} \qquad \text{(A28)}$$

and

$$\psi_3 = \sum AC \sin \frac{n\pi}{W} z \sinh \frac{n\pi}{W} y$$

<u>Solution for ψ_4</u>

Figure A6(d) gives the boundary conditions for ψ_4. Using the three conditions $\psi_1 (y = 0) = \psi_1(y = L) = \psi_1 (z = W) = 0$, the ψ_4 solution reduces to

$$\psi_4 = AC \sin \frac{n\pi}{L} y \sinh \frac{n\pi}{L} (z - W) \qquad \text{(A29)}$$

The fourth condition is

$$\psi_4 (z = 0) = f_3 y + f_2 y^2 = -AC \sinh \frac{n\pi W}{L} \sin \frac{n\pi}{L} y$$

Expanding $f_3 y + f_2 y^2$ in a $\sin \frac{n\pi}{L} y$ series gives

$$f_3 y + f_2 y^2 = \sum b_n \sin \frac{n\pi}{L} y$$

where

$$b_n = \frac{2}{L} \int_0^L (f_3 y + f_2 y^2) \sin \frac{n\pi}{L} y \, dy$$

$$= \frac{2f_3}{L} \int_0^L y \sin \frac{n\pi}{L} y \, dy + \frac{2f_2}{L} \int_0^L y^2 \frac{n\pi}{L} y \, dy$$

$$= \frac{2f_3}{L}\left[-\frac{L^2}{n\pi}(-1)^n\right] + \frac{2f_2}{L} \; - \left\{\frac{L^3}{n\pi}(-1)^n + \frac{2L^3}{(n\pi)^3} \quad [(-1)^n]-1\right\}$$

$$= -\frac{2f_3L(-1)^n}{n\pi} - \frac{2f_2L^2(-1)^n}{n\pi} + \frac{4L^2f_2}{(n\pi)^3}[(-1)^n-1]$$

and

$$-AC \sinh \frac{n\pi W}{L} = \left\{-\frac{2(-1)^n}{n\pi}(f_3L + f_2L^2) + \frac{4L^3}{(n\pi)^3} \quad [(-1)^n-1]\right\}$$

where

$$AC = -\left\{-\frac{2(-1)^n}{n\pi}(f_3L + f_2L^2) + \frac{4L^2f_2}{(n\pi)^3}[(-1)^n-1]\right\}\frac{1}{\sinh \frac{n\pi W}{L}}$$

and

$$\psi_4 = \sum AC \sin \frac{n\pi}{L} y \sinh \frac{n\pi}{L}(z-W)$$

<u>Summary of Solution for ψ</u>

$$\psi_T = \psi_1 + \psi_2 + \psi_3 + \psi_4$$

where

$$\begin{aligned}\psi_T = &\sum_{n=1}^{\infty} A_{n1} \sin \frac{n\pi}{W} z \sinh \frac{n\pi}{W}(y-L) \\ &+ \sum_{n=1}^{\infty} A_{n2} \sin \frac{n\pi}{L} y \sinh \frac{n\pi}{L} z \\ &+ \sum_{n=1}^{\infty} A_{n3} \sin \frac{n\pi}{W} z \sinh \frac{n\pi}{W} y \\ &+ \sum_{n=1}^{\infty} A_{n4} \sin \frac{n\pi}{L} y \sinh \frac{n\pi}{L}(z-W)\end{aligned} \tag{A30}$$

and

$$A_{n1} = -\left\{-\frac{2(-1)^n}{n\pi}\ \psi_1(W) + \frac{4f_2W^2}{(n\pi)^3}\left[(-1)^n-1\right]\right\}\ \frac{1}{\sinh \frac{n\pi}{W} L}$$

$$A_{n2} = \left\{-\frac{2(-1)^n}{n\pi}\ \psi_2(L) + \frac{2b_1}{n\pi} + \frac{4f_2L^2}{(n\pi)^3}\ \left[(-1)^n-1\right]\right\}\frac{1}{\sinh \frac{n\pi W}{L}} \tag{A31}$$

$$A_{n3} = \left\{-\frac{2(-1)^n}{n\pi}\ \psi_3(W) + \frac{2b_2}{n\pi} + \frac{4f_2W^2}{(n\pi)^3}\left[(-1)^n-1\right]\right\}\frac{1}{\sinh \frac{n\pi L}{W}}$$

$$A_{n4} = -\left\{-\frac{2(-1)^n}{n\pi}\ \psi_4(L) + \frac{4L^2f_2}{(n\pi)^3}\left[(-1)^n-1\right]\right\}\ \frac{1}{\sinh \frac{n\pi W}{L}}$$

DERIVATION OF $\vec{T}_1$ TORQUE FOR TWO CYLINDER PANELS

$$\vec{T}_1 = c^{-1} \int\int\int \vec{r} \times \{\nabla\phi \times \vec{H}\}\, dV \tag{A32}$$

where

$$dV = \tau\, dy\, dz$$

$$\vec{r} = a\,\hat{i} + (y-L_1)\,\hat{j} + (z - \tfrac{W}{2})\,\hat{k}$$

Expanding $\vec{T}_1$, we get

$$\begin{aligned}\vec{T}_1 = c^{-1}\int\int \Bigg\{ & \left[-(y-L_1)\, H_x\, \frac{\partial\phi}{\partial y} - (z - \frac{W}{2})\, H_x \frac{\partial\phi}{\partial z}\right]\hat{i} \\ & + \left[(z - \frac{W}{2})\left(H_z\ \frac{\partial\phi}{\partial y} - \frac{\partial\phi}{\partial z}\ H_y\right) + aH_x\ \frac{\partial\phi}{\partial y}\right]\hat{j} \\ & + \left[a\, H_x \frac{\partial\phi}{\partial z} - (y-L_1)\left(H_z\ \frac{\partial\phi}{\partial y} - \frac{\partial\phi}{\partial z}\ H_y\right)\right]\hat{k}\Bigg\}\ \tau\, dy\, dz\end{aligned}$$

Using the Cauchy-Riemann conditions

$$\frac{\partial \phi}{\partial y} = \frac{\partial \psi}{\partial z}$$

and

$$\frac{\partial \phi}{\partial z} = -\frac{\partial \psi}{\partial y}$$

then

$$\vec{T} = c^{-1} \iint \left\{ \left[-(y-L_1) H_x \frac{\partial \psi}{\partial z} + (z - \frac{W}{2}) H_x \frac{\partial \psi}{\partial y} \right] \hat{i} \right.$$

$$+ \left[(z - \frac{W}{2}) \left(H_z \frac{\partial \psi}{\partial z} + \frac{\partial \psi}{\partial y} H_y \right) + a H_x \frac{\partial \psi}{\partial z} \right] \hat{j} \qquad \text{(A33)}$$

$$\left. + \left[- a H_x \frac{\partial \psi}{\partial y} - (y-L_1) \left(H_z \frac{\partial \psi}{\partial z} + \frac{\partial \psi}{\partial y} H_y \right) \right] \hat{k} \right\} \tau \, dy \, dz$$

<u>Solution for x-Component of $\vec{T}_1$ Torque</u>

$$(\vec{T}_1)_x = c^{-1} \iint \left[-(y-L_1) H_x \frac{\partial \psi}{\partial z} + (z - \frac{W}{2}) H_x \frac{\partial \psi}{\partial y} \right] \tau \, dy \, dz \qquad \text{(A34)}$$

$$= -c^{-1} H_x \tau \iint y \frac{\partial \psi}{\partial z} dy \, dz + c^{-1} H_x \tau L_1 \iint \frac{\partial \psi}{\partial z} dy \, dz$$

$$+ c^{-1} H_x \tau \iint z \frac{\partial \psi}{\partial y} dy \, dz - \frac{c^{-1} H_x \tau W}{2} \iint \frac{\partial \psi}{\partial y} dy \, dz$$

And integrating over the panel, we get

$$(\vec{T}_1)_x = -c^{-1} H_x \tau \left[-\Sigma \frac{(A_{n2} + A_{n4}) (-1)^n L^2}{n\pi} \sinh \frac{n\pi W}{L} \right]$$

$$+ c^{-1} H_x \tau L_1 \left\{ \Sigma \frac{L}{n\pi} [1-(-1)^n] (A_{n2} + A_{n4}) \sinh \frac{n\pi W}{L} \right\}$$

$$+ \; c^{-1} H_x \tau \left[- \sum (A_{n1} + A_{n3}) \frac{W^2}{n\pi} (-1)^n \sinh \frac{n\pi L}{W} \right]$$

$$- \frac{c^{-1} H_x \tau W}{2} \left\{ \sum (A_{n1} + A_{n3}) \frac{W}{n\pi} [1-(-1)^n] \sinh \frac{n\pi L}{W} \right\}$$

Substituting in the A_{ni}'s and reducing, we get

$$(\vec{T}_1)_x = -c^{-1} H_x \tau \left\{ - \sum \frac{2b_1}{n\pi} [1-(-1)^n] \frac{(-1)^n L^2}{n\pi} \right\}$$

$$+ \; c^{-1} H_x \tau L_1 \left\{ \sum \frac{L}{n\pi} [1-(-1)^n] \quad \frac{2b_1}{n\pi} [1-(-1)^n] \right\}$$

$$+ \frac{c^{-1} H_x \tau}{2} \left\{ - \sum \frac{2b_2}{n\pi} [1-(-1)^n] \frac{W^2}{n\pi} (-1)^n \right\}$$

$$- \frac{c^{-1} H_x \tau W}{2} \left\{ \frac{2b_2}{n\pi} [1-(-1)^n] \frac{W}{n\pi} [1-(-1)^n] \right\}$$

For two panels

$$x = a, \; x = -a$$

it can be shown that

$$(\vec{T}_1)_x = 0 \qquad \text{(A35)}$$

<u>Solution for y-Component of $\vec{T}_1$ Torque</u>

$$(\vec{T}_1)_y = c^{-1} \iint \left\{ \left(z - \frac{W}{2}\right) \left| H_z \frac{\partial \psi}{\partial z} + \frac{\partial \psi}{\partial y} H_y \right| + a H_x \frac{\partial \psi}{\partial z} \right\} \tau \, dy \, dz \qquad \text{(A36)}$$

$$= c^{-1} \tau H_z \iint z \frac{\partial \psi}{\partial z} \, dy \, dz - \frac{c^{-1} \tau H_z W}{2} \iint \frac{\partial \psi}{\partial z} \, dy \, dz$$

$$+ c^{-1}\tau H_y \iint z \frac{\partial\psi}{\partial y}\, dy\, dz - \frac{c^{-1}\tau H_y W}{2} \iint \frac{\partial\psi}{\partial y}\, dy\, dz$$

$$+ c^{-1}\tau H_x a \iint \frac{\partial\psi}{\partial z}\, dy\, dz$$

Integrating, we get

$$\begin{aligned}
(\vec{T}_1)_y = {} & c^{-1}\tau H_z \Bigg\{ \Sigma \frac{WL}{n\pi} A_{n2} [1-(-1)^n] \sinh \frac{n\pi W}{L} \\
& + (A_{n1} - A_{n3}) \left(\frac{W}{n\pi}\right)^2 [1-(-1)^n] \left(\cosh \frac{n\pi L}{W} - 1\right) \\
& + (A_{n4} - A_{n2}) \left(\frac{L}{n\pi}\right)^2 [1-(-1)^n] \left(\cosh \frac{n\pi W}{L} - 1\right) \Bigg\} \\
& - \frac{c^{-1}\tau H_z W}{2} \left\{ \left(\frac{L}{n\pi}\right) [1-(-1)^n] (A_{n2} + A_{n4}) \sinh \frac{n\pi W}{L} \right\} \\
& \left.\begin{aligned}
& + c^{-1}\tau H_y \left\{ - (A_{n1} + A_{n3}) \left(\frac{W^2}{n\pi}\right) (-1)^n \sinh \frac{n\pi L}{W} \right\} \\
& - \frac{c^{-1}\tau H_y W}{2} \left\{ (A_{n1} + A_{n3}) \frac{W}{n\pi} \left[1-(-1)^n\right] \sinh \frac{n\pi L}{W} \right\}
\end{aligned}\right\} = 0 \text{ because } n \text{ is odd} \\
& + c^{-1}\tau H_x a \left\{ (A_{n2} + A_{n4}) \frac{L}{n\pi} [1-(-1)^n] \sinh \frac{n\pi W}{L} \right\}
\end{aligned}$$

Substituting in the A_{ni}'s and reducing, we get

$$(\vec{T}_1)_y = q_1(\omega_y H_z - \omega_z H_y) H_z + q_2(\omega_x H_y - \omega_y H_x) H_x$$

where

$$q_1 = \left\{ -\frac{1}{2}\sigma c^{-2}\,\tau\,WL\left(L_1 L - \frac{L^2}{2}\right) - \frac{1}{12}\,\sigma c^{-2}\,\tau\,WL^3 \right. \tag{A37}$$

$$+ 8\sigma c^{-2}\,\tau W^2\left(L_1 L - \frac{L^2}{2}\right)\Sigma\left(\frac{1}{m\pi}\right)^3\left[\tanh\frac{m\pi L}{2W} + \left(\frac{L}{W}\right)^2\tanh\frac{m\pi W}{2L}\right]$$

$$\left. + 16\,\sigma c^{-2}\,\tau\,W^4\,\Sigma\left(\frac{1}{m\pi}\right)^5\left[\tanh\frac{m\pi L}{2W} + \left(\frac{L}{W}\right)^4\tanh\frac{m\pi W}{2L}\right]\right\}$$

$$q_2 = -\frac{3}{4}\sigma c^{-2}\,\tau\,LW^3$$

$$m = 2n-1$$

Solution for z-Component of $\vec{T}_1$ Torque

From Equation (A33) we have

$$(\vec{T}_1)_z = c^{-1}\int\int\left[-a H_x\,\frac{\partial\psi}{\partial y} - (y-L_1)\left(H_z\,\frac{\partial\psi}{\partial y} + \frac{\partial\psi}{\partial y}H_y\right)\right]\tau\,dy\,dz \tag{A38}$$

$$= -c^{-1}a H_x\tau\int\int\frac{\partial\psi}{\partial y}\,dy\,dz - c^{-1}\,H_z\tau\int\int y\,\frac{\partial\psi}{\partial z}\,dy\,dz$$

$$- c^{-1}\tau H_y\int\int y\,\frac{\partial\psi}{\partial y}\,dy\,dz + c^{-1}\,\tau L_1\,H_z\int\frac{\partial\psi}{\partial z}\,dy\,dz$$

$$+ c^{-1}\,\tau L_1\,H_y\int\int\frac{\partial\psi}{\partial y}\,dy\,dz$$

Integrating, we get

$$(\vec{T}_1)_z = -c^{-1}\,a\,H_x\tau\left\{\Sigma(A_{n1} + A_{n3})\,\frac{W}{n\pi}\,[1-(-1)^n]\,\sinh\frac{n\pi L}{W}\right\}$$

$$-c^{-1}H_z\tau\left[-\Sigma\left(\frac{L^2}{n\pi}\right)(-1)^n\,(A_{n2} + A_{n4})\,\sinh\frac{n\pi W}{L}\right]$$

$$-c^{-1}\,\tau H_y\left[\Sigma\,\left\{A_{n3}\,\frac{LW}{n\pi}\,[1-(-1)^n]\,\sinh\frac{n\pi L}{W}\right.\right.$$

$$- (A_{n3} - A_{n1}) \left(\frac{W}{n\pi}\right)^2 \quad [1-(-1)^n] \quad \left(\cosh \frac{n\pi L}{W} - 1\right)$$

$$- (A_{n2} - A_{n4}) \left(\frac{L}{n\pi}\right)^2 \quad [1-(-1)^n] \quad \left(\cosh \frac{n\pi W}{L} \; - 1\right)\Bigg\}\Bigg]$$

$$+ c^{-1} \tau L_1 H_z \left\{\sum \frac{L}{n\pi} \quad [1-(-1)^n] \; (A_{n2} + A_{n4}) \sinh \frac{n\pi W}{L}\right\}$$

$$+ c^{-1} \tau L_1 H_y \left\{\sum \frac{W}{n\pi} \quad [1-(-1)^n] \; (A_{n1} + A_{n3}) \sinh \frac{n\pi L}{W}\right\}$$

Subsituting in the A_{ni}'s and reducing, we get

$$(\vec{T}_1)_z = q_3 H_x (\omega_y H_z - \omega_z H_y) + q_4 H_y (\omega_y H_z - \omega_z H_y)$$

where

$$q_3 = \frac{3}{4} \sigma c^{-2} \tau W^3 \tag{A39}$$

and

$$q_4 = \left\{\frac{1}{2} \sigma c^{-2} \tau LW \left(L_1 L - \frac{L^2}{2}\right) + \frac{1}{2} \sigma c^{-2} \tau LW \left(L_1 L - \frac{L^2}{2}\right) + \frac{1}{12} \sigma c^{-2} \tau LW^3\right.$$

$$- \sigma c^{-2} \tau L_1 W \left(L_1 L - \frac{L^2}{2}\right) - 8\sigma c^{-2} \tau W^2 \left(L_1 L - \frac{L^2}{2}\right) \sum \left(\frac{1}{m\pi}\right)^3 \left[\tanh \frac{m\pi L}{2W}\right.$$

$$\left.\left. + \left(\frac{L}{W}\right)^2 \tanh \frac{m\pi W}{2L}\right] - 16\sigma c^{-2} \tau W^4 \sum \left(\frac{1}{m\pi}\right)^5 \left[\tanh \frac{m\pi L}{2W} + \left(\frac{L}{W}\right)^4 \tanh \frac{m\pi W}{2L}\right]\right\}$$

Summary of $\vec{T}_1$ Torque

(1) $(\vec{T}_1)_x = 0$

$$(2)\quad (\vec{T}_1)_y = q_1(\omega_y H_z - \omega_z H_y)\, H_z + q_2(\omega_x H_y - \omega_y H_x)\, H_x \tag{A40}$$

$$(3)\quad (\vec{T}_1)_z = q_3(\omega_y H_z - \omega_z H_y)\, H_x + q_4(\omega_y H_z - \omega_z H_y)\, H_y$$

where

$$q_1 = \Bigg\{ -\frac{1}{2}\sigma c^{-2}\,\tau WL\left(L_1L - \frac{L^2}{2}\right) - \frac{1}{12}\sigma c^{-2}\,\tau WL^3$$

$$+ 8\sigma c^{-2}\,\tau W^2\left(L_1L - \frac{L^2}{2}\right)\Sigma\left(\frac{1}{m\pi}\right)^3\left[\tanh\frac{m\pi L}{2W} + \left(\frac{L}{W}\right)^2 \tanh\frac{m\pi W}{2L}\right]$$

$$+ 16\sigma c^{-2}\,\tau W^4\,\Sigma\left(\frac{1}{m\pi}\right)^5\left[\tanh\frac{m\pi L}{2W} + \left(\frac{L}{W}\right)^4 \tanh\frac{m\pi W}{2L}\right]$$

$$q_2 = -\frac{3}{4}\sigma c^{-2}\,\tau LW^3$$

$$q_3 = \frac{3}{4}\sigma c^{-2}\,\tau LW^3$$

$$q_4 = \Bigg\{\sigma c^{-2}\,\tau LW\left(L_1L - \frac{L^2}{L}\right) + \frac{1}{12}\sigma c^{-2}\,\tau LW^3 - \sigma c^{-2}\,\tau L_1W\left(L_1L - \frac{L^2}{2}\right)$$

$$-8\sigma c^{-2}\,\tau W^2\left(L_1L - \frac{L^2}{2}\right)\Sigma\left(\frac{1}{m\pi}\right)^3\left[\tanh\frac{m\pi L}{2W} + \left(\frac{L}{W}\right)^2 \tanh\frac{m\pi W}{2L}\right]$$

$$-16\sigma c^{-2}\,\tau W^4 \sum_{n=1}^{\infty}\left(\frac{1}{m\pi}\right)^5\left[\tanh\frac{m\pi L}{2W} + \left(\frac{L}{W}\right)^4 \tanh\frac{m\pi W}{2L}\right]\Bigg\}$$

$$m = 2n-1$$

DERIVATION OF $\vec{T}_2$ TORQUE FOR TWO CYLINDER PANELS

From Equation (A26)

$$\vec{T}_2 = \frac{\sigma c^{-2}}{2} \int\int\int \vec{r} \times \{ [(\vec{\omega} \times \vec{H}) \times \vec{r}\,] \times \vec{H} \} \, dV \tag{A41}$$

where

$$\vec{r} = a\hat{i} + (y-L_1)\,\hat{j} + \left(z - \frac{W}{2}\right)\hat{k}$$

$$dV = \tau \, dy \, dz$$

From Equation (A35), and expanding

$$\begin{aligned}[(\vec{\omega} \times \vec{H}) \times r] = {} & \left[(\omega_x H_y - \omega_y H_x)\, a - (\omega_y H_z - \omega_z H_y)\left(z - \frac{W}{2}\right)\right]\hat{j} \\ & + [\,(\omega_y H_z - \omega_z H_y)\,(y-L_1) - a(\omega_z H_x - \omega_x H_z)]\,\hat{k}\end{aligned} \tag{A42}$$

The x-component is satisfied because the panel is thin in the x-direction.

Then expanding

$$[(\vec{\omega} \times \vec{H}) \times \vec{r}\,] \times \vec{H} = (J_y H_z - J_z H_y)\,\hat{i} + (J_z H_x)\hat{j} - (J_y H_x)\hat{k} \tag{A43}$$

Then expanding

$$\begin{aligned}\vec{r} \times \{[(\vec{\omega} \times \vec{H}) \times \vec{r}\,] \times \vec{H}\} = {} & [-(y-L_1) J_y H_x - \left(z - \frac{W}{2}\right) J_z H_x]\,\hat{i} \\ & + [\,(z - \frac{W}{2})\,(J_y H_z - J_z H_y) + a J_y H_x\,]\,\hat{j} \\ & + [a J_z H_x - (y-L_1)\,(J_y H_z - J_z H_y)\,]\,\hat{k}\end{aligned}$$

Solution for x-Component of $\vec{T}_2$ (Two Panels)

$$(\vec{T}_2)_x = \frac{2\sigma c^{-3}}{2} \tau \iint [-(y-L_1) J_y H_x - (z - \frac{W}{2}) J_z H_x] \, dy \, dz$$

$$= -\frac{2\sigma c^{-2}}{2} \tau \iint (y-L_1) [a(\omega_x H_y - \omega_y H_x) - (z - \frac{W}{2}) (\omega_y H_z - \omega_z H_y)] H_x d_y d_z$$

$$= \frac{2\sigma c^{-2}}{2} \tau \iint (z - \frac{W}{2}) [(y-L_1)(\omega_y H_z - \omega_z H_y) - a(\omega_z H_x - \omega_x H_z] H_x d_y d_z$$

The terms involving "a" cancel out, and further reducing, we get

$$(\vec{T}_2)_x = + \sigma c^{-2} \tau \iint (y-L_1) (z - \frac{W}{2}) (\omega_y H_z - \omega_z H_y) H_x d_y d_z$$

$$- \sigma c^{-2} \tau \iint (y-L_1) (z - \frac{W}{2}) (\omega_y H_z - \omega_z H_y) H_x d_y d_z$$

Therefore,

$$(\vec{T}_2)_x = 0 \tag{A44}$$

Solution for y-Component of $\vec{T}_2$ (Two Panels)

$$(\vec{T}_2)_y = \sigma c^{-2} \tau \iint (z - \frac{W}{2}) \{[(\omega_x H_y - \omega_y H_x) a - (z - \frac{W}{2}) (\omega_y H_z - \omega_z H_y)] H_z$$

$$- [(y-L_1)(\omega_y H_z - \omega_z H_y) - a(\omega_z H_x - \omega_x H_z)] H_y\} d_y d_z$$

$$+ \sigma c^{-2} \tau a \iint [a(\omega_x H_y - \omega_y H_x) - (z - \frac{W}{2})(\omega_y H_z - \omega_z H_y)] H_x d_y d_z$$

The terms containing first power of "a" cancel over thesum of the two panels, so that

$$(\vec{T}_2)_y = -\sigma c^{-2}\ \tau H_z\ (\omega_y H_z - \omega_z H_y) \int\int (z - \frac{W}{2})^2\ d_y d_z$$

$$- \sigma c^{-2}\ \tau\ H_y\ (\omega_y H_z - \omega_z H_y) \int\int (z - \frac{W}{2})\ (y - L_1)\ d_y d_z$$

$$+ \sigma c^{-2}\ \tau\ a^2 H_x\ (\omega_x H_y - \omega_y H_y) \int\int d_y d_z$$

$$= -\sigma c^{-2}\ \tau H_z\ (\omega_y H_z - \omega_z H_y)\ \frac{\left(z - \frac{W}{2}\right)^3}{3}\ y\ \Bigg|_{0\ \ 0}^{W\ \ L}$$

$$- \sigma c^{-2}\ \tau\ H_y\ (\omega_y H_z - \omega_z H_y)\ \frac{\left(z - \frac{W}{2}\right)^2}{2}\ \frac{\left(y - L_1\right)^2}{2}\ \Bigg|_{0\ \ 0}^{W\ \ L}$$

$$+ \sigma c^{-2}\ \tau\ \frac{3W^2}{4}\ H_x\ (\omega_x H_y - \omega_y H_x)\ y\ z\ \Bigg|_{0\ \ 0}^{W\ \ L}$$

$$= -\sigma c^{-2}\ \tau\ H_z\ (\omega_y H_z - \omega_z\ H_y)\ \frac{1}{3}\left[\left(\frac{W}{2}\right)^3 - \left(\frac{W}{2}\right)^3\right]$$

$$+ \frac{3}{4}\,\sigma c^{-2}\ \tau\ W^3\ L\ H_x\ (\omega_x\ H_y - \omega_y H_x)$$

$$= -\frac{1}{12}\ c^{-2}\ \tau\ W^3 L\ (\omega_y H_z - \omega_z H_y)\ H_z + \frac{3}{4}\,\sigma c^{-2}\ \tau\ W^3 L\ (\omega_x H_y - \omega_y H_x)\ H_x$$

and

$$(\vec{T}_2)_y = q_5\ (\omega_y H_z - \omega_z H_y)\ H_z + q_6\ (\omega_x H_y - \omega_x H_y - \omega_y H_x)\ H_x$$

where (A45)

$$q_5 = -\frac{1}{12}\ c^{-2}\ \tau\ W^3 L,\ q_6 = 3/4\ \sigma c^{-2}\ \tau W^3\ L$$

Solution for z-Component of $\vec{T}_2$ (Two Panels)

$$(\vec{T}_2)_z = \sigma c^{-2} \int \int [a[(\omega_y H_z - \omega_z H_y)(y-L_1) - a(\omega_z H_x - \omega_x H_z)] H_x \tau d_y d_z$$

$$-\sigma c^{-2} \int \int (y - L_1) \{[a(\omega_x H_y - \omega_y H_x) - (z - \tfrac{W}{2})(\omega_y H_z - \omega_z H_y)] H_z \tau d_y d_z$$

$$+ \sigma c^{-2} \int \int (y - L_1) \{[(y - L_1)(\omega_y H_z - \omega_z H_y) - a(\omega_z H_x - \omega_x H_z)] H_y \tau d_y d_z$$

Terms containing first power of "a" are zero because of the sum over x = a and x = -a for two panels:

$$(\vec{T}_2)_z = -\sigma c^{-2} \tau a^2 H_x (\omega_z H_x - \omega_x H_z) \iint dy dz$$

$$+ \sigma c^{-2} \tau (\omega_y H_z - \omega_z H_y) H_z \underbrace{\int \int (y - L_1)(z - \tfrac{W}{2}) dy dz}_{0}$$

$$+ \sigma c^{-2} \tau H_y (\omega_y H_z - \omega_z H_y) \iint (y - L_1)^2 d_y d_z$$

$$= -\frac{3}{4} \sigma c^{-2} \tau W^3 L (\omega_z H_x - \omega_x H_z) H_x$$

$$+ \sigma c^{-2} \tau H_y (\omega_y H_z - \omega_z H_y) \left(\frac{(y - L_1)^3}{3}\right) \Bigg|_0^L z \Bigg|_0^W$$

$$= + q_7 (\omega_z H_x - \omega_x H_z) H_x + q_8 (Y_y H_z - \omega_z H_y) H_y \qquad \text{(A46)}$$

where

$$q_7 = -\frac{3}{4} \sigma c^{-2} \tau W^3 L$$

and

$$q_8 = +\frac{1}{3} \sigma c^{-2} \tau [(L - L_1)^3 + L_1{}^3] W$$

TORQUE DUE TO CYLINDER

<u>Sum of $\vec{T}_1$ and $\vec{T}_2$ due to Two Panels</u>

From Equations (A34), (A35), (A38), and (A39), the total torque

$$\vec{T} = \vec{T}_1 + \vec{T}_2$$

is

$$(1)\ (\vec{T})_x = 0$$

$$(2)\ (\vec{T})_y = (q_2 + q_6)(\omega_x H_y - \omega_y H_x) H_x + (q_1 + q_5)(\omega_y H_z - \omega_z H_y) H_z$$

$$(3)\ (\vec{T})_z = (q_3 + q_7)(\omega_z H_x - \omega_x H_z) H_x + (q_4 + q_8)(\omega_y H_z - \omega_z H_y) H_y$$

Let

$$K_{y1} = q_2 + q_6$$

$$= -\frac{3}{4} \sigma c^{-2} \tau L W^3 + \frac{3}{4} \sigma c^{-2} \tau W^3 L$$

$$= 0$$

$$
\begin{aligned}
K_{y2} &= q_1 + q_5 = \left\{ -\frac{1}{12}\,\sigma c^{-2}\,\tau W^3 L - \frac{1}{12}\,\sigma c^{-2}\,\tau W L^3 - \frac{1}{2}\sigma c^{-2}\,\tau W L\left(L_1 L - \frac{L^2}{2}\right)\right. \\
&\quad + 8\,\sigma c^{-2}\,\tau W^2\left(L_1 L - \frac{L^2}{2}\right)\Sigma\left(\frac{1}{m\pi}\right)^3\left[\tanh\frac{m\pi L}{2W} + \left(\frac{L}{W}\right)^2\tanh\frac{m\pi W}{2L}\right] \\
&\quad \left. + 16\,\sigma c^{-2}\,\tau W^4\,\Sigma\left(\frac{1}{m\pi}\right)^5\left[\tanh\frac{m\pi L}{2W} + \left(\frac{L}{W}\right)^4\tanh\frac{m\pi W}{2L}\right]\right\}
\end{aligned}
$$

$$
\begin{aligned}
K_{z1} &= (q_3 + q_7) \\
&= \frac{3}{4}\,\sigma c^{-2}\,\tau L W^3 - \frac{3}{4}\,\sigma c^{-2}\,\tau W^3 L \\
&= 0
\end{aligned}
$$

$$
\begin{aligned}
K_{z2} &= q_4 + q_8 \\
&= \left\{\frac{1}{3}\,\sigma c^{-2}\,\tau\left[(L - L_1)^3 + L_1^3\right] W + \sigma c^{-2}\,\tau L W\left[L_1 L - \frac{L^2}{2}\right]\right. \\
&\quad + \frac{1}{12}\,\sigma c^{-2}\,\tau L W^3 - \sigma c^{-2}\,\tau L_1 W\left(L_1 L - \frac{L^2}{2}\right) - 8\,\sigma c^{-2}\,\tau W^2\left(L_1 L - \frac{L^2}{2}\right)\Sigma\left(\frac{1}{m\pi}\right)^3\left[\tanh\frac{m\pi L}{2W} + \left(\frac{L}{W}\right)^2\tanh\frac{m\pi W}{2L}\right] \\
&\quad \left. - 16\,\sigma c^{-2}\,\tau W^4\,\Sigma\left(\frac{1}{m\pi}\right)^5\left[\tanh\frac{m\pi L}{2W} + \left(\frac{L}{W}\right)^4\tanh\frac{m\pi W}{2L}\right]\right\}
\end{aligned}
$$

Therefore,

$$
\begin{aligned}
(\vec{T})_x &= 0 \\
(\vec{T})_y &= K_{y2}\,(\omega_y H_z - \omega_z H_y)\,H_z \qquad \text{(A47)} \\
(\vec{T})_z &= K_{z2}\,(\omega_y H_z - \omega_z H_y)\,H_y
\end{aligned}
$$

where

$$K_{y2} = \left\{ -\frac{1}{12} c^{-2} \ {}_{\tau}W^3L - \frac{1}{12} \sigma c^{-2} \ {}_{\tau}WL^3 - \frac{1}{2} \sigma c^{-2} \ {}_{\tau}WL \left(L_1L - \frac{L^2}{2} \right) \right.$$

$$+ 8 \sigma c^{-2} \ {}_{\tau}W^2 \left(L_1L - \frac{L^2}{2} \right) \Sigma \left(\frac{1}{m\pi} \right)^3 \left[\tanh \frac{m\pi L}{2W} + \left(\frac{L}{W} \right)^2 \tanh \frac{m\pi W}{2L} \right]$$

$$\left. + 16 \sigma c^{-2} \ {}_{\tau}W^4 \Sigma \left(\frac{1}{m\pi} \right)^5 \left[\tanh \frac{m\pi L}{2W} + \left(\frac{L}{W} \right)^4 \tanh \frac{m\pi W}{2L} \right] \right\}$$

$$K_{z2} = \left\{ \frac{1}{3} \sigma c^{-2} \ {}_{\tau}WL^3 + \frac{1}{12} \sigma c^{-2} \ {}_{\tau}LW^3 - \frac{1}{2} \sigma c^{-2} \ {}_{\tau}L_1L^2W \right.$$

$$+ \sigma c^{-2} \ {}_{\tau}LW \left(L_1L - \frac{L^2}{2} \right) - 8 \sigma c^{-2} \ {}_{\tau}W^2 \left(L_1L - \frac{L^2}{2} \right) \Sigma \left(\frac{1}{m\pi} \right)^3 \left[\tanh \frac{m\pi L}{2W} + \left(\frac{L}{W} \right)^2 \tanh \frac{m\pi W}{2L} \right]$$

$$\left. - 16 \sigma c^{-2} \ {}_{\tau}W^4 \Sigma \left(\frac{1}{m\pi} \right)^5 \left[\tanh \frac{m\pi L}{2W} + \left(\frac{L}{W} \right)^4 \tanh \frac{m\pi W}{2L} \right] \right\}$$

Solution of $\vec{T}$ for All Six Panels

Figure A7shows the relationship of the ARRS spacecraft cylinder panels to each other. Equation(A47) represents the torque of two panels whose surfaces are normal to an x-axis.

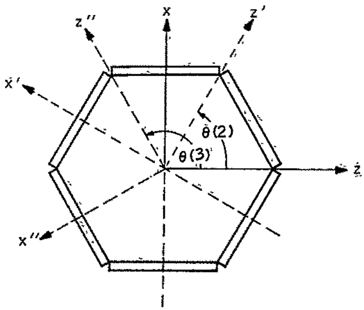

Figure A7. Relationship of Cylinder Panels to One Another

Therefore, the torque due to all panels in the unprimed frame is

$$\vec{T}_T = \vec{T} + R(\theta') \vec{T}' + R(\theta'') \vec{T}'' \tag{A48}$$

Equation (A47) represents the torque of two panels in the unprimed, the primed, and double primed frame. However, the torque is rotated into the unprimed frame and the $\vec{\omega}$'s and $\vec{H}$ are transformed to the unprimed frame:

$$T = R(\theta) T' \tag{A49}$$

where

$$R(\theta) = \begin{bmatrix} \cos\theta & 0 & s\theta \\ 0 & 1 & 0 \\ -s\theta & 0 & c\theta \end{bmatrix}$$

also

$$\vec{\omega} = R(\theta)\,\vec{\omega}'$$

$$\vec{H} = R(\theta)\,\vec{H}'$$

Therefore

$$\vec{T}_T = \sum_{i=1}^{3} R\,[\theta(i)]\,T'(i) \qquad \text{(A50)}$$

where

$$\theta(1) = 0°,\ \theta(2) = 60°,\ \text{and}\ \theta(3) = 120°$$

and

$$\begin{aligned} \vec{T}_T(i)_x &= [T'(i)_x \cos\theta + T'(i)_z \sin\theta] \\ \vec{T}_T(i)_y &= T'(i)_y \\ \vec{T}_T(i)_z &= [-T'(i)_x \sin\theta + T'(i)_z \cos\theta] \end{aligned} \qquad \text{(A51)}$$

From Equation (A47)

$$T'(i)_x = 0$$

Therefore

$$\vec{T}_T(i)_x = T'(i)_z \sin\theta$$

$$\vec{T}_T(i)_y = T'(i)_y$$

$$\vec{T}_T(i)_z = T'(i)_z \cos\theta$$

Using Equation (A47), we get

$$\vec{T}_T(i)_x = K_{z2} (\omega_y' H_z' - \omega_z' H_y') H_y' \sin \theta(i)$$

$$\vec{T}_T(i)_y = K_{y2} (\omega_y' H_z' - \omega_z' H_y') H_z' \qquad \text{(A52)}$$

$$\vec{T}_T(i)_z = K_{z2} (\omega_y' H_z' - \omega_z' H_y') H_y' \cos \theta(i)$$

Using the following

$$\vec{\omega}' = R^T(\theta) \vec{\omega}$$

$$\omega_x' = \omega_x \cos \theta - \omega_z \sin \theta$$

$$\omega_y' = \omega_y$$

$$\omega_z' = + \omega_x \sin \theta + \omega_z \cos \theta$$

and

$$\vec{H}_x' = H_x \cos \theta - H_z \sin \theta$$

$$H_y' = H_y$$

$$H_z' = H_x \sin \theta + H_z \cos \theta$$

From Equation (A52)

$$\vec{T}_T(i)_x = K_{z2}\,[\omega_y\,(H_x s\theta + H_z c\theta) - (\omega_x s\theta + \omega_z c\theta)\,H_y]\,H_y \sin\theta(i)$$

$$= K_{z2}\,(\omega_y H_x H_y\, s^2\theta + \omega_y H_y H_z\, s\theta\, c\theta - \omega_x H_y^2\, s^2\theta - \omega_z N_y^2\, c\theta\, s\theta)$$

$$= K_{z2}\,[\omega_y H_x H_y\,(\sum s^2\theta) + K_{z2}\omega_y H_y H_z \sum s\theta\, c\theta$$

$$- K_{z2}\,\omega_x H_y^2 \sum s^2\theta - K_{z2}\omega_z H_y^2 \sum c\theta\, s\theta]$$

where

$$\sum s^2\theta = s^2\,0° + s^2\,60° + s^2\,120°$$

$$= 0 + \left(\frac{\sqrt{3}}{2}\right)^2 + \left(\frac{\sqrt{3}}{2}\right)^2 = \frac{3}{4} + \frac{3}{4} = \frac{3}{2}$$

and

$$\sum s\theta\, c\theta = s0°\, c0° + s60°\, c60° + s120°\, c120°$$

$$= \left(\frac{\sqrt{3}}{2}\right)\frac{1}{2} + \left(\frac{\sqrt{3}}{2}\right) - \frac{1}{2} = 0$$

and

$$(\vec{T}_T)_x = \frac{3}{2} K_{z2}\,\omega_y H_x H_y - \frac{3}{2} K_{z2}\omega_x H_y^2$$

$$= -\frac{3}{2} K_{z2}\,(\omega_x H_y^2 - \omega_y H_x H_y)$$

From Equation (A52)

$$(\vec{T}_T)_y = 3K_{y2} (\omega_y{}' H_z{}' - \omega_z{}' H_y{}') H_z{}'$$

$$= 3K_{y2} [\omega_y(H_x s\theta + H_x c\theta) - (\omega_x s\theta + \omega_z c\theta) H_y] (H_x s\theta + H_z(\theta)$$

$$= 3K_{y2} \sum_\theta [\omega_y H_x{}^2 s^2\theta + \omega_y H_x H_z \underbrace{s\theta\, c\theta}_{0} + \omega_y H_x H_z \underbrace{s\theta\, c\theta}_{0} + \omega_y H_z{}^2 c^2\theta$$

$$-\omega_x H_x H_y s^2\theta - \omega_x H_y H_z \underbrace{s\theta\, c\theta}_{0} - \omega_z H_y H_x \underbrace{s\theta\, c\theta}_{0} - \omega_z H_y H_z c^2\theta$$

Using the value of $\sum\cos^2\theta$ and $\sum\sin^2\theta$, we get

$$= \frac{9}{2} K_{y2} [\omega_y(H_x{}^2 + H_z{}^2) - \omega_x H_x H_y - \omega_z H_y H_z]$$

From Equation (A52)

$$\vec{T}_T(i)_z = K_{z2} [\omega_y(H_x s\theta + H_z c\theta) - (\omega_x s\theta + \omega_z c\theta) H_y] H_y \cos\theta$$

and

$$(\vec{T}_T)_z = K_{z2} \sum_\theta (\omega_y H_x H_y \underbrace{s\theta\, c\theta}_{0} + \omega_y H_y H_z c^2\theta - \omega_x H_y{}^2 \underbrace{s\theta\ \theta}_{0} - \omega_z H_y^2 c^2\theta)$$

$$= -\frac{3}{2} K_{z2} (\omega_z H_y{}^2 - \omega_y H_y H_z)$$

<u>Summary of Torque Due to Spacecraft Cylinder</u>

(1) $(\vec{T}_T)_x = -\frac{3}{2} K_{z2} (\omega_x H_y{}^2 - \omega_y H_x H_y$

(2) $(\vec{T}_T)_y = \frac{9}{2} K_{y2} [\omega_y(H_x{}^2 + H_z{}^2) - \omega_x H_x H_y - \omega_z H_y H_z]$ (A53)

(3) $(\vec{T}_T)_z = -\frac{3}{2} K_{z2} (\omega_z H_y{}^2 - \omega_y H_y H_z)$

Let

$$P_1 = -\frac{3}{2}K_{z2}$$

and

$$P_2 = \frac{9}{2}K_{y2}$$

Then

$$\begin{aligned} P_1 = \Bigg\{ & -\frac{\sigma c^{-2}}{2}\,\tau W L^3 - \frac{1}{8}\,\sigma c^{-2}\,\tau L W^3 + \frac{3}{4}\,\sigma c^{-2}\,\tau L_1 L^2 W \\ & - \frac{3}{2}\,\sigma c^{-2}\,\tau L W \left(L_1 L - \frac{L^2}{2}\right) \\ & + 12\,\sigma c^{-2}\,\tau W^2 \left(L_1 L - \frac{L^2}{2}\right) \Sigma \left(\frac{1}{m\pi}\right)^3 \left[\tanh \frac{m\pi L}{2W} + \left(\frac{L}{W}\right)^2 \tanh \frac{m\pi W}{2L}\right] \\ & + 24\,\sigma c^{-2}\,\tau W^4\, \Sigma \left(\frac{1}{m\pi}\right)^5 \left[\tanh \frac{m\pi L}{2W} + \left(\frac{L}{W}\right)^4 \tanh \frac{m\pi W}{2L}\right] \Bigg\} \end{aligned}$$

and

$$\begin{aligned} P_2 = \Bigg\{ & -\frac{3}{8}\,c^{-2}\,\tau W^3 L - \frac{3}{8}\,\sigma c^{-2}\,\tau W L^3 - \frac{9}{4}\,\sigma c^{-2}\,\tau W L \left(L_1 L - \frac{L^2}{2}\right) \\ & + 36\,\sigma c^{-2}\,\tau W^2 \left(L_1 L - \frac{L^2}{2}\right) \Sigma \left(\frac{1}{m\pi}\right)^3 \left[\tanh \frac{m\pi L}{2W} + \left(\frac{L}{W}\right)^2 \tanh \frac{m\pi W}{2L}\right] \\ & + 72\,\sigma c^{-2}\,\tau W^4\, \Sigma \left(\frac{1}{m\pi}\right)^5 \left[\tanh \frac{m\pi L}{2W} + \left(\frac{L}{W}\right)^4 \tanh \frac{m\pi W}{2L}\right] \Bigg\} \end{aligned}$$

DERIVATION OF TORQUE DUE TO SPACECRAFT SOLAR PANELS

The torque is again given by Equation (A8). The current density in the solar panel must first be derived. Then, the integral Equation (A8) is evaluated.

SOLAR PANEL GEOMETRY

Solar panel geometry is shown in Figure A8.

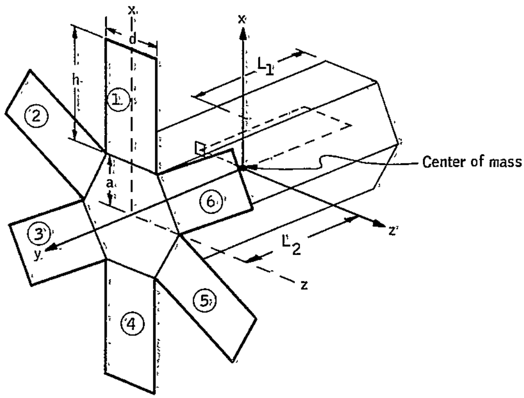

Figure A8. Solar Panel Configuration

METHOD OF TORQUE SOLUTION FOR SOLAR PANELS

The current density for panel 1 will be derived (Figure A8). The torque for panel 1 is then derived. By rotating the coordinate frame of Figure A8 60 degrees positively about y, the torque due to panel 2 is then the same as panel 1 except the $\vec{\omega}$ and $\vec{H}$ vector components are different. Therefore, continuing in the same manner, the torque for all panels is known. To obtain the torque for all panels in a common frame, only a series of coordinate transformations are required.

<u>Solution of Neumann Boundary Value Problem to Obtain ϕ (ψ stream function)</u>

The method used in this solution is identical to that discussed previously. Only, the boundary condition on the problem differs.

The boundary conditions for panel 1 are

$$
\begin{aligned}
J_x\,(y' = L_2,\ x' = a) &= 0 \\
J_x\,(y' = L_2,\ x' = a + h) &= 0 \\
J_z\,(y' = L_2,\ z = -d/2) &= 0 \\
J_z\,(y' = L_2,\ z = d/2) &= 0
\end{aligned}
\qquad (A54)
$$

The solution for ϕ is enhanced by translating the solar panel to a new frame, shown in Figure A9.

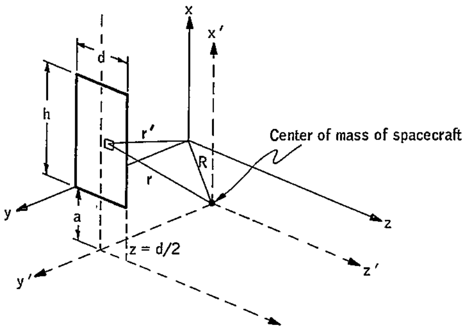

Figure A9. Relationship of Spacecraft Center of Mass to Translated Frame

The new boundary conditions are now

$$
\begin{aligned}
J_x\,(y = L_2,\ x = 0) &= 0 \\
J_x\,(y = L_2,\ x = h) &= 0 \\
J_z\,(y = L_2,\ z = 0) &= 0 \\
J_z\,(y = L_2,\ z = d) &= 0
\end{aligned}
\tag{A55}
$$

where $\vec{r}$ in Equation (A7) is

$$\vec{r} = (x+a)\ i\ X\ L_2\hat{j} + (z - d/2)\hat{k} \tag{A56}$$

Using Equation (A49) in Equation (A7), we get

$$J_x = \frac{1}{2}\sigma c^{-1}[\omega_z H_x - \omega_x H_x)(z-d/2) - (\omega_x H_y - \omega_y H_x)L_2] + \frac{\partial\phi}{\partial x}$$

$$J_y = \frac{1}{2}\sigma c^{-1}[\omega_x H_z - \omega_y H_x)(x+a) - (\omega_y H_z \; 0 \; \omega_z H_y)(z - d/2)] + \frac{\partial\phi}{\partial y} \quad (A57)$$

$$J_z = \frac{1}{2}\sigma c^{-1}[\omega_y H_z - \omega_z H_y) \; L_2 - (\omega_z H_x - \omega_x H_z)(x+a)] + \frac{\partial\phi}{\partial z}$$

Since the solar panel is very thin in the y-derivation, J_y is neglected. Therefore, only J_x and J_z will be considered.

The Neumann problem can be reduced to a Dirichlet problem using the following Cauchy-Riemann conditions:

$$\frac{\partial\phi}{\partial x} = \frac{\partial\psi}{\partial z}$$

and

$$\frac{\partial\phi}{\partial z} = -\frac{\partial\psi}{\partial y} \quad (A58)$$

Applying the boundary conditions and Cauchy-Riemann conditions, we get

$$J_x(y = L_2,\; x = 0) = 0 = V_1 + V_2\,(z - d/2) + \frac{\partial\psi}{\partial z}$$

$$J_x\,(y = L_2,\; x = h) = 0 = V_1 + V_2\,(z - d/2) + \frac{\partial\psi}{\partial z}$$

$$J_z\,(x = L_2,\; z = 0) = 0 = V_3 + V_4\,(x + a) - \frac{\partial\psi}{\partial x} \quad (A59)$$

$$J_z\,(y = L_2,\; z = j) = 0 = V_3 + V_4\,(x + a) - \frac{\partial\psi}{\partial x}$$

where

$$V_1 = -1/2\,\sigma\,c^{-1}\,L_2(\omega_x H_y - \omega_y H_x)$$

$$V_2 = 1/2\,\sigma\,c^{-1}(\omega_z H_x - \omega_x H_z) \quad (A60)$$

$$V_3 = 1/2\,\sigma\, c^{-1}(\omega_y H_z - \omega_z H_y)\, L_2 \qquad \text{(A60) (contd)}$$

$$V_4 = -\,1/2\,\sigma\, c^{-1}(\omega_z H_x - \omega_x H_z)$$

Equation (A 59) can now be integrated along the boundary of the solar panel to give the value of ψ along the boundary. Then, the solution ψ is determined in the interior of the boundary.

Figure A10 shows the new orientation of the solar panel to the x - z plane.

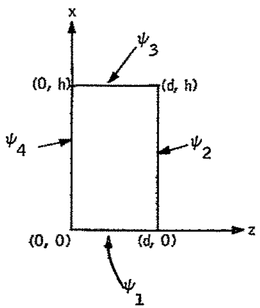

Figure A10. Relationship of Translated Solar Panel to x-z Coordinate Axes

The potential ψ_1 (z, x = 0) is given by

$$\psi_1(z,\; x = 0) = \int_{0\;\;0}^{z\;\;0} \frac{\partial \psi}{\partial z}\, dz$$

$$= \int_0^z -\left[V_1 + V_2\,(z - d/2)\right] dz$$

$$= \left[- V_1 z - \frac{V_2}{2} (z - d/2)\right]^2 \Bigg|_o^z$$

$$= - V_1 z - \frac{V_2}{2} (z - d/2)^2 + \frac{V_2}{2} (-d/2)^2$$

$$= - V_1 z - \frac{V_2}{2} z^2 + d/2\ V_2\ z$$

$$= - (V_1 - \frac{V_2}{2} d)\ z - \frac{V_2}{2} z^2$$

The potential $\psi_2(x,\ z = d)$ is given by

$$\psi_2(x, z=d) = \psi_1(z=d,\ x=0) + \int_{do}^{dx} + [V_3 + V_4\ (x + a)]\ dx$$

$$= -V_1 d + V_3 x + V_4\ (x + a)^2\ /2 \Bigg|_o^x$$

where

$$\psi_2 = - V_1 d + V_3 x + \frac{(x+a)^2}{2} V_4 - (a/2)^2\ V_4$$

$$= - V_1 d + V_3 x + \left(\frac{x^2}{2} + a\ x\right) V_4$$

$$= - V_1 d + (V_3 + a\ V_4)\ x + V_4 \frac{x^2}{2}$$

The potential ψ_3 is given by

$$\psi_3(x = h, z) = \psi_2(z = d, x = h) + \int - [V_1 + V_2(z - d/2)]\ dz$$

$$= -V_1 d + (V_3 + a\,V_4)h + V_4\,\frac{h^2}{2} - \left[V_1 z + \frac{V_2(z-d/2)^2}{2}\right]_d^z$$

$$= -V_1 d + (V_3 + a\,V_4)\,h + V_4\frac{h^2}{2} - \left(V_1 - \frac{V_2 d}{2}\right) z - \frac{V_2 z^2}{2}$$

$$= \left(V_3 h + a\,V_4 + V_4\,\frac{h^2}{2}\right) - \left(V_1 - \frac{V_2 d}{2}\right) z - \frac{V_2}{2}\,z^2$$

The potential $\psi_4(z = 0,\ x)$ is given by

$$\psi_4(z{=}0, x) \quad = \psi_3(x = h,\ z = 0) + \ [V_3 + V_4(x{+}a)\ ]\ dx$$

$$= \left[V_3 h + a\,V_4 h + V_4\,\frac{h^2}{2} + \quad V_3 x + V_4\,\frac{(x+a)^2}{2}\right]_h^x$$

$$= V_3 h + a\,V_4 h + V_4\,\frac{h^2}{2}\ X\ V_3 x + V_4\,\frac{(x+a)^2}{2} - V_3 h - V_4\,\frac{(h{+}a)^2}{2}$$

$$= (V_3 + a\,V_4)x + \frac{V_4 x^2}{2}$$

Summarizing ψ_1, ψ_2, ψ_3, and ψ_4 gives

$$\begin{aligned}
\psi_1 &= \bar{f}_1 z + \bar{f}_2 z^2 \\
\psi_2 &= b'_1 + \bar{f}_3 x + \bar{f}_2 x^2 \\
\psi_3 &= b'_2 + \bar{f}_1 z + \bar{f}_2 z^2 \\
\psi_4 &= \bar{f}_3 x + \bar{f}_2 x^2
\end{aligned} \tag{A61}$$

where

$$\bar{f}_1 = -\left(V_1 - \frac{V_2 d}{2}\right)$$

$$\bar{f}_2 = -\frac{V_2}{2}$$

$$b'_1 = -V_1 d$$

$$\bar{f}_3 = (V_3 - a\,V_2)$$

$$b'_2 = \left[V_3 h - \left(a\,h + \frac{h^2}{2}\right)V_2\right]$$

Compare Equation (A61) with Equation (A17).

The solution to the new panel can now be written using Equations (A30) and (A31):

$$\psi_T = \sum_{n=1}^{\infty} B_{n1} \sin \frac{n\pi}{d} z \quad \sinh \frac{n\pi}{d}(x-h)$$

$$+ \sum_{n=1}^{\infty} B_{n2} \sin \frac{n\pi}{h} x \quad \sinh \frac{n\pi}{h} z \tag{A62}$$

$$+ \sum_{n=1}^{\infty} B_{n3} \sin \frac{n\pi}{d} z \quad \sinh \frac{n\pi}{d} x$$

$$+ \sum_{n=1}^{\infty} B_{n4} \sin \frac{n\pi}{h} x \ \sinh \frac{n\pi}{h}(z-d)$$

where

$$B_{n1} = -\left\{-\frac{2(-1)^n}{n\pi}\psi_1(d) + \frac{4\bar{f}_2 d^2}{(n\pi)^3}\left[(-1)^n - 1\right]\right\} \frac{1}{\sinh \frac{n\pi}{d} h}$$

$$B_{n2} = \left\{-\frac{2(-1)^n}{n\pi}\psi_2(h) + \frac{2b'_1}{n\pi} + \frac{4\bar{f}_2 h^2\left[(-1)^n - 1\right]}{(n\pi)^3}\right\} \frac{1}{\sinh \frac{n\pi d}{h}} \tag{A63}$$

$$B_{n3} = \left\{ -\frac{2(-1)^n}{n\pi}\psi_3(d) + \frac{2b_2}{n\pi} + \frac{4\overline{f}_2 d^2}{(n\pi)^3}\left[(-1)^n - 1\right]\right\} \frac{1}{\sinh \frac{n\pi h}{d}} \qquad \text{(A63) (contd)}$$

$$B_{n4} = -\left\{ -\frac{2(-1)^n}{n\pi}\psi_4(h) + \frac{4h^2 \overline{f}_2\left[(-1)^n - 1\right]}{(n\pi)^3}\right\} \frac{1}{\sinh \frac{n\pi d}{h}}$$

The above is the solution for ψ_T for one solar panel. The following paragraphs will derive torque $\vec{T}_1$ for one solar panel.

Derivation of Torque $\vec{T}_1$ for One Solar Panel

Torque $\vec{T}_1$ is defined in Equation (A8):

$$\vec{T}_1 = c^{-1} \iiint \vec{r} \times \{\nabla\phi \times \vec{H}\}\, dV$$

where

$$dV = \epsilon\, dx\, dz$$

$$\vec{r} = (x + a)\,\hat{i} + L_2\,\hat{j} + (z - d/2)\hat{k}$$

Expanding $\vec{T}_1$, we get

$$\vec{T}_1 = c^{-1}\iint \left\{ \left[\left(L_2 H_y \frac{\partial\phi}{\partial x} - \left[z - \frac{d}{2}\right]\right)\left(H_x \frac{\partial\phi}{\partial z} - H_z \frac{\partial\phi}{\partial x}\right)\right]\hat{i}\right.$$

$$+ \left[-(z - d/2)\, H_y \frac{\partial\phi}{\partial z} - (x + a)\left(H_y \frac{\partial\phi}{\partial x}\right)\right]\hat{j} \qquad \text{(A64)}$$

$$\left. + \left[(x + a)\left(\frac{\partial\phi}{\partial z} H_x - H_z \frac{\partial\phi}{\partial x}\right) + L_2 H_y \frac{\partial\phi}{\partial z}\right]\hat{k} \right\} \epsilon\, dxdz$$

Using the Cauchy-Riemann conditions:

$$\frac{\partial \phi}{\partial x} = \frac{\partial \psi}{\partial z}$$

and

$$\frac{\partial \phi}{\partial z} = -\frac{\partial \psi}{\partial x}$$

then,

$$\vec{T}_1 = c^{-1}\iint\Bigg\{\left[\left(L_2H_y \frac{\partial \psi}{\partial z} - \left[z - \frac{d}{2}\right]\right)\left(H_x\left[-\frac{\partial \psi}{\partial x}\right] - H_z\frac{\partial \psi}{\partial z}\right)\right]\hat{i}$$

$$+\left[-(z - d/2)\,H_y\left(-\frac{\partial \psi}{\partial x}\right) - (x+a)\,H_y\frac{\partial \psi}{\partial z}\right]\hat{j}$$

$$+\left[(x+a)\left(-\frac{\partial \psi}{\partial x}H_x - H_z\frac{\partial \psi}{\partial z}\right) + L_2\,H_y\left(-\frac{\partial \psi}{\partial x}\right)\right]\hat{k}\Bigg\}\,\varepsilon\,dxdz$$

$$\vec{T}_1 = c^{-1}\iint\Bigg\{\left[L_2H_y\frac{\partial \psi}{\partial z} + (z - d/2)\left(H_x\frac{\partial \psi}{\partial x} + H_z\frac{\partial \psi}{\partial z}\right)\right]\hat{i}$$

$$+\left[+(z-d/2)\;H_y\frac{\partial \psi}{\partial x} - (x+a)\,H_y\frac{\partial \psi}{\partial z}\right]\hat{j} \qquad \text{(A65)}$$

$$+\left[-(x+a)\left(H_x\frac{\partial \psi}{\partial x} + H_z\frac{\partial \psi}{\partial z}\right) - L_2\,H_y\frac{\partial \psi}{\partial x}\right]\hat{k}\Bigg\}\,\varepsilon\,dxdz$$

Solution for the x-component of $\vec{T}_1$ --

$$(\vec{T}_1)_x = c^{-1}\iint\left[L_2H_y\frac{\partial \psi}{\partial z} + (z-d/2)\left(H_x\frac{\partial \psi}{\partial x} + H_z\frac{\partial \psi}{\partial z}\right)\right]\varepsilon\,dxdz \qquad \text{(A66)}$$

$$= c^{-1}\,\varepsilon\,L_2H_y\iint\frac{\partial \psi}{\partial z}\,dxdz + c^{-1}\,\varepsilon\,H_x\iint z\,\frac{\partial \psi}{\partial x}\,dxdz$$

$$-\frac{c^{-1}\ \varepsilon\, d\, H_z}{2}\iint \frac{\partial\psi}{\partial z}\ d\,x\,dz + c^{-1}\ \varepsilon\ H_z \iint z\ \frac{\partial\psi}{\partial z}\ dxdz$$

$$-\ \frac{c^{-1}\ \varepsilon\ d\ H_x}{2}\iint \frac{\partial\psi}{\partial x}\ dxdz$$

Integrating over the volume of the panel, we get

$$(\vec{T}_i)_x = c^{-1}\ \varepsilon\, L_2 H_y \left\{\sum\left(\frac{h}{n\pi}\right)[1-(-1)^n](B_{n2}+B_{n4})\ \sinh\ \frac{n\pi\, d}{h}\right\}$$

$$+\ c^{-1}\ \varepsilon\ H_x\left\{\sum\ (B_{n1}+B_{n3})\ \sinh\ \frac{n\pi h}{d}\left[-\ \frac{d^2}{n\pi}\ (-1)^n\right]\right\}$$

$$-\frac{c^{-1}\,\varepsilon\, d\, H_z}{2}\left\{\sum\left(\frac{h}{n\pi}\right)[1-(-1)^n]\ (B_{n2}+B_{n4})\ \sinh\ \frac{n\pi d}{h}\right\} \tag{A67}$$

$$+\ c^{-1}\ \varepsilon\, H_z\left[\left\{\ \frac{dh}{n\pi}\ \ B_{n2}\ [1-(-1)^n]\ \sinh\ \frac{n\pi d}{h} - (B_{n3}-B_{n1})\left(\frac{d}{n\pi}\right)^2\right.\right.$$

$$\left([1-(-1)^n]\quad \cosh\frac{n\pi h}{d} - 1\right)$$

$$\left.\left.-\ (B_{n2}-B_{n4})\ (\frac{h}{n\pi})^2\ [1-(-1)^n]\left(\cosh\left(\frac{n\pi d}{h}\right)-1\right)\right\}\right]$$

$$-\ \frac{c^{-1}\ \varepsilon\ d\ H_x}{2}\left\{\sum\ (B_{n1}+B_{n_3})\ \frac{d}{n\pi}\ [1-(-1)^n]\ \sinh\ \left(\frac{n\pi h}{d}\right)\right\}$$

Substituting in for the B_{ni}'s

$$(\vec{T}_1)_x = c^{-1}\ \varepsilon\ L_2 H_y\ \left\{\sum\left(\frac{h}{m\pi}\right)(2)\left[\frac{2b_1}{m\pi}(2)\right] + c^{-1}\ \varepsilon H_x \sum\left[\frac{2b_2{}'}{m\pi}(2)\left(\frac{d^2}{m\pi}\right)\right]\right\}$$

$$-\ \frac{c^{-1}\varepsilon\, d H_z}{2}\left[\sum\left(\frac{h}{m\pi}\right)(2)\ \left(\frac{2b_1{}'}{m\pi}\right)(2)\right] \tag{A68}$$

$$+ \; c^{-1} \epsilon \, H_z \left[\sum \left\{ \frac{dh}{m\pi} (2) \left[\frac{2}{m\pi} \; (b_1{}' + \bar{f}_3 h + \bar{f}_2 h^2) + \frac{2b_1'}{m\pi} - \frac{8\bar{f}_2 h^2}{(m\pi)^3} \right] \right. \right.$$

$$+ \; c^{-1} \epsilon \, H_z \left\{ \sum \left[-\frac{4}{m\pi} (b_2{}' + \bar{f}_1 d + \bar{f}_2 d^2) + \frac{16\bar{f}_2 d^2}{(m\pi)^3} \right] \left(\frac{d}{m\pi} \right)^2 (2) \tanh \left(\frac{m\pi h}{2d} \right) \right.$$

$$+ \; c^{-1} \epsilon \, H_z \left\{ \sum \left[-\frac{4}{m\pi} (b_1{}' + \bar{f}_3 h + \bar{f}_2 h^2) + \frac{16 f_2 h^2}{(m\pi)^3} \right] \left(\frac{h}{m\pi} \right)^2 (2) \tanh \left(\frac{m\pi d}{2h} \right) \right\} \right\}$$

$$- \frac{c^{-1} \epsilon \, d \, H_x}{2} \left\{ \sum \left[\frac{2b_2{}'}{m\pi} (2) \left(\frac{d}{m\pi} \right) \; (2) \right] \right\}$$

and reducing further to

$$(\vec{T}_1)_x = \frac{1}{2} \sigma \, c^{-2} \, \epsilon \, L_2^2 \, h \, d \, (\omega_x H_y - \omega_y H_x) \; H_y$$

$$+ \left\{ \frac{1}{4} \; \sigma \, c^{-2} \, \epsilon \, h \, d^2 \; L_2 - 4 \sigma \, c^{-2} \; \epsilon \; L_2 d^3 \sum \left(\frac{1}{m\pi} \right)^3 \left[\tanh \left(\frac{m\pi h}{2J} \right) + \left(\frac{h}{d} \right)^2 \tanh \left(\frac{m\pi d}{2h} \right) \right] \right\}$$

$$(\omega_x H_y - \omega_y H_x) \; H_z$$

$$+ \left\{ \frac{1}{4} \sigma \, c^{-2} \; \epsilon \, h^2 \; L_2 d - 4 \sigma \, c^{-2} \; \epsilon \; d^2 \; L_2 h \sum \left(\frac{1}{m\pi} \right)^3 \left[\tanh \frac{m\pi h}{2d} + \left(\frac{h}{d} \right)^2 \tanh \; \frac{m\pi d}{2h} \right] \right\}$$

$$(\omega_y H_z - \omega_z H_y) \; H_z$$

$$\left\{ - \frac{1}{4} \sigma \, c^{-2} \; \epsilon \; dh \left(a \, h + \frac{h}{2} \right)^2 + \frac{1}{24} \; \sigma \, c^{-2} \; \epsilon \; d \; h^3 \right. \qquad \text{(A69)}$$

$$+ 4\,\sigma\, c^{-2}\,\varepsilon\, d^2 \left(a h + \frac{h}{2}\right)^2 \sum \left(\frac{1}{m\pi}\right)^3 \left[\tanh\left(\frac{m\pi h}{2d}\right) + \left(\frac{h}{d}\right)^2 \tanh\left(\frac{m\pi d}{2h}\right)\right]$$

$$- 8\,\sigma\, c^{-2}\,\varepsilon\, d^4 \sum \left(\frac{1}{m\pi}\right)^5 \left[\tanh\left(\frac{m\pi h}{2d}\right) + \frac{h}{d}^4 \tanh\left(\frac{m\pi d}{2h}\right)\right]\Bigg\}$$

$$\cdot\ (\omega_z H_x - \omega_x H_z)\, H_z$$

<u>Solution for the y-component of $\vec{T}_1$ --</u>

$$(\vec{T}_1)_y = c^{-1} \iint \left[-(z - d/2)\, H_y \frac{\partial \phi}{\partial z} - (x + a)\, H_y \frac{\partial \phi}{\partial x}\right] \varepsilon\, dxdz$$

Using Cauchy-Riemann conditions, we get

$$(\vec{T}_1)_y = c^{-1} \iint \left[+ (z - d/2)\, H_y \frac{\partial \psi}{\partial x} - (x + a)\, H_y \frac{\partial \psi}{\partial z}\right] \varepsilon\, dxdz \qquad \text{(A70)}$$

$$= c^{-1} \varepsilon\, H_y \iint z \frac{\partial \psi}{\partial x} - c^{-1}\, \varepsilon\, H_y \iint x \frac{\partial \psi}{\partial z}\, dxdz$$

$$- c^{-1} \varepsilon\, H_y a \iint \frac{\partial \psi}{\partial z}\, dxdz \quad - \frac{c^{-1}\,\varepsilon d}{2} H_y \iint \frac{\partial \psi}{\partial x}\, dxdz$$

Integrating, we get

$$(\vec{T}_1)_y = c^{-1} \varepsilon\, H_y \left[-\sum (B_{n1} + B_{n3}) \frac{d^2}{n\pi} \cdot (-1)^n \sinh\left(\frac{n\pi h}{d}\right)\right]$$

$$- c^{-1} \varepsilon\, H_y \left[-\sum (B_{n2} + B_{n4})\, (-1)^n \frac{h^2}{n\pi} \sinh\left(\frac{n\pi d}{h}\right)\right]$$

$$- c^{-1} \varepsilon\, d/2\, H_y \left\{\sum (B_{n1} + B_{n3}) \frac{d}{n\pi} \left[1 - (-1)^n\right] \sinh\left(\frac{n\pi h}{d}\right)\right\}$$

$$- c^{-1} \varepsilon\, H_y a \left\{\sum \left(\frac{h}{n\pi}\right) \left[1 - (-1)^n\right] (B_{n2} + B_{n4}) \sinh\left(\frac{n\pi d}{h}\right)\right\}$$

Substitutions in the B_{ni}'s and reducing to get

$$(\vec{T}_1)_y = -1/2\,\sigma\, c^{-2}\varepsilon\, L_2 d\left(ah+\frac{h}{2}\right)^2 (\omega_x H_y - \omega_y H_x)\, H_y \quad \text{(A71)}$$

then

$$(\vec{T}_1)_y = S_7(\omega_x H_y - \omega_y H_x)\, H_y$$

Solution for the z-component of $\vec{T}_1$ --

$$(\vec{T}_1)_z = c^{-1}\iint\left[-(x+a)\left(H_x\frac{\partial\psi}{\partial x}+H_z\frac{\partial\psi}{\partial z}\right)-L_2 H_y\frac{\partial\psi}{\partial x}\right]\varepsilon\, dxdz$$

$$= c^{-1}\varepsilon H_x\iint x\,\frac{\partial\psi}{\partial x}\,dxdz - c^{-1}\varepsilon H_z\iint x\,\frac{\partial\psi}{\partial z}\,dxdz \quad \text{(A72)}$$

$$- c^{-1} a\varepsilon H_x\iint\frac{\partial\psi}{\partial x}\,dxdz - c^{-1}\varepsilon\, aH_z\iint\frac{\partial\psi}{\partial z}\,dxdz$$

$$- c^{-1} L_2\,\varepsilon H_y\iint\frac{\partial\psi}{\partial x}\,dxdz$$

Integrating, we get

$$(\vec{T}_1)_z = -c^{-1}\varepsilon H_x\left[\sum\left\{B_{n3}\,\frac{hd}{n\pi}\,[1-(-1)^n]\,\sinh\left(\frac{n\pi h}{d}\right)\right.\right.$$

$$+ (B_{n1}-B_{n3})\left(\frac{d}{n\pi}\right)^2[1-(-1)^n]\left(\cosh\left(\frac{n\pi h}{d}\right)-1\right)$$

$$\left.\left. + (B_{n4}-B_{n2})\left(\frac{h}{n\pi}\right)^2[1-(-1)^n]\left(\cosh\left(\frac{n\pi d}{h}\right)-1\right)\right\}\right.$$

$$- c^{-1}\varepsilon H_z\left[-\sum(B_{n2}+B_{n4})\,(-1)^n\frac{h^2}{n\pi}\,\sinh\left(\frac{n\pi d}{h}\right)\right]$$

$$- c^{-1} a \varepsilon H_x \left\{ \sum (B_{n1} + B_{n3}) \frac{d}{n\pi} [1 - (-1)^n] \sinh \left(\frac{n\pi h}{d} \right) \right\}$$

$$- c^{-1} \varepsilon a H_z \left\{ \sum \left(\frac{h}{n\pi} \right) [1-(-1)^n] (B_{n2} + B_{n4}) \sinh \left(\frac{n\pi d}{h} \right) \right\}$$

$$- c^{-1} L_2 \varepsilon H_y \left\{ \sum (B_{n1} + B_{n3}) \frac{d}{n\pi} [1-(-1)^n] \sinh \left(\frac{n\pi h}{d} \right) \right\}$$

Simplifying $(T_1)_z$, we get

$$(\vec{T}_1)_z = \left\{ -\frac{1}{2} \sigma c^{-2} \varepsilon h^2 L_2 d - \frac{1}{2} \sigma c^{-2} \varepsilon d L_2 a h + 4 \sigma c^{-2} \varepsilon h L_2 d^2 \sum \left(\frac{1}{m\pi} \right)^3 \right.$$

$$\left. \left[\tanh \frac{m\pi h}{2d} + \left(\frac{h}{d} \right)^2 \tanh \left(\frac{m\pi d}{2h} \right) \right] \right\} \left[H_x (\omega_y H_z - \omega_z H_y) \right]$$

$$+ \left\{ \frac{1}{2} \sigma c^{-2} \varepsilon h d (ah + h^2/2) + \frac{1}{2} \sigma c^{-2} a \varepsilon d (ah + h^2/2) - \frac{1}{24} \sigma c^{-2} \varepsilon d^3 h \right. \tag{A73}$$

$$- 4 \sigma c^{-2} \varepsilon d^2 (ah + h^2/2 \sum \left(\frac{1}{m\pi} \right)^3 \left[\tanh \left(\frac{m\pi h}{2d} \right) + \left(\frac{h}{d} \right)^2 \tanh \left(\frac{m\pi h}{2h} \right) \right]$$

$$\left. + 8 \sigma c^{-2} \varepsilon d^4 \sum \left(\frac{1}{m\pi} \right)^5 \left[\tanh \left(\frac{m\pi h}{2d} \right) + \left(\frac{h}{d} \right)^4 \tanh \left(\frac{m\pi d}{2h} \right) \right] \right\} \left[H_x (\omega_z H_x - \omega_x H_z) \right]$$

$$+ \left\{ -\frac{1}{4} \sigma c^{-2} \varepsilon L_2 h d^2 + 4 \sigma c^{-2} \varepsilon h^2 d L_2 \sum \left(\frac{1}{m\pi} \right)^3 \left[\tanh \left(\frac{m\pi d}{2h} \right) + \left(\frac{d}{h} \right)^2 \tanh \left(\frac{m\pi h}{2d} \right) \right] \right\}$$

$$\cdot H_x (\omega_x H_y - \omega_y H_x)$$

$$+ \left(- \frac{1}{4} \sigma c^{-2} \varepsilon h^2 L_2 d - \frac{1}{2} \sigma c^{-2} \varepsilon a L_2 h d\right) H_z (\omega_x H_y - \omega_y H_x)$$

$$+ \left[- \frac{1}{2} \sigma c^{-2} \varepsilon L_2^2 \, dh\right] H_y (\omega_y H_z - \omega_z H_y) + \frac{1}{2} \sigma c^{-2} \varepsilon L_2 d(ah + h^2/2) \cdot H_y (\omega_z H_x - \omega_x H_z)$$

Derivation of Torque $\vec{T}_2$ For One Solar Panel

Torque $\vec{T}_2$ is defined by equation

$$\vec{T}_2 = \frac{\sigma c^{-2}}{2} \iiint \vec{r} \times \left\{ [(\vec{\omega} \times \vec{H}) \times \vec{r}] \times \vec{H} \right\} dV \tag{A74}$$

Expanding for solar panels with $J_y = 0$, we get

$$\vec{T}_2 = \frac{\sigma c^{-2}}{2} \iint \left\{ \left[L_2 H_y J_x - (z - d/2)(H_x J_z - H_z J_x) \right] \hat{i} + [-(z-d/2) H_y J_z - (x+a) H_y J_x] \hat{j} + \left[(x+a)\left(H_x J_z - H_z J_x\right) + L_2 J_z H_y \right] \hat{k} \right\} \varepsilon \, dx dz \tag{A75}$$

Solution for $(\vec{T}_2)$ x-Component --

$$(\vec{T}_2)_x = \frac{\sigma c^{-2}}{2} \iint [L_2 H_y (z-d/2)(\omega_z H_x - \omega_x H_z) - L_2^2 H_y (\omega_x H_y - \omega_y H_x)] - (z-d/2) \left\{ H_x \left[L_2 (\omega_y H_z - \omega_z H_y) - (x+a)(\omega_z H_x - \omega_x H_z) \right] - H_z \left[(z-d/2)(\omega_z H_x - \omega_x H_z) - L_2 (\omega_x H_y - \omega_y H_x) \right] \right\} \varepsilon \, dx dz \tag{A76}$$

Integrating, we get

$$(\vec{T}_2)_x = -\frac{\sigma c^{-2}}{2} \varepsilon L_2^2 \, d h \, (\omega_x H_y - \omega_y H_x) H_z + \frac{\sigma c^{-2}}{24} \varepsilon h d^3 \, H_z(\omega_z H_x - \omega_x H_z) \tag{A77}$$

Solution for $(\vec{T}_2)_y$ --

$$(\vec{T}_2)_y = \frac{\sigma c^{-2}}{2} \int_0^{n} \int_0^{d} \Big\{ -(z-d/2)H_y \, [L_2(\omega_y H_z - \omega_z H_y) - (x+a)(\omega_z H_x - \omega_x H_z)] - (x+a)H_y \, [(z-d/2)(\omega_z H_x - \omega_x H_z) - L_2(\omega_x H_y - \omega_y H_x)] \Big\} \, \varepsilon \, dxdz$$

Integrating, we get

$$(\vec{T}_2)_y = \frac{\sigma c^{-2}}{2} \varepsilon L_2 d \left(\frac{h}{2}^2 + ah\right) H_y(\omega_x H_y - \omega_y H_x) \tag{A78}$$

Solution of $(\vec{T}_2)_z$ --

$$(\vec{T}_2)_z = \frac{\sigma c^{-2}}{2} \int_0^d \int_0^h \Big[(x+a) \, \{ H_x [L_2(\omega_y H_z - \omega_z H_y) - (x+a)(\omega_z H_x - \omega_x H_z)] - H_z[(z-d/2)(\omega_z H_x - \omega_x H_z) - L_2(\omega_x H_y - \omega_y H_x)] \} + L_2 H_y \, [L_2(\omega_y H_z - \omega_z H_y) - (x+a)(\omega_z H_x - \omega_x H_y)] \Big] \, \varepsilon \, dxdz \tag{A79}$$

Integrating, we get

$$(\vec{T}_2)_z = \frac{\sigma c^{-2}}{2} \varepsilon L_2 d(ah + h^2/2) H_x(\omega_y H_z - \omega_z H_y)$$

$$- \frac{\sigma c^{-2}}{2} \varepsilon \left(\frac{dh^3}{3} + a\,d\,h^2 + a^2\,hd \right) H_x \left(\omega_z H_x - \omega_x H_z \right)$$

$$+ \frac{\sigma c^{-2}}{2} \varepsilon\, L_2 d\, (ah + h^2/2)\, H_z (\omega_x H_y - \omega_y H_x) \tag{A80}$$

$$+ \frac{\sigma c^{-2}}{2} \varepsilon\, L_2{}^2 h\, d\, H_y (\omega_y H_z - \omega_z H_y)$$

$$- \frac{\sigma c^{-2}}{2} \varepsilon\, L_2\, d(ah + h^2/2)\, H_y (\omega_z H_x - \omega_x H_z)$$

Total Torque for Six Panels

Sum of $\vec{T}_1 + \vec{T}_2$ for one Panel --

Using Equations (A69) and (A77), then

$$(\vec{T}_1)_x + (\vec{T}_2)_x = (\vec{T}_T)_x$$

$$(\vec{T}_T)_x = \left\{ \frac{1}{4} \sigma c^{-2} \varepsilon\, L_2 h\, d^2 - 4 \sigma c^{-2} \varepsilon\, L_2\, d^3 \sum \left(\frac{1}{m\pi} \right)^3 \left[\tanh \left(\frac{m\pi h}{2d} \right) + \left(\frac{h}{d} \right)^2 \tanh \left(\frac{m\pi d}{2h} \right) \right] \right\} H_z (\omega_x H_y - \omega_y H_x)$$

$$+ \left\{ \frac{1}{4} \sigma c^{-2} \varepsilon\, L_2 h^2 d - 4 \sigma c^{-2} \varepsilon L_2 d^2 h \sum \left(\frac{1}{m\pi} \right)^3 \left[\tanh \left(\frac{m\pi h}{2d} \right) + \left(\frac{h}{d} \right)^2 \tanh \left(\frac{m\pi d}{2h} \right) \right] \right\} H_z (\omega_y H_z - \omega_z H_y)$$

$$+ \left\{ - \frac{1}{4} \sigma c^{-2} \varepsilon\, d\, h(ah + h^2/2) + \frac{1}{12} \sigma c^{-2} \varepsilon\, dh^3 \right.$$

$$+ 4\sigma c^{-2} \varepsilon\, d^2 (ah + h^2/2) \sum \left(\frac{1}{m\pi}\right)^3 \left[\tanh\left(\frac{m\pi h}{2d}\right) + \left(\frac{h}{d}\right)^2 \tanh\left(\frac{m\pi d}{2h}\right) \right]$$

$$\left. - 8 \sigma c^{-2} \varepsilon\, d^4 \sum \left(\frac{1}{m\pi}\right)^5 \left[\tanh\left(\frac{m\pi h}{2d}\right) + \left(\frac{h}{d}\right)^4 \tanh\left(\frac{m\pi d}{2h}\right) \right] \right\}$$

$$\cdot\ H_z(\omega_z H_x - \omega_x H_z)$$

and

$$(\vec{T}_T)_y = 0 \tag{A81}$$

Using Equations (A73) and (A80), then

$$(\vec{T}_1)_z + (\vec{T}_2)_z = \left\{ - \frac{1}{4} \sigma c^{-2} \varepsilon L_2 dh^2 + 4\sigma c^{-2} \varepsilon\, h L_2\, d^2 \sum \left(\frac{1}{m\pi}\right)^3 \tanh\left(\frac{m\pi h}{2d}\right) \right.$$

$$\left. + \left(\frac{h}{d}\right)^2 \tanh\left(\frac{m\pi d}{2h}\right) \right\} H_x(\omega_y H_z - \omega_z H_y)$$

$$+ \left\{ \sigma c^{-2} \varepsilon\, \frac{h^3 d}{3} + \frac{3}{4} \sigma c^{-2} \varepsilon\, adh^2 \right.$$

$$- \frac{1}{24} \sigma c^{-2} \varepsilon\, d^3 h \tag{A82}$$

$$- 4 \sigma c^{-2} \varepsilon\, d^2 (ah + h^2/2) \sum \left(\frac{1}{m\pi}\right) \left[\tanh\left(\frac{m\pi h}{2d}\right) + \left(\frac{h}{d}\right)^2 \tanh\left(\frac{m\pi d}{2h}\right) \right]$$

$$+ 8\sigma c^{-2}\varepsilon\, d^4 \sum \left(\frac{1}{m\pi}\right)^5 \left[\tanh\left(\frac{m\pi h}{2d}\right) + \left(\frac{h}{d}\right)^4 \tanh\left(\frac{m\pi d}{2h}\right)\right]\Bigg\}$$

$$\bullet\ H_x (\omega_z H_x - \omega_x H_z)$$

$$+ \Bigg\{ - \frac{1}{4}\sigma c^{-2}\varepsilon\, L_2 h d^2 + 4\sigma c^{-2}\varepsilon\, h^2 L_2\, d \sum \left(\frac{1}{m\pi}\right)^3$$

$$\left[\tanh\left(\frac{m\pi d}{2h}\right) + \left(\frac{h}{d}\right)^2 \tanh\left(\frac{m\pi d}{2d}\right)\right]\Bigg\}\ H_x(\omega_x H_y - \omega_y H_x)$$

SUMMARY OF $\vec{T}$ DUE TO ONE SOLAR PANEL (IN PRIMED FRAME)

$$(\vec{T})_x{}' = K_{x1} H_z{}'(\omega'_x H'_y - \omega'_y H'_x) + K_{x2} H'_z(\omega'_y H'_z - \omega'_z H'_y)$$

$$+ K_{x3} H'_z (\omega'_z H'_x - \omega'_x H'_z) \qquad \text{(A83)}$$

$$(\vec{T})_y{}' = 0$$

$$(T)_z{}' = K_{z1} H'_x(\omega'_y H'_z - \omega'_z H'_y) + K_{z2} H'_x(\omega'_z H'_x - \omega'_x H'_z)$$

$$+ K_{z3} H'_x(\omega'_x H'_y - \omega'_y H'_x)$$

Using the technique discussed under "Torque Due to Cylinder" the torque for six solar panels is derived in the following paragraphs.

The torque resolved in one frame is

$$\vec{T}(i)_x = T'(i)_x \cos\theta + T'(i)_z \sin\theta$$

$$\vec{T}(i)_y = T'(i)_y$$

$$\vec{T}(i)_z = [- T'(i)_x \sin\theta + T'(i) \cos\theta]$$

where the prime indicates the torque for i^{th} panel in the i^{th} frame,

and where

$$H_x' = H_x \cos\theta - H_z \sin\theta$$

$$H_y' = H_y$$

$$H_z' = H_x \sin\theta + H_z \cos\theta$$

The solution for $(\vec{T}_x)$ (six panels) is

$$\begin{aligned}
\left(\vec{T}(i)\right)_x = & \Big[K_{x1}H_z' (\omega_x'H_y' - \omega_y'H_x') + K_{x2}H_z'(\omega_y' H_z' - \omega_z'H_y') \\
& + K_{x3}H_z'(\omega_z'H_x' - \omega_x'H_z')\Big]\cos\theta\,(i) \qquad \text{(A84)} \\
& + \Big[K_{z1}\, H_x'(\omega_y'H_z' - \omega_z'H_y') + K_{z2}H_x'(\omega_z'H_x' - \omega_x'H_z') \\
& + K_{z3}\, H_x'(\omega_x'H_y' - \omega_y' H_x')\Big] \sin\theta(i)
\end{aligned}$$

$$\begin{aligned}
\sum_{i=1}^{6} T(i)_x = (\vec{T})_x &= -3K_{x3}(\omega_x H_z{}^2 - \omega_z H_x H_z) + 3K_{z2}(\omega_x H_z{}^2 - \omega_z H_x H_z) \\
&= -3(K_{x3} - K_{z2})\,\omega_x H_z{}^2 + 3(-K_{z2} + K_{x3})\,\omega_z H_x H_z
\end{aligned}$$

where

$$\begin{aligned}
K_{x3} - K_{z2} = \Bigg\{ & -\frac{1}{4}\sigma c^{-2}\epsilon dh(ah + h^2/2) + \frac{1}{12}\sigma c^{-2}\epsilon\, dh^3 \\
& + 4\sigma c^{-2}\epsilon\, d^2(ah + h^2/2)\sum \left(\frac{1}{m\pi}\right)^3 \left[\tanh\left(\frac{m\pi h}{2d}\right) + \left(\frac{h}{d}\right)^2 \tanh\left(\frac{m\pi d}{2h}\right)\right] \\
& - 8\sigma c^{-2}\epsilon\, d^4 \sum{}' \left(\frac{1}{m\pi}\right)^5 \left[\tanh\left(\frac{m\pi h}{2d}\right) + \left(\frac{h}{d}\right)^4 \tanh\left(\frac{m\pi d}{2h}\right)\right]\Bigg\}
\end{aligned}$$

$$- \Bigg\{ \sigma c^{-2} \varepsilon \frac{h^3 d}{3} + \frac{3}{4} \sigma c^{-2} \varepsilon\, a d h^2 - \frac{1}{24} \sigma c^{-2} \varepsilon d^3 h$$

$$- 4 \sigma c^{-2} \varepsilon d^2 (ah + h^2/2) \sum \left(\frac{1}{m\pi}\right)^3 \left[\tanh\left(\frac{m\pi h}{2d}\right) + \left(\frac{h}{d}\right)^2 \tanh\left(\frac{m\pi d}{2h}\right) \right]$$

$$+ 8 \sigma c^{-2} \varepsilon d^4 \sum \left(\frac{1}{m\pi}\right)^5 \left[\tanh\left(\frac{m\pi h}{2d}\right) + \left(\frac{h}{d}\right)^4 \tanh\left(\frac{m\pi d}{2h}\right) \right] \Bigg\}$$

Reducing further to

$$(K_{x3} - K_{z2}) = \Bigg\{ - \sigma c^{-2} \varepsilon\, a d h^2 - \frac{9}{24} \sigma c^{-2} \varepsilon\, d h^3 - \frac{1}{24} \sigma c^{-2} \varepsilon d^3 h$$

$$+ 8 \sigma c^{-2} \varepsilon d^2 (ah + h^2/2) \sum \left(\frac{1}{m\pi}\right)^3 \left[\tanh \frac{m\pi h}{2d} + \left(\frac{h}{d}\right)^2 \tanh\left(\frac{m\pi d}{2h}\right) \right]$$

$$- 16 \sigma c^{-2} \varepsilon d^4 \sum \left(\frac{1}{m\pi}\right)^5 \left[\tanh\left(\frac{m\pi h}{2d}\right) + \left(\frac{h}{d}\right)^4 \tanh\left(\frac{m\pi d}{2h}\right) \right] \Bigg\}$$

and the solution for $(\vec{T}_1)_y$ is

$$(\vec{T})_y = 0 = \Sigma \; [\, T(i)]_y$$

and solution for $(\vec{T})_z$ is

$$\Sigma \; T(i)_z = \vec{T}_z = 3(K_{z2} - K_{x3}) \; (\omega_z H_x{}^2 - \omega_x H_x H_z) \qquad \text{(A85)}$$

SUMMARY OF TORQUE DUE TO SOLAR PANEL

$$\vec{T}_x = -3 \; (K_{x3} - K^1_{z3})(\omega_x H_z{}^2 - \omega_z H_x H_z)$$

$$\vec{T}_y = 0 \qquad \text{(A86)}$$

$$T_z = - 3(K_{x3} - K'_{z2})(\omega_z H_x{}^2 - \omega_x H_x H_z)$$

where $(K_{x3} - K_{z2})$ is given above.

SUM OF TORQUE DUE TO PANEL'S AND CYLINDER

EQUATIONS

$$(\vec{T})_x = -\underbrace{3/2\ K_{z2}}_{P_{x1}}(\omega_x H_y{}^2 - \omega_y H_x H_y) - 3\underbrace{(K_{x3} - K}_{P_{x2}}{}_{z2})(\omega_x H_z{}^2 - \omega_z H_x H_z)$$

$$(\vec{T})_y = \underbrace{9/2\ K_{y2}}_{P_y}\ [\omega_y(H_x{}^2 + H_z{}^2) - \omega_x H_x H_y - \omega_z H_y H_z] \qquad \text{(A87)}$$

$$(\vec{T})_z = -\underbrace{3/2\ K_{z2}}_{P_{x1}}(\omega_z H_y{}^2 - \omega_y H_y H_z) - \overbrace{3(K_{x3} - K_{z2})}^{P_{x2}}\ (\omega_z H_x{}^2 - \omega_x H_x H_z)$$

where

$$\begin{aligned} P_{x1} &= 3/2K_{z2} \\ &= \Big\{\tfrac{1}{2}\ \sigma c^{-2}\ \tau W L^3 + \tfrac{1}{8}\sigma c^{-2}\ \tau\ LW^3 - \tfrac{3}{4}\sigma c^{-2}\ \tau\ L_1 L^2 W \\ &+ \tfrac{3}{2}\ \sigma c^{-2}\ \tau\ L\ W\ (L_1 L - L^2/2 - 12\ \sigma c^{-2}\ \tau\ W^2(L_1 L - L^2/2) \\ &\quad \cdot \sum\left(\frac{1}{m\pi}\right)^3 \left[\tanh\left(\frac{m\pi L}{2W}\right) + \left(\frac{L}{W}\right)^2 \tanh\left(\frac{m\pi W}{2L}\right)\right] \\ &- 24\ \sigma c^{-2}\ \tau\ W^4 \sum\left(\frac{1}{m\pi}\right)^5 \left[\tanh\left(\frac{m\pi L}{2W}\right) + \left(\frac{L}{W}\right)^4\ \tanh\left(\frac{m\pi W}{2L}\right)\right] \end{aligned} \qquad \text{(A88)}$$

and

$$P_{x2} = P_{z2} = 3(K_{x3} - K_{z2})$$

$$= \Bigg\{ - 3\,\sigma\, c^{-2} \varepsilon\, a d h^2 - \frac{9}{8}\,\sigma c^{-2} \varepsilon\, a d h^3 - \frac{1}{8}\sigma c^{-2} \varepsilon\, d^3 h$$

$$+ 24\,\sigma\, c^{-2} \varepsilon\, d^2 (ah + h^2/2) \sum \left(\frac{1}{m\pi}\right)^3 \left[\tanh \frac{m\pi h}{2d} + \left(\frac{h}{d}\right)^2 \tanh\left(\frac{m\pi d}{2h}\right)\right] \quad \text{(A89)}$$

$$- 48\,\sigma c^{-2} \varepsilon\, d^4 \sum \left(\frac{1}{m\pi}\right)^5 \left[\tanh\left(\frac{m\pi h}{2d}\right) + \left(\frac{h}{d}\right)^4 \tanh\left(\frac{m\pi d}{2h}\right)\right] \Bigg\}$$

$$P_y = 9/2\, K_{y2}$$

$$= \Bigg\{ - \frac{3}{8} c^{-2} \sigma\,\tau\, W^3 L - \frac{3}{8}\sigma c^{-2} \tau\, W L^3 - \frac{9}{4}\sigma\, c^{-2}\, \tau\, W L\, (L_1 L - L/2^2)$$

$$+ 36\,\sigma\, c^{-2}\, \tau\, W^2 (L_1 L - L^2/2) \sum \left(\frac{1}{m\pi}\right)^3 \left[\tanh\left(\frac{m\pi L}{2W}\right) + \left(\frac{L}{W}\right)^2 \tanh\left(\frac{m\pi W}{2L}\right)\right]$$

$$+ 72\,\sigma\, c^{-2}\, \tau\, W^4 \sum \left(\frac{1}{m\pi}\right)^5 \left[\tanh\left(\frac{m\pi L}{2W}\right) + \left(\frac{L}{W}\right)^4 \tanh\left(\frac{m\pi W}{2L}\right)\right] \Bigg\} \quad \text{(A90)}$$

DISCUSSION

The solution given by Equations (A87), (A89), and (A90) represent the torque for the geometry described for the ARRS spacecraft. The coefficients are in terms of the spacecraft dimension and can be used to aid in the design of the spacecraft to minimize the eddy current losses. Three coefficients exist for the spinning hat configuration. Evaluation of the coefficient will establish the relative significance.

The solution for the potential, ϕ presented initially a problem which was eventually overcome. First, numerical techniques were considered to evaluate ϕ, but were quickly overruled because numerical solution would be needed every time the torque is evaluated (0.4 sec per HDMP Phase A, Part II).

Secondly, the two-dimensional Neumann problem can be be reduced to a Dirichlet boundary value problem and a solution for the stream function, ψ, made. Two approaches were considered in the solution for ψ: (1) solution by application of Green's function, and (2) series of sine, cosine, and hyperbolic sine and cosine.

The second solution method had initial difficulty. The solution for the plate was a series of sines and hyperbolic sine for the stream function, ψ. Since $\nabla\psi$ was required, it was clear $\nabla\psi$ could not be obtained from ψ. However, because the torque equation is a volume integral and by applying integration by parts, the gradient of ψ was not required. The solution for the torque was then good. Further effort to apply Green's function was suspended.

APPENDIX B
AERODYNAMIC TORQUE

PRECEDING PAGE BLANK NOT FILMED.

APPENDIX B
AERODYNAMIC TORQUE

The aerodynamic effect on the spacecraft is discussed in the following paragraphs. The torque produced consists of aerodynamic pressure torque due to the spacecraft's center of mass velocity and a dissipative torque due to the spacecraft's angular rate. The torque equation including these two effects is taken from Beletskii's work(ref.3). The torque equation including these two effects is craft's angular velocity is large compared with the rotation of the atmosphere (earth's rate approximately), the linear surface velocities due to the spin of the satellite is small compared with the spacecraft's center of mass velocity, and the angle of attack of each surface encountered is less than $\frac{\pi}{2}$. The torque equation is then given by

$$\vec{T} = \frac{1}{2} c \rho_a V_o^2 \int_{S(\vec{n}\cdot\vec{e}_v > o)} (\vec{n}\cdot\vec{e}_v)(\vec{e}_v \times \vec{r}_s)\, dS$$

$$+ \frac{1}{2} c \rho_a V_o \int_{S(\vec{n}\cdot\vec{e}_v > o)} \left[\left(\vec{n}\cdot\left[\vec{\omega}\times\vec{r}_s\right]\right) \left(\vec{e}_v \times \vec{r}_s\right) + (\vec{n}\cdot\vec{e}) \left[\vec{\omega}\times\vec{r}_s\right] \times \vec{r}_s \right] dS \qquad \text{(B1)}$$

where

$\vec{n}$ = Unit vector in direction of normal to surface, dS

$\vec{e}_v = \frac{\vec{V}_o}{|\vec{V}_o|}$ = Unit vector in direction of translational velocity of center of mass relative to incident stream

$\vec{r}_s$ = Radius vector joining surface element center and spacecraft center of mass

The first term of Equation (B1) represents torque due to misalignment of spacecraft center of mass and center of pressures. The second term represents dissipative torque due to spacecraft spin. Upon examining the coefficient of each term, the torque due to center of pressure misalignment is approximately a factor of V_o larger than the dissipative torque coefficient when $\omega r << V_o$. For ARRS spacecraft in a 270-nautical-mile orbit, V_o is 2.624×10^4 ft/sec.

Previous investigations estimated that $\frac{1}{2} c \rho_a V_o^2$ is 2×10^{-7} lb/ft^2. Then, dividing by V_o, we get 0.76×10^{-11} lb-sec/ft^3. Multiplying by $\omega r = 2$ ft for ARRS spacecraft, $\frac{1}{2} c \zeta_a V_o \omega r \approx 10^{-12}$ lb/ft^2.

Dissipative torque is a factor of 10^{-4} less than pressure torque and is sufficiently small that the second term of Equation (B1) will be neglected. Then, the aerodynamic torque equation is given by

$$\vec{T} = \frac{1}{2} c \rho_a V_o^2 \int_{S(\vec{n} \cdot \vec{e}_v > 0)} (\vec{n} \cdot \vec{e}_v)(\vec{e}_v x \vec{r}_s)\, dS \tag{B2}$$

The domain of integration is indicated by $S(\vec{n} \cdot \vec{e}_v > 0)$. This means the angle of attack of each surface element is less than $\frac{\pi}{2}$. The ARRS spacecraft surfaces consist of a hexagonal cylinder and rectangular solar panels.

The direction of the stream is in the orbit plane, and for this reason the spacecraft will present a different surface to the stream, depending on the attitude of the vehicle.

Figure B1 illustrates two orientations of the spacecraft that give two different domains for Equation (B2).

The aerodynamic torque will be represented by two equations because of the different surfaces presented to the stream as shown in Figure B1. In Figure 1b, the force along the y-axis due to the stream is positive. Figure B1a illustrates that the force along the y-axis is negative.

DERIVATION OF TORQUE FOR $F_y \leq 0$

The computation can be done on each surface and summed over the domain of integration. The spacecraft has two basically different geometries -- a hexagonal cylinder and solar panels. The hexagonal cylinder is comprised of six planes as shown in Figure B2. The body coordinates are also shown in Figure B2.

Torque on the cylinder is computed by integrating over each of the surfaces ($i = 1, \ldots 6$) and using only those torques on the surfaces which satisfy $n_i \cdot \vec{e}_v > 0$.

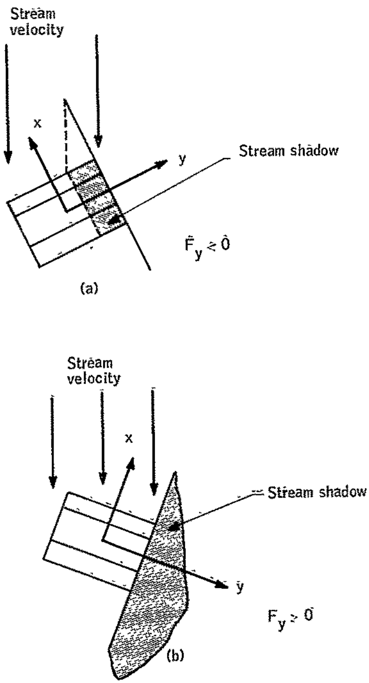

Figure B1. Spacecraft Shadowing

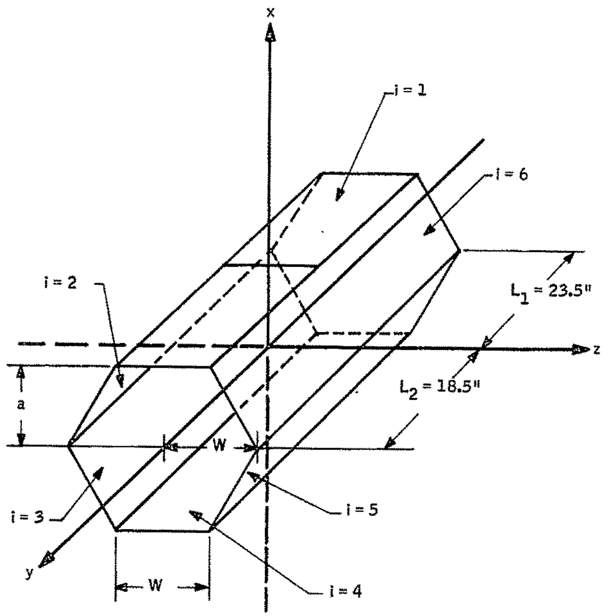

Note:
Surfaces, i = 1, 2, . . ., 6 are indicated in the figure. The normal to each one of the six surface is given by n_i. The origin of coordinate system is located at spacecraft's center of mass.

Figure B2. Spacecraft Hexagonal Cylinder Configuration

Surface i = 1 The outer normal of surface 1 is

$$n_1 = \hat{i} \tag{B3}$$

The radius vector, $\vec{r}_{s1}$, is given by

$$\vec{r}_{s1} = a\hat{i} + y\hat{j} + z\hat{k} \tag{B4}$$

The integral from Equation (B2) becomes

$$\vec{T}_{c1} = q_2(\vec{n}_1 \cdot \vec{e}_v)\, e_v x \int r_{s1} dS_1 \tag{B5}$$

The integral to be solved is

$$\iint (a\hat{i} + y\hat{j} + z\hat{k})\, dydz \tag{B6}$$

The limits of integration are

$$- L_1 \le y \le L_2, \; - \frac{W}{2} \le z \le \frac{W}{2}$$

$$a = \frac{\sqrt{3}W}{2} \text{ a constant} \tag{B7}$$

Integrating Equation (B6), one gets

$$\frac{\sqrt{3}W^2}{2} L\hat{i} + \frac{W}{2} \left(L_2^2 - L_1^2\right) \hat{j} \tag{B8}$$

Therefore,

$$\vec{T}_{c1} = q_2 (\vec{n}_1 \cdot \vec{e}_v)\, \vec{e}_v x \left[\frac{\sqrt{3}W^2}{2} L\hat{i} + \frac{W}{2} \left(L_2^2 - L_1^2\right) \hat{j}\right] \tag{B9}$$

Surface i = 2 Notice that the integration of each surface can be done in a coordinate frame like the i = 1 surface. To represent the results in the coordinate frame shown in Figure B2, a coordinate transformation involving a single rotation about the y-axis will do. Figure B3 illustrates the technique.

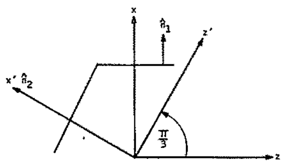

Figure B3. Relationship of Integration Coordinate Frame to Spacecraft Body Frame

A positive 60-degree rotation about the y-axis places $\dot{x}'$ along surface n_2 normal. The integration in the prime system is identical to the unprimed on the n_1 surface. Therefore, the integration of each surface can be carried out in the primed system and then transformed to the unprimed system by the following:

$$\begin{bmatrix} x \\ \dot{y} \\ z \end{bmatrix} = \begin{bmatrix} \cos \frac{\pi}{3}(i-1) & 0 & \sin \frac{\pi}{3}(i-1) \\ 0 & 1 & 0 \\ -\sin \frac{\pi}{3}(i-1) & 0 & \cos \frac{\pi}{3}(i-1) \end{bmatrix} \cdot \begin{bmatrix} x^{(i-1)} \\ y^{(i-1)} \\ z^{(i-1)} \end{bmatrix} \qquad \text{(B10)}$$

where

$$x^{(i-1)} = x = \frac{\sqrt{3}W^2}{2} L \qquad \text{(B11)}$$

$$y^{(i-1)} \doteq y = \frac{W}{2}\left(L_2^2 - L_1^2\right)$$

$$z^{(i-1)} = z = 0$$

Therefore,

$$\vec{T}_{ci} = q_2(\vec{n}_i \cdot \vec{e}_v)\vec{e}_v x \left[\cos\frac{\pi}{3}(i-1)\frac{\sqrt{3}W^3}{2}L\right]\hat{i} + \frac{W}{2}\left(L_2^2 - L_1^2\right)\hat{j} - \frac{\sqrt{3}W^3}{2}L\sin\frac{\pi}{3}(i-1)\hat{k} \tag{B12}$$

where

$$n_i = \sin\ 90+\frac{\pi}{3}(i-1)\ \hat{i}+\cos\ 90+\frac{\pi}{3}(i-1)\hat{k} = \cos\frac{\pi}{3}(i-1)\hat{i} - \sin\frac{\pi}{3}(i-1)\hat{k}$$

Equation (B12) represents the torque for each plane describing the hexagonal cylinder. To obtain the torque on the cylinder each surface must be tested for

$$\vec{n}_i \cdot \vec{e}_v > 0 \tag{B13}$$

For surfaces which satisfy $\vec{n}_i \cdot \vec{e}_v > 0$, the torque is given Equation (B20). The sum is then taken over all surfaces that satisfy Equation (B13).

Torque due to the solar panels will now be computed in the same manner. Assume that the solar panels can be approximated by a disk as shown in Figure B4.

The torque equation for the disk when $F_y \geq 0$ is given by

$$\vec{T} = \frac{1}{2}c\rho_a V_o^2 \int_{S(\vec{n}\cdot\vec{e}_v > 0)} (\vec{n}\cdot\vec{e}_v)(\vec{e}_v x\vec{r}_s)dS$$

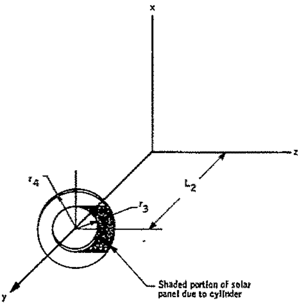

Figure B4. Shadowing on Solar Panel due to Spacecraft Cylinder

For the disk the normal to the surface is

$$n = -\hat{j} \tag{B14}$$

Figure B4 shows the shadow when e_v is directed along the negative z-axis. The shadow moves around the disk as the spacecraft rotates. The integral

$$r_s dS \tag{B15}$$

must be evaluated for each time because the domain of integration is changing with time. The approach will be to integrate over the domain shown in Figure B4 and make a time-varying transformation about the body y-axis to give the integrated result as a function of time.

The integration will be performed over the shaded area of Figure B4, and the results subtracted from the integrated result over the entire disk defined between r_3 and r_4. The result will be good for $\theta = 0$ when $\hat{e}_v \cdot k = -1$. The shaded area rotates negatively about the y-axis; therefore, the transformation from the primed system (system in which the shaded area has the relation shown in Figure B5 to the unprimed (the body axis where the shade rotates about the body y-axis) will be made to give the result for all time.

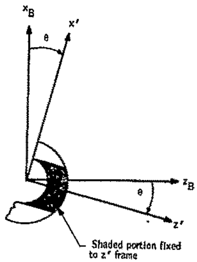

Figure B5. Transformation of Rotating Shade Frame Relative to Body Fixed Axis

The transformation is

$$\begin{bmatrix} x \\ y \\ z \end{bmatrix} = \begin{bmatrix} \cos\theta & 0 & -\sin\theta \\ 0 & 1 & 0 \\ \sin\theta & 0 & \cos\theta \end{bmatrix} \begin{bmatrix} x' \\ y' \\ z' \end{bmatrix} \tag{B16}$$

The integral is given by Equation(B15) and r_s is

$$x\hat{i} + L_2\hat{j} + z\hat{k} \tag{B17}$$

and $dS = dxdz$.

Therefore,

$$\int xdxdz\hat{i} + \int L_2 dxdz\hat{j} + \int zdxdz\hat{k} \tag{B18}$$

The integration will first be conducted over the entire disk defined between r_3 and r_4. Call this surface S'. The integration over S' is obtained by integrating over the large disk whose radius is r_4 and subtracting the value obtained by integrating over the small disk whose radius is r_3.

Let S'' be the large disk, and S''' be the small disk. Therefore,

$$\int_{S'} r ds = \int_{S''} r ds - \int_{S'''} r ds \tag{B19}$$

The limits of integration over S'' are

$$-r_4 \leq x \leq r_4$$

$$-\sqrt{r_4^2 - x^2} \leq z \leq \sqrt{r_4^2 - x^2}$$

The integal then is

$$\int_{-r_4}^{r_4} \int_{-\sqrt{r_4^2 - x^2}}^{\sqrt{r_4^2 - x^2}} (x dx dz \hat{i} + L_2 dx dz \hat{j} + z dx dz \hat{k}) \tag{B20}$$

and gives

$$\int_{-r_4}^{r_4} \left[2 x \sqrt{r_4^2 - x^2} \; dx \hat{i} + 2L_2 \sqrt{r_4^2 - x^2} \; dx \hat{j}\right] \tag{B21}$$

$$\int_{S''} r ds = L_2 \pi r_4^2 \hat{j} \tag{B22}$$

Integrating over S''' surface, a similar result is obtained

$$\int_{S'''} \vec{r}ds = L_2 \pi r_3^2 \hat{j} \tag{B23}$$

Therefore,

$$\int_{S'} \vec{r}ds = L_2 \pi (r_4^2 - r_3^2) \hat{j} \tag{B24}$$

The integration over the shaded area given in Figure B4 will now be carried out. The limits of integration are given by

$$-r_3 \leq x \leq r_3$$

$$\sqrt{r_3^2 - x^2} \leq z \leq \sqrt{r_4^2 - x^2}$$

The integral is

$$\int_{-r_3}^{r_3} \int_{-\sqrt{r_3^2 - x^2}}^{\sqrt{r_4^2 - x^2}} (xdxdz\hat{i} + L_2 dxdz\hat{j} + zdxdz\hat{k}) = \int_{S^*} \vec{r}dS \tag{B25}$$

where S^* is the domain of integration of the shaded area.

Therefore,

$$\int_{S^*} \vec{r}dS = \left[\left[L_2 r_3 \left(r_4^2 - r_3^2\right)^{1/2} + L_2 r_4^2 \sin^{-1}\left(\frac{r_3}{r_4}\right) \frac{-L_2 \pi r_3^2}{2}\right]\hat{j} + r_3 \left(r_4^2 - r_3^2\right) \hat{k}\right] \tag{B26}$$

The integral of the unshaded portion of the disk in Figure B4 is given by

$$\int_{S'} r dS - \int_{S^*} r dS \tag{B27}$$

For Equation (B27) is true for all time $t \geq t_o$ when Equation (B26) is modified by Equation (B16) to give

$$\begin{aligned} x &= \sin\theta \; r_3 \left(r_4^2 - r_3^2\right) \\ y &= L_2 r_3 \left(r_4^2 - r_3^2\right)^{1/2} + L_2 r_4^2 \sin^{-1}\left(\frac{r_3}{r_4}\right) - \frac{\pi}{2} L_2 r_3^2 \\ z &= \cos\theta \; r_3 \left(r_4^2 - r_3^2\right) \end{aligned} \tag{B28}$$

Then,

$$\begin{aligned} \int_{S'} r dS - \int_{S^*} r dS \\ &= \left[r_3\left(r_4^2 - r_3^2\right) \sin\theta\right] \hat{i} \\ &+ \left[L_2 \pi\left(r_4^2 - r_3^2\right) - L_2 r_3 \left(r_4^2 - r_3^2\right)^{1/2} - L_2 r_4^2 \sin^{-1}\left(\frac{r_3}{r_4}\right) + \frac{\pi}{2} L_2 r_3^2\right] \hat{j} \\ &- \left[r_3\left(r_4^2 - r_3^2\right) \cos\theta\right] \hat{k} \end{aligned} \tag{B29}$$

The torque for the solar panels is

$$\vec{T} = \frac{1}{2} c \rho_a V_o^2 (\vec{n} \cdot \vec{e}_v) \vec{e}_v x \left[r_3 \left(r_4^2 - r_3^2 \right) \sin \theta \right] \hat{i}$$

$$+ \left[L_2 \pi r_4^2 - \frac{L_2}{2} \pi r_3^2 - L_2 r_3 \left(r_4^2 - r_3^2 \right)^{1/2} - L_2 r_4^2 \sin^{-1} \left(\frac{r_3}{r_4} \right) \hat{j} \right. \tag{B30}$$

$$\left. - r_3 \left(r_4^2 - r_3^2 \right) \cos \theta \ \hat{k} \right]$$

Torque due to the cylinder and solar panels is summarized below for the case where $\vec{e}_v \cdot \hat{j} \leq 0$ or $F_y \geq 0$.

Torque due to each plane surface of the cylinder is given by

$$\vec{T}_{ci} = q_2 (\vec{n}_i \cdot \vec{e}_v) \vec{e}_v x \left[\frac{\sqrt{3} W^3}{2} L \cos \frac{\pi}{3} (i-1) \hat{i} + \frac{W}{2} \left(L_2^2 - L_1^2 \right) \hat{j} \right.$$

$$\left. - \frac{\sqrt{3} W^3}{2} L \sin \frac{\pi}{3} (i-1) \hat{k} \right] \tag{B31}$$

where

$$q_2 = \frac{1}{2} c \rho_a V_o^2$$

$$n_i = \cos \frac{\pi}{3} (i-1) \hat{i} - \sin \frac{\pi}{3} (i-1) \hat{k}$$

$$\vec{T} = \frac{1}{2} c \rho_a V_o^2 (\vec{n} \cdot \vec{e}_v) \vec{e}_v x \left[\left(r_3 \left(r_4^2 - r_3^2 \right) \sin \theta \right) \hat{i} \right.$$

$$+ L_2 \pi r_4^2 - \frac{L_2 \pi r_3^2}{2} - L_2 r_3 \left(r_4^2 - r_3^2 \right)^{1/2} - L_2 r_4^2 \sin^{-1} \left(\frac{r_3}{r_4} \right) \hat{j}$$

$$\left. - \left(r_3 \left(r_4^2 - r_3^2 \right) \cos \theta \right) \hat{k} \right] \tag{B32}$$

where $n = -\hat{j}$. The torques expressed in Equations (B30) and (B31) are valid when $\vec{e}_v \cdot j \leq 0$ or $F_y \geq 0$.

The angle, θ, is given by

$$\sin\theta = v_x / \sqrt{1 - v_y^{\,2}}$$

$$\cos\theta = -v_z / \sqrt{1 - v_y^{\,2}}$$

where v_x, v_y, and v_z are the components of the $\vec{e}_v$ vector in body axes.

The end of the cylinder (opposite solar panel end - see Figure B1b) contributes a torque when $\hat{e}_v \cdot (-\hat{j}) > 0$.

The torque is given by

$$\vec{T}_{CE} = q_2(\vec{n} \cdot \vec{e}_v)\vec{e}_v x \int r_{SE} dS_E$$

$$r_{SE} = x\hat{i} - L_1\hat{j} + z\hat{k}$$

Integrating

$$\int r_{SE} dS_E = -L_1 \pi r_3^2 \,\hat{j} \qquad \text{(B33)}$$

This assumes that the end is a disk of radius r_3 located at a $-L_1$ distance along the y-axis.

DERIVATION OF TORQUE FOR $e_v \cdot \hat{j} > 0$ or $F_y \leq 0$

Torque due to aerodynamic pressure is different for $\vec{e}_v \cdot \hat{j} > 0$ because the surface presented to the stream density is different (Figure B1a.) The solar panels are not shadowed, but the cylinder is as shown in Figure B6. The shadow, however, on the cylinder will be limited due to the attitude control limits for ARRS.

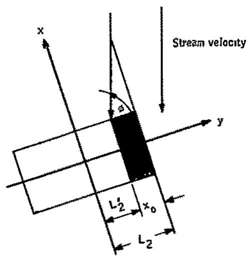

Figure B6. Shadowing on Cylinder due to Solar Panels

The shadow on the cylinder will effect the limits of integration for the torque due to the cylinder.

In the derivation of the torque for the solar panels, we again assume a solid disk as before.

The torque on the cylinder for $\vec{e}_v \cdot \hat{j} > 0$ is derived the same as for $\vec{e}_v \cdot \hat{j} \leq 0$. Only the limit of integration for L_2 is changed.

The limit of integration for L_2 is a function of the spacecraft attitude relative to the stream. The new limit of integration is given by L_2'.

The inner product

$$\vec{e}_v \cdot \hat{j} = \cos \phi$$

where ϕ is the angle between the body j-axis and the mass center velocity. In Figure B6 note that

$$\frac{r_4 - r_3}{y_o} = \tan \phi \tag{B34}$$

Therefore,

$$L_2' = L_2 - y_o \tag{B35}$$

where y_o can be represented as

$$y_o = (r_4 - r_3)\sqrt{\frac{\cos 2\phi}{1 - \cos^2 \phi}} \tag{B36}$$

and reducing further,

$$y_o = (r_4 - r_3)\ \frac{e_v \cdot j}{\sqrt{1-(e_v \cdot j)^2}} \tag{B37}$$

Then the integration limit becomes

$$L_2' = L_2 - \frac{(r_4 - r_3)(\vec{e}_v \cdot \hat{j})}{\sqrt{1-(e_v \cdot \hat{j})^2}} \tag{B38}$$

The limits of integration are now

$$-L_1 \le y \le L_2'$$

$$-\frac{w}{2} \le z \le \frac{w}{2}$$

Using the results of Equation (B12), we get

$$T_{ci} = q_2(\vec{n}_i \cdot \vec{e}_v) x \left[\frac{\sqrt{3}}{2} W^3 \left(L_1 + L_2'\right) \cos \frac{\pi}{3}(i-1) + \frac{W}{2}\left(L_2'^2 - L_1^2\right) \hat{j} \right.$$
$$\left. - \frac{\sqrt{3}}{2} W^3 \left(L_1 + L_2\right) \sin \frac{\pi}{3}(i-1)\, \hat{k} \right] \qquad \text{(B39)}$$

where

$$n_i = \cos \frac{\pi}{3}(i-1)\, \hat{i} - \sin \frac{\pi}{3}(i-1)\, \hat{k}$$

This torque is valid for $e_v \cdot \hat{j} > 0$ and zero for $e_v \cdot j \le 0$.

Equation (B39) represents the torque for each plane (i = 1, 2, 3, 4, 5, and 6). A sum of the torques for each plane that meets the following conditions ($\vec{e}_v \cdot \vec{n}_i \ge 0$) must be performed to obtain the total torque due to the cylinder.

The torque due to the disk (see Figure B4) for $\vec{e}_v \cdot \hat{j} > 0$ is just the result shown by Equation (B24). Equation (B24) is substituted into Equation (B2) to give

$$\vec{T}_{sp} = q_2 \left(\vec{e}_v \cdot \vec{n}'\right) \left(\vec{e}_v x L_2 \pi \;\; r_4^2 \;\; \hat{j}\right) \qquad \text{(B40)}$$

where $\vec{n}' = \hat{j}$, and the torque is valid for $(\vec{e}_v \cdot \hat{j}) \le 0$.

$$T_a = \begin{cases} q_2 \vec{e}_v x \left(\sum\limits_{\substack{i \\ (\vec{n}_i \cdot \vec{e}_v > 0)}} (\vec{n}_i \cdot \vec{e}_v) \vec{v}_i + (\vec{n} \cdot \vec{e}_v)(\vec{v} + \vec{v}_E) \right) & \text{for } \vec{e}_v \cdot \hat{j} \leq 0 \text{ or } F_y \geq 0 \\ q_2 \vec{e}_v x \left(\sum\limits_{\substack{i \\ (n_i \cdot e_v > 0)}} (\vec{n}_i \cdot \vec{e}_v) \vec{v}_i + (\vec{n}' \cdot \vec{e}_v) \vec{v}' \right) & \text{for } e_v \cdot \hat{j} > 0 \text{ or } F_y < 0 \end{cases} \tag{B41}$$

where

$$\vec{v}_i = \frac{\sqrt{3} W^3}{2} L \cos \frac{\pi}{3} (i-1) \hat{i} + \frac{W}{2} \left(L_2^2 - L_1^2 \right) \hat{j} - \frac{3}{2} W^3 \sin \frac{\pi}{3} (i-1) \hat{k}$$

$$\vec{n}_i = \cos \frac{\pi}{3} (i-1) \hat{i} - \sin \frac{\pi}{3} (i-1) \hat{k} \quad \text{for } i=1, \ldots 6.$$

$$\vec{n} = -\hat{j}$$

$$\vec{n}' = \hat{j}$$

$$v_i' = \frac{3}{2} W^3 \left(L_1 + L_2' \right) \cos \frac{\pi}{3} (i-1) \hat{i} + \frac{W}{2} \left(L_2'^2 - L_1^2 \right) \hat{j} - \frac{3W^3}{2} \left(L_1 + L_2' \right) \sin \frac{\pi}{3} (i-1) \hat{k}$$

$$L_2' = L_2 - \frac{(r_4 - r_3)(e_v \cdot \hat{j})}{\sqrt{1 - (\vec{e}_v \cdot \hat{j})^2}}$$

$$\vec{v}' = L_2 \pi \ r_4^2 - r_3^2 \ \hat{j}$$

$$V_E = L_1 \pi \ r_3^2 \hat{j}$$

$$\vec{v} = \left[\left(r_3 (r_4^2 - r_3^2) \sin\theta\right) \hat{i}\right.$$

$$+ \left(L_2 \pi r_4^2 - L_2 \pi r_3^2 - L_2 r_3 (r_4^2 - r_3^2)^{1/2} - L_2 r_4^2 \sin^{-1}\left(\frac{r_3}{r_4}\right)\right) \hat{j}$$

$$\left. - \left(r_3 (r_4^2 - r_3^2) \cos\right) \theta \;\; k\right]$$

where

$$\sin\theta = \frac{v_x}{\sqrt{1 - v_y^2}}$$

$$\cos\theta = \frac{v_z}{\sqrt{1 - v_y^2}}$$

and the symbol

$$\sum_i$$

$$(\vec{n}_1 - e_v > 0)$$

means sum over the surfaces whose angle of attack is positive.

The torque equation derived above is not an exact representation of the vehicle's aerodynamic torque. Frictional or dissipative torques are small compared with pressure torques; therefore, frictional torques were neglected.

In the derivation of pressure torque, the solar panels were assumed to be a solid disk, where in actuality, six rectangular panels are the solar panels (see Figure B7).

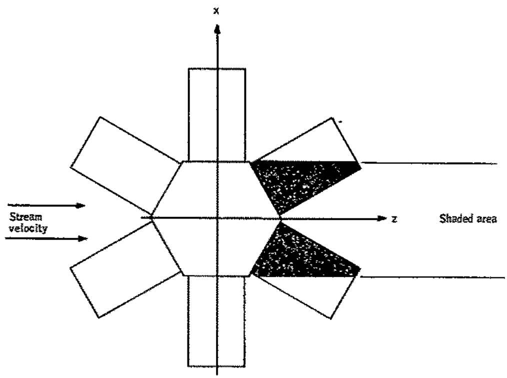

Figure B7. Solar Panel Configuration

The torque due to the solar panels in reality is varying with a frequency six times the spin rates as opposed to the result obtained in this analysis. The result derived in this analysis is varying relative to the body axis only, but not the magnitude of the torque. In Figure B7, the shaded area covers only part of the two solar panels, and as the spacecraft rotates, varying amounts of solar panel area are shaded. It is for this reason the magnitude of the solar panel torques is varying approximately six times the spin rate. The disk-shaped panels give a larger magnitude of torque but remain constant in absolute value.

CENTER OF MASS VELOCITY IN BODY PRINICPAL AXES

The vector, $\vec{e}_v$, used throughout the development represents the direction of the spacecraft center of mass travel. This vector is used because the stream velocity is assumed to lie in the orbit plane of the vehicle. The velocity of the stream due to earth's rate is amll in comparison with the velocity of the spacecraft center of mass. Therefore, a transformation from local vertical coordinate to inertial, then to body principal coordinates is required (See Figure B8).

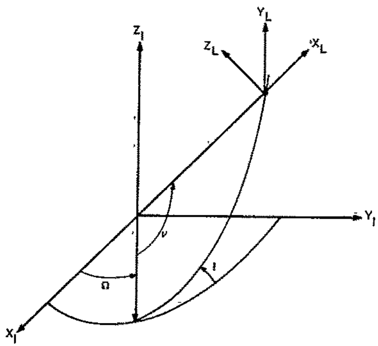

Figure B8. Relationship of Local Vertical Frame to Inertial Frame

The transformations are

$$\bar{X}_I = F(\Omega, i, \gamma)^T \bar{X}_L \tag{B42}$$

PRECEDING PAGE BLANK NOT FILMED.

where

$\gamma = \omega_o (t - t_o')$

ω_o = orbit rate.

t_o' = initial time of spacecraft reference point.

APPENDIX C

DERIVATION OF THE MAGNETIC AND GRAVITATIONAL TORQUES IN TERMS OF THE STATE VARIABLES

PRECEDING PAGE BLANK NOT FILMED.

APPENDIX C

DERIVATION OF THE MAGNETIC AND GRAVITATIONAL TORQUES IN TERMS OF THE STATE VARIABLES

Appendix C derives the magnetic and gravitational torques of Equation (27) in terms of the state variables and their rates. Equation (27) after substitution of the Euler matrix in vector form becomes

$$
\begin{aligned}
T_{M_X} = {} & B_z\left[M_x\left(c\psi s\phi + c\theta c\phi s\psi\right) + M_y\left(-s\psi s\phi + c\theta c\phi c\psi\right)\right. \\
& \left. - M_z s\theta c\phi\right] - B_y\left[M_x s\psi s\theta + M_y c\psi s\theta + M_z c\theta\right] \\
T_{M_y} = {} & B_x\left[M_x s\psi s\theta + M_y c\psi s\theta + M_z c\theta\right] \\
& - B_z\left[M_x\left(c\psi c\phi - c\theta s\phi s\psi\right) - M_y\left(s\psi c\phi + c\theta s\psi s\phi\right)\right. \\
& \left. + M_z s\theta s\phi\right] \\
T_{M_z} = {} & B_y\left[M_x\left(c\psi c\phi - c\theta s\psi s\phi\right) - M_y\left(s\psi c\phi + c\theta s\phi c\psi\right)\right. \\
& \left. + M_z s\theta s\phi\right] - B_x\left[M_x\left(c\psi s\phi + c\theta c\phi s\psi\right)\right. \\
& \left. + M_y\left(-s\psi s\phi + c\theta c\phi c\psi\right) - M_z s\theta c\psi\right]
\end{aligned}
\qquad \text{(C1)}
$$

(Note for the symmetric body case that since both ψ and ϕ are each periodic with non-integer periods, the only net average nonzero term is the $M_z \cos\theta$ in the first two equations.)

After substitution

$$
\begin{aligned}
T_{E_X} &= K\Big[\big((B_x^2 - B^2)\,c\phi + B_x B_y\, s\phi\big)\,\dot{\theta} + \big((B_x^2 - B^2)\, s\phi s\theta \\
&\qquad - B_x B_y\, c\phi\, s\theta + B_x B_z\, c\theta\big)\,\dot{\psi} + B_x B_z\,\dot{\phi}\Big] \\
T_{E_Y} &= K\Big[\big((B_y^2 - B^2)\, s\phi + B_y B_x\, c\phi\big)\,\dot{\theta} + \big(-(B_y^2 - B^2)\, c\phi s\theta \\
&\qquad + B_y B_x\, s\phi s\theta + B_y B_z\, c\theta\big)\,\dot{\psi} + B_y B_z\,\dot{\phi}\Big] \\
T_{E_z} &= K\Big[(B_x B_z\, c\phi + B_y B_z\, s\phi)\,\dot{\theta} + \big(B_x B_z\, s\phi s\theta - B_y B_z\, c\phi s\theta \\
&\qquad + (B_z^2 - B^2)\,c\theta\big)\,\dot{\psi} + \big(B_z^2 - B^2\big)\,\dot{\phi}\Big]
\end{aligned}
\tag{C2}
$$

The gravity gradient torques are somewhat more involved since they are related to the spacecraft symmetry. In order to include both symmetric and nonsymmetric inertia conditions, the inertia matrix is written as

$$
\underline{I} = I\begin{pmatrix} 1 & 0 & 0 \\ 0 & 1 & 0 \\ 0 & 0 & a \end{pmatrix} + \begin{pmatrix} -\epsilon & 0 & 0 \\ 0 & -\epsilon & 0 \\ 0 & 0 & 0 \end{pmatrix}
$$

where

$$a \equiv I_z / I$$

$$\epsilon \equiv \frac{I_y - I_x}{2}$$

$$I \equiv \frac{I_y + I_x}{2}$$

From Equation (27), the term E^{-1} IE is the only term containing the Euler angle terms, so the averaging of this matrix is sufficient. The product of E^{-1} IE for the first term of Equation (C3) is the symmetric matrix

$$H = \begin{bmatrix} 1 - s^2\phi s^2\theta\ (1-a) & c\phi s\phi s^2\theta\ (1-a) & -s\phi c\theta s\theta\ (1-a) \\ - & 1 - c^2\phi s^2\theta\ (1-a) & c\phi c\theta s\theta\ (1-a) \\ - & & 1 - c^2\theta\,(1-a) \end{bmatrix} \quad (C3)$$

The product of E^{-1} IE for the second term of Equation (C3) is the symmetric matrix C whose terms are

$$C_{11} = \varepsilon\left(-(c^2\psi - s^2\psi)(c^2\phi - c^2\theta s^2\phi) + 4c\phi s\phi c\psi s\psi c\theta\right)$$

$$C_{12} = -\varepsilon\left((c^2\psi - s^2\psi)\left(c\phi s\phi\left(1 + c^2\theta\right)\right) + 2c\psi s\psi c\theta\left(c^2\phi - s^2\phi\right)\right)$$

$$C_{13} = -\varepsilon\left(c\theta s\theta s\phi(c^2\psi - s^2\psi) + 2c\psi s\psi c\phi s\theta\right)$$

$$C_{22} = \varepsilon\left(-(c^2\psi - s^2\psi)\ s^2\phi c^2\theta\right) + 2c\psi s\psi c\phi s\phi c\theta)$$

$$C_{23} = -\varepsilon\left(c\theta s\theta c\phi(c^2\psi) - s^2\psi) + 2c\psi s\psi s\phi s\theta\right)$$

$$C_{33} = -\varepsilon\left(s^2\theta(c^2\psi - s^2\psi)\right)$$

The torques can be written in terms of the matrix $D = H + C$ and the components of Equation (41) as

$$\begin{array}{l} T_{G_x} = \\ T_{G_y} = \\ T_{G_z} = \end{array} \left(\begin{array}{l} I \left[(D_{33} - D_{22}) r_2 r_3 + D_{23} (r_2^2 - r_3^2) + D_{13} r_1 r_2 - D_{12} r_1 r_3 \right] \\ I \left[(D_{11} - D_{33}) r_1 r_3 + D_{13} (r_3^2 - r_1^2) + D_{12} r_2 r_3 - D_{23} r_1 r_2 \right] \\ I \left[(D_{22} - D_{11}) r_1 r_2 + D_{12} (r_1^2 - r_2^2) + D_{23} r_1 r_2 - D_{13} r_2 r_3 \right] \end{array} \right) \tag{C4}$$

APPENDIX D

APPROXIMATE CLOSED-FORM SOLUTION FOR THE ATTITUDE OF A WEAKLY TORQUED ASYMMETRIC SPACECRAFT

PRECEDING PAGE BLANK NOT FILMED.

APPENDIX D

APPROXIMATE CLOSED-FORM SOLUTION FOR THE ATTITUDE OF A WEAKLY TORQUED ASYMMETRIC SPACECRAFT

The objective was to develop efficient means of computing the spacecraft state over a time interval $0 \geq t \geq T$, with only knowledge of the principal moments of inertia, spacecraft attitude and angular velocity at time zero, and applied torque over the time interval of interest. This problem has been studied by a wide variety of people and indeed is somewhat "classical". Studies have concentrated on the problem as applied to the Attitude-Referenced Radiometer Study (ARRS) spacecraft which has a favorable inertia condition (i.e., almost completely symmetric with $(I_y - I_z)/I_y \sim 0.1$ and $|I_x - I_z|/I_x \sim 0.01$ and with torques that, while not simple, are manageable.

Reference 19 provides a baseline for further study of the general ARRS attitude determination problem. The approach to the spacecraft modeling problem was that of application of a fourth-order Runge-Kutta numerical integration technique, first to the equation for the time rate of change of angular velocity in spacecraft (principal) axes and secondly to the equations relating Euler angle rates to body (spacecraft) rates (i.e., six integrations for $\dot{\omega}_X$, $\dot{\omega}_Y$, $\dot{\omega}_Z$, $\dot{\theta}$, $\dot{\varphi}$, $\dot{\psi}$). Results indicated good numerical stability (and accuracy) could be achieved with an integration step size of 0.4 second for time durations as long as one full orbit (90 minutes). Thus, performance accuracy was excellent, but the efficiency of this calculation was thought to be poor ("efficiency" measured in terms of computer time to real time ratio). Hence, other means of medeling the spacecraft were sought.

This Appendix is divided into the following technical sections: Coordinate Frame and Angular Rates: Problem Separation; The Untorqued Case: The Torqued Case; Computer Mechanization: and Torque Averaging. Several comments are made relative to this organization. The equation of motion is divided inot two parts, the first of which is the untorqued case and the second, of course, with torque. The untorqued case has a known general solution in terms of elliptic functions. The work of that section is obtain efficient and accurate means for implementing the solution. While these approximations can be analyzed analytically, it is much more practical to experimentally test them with a computer. The section on computer mechanization is not meant to be a computer program, but rather to indicate all of the required computation in a means that is easily programmable.

COORDINATE FRAMES AND ANGULAR RATES

This section describes the kinematic relationship which forms the framework of the analysis to follow. Attachment I provides a derivation of these relationships.

Three coordinate frames will be used: inertial, angular momentum, and body principal axes. These are labeled respectively:

$(\hat{I}_i, \hat{J}_i, \hat{K}_i)$ = Inertial frame

$(\hat{I}_H, \hat{J}_H, \hat{K}_H)$ = Angular momentum frame

$(\hat{I}_B, \hat{J}_B, \hat{K}_B)$ = Body principal axes frame

Relationships between these are described below.

BODY-TO-SPACE TRANSFORMATION - THE "E" MATRIX

By definition, the body axes are related to inertial axes by the "E" matrix, viz:

$$\begin{pmatrix} \hat{I}_B \\ \hat{J}_B \\ \hat{K}_B \end{pmatrix} = \begin{pmatrix} E(\psi, \varphi, \theta) \end{pmatrix} \begin{pmatrix} \hat{I}_i \\ \hat{J}_i \\ \hat{K}_i \end{pmatrix} = \begin{bmatrix} (c\theta c\psi - s\psi s\varphi s\theta) & (s\psi c\theta + c\psi s\varphi s\theta) & (-s\theta c\varphi) \\ -s\psi c\varphi & (c\psi c\varphi) & (s\varphi) \\ (s\theta c\psi + s\psi s\varphi c\theta) & (s\theta s\psi - c\psi s\varphi c\theta) & (c\varphi c\theta) \end{bmatrix} \begin{pmatrix} \hat{I}_i \\ \hat{J}_i \\ \hat{K}_i \end{pmatrix} \tag{D1}$$

and the Euler rates are

$$\begin{aligned} \dot{\psi} \cos \varphi &= -\omega_{X_B} \sin \theta + \omega_{Z_B} \cos \theta \\ \dot{\varphi} &= \omega_{X_B} c\theta + \omega_{Z_B} s\theta \\ \dot{\theta} &= \omega_{Y_B} - \dot{\psi} \sin \varphi \end{aligned} \tag{D2}$$

where $(\omega_{X_B}, \omega_{Y_B}, \omega_{Z_B})$ are the components of the angular rate of the body principal axis frame with respect to (WRT) inertial space expressed in body axes.

ANGULAR MOMENTUM FRAME

The angular momentum frame is an intermediate frame between inertial and body axes and is defined as follows:

$$\begin{pmatrix} \hat{I}_H \\ \hat{J}_H \\ \hat{K}_H \end{pmatrix} = \begin{pmatrix} F(\mu, \nu, \sigma) \end{pmatrix} \begin{pmatrix} \hat{I}_i \\ \hat{J}_i \\ \hat{K}_i \end{pmatrix} = \begin{bmatrix} (c\sigma c\mu - s\mu s\nu s\sigma) & (s\mu c\sigma + c\mu s\nu s\sigma) & (-s\sigma c\nu) \\ (-s\mu c\nu) & (c\mu c\nu) & (s\nu) \\ (s\sigma c\mu + s\mu s\nu c\sigma) & (s\sigma s\mu - c\mu s\nu c\sigma) & (c\nu c\sigma) \end{bmatrix} \begin{pmatrix} \hat{I}_i \\ \hat{J}_i \\ \hat{K}_i \end{pmatrix} \tag{D3}$$

and

$$\begin{pmatrix} \hat{I}_B \\ \hat{J}_B \\ \hat{K}_B \end{pmatrix} = \begin{pmatrix} A(\xi,\eta,\zeta) \end{pmatrix} \begin{pmatrix} \hat{I}_H \\ \hat{J}_H \\ \hat{K}_H \end{pmatrix} = \begin{bmatrix} (c\eta c\xi) & (s\eta) & (-c\eta s\xi) \\ (-c\zeta s\eta c\xi + s\zeta s\xi) & (c\zeta c\eta) & (c\zeta s\eta s\xi + s\zeta c\xi) \\ (s\zeta s\eta c\xi + c\zeta s\xi) & (-s\zeta c\eta) & (-s\zeta s\eta s\xi + c\zeta c\xi) \end{bmatrix} \begin{pmatrix} \hat{I}_H \\ \hat{J}_H \\ \hat{K}_H \end{pmatrix} \tag{D4}$$

so that

$$E(\psi,\varphi,\theta) = A(\xi,\eta,\zeta) \cdot F(\mu,\nu,\sigma) \tag{D5}$$

The Euler rates are given by:

$$\begin{aligned} \dot{\mu} c\nu &= -V_{X_H} s\sigma + V_{Z_H} c\sigma \\ \dot{\nu} &= V_{X_H} c\sigma + V_{Z_H} s\sigma \\ \dot{\sigma} &= V_{Y_H} - \dot{\mu} s\nu \end{aligned} \tag{D6}$$

where (V_{X_H}, V_{Y_H}, V_{Z_H}) are the components of angular rate of the angular momentum frame WRT inertial space expressed in angular momentum coordinates.

Further

$$\begin{aligned} \dot{\eta} &= U_{Y_B} s\zeta + U_{Z_B} c\zeta \\ \dot{\xi} c\eta &= U_{Y_B} c\zeta - U_{Z_B} s\zeta \\ \dot{\zeta} &= U_{X_B} - \dot{\xi} s\eta \end{aligned} \tag{D7}$$

where (U_{X_B}, U_{Y_B}, U_{Z_B}) are the components of angular rate of the body axis frame WRT the angular momentum frame expressed in body axes.

Hence,

$\vec{\omega} = \vec{U} + \vec{V}$ = (body rate WRT inertial space) = (rate of angular momentum frame WRT inertial space) + (rate of body axes WRT angular momentum frame)

Details of these relationships may be found in Attachment I. As will be seen in the work to follow, the transformation $F(\mu, \nu, \sigma)$ is essentially an initial condition matrix. However, angles μ and ν will vary as the direction of the spacecraft's angular momentum vector varies due to the presence of torque. The matrix $A(\xi, \eta, \zeta)$ varies as the attitude of an untorqued spacecraft varies.

PROBLEM SEPARATION

The equations of motion for the spacecraft

$$
\begin{aligned}
A\dot{\omega}_{X_B} - (B - C)\,\omega_{Y_B}\omega_{Z_B} &= \tau_{X_B} \\
B\dot{\omega}_{Y_B} - (C - A)\,\omega_{Z_B}\omega_{X_B} &= \tau_{Y_B} \\
C\dot{\omega}_{Z_B} - (A - B)\,\omega_{X_B}\omega_{Y_B} &= \tau_{Z_B}
\end{aligned}
\tag{D8}
$$

where A, B, and C are the inertia tensor components in diagonal representation and τ_{X_B}, τ_{Y_B}, τ_{Z_B} are the components of the total external torque expressed in body axes.

In vector notation, the equation of motion is

$$I \cdot \dot{\vec{\omega}} + \vec{\omega} \times I \cdot \vec{\omega} = \vec{\tau}$$

where

$$I = (\hat{I}_B, \hat{J}_B, \hat{K}_B) \begin{pmatrix} A & 0 & 0 \\ 0 & B & 0 \\ 0 & 0 & C \end{pmatrix} \begin{pmatrix} \hat{I}_B \\ J_B \\ K_B \end{pmatrix}$$

and the "dot" over the $\vec{\omega}$ means WRT body axes. As given previously,

$$\vec{\omega} = \vec{U} + \vec{V}$$

and therefore

$$I \cdot (\dot{\vec{U}} + \dot{\vec{V}}) + (\vec{U} + \vec{V}) \times I \cdot (\vec{U} + \vec{V}) = \vec{\tau}$$

or

$$(I \cdot \vec{U} + \vec{U} \times I \cdot \vec{U}) + (I\dot{\vec{V}} + \vec{U} \times I \cdot \vec{V} + \vec{V} \times I \cdot \vec{U} + \vec{V} \times I \cdot \vec{V} - \vec{\tau}) = \vec{0} \qquad \text{(D9)}$$

The first term of Equation (D9) in form is precisely that of an untorqued vehicle, while the second term is all that remains. In component form, Equation (D9) may be expressed as:

$$\begin{aligned} A\dot{U}_1 - (B-C)\,U_2U_3 &= 0 \\ B\dot{U}_2 - (C-A)\,U_3U_1 &= 0 \\ C\dot{U}_3 - (A-B)\,U_1U_2 &= 0 \end{aligned} \qquad \text{(D10)}$$

and

$$\begin{aligned} A\dot{V}_1 - (B-C)\,(U_2V_3 + U_3V_2 + V_2V_3) - \tau_1 &= 0 \\ B\dot{V}_2 - (C-A)\,(U_3V_1 + U_1V_3 + V_3V_1) - \tau_2 &= 0 \\ C\dot{V}_3 - (A-B)\,(U_1V_2 + U_2V_1 + V_1V_2) - \tau_3 &= 0 \end{aligned} \qquad \text{(D11)}$$

where for brevity the indices 1, 2, and 3 replace "X_B, Y_B, Z_B" respectively.

Equation (D10) has a general solution, while Equation (D11) is, in general, not solvable explicitly. Essentially, however, for the purposes of spacecraft modeling, Equation (D10) may be used as a baseline solution, and Equation (D11) may be used as a perturbation.

THE UNTORQUED CASE

This section deals with the general Euler equation solution for an untorqued spacecraft and then the specialized solution for the ARRS baseline configuration.

FUNDAMENTAL SOLUTION

The fundamental solution of Equation (D10) is given conditionally in Table D1. where the angle, φ, is defined by:

$$p(t - t_0) = \int_{\varphi=\varphi(t_0)}^{\varphi=\varphi(t)} \frac{d\varphi}{\sqrt{1 - k^2 \sin^2 \varphi}} \tag{D12}$$

Attachment II outlines this solution. Paragraphs to follow will develop how Equation (D12) may be implemented practically.

$t = t(\varphi)$ RELATIONSHIP

The elliptic integral is defined by

$$p\,dt = (1 - k^2 \sin^2 \varphi)^{-1/2} \, d\varphi \tag{D13}$$

where

$$k^2 = \begin{cases} \dfrac{(C-A)\,(2BT-H^2)}{(B-C)\,(H^2-2AT)} & \text{Case 1 with } B > C \geq A \\[2ex] \dfrac{(A-C)\,(2BT-H^2)}{(B-A)\,(H^2-2CT)} & \text{Case 2 with } B > A \geq C \end{cases}$$

In either case, the magnitude of k^2 is given by

$$k^2 = \left(\frac{C-A}{B-C}\right)\left[\frac{A(B-A)U_1^2 + C(B-C)U_3^2}{B(B-A)U_2^2 + C(C-A)U_3^2}\right] \approx \left(\frac{C-A}{B-A}\right)\left(\frac{U_1^2 + U_3^2}{U_2^2}\right)$$

$$= \left(\frac{C-A}{B-A}\right) \tan^2 (\text{cone angle})$$

The "x" and "z" body principal moments will be matched to 1.0 percent or better, while the difference between the "spin" inertia and the "x" or "z" inertias is approximately 10 percent. The baseline configuration further calls for the cone angle to be damped under five degrees or $\sim$0.1 radian. Hence:

$$k^2 \lesssim \frac{(0.01)}{(0.1)} (0.1)^2 \sim 10^{-3}$$

Now, expand Equation (D13) in a Taylor's series and integrate term by term:

$$p \int dt = \int (1-k^2 \sin^2 \varphi)^{-1/2} d\varphi$$

$$= \int \left(1 + \frac{k^2}{2} s^2\varphi + \frac{3}{8} k^4 s^4\varphi + \ldots\right) d\varphi$$

so that

$$pt = \varphi + \frac{k^2}{2}\left(\frac{\varphi}{2} - \frac{s\varphi c\varphi}{4}\right) + \frac{3k^4}{8}\left(\frac{3\varphi}{8} - \frac{3s\varphi c\varphi}{8} - \frac{s^3\varphi c\varphi}{4}\right) + 0(k^6)$$

$$= \left(1 + \frac{k^2}{4} + \frac{9k^4}{64} + \ldots\right)\varphi - \frac{k^2}{4}\, s\varphi c\varphi + \frac{3k^4}{8}\left(\frac{-3s\varphi c\varphi}{8} - \frac{s^3\varphi c\varphi}{4}\right) + 0(k^6)$$

and

$$\frac{pt}{\left(1 + \frac{k^2}{4} + \frac{9k^4}{64} + \ldots\right)} = \varphi - \frac{k^2}{4}\left(1 - \frac{k^2}{4}\right)s\varphi c\varphi - \frac{9k^4}{64}\, s\varphi c\varphi - \frac{3k^4}{32} s^3\varphi c\varphi + 0(k^6)$$

Let

$$\omega = \frac{p}{\left(1 + \frac{k^2}{4} + \frac{9k^4}{64} + \ldots\right)}$$

Then

$$t = t(\varphi) = \frac{\varphi}{\omega} - \frac{k^2}{4\omega}\, s\varphi c\varphi \left[\left(1 - \frac{5k^2}{16}\right) + \frac{3k^2 s^2\varphi}{8}\right] + 0(k^6) \qquad \text{(D14)}$$

This is the desired relationship.

$\varphi = \varphi(t)$ RELATIONSHIP

It is found convenient to invert the $t = t(\varphi)$ relationship, Equation (D14). Thus, let

$$\varphi = \omega t + \alpha + \Delta\varphi$$

Then

$$t = \frac{\omega t + \alpha + \Delta\alpha}{\omega} - \frac{k^2}{4\omega} [\sin \omega t \cos (\alpha + \Delta\alpha) + \cos \omega t \sin (\alpha + \Delta\alpha)]$$

$$[\cos \omega t \cos (\alpha + \Delta\alpha) - \sin \omega t \sin (\alpha + \Delta\alpha)] \left(1 - \frac{5k^2}{16} + \frac{3k^2 s^2 \varphi}{8}\right) + 0(k^6)$$

and therefore

$$\Delta\varphi = \frac{k^2}{4} s\omega t c\omega t \left(1 + \frac{5k^2}{16} + \frac{3k^2}{8} s^2 \omega t\right)$$

$$-\alpha \left[1 + \frac{k^2}{4}(s^2\omega t - c^2\omega t)\left(1 + \frac{5k^2}{16} + \frac{3k^2}{8} s^2\omega t\right)\right] + 0(k^6)$$

Now choose α such that $\Delta\varphi = 0(k^6)$. Hence,

$$\varphi = \omega t + \frac{k^2}{4} s\omega t c\omega t \left[\left(1 + \frac{9k^2}{16}\right) - \frac{k^2}{8} s\omega t\right] + 0(k^6) \tag{D15}$$

EULER ANGLES

The angular momentum associated with the angular velocity, $\vec{U}$, is given by

$$\vec{H} = AU_1\hat{I}_B + BU_2\hat{J}_B + CU_3\hat{K}_B$$

Now, from the coordinate frame definition of Section II, choose the angles (ξ, η, ζ) such that

$$\vec{H} = H\hat{J}_H = H(s\eta\hat{I}_B + c\zeta c\eta\hat{J}_B - s\zeta c\eta\hat{K}_B)$$

and therefore,

$$AU_1 = Hs\eta$$

$$BU_2 = Hc\zeta c\eta$$

$$CU_3 = -Hs\zeta c\eta$$

Hence,

$$\zeta = \tan^{-1}\left(\frac{-CU_3}{BU_2}\right), \quad -\pi \le \zeta \le \pi \tag{D16}$$

$$\eta = \sin^{-1}\left(\frac{AU_1}{H}\right), \quad -\pi \le \eta \le \pi \tag{D17}$$

The value of ξ may be obtained from Equation (D7), viz.,

$$\dot{\xi} c\eta = U_2 c\zeta - U_3 s\zeta$$

$$= c\zeta\left(\frac{Hc\zeta c\eta}{B}\right) - s\zeta\left(\frac{-Hs\zeta c\eta}{C}\right)$$

so that

$$\dot{\xi} = \frac{H}{B}\left[1 + \left(\frac{B-C}{C}\right)\sin^2\zeta\right] \tag{D18}$$

But, from Equation (D16),

$$\sin^2\zeta = \frac{C^2U_3^2}{B^2U_2^2 + C^2U_3^2}$$

The two inertia cases must now be considered.

<u>Case 1:</u> $A > B \geq C$

From Table D1,

$$\sin^2\zeta = \frac{C^2\beta^2 \sin^2\varphi}{B^2\alpha^2(1-k^2\sin^2\varphi) + C^2\beta^2\sin^2\varphi} = \frac{(C^2\beta^2/B^2\alpha^2)\sin^2\varphi}{1 - [k^2 - (C\beta/B\alpha)^2]\sin^2\varphi}$$

But, using Table D1,

$$\left(\frac{C\beta}{B\alpha}\right)^2 - k^2 = \frac{A^2\gamma^2}{B^2\alpha^2}$$

so that

$$\sin^2\zeta = \frac{(C\beta/B\alpha)^2\sin^2\varphi}{1 + \left(\frac{A^2\gamma^2}{B^2\alpha^2}\right)\sin^2\varphi} \tag{D19}$$

<u>Case 2:</u> $A > C \geq B$

From Table D1,

$$\sin^2\zeta = \frac{C^2\gamma^2\cos^2\varphi}{B^2\alpha^2(1-k^2\sin^2\varphi) + C^2\gamma^2\cos^2\varphi} = \frac{\left[\frac{C^2\gamma^2}{B^2\alpha^2 + C^2\gamma^2}\right]\cos^2\varphi}{1 - \left[\frac{C^2\gamma^2 + B^2\alpha^2k^2}{B^2\alpha^2 + C^2\gamma^2}\right]\sin^2\varphi}$$

But, using the equations of Table D1, this expression may be reduced to

$$\sin^2\zeta = \frac{(C\gamma/H)^2 \cos^2\varphi}{1 - (A\beta/H)^2 \sin^2\varphi} \tag{D20}$$

For approximation purposes it is noted that

$$\left(\frac{C\beta}{B\alpha}\right)^2 \sim \left(\frac{A\gamma}{B\alpha}\right)^2 \sim \left(\frac{C\gamma}{H}\right)^2 \sim \left(\frac{A\beta}{H}\right)^2 \lesssim (\text{cone angle})^2 \lesssim 0.01$$

Since φ is a known function of time [Equation D16)], Equation (D18) may be integrated directly. The angle, ξ, is, roughly speaking, the spin coordinate. To place a numerical value on the precision to which ξ must be calculated, it will be assumed that an "open loop" integration to an accuracy of two arc seconds for one-third of an orbit will be required. For a constant error rate, $\Delta\omega$, then,

$$\Delta\omega t \lesssim 10^5$$

where

$$t = \frac{1}{3}(90 \text{ minutes}) = 1800 \text{ seconds}$$

to that

$$\Delta\omega \lesssim 5 \times 10^{-9} \text{ radians/second}$$

Hence, $\sin^2\zeta$ must be expanded to an accuracy corresponding to this precision. That is;

$$\Delta(\sin^2\zeta)\left(\frac{B-C}{B}\right)\frac{H}{B} \leq 5 \times 10^{-9}$$

or

$$\Delta(\sin^2\zeta) \le \frac{(5 \times 10^{-9})}{\frac{B-C}{C} \quad \frac{B\omega}{B}} \sim \frac{5 \times 10^{-8}}{(0.1)\ \frac{2\pi}{20}} \sim 10^{-7}$$

Now examine φ for accuracy. The perturbation term of Equation (D15) occurs approximately at $\omega t = \pi/4$, so that this term at maximum value is

$$\frac{k^2}{8}\left(1 + \frac{9k^2}{16} - \frac{k^2}{8}\sin^2\omega t\right)$$

but

$$\frac{9k^4}{(8)(16)} \lesssim \frac{10^{-6}}{16}$$

which is negligible compared with 10^{-6}. The same is true of the sine squared term. Hence for an accuracy of 10^{-6} for $\sin^2\varphi$, φ may be approximated to

$$\varphi = \omega t + \frac{k^2}{4} s\omega t c\omega t$$

Further,

$$\frac{k^2}{4} s\omega t c\omega t \le \frac{10^{-6}}{8} \le 10^{-4}$$

so that $\varphi = \omega t$ is sufficiently accurate for all powers of $\sin\varphi$ above two. Therefore,

$$\sin^2\varphi = [\sin(\omega t + \alpha)]^2 \sim (\sin\omega t \quad \cos\alpha + \cos\omega t \sin\alpha)^2$$

$$\sim \quad \sin^2\varphi = \sin^2\omega t + \frac{k^2}{2}\sin^2\omega t \cos^2\omega t$$

$$= \left(1 + \frac{k^2}{2}\right)\sin^2\omega t - \frac{k^2}{2}\sin^4\omega t$$

The expressions of Equations (D19) and (D20) for $\sin^2 \zeta$ may be expanded yielding

$$\sin^2\zeta = \begin{cases} \left(\frac{C\beta}{B\alpha}\right)^2 \sin^2\varphi \left[1 - \varepsilon^2 \sin^2\varphi + \varepsilon^4 \sin^4\varphi - \varepsilon^6 \sin^6\varphi\right] \\ \text{for } \varepsilon^2 = (A\gamma/B\alpha)^2 \qquad \text{(Case 1)} \\ \\ \left(\frac{C\gamma}{H}\right)^2 (1 - \sin^2\varphi)\left[1 + \varepsilon^2 \sin^2\varphi + \varepsilon^4 \sin^4\varphi + \varepsilon^6 \sin^6\varphi\right] \\ \text{for } \varepsilon^2 = (A\beta/H)^2 \qquad \text{(Case 2)} \end{cases} \qquad \text{(D21)}$$

which are accurate to 10^{-8} if the spacecraft cone angle is kept under approximately six degrees (five in the specification). The angle, φ, is expressed as a function of time by Equation (D15) and is accurate to the order of k^6. It was shown earlier in this section that $k^2 \lesssim 10^{-3}$, so that $k^6 \lesssim 10^{-9}$ and $k^4 \lesssim 10^{-6}$. Table D2, then, expresses the required accuracy of $\sin^2\varphi$ as a function of k in order to achieve an accuracy of 10^{-8} (over-designed) for $\sin^2\zeta$ to an accuracy of better than 10^{-6}.

TABLE D2.– ACCURACY REQUIREMENTS FOR SINφ

Function	Required Accuracy	Order of k
$\sin^2\varphi$	10^{-6}	$0(k^4)$
$\sin^4\varphi$	10^{-4}	$0(k^4)$
$\sin^6\varphi$	10^{-2}	$0(k^2)$
$\sin^8\varphi$	10^0	$0(k^0)$

Substitution of these approximations into Equation (D21) yields:

$$\sin^2\zeta = \begin{cases} \left(\frac{C\beta}{B\alpha}\right)^2 \left[\left(1 + \frac{k^2}{2}\right) s^2\omega t - \left(\varepsilon^2 + \frac{k^2}{2}\right) s^4\omega t + \varepsilon^4 s^6\omega t - \varepsilon^6 s^8\omega t \right] \\ \text{for } \varepsilon^2 = (A\gamma/B\alpha)^2 \qquad \text{(Case 1)} \\ \\ \frac{C\gamma}{H}^2 \left[1 - \left(1 - \varepsilon^2 + \frac{k^2}{2}\right) s^2\omega t - \left(\varepsilon^2 - \varepsilon^4 - \frac{k^2}{2}\right) s^4\omega t - (\varepsilon^4 - \varepsilon^6) s^6\omega t \right. \\ \left. \quad - \varepsilon^6 s^8 \omega t \right] \end{cases}$$

$$\text{for } \varepsilon^2 = (A\beta/H)^2 \qquad \text{(Case 2)} \qquad \text{(D22)}$$

Finally, then, to a total accuracy of 5×10^{-9} radians per second

$$\dot{\xi} = \frac{H}{B}[C_0 + C_2 \sin^2\omega t + C_4 \sin^4\omega t + C_6 \sin^6\omega t + C_8 \sin^8\omega t] \qquad \text{(D23)}$$

where the C coefficients are computed according to whether Case 1 or Case 2 applies by the formulas of Table D3.

TABLE D3. COEFFICIENTS FOR $\dot{\xi}$ EXPANSION

Coefficient	Value for Case 1	Value for Case 2
d_1	$(B-C/C)\,(C\beta/B\alpha)^2$	$(B-C/C)\,(C\gamma/H)^2$
d_2	$(A\gamma/B\alpha)^2$	$(A\beta/H)^2$
C_0	1.0	$1.0 + d_1$
C_2	$d_1(1 + k^2/2)$	$-d_1(1-d_2 + k^2/2)$
C_4	$-d_1(d_2 + k^2/2)$	$-d_1(d_2 - d_2^2 - k^2/2)$
C6	$d_1 d_2^2$	$-d_1(d_2^2 - d_2^3)$
C_8	$-d_1 d_2^3$	$-d_1 d_2^3$

Attention is now turned toward the integration of $\dot{\xi}$ to obtain the third Euler angle. Thus,

$$\xi(t_{n+1}) = \xi(t_n) + \int_{t_n}^{t_{n+1}} \dot{\xi}(\tau)d\tau$$

$$= \xi(t_n) + \int_{t_n}^{t_{n+1}} \frac{H}{B}(C_0 + C_2 \sin_2\omega\tau + C_4 \sin^4\omega\tau + C_6 \sin^6\omega\tau + C_8 \sin^8\omega\tau)d\tau$$

$$= \xi(t_n) + d_3 \Big\{ C_0[H_0(t_{n+1}) - H_0(t_n)] + C_2[H_1(t_{n+1}) - H_1(t_n)]$$
$$+ C_4[H_2(t_{n+1}) - H_2(t_n)] + C_6[H_3(t_{n+1}) - H_3(t_n)]$$
$$+ C_8[H_4(t_{n+1}) - H_4(t_n)] \Big\}$$

where

$$d_3 = H/B\omega$$
$$H_0(\tau) = \omega\tau$$
$$G_0(\tau) = \sin\omega\tau \cos\omega\tau$$
$$H_m(\tau) = -\frac{G_{m-1}(\tau)}{2m} + \left(\frac{2m-1}{2m}\right)H_{m-1}(\tau)$$

and

$$G_m(\tau) = \sin^2\omega\tau \, G_{m-1}(\tau)$$

so that

$$\int_{t_n}^{t_{n+1}} \sin^{2m}\omega\tau \, d(\omega\tau) = H_m(t_{n+1}) - H_m(t_n)$$

The development of the integral recursion formula may be found in Attachment III.

SUMMARY

Table D4 summarizes the computation required for the untorqued solution within the ground rules set forth herein. The following notes are applicable to Table D4.

1) Indices "B" and "A" denote "Before" and After".

2) The angle, φ_B, must be obtained in the correct quadrant initially. Signs and phase depend on the inequality conditions for Cases 1 and also that $U_2 > 0$.

3) Δt is the computing interval step size.

4) ζ and η should be computed initially with $U = U(\varphi_B)$. (i. e., at time $t = 0$ and U's used to compute ζ and η should be initial values.

5) Arbitrarily set $\xi = 0$ at $t = 0$.

THE TORQUED CASE

This section develops the computational means to obtain change in spacecraft attitude due to the presence of a torque.

PROBLEM DEFINITION

From a previous section, the spacecraft modeling problem has been divided into two parts, the first of which was dealt with previously. This selection will deal with the solution of Equation (D11), which is repeated here for convenience:

$$A\dot{V}_1 - (B-C)(U_2V_3 + U_3V_2 + V_2V_3) - \tau_1 = 0$$

$$B\dot{V}_2 - (C-A)(U_3V_1 + U_1V_3 + V_3V_1) - \tau_2 = 0$$

$$C\dot{V}_3 - (A-B)(U_1V_2 + U_2V_1 + V_1V_2) - \tau_3 = 0$$

It is noted that the equation for V_2 accounts principally for the change in spin speed. Any change in speed is due solely to torque T_2 if there is a perfect inertia match (i.e., if A = C). Further, the terms in parentheses are all small, so that on a first-approximation basis:

$$\dot{V}_2 \approx \frac{\tau_2}{B} \tag{D25}$$

Now, rearrange the first and third lines of Equation (11):

$$\dot{V}_1 - \left(\frac{B-C}{A}\right)(U_2 + V_2)V_3 = \frac{\tau_1}{A} + \left(\frac{B-C}{A}\right)U_3V_2$$

$$\dot{V}_3 - \left(\frac{A-B}{C}\right)(U_2 + V_2)\,V_1 = \frac{\tau_3}{C} + \left(\frac{A-B}{C}\right)U_1V_2$$

Consider $U_2 + V_2 = \omega_2$ to be a constant relative to variation of the V's. Then

$$\ddot{V}_1 - \left(\frac{B-C}{A}\right)\omega_2\dot{V}_3 \approx \frac{\dot{\tau}_1}{A}$$

$$\ddot{V}_3 - \left(\frac{A-B}{C}\right)\omega_2\dot{V}_1 \approx \frac{\dot{\tau}_3}{C}$$

and, therefore,

$$\ddot{V}_1 + \left[\left(\frac{B-C}{A}\right)\left(\frac{B-A}{C}\right)\omega_2^2\right]V_1 = \left[\left(\frac{B-C}{A}\right)\right]\omega_2\,\left(\frac{\tau_3}{C}\right)$$

$$\ddot{V}_3 + \left[\left(\frac{B-C}{A}\right)\left(\frac{B-A}{C}\right)\omega_2^2\right]V_3 = -\left[\left(\frac{B-A}{C}\right)\right]\omega_2\,\left(\frac{\tau_1}{A}\right)$$

Let

$$\lambda^2 = \left[\left(\frac{B-C}{A}\right)\left(\frac{B-A}{C}\right)\omega_2^2\right]$$

so that approximately

$$\ddot{V}_1 + \lambda^2 V_1 = \frac{\lambda T_3}{C}; \qquad T_3 = \sqrt{\left(\frac{B-C}{B-A}\right)\frac{C}{A}}\,\tau_3$$

$$\ddot{V}_3 + \lambda^2 V_3 = \frac{-\lambda T_1}{C}; \qquad T_1 = \sqrt{\left(\frac{B-A}{B-C}\right)\frac{C}{A}}\,\tau_1 \qquad \text{(D26)}$$

Equation (D26) represents a pure undamped second-order system with a natural frequence of λ which is approximately equal to $(B-A/C)\omega_2$. The ARRS baseline system calls for an inertia mismatch of the order of 10 percent so that λ is of the order of 0.1 of the spin frequency. Hence, forcing functions (e.g.,

$T_3\frac{\lambda}{C}$) with harmonic content above, say, $0.1\omega_2$, is attenuated by λ/ω where ω is the angular frequency of the forcing function. Thus, in particular, forcing functions at the spin frequency are attenuated by roughly a factor of 10. It may now be argued backwards that the approximations used to obtain Equation (D26) are indeed justified. In actual fact, however, the final justification for these approximations will be whether they indeed yield adequate solution accuracy. This approach leads to the conclusion that the only torques of consequence are those which are constants or whose average is a constant, since constants alone come through the filter unattenuated. Thus, in the work to follow, torques will be assumed constant over the region of interest.

RECURSION EQUATIONS

Equation (D26) has the solution

$$V_1(t) = V_1(0)\cos\lambda t + \frac{\dot{V}_1(0)}{\lambda}\sin\lambda t + \frac{1}{C}\int_0^t T_3(x)\sin\lambda(t-x)dx$$

$$V_3(t) = V_3(0)\cos\lambda t + \frac{\dot{V}_3(0)}{\lambda}\sin\lambda t - \frac{1}{C}\int_0^t T_1(x)\sin\lambda(t-x)\,dx \qquad \text{(D27)}$$

Appendix D makes use of Equation (D27) to derive a recursion equation relating successive solutions of V at times t_n and t_{n+1}, where $t_{n+1} - t_n = \Delta t$.

$$\begin{Bmatrix} V_1(t_{n+1}) \\ \left[\frac{\dot{V}_1(t_{n+1})}{\lambda}\right] \end{Bmatrix} = \begin{pmatrix} \cos\lambda\Delta t & \sin\lambda\Delta t \\ -\sin\lambda\Delta t & \cos\lambda\Delta t \end{pmatrix} \begin{Bmatrix} V_1(t_n) \\ \left[\frac{\dot{V}_1(t_n)}{\lambda}\right] \end{Bmatrix} + \begin{bmatrix} \frac{1}{C}\int_{t_n}^{t_{n+1}} T_3(x)\sin\lambda(t_{n+1}-x)dx \\ \frac{1}{C}\int_{t_n}^{t_{n+1}} T_3(x)\cos\lambda(t_{n+1}-x)dx \end{bmatrix}$$

$$\begin{Bmatrix} V_3(t_{n+1}) \\ \\ \left[\dfrac{\dot{V}_3(t_{n+1})}{\lambda}\right] \end{Bmatrix} = \begin{pmatrix} \cos\lambda\Delta t & \sin\lambda\Delta t \\ \\ -\sin\lambda\Delta t & \cos\lambda\Delta t \end{pmatrix} \begin{Bmatrix} V_3(t_n) \\ \\ \left[\dfrac{\dot{V}_3(t_n)}{\lambda}\right] \end{Bmatrix} - \begin{bmatrix} \dfrac{1}{C}\displaystyle\int_{t_n}^{t_{n+1}} T_1(x)\sin\lambda(t_{n+1}-x)dx \\ \\ \dfrac{1}{C}\displaystyle\int_{t_n}^{t_{n+1}} T_1(x)\cos\lambda(t_{n+1}-x)dx \end{bmatrix}$$

By virtue of the argument given earlier, assume that both T_1 and T_3 are constants over the interval from t_n to t_{n+1}. Then

$$\begin{Bmatrix} V_1(t_{n+1}) \\ \\ \left[\dfrac{\dot{V}_1(t_{n+1})}{\lambda}\right] \end{Bmatrix} = \begin{pmatrix} \cos\lambda\Delta t & \sin\lambda\Delta t \\ \\ -\sin\lambda\Delta t & \cos\lambda\Delta t \end{pmatrix} \begin{Bmatrix} V_1(t_n) \\ \\ \left[\dfrac{\dot{V}_1(t_n)}{\lambda}\right] \end{Bmatrix} + \begin{bmatrix} \dfrac{T_3(t_n)}{\lambda C}(1-\cos\lambda\Delta t) \\ \\ \dfrac{T_3(t_n)}{\lambda C}\sin\lambda\Delta t \end{bmatrix} \tag{D28}$$

$$\begin{Bmatrix} V_3(t_{n+1}) \\ \\ \left[\dfrac{\dot{V}_3(t_{n+1})}{\lambda}\right] \end{Bmatrix} = \begin{pmatrix} \cos\lambda\Delta t & \sin\lambda\Delta t \\ \\ -\sin\lambda\Delta t & \cos\lambda\Delta t \end{pmatrix} \begin{Bmatrix} V_3(t_n) \\ \\ \left[\dfrac{\dot{V}_3(t_n)}{\lambda}\right] \end{Bmatrix} - \begin{bmatrix} \dfrac{T_1(t_n)}{\lambda C}(1-\cos\lambda\Delta t) \\ \\ \dfrac{T_1(t_n)}{\lambda C}\sin\lambda\Delta t \end{bmatrix} \tag{D29}$$

EULER ANGLES

Ultimately, it is desired to compute μ, ν, and σ to complete the attitude determination. This may be done by considering Equation (D6), which is repeated here for convenience.

$$\dot{\mu} c\nu = -V_{X_H} \sin\sigma + V_{Z_H} \cos\sigma$$

$$\dot{\nu} = V_{X_H} \cos\sigma + V_{Z_H} \sin\sigma$$

$$\dot{\sigma} = V_{Y_H} - \dot{\mu} \sin\nu$$

$$= V_{Y_H} - \tan\nu(-V_{X_H} \sin\sigma + V_{Z_H} \cos\sigma)$$

where

$$\begin{pmatrix} V_{X_H} \\ V_{Y_H} \\ V_{Z_H} \end{pmatrix} = \begin{bmatrix} (c\eta c\xi) & (-c\zeta s\eta c\xi + s\zeta s\xi) & (s\zeta s\eta c\xi + c\zeta s\xi) \\ (s\eta) & (c\zeta c\eta) & (-s\zeta c\eta) \\ (-c\eta s\xi) & (c\zeta s\eta s\xi + s\zeta c\xi) & (-s\zeta s\eta s\xi + c\zeta c\xi) \end{bmatrix} \begin{pmatrix} V_1 \\ V_2 \\ V_3 \end{pmatrix}$$

From Equation (D8), and it is remembered that

$$V_1 = V_{X_B}, \quad V_2 = V_{Y_B}, \text{ and } V_3 = V_{Z_B}$$

Therefore

$$\begin{pmatrix} \dot{\mu} c\nu \\ \dot{\nu} \\ \dot{\sigma} \end{pmatrix} = \begin{pmatrix} -\sin\sigma & 0 & \cos\sigma \\ \cos\sigma & 0 & \sin\sigma \\ \tan\nu\sin\sigma & 1 & -\tan\nu\cos\sigma \end{pmatrix} \begin{bmatrix} (c\eta c\xi) & (-c\zeta s\eta c\xi + s\zeta s\xi) & (s\zeta s\eta c\xi + c\zeta s\xi) \\ (s\eta) & (c\zeta c\eta) & (-s\zeta c\eta) \\ (-c\eta s\xi) & (c\zeta s\eta s\xi + s\zeta c\xi) & (-s\zeta s\eta s\xi + c\zeta c\xi) \end{bmatrix} \begin{pmatrix} V_1 \\ V_2 \\ V_3 \end{pmatrix}$$

$$= \begin{bmatrix} -\sin(\sigma + \xi)V_1 + \cos(\sigma + \xi)V_3 \\ \cos(\sigma + \xi)\, V_1 + \sin(\sigma + \xi)V_3 \\ V_2 - \dot{\mu} s\nu \end{bmatrix} + \begin{pmatrix} \text{first order} \\ \text{misalignment} \\ \text{terms } \eta \text{ and } \zeta \end{pmatrix} \qquad \text{(D30)}$$

Next consider the integration of Equation (D30). The most significant variable on the right hand side is the angle ξ, and that portion of the V's which vary with ξ. The rest of the variation is "slow" relative to ξ. Therefore, let ν and σ be considered constant over the sample period as far as $\dot{\mu}$ and $\dot{\nu}$ are concerned. Further, recall that [Equation(D18)] $\dot{\xi} \approx \frac{H}{B}$. Then, let

$$\rho_n = \sigma(t_n) + \xi(t_n) \tag{D31}$$

and let the variation of ξ be

$$\omega_H \tau, \quad 0 \le \tau \le (t_{n+1} - t_n)$$

where

$$\omega_H = \frac{H}{B}$$

Then

$$\dot{\mu}(t_n + \tau) = \frac{1}{\cos\nu(t_n)} \left\{ -\sin(\rho_n + \omega_H \tau) V_1(t_n + \tau) + \cos(\rho_n + \omega_H \tau) V_3(t_n + \omega_H \tau) \right\} \tag{D32}$$

and

$$\dot{\nu}(t_n + \tau) = \cos(\rho_n + \omega_H \tau) V_1(t_n + \omega_H \tau) + \sin(\rho_n + \omega_H \tau) V_3(t_n + \omega_H \tau) \tag{D33}$$

Now substitute the values of V_1 and V_3 from Equations (D28) and (D29), with τ replacing the parameter Δt. The result is:

$$\begin{aligned} \cos\nu(t_n)\dot{\mu}(t_n + \tau) = {} & -\sin(\rho_n + \omega_H \tau) \left\{ V_1(t_n)\cos\lambda\tau + \left[\frac{\dot{V}_1(t_n)}{\lambda}\right]\sin\lambda\tau + \frac{T_3(t_n)}{\lambda C}(1 - \cos\lambda\tau) \right\} \\ & + \cos(\rho_n + \omega_H \tau) \left\{ V_3(t_n)\cos\lambda\tau + \left[\frac{\dot{V}_3(t_n)}{\lambda}\right]\sin\lambda\tau - \frac{T_1(t_n)}{\lambda C}\sin\lambda\tau \right\} \end{aligned} \tag{D34}$$

and

$$\dot{\nu}(t_n+\tau) = \cos(\rho_n+\omega_H\tau)\left\{V_1(t_n)\cos\lambda\tau + \left[\frac{\dot{V}_1(t_n)}{\lambda}\right]\sin\lambda\tau + \frac{T_3(t_n)}{\lambda C}(1-\cos\lambda\tau)\right\}$$
$$+\sin(\rho_n+\omega_H\tau)\left\{V_3(t_n)\cos\lambda\tau + \left[\frac{\dot{V}_3(t_n)}{\lambda}\right]\sin\lambda\tau - \frac{T_1(t_n)}{\lambda C}\sin\lambda\tau\right\} \tag{D35}$$

Equations (D34) and (D35) are integrated over the interval from t_n to t_{n+1}, which results in

$$\mu(t_{n+1}) = \mu(t_n) + \frac{1}{\cos\nu_0}\left\{-V_1(t_n)I_1(t_{n+1}) \frac{-\dot{V}_1(t_n)}{\lambda}I_2(t_{n+1}) - \frac{T_3(t_n)}{\lambda C}\left[I_5(t_{n+1}) - I_1(t_{n+1})\right]\right.$$
$$\left. +V_3(t_n)I_3(t_{n+1}) + \dot{V}_3(t_n I_4(t_{n+1}) - \frac{T_1(t_n)}{\lambda C}\left[I_6(t_{n+1})-I_3(t_{n+1})\right]\right\} \tag{D36}$$

and

$$\nu(t_{n+1}) = \nu(t_n) + \left\{V_1(t_n)I_3(t_{n+1}) + \frac{\dot{V}_1(t_n)}{\lambda}I_4(t_{n+1}) + \frac{T_3(t_n)}{\lambda C}\left[I_6(t_{n+1})-I_3(t_{n+1})\right]\right.$$
$$\left. +V_3(t_n)I_1(t_{n+1}) + \frac{\dot{V}_3(t_n)}{\lambda}I_2(t_n) - \frac{T_1(t_n)}{\lambda C}\left[I_5(t_{n+1})-I_1(t_{n+1})\right]\right\} \tag{D37}$$

Table D5 lists the functions I_1, I_2, --- I_6.

SUMMARY

This section has developed the computation method for Euller angles μ, ν, and σ using the torque components τ_1, τ_2, amd τ_3 in body axes and assuming that they are constant over the computation interval. Table D5 lists the computation.

COMPUTER MECHANIZATION

This section summarizes the computation to be carried out as developed in the previous three sections. While this does not represent a program in the normal sense, a program could be constructed easily from it. It is intended that the contents of this section bridge the gap that usually exists between analysis language and programming language. Table D6 lists initial computation (computed only at time zero or on reinitialization), while Table D7 represents on-going computation.

The following notes are applicable to Tables D6 and D7:

1) A, B, C are spacecraft principal inertia values about the X_B, Y_B, Z_B axes respectively and are assumed available for this computation. Unless special precautions are taken (not delineated in this report), one of the two inequality conditions must be met for the formulas to be valid:

   Case 1: $B > C \geq A$

   Case 2: $B > A \geq C$

   ω_1, ω_2, ω_3 are spacecraft angular rate components in body axes about (X_B, Y_B, Z_B) axes respectively and are used here for initialization. They are also computed on-line (Table D7).

2) θ, φ, ψ are spacecraft attitude angles relating the transformation between the inertial reference and spacecraft principal axes and are assumed known at initialization. Thereafter, they are computed on-line (Table D7).

3) Subscript "B"" denotes "before" a step Δt in time is taken, while subscript "A" denotes "after" the step is taken. It is assumed that Δt is supplied externally to the listed computation.

4) These may be made a constant on initialization for fixed Δt.

TORQUE AVERAGING

Previously, an approximation for the "perturbed" equation of motion [Equation (D11)] was developed. This section develops a physical interpretation of the approximation and, secondly, torque approximations which may be used as trial solutions for computer experimentation.

EQUATION OF MOTION APPROXIMATION

In vector form, the separated equation of motion, Equation (D9), is

$$I \cdot \dot{\vec{V}} + \vec{U} \times I \cdot \vec{V} + \vec{V} \times I \cdot \vec{U} + \vec{V} \times I \cdot \vec{V} = \vec{\tau}$$

Let

$$\Delta\vec{H} = I \cdot \vec{V} \quad \text{and} \quad \vec{H} = I \cdot \vec{U}$$

Then

$$\left(\frac{d\Delta\vec{H}}{dt}\right)_{\substack{\text{body}\\ \text{axes}}} + (\vec{U} + \vec{V}) \times \Delta\vec{H} + \vec{V} \times \vec{H} = \vec{\tau}$$

so that the separated equation of motion becomes

$$\left(\frac{d\Delta\vec{H}}{dt}\right)_{\substack{\text{inertial}\\ \text{space}}} = \vec{\tau} - \vec{V} \times \vec{H}$$

The term $\vec{V} \times \vec{H}$ represents the interaction between the torqued portion of the solution and the untorqued portion. This result is of no particular significance except to keep the mathematics in perspective.

Now consider the approximations used to obtain Equation (D26). In vector form, these are noted as:

$$I\vec{V} + \underbrace{\vec{U}}_{\vec{U} \approx U_2 \hat{J}_B} \times I \cdot \vec{V} + \vec{V} \times \underbrace{I \cdot \vec{U}}_{I \cdot \vec{U} \approx BU_2 \hat{J}_B} + \vec{V} \times \underbrace{I \cdot \vec{V}}_{I \cdot \vec{V} \approx BV_2 \hat{J}_B} = \vec{\tau}$$

This amounts to approximating the spacecraft angular rate to be along the principal "Y" axis only, with the other components zero. Hence, for computational purposes, the drift of the spacecraft angular momentum vector is computed as though the spacecraft spins solely about its own "Y" principal body axis.

TORQUE CONSIDERATIONS

From the torque analysis performed, it appears that three torque sources are large enough to be modeled in the attitude determination process. These are gravity gradient, eddy current, and residual magnetic moment. These torques are functionally indicated below as:

$$\begin{aligned} \vec{\tau}_{\text{gravity gradient}} &= \vec{\tau}_{GG}(\theta, \varphi, \psi, \vec{R}) \\ \vec{\tau}_{\text{magnetic moment}} &= \vec{\tau}_{mm}(\theta, \varphi, \psi, \vec{R}) \\ \vec{\tau}_{\text{eddy current}} &= (\theta, \varphi, \psi, \vec{R}, \vec{\omega}) \end{aligned} \tag{D38}$$

where

$\vec{R}$ = spacecraft position in orbit

$\vec{\omega}$ = spacecraft angular rate

If θ, φ, ψ, $\vec{R}$, and $\vec{\omega}$ were known functions of time, the particular integral of the approximate solution given previouslv [e.g., Equation (D27)] could be calculated analytically. Previously established was how the angles (ξ, η, ζ) are computed as known functions of time and the untorqued angular rate $\vec{U} = \vec{U}(t)$ is known. For the purposes of calculating the torque, and ultimately the drift of the angular momentum axes, the variation in the angles (μ, ν, σ) may easily by neglected. Thus, to a high degree of approximation the Euler angles (θ,φ,ψ) may be computed as known functions of time from the relationship of Equation (D5). That is, if

$$E(\theta, \varphi, \psi) = A(\xi, \eta, \zeta) \cdot F(\mu, \nu, \sigma) \tag{D39}$$

and

$$\xi = \xi(t),\ \eta = \eta(t),\ \zeta = \zeta(t)$$

$$\mu = \mu(0),\ \nu = \nu(0),\ \sigma = \sigma(0)$$

then

$$\begin{aligned}
\theta &= \theta[\xi(t),\ \eta(t),\ \zeta(t),\ \mu_0,\ \nu_0,\ \sigma_0] \\
\varphi &= \varphi[\xi(t),\ \eta(t),\ \zeta(t),\ \mu_0,\ \nu_0,\ \sigma_0] \\
\psi &= \psi[\xi(t),\ \eta(t),\ \zeta(t),\ \mu_0,\ \nu_0,\ \sigma_0]
\end{aligned} \tag{D40}$$

Further,

$$\vec{\omega} = \vec{U}(t) + \vec{V}(t) \approx \vec{U}(t) \tag{D41}$$

Hence, substitution of these relationships into the torque formulas would yield the torque as a function of time which could then be integrated directly. Equation(D40), however, is extremely complex insofar as these operations are concerned. An attempt has been made to redefine coordinates so that the initial conditions on μ, ν, σ are zero and $(\xi, \eta, \zeta) = (\theta, \varphi, \psi)$. In this way, except for the variation of μ, ν, σ, which is negligible, (θ, φ, ψ) would be directly known functions of time. The most obvious method to achieve this notion would be to redefine the angular momentum axes so that, analogously with Equation (D39),

$$E(\theta, \varphi, \psi) = E(\xi, \eta, \zeta) \cdot E(\mu, \nu, \sigma)$$

and

$$(\theta, \varphi, \psi)_{t=0} = (\xi, \eta, \zeta)_{t=0}$$

$$(\mu, \nu, \sigma)_{t=0} = 0$$

This redefinition will achieve the desired result, but, unfortunately no simple solution for the angles in terms of the rates have been found for this coordinate frame. Solution of the form or simplicity of Equations (D16), (D17), and (D18) have thus far eluded all efforts. A compromise solution is next outlined.

TORQUE APPROXIMATIONS

A previous section argued that the effect of the torque (i.e., drift rate) would be attenuated for all frequencies above approximately $\lambda \approx (B-A/C)U_2$. In particular, then, the sinusoidal motion of the angle, θ (i.e., the spin coordinate), in the torque should contribute little to the total drift. Thus, it is suggested that the torque be averaged over a spin period.

Thus, let

$$\langle \vec{\tau} \rangle = \frac{1}{2\pi} \int_0^{2\pi} \vec{\tau}(\theta) d\theta$$

Gravity Gradient Approximations

The gravity gradient torque is given in Ref. 3 as

$$\vec{\tau}_{GG} = \frac{3\mu}{R^3} \hat{r} \times \bar{\bar{I}} \cdot \hat{r}$$

where

μ = Earth's gravitational constant ≈ 1.4082 x 10^{16} ft^3/sec^2

$\hat{r}$ = Unit vector in directional of radius vector to spacecraft from Earth's center

R = Distance from earth's center to spacecraft center of mass

$\bar{\bar{I}}$ = Moment of inertia dyadic of spacecraft.

In spacecraft body axes, the torque is

$$\begin{bmatrix} (\tau_{GG})_{X_B} \\ (\tau_{GG})_{Y_B} \\ (\tau_{GG})_{Z_B} \end{bmatrix} = \frac{3\mu}{R^3} \begin{bmatrix} (C-B) r_{Y_B} r_{Z_B} \\ (A-C) r_{Z_B} r_{X_B} \\ (B-A) r_{X_B} r_{Y_B} \end{bmatrix}$$

where

$$\begin{pmatrix} r_{X_B} \\ r_{Y_B} \\ r_{Z_B} \end{pmatrix} = E(\theta, \varphi, \psi) \begin{pmatrix} r_{X_I} \\ r_{Y_I} \\ r_{Z_I} \end{pmatrix}$$

It is easily established that

$$\frac{1}{2\pi}\int_0^{2\pi} r_{Y_B}(\theta) r_{Z_B}(\theta) d\theta = 0$$

$$\frac{1}{2\pi}\int_0^{2\pi} r_{Z_B}(\theta) r_{X_B}(\theta) d\theta = \frac{r_{Y_I} r_{Z_I}}{2} \sin\varphi$$

$$\frac{1}{2\pi}\int_0^{2\pi} r_{X_B}(\theta) r_{Y_B}(\theta) d\theta = 0$$

But

$$r_{Y_I} = c\nu s\Omega + s\nu c i c\Omega$$

and

$$r_{Z_I} = s\nu s i$$

Thus

$$\langle \tau_{GG} \rangle \doteq \frac{3\mu}{R^3} \frac{(A-C)\sin\varphi}{2} (s\nu s i)(c\nu s\Omega + s\nu c i c\Omega)\hat{J}_B$$

Magnetic Moment Approximations

The magnetic moment torque is

$$\vec{\tau}_{mm} \equiv \vec{M} \times \vec{B}$$

where the components of $\vec{M}$ are fixed with respect to the spacecraft and the components of $\vec{B}$ are earth-fixed. Thus

$$\begin{pmatrix} B_{X_B} \\ B_{Y_B} \\ B_{Z_B} \end{pmatrix} = E(\theta, \varphi, \psi) \begin{pmatrix} B_{X_I} \\ B_{Y_I} \\ B_{Z_I} \end{pmatrix}$$

Further

$$\langle \vec{\tau}_{mm} \rangle = \frac{1}{2\pi} \vec{M} \times \int_0^{2\pi} \vec{B}(\theta) d\theta$$

$$= \begin{vmatrix} \hat{I}_B & \hat{J}_B & \hat{K}_B \\ M_{X_B} & M_{Y_B} & M_{Z_B} \\ \langle B_{X_B} \rangle & \langle B_{Y_B} \rangle & \langle B_{Z_B} \rangle \end{vmatrix}$$

But

$$\langle B_{X_B} \rangle = 0$$

$$\langle B_{Y_B} \rangle = -s\psi c\varphi B_{X_I} + c\psi c\varphi B_{Y_I} + s\varphi B_{Z_I}$$

$$\langle B_{Z_B} \rangle = 0$$

Hence,

$$\langle \vec{\tau}_{mm} \rangle = \hat{I}_B \left[-M_{Z_B} (-s\psi c\varphi B_{X_I} + c\psi c\varphi B_{Y_I} + s\varphi B_{Z_I} \right]$$
$$+ K_B \left[+M_{X_B} (-s\psi c\varphi B_{X_I} + c\psi c\varphi B_{Y_I} + s\varphi B_{Z_I} \right]$$

Eddy Current Torque

The eddy current torque has been averaged as the previous two torques and the result is found to be

$$(\tau_{EC})_{X_B} = 0$$

$$(\tau_{EC})_{Y_B} = -K\omega_{Y_B} \left\{ \frac{1}{2} (1-\cos^2\varphi \sin^2\psi) B_{X_I}^2 + (1-\cos^2\varphi \cos^2\psi) B_{Y_i}^2 \right.$$
$$+ \frac{1}{2} (1+\cos^2\varphi \cos^2\psi) B_{Z_I}^2 + \sin 2\psi \cos^2\varphi B_{X_I} B_{Y_I}$$
$$\left. + \sin 2\varphi \sin\psi B_{Y_I} B_{Z_I} - \sin 2\varphi c\psi B_{Y_I} B_{Z_I} \right\}$$

$$(\tau_{EC})_{Z_B} = 0$$

where

$$K = 2.86 \times 10^{-5} \text{ ft-lb-sec/gauss}^2$$

ATTACHMENT I
COORDINATE FRAMES

This appendix documents the details of the transformations and angular rates between three coordinate frames:

$(\hat{I}_i, \hat{J}_i, \hat{K}_i)$ = Inertial frame

$(\hat{I}_H, \hat{J}_H, \hat{K}_H)$ = Angular Momentum frame

$(\hat{I}_B, \hat{J}_B, \hat{K}_B)$ = Body principal axes frame

RELATIONSHIP BETWEEN BODY AXES AND INERTIAL SPACE

Figure I1 illustrates the three rotations (ψ, φ, θ) from inertial to body axes respectively. The mathematical relationships are

$$\begin{pmatrix} \hat{I}_i \\ \hat{J}_i \\ \hat{K}_i \end{pmatrix} = \begin{pmatrix} c\psi & -s\psi & 0 \\ s\psi & c\psi & 0 \\ 0 & 0 & 1 \end{pmatrix} \begin{pmatrix} \hat{I}_i' \\ \hat{J}_i' \\ \hat{K}_i' \end{pmatrix}$$

$$\begin{pmatrix} \hat{I}_i' \\ \hat{J}_i' \\ \hat{K}_i' \end{pmatrix} = \begin{pmatrix} 1 & 0 & 0 \\ 0 & c\varphi & -s\varphi \\ 0 & s\varphi & c\varphi \end{pmatrix} \begin{pmatrix} \hat{I}_i'' \\ \hat{J}_i'' \\ \hat{K}_i'' \end{pmatrix}$$

$$\begin{pmatrix} \hat{I}_i'' \\ \hat{J}_i'' \\ \hat{K}_i'' \end{pmatrix} = \begin{pmatrix} c\theta & 0 & s\theta \\ 0 & 1 & 0 \\ -s\theta & 0 & c\theta \end{pmatrix} \begin{pmatrix} \hat{I}_B \\ \hat{J}_B \\ \hat{K}_B \end{pmatrix}$$

and

$$\begin{pmatrix} \hat{I}_B \\ \hat{J}_B \\ \hat{K}_B \end{pmatrix} = \begin{pmatrix} c\theta & 0 & -s\theta \\ 0 & 1 & 0 \\ s\theta & 0 & c\theta \end{pmatrix} \begin{pmatrix} 1 & 0 & 0 \\ 0 & c\varphi & s\varphi \\ 0 & -s\varphi & c\varphi \end{pmatrix} \begin{pmatrix} c\psi & s\psi & 0 \\ -s\psi & c\psi & 0 \\ 0 & 0 & 1 \end{pmatrix} \begin{pmatrix} \hat{I}_i \\ \hat{J}_i \\ \hat{K}_i \end{pmatrix}$$

$$= \begin{bmatrix} (c\theta c\psi - s\psi s\varphi s\theta) & (s\psi c\theta + c\psi s\varphi s\theta) & (-s\theta c\varphi) \\ -s\psi c\varphi & c\psi c\varphi & s\varphi \\ (s\theta c\psi + s\psi s\varphi c\theta) & (s\theta s\psi - c\psi s\varphi c\theta) & (c\varphi c\theta) \end{bmatrix} \begin{pmatrix} \hat{I}_i \\ \hat{J}_i \\ \hat{K}_i \end{pmatrix} = E(\psi, \varphi, \theta) \begin{pmatrix} \hat{I}_i \\ \hat{J}_i \\ \hat{K}_i \end{pmatrix}$$

The angular rate of the body axes WRT inertial space is

$$\vec{\omega} = \dot{\psi}\hat{K}_i' + \dot{\varphi}\hat{I}_i + \dot{\theta}\hat{J}_B = \dot{\psi}(s\varphi\hat{J}_i'' + c\varphi\hat{K}_i'') + \dot{\varphi}\hat{I}_i'' + \dot{\theta}\hat{J}_B$$

$$= (\dot{\varphi},\ \dot{\psi}s\varphi,\ \dot{\psi}c\varphi) \begin{pmatrix} c\theta & 0 & +s\theta \\ 0 & 1 & 0 \\ -s\theta & 0 & c\theta \end{pmatrix} \begin{pmatrix} \hat{I}_B \\ \hat{J}_B \\ K_B \end{pmatrix} + \dot{\theta}\hat{J}_B$$

$$= (\dot{\varphi}c\theta - \dot{\psi}c\varphi s\theta)\hat{I}_B + (\dot{\theta} + \dot{\psi}s\varphi)\hat{J}_B + (+\dot{\varphi}s\theta + \dot{\psi}c\varphi c\theta)\hat{K}_B$$

Thus

$$\omega_{X_B} = \dot{\varphi}c\theta - \dot{\psi}c\varphi s\theta$$
$$\omega_{Y_B} = \dot{\theta} + \dot{\psi}s\varphi$$
$$\omega_{Z_B} = \dot{\varphi}s\theta + \dot{\psi}c\varphi c\theta$$

so that

$$\begin{aligned}
\dot{\psi} c\varphi &= -s\theta \omega_{X_B} + c\theta \omega_{Z_B} \\
\dot{\varphi} &= c\theta \omega_{X_B} + s\theta \omega_{Z_B} \\
\dot{\theta} &= \omega_{Y_B} - \dot{\psi} s\varphi
\end{aligned}$$

RELATIONSHIP BETWEEN BODY AND ANGULAR MOMENTUM COORDINATES

Figure I2 illustrates the successive rotations (ξ, η, ζ) from the angular momentum frame to the body axis frame. The mathematical relationships are:

$$\begin{pmatrix} \hat{I}_H \\ \hat{J}_H \\ \hat{K}_H \end{pmatrix} = \begin{pmatrix} c\xi & 0 & s\xi \\ 0 & 1 & 0 \\ -s\xi & 0 & c\xi \end{pmatrix} \begin{pmatrix} \hat{I}'_H \\ \hat{J}'_H \\ \hat{K}'_H \end{pmatrix}$$

$$\begin{pmatrix} \hat{I}'_H \\ \hat{J}'_H \\ \hat{K}'_H \end{pmatrix} = \begin{pmatrix} c\eta & -s\eta & 0 \\ s\eta & c\eta & 0 \\ 0 & 0 & 1 \end{pmatrix} \begin{pmatrix} \hat{I}''_H \\ \hat{J}''_H \\ \hat{K}''_H \end{pmatrix}$$

$$\begin{pmatrix} \hat{I}''_H \\ \hat{J}''_H \\ \hat{K}''_H \end{pmatrix} = \begin{pmatrix} 1 & 0 & 0 \\ 0 & c\zeta & -s\zeta \\ 0 & s\zeta & c\zeta \end{pmatrix} \begin{pmatrix} \hat{I}_B \\ \hat{J}_B \\ \hat{K}_B \end{pmatrix}$$

and

$$\begin{pmatrix} \hat{I}_B \\ \hat{J}_B \\ \hat{K}_B \end{pmatrix} = \begin{pmatrix} 1 & 0 & 0 \\ 0 & c\zeta & s\zeta \\ 0 & -s\zeta & c\zeta \end{pmatrix} \begin{pmatrix} c\eta & s\eta & 0 \\ -s\eta & c\eta & 0 \\ 0 & 0 & 1 \end{pmatrix} \begin{pmatrix} c\xi & 0 & -s\xi \\ 0 & 1 & 0 \\ s\xi & 0 & c\xi \end{pmatrix} \begin{pmatrix} \hat{I}_H \\ \hat{J}_H \\ \hat{K}_H \end{pmatrix}$$

$$= \begin{bmatrix} c\eta c\xi & (s\eta) & (-c\eta s\xi) \\ (-c\zeta s\eta c\xi + s\zeta s\xi) & (c\zeta c\eta) & (c\zeta s\eta s\xi + s\zeta c\xi) \\ (s\zeta s\eta c\xi + c\zeta s\xi & (-s\zeta c\eta) & (-s\zeta s\eta s\xi + c\zeta c\xi) \end{bmatrix} \begin{pmatrix} \hat{I}_H \\ \hat{J}_H \\ \hat{K}_H \end{pmatrix}$$

The angular rate of body axes WRT the angular momentum axes is

$$\begin{aligned} \vec{\omega} &= \dot{\xi}\hat{J}'_H + \dot{\eta}\hat{K}''_H + \dot{\zeta}\hat{I}_B \\ &= \dot{\xi}(s\eta\hat{I}''_H + c\eta\hat{J}''_H) + \dot{\eta}\hat{K}''_H + \dot{\zeta}\hat{I}_B \\ &= (\dot{\xi}s\eta,\ \dot{\xi}c\eta,\ \dot{\eta}) \begin{pmatrix} 1 & 0 & 0 \\ 0 & c\zeta & -s\zeta \\ 0 & s\zeta & c\zeta \end{pmatrix} \begin{pmatrix} \hat{I}_B \\ \hat{J}_B \\ \hat{K}_B \end{pmatrix} + \dot{\zeta}I_B \\ &= (\dot{\xi}s\eta + \dot{\zeta})\hat{I}_B + (\dot{\xi}c\eta c\zeta + \dot{\eta}s\zeta)\hat{J}_B + (-\dot{\xi}c\eta s\zeta + \dot{\eta}c\zeta)\hat{K}_B \end{aligned}$$

Thus

$$\begin{aligned} \omega_{X_B} &= \dot{\xi}s\eta + \dot{\zeta} \\ \omega_{Y_B} &= \dot{\xi}c\eta c\zeta + \dot{\eta}c\zeta \\ \omega_{Z_B} &= \dot{\xi}c\eta s\zeta + \dot{\eta}c\zeta \end{aligned}$$

and

$$\dot{\eta} = \omega_{Y_B} s\zeta + \omega_{Z_B} c\zeta$$

$$\dot{\xi} c\eta = \omega_{Y_B} c\zeta - \omega_{Z_B} s\zeta$$

$$\dot{\zeta} = \omega_{X_B} - \dot{\xi} s\eta$$

RELATIONSHIP BETWEEN ANGULAR MOMENTUM AXES AND INERTIAL SPACE

This transformation is defined exactly as the relationship between body axes and inertial space. Hence the following strict analogy holds:

$$\mu \sim \psi$$

$$\nu \sim \varphi$$

$$\sigma \sim \theta$$

Therefore, from those relationships it follows that

$$\begin{pmatrix} \hat{I}_H \\ \hat{J}_H \\ \hat{K}_H \end{pmatrix} = \begin{bmatrix} (c\sigma c\mu - s\mu s\nu s\sigma) & (s\mu c\sigma + c\mu s\nu s\sigma) & (-s\sigma c\nu) \\ (-s\mu c\nu) & (c\mu c\nu) & (s\nu) \\ (s\sigma c\mu + s\mu s\nu c\sigma) & (s\sigma s\mu - c\mu s\nu c\sigma) & (c\nu c\sigma) \end{bmatrix} \begin{pmatrix} \hat{I}_i \\ \hat{J}_i \\ \hat{K}_i \end{pmatrix} = F(\mu, \nu, \sigma) \begin{pmatrix} \hat{I}_i \\ \hat{J}_i \\ \hat{K}_i \end{pmatrix}$$

while the Euler rates are given by

$$\dot{\mu} c\nu = -V_{X_H} s\sigma + V_{Z_H} \cos\sigma$$

$$\dot{\nu} = V_{X_H} c\sigma + V_{Z_H} s\sigma$$

$$\dot{\sigma} = V_{Y_H} - \dot{\mu} s\nu$$

ATTACHMENT II
THE FUNDAMENTAL SOLUTION

This appendix deals with the solution to the equation set

$$
\begin{aligned}
AU_1 - (B-C)U_2U_3 &= 0 \\
B\dot{U}_2 - (C-A)U_3U_1 &= 0 \\
C\dot{U}_3 - (A-B)U_1U_2 &= 0
\end{aligned}
$$

where either one of two cases prevail:

Case 1	$B > C \geq A$
Case 2	$B > A \geq C$

By the physical laws of momentum and energy conservation, it is known that the following constants exist:

$$
\begin{aligned}
2T &= AU_1^2 + BU_2^2 + CU_3^2 = \text{constant} \\
H^2 &= A^2U_1^2 + B^2U_2^2 + C^2U_3^2 = \text{constant}
\end{aligned}
$$

Now obtain a single differential equation, a function solely of a single-velocity component.

CASE 1

Choose U_3, then

$$2AT - H^2 = B(A-B)U_2^2 + C(A-C)U_3^2$$

or

$$U_2^2 = \frac{(2BT - H^2 - C(A - C)U_3^2}{B(A-B)}$$

and note that $(H^2 - 2AT) > 0$ when U_2 is sufficiently greater than U_3 (the case at hand).

Further

$$2BT - H^2 = A(B-A)\, U_1^2 + C(B-C)\, U_3^2$$

or

$$U_1^2 = \frac{(2BT - H^2) - C(B-C)U_3^2}{A(B-A)}$$

and note that $(2BT - H^2) > 0$. Then

$$U_3^2 = \left(\frac{A-B}{C}\right)^2 \left[\frac{(2AT - H^2) - C(A-C)U_3^2}{B(A-B)}\right]\left[\frac{(2BT - H^2) - C(B-C)U_3^2}{A(B-A)}\right]$$

$$= \left[\frac{(H^2 - 2AT)\,(2BT - H^2)}{C^2AB}\right]\left\{1 - \left[\frac{C(C-A)}{H^2-2AT}\right] U_3^2\right\}\left\{1 - \left[\frac{C(B-C)}{2BT - H^2}\right] U_3^2\right\}$$

Let

$$\frac{1}{\beta^2} = \frac{C(B-C)}{2BT - H^2}$$

and

$$\frac{k^2}{\beta^2} = \frac{C(C-A)}{H^2 - 2AT}$$

so that

$$\beta^2 = \frac{2BT - H^2}{C(B-C)}$$

and

$$k^2 = \frac{(C-A)(2BT - H^2)}{(B-C)(H^2 - 2AT)}$$

Let

$$\xi = \mu_3/\beta$$

Then

$$\frac{C^2AB}{(H^2-2AT)(2BT-H^2)}\left(\frac{dU_3}{dt}\right)^2 = (1-\xi^2)(1-k^2\xi^2)$$

$$= \left\{\frac{C^2AB}{(H^2-2AT)(2BT-H^2)}\left[\frac{d(\omega_3/\beta)}{d(pt)}\right]^2 \beta^2 p^2\right\}$$

Then define p so that

$$p^2 = \left[\frac{H^2-2AT)(2BT-H^2)}{C^2AB}\right]\left[\frac{C(B-C)}{2BT-H^2}\right]$$

$$= \frac{(B-C)(H^2-2AT)}{ABC}$$

Thus

$$\left(\frac{d\xi}{d\tau}\right)^2 = (1-\xi^2)(1-k^2\xi^2)$$

where

$$\xi = U_3/\beta \text{ and } \tau = pt$$

Following conventional notation,

$$U_3 = \beta \mathrm{sn}[p(t-t_0)]$$

Hence,

$$U_1^2 = \frac{(2BT-H^2) - C(B-C)\left[\frac{2BT-H^2}{c(B-C)}\right] \mathrm{sn}^2[p(t-t_0)]}{A(B-A)}$$

$$= \frac{(2BT-H^2)}{A(B-A)} \left[1 - \mathrm{sn}^2[p(t-t_0)]\right]$$

Let

$$\gamma^2 = \frac{2BT - H^2}{A(B-A)}$$

Further,

$$U_2^2 = \frac{(2AT - H^2) - C(A-C)\left[\frac{2BT - H^2}{C(B-C)}\right] \mathrm{sn}^2 [p(t-t_0)]}{B(A-B)}$$

$$= \frac{H^2-2AT}{B(B-A)} \left\{1 - \left[\frac{(C-A)(2BT-H^2)}{(H^2-2AT)(B-C)}\right] \mathrm{sn}^2 \; [p(t) - t_0)]\right\}$$

$$= \alpha^2 \left\{1 - k^2 . \mathrm{sn}^2 [p(t - t_0)]\right\}$$

where

$$\alpha = \frac{H^2 - 2AT}{B(B-A)}$$

$$= \cos\lambda\Delta t \; V(t_n) + \frac{\sin\lambda\Delta t}{\lambda} \quad V(t_n) + \frac{1}{c}\int_{t_n}^{t_{n+1}} T(x)\sin\lambda(t_{n+1}-x)\,dx$$

The same expansion technique may be carried out for the V equation, yielding

$$\dot{V}(t_{n\pm 1}) = \cos\lambda\Delta t \; V(t_n) = \lambda\sin\lambda\Delta t \; V(t_n) + \frac{\lambda}{c}\int_{t_n}^{t_{n+1}} T(x)\cos\lambda(t_{n+1}-x)\,dx$$

which establishes the recursion equation.

Hence,

$$U_1 = \gamma \cos \varphi$$

$$U_2 = \alpha\sqrt{1 - k^2 \sin^2 \varphi} \qquad \text{where} \quad \sin \varphi = \operatorname{sn}\,[p(t-t_0)]$$

$$U_3 = \beta \sin \varphi$$

$$\alpha = \sqrt{\frac{H^2-2AT}{B(B-A)}}$$

$$\beta = \sqrt{\frac{2BT-H^2}{C(B-C)}}$$

$$\gamma = -\sqrt{\frac{2BT-H^2}{A(B-A)}}$$

$$k = \sqrt{\frac{(C-A)\;(2BT-H^2)}{(B-C)(H^2-2BT)}}$$

$$p = \sqrt{\frac{(B-C)(H^2-2AT)}{CAB}}$$

CASE 2

Solve for U_1 above. Carrying out the method outlined in Case 1 yields:

$$U_1 = \beta \sin \varphi$$

$$U_2 = \alpha\sqrt{1 - k^2 \sin^2\varphi}$$

$$U_3 = \gamma \cos \varphi$$

where

$$\alpha = \sqrt{\frac{H^2-2CT}{B(B-C)}}$$

$$\beta = \sqrt{\frac{2BT-H^2}{A(B-A)}}$$

$$\gamma = -\sqrt{\frac{2BT-H^2}{C(B-C)}}$$

$$k = \sqrt{\frac{(A-C)(2BT-H^2)}{(B-A)(H^2-2CT)}}$$

$$p = \sqrt{\frac{(H^2-2CT)(B-A)}{ABC}}$$

ATTACHMENT III
RECURSION EQUATION FOR $\int \sin^{2n}\varphi\, d\varphi$

It is desired to recursively compute $\int \sin^{2n}\varphi d\varphi$ for values of n running from 1 to at least 4. The derivation starts with the integral formula:

$$F_n(\varphi) = \int \sin^{2n}\varphi d\varphi = -\frac{\sin^{2n-1}\varphi \cos\varphi}{2n} + \left(\frac{2n-1}{2n}\right)\int \sin^{2n-2}\varphi\, d\varphi$$

$$= -\left[\cos\varphi(\sin\varphi)^{2(n-1)-1}\right]\frac{\sin^2\varphi}{2n} + \left(\frac{2n-1}{2n}\right)F_{n-1}(\varphi)$$

Let

$$G_n = \sin^2\varphi\, G_{n-1}$$

Then

$$F_n(\varphi) = \left(\frac{2n-1}{2n}\right)F_{n-1}(\varphi) - \frac{G_{n-1}(\varphi)}{2n}$$

and

$$G_n(\varphi) = \sin^2\varphi\, G_{n-1}(\varphi)$$

for large n values.

For $n = 0$,

$$F_0 = \int d\varphi = \varphi$$

then let

$$G_0 = \sin\varphi\cos\varphi$$

Then,

$$
\begin{aligned}
F_1 &= \int \sin^2\varphi \, d\varphi \\
&= \frac{\varphi}{2} - \frac{s\varphi c\varphi}{2} \\
&= \left(\frac{2(1)-1}{2(1)}\right) F_0 - \frac{G_0}{2(1)}
\end{aligned}
$$

It is easily verified that this relationship holds for n = 2, thus proving the relationship; hence, the mechanization shown in Figure III 1.

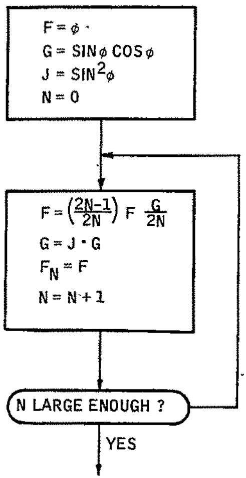

Figure III 1. Recursion for $\int \sin^{2n}\phi \, d\phi$

ATTACHMENT IV

RECURSION EQUATION FOR SUCCESSIVE TIME SOLUTIONS OF DIFFERENTIAL EQUATION

The objective of this attachment is to derive a recursion equation relating successive time solutions of the differential equation:

$$\ddot{V} + \lambda^2 V = \frac{\lambda T(t)}{c}$$

which has the fundamental solution

$$V(t) = V(0)\cos\lambda t + \frac{\dot{V}(0)\sin\lambda t}{\lambda} + \frac{\lambda}{c}\int_0^t T(x)\sin\lambda(t-x)dx$$

First, it is noted that

$$V(t) = -\lambda V(0)\sin\lambda t + V(0)\cos\lambda t + \frac{\lambda}{c}\int_0^t T(x)\,\mathrm{cox}\lambda(t-x)dx$$

Then

$$V(t_{n+1}) = V(t_n + \Delta t) = V(0)\cos\lambda(t_n+\Delta t) + \frac{\dot{V}(0)}{\lambda}\sin\lambda(t_n+\Delta t)$$
$$+ \frac{1}{c}\int_0^{t_n} T(x)\sin\lambda(t_n+\Delta t - x)\,dx + \frac{1}{c}\int_0^{t_{n+1}} T(x)\sin\lambda(t_n\Delta t-x)dx$$

Now, expand the trigonometric functions and collect terms so that

$$V(t_{n+1}) = \cos\lambda\Delta t\left\{V(0)\cos\lambda t_n + \frac{\dot{V}(0)}{\lambda}\sin\lambda t_n + \frac{1}{c}\int_0^{t_n} T(x)\sin\lambda(t_n-x)dx\right\}$$
$$+ \frac{\sin\lambda\Delta t}{\lambda}\left\{-\lambda V(0)\sin\lambda t_n + \frac{\dot{V}(0)}{\lambda}\cos\lambda t_n + \frac{1}{c}\int_0^{t_n} T(x)\cos\lambda(t_n-x)\,dx\right\}$$
$$+ \frac{1}{c}\int_{t_n}^{t_{n+1}} T(x)\sin\lambda(t_n - x)\,dx$$

APPENDIX E

ARRS PHOTOMULTIPLIER SENSITIVITY AND OVERLOAD PROTECTION

PRECEDING PAGE BLANK NOT FILMED.

APPENDIX E

ARRS PHOTOMULTIPLIER SENSITIVITY AND OVERLOAD PROTECTION

The starmapper considered for the ARRS includes a photomultiplier cathode which is alternatively exposed to bright light sources, such as the moon or sun illuminated Earth, and the low light levels presented by a star field viewed under shaded conditions. Of particular interest are the effects of cathode exposure when the starmapper is in a 500-km orbit above the sunlit portion of the earth. One of the requirements for the ARRS is to determine the star magnitude which can be reliably detected for the shaded conditions on the sunlit side of the earth but with the increased photomultiplier dark current due to the periodic cathode exposures to the high intensity of the earth's albedo.

Limited data for the increased photomultiplier dark current are presented in reference 12; however, this report was primarily concerned with establishing permanent, long-term increases of photomultiplier dark current caused by extended exposure to simulated space radiation. As a consequence, most of the dark current data presented in this report were taken after the cathode was dark adapted for a four-hour period. (The data showed some degradation in quantum efficiency on long exposure to combined flux of electrons, protons, and Earth and Earth-Moon albedo.) However, the 35 KeV electrons used could not be expected to penetrate more than about 0.3 mil. Thus, any effects observed must have been due to luminescence of the photocathode substrate.

The data did show that cathode dark current recovered to the initial values before exposure. But, for the ARRS, it is necessary to know the dark current immediately after exposure since this parameter is a major factor determining the limiting star magnitude which may be detected during the portion of the scan period that the starmapper is shaded from the sun-illuminated Earth.

Figure 3.5.3-1, page 64, reference 12, gives the only data currently published on the cathode current immediately after radiation exposure. These data were obtained from measurements of EMR 541N anode currents immediately after the simulated exposures during 400 orbits. For a multiplier gain of 10^6, the largest anode dark current was recorded as 10^{-9} A for a tube exposed only to particle radiation. The anode dark currents for tubes exposed only to particle and visible electromagnetic radiation measured no more than 10^{-10} A. Based on these values of cathode dark current, an analysis of limiting detectable magnitude will be made for a wide range of dark current values which includes the values stated above.

To further the analysis, use the notation and results described in the main body. The peak signal-to-rms noise ratio at the output of a photomultiplier which is generating a star pulse from the radiation of a star image transmitting a slit mask is given by

$$\frac{S}{N} = \frac{(0.597)\, I_s}{1.23\, [2e\, (0.8\, I_s + I_B + I_D)\, \Delta f]^{1/2}} \tag{E1}$$

where

I_s = the average current produced by 100 percent of the star radiation striking the cathode

I_B = the average current produced by stellar background radiation striking the cathode

I_D = the average dark current of the cathode

Δf = the noise equivalent bandwidth of the electronic filter

Equation (E1) was derived assuming that 80 percent of the star image radiation passes through the slit when the star image is centered in the slit. The numerator factor accounts for decrease of pulse height caused by the filter. The factor 1.23 in the denominator accounts for noise introduced by the photomultiplier dynode chain.

To preserve star pulse symmetry for high-accuracy, threshold-crossing signal detection, it is required that the electronic filter exhibit a near linear phase shift versus frequency characteristic. A six-pole Paynter filter exhibits a suitable linear phase characteristic. The noise equivalent bandwidth for this filter can be shown to be

$$\Delta f = 1.020\, f_c$$

where $f_c = \omega_c / 2\pi$ is the filter frequency parameter. Moreover, for maximum signal to noise, the frequency parameter is

$$\omega_c \approx 0.7/\sigma$$

for a slit width such that 80 percent of the star energy passes through the slit when the star is centered. For this case,

$$T_s = 2.56\sigma$$

where $T_s = \alpha/\omega$ is the star crossing time. Then

$$\Delta f = \frac{1.020 \times 0.7 \times 2.56}{2\pi\, T_s} = 314 \text{ Hz} \tag{E2}$$

The signal current at magnitude M_B and type A_o is

$$I_s = e\,\gamma(11{,}000°K)\ \epsilon_{op}\ \epsilon_{qmax}\ A_o$$

$$= 1.602 \times 10^{-19}\ 1.76 \times 10^{6} \times 0.85 \times 0.215 \times 26.72\ 10^{-0.4M_B}$$

$$= 1.38 \times 10^{-12} \times 10^{-0.4M_B}\ A \qquad \text{(E3)}$$

The signal due to faint star background is

$$I_B = e\,n_s/T = \frac{1.602 \times 10^{-19} \times 192}{0.926 \times 10^{3}} \qquad \text{(E4)}$$

$$= 3.33 \times 10^{-14}\ A$$

A range of dark currents

$$I_D = 10^{-17+k},\ k = 0,\ 1, \ldots,\ 8 \qquad \text{(E5)}$$

is used in Equation (E1) together with Equations (E2) through (E5). Signal to noise is set equal to 10 and the result is solved for M_B. One gets the plot of Figure E1. Note that little deterioration in minimum magnitude at (S/N) = 10 occurs until the dark current becomes comparable to the background, whereupon a rapid decay occurs. It is plain that bright objects in the field will make the sensor unoperative.

Other questions of interest related to the ARRS concern the protection of the photomultiplier from overload conditions. Two possible methods may be used to provide adequate protection and overload safety margin. One method is to operate the multiplier chain at the lowest possible voltage so that the anode current level is kept to a minimum. This could also include operating only the number of dynode stages to provide the minimum required multiplier gain. The other method involves switching the cathode first dynode voltage when an overload condition does exist.

To establish the minimum required multiplier gain, it is necessary to consider the basic sources of noise in photocurrent detection. An always present noise factor is the shot noise of the cathode current. The other basic noise is the Johnson noise of the anode resistor. Therefore, the mean square noise voltage at the photomultiplier anode is given by

$$\overline{v_n^{\,2}} = R^2G^2\ (2e\ I_k\Delta f) + 4k\,T\,R\,\Delta f = e\,R\,\Delta f\,(2G^2\,R\,I_k + \frac{4K\ T}{e}\ )$$

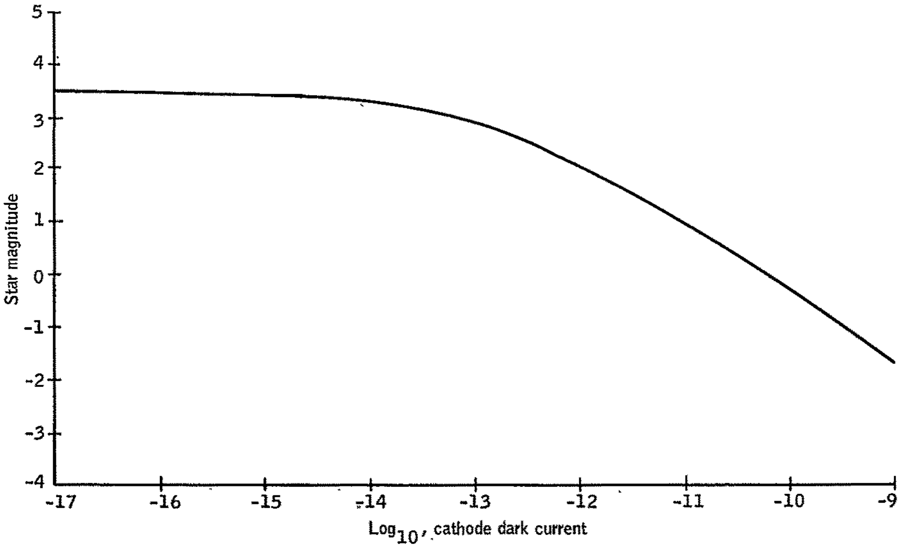

Figure E1. Recovery of Input Signal from Output Signal

where

R = anode load resistor

G = the multiplier gain

I_k = average cathode current

Δf = electrical bandwidth

$4kT$ = 1.62×10^{-20} for $T = 23°C = 296°K$

Here the multiplier gain is assumed to be noise-free. It is desirable to have multiplier gain which is sufficiently large so that the shot noise dominates. This occurs when

$$2G^2 R I_k >> \frac{4kT}{e}$$

Therefore, require that

$$2G^2 R I_k = 10\left(\frac{4kT}{e}\right) = 1$$

where

$$\frac{4kT}{e} \doteq 10^{-1} \text{ for } T = 20°C$$

Now the upper limit on R is determined by the maximum allowable RC_s time constant where C_s is the stray capacitance at the anode. This RC_s time constant should be less than the transit time of a point image to cross the slit. For ARRS the slit transit time is given by

$$T_s = \alpha/\omega = 1/18 \times 60 = 0.926 \times 10^{-3} \text{ sec}$$

If one assumes that $C_s = 20 \times 10^{-12}$ farad and $R = 10^7$ ohms, $RC_s = 0.2 \times 10^{-3}$ second $< T_s$, then

$$G^2 = \frac{1}{2 \times 10^7 I_k}$$

Next, assume that the smallest value for I_k when a star signal is present occurs for a fourth magnitude star. In this case for D = 1 inch

$$I_k = \frac{2.35}{3^2} \times 10^{-12} \times 10^{-0.4 \times 4} = 0.386 \times 10^{-14} A$$

Hence, the multiplier gain need not exceed

$$G = (2 \times 10^7 \times 0.386 \times 10^{-14})^{-1/2} = 3.60 \times 10^3$$

It is possible to estimate the number of dynodes required to provide the minimum value of dynode gain. For the EMR 531N data sheet, the gain per dynode stage, g, is given by

$$g^{14} = 10^4$$

for 1690 volts applied across the multiplier chain. This reduces to a per stage gain of

$$g = 1.93$$

Now, let n such stages be required to provide an overall gain of 2.75×10^3. Thus,

$$(1.93)^n = 3.60 \times 10^3$$

or

$$n = 12.45 \approx 12 \text{ stages}$$

This implies that the last two dynode stages of the EMR 531N need not be used.

If the maximum allowable current level of the last active dynode stage is one microampere, as is indicated for the 531N, then the cathode current for this limiting condition is

$$I_k = \frac{10^{-6}}{2.24 \times 10^3} = 0.446 \times 10^{-9} A$$

When the photomultiplier cathode is exposed to a high-intensity light source and the anode current level exceeds the maximum allowable ration, it is necessary to switch the photomultiplier bias voltage so that the overload currents are reduced or interrupted. Figure E1 shows a schematic for switching the photomultiplier cathode voltage. The cathode is at ground potential and the anode is connected to positive high voltage through a load resistor, R_L. The first dynode is connected to a positive bias voltage through a resistor R and a transistor switch. When the transistor switch is OFF, the positive voltage is applied to the first dynode and free electrons from the cathode are accelerated toward the first dynode. When the transistor switch is ON, the transistor shunts a small negative voltage to the first dynode. This small negative voltage will repel electrons back to the cathode, thus preventing cathode current from reaching the multiplier chain. Preventing cathode current from flowing to the dynode chain in this manner should prevent cathode and dynode degradation even when the cathode is exposed to high-intensity light sources.

After the photomultiplier cathode-first dynode voltage has been switched to cutoff the electron flow from the cathode, a signal must be available which indicates that no bright source is in the field of view in order to turn the cathode-first dynode voltage back to the operational condition. This signal can be generated by a solid-stage detector whose relatively wide optical field of view always scans at a fixed azimuth preceding the scan of the star-mapper field of view.

APPENDIX F

ANALYSIS OF CATHODE TEMPERATURES RESULTING FROM EXPOSURE TO SOLAR RADIATION

APPENDIX F

ANALYSIS OF CATHODE TEMPERATURES RESULTING FROM EXPOSURE TO SOLAR RADIATION

The "N" type cathode in the EMR 531N-01-14 multiplier phototube has an upper temperature limit of 150°C. It is of interest to know whether or not this temperature is exceeded as a consequence of exposing the cathode to direct sunlight under the conditions attending the application of the 531N tube in the ARRS starmapper in a design which has no sun shutter.

Solar energy entering the starmapper aperture (3.25 inch for 20° field of view) is concentrated by the optics and focused as an image 33 arc min in diameter (0.063 inch for the 6.5-inch focal length optics) at the focal surface. If the sun's image passes over one of the celestial viewing slits at the focal plane some of the solar energy will reach the cathode of the photomultiplier tube (PMT) via optical fibers between the slit and the PMT. However, not all of the solar energy reaching the cathode is absorbed -- some is transmitted. Unfortunately, data are lacking on the absorption of solar energy by the cathode. The information that is published relates to the quantum efficiency, or response, of the cathode. In a program conducted for NASA Langley, Brown, et al., (ref. 12) calculated the total irradiance of the sun in the range of the N-type cathode to be 0.0312 W/cm^2. This value is less than the 0.140 W/cm^2 solar constant. The use of the lower value for thermal calculations is justifiable if it is assumed that the optical design provides for a filter to remove radiation of wavelengths longer than the 700-mμ cutoff point for the response of the 531N tube. Such a filter would thus remove the infrared portion of the solar spectrum.

The irradiance of 0.0312 W/cm^2 applies at the aperture of the starmapper. The intensity of the solar energy reaching the focal plane is obtained by multiplying the 0.0312 W/cm^2 by the ratio of aperture area to image area and by an optical efficiency factor. Thus, the intensity at the focal plane is

$$p = 0.0312 \times \left(\frac{3.25}{0.063}\right)^2 \times 0.8 = 67 \text{ W/cm}^2$$

where 0.8 is an assumed value of optical efficiency.

The fiber optics between the viewing slit and the PMT will attenuate the energy because the energy transmitted through any given fiber enters over a part of the end surface but leaves over the total surface of the opposite end, as shown in Figure F1.

The energy will be attenuated in proportion to the ratio of slit area to total end surface area; i.e.,

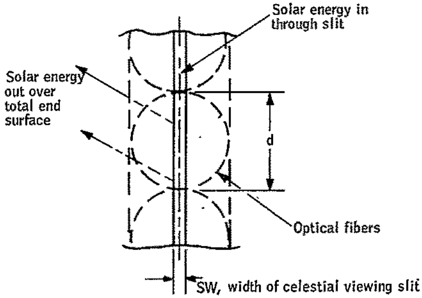

Figure F1

$$p' = p \times \frac{Sw \times d}{\frac{\pi}{d} d^2} = p \times \frac{4\,Sw}{\pi\, d} \qquad \text{(F1)}$$

The slit width is 60 arc sec or 0.002 inch for the 6.50inch focal length system. Optical fibers of 0.010-inch diameter will be assumed. Therefore,

$$p' = 67 \times \frac{4 \times 0.002}{\pi \times 0.010} = 17.1\ \text{W/cm}^2$$

This energy will be absorbed by the cathode at the surface of the PMT window during the period of time during which the sun's image is over the viewing slit.

The time of exposure to the 17.1 W/cm^2 energy input is dependent on the spin rate, N, of the satellite. Since the sun subtends an angle of 33 arc min, the exposure time is

$$t = \frac{33}{\frac{N}{60} \times 360 \times 60} = \frac{0.092}{N} \qquad \text{(F2)}$$

where the units for t and N are seconds and revolutions per minute, respectively.

To obtain an approximation of the temperature rise of the cathode layer resulting from exposure to 17.1 W/cm^2, the heat transfer problem can be treated as an infinite body with a plane surface exposed to a permanent heat source at the surface. The heat source is the energy-absorbing cathode layer and the surface temperature is the cathode temperature of interest.

Ingersoll, Zobel, and Ingersoll (ref. 20) present the solution for the problem of a continuous heat source acting over a surface of an infinite body. The temperature at the surface is expressed by the equation

$$T = \frac{Q'\sqrt{\alpha t}}{k\sqrt{\pi}} \qquad \text{(F3)}$$

where

T = surface temperature at any time, t, for an initial temperature, T_o = 0°C

Q' = continuous heat source at the surface

α = thermal diffusivity of the body; $\alpha = \frac{k}{c\rho}$

where

k = thermal conductivity

c = specific heat

ρ = density

t = time

The actual cathode heating problem is one of a number of localized heat sources rather than a continuous heat source; therefore, Equation (F3) should yield a conservative temperature value. This is sufficient for obtaining an approximation of the cathode temperature rise.

Before substituting in Equation (F3), values must be expressed in consistent units. Thus, since 1 W = 0.239 cal/sec,

$$p' = Q' = 17.1 \times 0.239 = 4.1 \text{ cal/sec-cm}^2$$

Thermal properties of the particular glass used for the window in the PMT are not available, but using values for a typical glass with equilibrium temperature must be less than the 150°C maximum by the amount of the temperature rise occurring in a single pass of the sun; i.e., 120°C and 138°C for 1 and 3 rpm, respectively.

Rather than attempting a solution of the complete heat transfer problem, the heat loss by conduction will be neglected and an approximate solution based on radiative exchange alone will be used to show that the cathode will not reach destructive temperatures.

The solution will be restricted to the events associated with a single optical fiber transmitting energy from a portion of a viewing slit to a spot on the PMT window or cathode as was done in calculating the temperature rise for a single pass of the sun. This spot will be losing heat by radiative exchange with surrounding surfaces. The rate of heat transfer by radiation is given by the equation

$$\frac{q}{A} = F_1 F_2 \sigma (T_1^4 - T_2^4) \qquad \text{(F4)}$$

where

- q = heat transfer per unit time
- A = area
- F_1 = geometric form factor
- F_2 = emissivity factor
- σ = Stefan-Boltzmann constant
- T_1 = absolute temperature of warmer surface
- T_2 = absolute temperature of cooler surface

For a surface which is small relative to enclosing surfaces, Kern (ref. 21) gives $F_1 = 1$ and $F_2 = \epsilon_1$, where ϵ_1 = emissivity of the small surface. For the glass window of the PMT, $\epsilon_1 = 0.9$ (approximately).

Since the heat lost by radiative cooling must equal the heat gained by solar heating, the heat transfer rate, q/A, is obtained by multiplying the solar heating input rate, Q', by the ratio of heating time to cooling time. Thus,

$$\frac{q}{A} = Q' \times \frac{t}{\frac{60}{N}}$$

or substituting from Equation (F2)

$$\frac{q}{A} = Q' \times \frac{\frac{0.092}{N}}{\frac{60}{N}} = 1.53 \times 10^{-3}\, Q' \qquad \text{(F5)}$$

For $Q' = 4.1$ cal/(sec) (cm^2), $\frac{q}{A} = 6.3 \times 10^{-3}$ cal/(sec) (cm^2). The Stefan-Boltzman constant

$$\sigma = 1.362 \times 10^{-12} \text{ cal/(sec) (cm}^2\text{) (°K}^4\text{)}$$

The temperature of surrounding surfaces which the spot in question is radiating to will be taken as the 200°K planned operating temperature; i.e., T_2 = 200°K.

Substituing appropriately in Equation (F4) and solving for T_1 gives

$$T_1 = \left[\frac{q/A}{F_1 F_2 \sigma} + T_2^{\,4}\right]^{1/4}$$

$$T_1 = \left[\frac{6.3 \times 10^{-3}}{1 \times 0.9 \times 1.362 \times 10^{-12}} + (200)^4\right]^{1/4} = 287°K \text{ or } 14°C$$

Thus, it has been shown that radiative cooling alone is adequate to remove the solar energy reaching any spot on the PMT cathode by transmission from the celestial viewing slit through the fiber optics to the cathode. The relatively low equilibrium temperature of 14°C occurs because the period of cooling is significantly longer than the period of solar heating.

The temperature rise of 20.8°C for a spot on the cathode which was calculated for a spin rate of 1 rpm for one pass of the sun is also relatively low. Thus, a substantial safety factor exists if the solar energy is attenuated by using a filter to remove wavelengths beyond the range of the 531N PMT. The fiber optics also act to attenuate the intensity of solar energy passing through the viewing slits and reaching the cathode.

APPENDIX G
MAIN REFERENCE FRAME

PRECEDING PAGE BLANK NOT FILMED.

APPENDIX G
MAIN REFERENCE FRAME

This Appendix defines the main reference frames used in the spacecraft dynamics modeling and the attitude determination data reduction simulation. The main reference frames are (1) the body frame, (2) the experiment frame, (3) the local vertical frame, and (4) the inertial frame.

The body frame refers to a body-fixed triad aligned to the spacecraft principal moment of inertial axes. The axes are denoted X_B, Y_B, and Z_B.

The experiment frame refers to an instrument-fixed triad denoted by X_E, Y_E, and Z_E.

The local vertical frame has its origin fixed to the spacecraft center of mass in orbit with X_L as directed along a radius vector from the earth's center. The X_L lies in the orbit plane in the direction of the spacecraft velocity vector.

The inertial frame has its origin fixed at the earth's center with the Z_I axis along the earth's polar axis, the X_I axis directed toward the vernal equinox, and the Y_I and X_I lying in the equatorial plane.

REFERENCE FRAME TRANSFORMATIONS

The transformations used in this report are

1) Inertial to body axis
2) Body to experimental axes
3) Local vertical to inertial axes

Inertial to Body Axes

The inertial axes are related to the spacecraft body axes by the sequence of Euler rotations

- ψ about the Z_I axis
- ϕ about the first displaced X axis
- θ about the second displaced y axis

A vector in inertial space is then given in body coordinates by

$$\vec{X}_B = E(\psi, \phi, \theta)\ \vec{X}_I$$

where

$$E = \begin{bmatrix} (\cos\theta\cos\psi - \sin\theta\sin\phi\sin\psi) & (\cos\theta\sin\psi + \sin\theta\sin\phi\cos\psi) & -\sin\theta\cos\theta \\ -\cos\phi\sin\psi & \cos\phi\cos\psi & \sin\phi \\ (\sin\theta\cos\psi + \cos\theta\sin\phi\sin\psi) & (\sin\theta\sin 1 - \cos\theta\sin\phi\cos\psi) & \cos\theta\cos\phi \end{bmatrix}$$

Body to Experimental Axes

The body axes are related to the experimental by the sequence of Euler angle rotations

- ϵ_1 about the Z body axis
- ϵ_2 about the firat displaced X axis
- ϵ_3 about the second displaced y axis

A vector in body axes is given by experimental frame by

$$\vec{X}_E = C(\epsilon_1, \epsilon_2, \epsilon_3)\,\vec{X}_B$$

where

$$C = \begin{bmatrix} (\cos \epsilon_3 \cos \epsilon_1 - \sin \epsilon_2 \sin \epsilon_1) & (\cos \epsilon_3 \sin \epsilon_1 + \sin \epsilon_2 \sin \epsilon_2 \cos \epsilon_1) & (-\sin \epsilon_3 \cos \epsilon_2) \\ - \cos \epsilon_2 \sin \epsilon_1 & \cos \epsilon_2 \cos \epsilon_1 & \sin \epsilon_2 \\ (\sin \epsilon_3 \cos \epsilon_1 + \cos \epsilon_3 \sin \epsilon_2 \sin \epsilon_1) & (\sin \epsilon_3 \sin \epsilon_1 - \cos \epsilon_3 \sin \epsilon_2 \cos \epsilon_1) & (\cos \epsilon_3 \cos \epsilon_2) \end{bmatrix}$$

Local Vertical to Inertial Axes

The local vertical axes are realted to the inertial axes by the sequence of Euler angle rotations

- Ω about the Z_I axis
- i about the first displaced x axis
- ν about the first displaced z axis

where

Ω is the right ascension of the ascending node

i is the inclination of the orbit, and

ν is the angle from the ascending node

The transformation matrix from inertial frame to local vertical frame is

$$\vec{X}_L = F(\Omega, i, \nu) \vec{X}_I$$

where

$$F(\Omega, i, \nu) = \begin{bmatrix} \cos \nu \cos \Omega - \sin \nu \cos i \sin \Omega & \cos \nu \sin \Omega + \sin \nu \cos i \cos \Omega & \sin \nu \sin i \\ -\sin \nu \cos \Omega - \cos \nu \cos i \sin \Omega & -\sin \nu \sin \Omega + \cos \nu \cos i \cos \Omega & \cos \nu \sin i \\ \sin i \sin \Omega & - \sin i \cos \Omega & \cos i \end{bmatrix}$$

OTHER REFERENCE FRAME RELATIONSHIPS

Equatorial inertial frame (X_I, Y_I, Z_I) to ecliptic inertial reference frame transformation is given by a single rotation ε about the X_I axis, where ε is the obliquity of the ecliptic (mean value in 1960 is 23° 6' 40.16").

A vector $\vec{X}_I$ in the equatorial frame is given by

$$\vec{X}_\varepsilon = G(\varepsilon)\,\vec{X}_I$$

in the ecliptic inertial reference frame where

$$G(\varepsilon) = \begin{bmatrix} 1 & 0 & 0 \\ 0 & \cos\varepsilon & \sin\varepsilon \\ 0 & -\sin\varepsilon & \cos\varepsilon \end{bmatrix}$$

A primed reference frame is defined to relate spacecraft geometry to the fixed body frame. The spacecraft geometry relation to the body axis requires a single rotation from any i^{th} surface, primed frame, to the body frame. The primed frame is related to the body frame by

$$\vec{X}_B = M(i)\,\vec{X}^{\,1}$$

where i denotes the reference and

$$M(i) = \begin{bmatrix} \cos\frac{\pi}{3}(i-1) & 0 & \sin\frac{\pi}{3}(i-1) \\ 0 & 1 & 0 \\ -\sin\left(\frac{\pi}{3}\right)(i-1) & 0 & \cos\left(\frac{\pi}{3}\right)(i-1) \end{bmatrix} \qquad i = 1,2,3,4,5, \text{ and } 6$$

The angle, $\frac{\pi}{3}$ is due to the spacecraft Hexagonal shape.

REFERENCES

1. Smith, Louis G.: A Theoretical Study of the Torques Induced by a Magnetic Field on Rotating Cylinders and Spinning Thin-Wall Cones, Cone Frustums, and General Body of Revolution. NASA TR-R-129, 1962.

2. Vinti, John P.: Theory of the Spin of a Conducting Satellite in the Magnetic Field of the Earth. Report No. 1020, Ballistic Research Labs., Aberdeen Proving Ground, Md., July 1957.

3. Beletskii, V. V.: Motion of an Artificial Satellite About its Center of Mass. NASA TT F-429, 1966.

4. Hausner, C. W.; and Hudson, D. E.: Applied Mechanics Dynamics. Second ed., D. Van Nostrand Co., 1959, Chapter 7.

5. Goldstein, H.: Classical Mechanics. Addison-Wesley Publishing Co., Reading Mass., 1957, Chapter 5.

6. Tidwell, N. W. ; and others: Conceptual Mechanization Studies for a Horizon Definition Spacecraft - Attitude Control Subsystem. NASA CR-66382, May 1967.

7. Rathmann, C. L.; Mann, G. H.; and Nordberg, M. E.: A New Ultralow-Expansion, Modified Fused-Silica Glass. Applied Optics, Vol. 7, No. 5, May 1968, pp. 819-823.

8. Plummer, W. A.; and Hagy, H. E.: Precision Thermal Expansion Measurements on Low Expansion Optical Materials. Applied Optics, Vol. 7, No. 5, May 1968, pp. 825-831.

9. Malitson, I. H.: Interspecimen Comparison of the Refractive Index of Fused Silica. J. of Optical Society, Vol. 55, No. 10, pp. 1205-1209.

10. Sosman, R. B.: The Properties of Silica. Chemical Catalog Company, Inc., N. Y., 1927, p. 687, Table 34.7.

11. Jensen, Niels: Optical and Photographic Reconnaissance Systems. Wiley and Sons, N. Y., 1968, Table 6.2, p. 59.

12. Brown, N. J., Pai, M. S.; and Park, S.: Degradation of Multiplier Phototubes Exposed to Spatial Radiations. EMR-Aerospace Sciences, College Park, Md., October 1968.

13. Greenstein, ed.: Stellar Energy Distribution in Stars and Stellar Systems. U. of Chicago Press.

14. Allen: Astrophysical Quantities Second ed., Athelone Press.

15. Anon.: J. Astro Phys., Vol. 133, No. 229, 1961.

16. Anon.: Special Techniques for Space Navigation Control Data Corp., 1964.

17. Farrel, E. J. and Others: A Theorectical Investigation of Information Limits Scanning Optical Systems. NASA CR-672, December 30, 1965.

18. Petrovsky, I. G.: Lectures on Partial Differential Equations. Interscience Publishers, 1954, pp. 192-196.

19. Vogelzang, W. F.; Baltes, J. J.; and Sharmack, D. K.: Orbital Operations and Analysis for a 15-micron Horizon Radiance Measurement Experiment. NASA CR-66376, May 1967.

20. Ingersoll; Zobel; and Ingersoll: Heat Conduction. McGraw-Hill, N. Y., 1948, p. 156.

21. Kern, D. Q.: Process Heat Transfer. McGraw-Hill, N. Y., 1950, p. 82.

22. Schmidt, S. F.: Compensation for Modeling Erros in Orbit Determination Problems. Analytical Mechanics Assoc., Inc., Interim Report No 67-16, Contract NAS5-11048, November 1967.

23. Bellantoni, J. F.; and Dodge, K. N.: A Square Root Formulation of the Kalman-Schmidt Filter. AIAA Journal, Vol. 5, No 7, July 1967, pp. 1309-1314.

24. Hildebrand, F. B.: Introduction to Numerical Analysis. McGraw-Hill, N. Y., 1956.

25. Boss, B; et. al: Albany Star Catalog. Carnegie Institute of Washington, 1963.

26. Heun, K.: Neue Methode zur Approximativen Integration der Differentialgleichungen einer unabhangigen Variable, Z. angew. Math. v. Phys., 45;23-38 (1900)

27. Foudriat, E. C.: Analysis of Limited Memory Estimators and Their Application to Spacecraft Attitude Determination. Marquette University, NASA Grant NGR-50-001-009, September 1969.

HONEYWELL

INC.

17 March 1970

National Aeronautics & Space Administration
Langley Research Center
Langley Station M.S. 126
Hampton, Virginia 23365

EDM-3-009

Attention: Mr. Willis A. Simmons
Contracting Officer

Subject: Contract NAS1-8801, Data Submittal
Volume I of Final Report

Reference: Letter NAS1-8801 (MFC) of 11/7/69

Gentlemen:

Enclosed is a copy of "Attitude Referenced Radiometer Study Volume I - Attitude Determination System Design," CR-66852, required by NASA/LRC contract NAS1-8801, Design Study of An Attitude-Referenced Radiometer, and the referenced letter. The report has been revised in compliance with the items of the referenced letter.

Mailing of the copies required by the distribution list included in the referenced letter is being done simultaneously with this information submission to you.

If there are any questions, please do not hesitate to contact the undersigned.

Very truly yours,

E. D. Maurer

E. D. Maurer
Sr. Program Administrator

EDM:sdc

Enclosures

cc: Mr. M. F. Cavelli